Université de Lille
Vrije Universiteit Amsterdam

Ecole doctorale « Science de la Matière, du Rayonnement, et de l'Environnement »
Laboratoire d'Océanologie et de Géosciences – UMR 8187 LOG

High resolution study of the deep-water Southern Ocean circulation during the last climatic cycle using geochemical and mineralogical proxies in marine sediments: implication for the CO_2 cycle.

Etude à haute résolution de la circulation océanique profonde dans l'Océan Austral pendant le dernier cycle climatique à l'aide de traceurs géochimiques et minéralogiques dans les sédiments marins : implications pour le cycle du CO_2.

Thèse préparée et soutenue publiquement par **François Beny** le 07/10/2020
pour obtenir le grade de Docteur de l'Université de Lille et de la Vrije Universiteit Amsterdam.
Sépcialités : Géochimie sédimentaire, Paléoclimatologie, Paléocéanographie

Devant le jury composé de :

Nicolas TRIBOVILLARD, Professeur, Université de Lille – rapporteur
Nadine MATTIELLI, Professeur, Université Libre de Bruxelles – rapporteuse
Ronald VAN BALEN, Professeur, Vrije Universiteit Amsterdam – examinateur
Martin FRANK, Professeur, GEOMAR – examinateur
Tina VAN DE FLIERDT, Professeur, Imperial College London – examinatrice
Charlotte SKONIECZNY, Maitre de conférences, Université Paris-Saclay –examinatrice
Sylvie PHILIPPE, Maitre de conférences, Université Littoral Côte d'Opale – invitée

Viviane BOUT-ROUMA ZEILLES, Directrice de recherche CNRS, LOG – directrice de thèse
Gareth R. DAVIES, Professeur, Vrije Universiteit Amsterdam – directeur de thèse
Aloys BORY, Maitre de conference, Université de Lille – co encadrant de thèse

A Juliette. J'espère que la science fera un jour suffisament d'avancée pour permettre de soigner ce qui a eu raison de toi trop tôt.

To Juliette. I hope that one day, science will make enough progresses to cure the disease that took you too young.

Table of content

Abstract

This PhD thesis provides new insights into both the deep Southern Ocean circulation and CO_2 cycle based on geochemical, radiogenic isotopes and clay mineralogical signatures of the terrigenous fractions transported by the main deep-water masses using sediment cores recovered in the South Atlantic sector (core MD07-3076Q, central South Atlantic) and in the South Indian sector (core MD12-3396Q) of the Southern Ocean.

A careful preliminary study of the geological (e.g. mineralogical, geochemical) properties of the potential sediments sources to the Southern Ocean and of the source-to-sink transportation patterns of detrital particles (i.e. oceanic and atmospheric settings) was crucial to develop a well constrained provenance study in this rather complex area. These prelimnary data demonstrated that it was abolsutely necessary to work on distinct grain-size fractions in the South Atlantic Ocean in order to efficiently track different water masses. Such an approach successfully permits: (1) provenance identification of the various grain-size fractions (clay, cohesive silt and sortable silt); (2) an assignment of each grain-size fraction to a specific water-mass; (3) the reconstruction of the main deep water-mass pathways past changes, (4) to reconstruct paleoenvironmental changes over South America during the Holocene. In the South Indian Ocean, the study of the clay size fraction enabled to compare the relative contribution of the two main deep-water masses in the area (i.e. Antarctic Bottom Water - AABW, Antarctic Circumpolar Current - ACC).

Overall, our data support the idea of strong southern deep-water masses (i.e. AABW and Circumpolar Deep Water, CDW) and weak southern North Atlantic deep-water (NADW) during the last glacial period. The transition between this glacial state and the Modern period likely happened during the Bølling Allerød (B/A). This transition is associated with (1) a southward migration of the NADW into the South Atlantic sector of the Southern Ocean, (2) a retreat of the southern deep-water masses, and (3) a slowdown of the Lower CDW (LCDW) in the South Atlantic sector and of the ACC in the Indian sector of the Southern Ocean.

In addition, this study successfully permits the distinction between the AABW and the ACC (that includes CDW) in both sectors of the Southern Ocean, using the sedimentological and geochemical charactertics of terrigenous particles. This enabled the quantification of the relative contribution to sedimentation of all the main deep-water masses in each sector (i.e. AABW, CDW and NADW in the South Atlantic sector; ACC and AABW in the South Indian sector). Thanks to this distinction, it was possible to provide evidences of previously unknown

AABW activities through time, and to study the dynamical interactions between the AABW and the LCDW in the South Atlantic sector of the Southern Ocean. We show that Heinrich Events (HE) 1, 2 and 3 are preceded by a modification of the Southern Ocean overturning circulation, and especially associated to a significant increase in AABW contribution to sediment deposition. Consequently, this work highlights that a change in the Southern Ocean overturning circulation can play a major role or even trigger the Heinrich Events. Our data also indicates that the turbulent mixing was stronger during HE 2 than during HE 1, even though HE 2 is muted in atmospheric CO_2 records. This suggests that the exchanges between the deep ocean and the atmosphere might have been disabled due to dynamical/physical barrier resulting from background conditions involved by low obliquity during the last glacial period. At the very end of this glacial period, our data indicate a substantial "pulse" of AABW speed and northern extent in the South Atlantic sector of the Southern Ocean. This "pulse" is concomitant with the first increase of the ventilation recorded in the same sediment core and ends with the beginning of the HS 1, a period of rising atmospheric CO_2. These observations suggest that this rapid incursion of AABW into the South Atlantic Ocean may be responsible of the breakdown of the physical/dynamical barrier between the deep CO_2-rich ocean and the surface, enabling the exchange between these CO_2-rich waters and the atmosphere during the HS 1, and thus, the rise of atmospheric CO_2 during the last deglaciation.

Acknowledgments

I express my greatest thanks to my main PhD supervisors Viviane Roumazeilles and Gareth Davies for letting me make this PhD at the University of Lille and at the Vrije Universiteit of Amsterdam. Thank you for your trust and for your scientific/technical guidance and advice when I needed them. I also wish to express my particular thanks to Viviane for letting me so much freedom on all these subjects that were not part of the PhD but that shall be very good for my future career, and for giving funds for it when it was needed. The list is quite long: the writing and the publication of a paper from the work done during my master's degree thesis, the scientific expedition ACCLIMATE on the Marion Dufresne, the expedition with IODP on the Joides Resolution in the Ross Sea to prepare a post-doc, and the incoming one on the Kerguelen Islands. I am aware of the luck I had to participate to that much expeditions (5 months cumulated) in one single PhD.

I am very grateful to Charlotte Skonieczny, my master's degree thesis supervisor, that made everything and spend hours at the phone to sell me to Viviane and Aloys, and to ask them to postpone the application deadline for me. Without her help, someone else would be writing these lines.

I wish to thank all of those that helped me in the different labs that I visited. In Lille I want to thank Marion Delattre, Romain Abraham, and Philippe Recourt for their help in the lab and for the analyses that they made for the PhD before and during the PhD. In Amsterdam, I am very grateful to Richard Smeets, Kirsten van Zuilen, Alice Knaff, Michael Gress, and Janne Koornneef for their numerous suggestions and tremendous help in the clean lab and for the isotopic measurements on TIMS and on the Neptune. I also thank Paulo d'Imporzano, Emmeke Bos, Mathijs van de Ven, Bas van der Wagt, for running an important part of my samples on the instruments (TIMS, Neptune, ICP-MS) when I was in France. I also want to thank all the students and other scientist that had to work and to support my invasions of the clean lab.

I sincerely thank Aloys Bory, Claire Waelbroeck, Elisabeth Michel, Alain Mazaud and Julia Gottschalck for the very interesting discussions about my PhD. Your advices, comments and suggestions helped me a lot to make a better use of my data. In particular, your view "from the outside" was very usefull to better understand the main challenges in paleoceanography, a topic that I discovered during this PhD.

I express my sincere thanks to the University of Lille and to the Vrije Universiteit of Amsterdam to permit myself to make this PhD in their institutions. I also express my sincere thanks to the école doctoral SMRE, to the Région Haut de France, and to Europlanet 2020 RI, which received funding from the European Union's Horizon 2020 research and innovation programme under grant agreement No 654208, for their financial support to the PhD.

I want to express my deepest thanks to Nicolas Tribovillard for its financial support to the extension of the PhD that permit myself to fulfil all the requirement from both universities, to participate to the expedition on the Kerguelen Island, and to have something eat at the end of the month during this extra year. I also take advantage of this opportunity to thank you for making me like geology almost 10 years ago when I followed your courses in the first year of the bachelor's degree at the University of Lille… I was initially planning to study biology!

I am grateful to Monique Gentric for her precious help with administrative things, in particular when I was stuck at the other side of the world. I am also grateful to Sylvie Philippe that received me in her office and in her clean lab for at least the second half of my PhD, and for her precious help in Wimereux (in particular for helping me to find reliable literature on radiogenic isotopes). I also want to thank Meryll Le Quilleuc who joined me in my office in Lille and that had to support myself when I was cursing the French administration (and provided me a valuable help when I deleted important emails too quickly).

Bon, maintenant trêves de mondanités, il faut aussi remercier la famille et les copains qui m'ont aidé et supporté à leur façon dans cette thèse. Et là, pas le choix, je dois l'écrire en français, sinon, certaines personnes citées ne comprendraient rien du tout. Je dois évidemment commencer par mes deux parents. Malheureusement, je ne pourrai pas faire la liste des choses pour lesquelles je dois vous remercier car il faudrait que j'écrive une deuxième thèse. Je tiens aussi à remercier Christophe, Hélène, Arnaud, Catherine, Elora, Nanou, et Garance pour m'avoir hébergé sur Lille quand j'en avais besoin une fois mon logement sur place rendu. Même si la plupart ne sont plus là aujourd'hui, je veux remercier mes quatre grands parents pour les efforts qu'ils ont faits pour financemes études alors que je n'étais encore qu'enfant. Je tiens aussi à remercier mon petit frère Nicolas, le geek, qui m'a aidé de nombreuses fois à régler des problèmes informatiques (comme le décès de mon disque dur en fin de thèse), et m'a proposé des moyens d'analyser automatiquement certaines données (on aura essayé !). Et puis enfin, je veux remercier mes amis (Nico, Coincoin, Pierre « Moustache », Lucas, Tim, Valou, Toto, Alex, Boubou, Vianney, Elora, Zélie, Lisa), qui m'ont permis d'avoir le moral pendant

l’essentiel de la thèse. Des mercis particuliers à Toto et Lucas qui ont su trouver les mots justes dans les rares moments de doutes que j’ai pu avoir.

Pour finir, je voudrai dédier cette thèse à Juliette. J’espère que la science fera un jour suffisament d’avancée pour permettre de soigner ce qui a eu raison de toi trop tôt.

Chapter 1. General introduction

I. Presentation

Today the importance of acting for the Planet health is taking an increasing place in many people's mind. Indeed, the effect of a falling biodiversity and the impacts of climatic changes caused by rising anthropogenic greenhouse gas emissions are becoming one of society's most important preoccupations. In fact, the increase in the frequency and intensity of extreme climate events such as major cyclones, prolonged droughts, temperature records being surpassed year after year, or even the recent extreme cold in Northern USA has captured people's attention. Despite many countries signing the Paris climate agreement at the 21st Conference of the Parties to the United Nations Framework Convention on Climate Change (COP 21), with the objective to reduce CO_2 emissions to limit the global warming to less than 2°C by 2050 compared to preindustrial levels, recent political and societal events have taken these problematics from the consciousness of a large part of the population. In this context the election of Donald Trump, a climatosceptic, to the presidency of the United States of America has had major impact. Moreover, the social movement of the "gilets jaunes" in France, triggered by high petrol prices, has completely muted the COP 24 in the mainstream media in France and is making all talk of climate change inaudible to general public. This makes it more challenging for scientist's to guide political decision, and to improve people consciousness about the risks of living in a fast warming world which will lead of sea level rise, rainfall distribution changes causing stronger droughts and stronger floods, food security hazards etc.

To make effective impact in the climate change debate, it is critical that scientists understand how the climate is likely to change and to draw scenarios according to the amount of CO_2 released to the atmosphere by anthropic activity. In that way, understanding all the processes involved in the global carbon cycle at different time scales is necessary. In particular, the role of oceans is vital to define, since there is 60 times more CO_2 in the deep ocean than in the atmosphere (Adkins, 2013) and that it currently takes up about 30% of the CO_2 released by the humans. Numerous studies have attempted to reconstruct past (Piotrowski et al., 2004, 2008; Weber and Drijfhout, 2007; Zhang and Delworth, 2007; Barker et al., 2009, 2010; Vasquez Riveiros et al., 2010; Waelbroeck et al., 2011; Adkins et al., 2013; Howe et al., 2016; and many others) and present day (Reid, 1989, 1994, 1997, 2003; Tsuchiya et al., 1994; Park et al., 1991; Park and Gambéroni, 1995; Orsi et al., 1995, 1999; Larqué et al., 1997; Rintoul 1985; Rintoul et al., 2001; all geotrace project members; and many others) oceanic circulation, and its impact on the atmospheric CO_2 (Ahn and Brook, 2008; Anderson et al., 2009; Skinner et al., 2010, 2013, 2014; Burke and Robinson, 2012; Adkins, 2013; Levy et al., 2013; Ziegler et al., 2013;

Boer and Hogg, 2014; Menviel et al., 2014, 2015a,b; Yu et al., 2014; and many others). These reconstructions are then used to test numerical models that aim to estimate the evolution of climate in a global warming world induced by anthropogenic CO_2 liberation. If it can be shown that these models are able to simulate the climate of the past, then, they are used to simulate the future climate changes (sea level rise, temperature changes,…) generated by increased atmospheric CO_2.

In all these studies of CO_2, the Southern Ocean appears as a key area for the understanding of present and past carbon cycle. Being a sink today, it acted as a source of atmospheric CO_2 during the last deglaciation and caused a rise of ~100 ppm of the atmospheric CO_2 in few thousand years (Petit et al., 1990; Ahn and Brook, 2008; Bereiter et al., 2015). Many processes have been invoked in the extensive literature to explain this deglacial atmospheric CO_2 rise. However, there is a consensus today that the upwelling of deep and CO_2-rich water masses in the Southern Ocean is the main contributor to this variation (Anderson et al., 2009; Fischer et al., 2010; Burke and Robinson, 2012; Skinner et al., 2014; Menviel et al., 2018). As a consequence, the organization, the extension, and the ventilation/stratification of the deep-water masses (i.e. Atlantic Meridional Overturning Circulation, AMOC) have been widely studied using proxies of the water column properties (Mc Manus et al., 2004; Barker et al., 2009; Robinson and van de Flierdt., 2009; Vasquez-Riveiros et al., 2010; Skinner et al., 2010, 2013, 2014; Thornalley et al., 2010, 2011; Waelbroeck et al., 2011; Gottschalk et al., 2015a,b, 2018a; Howe et al., 2016; and many others). Yet, the signal carried by the terrigenous particles in these deep-water masses in the sub-Antarctic Atlantic Ocean remain poorly studied (Diekmann et al., 2000 – Scotia Sea; Walter et al., 2000– Scotia Sea and South-West South Atlantic; Kuhn and Diekmann, 2002– Cape Basin; Borchers et al., 2011– South Kerguelen Plateau-Prydz Bay). The interest for such studies remains low despite transport of terrigenous particles has the potential to reconstruct the dynamic components of deep ocean circulation. In fact, grain-size distribution has already been used successfully to distinguish the contribution of different transport vectors such as wind or oceanic currents (Weltje and Prins, 2007; Weltje, 2012), and to reconstruct past flow speeds (Hall et al., 2001; McCave and Hall, 2006; Krueger et al., 2012; Spooner et al., 2018). In the same way, clay minerals are known to be a useful tracer of provenance, weathering and transportation pattern of marine sediments (Moriarty et al., 1977; Petschik et al., 1996; Kuhn and Diekmann, 2002; Krueger et al., 2008). Coupled with radiogenic isotope compositions, terrigenous particles of sediments furnish a robust tool to decipher the provenance of marine sediments through time (Walter et al., 2000; Bayon et al.,

2009; Meyer et al., 2011; Toucanne et al., 2015). Due to the relationship between grain-size distribution and transportation pattern, several studies have explored the isotopic composition of distinct grain-size fractions (Meyer et al., 2011; Bayon et al., 2015; Zhao et al., 2017; Beny et al., 2018). In fact, a grain-size mode can be associated with an energy of transport, and thus, to a particular vector of transport. In other words, grain-size modes could be associated to deep-water masses, thus, allowing the isotopic composition of terrigenous particles transported by each water mass to be determined. To understand these associations, it is crucial to understand the history of the terrigenous particles from their formation to their deposition in the deep ocean, i.e., their source-to-sink history.

The transfer of sediments from the continents to the oceans is influenced by both geodynamical forcing (internal forcing) and climatic forcing (external forcing). In the present work, the interval studied (one climatic cycle, ~30 000 years) is obviously too short to observe any change due to internal forcing (the exception being volcanic eruptions that are easily recognizable), but this timescale is ideal to explore the impact of the external forcing onto the continent-ocean sediment transfer. The latter can be decomposed in several steps: the emission of terrigenous particles from a bed rock, the transport of these particles to the ocean, and their transport and deposit on the ocean floor. The nature of the sediment deposited (i.e. chemical and physical properties) depends on the nature of the bedrock and the climatic conditions under which the particle is generated (i.e. winds and rainfalls intensities, presence of ice, volcanism). Sedimentary particles can be transported to the ocean by a combination of transportation vectors such as wind, glaciers, and rivers, all related to climatic conditions. Finally, when the particle is delivered to the open ocean, it reaches the site where it is deposited thanks to the oceanic currents. To decipher the signal preserved in the detrital fraction of deep marine sediments, it is obviously crucial to understand all these steps and how they impact the final composition of the sediment.

II. Objectives

The general objective of this PhD is to decipher the terrigenous signal in three sediment cores recovered by the french vessel Marion Dufresne in order to provide a new kind of information on the variation of the deep circulation in the Southern Ocean, and more generally to give new insights on climate changes through the last climatic cycle (i.e., ~30 000 years). One core is located in the South Atlantic sector of the Southern Ocean (MD07-3076Q), and two are located east of the Kerguelen Plateau (MD12-3396Q and MD12-3401Q).

To achieve this general objective, the main goals are:

- To characterise the composition of all the potential source of sediment for the studied sites. This includes the original composition of the source regions (i.e., geological background) and the estimation of the effect of onland climatic conditions on both mineral composition and transfer of the particles from the continent to the ocean.
- To estimate the composition of the terrigenous particles transported by each deep-water mass. The ultimate goal of this objective is to obtain an isotopic composition of the terrigenous particles transported by deep-water masses as well as the clay mineral assemblage. It includes the potential variation in the composition of the terrigenous particles transported within one deep-water mass caused by changes in the delivery from the continent by on-land climatic variations. There will be a particular focus on the isotopic composition of grain-size modes from the South Atlantic sediment core.
- To use outcomes from the previous objective to compare the relative contributions of the deep-water masss through time and to understand the implication for the Southern Ocean deep-water circulation. This will include an estimation of the relative contribution of the deep-water masses to sedimentation and an estimation of their respective velocity changes through time.
- To compare the data from the Atlantic and Kerguelen sectors with literature observations to draw global scenarios and link to variations in atmospheric CO_2. A particular focus is made on Heinrich Stadials, and on the Younger Dryas in this objective.

III. Organization of the manuscript

In order to respond to the objectives of the thesis, the present manuscript is organized in 9 chapters, including this general introduction. The results from the PhD resulted in 5 scientific articles (4 being written by the PhD candidate as first author), consequently, the PhD manuscript is articulated around these “ready to submit” or accepted papers that corresponds to chapter 4 to 8, while chapters 2, 3 and 9 present the general settings, the material and methods, and the conclusions and perspectives, respectively.

Chapter 2, the general settings, aim to help the reader understand the regional context of the work. In this chapter, the sedimentological and geochemical tools used during the PhD

are explained in part I. Part II describes the present day and past atmospheric settings from the global to the regional scale. A particular focus is made on the highly variable climatic conditions over South America. Part III depicts the present day and past oceanic circulation. In this part, both surface and deep circulation are described, and a particular focus is made on the South Atlantic and on the South Atlantic sector of the Southern Ocean. The last part of this chapter (part IV) provides a general description of the geology of almost the entire Southern Hemisphere (only the Australia and the New Zealand are not described). This part includes the general geodynamical context (including bed rock associations) of Antarctica, South America, Africa, and of the circumpolar volcanic islands. The clay mineralogy produced and the geochemical composition of the rocks are given in this part by taking into account the impact of climatic conditions on-land.

Chapter 3, the material and methods, is split into three parts: the material used for the study, the analytical methods used, and the quality control of the data produced. The first part described the sediment cores used for the PhD and how they have been dated. The second part details the protocols used for all the analyses (grain-size distribution, clay mineralogy, geochemistry) and the instruments used for the measurements. The last part discusses the data quality, and choices made on the viability of this data. Based on this review, some data have been excluded from the rest of the manuscript.

Chapter 4 represents the first paper of the PhD. This paper focuses on deciphering the terrigenous signal of particles transported by deep-water masses in the South Atlantic Ocean using the sediment core from the South Atlantic (MD07-3076Q). In this paper, the isotopic composition of the terrigenous particles and the clay mineral assemblages transported by deep-water masses is given for each of the three main deep-water masses in the South Atlantic Sector of the Southern Ocean. These associations are then used to reconstruct the past extent and velocities of deep-water masses during the Last Glacial Maxima (LGM) and the deglaciation.

Chapter 5 corresponds to the second paper of the PhD. It focuses on the time interval from the sediment core MD07-3076Q not examined in the previous chapter: the Holocene. It uses the conclusions from the chapter four to explore the palaeoenvironnemental changes on the Southern South American continent using marine terrigenous sediments. This study gives new insights free of potential local bias on rainfalls and winds distribution and intensity through the Holocene in the eastern side of the Andes.

Chapter 6 is a paper focusing on the sediment core MD12-3396Q located in the Kerguelen Sector of the Southern Ocean. This paper examines the provenance of terrigenous sediments from this sediment core to reconstruct the past contributions of the ACC vs the Antarctic Bottom Water (AABW). For the first time, robust evidence of AABW episodic northward expansion via the local Deep Western Boundary Current (DWBC) is given using clay mineral properties, radiogenic isotopes, and geochemical composition (i.e. trace and rare earth elements).

Chapter 7, the final paper from the PhD focuses on rapid climatic changes that happened during Heinrich Stadials and the Younger Dryas, and the implication for atmospheric CO_2 variations. This paper uses the conclusions derived from all the four previous papers to give new insights on the mechanisms involved in the Northern Hemisphere Heinrich Events, deglacial CO_2 rise, Southern Ocean upwelling, and Atlantic Meridional Overturning Circulation (AMOC) shut-down/recovery.

The last chapter 8, presents the general conclusions of the PhD, and the perspectives that can be drawn from this work.

Chapter 2. General settings

I. Sedimentological and geochemical tools

A. Grain-size distribution

Grain-size distribution is a useful tool to understand the dynamic processes occurring during the transport of sediment and its deposition. Indeed, the size and the morphology of the particles directly result from the processes involved during the transport. On Earth, the particles are generally transported by wind, liquid water, ice, and/or gravity induced mass transport. In the sediment cores of this study, gravitational processes have not been identified in the sediment, and it is assumed that winds, oceanic currents, as well as icebergs are the only processes that can bring sediments to our sites. Generally, ice transported sediments present a very heterogeneous grain-size distribution because ice does not sort the particles according to their size. In contrast, the sediments transported by winds and oceanic currents can be well sorted. This sorting results from 3 transporting processes that are involved during the transport of a particle by a fluid: crawling, saltation, and suspension (figure 1).

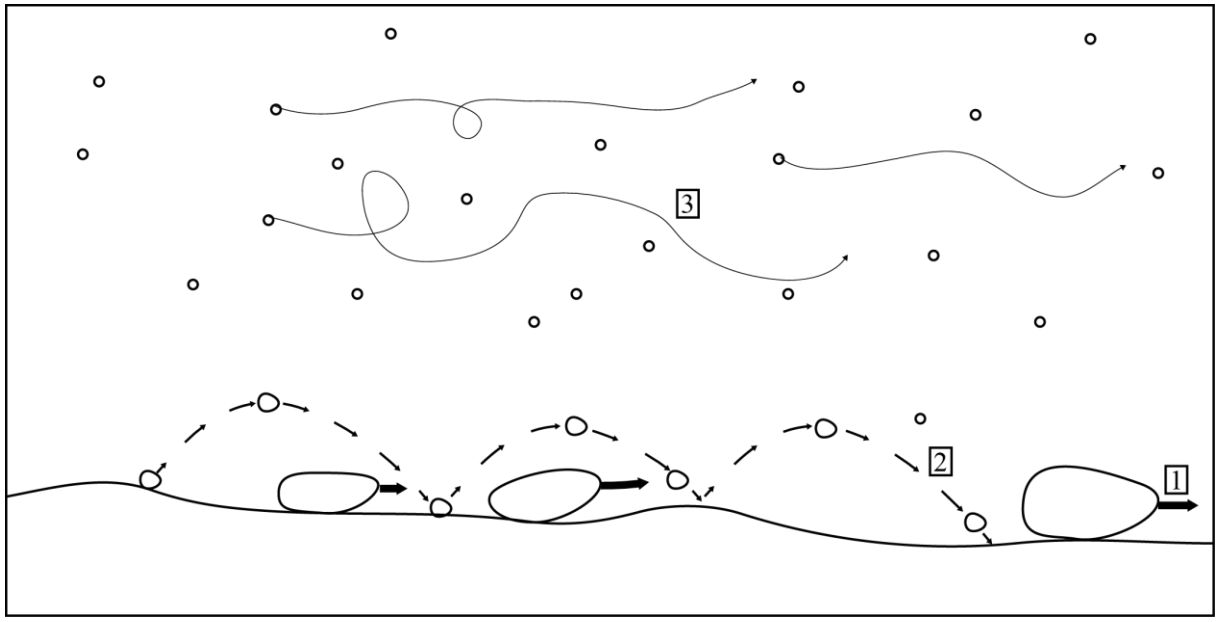

Figure 1: Scheme showing transportation processes of detrital particles. 1: crawling, 2: saltation, 3: suspension.

Crawling is the process that defines the movement of a particle that maintains contact with the ground and moves (crawl) on it. It is the process that requires the least energy to move a particle in fluid, but it is also the slowest in term of particle speed. Saltation requires more energy and corresponds to a transport in the fluid with intermittent contact with the ground where the particle is chocked. This phenomenon is very powerful in breaking particles and creating smaller ones. The last process is suspension and is the one that requires the most energy

in the fluid. This phenomenon corresponds to the transport of a particle in the fluid without contact with the ground. Because coarse particles need more energy to be moved than fine particles, they are likely transported by crawling, the finer one by saltation, and the finest ones by suspension. Similarly, the finer the particle, the greater the distance it can be transported. Consequently, the size of the particles decreases with distance from the particle source. To conclude, the size of the particles transported by a fluid directly results from the speed and nature of the fluid.

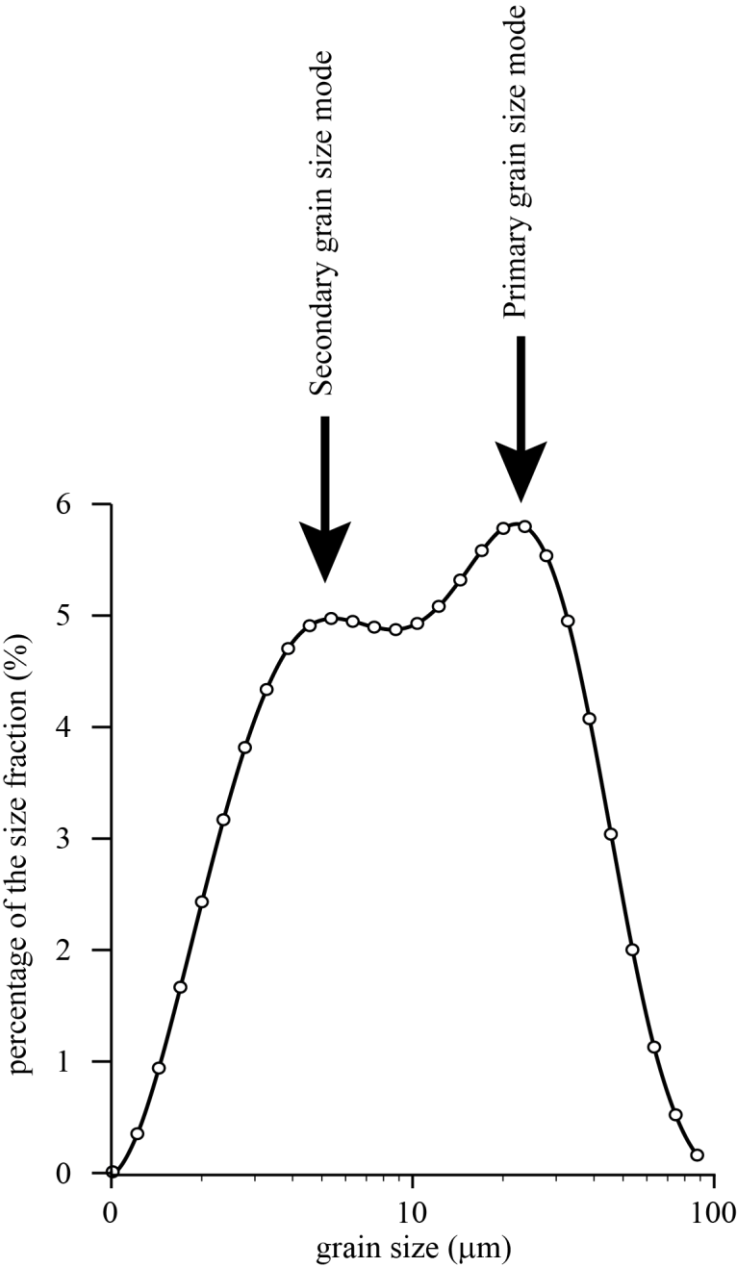

<u>Figure 2:</u> Example of grain-size distribution curve (sample from the core MD07-3076Q used in this PhD).

Grain-size distribution has already been used successfully to distinguish the contribution of different transporting agents such as wind or oceanic currents (Weltje and Prins, 2007; Weltje, 2012), and to reconstruct past flow speeds (McCave and Hall, 2006). In grain-size distribution analyses, the granulometric mode is identified as a "peaks" on the grain-size distribution curve and corresponds to the particle size that is the most represented in the sediment (figure 2). These grain-size modes can be interpreted as the grain-size most easily transported by a fluid and is characteristic of the flow speed and of the nature of the fluid (most likely wind or water in our case). Consequently, when observing these grain-size modes, we can reconstruct the past evolution of the fluid speed (wind or oceanic current, figure 3).

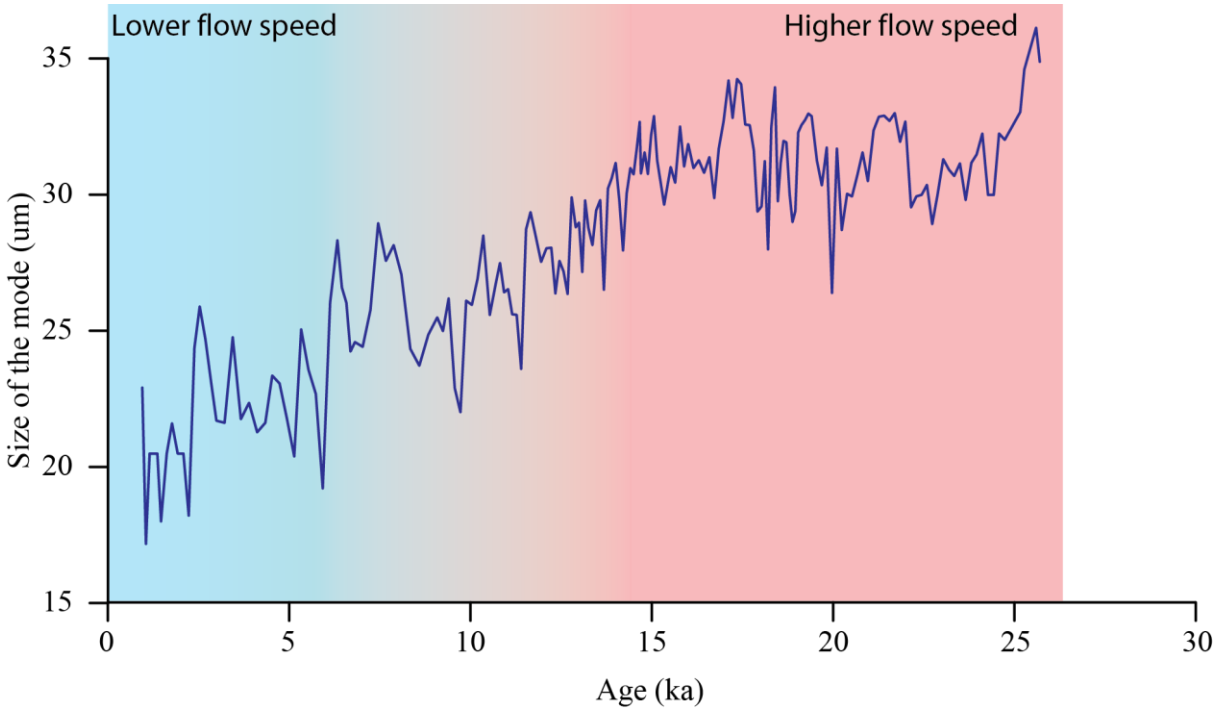

Figure 3: *Value of a grain-size mode through time showing flow speed variations. Values used are from the coarse grain-size mode of the core MD07-3076Q used in this PhD.*

B. Clay minerals

The clay minerals correspond to very small minerals (< 2 µm) with a very high surface area (specific surface; surface per weight, measured in m^2/g), making them easily transportable over long distance. They belong to the family of alumina phyllosilicates. This mineral family is constituted by layers of octahedrons $Al(OH)_6$ and by silica tetrahedron SiO_4 linked by O atoms and OH molecules (figure 4). Based on the layer organization, 1/1 clays are distinguished from 2/1 clays. The 1/1 clays are composed of one tetrahedron layer and one octahedron layer, whereas 2/1 clays are composed of 2 tetrahedron layers and one octahedron layer. The

formation of the clay minerals is controlled by the mineralogy of the primary rock, by the climatic conditions, and also by the topography, i.e. the erosional environment (figure 5). In this study, we focus on four types of clay minerals: smectite, illite, chlorite, and kaolinite.

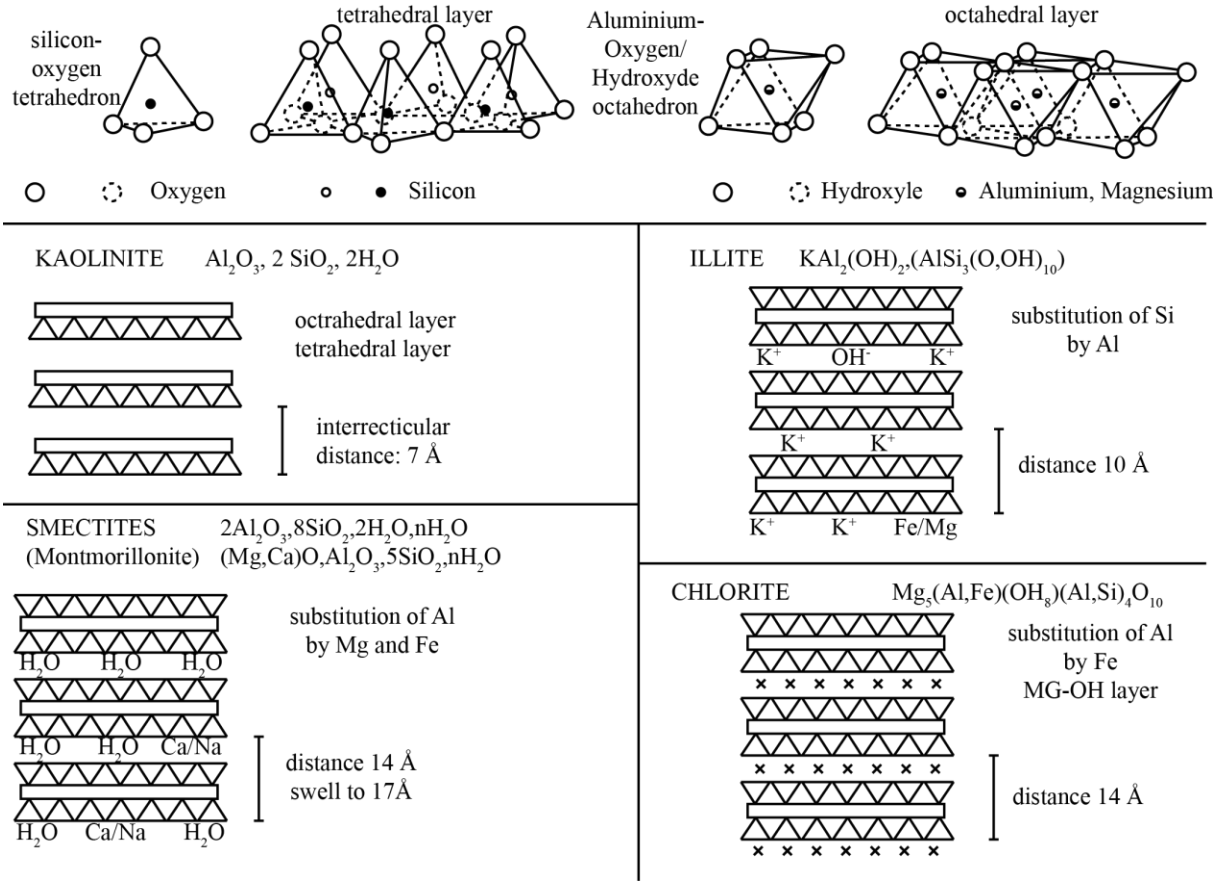

Figure 4: Structure of main clay mineral families (redrawn from Chamley, 1989).

Chlorite is the clay mineral most sensitive to chemical weathering, and is mainly found under dry climate conditions (i.e., high latitude mineral). Chlorite is abundant in metamorphic rocks such as gneiss and schist, but is also present in magmatic and sedimentary rocks. The chemical formula of chlorite is $(Fe,Mg,Al)_6(Si,Al)_4O_{10}(OH)_8$. Its density is between 2.6 and 3.3, and its specific surface is between 100 and 175 m²/g (Morel, 1996).

In contrast, kaolinite is the final product of the chemical weathering, and is the dominant mineral in most of the equatorial and tropical areas (i.e., low latitude mineral). The chemical formula of kaolinite is $Al_2K_2Si_2O_5(OH)_4$. Its density is between 2.5 and 2.6 and its specific surface 10 and 35 m²/g making kaolinite the clay mineral with the lowest specific surface.

Smectite is the product of the alteration of basic rocks such as basalt, and is dominant in most volcanic areas. The chemical formula of the smectite is $(Na,Ca)_{0.3}(Al,Mg)_2Si_4O_{10}(OH)n(H_2O)$ and its density is between 2 and 2.75. The specific

surface of the smectite is between 700 and 800 m²/g. The high specific surface and the chemical composition of the smectite make it chemically very reactive, and its behavior in the water column may differs from the other clay minerals. As an example, smectite is likely to remain "locked" between two distinct water masses that are characterized by distinct physicochemical properties.

Illite can be considered as a "detrital" clay mineral and is found in areas with moderate to low chemical weathering such as desert. The chemical formula of illite is $(K,H_3O)(Al,Mg,Fe)_2(Si,Al)_4O_{10}[(OH)_2,(H_2O)]$. Its density is between 2.6 and 2.9 and its specific surface is between 100 and 175m²/g.

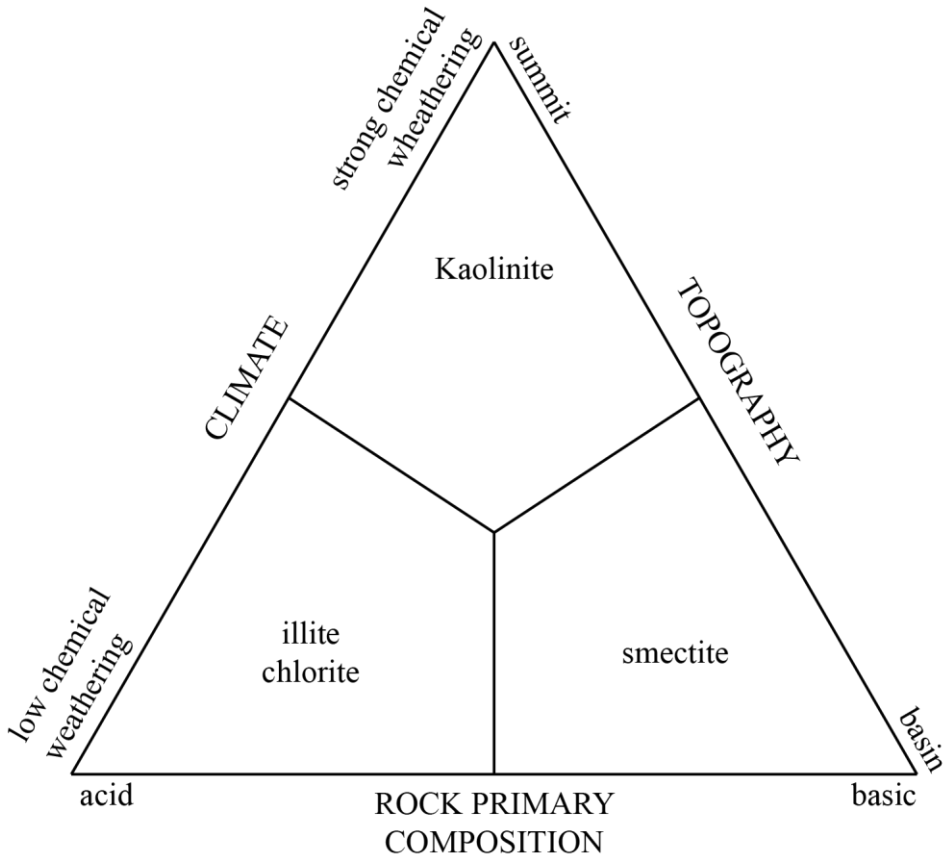

Figure 5: *Relation between environmental conditions and clay mineralogy formation.*

C. Trace and Rare Earth Elements

1. *Rare Earth Elements (REE)*

Rare earth elements (REE), or lanthanides, correspond to the group of atoms with atomic numbers between 57 and 71 (i.e., from La to Lu). Some workers include scandium (Sc) and yttrium (Y) in this group. The latter is characterized by very specific electronic configuration making it very reactive. REE are useful in many fields of the industry and hence they are

considered “strategic” (or “critical”) elements. It is particularly true for the heavy rare earth elements (HREE) which include the element from the Tb to the Lu. The lighter REE are called light rare earth elements (LREE). In our study, REE are useful to identify the provenance of the sediment. Indeed, the REE composition is characteristic of a rock formation, and thus can be used to identify the provenance of sediments.

To avoid the odd even effect of element abundances (Oddo–Harkins rule), REE are usually reported normalized to a standard composition. Many standard REE compositions are used to allow comparisons between the different potential provenances. The most widely used in the context of sediments are the North American Shale Composite (NASC), the chondrite composition, the upper continental crust (UCC), and the Post Archaean Australian Shales (PAAS). In the study of marine sediment, the REE composition of the sediment is usually normalized to PAAS. This normalization corresponds to the ratios sample/PAAS for each element. It allows to compare the composition of the sample to the PAAS standard which is close to the average composition of the superficial Earth (UCC may also be used). Thanks to the normalization, it is possible to produce REE spectra, which immediately show enrichments and/or depletions of elements in the sediment. Recently, a study by Bayon et al. (2015) explored the composition of river’s runoff to the ocean on clays as well as on silts to develop a new standard: the World River Average Silts (WRAS).

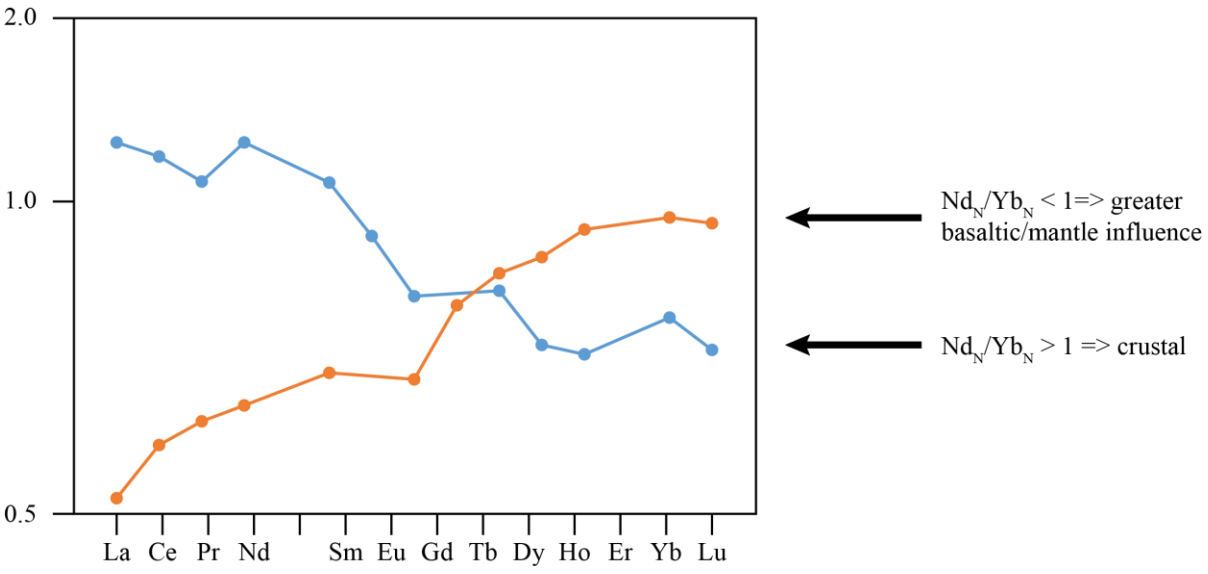

Figure 6: *Examples of WRAS normalized REE spectra from two distinct areas. Values used to trace the orange and blue spectra are from a tephra layer from dite IODP346 U1429 (Nd_N/Yb_N = 0.66; Beny et al., 2018) and from river sediments from located in cristaline environment from Korea (Nd_N/Yb_N = 1.48; Lee et al., 2003).*

Elemental ratios are also used for comparison. As an example, the Nd_N/Yb_N ratio (the "N" in index means that the values used are normalised) is commonly used to compare the HREE with the LREE composition as they may help to discriminate the origin of the sources (Bayon et al., 2015). In fact, ratios close to 1 are related to the WRAS composition, whereas lower ratios (i.e., enrichment in HREE compared to LREE, see figure 6) contain material derived more directly from Earth's mantle (such as basaltic rocks). Changes in Nd_N/Yb_N can be very useful to identify the poorly evolved volcanic-born material compared to mainly granitic crustal material.

Europium (Eu) also has a particular behavior because of its divalent characteristic in reductive environment, such as in the mantle. As a consequence, this element is favorably partitioned into plagioclase feldspar, and the REE spectrum of plagioclase-rich rocks is generally characterized by positive Eu anomaly. In contrast, this anomaly is negative in the upper continental crust. This anomaly is evaluated by the ratio Eu/Eu* where $Eu^* = (Gd \times Sm)^{1/2}$.

2. *Trace elements*

According to the definition given by White (2007), trace elements are "those elements that are not stoichiometric constituents of phases in the system of interest". Trace elements correspond to elements that are rare and represent less than 0.1% of a rock composition. Consequently REE can also be considered as trace elements, but they are studied separately in this work. Because all these trace elements have distinct behavior during magmatic processes and during supergene weathering, their concentrations are very heterogeneous. Consequently, they can give clues on the processes involved from rock formation, to its deposition in deep marine environments. Similarly, trace elements can give insights on the provenance of detrital sediments.

Trace elements can be divided into 2 groups: compatible, and incompatible elements. The compatible elements are also called mantle rock forming elements (MRFE) because they partition into the main constituent minerals in the mantle. MRFE are characterized by a low to moderate cationic charge, and low to moderate cationic radius (such as Al, Si, Mg, Cobalt). The other elements are termed incompatible because they partition into the melt during partial melting of the mantle and during the crystallization processes of a magma. Consequently, these elements are abundant in the continental crust. These incompatibles elements can also be divided into two groups according to the ratio cationic charge/cationic radius (z/r). Elements whose z/r ratio is below 2 corresponds to the large ion lithophile elements (LILE), while those

with a z/r ratio is above 2 are called high field strength elements (HFSE). By definition, HFSE are characterized by a small radius compared to their charge. Consequently, they have a high electrical field strength (from where their name comes from) and can create strong bounding with adjacent ions. The result is that HFSE are not mobilized by fluids during weathering processes while LILE are mobile. Thus, the ratios of HFSE and LILE can give insights on these weathering processes.

D. Radiogenic isotopes

Isotopes are atoms with the same number of protons (positive charge particle of the core), but a different number of neutrons (neutral charge particle of the core). Two types of isotopes are commonly used in geology and paleoclimatology: stable isotopes and radiogenic isotopes; but recently, several scientists also start to explore clumped isotopes, by working on molecules instead of on atoms. The study of stable isotope is mainly makes use of the different behavior of different isotopes based on the mass difference whereas the study of radiogenic isotope is mainly based on radioactive decay and ingrowth. Radiogenic isotopes are used to the study the history of magmas as well as to track the provenance of terrigenous sediments.

Terrigenous sediments are the result of the erosion of older rocks; magmatic, metamorphic, or older sedimentary. In all cases, these rocks had an ultimate origin as crystallization products of a magma. The geochemical properties of the magma – and by extension of the rock formed during their crystallisation – depend on several parameters such as the geological context (hot-spot, subduction zone, collision zone…), the period of Earth evolution (pre- or post- modern plate tectonics), the mode of crystallization (fractioned, slow/fast, intrusive/extrusive,…). Even though this list is not comprehensive, it serves to stress that all these processes may change the chemical composition of the magma, and thus, of the rock formed when the magma cools. It implies major spatial and temporal heterogeneity of the chemical composition of rocks. These characteristics can be used to track the provenance of terrigenous sediment. In particular, each rock is characterized by specific isotopic ratios at its formation. This ratio changes through time due to the natural decay of radioactive isotopes. Simultaneously, other parameters can impact the isotopic ratio, such as weathering, but the changes involved are specific to the element studied and are detailed below and schematized on figure 7.

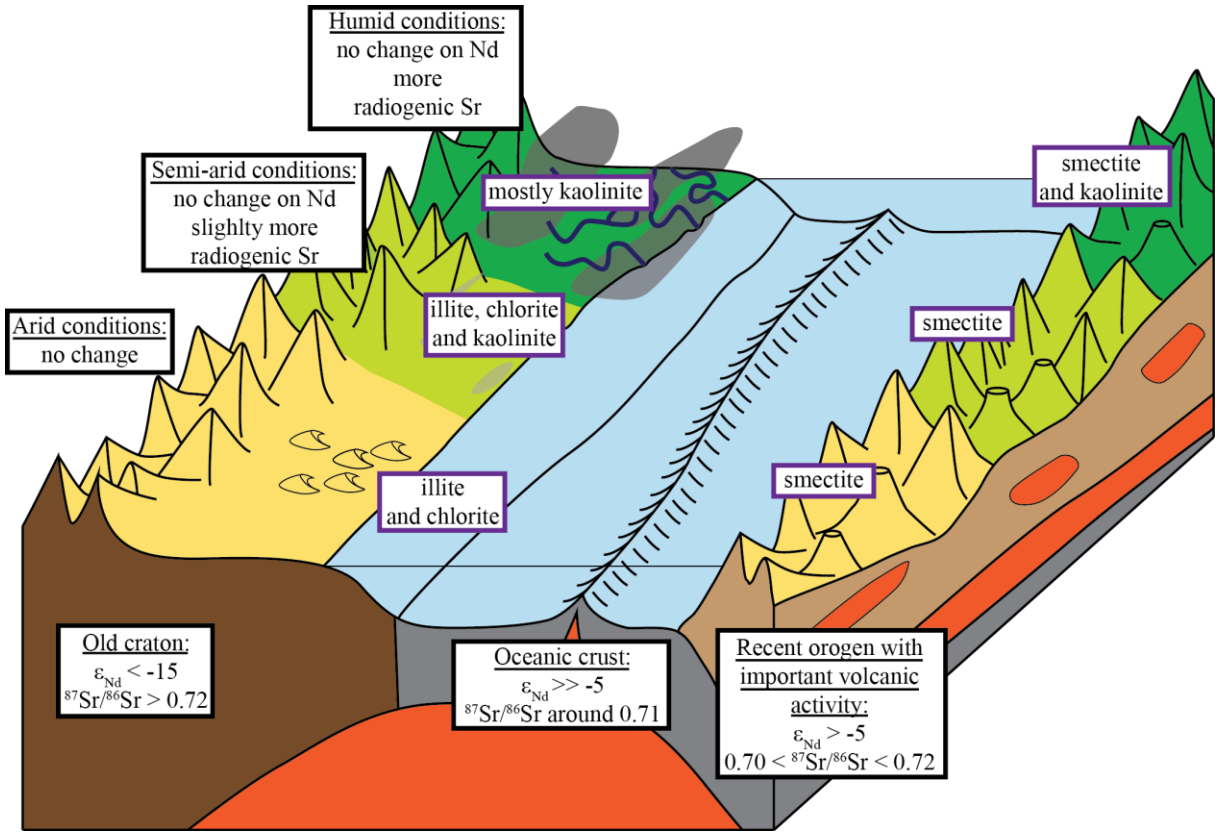

Figure 7: *3D bloc diagram showing the impact of the geological context and weathering environment on isotopic composition of Sr and Nd, and the clay minerals produced onland. Clay minerals indicated on this diagram correspond to the clay mineral assemblage delivered to the ocean. On the left, is represented a passiv margin, similar to what is found along the west African coast. On the right is shown an active margin, similar to what is found along the west South American coast. Note that the impact of grain-size on Sr is not shown on this figure nor the influence of wind sorting.*

1. Samarium-Neodymium (Sm-Nd) system

Neodymium is a Light Rare Earth Element (LREE). Its atomic number is 60 and its atomic mass is 144.24. It possesses 5 stable isotopes, and 5 radioactive. ^{144}Nd and ^{150}Nd's half-life time is very long (6 and 9 orders of magnitude longer than the Earth life, respectively) and can be considered as stable at geological time scale. ^{143}Nd is formed by the natural decay of the ^{147}Sm according to the following equation:

$$^{147}Sm \rightarrow {}^{143}Nd + \alpha \qquad (\alpha \text{ radioactivity})$$

Samarium (Sm) is also a LREE. Its atomic number is 62, and its atomic mass is 150.36. Similarly to Nd, 7 Sm isotopes are found in nature. 6 are stable, whereas the ^{147}Sm is radioactive with a half-life of 1.06×10^{11} years (Faure and Mensing, 2005). Due to their similar properties,

Sm and Nd react similarly to surficial weathering, making this system very useful to track provenance changes. However, due to the small difference between the two ionic radii of these elements, Nd is preferentially concentrated in the liquid phase during partial melting of silicate mineral while Sm preferentially stays in the residual solid. Consequently, the continental crust appears enriched in Nd relative to Sm compared to the mantle. This causes less production of radiogenic Nd into the continental crust than the mantle.

The ratio used to study the isotopic composition of Nd is $^{143}Nd/^{144}Nd$. Because the variations of this ratio are low, the index ε_{Nd} is commonly used to express the isotopic ratio. This ratio is calculated by comparing the $^{143}Nd/^{144}Nd$ of the rock/sediment analyzed to the material thought to have formed the Earth, chondritic meteorites. The material is names CHUR (CHondritic Uniform Reservoir) and ε_{Nd} is defined following the equation presented by DePaolo and Wasserburg (1976):

$$\varepsilon Nd(t) = \left(\frac{\frac{143Nd}{144Nd} sample}{\frac{143\mathrm{Nd}}{144\mathrm{Nd}} CHUR} - 1 \right) \times 10000$$

In this equation, the value of the CHUR is dependent of the age chosen. To study the paleo-provenance during the quaternary, the value for the CHUR (at t=0; i.e. $\varepsilon_{Nd}(0)$) is 0.512638. The higher ε_{Nd} value, the more abundant the radiogenic isotope (^{143}Nd) is compared to the non-radiogenic isotope (^{144}Nd); i.e., the higher the $^{143}Nd/^{144}Nd$ ratio. High ε_{Nd} (close to 0 and higher) are considered as radiogenic, and lower ε_{Nd} are considered as non-radiogenic (or unradiogenic). Usually, crustal rocks have very unradiogenic values (often below -10) whereas basaltic provinces derived from the Earth's mantle have radiogenic values (higher than 0).

2. Rubidium-Strontium (Rb-Sr) system

Strontium is an alkaline-earth element. Its atomic number is 38 and its atomic mass is 87.62. The 4 stable Sr isotopes found in nature are: ^{84}Sr (0.56%), ^{86}Sr (9.87%), ^{87}Sr (7.04%), and ^{88}Sr (82.53%). Not all ^{87}Sr is primordial and is partially formed from the natural β decay of radioactive ^{87}Rb.

In contrast rubidium is an alkaline element. Its atomic number is 37 and its atomic mass is 85.47. Rubidium possesses 2 isotopes in the nature: ^{85}Rb (72.2%) is stable, whereas the ^{87}Rb (27.8%) is radioactive (half-life of 4.88×10^{10} years; Faure and Mensing, 2005).

In contrast to Nd and Sm, Rb and Sr have distinct geochemical properties and hence changes in Rb/Sr ratio can impact the $^{87}Sr/^{86}Sr$ ratio that is used to reconstruct provenances.

The Rb/Sr ratio tends to change according to the magmatic processes involved during the crystallization of magma. During crystallization, Sr tends to concentrate in plagioclases, while Rb tends to stay in the liquid phase. As a result, Rb/Sr ratio of the residual liquid progressively increases during magma differentiation. As an example, mantle-derived rocks generally have lower Rb/Sr ratios than crustal rocks. This implies that the $^{87}Sr/^{86}Sr$ of crustal rocks rises faster than the mantle due to higher Rb concentrations. It means that the continental granites are characterized by higher $^{87}Sr/^{86}Sr$ ratios than the oceanic basalts.

The distinct geochemical behaviors during magma crystallization also imply that Sr and Rb are found in different mineral phases. The Sr^{2+} ion has a comparable radius to Ca^{2+}, which it can replace in many minerals. Consequently, Sr is mostly found in Ca-bearing minerals such as plagioclase, apatite, or calcium carbonate (especially aragonite). The ion Sr^{2+} can also replace the ion K^{+} in K-feldspars, but it must be coupled to a substitution of Si^{4+} by Al^{3+} to preserve electrical neutrality. In contrast, the Rb^{+} ion can substitute for K^{+} in all K-bearing minerals. Consequently, Rb is commonly found in micas (such as muscovite and biotite), K-feldspar, clays, and evaporites. In detrital sediments, this mineralogical segregation of Rb and Sr causes changes in the Rb/Sr ratios according to the mineralogy, which is often related to grain-size with fine-grained clays being more Rb rich. Indeed, Sr-bearing minerals (plagioclases) are generally more resistant during transport than Rb-bearing minerals (clays and micas). In addition, clays and micas are generally smaller than plagioclases. As a result, in detrital sediments, Rb/Sr ratios are higher in the fine fractions of the sediment than in the coarse fractions, and $^{87}Sr/^{86}Sr$ ratios increase when the grain-size is smaller.

The different properties of Rb and Sr also lead to chemical fractionation during surficial chemical weathering. Rb is less compatible in fluids than Sr, meaning that Sr tends to be washed out during chemical weathering whereas Rb tends to stay in the solid residue. As a result, strongly weathered rocks –and especially those with high original Rb/Sr ratios- generally have higher $^{87}Sr/^{86}Sr$ than well-preserved rocks.

To summarize, $^{87}Sr/^{86}Sr$ ratios in detrital sediments increase when the weathered rock is old, derived from an evolved magma, chemically weathered, and when the grain-size is finer.

3. Uranium-Thorium-Lead (U-Th-Pb) systems

The Pb is a post transition metal. Its atomic number is 82 and its atomic mass is 207.2. Pb possesses 4 natural stable isotopes: ^{204}Pb (1.4%), ^{206}Pb (24.1%), ^{207}Pb (22.1%), and ^{208}Pb (52.4%). ^{204}Pb is primordial, but ^{206}Pb, ^{207}Pb, and ^{208}Pb are all partially formed as the final

product of complex decay chains of the ^{238}U ($t_{1/2}$=4.47 x 10^9), ^{235}U ($t_{1/2}$=0.70 x 10^9), and ^{232}Th ($t_{1/2}$=14.01 x 10^9), respectively

U and Th are both members of the actinide series of elements. Because their electron configurations are similar, they have similar chemical properties. In addition, they both occur in a tetravalent oxidation state in nature and have similar radii (U^{4+} = 1.05 Å; Th^{4+} = 1.10 Å; Faure and Mensing, 2005). As a consequence, they can easily substitute for each other. However, under oxidizing conditions, U forms uranyl ions (UO_2^{2+}), which correspond to a valence of +6 for U. Uranyl ions are soluble in water, making it mobile under oxidizing conditions. Consequently, it is separated from Th, which only exists in the tetravalent state which is insoluble in water. As a result, under oxidizing condition, chemical weathering on-land may progressively wash away U from rocks. This U-removal reduces the proportion of the radioactive parents of ^{206}Pb and ^{207}Pb that ultimately reduces their production, and thus, their abundance in rocks. Becaue Th is not washed away by this process, the removal of U form rocks as uranyl in water may decrease the production of ^{206}Pb and ^{207}Pb compared to ^{208}Pb, which results from Th decay.

Even if U and Th generally occurs in similar accessory minerals, there are some Th-bearing and U-bearing minerals such as uraninite (UO_2) and thorianite (ThO_2). Similarly, apatite is sometime considered as an urogenic mineral, whereas monazite is considered as a thorogenic mineral. These kinds of minerals are not always ubiquitous in crustal rocks. As a consequence, the type of mineral carrying the radioactive parent of the Pb radiogenic isotopes may also have an impact onto the isotopic composition of the ^{206}Pb and ^{207}Pb compared to ^{208}Pb.

Lead is often classified into two types of Pb: the “common Pb” and the “radiogenic Pb”. Common Pb is the primordial Pb (i.e., ^{204}Pb), while the radiogenic Pb corresponds to all the Pb isotopes formed by the radioactive decay of U and Th. These two kind of Pb are not in the same proportion in all the mineral phases. In minerals characterized by low original U/Pb and Th/Pb ratios such as plagioclase and K-feldspar, the evolution of Pb isotopes by radioactive decay is rather low due to the low production of radiogenic Pb by radioactive decay. As a result, these minerals are “enriched” in common Pb (Erel et al., 1994). On the other hands, radiogenic Pb is abundant in minerals with high original U/Pb and Th/Pb ratios that are old enough to produce radiogenic isotopes by radioactive decay. These minerals include zircon, apatite, epidolite, monazite, sphene, and uraninite (Erel et al., 1994). Because all these last minerals are generally accessories, the Pb isotopic composition is usually controlled by the plagioclase and the K-feldars (Erel et al., 1994). This heterogenous distribution of common and radiogenic Pb in

mineral phases is responsible of a differential reaction of common and radioactive Pb during chemical weathering. Indeed, phosphates such as apatite and monazite are less resistant to chemical weathering than feldspars and silicate accessory minerals (Shirahata et al., 1980; Allen and Hajek, 1989). Consequently, radioactive Pb is generally easierly washed away from rocks than the common Pb, resulting a decrease of the relative proportion of radiogenic Pb in rocks.

Similarly, radiation dommage to the crystal structure can be caused during the production of radioactive Pb, leading to the creation of a pathway favorising the migration of radiogenic Pb to the liquid phase (Silver et al., 1984). Finally, Silver et al. (1984) also showed that grain boundary effects can impact the reaction of the Pb isotopic composition of a rock to chemical weathering. Indeed, minor phases as well as mineral impurities concentrating incompatibles elements (including U and Th) are concentrated at the surface of the minerals. This configuration exposes them more to chemical weathering processes, and thus eases the removal of radiogenic Pb from rocks during chemical weathering.

Finally, to conclude on the Pb isotopes, there is more radiogenic isotopes in old rocks containing substantial accessory mineral phases, while chemical weathering tends to wash them away and to reduce their proportion in rocks.

II. Atmospheric Settings

The world's climate is controlled by many parameters such as orbital forcing and the position of the continents that specifically constrain the oceanic transport of heat. These parameters are known to have a strong impact on rocks weathering, sediments transport, and oceanic and atmospheric circulations. Due to the shortness of the time period under study (25-50 kyr), the position of the continents can be considered as constant. Here, we only consider the main climatic phenomena occurring over our study area, and their variations through time.

The Earth's atmosphere is composed of several layers: the troposphere, the stratosphere, the mesosphere, the thermosphere, and the exosphere. However, most of the climatic structures studied in this work are located in the troposphere. Consequently, when talking about the atmosphere, we only refer to the lowest layer that contains most of the water vapor: the troposphere. This troposphere is ~8-16 km thick and is thicker at the equator than at the poles.

A. Modern atmospheric circulation

1. General circulation

a. Latitudinal atmospheric circulation

The Earth's atmosphere is constituted by three main hemispheric cells: the Hadley cell, the Ferrell cell, and the Polar cell (figure 8). These cells are the direct result of pressure gradients caused by the latitudinal insolation gradient. However, the Coriolis force, corresponding to an inertial force generated by the rotation of an object, strongly modifies the atmospheric circulation on Earth.

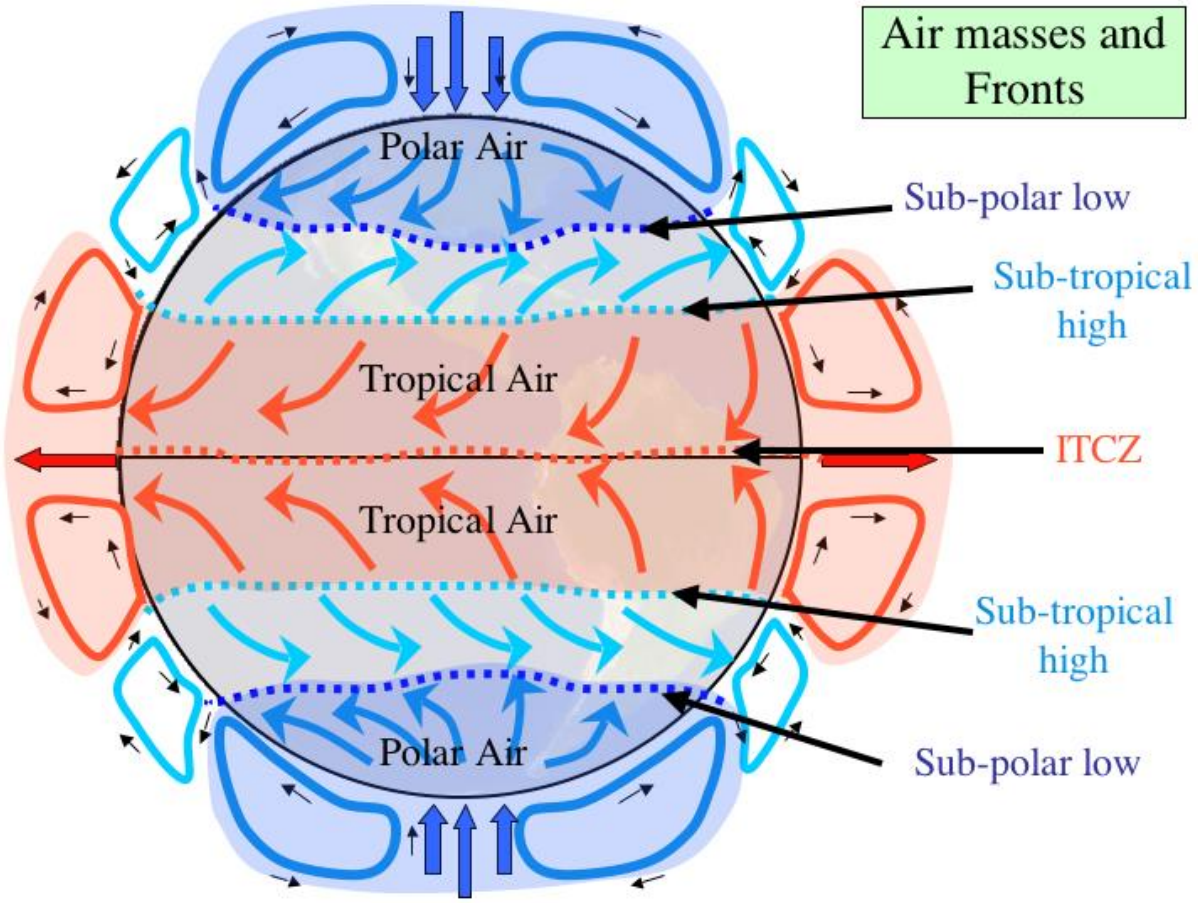

Figure 8: General atmospheric circulation (Urbano, 2011). The Hadley circulation cells are represented in red, the Ferrel circulation cells in light blue, and the Polar circulation cells in dark blue.

At the equator, the insolation is maximum, and the air is characterized by high temperature and low pressure. It implies a convergence of the air masses in the area, which is called the Inter Tropical Convergence Zone (ITCZ). This air migrates from higher latitude characterized by higher pressures, and is loaded in moisture due to high evaporation involved by the high temperature of these regions. At the ITCZ position, the warm and humid air rises,

generating strong rainfalls (including thunderstorms) until it meets the tropopause. Locked by this tropopause, the humid air is then pushed poleward by the constant flux of air coming from below. When migrating poleward, the air is also deviated eastward by the Coriolis force. Simultaneously, the air cools, loses its moisture, and starts to sink between the latitudes 30° and 35° called the "Horse Latitudes". Because the air has lost his entire moisture when reaching these latitudes, it generates vast desert areas, including the most famous one: the Sahara. Finally, due to the high pressures prevailing in these areas, the air that sank starts to move equatorward again and is deviated to the West by the Coriolis force, generating winds called North (South) easterly trades in the northern (southern) hemisphere. All this circulation is known as the Hadley cell.

In contrast, the insolation is minimum at the poles, where the air is consequently characterized by high pressure and very low temperature. This cold and dry air migrates to temperate areas through the lower part of the atmosphere, explaining the occurrence of dry cold deserts around the poles (such as Antarctica). During this migration, the air is again deviated westward by the Coriolis force, and is also progressively warmed and loaded with moisture. At the latitude 60°, so called "Polar Front" (PF), the air starts to rise and to loose moisture, generating humid areas over temperate latitudes. In the upper part of the atmosphere, the air is pushed similarly than at the ITCZ, and migrates to its initial polar position. During this migration, the air is deviated to the East by the Coriolis forces, and releases it moisture as rainfall. This polar circulation constitutes the Polar cell.

The third atmospheric cell directly results from the Polar and Hadley cell circulations and is known as the Ferrell cell. In the lower part of the atmosphere, the Hadley cell generates high pressure in the tropical areas, while the Polar cell generates low pressure at 60° latitudes. The warm and dry air close to the ground from the tropics (~30° latitude) migrates to the 60° latitudes. It is deviated eastward forming winds called Westerlies, and is loaded with moisture. When reaching the lower pressure areas, the wet air meets the wet air from the Polar cell and they rise together. Then, it migrates to its initial tropical position in the higher part of the atmosphere. During this migration, the air looses its moisture as rainfall, which also explains the humidity of the temperate areas. When back to the tropical latitudes, the air sinks and migrates again to higher latitudes.

b. ITCZ motion, and monsoon Activity

The monsoon is very well known in India since it is associated with very strong rainfall. However, this phenomenon is present at almost all tropical latitudes. In fact, a transitional zone

with alterning seasonal dry and wet seasons (the so-called "monsoon") is often observed between wet equatorial and dry tropical areas, resulting from the seasonal migrations of the ITCZ. This phenomenon is mostly caused by the thermal gradient between the ocean and the continent due to high thermal ocean inertia. At the beginning of the summer, the continent warms faster than the ocean, promoting the development of warm and low pressure atmospheric areas over the continent, while high pressure cells appear over the ocean surface. As a result, the humid air evaporating from the ocean migrates toward the continental low pressure areas generating strong precipitations on land.

In January, the ITCZ is at its southernmost position. As a result, strong rainfalls are observed in tropical regions in the southern hemisphere, and dry and windy conditions are observed in the same areas in the northern hemisphere: it is the summer monsoon in the southern hemisphere, and the winter monsoon in the northern one. Then the ITCZ migrates northward until it reaches it northernmost position at the end of June or early July. The situation is then reversed with summer monsoon in the northern hemisphere, and winter monsoon in the southern one. From August to December, the ITCZ migrates southward back to its initial position. The timing and the duration of winter and summer monsoons vary from a few weeks due the complex latitudinal position of the ITCZ, and to some discrepnacies in migration and displacement timing.

2. Impact of atmospheric circulation at the regional scale

a. Antarctica

The entire continent is located in the southern hemisphere Polar cell, and is consequently under the influence of the cold and dry polar easterlies. The climate over Antarctica is very uniform and polar. Almost all the continent is covered by thick ice sheets (99%), and this area records the coldest temperature ever measured on Earth at the Vostok station (-89.2°C). The entire continent is a cold desert, making it the largest desert area on Earth.

b. South America

The climate in South America is strongly influenced by the Andes Mountains, which constitutes a continuous North-South barrier to easterlies and westerlies. It is responsible for different humidity conditions on each side of the Andes (figure 9). In a general way, at tropical latitudes, the easterly trades transport moisture from the Atlantic Ocean towards the East. This moisture is blocked by the Andes piedmont where humid conditions develop, while dry and arid conditions prevail on the western sides of the Andes. By contrast, at temperate latitudes, the westerlies promote transport moisture from the Pacific Ocean toward the western part of

the Andes, whereas the eastern part stays dry and arid. Modern moisture and climatic conditions are described thereafter.

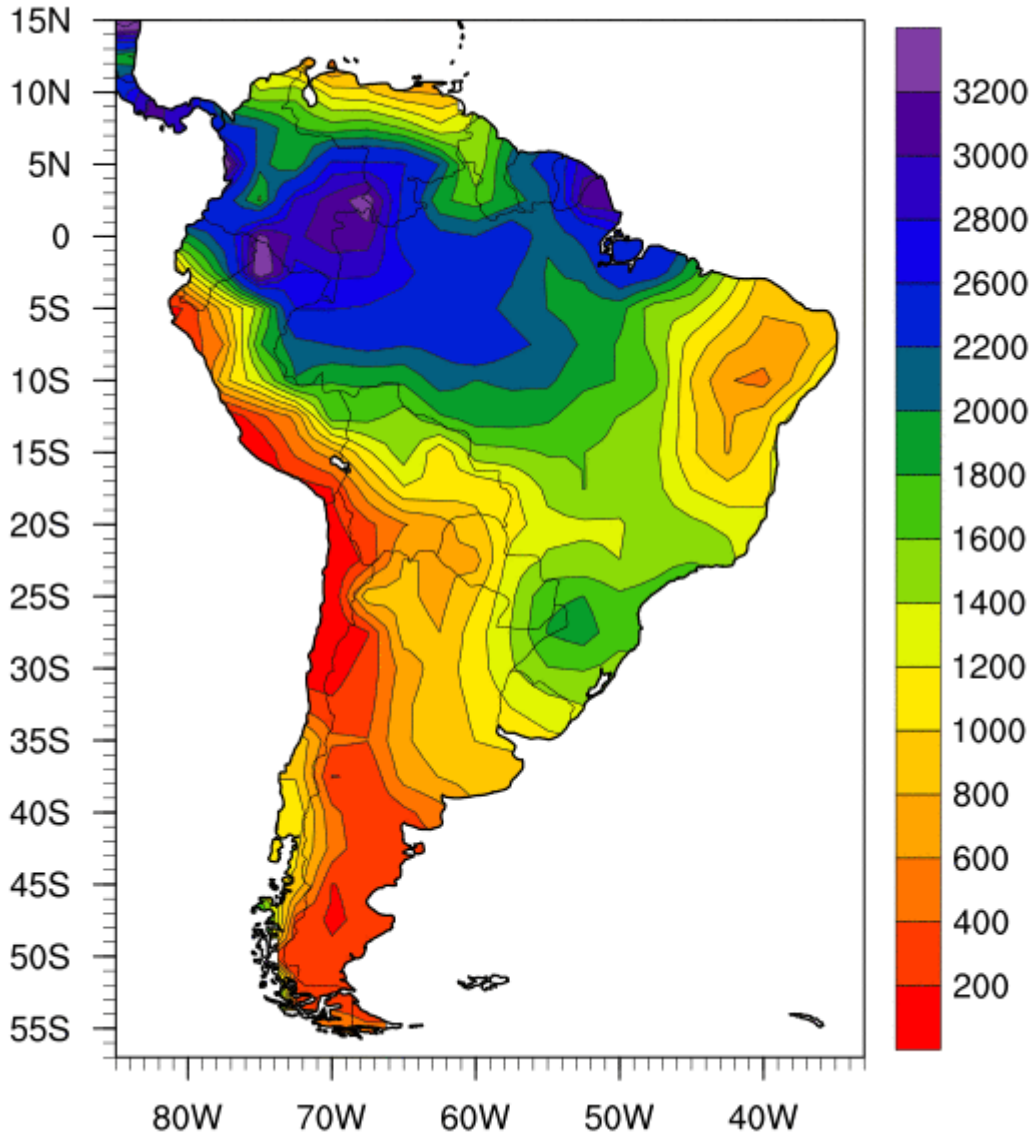

Figure 9: Observed annual total precipitation (in millimetres) from 1976 to 2009. Figure from the NOAA's website (National Oceanic and Atmospheric Administration; https://www.esrl.noaa.gov/psd/; using the data from (Libmann and Allured, 2005).

East of the Andes, four latitudinal areas can be distinguished: equatorial and tropical latitudes, subtropical latitudes, and cool-warm temperature zone. Equatorial and tropical latitudes are controlled by the South American Monsoon System (SAMS). Like other monsoon systems, the SAMS is strongly influenced by the ITCZ position and by land-sea surface gradient (Vera et al., 2006). However, the SAMS is also influenced by an important convection band named the South Atlantic Convergence Zone (SACZ). This cloudy band extends from the

southern Amazonia toward the southeastern Brazil and the surrounding Atlantic Ocean (Vera et al., 2006; Cruz et al., 2009; figure 10 and 11). The equatorial area is characterized by warm conditions associated with significant rainfall. This rainfall is quite homogeneous over the Amazon basin, however, the coastal areas and the Andean foothills receive much higher rainfalls (up two 3 times higher; Clapperton, 1993). The vegetation in this area is mostly composed of dense forests. The tropical areas know intense summer rainfalls, dry winters, and moderate rainfalls the rest of the year. These areas correspond to northern Venezuela, and eastern Columbia, north of the equator, and to the Brazilian highlands south of the equator. The vegetation cover of these areas is mostly composed of woodland savannas, but tropical forests occur near the Andes, and tropical scrub woodlands dominate the San Francisco River drainage basin. The third area corresponds to the subtropical zone lying between 25 and 40°S. It is characterized by highly seasonal rainfall concentrated during the summer. The vegetation is characterized by tropical forests, and by tropical scrub woodlands close to the Andes. Over the Pampa, the rainfall occurs as heavy showers concentrated into a few annual rainy days (Clapperton, 1993). The vegetation is adapted to this very particular climate and is known as Pampa grassland. The last area is the cool-warm temperate zone. This area is dry and can be classified as a semi-arid desert and is called Patagonia. The very dry conditions characterizing over this area (figure 9) are responsible for the very poor vegetation cover, mainly composed of shrubs and grasses known as the Patagonian steppe (Clapperton, 1993).

Another important feature characterizing South America is the South Westerly Wind Belt (SWWB; figure 11). This belt, briefly described hereafter, is responsible of important rainfalls over southernmost Patagonia, and particularly on the west side of the Andes.

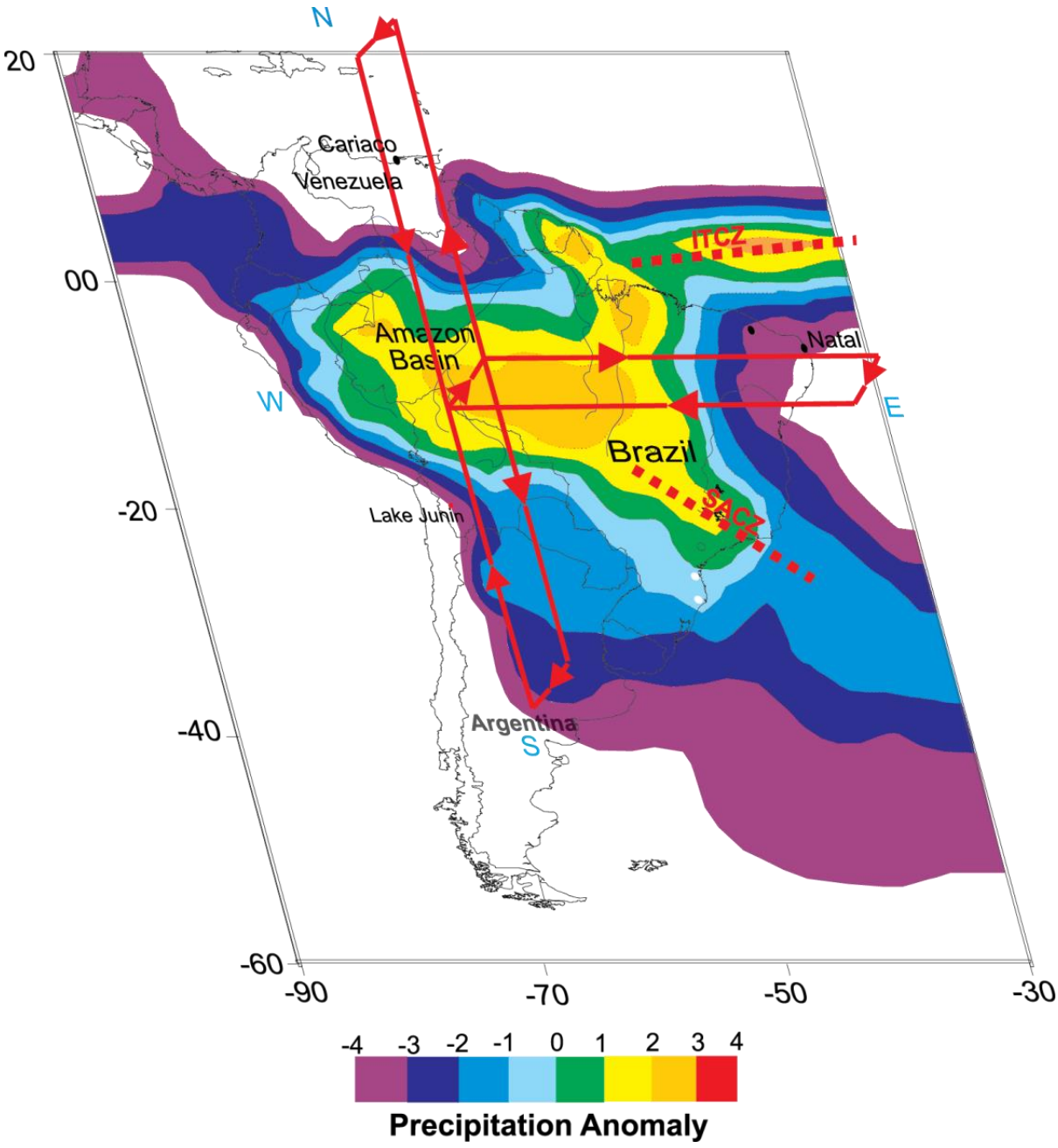

Figure 10: *Schematic diagram showing precipitation patterns in summer and atmospheric circulation over South America for the last 4 000 years (Cruz et al., 2009). Red arrows represent the atmospheric convection cells. Note that the westerly wind belt is not represented on this figure.*

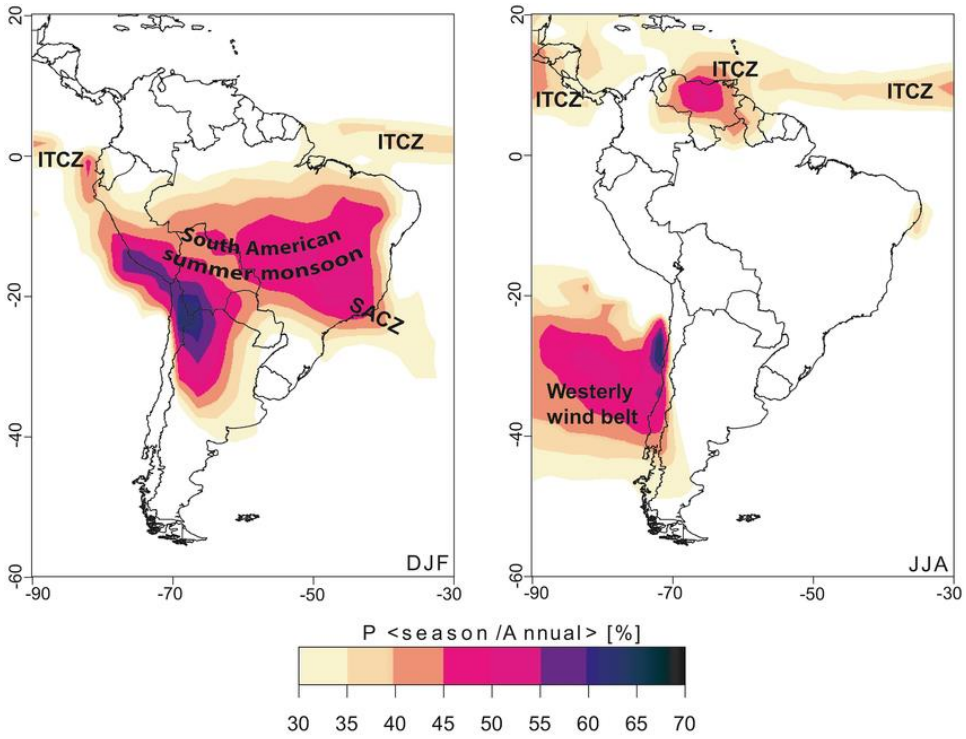

<u>Figure 11:</u> Percentage of annual precipitation received during December, January, and February (left part); and during June, July, and August (right part). Figure from Flantua et al. (2016).

The western part the Andes is not likely to supply any sediment toward our studied sites, with the exception of the southernmost part, this area is only briefly described. Equatorial climate dominates north of ~5°S. From 5 to 30°S, the climate is arid and warm. From 30°S to 40°S, the climate is more humid, with strong summer rainfall. The southernmost part, south of 40°S, is characterized by very strong winds and significant rainfall, largely received as snow because of the high relief in the area. This important snowfall is the origin of important land glaciers in the area (Clapperton, 1993).

c. Africa

Based on the main oceanographic and atmospheric configurations, Africa is not expected to be a major contributor to sedimentation in our studied sites. However, in order to be able to identify or to rule out any contribution from this continent, it is necessary to have a general idea of its characteristics, even if only focusing on the main sources area. Africa includes various climatic conditions. However, even if the East African Rift can acts as a small climatic barrier, there is no major mountain chain such as the Andes as in South America. Consequently, the spatial distribution of these climates in Africa is mostly latitudinally controlled. Here we describe these different climate zonations.

Desert and Humid areas

As in most parts of the world, the latitudes around 30° in Africa experience very dry climatic conditions. These deserts are the direct result of the Hadley Cell described in part II.A.1.a. These areas correspond to the Sahara in the northern hemisphere, and to the Namibian desert in the southern hemisphere.

The African Monsoon

The African monsoon is strongly related to the ITCZ position, which is in turn strongly linked to Earth obliquity. The geographical organization of the African monsoon is mostly latitudinally controlled (see figures 12 and 13). Indeed, today, in the northern hemisphere, the summer monsoon is generally located south of a line between northern Senegal and southern Sudan. In the southern hemisphere, the southern limit of the summer monsoon is generally located north of Namibia.

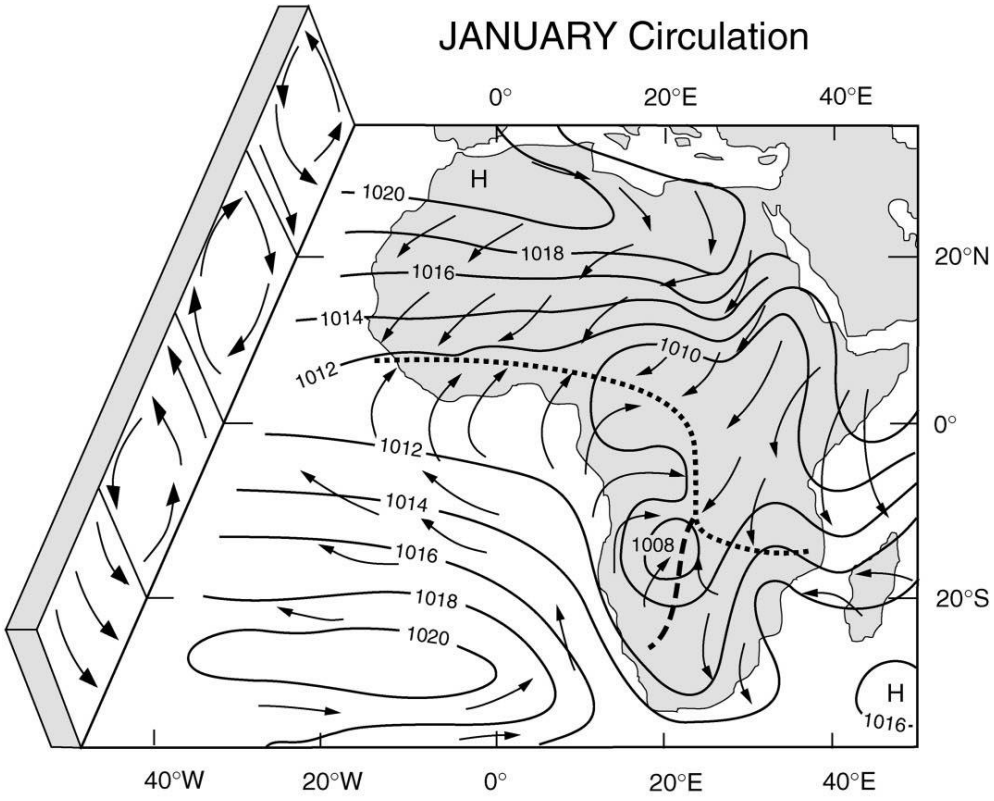

Figure 12: Schematic diagram of the general circulation pattern of winds and pressure over Africa in January (Nicholson, 1996). Dotted line represent the ITCZ. Pressures are indicated in hPa.

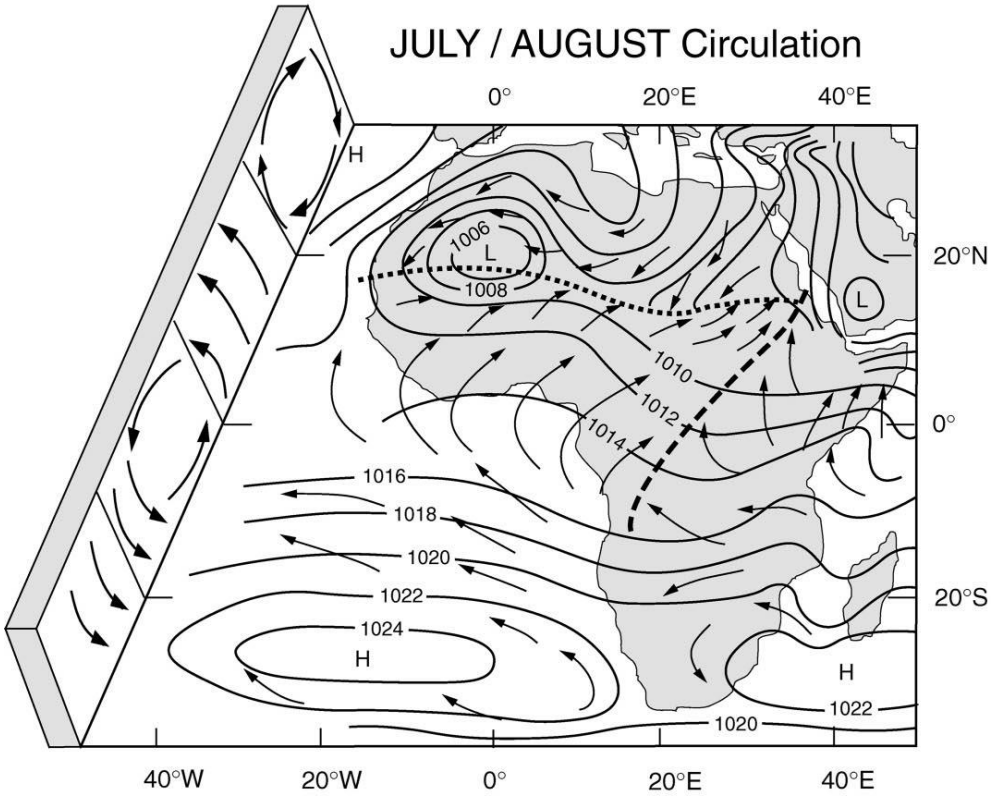

Figure 13: Schematic diagram of the general circulation pattern of winds and pressure over Africa in January (Nicholson, 1996). Dotted line represent the ITCZ. Pressures are indicated in hPa.

3. *Circumpolar Islands*

The climate over the circumpolar islands (i.e., volcanic islands located on the Antarctic circumpolar current pathway) is cold to cold temperate climate. The seasonal thermal amplitude is relatively low and regulated by the oceanic conditions (i.e., Antarctic circumpolar current). All these islands are located on the westerlies pathways. As a consequence, they are regularly submitted to strong winds and to frequent storms. Most of them, such as the Kerguelen Islands, are partially covered by ice sheets.

B. Past atmospheric circulation

1. *General circulation changes*

The quaternary period of Earth history started 2.6 million years ago and is characterized by a succession of glacial and interglacial periods. These cycles are mainly controlled by the orbital parameters of the Earth defined by Milankovitch (1941, see figure 14). They are caused by the eccentricity of Earth's orbit (cycle of 100 000 and 400 000 years), the obliquity of Earth's rotation axis (cycle of 40 000 years), and the equinox's precession (19 000 and 23 000 years). These variations are at the origin of temporal variations of solar insolation.

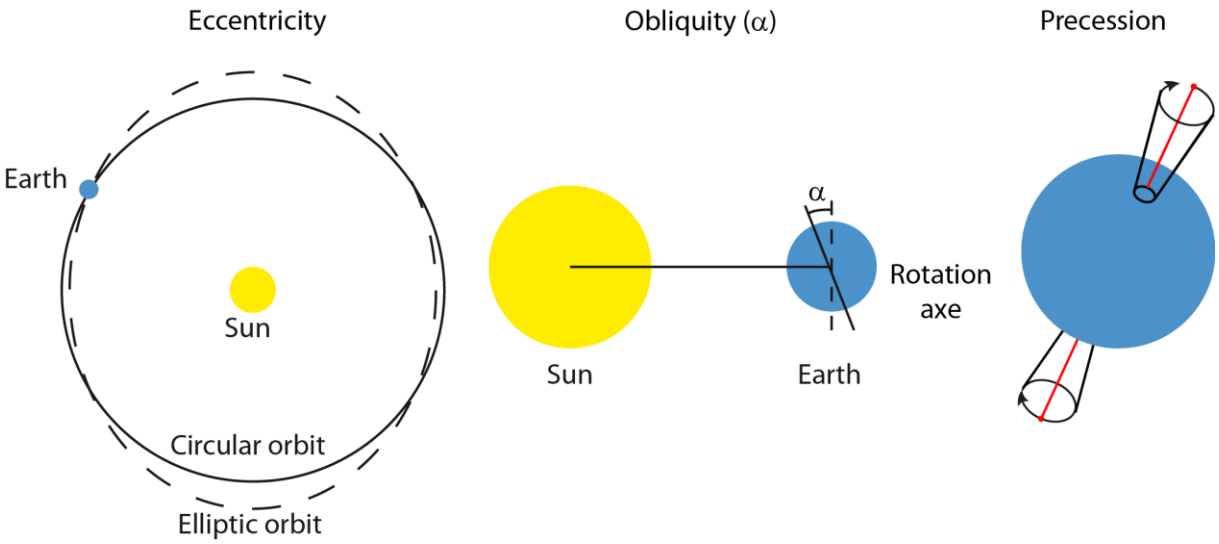

Figure 14: Orbital parameters of the Earth.

These glacial-interglacial variations induce major changes in climatic conditions that lead to temperature and salinity variations in the oceans. These variations can be recorded in oxygen isotope ratios ($\delta^{18}O$) measured in the skeletons of organisms, as foraminifera: This proxy is calculated using the following formula: $\delta^{18}O = 1000 \times [\frac{(\frac{18O}{16O})sample}{(\frac{18O}{16O})SMOW} - 1]$ were the SMOW is the Standard Mean Ocean Water. The response of the oxygen isotopes to changes in insolation is not linear (figure 15), but the major temporal variations in $\delta^{18}O$ are used to delimit marine isotopic stages (MIS) corresponding to a glacial or interglacial period. Even MIS correspond to interglacial periods, and odd MIS correspond to glacial periods. The abrupt and large climatic variations that occur during major deglaciation phases are called terminations (figure 15). Terminations are labelled using roman numbers, and Termination I corresponds to the last major deglaciation. The present study will focus on this particular termination. For this latter (Termination I), the climatic changes represent a sea level rise of ~120 m (Grant et al., 2014), and a global warming of more than 15°C at the poles (Cuffey and Clow, 1997) in less than 10 000 years.

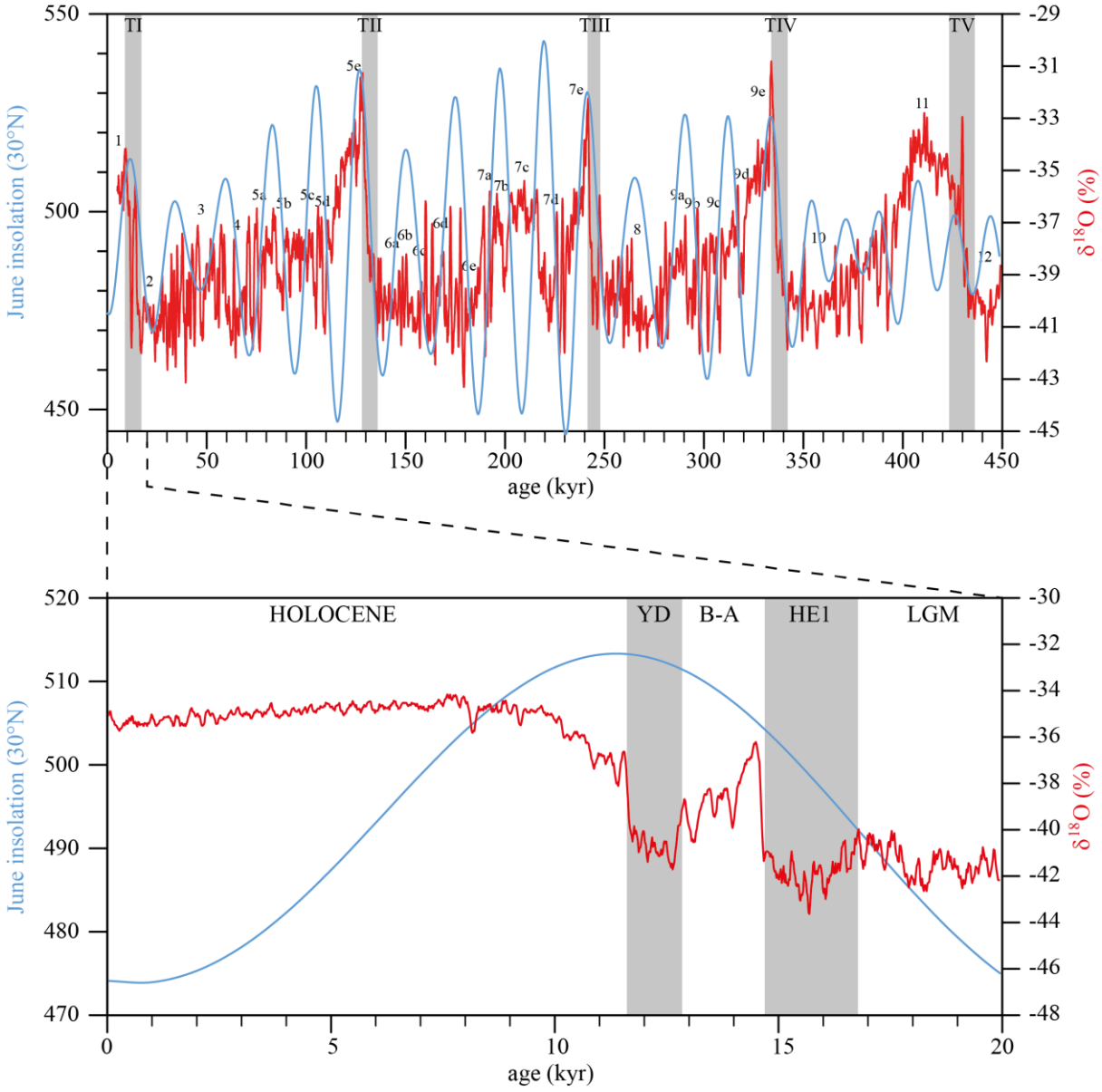

Figure 15: NGRIP ice cores $\delta^{18}O$ from Andersen et al. (2004) (zoom only) and GLT_syn simulation of $\delta^{18}O$ from Barker et al., (2011) (0-450 ka) and June insolation at 30°N. Terminations on the first part of the figure are highlighted by grey areas and numerated from TI to TV. The MIS are numerated on the $\delta^{18}O$ curve from MIS 1 to MIS 12. On the second part, a zoom is made on the last 20 kyr, including the last termination. The Younger Dryas (YD) and the Heinrich Event 1 (HE 1) are highlighted by grey areas. The latters also delimite the Holocene, the Bolling Allerod (B-A) and the Last Glacial Maxima (LGM) periods. On this figure the discrepancy between $\delta^{18}O$ and insolation is visible at both scale (20 kyr and 450 kyr) and demonstrate that the climate does not react linearly to insolation.

The Termination I is not a linear deglaciation and is composed of three main phases. The first one starts with the collapse of the Laurentide ice sheet, generating the huge liberation

of icebergs and fresh water to the ocean. This event is known as Heinrich Event 1 (HE 1), characterized by the occurrence of ice rafted debris (IRD) in North Atlantic Ocean sediments (Heinrich, 1988). This event is responsible for the cooling of the northern hemisphere between ~17 ka and 14.8 ka and is concomitant with a warming of the southern hemisphere called Antarctic Warm Event. This transmission of the perturbation from one atmosphere to the other is often referred as interhemispheric seesaw (Barker et al., 2009). These interhemispheric seesaw processes generally involved opposite variation in the two hemisphere: a warming in one hemisphere is generally followed by a cooling in the other (Barker et al., 2009). Other Heinrich Events (HE) and their associated Antarctic Warm Events have been recorded in various records. These events must not be confused with the term Heinrich Stadials (HS) that is also commonly used. The term "Heinrich Stadials" encompass Heinrich Events and correspond to a period were stadial climatic conditions occurred (cold northern hemisphere) while the term "Heinrich Events" only refer to northern hemisphere ice sheet collapse events that lead to fresh water input and ice rafting surge in the North Atlantic Ocean. Heinrich Stadials usually starts slightly before Heinrich Events (0-2 kyr) and most of them are associated to Antarctic Warm Events. The second deglaciation phase is called the Bølling-Allerød (B-A) and corresponds to a warming of the northern hemisphere (from 14.7 to 12.7 ka). Meanwhile, the southern hemisphere underwent cooling conditions, known as the Antarctic Cold Reversal (ACR). The third phase of the deglaciation, the Younger Dryas, starts in the northern hemisphere when the ACR is still ongoing in the southern hemisphere, and is characterized by a cooling of the northern hemisphere. It corresponds to the last oscillation of the deglaciation betwwen 12.7 and 11.5 ka. This period, also referred as the HE 0, experience important iceberg activity. Finally, the Younger Dryas is marked in the Southern Hemisphere by a slight warming. This last oscillation marks the end of the deglaciation, and the beginning of the actual Holocene interglacial period. In our study, two of the sediment cores record the last 50 ka: HE 2, 3, and 4 are visible between 22 and 24 ka, 29 and 31 kyr, and 35 and 38 ka, respectively (Bond and Lotti, 1995; Vidal et al., 1999; Hemming, 2004).

All these changes in orbital forcing, insolation distribution, and climatic conditions resulted in a continuous reorganization of atmospheric conditions. In particular, the boundaries between atmospheric cells were subject to latitudinal shifts in response to these forcings. As an example, the position of the ITCZ is generally more northerly during interglacial periods, and more southerly during glacial periods. Past evolutions of the ITCZ have been recorded in many palaeo-proxy records: in speleothems (Ayliffe et al., 1998; Cruz et al., 2005, 2006a,b, 2009;

Wang et al., 2008; Cheng et al., 2006, 2012; Caley et al., 2014; Jo et al., 2014; Novello et al., 2017), paleosols (An et al. 2000; Jo et al., 2014; Rousseau et al., 2009), as well as in marine sediments (Kaplan et al., 2016; Beny et al., 2018; Zhao et al., 2018). This latitudinal variation implies significant variation of summer and winter monsoon activities through time. For example, it is well established that the northern hemisphere had enhanced summer monsoon rainfalls during interglacial periods (Ayliffe et al., 1998; An et al. 2000; Wang et al., 2008; Cheng et al., 2009, 2012; Rousseau et al., 2009; Caley et al., 2014; Jo et al., 2014; Beny et al., 2018), and that enhanced winter monsoon winds occurred during glacial periods (An et al., 2000; Hu et al., 2012; Beny et al., 2018).

Similarly, although still subject to debate (Hesse and McTainsh, 1999; Kohfeld et al., 2013; Sime et al., 2013), several studies suggest that the Southern Hemisphere westerlies were stronger and shifted equatorward during the last glacial periods (Moreno et al., 1999; Lamy et al., 2001; Toggweiler et al., 2006). In particular, Moreno et al. (1999) suggest, based on pollens recovered from the Canal de la Puntilla (41°S), that the westerlies were located north of 41°S during the last glacial period, whereas they are located at 50°S today.

2. Regional circulation changes

a. Antarctica

Antarctica was submitted to stronger easterlies during cold periods, resulting from a northward migration of the circumpolar climatic front associated with a stronger southern hemisphere Polar cell. This phenomenon is particularly clear in Antarctic Ice cores in which higher aeolian activitie are observed in the Dome C ice core (Grousset et al. 1992) and in the Vostok ice core (Petit et al., 1990) during glacial periods.

b. South America

The position of South American climatic structures (i.e. ITCZ, SACZ, SWWB) is controlled by summer insolation (Cruz et al., 2009), oceanic conditions (Kilian and Lamy, 2012), and thus, by the orbital parameters. As a result, important climatic changes occurred during the deglaciation and during the Holocene in South America, and more generally during all glacial terminations.

At a global scale, the ITCZ was located southward during glacial periods compared to interglacials (Jo et al., 2014). These shifts have mainly been identified in speleothem records worldwide (East Asia: Wang et al., 2001, 2008; Yuan et al., 2004; Dykoski et al., 2005; Cheng et al., 2016; Australia: Ayliffe et al., 1998; India: Dutt et al., 2015; Raza et al., 2017; South

America: Cruz et al., 2005, 2009; Novello et al., 2017) and resulted in an anti-phasing of summer monsoon rainfall intensities between the southern and the northern hemispheres. In South America, although past moisture conditions are still highly debated, some consensual conclusions can be drawn (Kilan and Lamy, 2012). During the LGM, the South American monsoon rainfall was lower than today (Anhuf et al., 2006; Cook and Vizy, 2006; Fontes et al., 2017) partly due to a rather short wet season (Cook and Vizy, 2006). This change is likely due to reduced evaporation from a cooler sea surface in the Atlantic (Cook and Vizy, 2006).

In southern Brazil, speleothem records indicate that rainfall intensities were controlled by the austral summer insolation at orbital time scale (Cruz et al., 2006, 2009) while abrupt increases of rainfall were likely driven by changes in the AMOC (Atlantic Meridional Overturning Circulation) during Heinrich Stadials and the Younger Dryas (Cruz et al., 2006, EPSL). As a result, rainfall over southern Brazil during the LGM was likely similar to today, while it was probably weaker during the Early-Mid Holocene and stronger during the deglaciation (Cruz et al., 2006, EPSL). Indeed during the Early Holocene (12 to 8 ka), the SWWB retracted to the South, causing relatively weak winds and low rainfalls over southern Brazil and Patagonia (Razik et al., 2013; Mansilla et al., 2016). However, forest expansion in southern Patagonia suggests that this area could have received stronger rainfalls during this interval compared to the deglaciation (Mansilla et al., 2016). During the Early to Mid-Holocene transition, Patagonia experienced Holocene driest conditions likely due to the northward migration of the SWWB (Razik et al., 2013; Mansilla et al., 2016). This migration promoted maximum ice field growth and sea ice expansion in Patagonia between 6.1 and 4.5 ka (Kaplan et al., 2016). Cold and dry Mid Holocene conditions were followed by warm and humid conditions during the Late Holocene (since 4 ka). The transition between these two periods is marked by a southward shift of the SWWB causing weaker winds but stronger rainfall over the southern Brazil and southern Patagonia (Behling et al., 2001; Glasser et al., 2004; Mathias et al., 2012; Razik et al., 2013; Kaplan et al., 2016; Mansilla et al., 2016) leading to conditions close to the present day climate. All these observations highlight the particularly high variability of the South American climate during the Holocene.

c. Africa

As described in part II.A.2.c, climate over Africa is strongly influenced by the ITCZ migrations. Most records indicate that dry conditions prevailed during the LGM (23-18 ka; Gasse, 2000) due to a weak global hydrological cycle. At the beginning of the HS 1 (17-16 ka), a wetting and warming phase occurred (Gasse, 2000). Two rapid arid to humid transitions are

observed between 15 and 14.5 ka and between 11.5 and 11 ka (Gasse, 2000). During the Holocene, two dry periods are recorded at the vicinity of the 8.2 ka event (from 8.4 to 8 ka) and between 4.2 to 4 ka (Gasse, 2000).

d. Circumpolar Islands

The variation of the climate in the circumpolar islands is tightly linked to the changes in oceanic condition, as well as shifts in the SWWB. As described in part II.B.1, the SWWB was stronger during the LGM, causing windier conditions over the circumpolar islands. Similarly, circumpolar oceanic fronts (see part III.A.2 for details) were pushed equatorward (Anderson et al., 2009) during the LGM. Consequently, the climatic conditions were colder over these islands.

III. Oceanographic settings

A. Modern Surface Circulation

1. Atlantic surface circulation

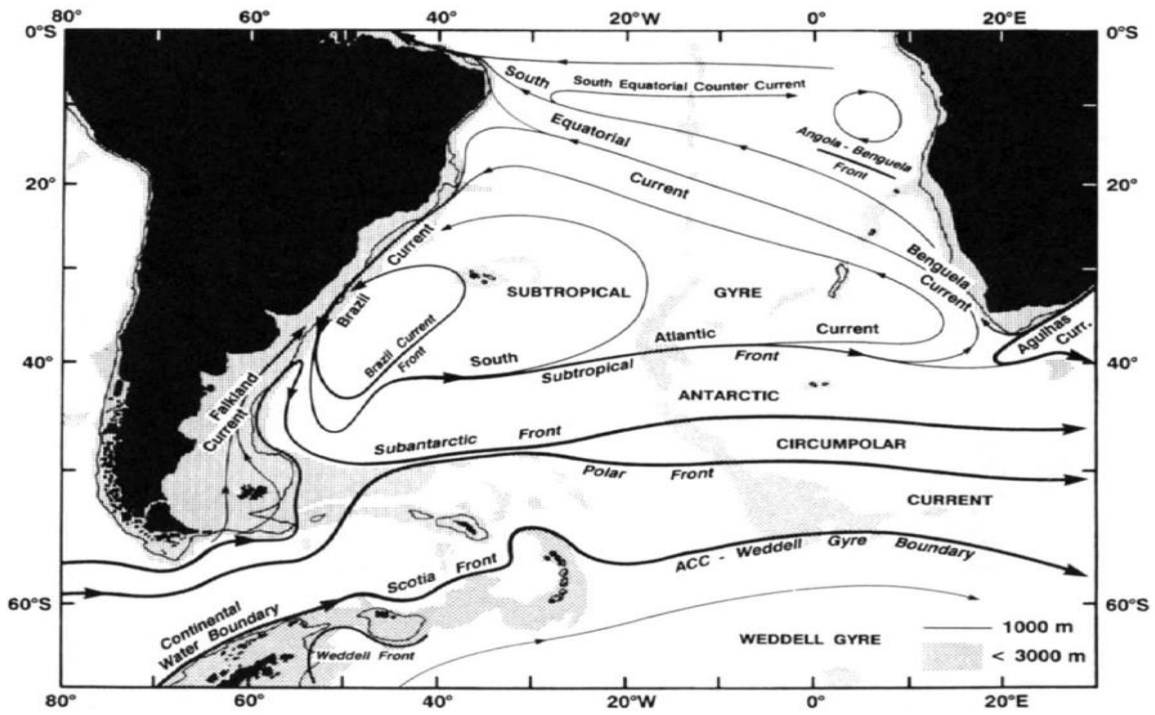

Figure 16: Schematic representation of the South Atlantic surface circulation (Peterson and Stramma, 1991).

Figure 16 shows the general surface circulation in the South Atlantic. The main features in the South Atlantic are the Subtropical Gyre, and the Angola Gyre. The Angola Gyre is delimited to the north by the South Equatorial Counter Current, to the east by the Africa

continent, and to the south-west by the South Equatorial Current. This last current corresponds to the northern limit of the Subtropical Gyre and flows westward to the eastern South America. Here it splits into two branches: North Brazil Current which flows northward, and Brazil Current which flows southward along the South American coast (Peterson and Stramma, 1991). At this location, the Brazil current meets the cold Falkland Current, shifts to the east, and leaves the coast. There, part of the Brazil current flows northward to form the Brazil Current Front, and another part flows to the east until the South Atlantic Current. This current goes east until it meets the African continent where a part reaches the Benguela Current, which flows directly into the South Equatorial Current, and the other part enters the Agulhas Current. The South Equatorial Current, the Brazil current, and the South Atlantic Current together define the limits of the Subtropical Gyre. The southern limit of this gyre corresponds to an important convergence zone: the Subtropical Front (STF, also called subtropical convergence, Orsi et al., 1995). The STF corresponds to the northern limit of the Antarctic Circumpolar Current (ACC), and thus marks the northern limit of the Southern Ocean. North of this front, surface water minimum temperatures range from 11°C in winter to 14.5°C in summer (Deacon, 1937) and salinities are ca. 34.9 psu (practical salinity unit, Orsi et al., 1995).

2. Southern Ocean surface circulation

The Southern Ocean connects the three main oceans (i.e. Atlantic, Indian, and Pacific). It is a one of the main features of the global overturning circulation and monitors the global transport of heat, of fresh water and other properties influencing climate (Rintoul et al., 2001). The most remarkable feature in the Southern Ocean is the ACC, which flows eastward without being stop by any land barrier. The northern limit of this ACC is delimited by the STF, whereas it is limited to the south by the Antarctic Divergence (Orsi et al., 1995). The STF is remarkable because it is marked by rapid changes of sea water temperature and salinity corresponding to the northern limit of cold circumpolar waters - at least 4°C and 0.5 psu - (Deacon, 1982; Peterson and Stramma, 1991; Orsi et al., 1995). This front is located around 40°S in the southern Ocean and is only interrupted by the South American continent (Orsi et al., 1995). The Antarctic Divergence defined as “the limit between the eastward flowing ACC and the westward flowing Antarctic Coastal Current” (Dunlop, 2008) marks the southern ACC boundary. Other oceanic fronts are present within the ACC: the sub-Antarctic Front (SAF), and the Antarctic Convergence called the Polar Front (PF). The SAF corresponds to a salinity minimum (Orsi et al., 1995), while the PF is a convergence zone where the surface waters sink due to buoyancy loss and form intermediate and deep waters.

B. Modern intermediate and deep circulation

1. South Atlantic sector

The South Atlantic deep and intermediate circulation is characterized by a conflict between northern sourced water masses, and southern sourced water masses (figure 17). Four water masses flow northward (so-called southern sourced water masses): the AntArctic Intermediate Water (AAIW), the Lower and the Upper Circumpolar deep-water (LCDW and UCDW), and the AntArctic Bottom Water (AABW); and one water mass flows southward: the North Atlantic deep-water (NADW).

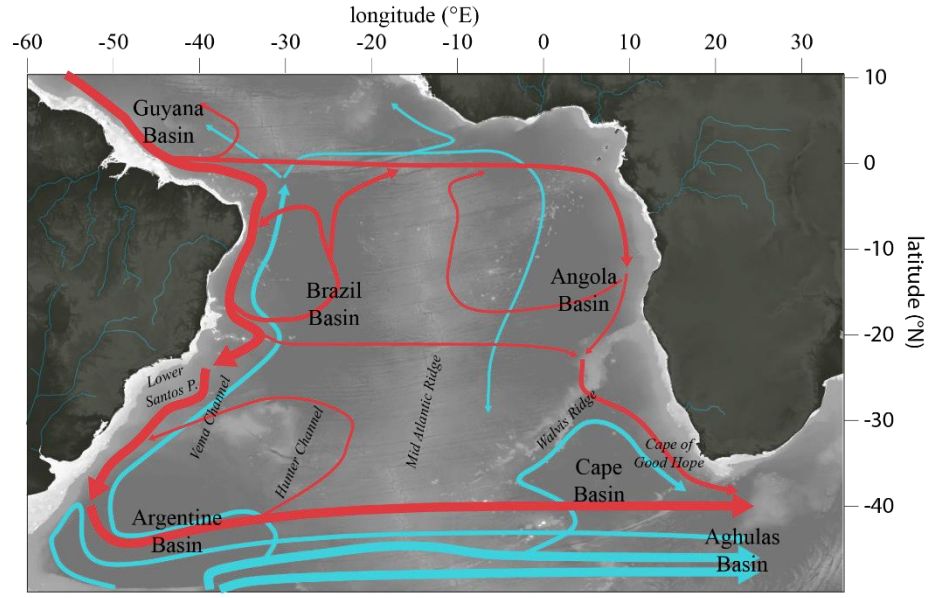

<u>Figure 17:</u> Schematic representation of the large scale NADW (red arrows) and AABW/LCDW (light blue arrows) flow (redrawn from Stramma and England, 1999).

The North Atlantic deep-water (NADW) is formed in the North Atlantic, particularly in the Labrador and the Nordic Seas. The NADW propagates southward in the South Atlantic Ocean via the deep western boundary current (DWBC) that flows along the South American shelf until ~45°S where it diverges eastward (Reid, 1989; Stramma and England, 1999, figure 17). A second branch of the NADW leaves the South American shelf near the equator and further reaches the African shelf in the Angola Basin (figure 17). This branch flows south until the Cape of Good Hope where it enters the Indian Ocean. Along all these pathways, the NADW contains circulation cells, responsible for important water export in the Angola Basin, Argentine Basin, and particularly in the Brazil Basin (figure 17, Stramma and England, 1999). The NADW is characterized by high temperature (between 2 and 4°C), high salinity (around 35 psu, Schlitzer et al., 2018), high oxygen content (~250 µmol/kg), and low nutrient content

([PO_4^{3-}] ~1.5 µmol/kg) compared to southern waters. Its density is 27.76 kg/m^3 and the volume transport ranges between 18 and 26 Sv. The NADW penetrates the Circumpolar Deep-Water (CDW) in the Southern Ocean between 45°S and 55°S (Reid, 1989) where this CDW splits into two distinct water masses: the Upper, and the Lower Circumpolar deep-water (UCDW and LCDW). The UCDW flows northward above the NADW, while LCDW flows northward beneath the NADW (figure 18).

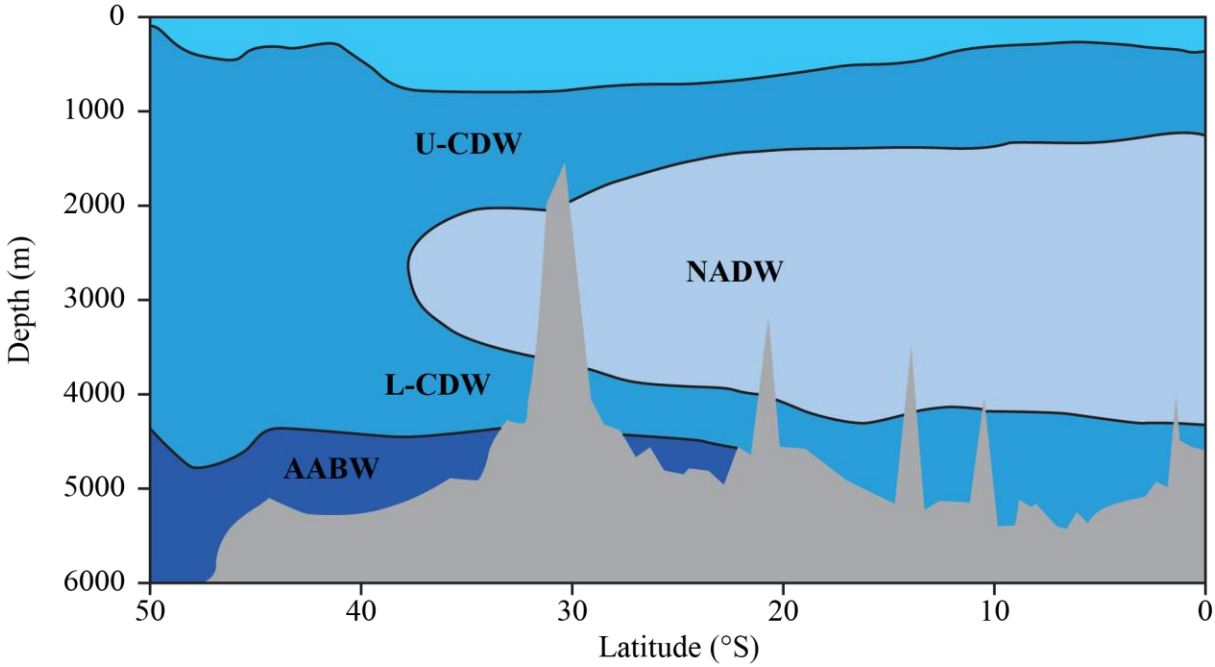

Figure 18: Deep-water masses, as observed on the CTD profile GA02 from GEOTRACE data. Delimitations between CDW and all other water masses (except the AABW) are drawn following the isoline [PO_4^{3-}]=1.75 µmol/kg (Data from Rijkenberg et al., 2014; Salt et al., 2015). Delimitation between CDW and AABW is drawn following the isoline 0°C using the data from Mawji et al. (2015)

Although some part of the CDW flow northward in the South Atlantic, as described above, most of the CDW flows eastward around Antarctica. The UCDW is characterized by low dissolved oxygen (<200 µmol/kg), high nutrient concentration ([PO_4^{3-}] >2 µmol/kg), and low salinity (~34.6 psu Orsi et al., 1995). South of the Polar Front, it forms a potential temperature maximum of at least 1.7°C. The northern extension of UCDW is very asymmetric as it is more developed in eastern part of the South Atlantic than in the western part (Larqué et al., 1997). West of the Mid-Atlantic Ridge (MAR), the UCDW thickness progressively decreases until 20-22°S (Larqué et al., 1997) where only a diluted version is found. From this point, the UCDW characteristics vanish very rapidly (Larqué et al., 1997). East of the MAR,

the UCDW contribution is much stronger, while the stratification of the Atlantic is much weaker (Larqué et al., 1997). The LCDW exhibits a similar longitudinal distribution than the UCDW, although it is much more constrained by the sea floor topography. West of the MAR, the LCDW enters the Argentine Basin via the Drake Passage. It reaches the Brazil Basin via the Vema Channel, the Hunter Channel, and the Lower Santos Plateau (figure 17; Speer and Zenk, 1993). East of the MAR, the LCDW is abundant in the Cape Basin, but almost absent and diluted in the Angola Basin because of weak but thick NADW (Larqué et al., 1997). The lower part of the LCDW mixes with the upper part of the AABW, which allows the export of AABW further north.

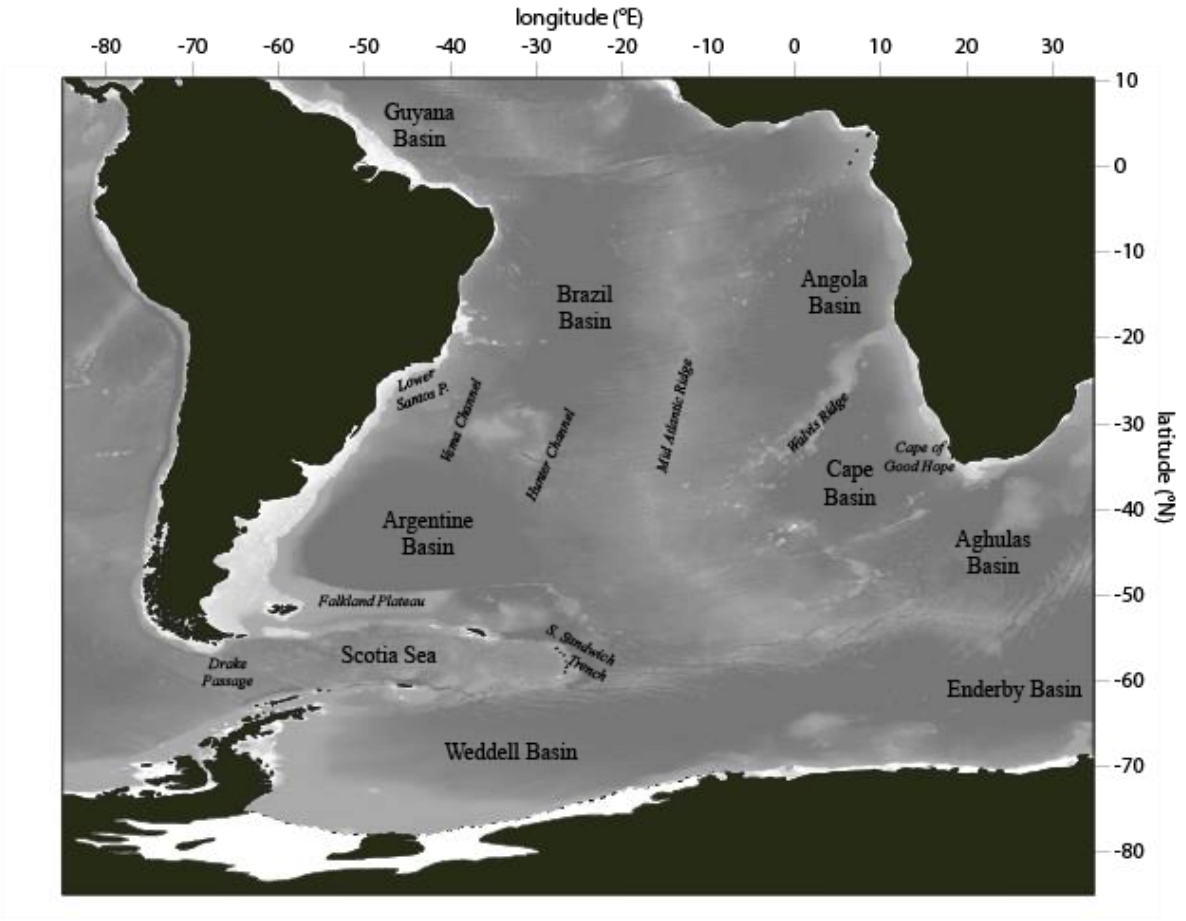

Figure 19: *Bathymetric map and toponimy of the South Atlantic Ocean.*

The AABW constitutes the southernmost-born water mass as it is produced along the Antarctic continental shelf. Currently, this formation takes place in winter when the sea water, already close to freezing, becomes saltier due to sea ice formation, which increases its density (Foster and Camarck, 1975; Orsi et al., 1999). The properties of AABW mostly depend on their production area. For example, the AABW that forms in the Ross Sea is saltier than the AABW originating from the Weddell Sea (Orsi et al., 1999). However, the Drake Passage prevents any

exchanges between these two types of AABW (Orsi et al., 1999), and the AABW in the Atlantic sector is almost exclusively generated in the Weddell Sea. The AABW production takes place at only a few places. Foster and Camarck (1975) demonstrated the formation of a very cold type of bottom water in the vicinity of the shelf break between 29 and 40°W. They also showed important formation of bottom water along the Antarctic Peninsula's tip, between 35 and 55°W and north of 65°S. This mode of formation of bottom water is called the Polynas Mode. However, in the Weddell Sea, even if poorly represented today, a second mode of formation of bottom water likely occurred in the past: the Ice Shelf Water mode, which corresponds to bottom water formation under the Antarctic ice shelves due to super-cooling (Krueger et al. and references therein, 2012). After sinking, the AABW flows into the Weddell Gyre where it is very thick (more than 4000m, Orsi et al., 1999). A part of AABW reaches the Argentine basin, where it is partly exported to the Brasil basin via the Vema Channel, the Agulhas Basin (Atlantic Ocean; figure 17 and 19; Larqué et al., 1997; Stramma and England, 1999), and the Crozet Basin (Indian Ocean, not shown on the figure; Stramma and England, 1999). The northernmost expansion of AABW is about 10°S (Reid, 1989). However, most of the AABW does not flow north of 50°S. The AABW is very cold (θ<0.1°C), moderately salty (34.6-34.7 psu, Schlitzer et al., 2018), oxygen poor ([O_2] ~220 µmol/kg), and nutrient rich ([PO_4^{3-}] ~2.1 µmol/kg). It is also interesting to note that the AABW has a high content in dissolved silicates (>100 µmol/kg), and nitrates (>30 µmol/kg; Rijkenberg et al., 2014; Salt et al., 2015).

The last important water mass is the AAIW, which is mainly generated north of the Polar Front (PF) around Antarctica by buoyancy loss of the ACC. This water represents a salinity minimum that flows northward to reach up to 1000 m depth at the Equator (Larqué et al., 1997). Because AAIW formation occurs far from the continental margin, its capacity to transport sediment is likely low compared to the other deep-water masses. In addition, the AAIW is thinner than other deep-water masses. Consequently, in this study, the contribution of AAIW is considered negligible compared to the three main deep-water masses.

2. *Kerguelen Sector*

The Kerguelen Plateau is located in the South Indian Sector of the Southern Ocean. It constitutes a major obstacle to the ACC flowing eastward and splits it into several branches (figure 20). Presently, two thirds of the ACC flow is deviated north of the Kerguelen-Crozet Plateau (i.e. ACC-core; 89-94 Sv; Park et al., 2009) and lies south of the Sub-Antarctic Front (SAF). The remaining one third of the ACC flow is flowing through the Fawn Trough (i.e. Fawn Trough Current; 43Sv; Park et al., 2009). This southern branch then deviates northward

along the eastern flank of the Kerguelen-Crozet Plateau to rejoin the ACC-core (Park et al., 2009). Secondary branches (8Sv) flowing onto the Kerguelen Plateau are also reported by Park et al. (2009, 2014) and are associated to the Polar Front (PF). These branches move slowly when crossing the Kerguelen Plateau (<5 cm/s; Park et al., 2014).

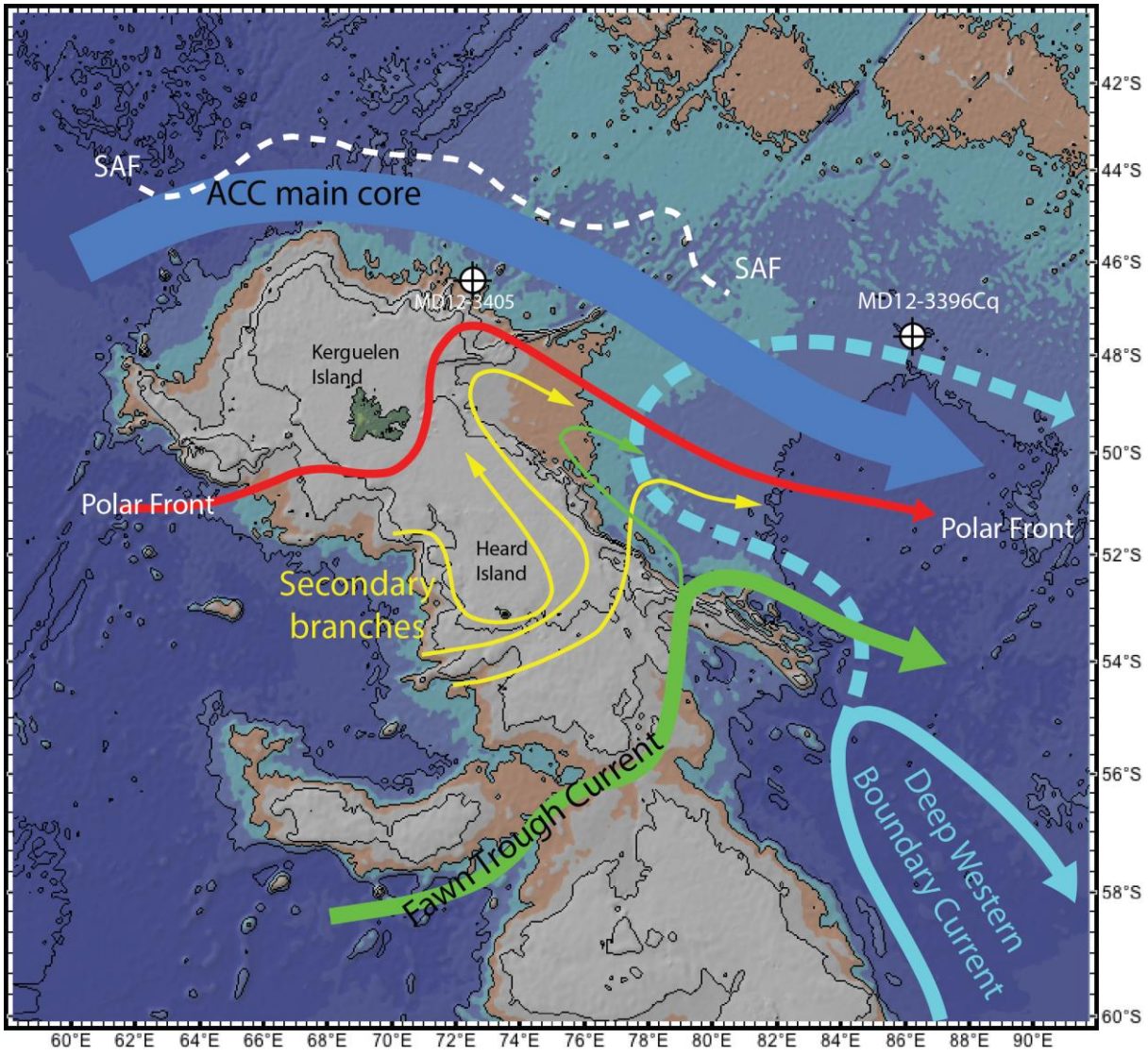

Figure 20: Present day deep and bottom circulation of the Kerguelen sector of the Southern Ocean. Dark blue, red, yellow and green arrows: present day organisation of ACC branches according to Park et al. (2009); light blue arrow: present day DWBC (i.e. AABW) according to Fukamachi et al. (2010); dashed light blue arrow: position of the DWBC during Heinrich Stadial period suggested by geochemical data from this study. SAF: Sub Antarctic Front.

The Kerguelen Plateau also acts as a barrier for the westward flow of AABW, which is deviated northward as the so-called Deep Western Boundary Current (DWBC). The northwestward transport of this current is estimated to be 16 to 22 Sv (Aoki et al., 2008;

Fukamachi et al, 2010), of which 8.4 Sv are redirected to the Southeast, resulting in a net equatorward export of AABW of 8 Sv. According to Aoki et al. (2008), the AABW transported by the DWBC originates from both the Adélie Land (between 140 and 150°E, Bindoff et al., 2000) and the Princess Elisabeth Trough (i.e. in the Prydz Bay). Close to the Antarctic continent, the AABW interacts (e.g. mixing; Orsi et al. 1999) with the westward along slope current from Antarctica (Antarctic Slope Current, ASC). This current remains restricted to the Antarctic continental slope while the AABW formed on the continental shelf flows below the ASC and is exported to the deep oceanic basins (figure 21).

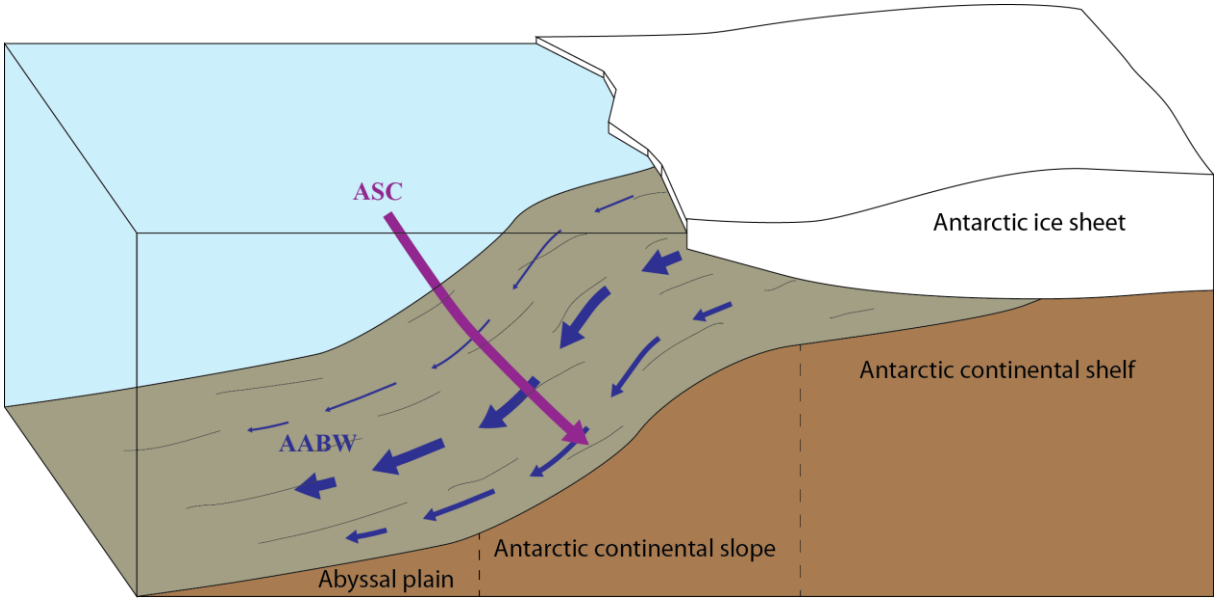

Figure 21: *Organisation of AABW and ASC circulations around Antarctica. AABW forms on the continental shelf via interaction with sea ice and/or the Antarctic ice sheet and falls from the shelf to the abyssal plain by flowing below the ASC on the continental slope. The ASC flows along the continental slope and is not exported to the abyssal plain.*

C. Past oceanic circulation

1. Atlantic sector

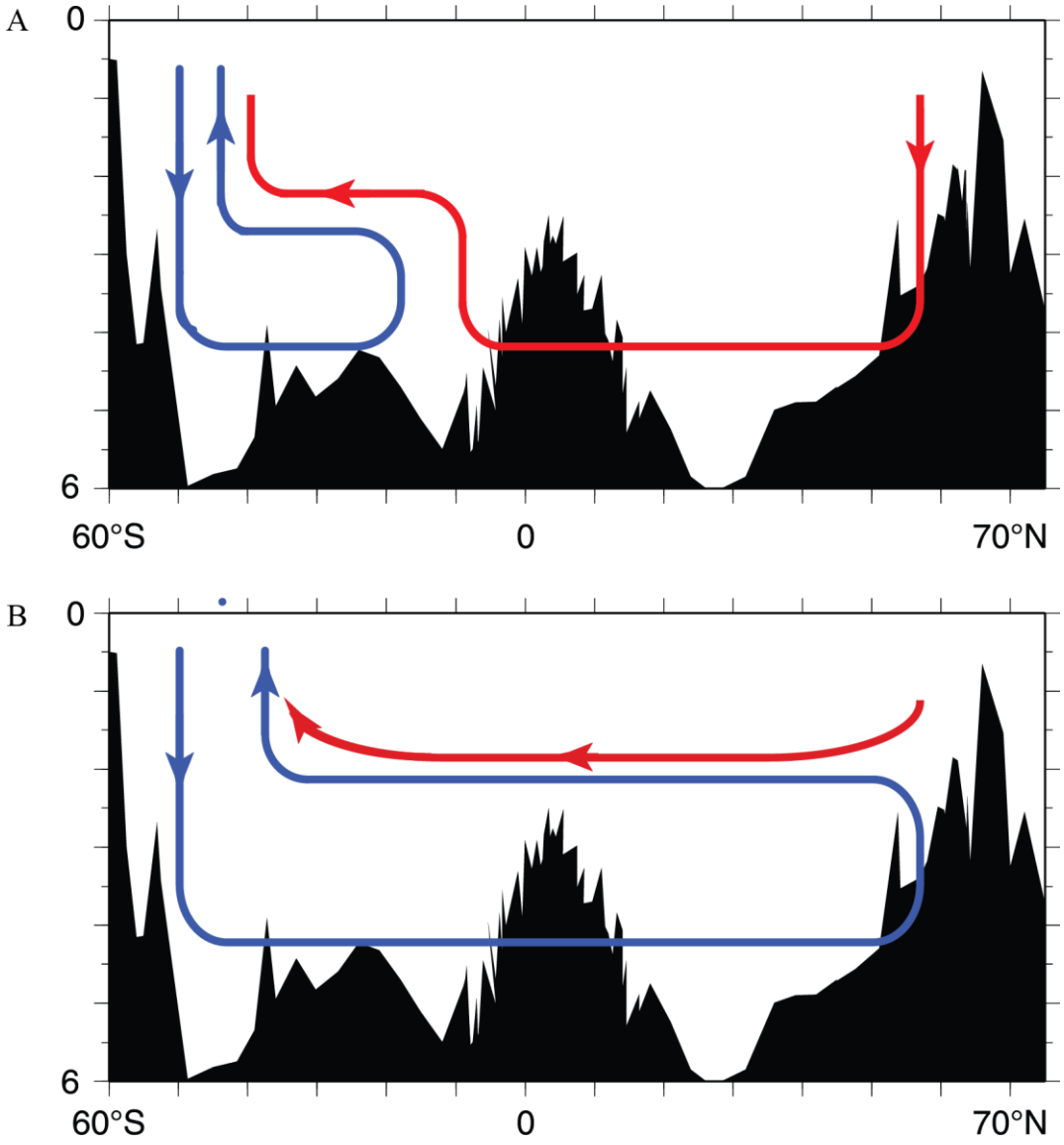

Figure 22: Simplified deep Atlantic circulation (Adkins, 2013). A: Modern deep circulation; B: Last Glacial deep circulation.

During the Quaternary, the characteristics of deep-water masses were not constant. The past evolution of the Atlantic Meridional Overturning Circulation (AMOC) is still a matter of debate (Weber and Drijhout., 2007; Vasquez Riveiros et al., 2010; Waelbroeck et al., 2011; Howe et al., 2016). However, some common features are accepted by a majority of the scientist community: 1) the southern extent of the NADW is reduced during glacial periods, whereas the northern extent of southern-born water masses is maximum (see figure 22; Kuhn and Diekmann, 2002; Adkins, 2013), 2) the Antarctic Circumpolar Current (ACC, including the CDW) likely displayed high velocities associated with enhanced westerly winds during the

LGM (Dezileau et al., 2000; Walter et al., 2000; Mazaud et al., 2010), and 3) the South Atlantic and the Southern Ocean are rather highly stratified during the LGM, and the ventilation recovery during the deglaciation is known to enable the release of CO_2 from the ocean to the atmosphere (Toggweiler et al., 2006; Barker et al., 2010; Skinner et al., 2010, 2013, 2014). Finally, abrupt variations during the deglaciation have also been observed during the Heinrich Stadial 1 (HS 1, which encompasses the Heinrich Event), the Bolling-Allerod (BA), and the Younger Dryas (YD, Anderson et al., 2009; Barker et al., 2009; Gottshalk et al., 2015a). The release of cold and fresh water during Heinrich Events 0 (i.e. YD) and 1 likely caused a shutdown of the AMOC during these periods. The Bølling Allerød is marked by a deepening of the AMOC, and a recovery of the NADW strength. Similarly, similar shutdown of the AMOC generated by the release of fresh waters are associated to ventilation overshoots in the Southern Ocean during HS 1 and the YD, raising the atmospheric CO_2 from 180 ppm to 280 ppm in two steps (Anderson et al., 2009; Skinner et al., 2010, 2013, 2014; Bereiter et al., 2015).

2. Kerguelen sector

The evolution of the ACC and the AABW are controversial. Studies close to our Kerguelen sites suggest stronger ACC during the Last Glacial Maxima (LGM) compared to the Holocene (Bareille et al., 1994; Dezileau et al., 2000, Mazaud et al. 2010), whereas a study based on sortable silts in the Scotia Sea (Southwest Atlantic sector of the Southern Ocean) show no major changes during the LGM (McCave et al., 2014). The evolution of the DWBC is poorly known, however, northward expansion of AABW during glacial periods has been reported in other areas (McCave et al., 2008; Govin et al., 2009; Spooner et al., 2018).

IV. Geological Settings

Our study sites (South Indian and South Atlantic sectors of the Southern Ocean) may receive sediments from many geological formations under multiple climatic conditions. These background conditions may have a substantial impact on the flux and on the composition of the sediment delivery to our sites. Thus, it is necessary to constrain the regional geology and the effects of climatic conditions on this geological background before interpreting any possible provenance informations. However, since the size of potential source areas corresponds to ~20 % of the Earth's surface, the provenance signal is smoothed and local bias are likely negligeable. Consequently, we focus on large-scale features and general properties of potential sources. In addition, the isotopic data from the literature are detailed in annex 1. Some maps (annexes 2 to 6), generated from this database, are used to constrain the geographical

distribution for all the isotopic ratios used in this study (ε_{Nd}, $^{87}Sr/^{86}Sr$, $^{206}Pb/^{204}Pb$, $^{207}Pb/^{204}Pb$, and $^{208}Pb/^{204}Pb$).

A. Antarctica

1. General geology

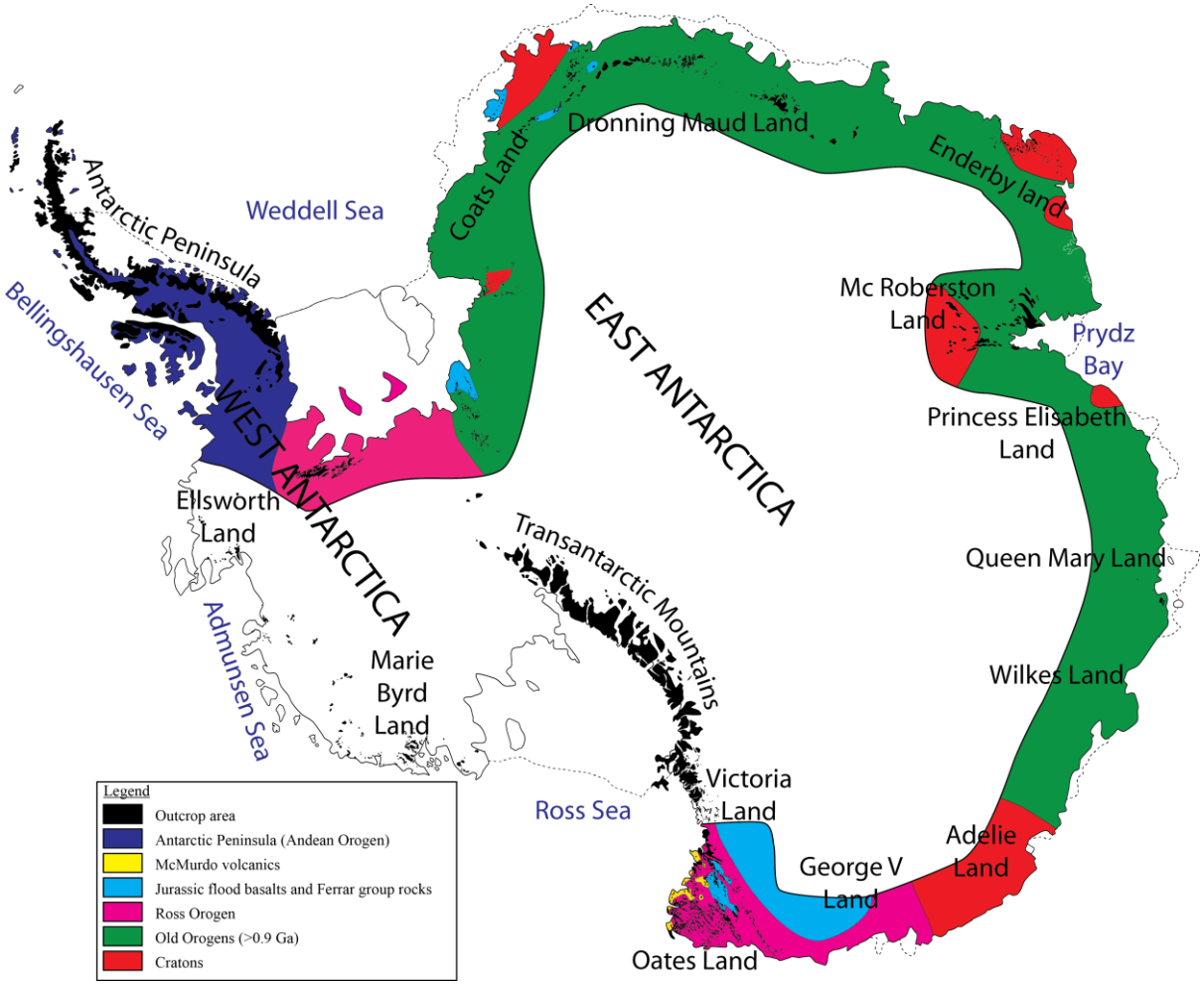

Figure 23: Simplified geology of Antarctica's coasts. Note that the geological limits has been placed approximatively due to lack of outcrops (especially from the Wilkes Land to George V Land).

The knowledge of Antarctica's geology is mainly based on coastal observations, and sparse nunataks due to the thick ice sheet covering 99% of the continent (figure 23). This information is biased since the non-competent rocks are much less represented in nunataks. However, this lack is balanced by the study of coastal marine sediments. Antarctica is composed of two important blocks: East Antarctica and West Antarctica. West Antarctica is similar to the Andes, whereas East Antarctica corresponds to a very old continental crust overlain by undeformed sediments (Nordenskjöld, 1913 *In* Elliot, 1975). Due to the difficulty of exploring

the geology of Antarctica, we will describe its geology in this section by organizing the information around the known outcrops, and try to fill the gaps using clues given by marine sediments.

a. West Antarctica

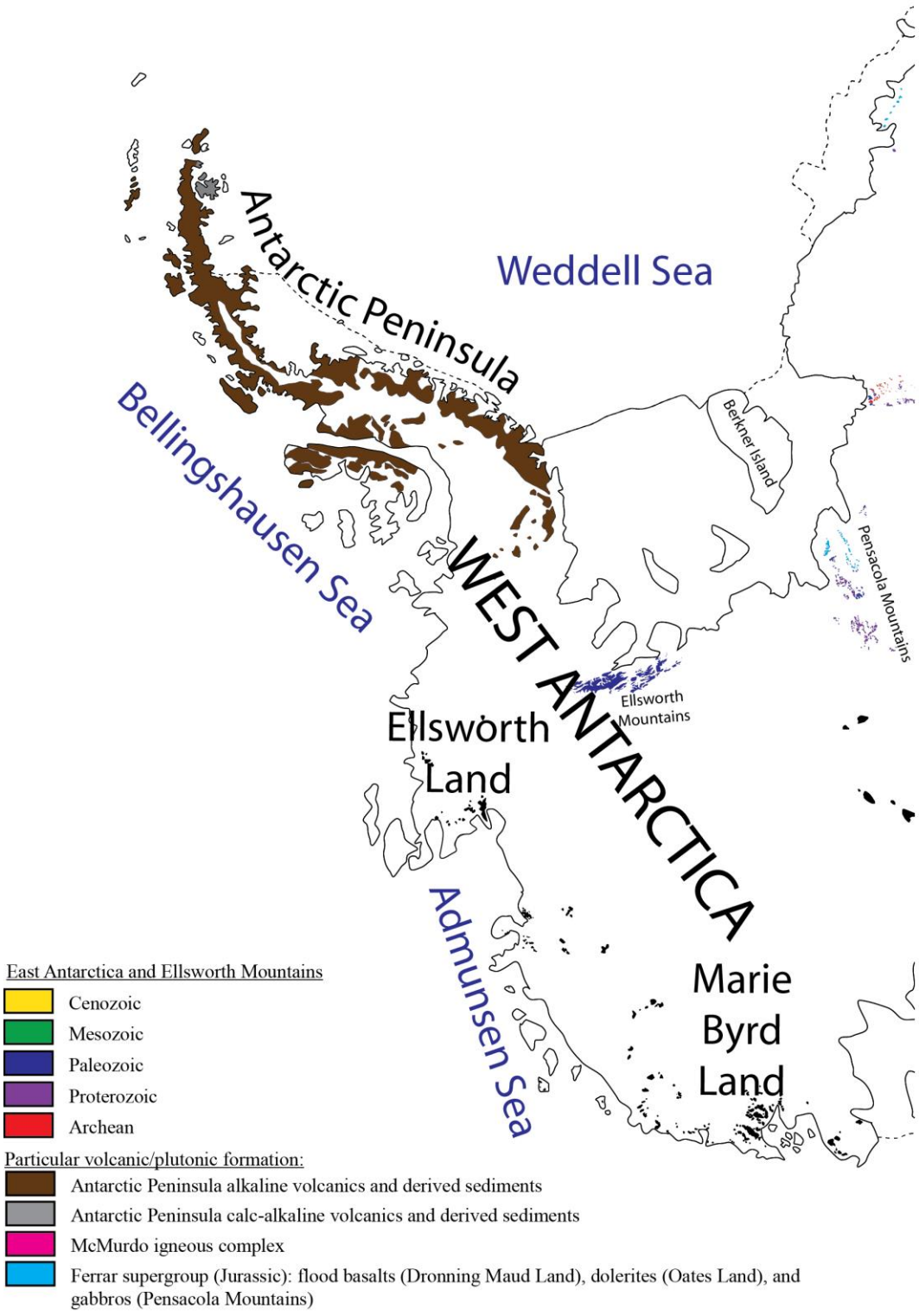

Figure 24: Outcrop map of West Antarctica. Black areas represent unclassified outcrops.

West Antarctica includes the Antarctic Peninsula, the Scotia Arc region, the Ellsworth Land, the Ellsworth Mountains, and the Marie Byrd Land (figure 23 and 24). Outcrops are dominated by plutonic and volcanic rocks, but sedimentary and metamorphic rocks are also present. Marie Byrd Land is mainly composed of alkaline volcanic rocks (Anderson, 1965; Tingey et al., 1991). However, it is located in the Pacific part of Antarctica, and its contribution as a sediment source to our study site looks unlikely. The Ellsworth Land is located more easterly than the Marie Byrd Land, but is still mainly in the Pacific part of Antarctica, and its contribution at our study site may remain very limited. It is composed of Precambrian rocks, corresponding mainly to granodiorite orthogneiss intruded by granitic and pegmatitic sheets (Tingey et al., 1991). However, the lack of outcrops in the area (only 3 locations) makes geological investigation complicated.

In contrast, Ellsworth Mountains present much better outcrops and are located near the southwest part the Weddell Sea ice shelf. This area contains a wide variety of rocks ranging in age from Late Proterozoic to Late Paleozoic (Tingey et al., 1991; Anderson, 1965). However, these rocks are mainly sedimentary rocks (quartzite, volcanic diamictite, conglomerate) derived from acid volcanic and plutonic material (Anderson, 1965; Tingey et al., 1991), and some carbonate formations are also present.

The Antarctic Peninsula is one of the most probable sources of sediment for CDW and AABW. It is mainly composed of calc-alkaline magmatic rocks, associated with deformed sediments of similar composition. It is interesting to note the occurrence of alkaline volcanic rocks and associated detrital sediments near the AABW formation location identified by Foster and Camarck (1975) between 35 and 55°W and North of 65°S.

b. Transantarctic Mountains

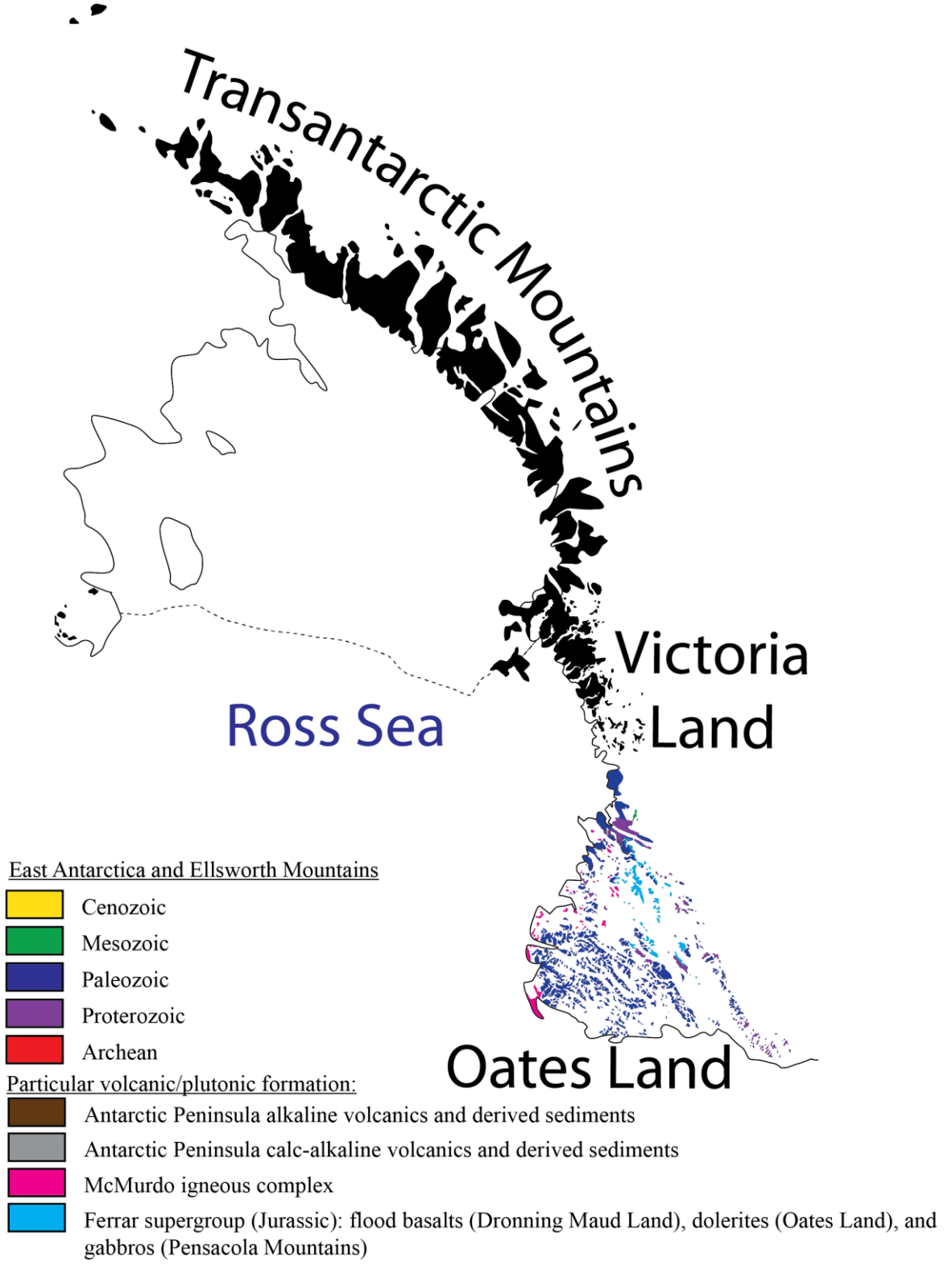

Figure 25: Outcrop map of Transantarctic Mountains. Black areas represent unclassified outcrops.

The Transantarctic Mountains are one of the most striking geological features in East Antarctica. However, because of their size and geological diversity, they are discussed regionally. They correspond to an important relief and hence sediment source from Oates Land, northern Victoria Land and Marie Byrd Land in the south (figure 23 and 25). They constitute the western limit of the Ross Ice Shelf.

The basement of the Transantarctic Mountains is composed of Proterozoic to Cambrian metamorphic rocks of variable grades intruded by Cambrian-Ordovician acid plutons (Hauptvogel and Passchier and references therein, 2012; Tingey, 1991a). This basement is overlain by Devonian-Triassic sediments in turn intruded by dolerite sills and dykes mostly from the Jurassic (Laird, 1991; Hauptvogel and Passchier and references therein, 2012; Tingey, 1991a). This Jurassic intrusion is a major event that is observed in most of East Antarctica and known as the Ferrar supergroup. Along with contemporary volcanic extrusion of basalt, this magmatic activity was related to the breakup of a supercontinent and the separation of Antarctica from Africa, India and Australia. Recent episodes of volcanic activity include trachytic eruption at 25 Ma and undersaturated volcanic series from 19 to 12 Ma (Hauptvogel and Passchier and references therein, 2012).

Oates Land and northern Victoria Land

Oats Land can be divided into three main formations: (1) Late Proterozoic phylites (Laird, 1991) (2) Jurassic dolerites, and (3) metamorphic rocks (called the Wilson Group) of amphibolite facies that includes layered gneisses (some of sedimentary origin), granitoids, and pegmatite veins. Northern Victoria Land can also be divided in three formations. The Wilson Group is also present in this area. However, the two other formations are different and composed of Cambro-Ordovician sediments and mildly metamorphosed basic volcanic rocks.

South Victoria Land

The South Victoria Land contains one of the largest outcrops in Antarctica: the Victoria Land Dry Valleys. The basement is represented by a low-grade metamorphic complex, mainly composed of marbles, schists and gneisses of sedimentary origin (Tingey, 1991a). This basement is intruded by granitoids and overlain by Devonian quartzose sandstones, and by Late Carboniferous to Early Jurassic sequence including glacial beds, sandstones, shales, conglomerates and coal (Barrett, 1991). All of these rocks are intruded by Jurassic dolerites (Tingey, 1991a).

Central Transantarctic Mountains

The Central Transantarctic Mountains are largely composed of amphibolite facies metamorphic rocks. This group includes quartzo-feldspathic gneiss, migmatite, quartzite, semipelitic schist, amphibolite, calcsilicate schist, and marbles formed from metamorphism of sandstone, limestone, dolomite, and interbedded mafic volcanic rocks. These metamorphic rocks are intruded by granitoid plutons.

c. East Antarctica

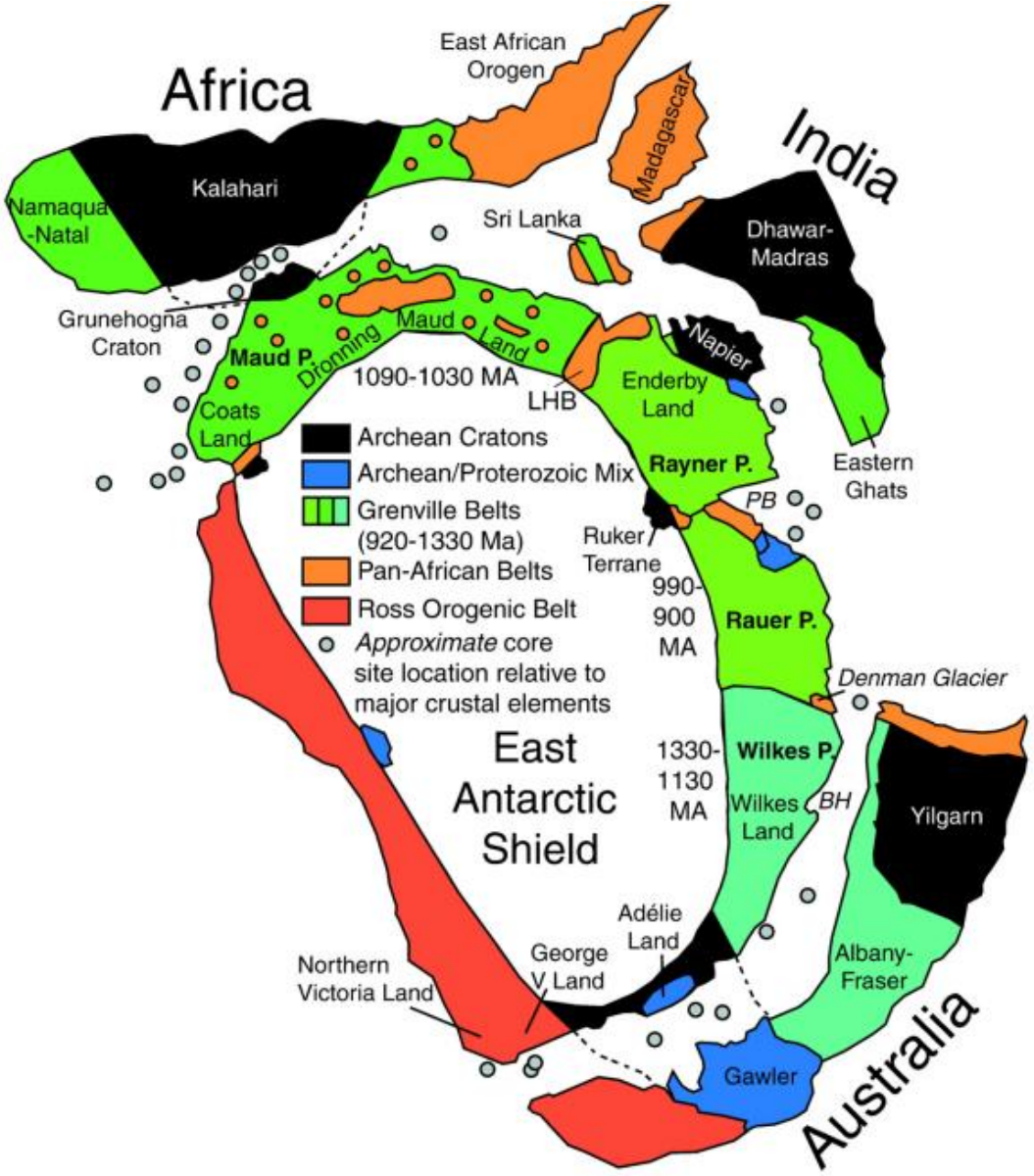

Figure 26: Structural map of East Antarctica (Pierce et al., 2014). BH: Bunger Hills, LHB: Lützow-Holm Belt, PB: Prydz Bay.

The East Antarctica region is much wider than West Antarctica. The main geological structures are shown on figure 26). Because most of the geological knowledge comes from coastal outcrops and mountains, the main features are described hereafter from west to east, and from the Weddell Sea to the Ross Sea. Particular focus is made on the eastern part of the Weddell Sea, and on the Prydz Bay inlet where the AABW may be formed (see part III of this chapter for details on AABW formation).

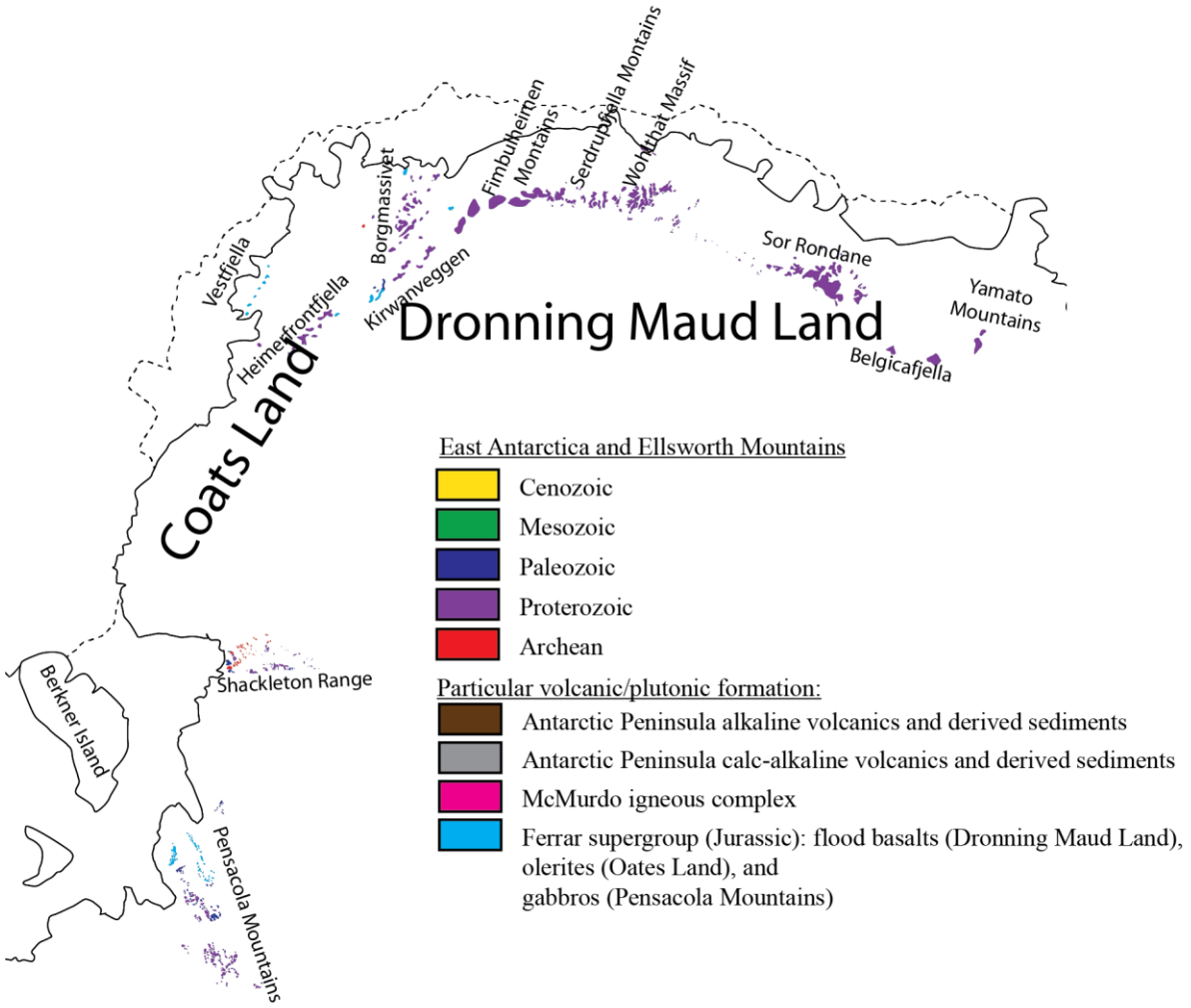

Figure 27: Outcrop map of Eastern Weddell Sea Embayment and Dronning Maud Land.

Pensacola Mountains

In the central-east part of the Weddell Sea, the first feature of East Antarctica corresponds to the Pensacola Mountains (figures 23 and 27). These mountains are characterized by rocks from Late Proterozoic to Late Devonian ages (Laird, 1991). Late Proterozoic rocks are characterized by slightly metamorphosed (green schists) slate and sandstones, and by basalts (mainly pillow lavas). There are some occurrences of dolerites and minor rhyolite intrusions. The Cambrian succession comprises limestones, a felsic volcanic unit, and interbedded

siltstones and shales. The Ordovician is characterized by sedimentary successions with variable clast compositions: limestone, volcanic clasts, and quartz. The grain-size varies from argillaceous siltstones to conglomerates. The Late Devonian that unconformably overlies these formations is composed of quartzite (Laird, 1991). In the northernmost part of the Pensacola Mountains, Jurassic gabbroic rocks of the Ferrar Supergroup formation (i.e. mostly flood basalt) represent most of the exposed rocks (Ford and Kistler, 1980).

Berkner Island

Little is known on the geology of this island because it is totally covered by the ice sheet (figure 27). However, the study of marine sediments close to this island suggests that it has a particular composition. Indeed, important amount of kaolinite has been recognized (Petschick et al., 1996) in the vicinity of the island. In Antarctica, kaolinite is only found in the Transantarctic Mountains, more specifically in the Beacon Supergroup (Tingey et al., 1991), and in the Prince Charles Moutains in the McRobertson Land (see below).

Shackleton Range

The Shackleton Range is located in the eastern coast of the Weddell Sea (figures 23 and 27). The geological formations are Archaean to Paleozoic (the youngest being Devonian). Most of the rocks are metamorphics and can be divided in three groups on the basis of the metamorphic grade and composition: (1) granitic gneisses, sillimanite-garnet gneisses, marbles, pyroxene granulites, and garnetiferous dioritic gneisses; (2) amphibolites, garnet-mica schists, mica schists, quartzites, marbles, and calcshists; (3) slates and quartzites (Anderson, 1965). Some sedimentary rocks occur in the western part of these mountains and are ferruginous shales, feldspathic sandstones, calcareous sandstones and quartzite conglomerate (Anderson, 1965).

Theron Mountains

Theron Mountains are located ~100 km north of the Shackleton Range (figures 23 and 27). They are mainly composed of Devonian-Permian formations (Anderson, 1965; Tingey et al., 1991) that comprise feldspathic sandstones, arkoses, and black carbonaceous shales. These sedimentary formations are intruded by Jurassic tholeiitic dolerite dykes (Anderson, 1965).

Coats Land

Coats Land is located north of the Theron Mountains along the Weddell Sea coast (figures 23 and 27). In this area, only few nunataks give insights on the geology, and their geological significance is uncertain. These nunataks are mainly composed of ~1 billion years

old porphyry (Tingey, 1991a; Loewy, 2011). Capurro (1955) reported one coastal nunatak as being granophyric granite, impure crystalline limestone, and spillite.

Western Dronning Maud Land

Dronning Maud Land is an area between 20°W and 45°E with outcrops mainly concentrated in mountains close to the coast (figure 23 and 27). The western part includes several outcrops known as Vestfjella (or Kraul Mountains), Mannefalknausane, Heimefrontfjella (or Kottasberg), and Sembberget. Vestfjella and Mannefalknausane are located close to the coast, whereas the two others are more in the hinterland. North-east of these outcrops, are found the important exposure region of the Jutulstraumen Glacier which bring sediments to the Weddell-Enderby oceanic basin.

Vestfjella is mainly composed of Permian clastic sediments (sandstones and shales), and strongly altered basic lavas (mostly tholeiitic to alkaline basalts; Tingey et al., 1991). Minor pyroclastics and volcanogenic sediments are present. All of these formations are intruded by dolerite dykes and olivine gabbro (Tingey, 1991). 80 km south of Vestfjella, the outcrop of Mannefalknausane is mainly composed of gneisses. Four main rocks are recognizable: red granite gneiss, charnockite gneiss, porphyroblastic gneiss, and intrusive dolerite (Tingey, 1991). Heimerfrontfjella is an important outcrop and is also mainly composed of gneisses. It includes biotite-quartz-feldspar paragneisses, amphibolites, and marbles, sometimes intruded by granites or gneissic granites. This basement is sometimes overlain by terrestrial coal-bearing sediments (Barrett, 1991) and Jurassic tholeiitic basalts containing rare olivines (Tingey et al., 1991). The last outcrop, Sembberget, is entirely composed of this Jurassic tholeiitic basalt (Tingey, 1991).

The Jutulstraumen Glacier can be divided into four geological provinces. The first, known as the Annandagstoppane-Juletopanne area, comprises Archean granitoids intruded by Early Proterozoic gabbros. The second is the central Borgmassivet-Ahlmannryggen area formed of Proterozoic sediments (mainly detrital) and volcanic rocks (basalts to andesitic basalt, rare pyroclastic rocks) intruded by mafic/ultramafic and felsic sills. These first two provinces correspond to the Grunehogna Craton (Pierce et al., 2014; Mieth and Jokat, 2014). The third province is located in the Sverdrupfjella Mountains and is the easternmost province. It is constituted by high grade metamorphic rocks intruded by Mesozoic alkali granitoids. These high grades metamorphic contain a wide range of gneisses, which can bear garnet, sillimanite, biotite, hornblende, and/or cordierite. Chert bands, marbles and skarns are also present. The last

province is located in the South and named Kirwanveggen area. It is composed of high-grade metamorphic basement, overlain by Cambrian and Permian sediments and Jurassic basalts.

Central Dronning Maud Land

Central Dronning Maud Land is largely formed by the Fimbulheimen Mountains (~300 km long), located just east of the Sverdrupfjella Mountains (figures 23 and 27). Other important features in the Central Dronning Maud Land are the Wolthat Massif, east of the Fimbulheimen Mountains, and the Schimacher Oasis, north of the Wolthat Massif (figures 23 and 27).

Fimbulheimen Mountains are also characterized by a variety of metamorphic rocks that vary from the amphibolite facies in the west to granulite facies to the east. Charnockitic rocks represent a large percentage of the outcrop. The Wolthat Massif is composed of a gabbro anorthosite complex cut by rare lamprophyre dyke and altered gabbro, peridotite, and pyroxenite. These rocks are rich in plagioclase (up to 80%; Tingey, 1991), and the other main minerals are pyroxenes, magnetite (1-4%), potash feldspar (0-3%), and quartz (0-1%; Tingey, 1991). Schirmarcher Hills are composed of biotite-garnet gneiss, pyroxene granulite, and schist with minor intercalation of basic and ultramafic metamorphosed rocks (Tingey, 1991)

Eastern Dronning Maud Land

The eastern part is characterized by sparser outcrops than the coastal Dronning Maud Land. It comprises two main outcrops: the Sor-Rondane between 20 and 30°E and the Yamato Mountains around 35°E (figures 23 and 27). A smaller outcrop - the Belgicafjella - exists in between. Sor Rondane and Belgicagjella are composed of metamorphic rocks similar with the previously described Fimbulheimen Mountains, but they are not intruded by unmetamorphosed material. The Yamato Mountains are mainly composed of migmatites, granite, syenite, and layered gneisses. Rare metabasites are also present (Tingey, 1991).

Enderby Land

Enderby Land corresponds to an area located between 45 and 60°E (figure 23 and 28). The coastal region of this land is characterized by the presence of two metamorphic complexes: the Napier and Rayner Complexes (figure 26). The Napier Complex represents an old craton. It is composed of two gneisses groups: (1) massive pyroxene-quartz-feldspar gneiss with minor mafic to ultramafic intercalations; (2) layered garnet-quartz-feldspar gneiss with subordinate siliceous, ferruginous, and aluminous metasediments. The Rayner Complex is exposed in the southern and the western part of the Enderby Land (see cratonic areas on figure 23). Its

composition is similar to high-grade metamorphic rocks of Dronning Maud Land (Tingey, 1991).

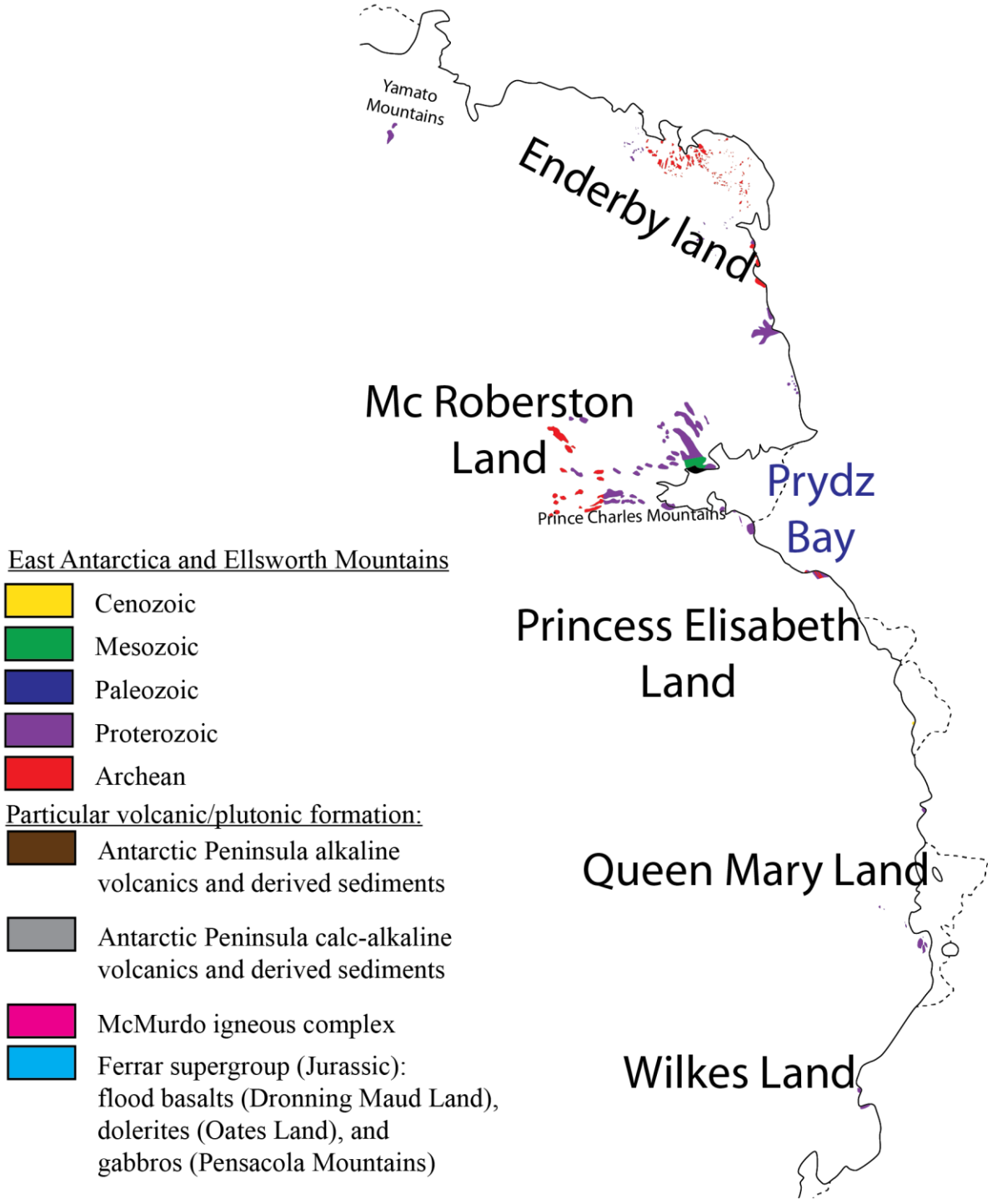

Figure 28: *Map from Enderby to Wilkes Land. Black areas represent outcrops.*

MacRobertson Land

MacRobertson Land is located east of the Prydz Bay, and constitutes the western part of the Prydz Bay inlet (figures 23 and 28). Two areas can be distinguished: the Mawson Coast,

and the Prince Charles Mountains in the southeastern part of Prydz Bay's watershed. The Mawson coast is mainly constituted by Precambrian (620-1250Ma, Tingey, 1991 and references therein) high-grade granulite facies, intruded by charnockite plutons.

The Prince Charles Mountains have more diverse rock formations ranging from the Archean to Eocene (Tingey, 1982a,b). It can be divided into a northern and a southern province. The Northern Province is composed of high-grade metamorphic rocks regarded as the eastward extension of the Rayner Complex (Tingey, 1991). The southern province corresponds to the Ruker Terrane (figure 26) and is composed of an Archean granitic orthogneiss basement overlain by terrestrial metasediments (Permo-triassic sandstones, shale, coal and basal conglomerate; Barret, 1991; Mond, 1972). These rocks are intruded by metamorphosed tholeiitic dykes. The metasediments were deposited during warm and wet conditions (Whitehead and McKelvey, 2001), which promoted the formation of kaolinite. The imprint of this kaolinite is recognizable in the clay mineralogy of the Weddell-Enderby Basin (Petschik et al., 1996), but is less obvious in the Australian-Antarctic Basin (Moriarty et al., 1977).

Princess Elizabeth Land

Princess Elizabeth Land represents the eastern part of the Prydz Bay and is located between 73.5 and 88°E (figures 23 and 28). This area exposes isolated mountains and nunataks, and some coastal outcrops. The Grove Mountains, east of the South Prince Charles Mountains have similar geological properties than the North Prince Charles Mountains. Coastal outcrops of the Prydz Bay are mainly composed of high grade metamorphic rocks intruded by a few granitic plutons. These rocks are dominantly granulite facies in the southwest, and amphibolite facies migmatites the central-northeast (Tingey, 1981). The Vestfold Hills are located on the northeastern coast of Prydz Bay and are mainly composed of Archean gneisses intruded by mafic dykes. The gneisses comprise 3 units: (1) basic to intermediate metavolcanic rocks with layered pyroxenites and metagabbros; (2) heterogeneous layered felsic orthogneiss mainly composed of quartz, pyroxenes, and plagioclases; (3) paragneisses mainly composed of garnet, biotite, pyroxenes, quartz and feldspar, and basic metavolcanics rocks.

Shackleton ice shelf – Bunger Hills region

This area includes Queen Mary Land and the western part of Wilkes Land. It is located between 98 and 101°E (figures 23 and 28). Two areas separated by the Denman Glacier located west of 100°E can be distinguished. The western part is mainly composed of migmatitic orthogneisses of tonalitic to granitic composition intruded by plutonic rocks such as gabbro, diorite, syenite, monzonite and granite. The eastern part is composed of felsic gneisses of

predominantly tonalitic composition, and subordinate mafic and ultramafic granulites. These complexes are locally intruded by charnockitic plutons. Some Cambrian red siltstones and sandstones are also present (Tingey, 1991).

Wilkes Land

The Wilkes Land corresponds to an area between 100°E to 136°E largely covered by ice (figures 23 and 28). The only significant outcrops are located in the Bunger Hills region described above, the Windmill Islands (around 110.5°E) and very isolated nunataks mainly composed of Proterozoic felsic intrusive rocks. The Windmill Islands consist in layered schists, gneisses, and migmatites intruded by pluton of charnockitic and porphyritic granites. All of these rocks are intruded by dolerites dykes from the Jurassic (Tingey, 1991). Despite this lack of outcrop, it is thought that the age of most of the rocks from Wilkes Land are grenvillian and thus correspond to an ald orogeny (Pierce et al., 2014).

Adelie Land and George V Land

The geology of Adelie Land and the George V Land is very difficult to draw with precision due to the lack of outcrops. Overall, the Adélie Land and the westernmost part of George V Land represent a vast old craton (Tingey et al., 1991; Pierce et al., 2014), while the rest of George V Land is probably dominated by the Ross Orogen and by rocks of the Ferrar supergroup (i.e. mafic rocks; Cook et al. 2017). Garnet bearing granite gneiss largely composes the coastal outcrops of the Adelie Land and a part of the George V Land (figures 23 and 28). The other formations consist in garnet cordierite sillimanite metapelites in the Adelie Coast, granitic orthogneiss intruded by amphibolized mafic dykes and muscovite aplite and pegmatite veins at the Cape Dension (between the two lands), and felsic orthogneisses largely outcrop in George V Land. Isolated Triassic continental sediments intruded by Jurassic dolerites are found in the Adelie Coast. The last formation is represented by the phylite of the Cape Hunter (Tingey, 1991). The sediment delivery from this formation is rich in chlorite and is recognizable in the data of Moriaty et al. (1977) where chlorite concentration are higher along the Adelie Coast in the Australian Antarctic Basin.

2. *Impact of climate on clay mineralogy, and isotopic composition*

Under dry and cold condition, chemical weathering is absent or occurs at a very low rate, which leads to the preservation of chlorite. This mineral is very characteristic of Antarctica's provenance and represent ~30% of the clay mineral delivered to the Ocean by the Antarctic (Petschick et al., 1996; Diekmann et al., 2000). No kaolinite is formed under dry condition but may be inherited from old rocks weathered under wet conditions when Antarctica

was located at lower latitudes. Such rocks are found in the east of the Dronning Maud Land (in the Prydz Bay), but are almost absent in the Weddell Sea (Petschick et al., 1996). Some smectite are found where basic rocks are exposed, especially in West Antarctica, where smectite is one of the most abundant clay minerals (up to 90%; Petschick et al., 1996; Diekmann et al., 2000; Walter et al., 2000). In east Antarctica, smectite does not represent more than 15% of the clay minerals (Petschick et al., 1996). In Antarctica, illite is ubiquitous and usually well crystallised (Petschick et al., 1996), it corresponds to half of the clay mineral delivered by Antarctica (Petschick et al., 1996; Diekmann et al., 2000; Walter et al., 2000). The isotopic composition of West Antarctica strongly differs from East Antarctica (see annex 1 for detailed references). Radiogenic neodymium is found in West Antarctica (annexes 1 and 2), while very unradiogenic neodymium is found in East Antarctica (down to ε_{Nd} = -50 for the old cratons identified above, annexes 1 and 2). Pb and Sr isotope ratios record highly radiogenic values in East Antarctica, and unradiogenic values in West Antarctica (annexes 1, 3, 4, 5 and 6).

B. South America

1. General geology

South America can also be divided into two major geomorphology-geological regions. The first corresponds to the Andean Chain, and the second to the South American shield partly covered by younger sediments.

a. Andean Chain

Argentinian Fuegian Andes (Southern Patagonia)

The Argentinian Fuegian Andes can be divided into seven stratigraphic units organized from south/southwest to north/northeast (Olivero and Martinioni, 2001). The basement rocks (Paleozoic-Jurassic) are composed of schists and amphibolites and are unconformably overlain by the Lemaire Formation formed during extensional tectonism (upper Jurassic). This formation comprises rhyolites, basalts, slates, acidic volcanic breccias, tuffs, conglomerates, and turbidites (Olivero and Martinioni, 2001). The Yahgan-Beauvoir formations (Lower Cretaceous) formed in a post-rift tectonic context and included black mudstones, andesitic volcaniclastic turbidites, and tuffs. The Cerro Matrero Formation (Late Cretaceous) marks the tectonic inversion and the beginning of the uplift of the Argentinian Fuegian Andes generating the molasses deposits of the Rio Claro Formation (Paleocene). The Despedida Group (Eocene) corresponds to fold and thrust belts deposits overlain by the Cabo Pena Formation (uppermost Eocene-earliest Oligocene; Olivero and Martinioni, 2001).

Patagonia and Pampa loess basins

Patagonia is the southernmost part of the Andes located south of 40°S. In term of geomorphology, this area can be divided into two parts: the Andean mountains located along the western and southern coasts (previously described), and loess basins in the central part and the Atlantic coast. The loess basin includes Patagonia and the Pampa area located on the South American Shield. The Pampa basin is mainly made up with reworked material from the Andes. The provenance of the loess is however debated. The first hypothesis proposes the Puna Altiplano as the source of loess material (Sayago et al. and references therein, 2001). The second hypothesis suggests that this loess is transported from the south and southwest Andes by vertical advection of fine material at high altitude and by strong wind transport of sandy material over short distance (Sayago et al., 2001). However, Sayago et al. (2001), explained that the morphology and loess structures (such as dunes) rather suggest a transport by winds from the south and southeast, which is more consistent with the second hypothesis.

b. South American Shield and sediment cover

The South American Shield comprises Pre-Cambrian crystalline rocks. It is exposed to the surface over wide areas: the Guyana Highlands, the Brazilian Highlands, and over a large coastal band from the Parana River to the north of the San Francisco River (figure 29). This Pre-Cambrian shield is covered by Paleozoic to Cenozoic sedimentary and volcanic rocks (Clapperton, 1993).

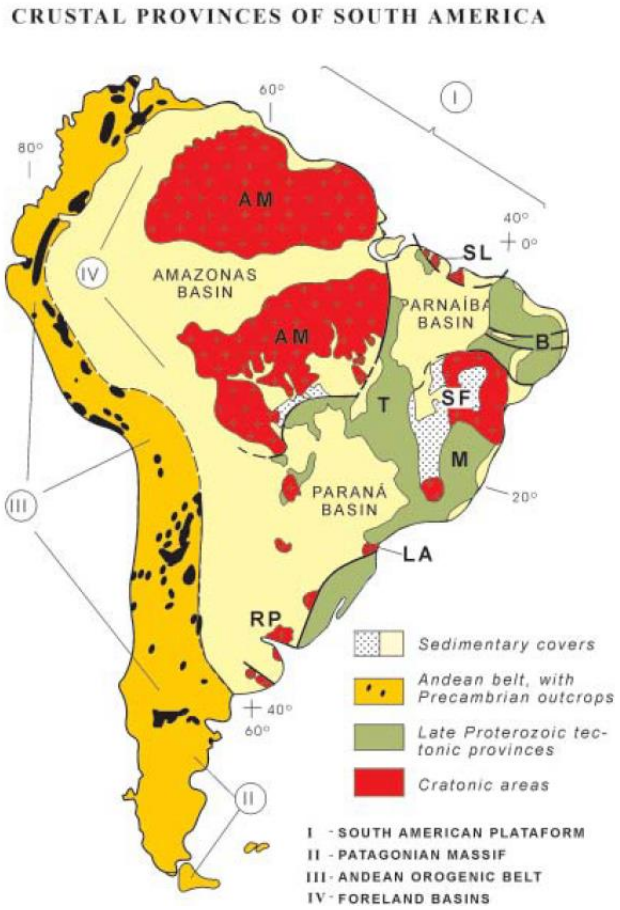

Figure 29: Structural map of the South America (Cordani and Sato, 1999); AM: Amazonian Craton, SL: Sao Luis Craton, SF: Sao Francisco Craton, LA: Luiz Alves Craton, RP: Rio de la Plata Craton, B: Borborema Province, T: Tocantins Province, M: Mantiqueira Province.

The Guyana Highlands and Northernwestern Brazilian Highlands

The Guyana Highlands and the northwestern part of the Brazilian Highlands constitute the Amazonian Craton, formed of 6 major geological provinces oriented NW-SE (Engler, 2009). (1) The Maroni-Itacaiunas Province (2.25-1.95 Ga) corresponds to the northernmost province and is located along the Guyana coast. It is mainly composed of metasedimentary and metavolcanic units associated with granite-greenstone terrane (greenschists to amphibolite facies), granulite facies rocks, gneiss-migmatites terranes, and granitoid plutons (Engler, 2009). (2) The Central Amazonian Province (older than 2.3 Ga) is located south of the Maroni-Itacaiunas Province. This province corresponds to high-grade metamorphic terranes, granite-greenstone belt sequences, granitoids, ultramafic intrusions, gneiss, amphibolite, metavolcano-sedimentary sequences, and mafic dykes (Engler, 2009). (3) The Venturi-Tapajos Province (1.95-1.8 Ga) is located west and south of the two previous provinces. It is mainly composed of calc-alkaline granitoids. It also contains calc-alkaline and alkaline to intermediate volcanic

rocks, mafic dykes, and a sedimentary platform cover. (4) The Rio Negro-Juruena Province (1.8-1.55 Ga) is located Southwest of the Venturi-Tapajos Province. It is composed of volcano-sedimentary sequences, felsic plutonic-gneiss and granitoids, molasses platforms and marine sediments from the Mesoproterozoic to the Mesozoic. (5) The Rondonian-San Ignacio Province (1.55-1.3 Ga) is located southwest of the Rio Negro-Juruena Province and is only south of the Amazon at the westernmost area of the Brazilian Highlands. It is composed of granite-migmatite terranes, granulitic rocks, metavolcano-sedimentary sequences, intrusive rocks, and sedimentary sequence associated with alkaline basalts. (6) The Sunsas Province (1.25-1.0 Ga) is exposed over a very small area compared to the other provinces and located in the southwest of the Brazilian Highlands. It is composed of metavolcano-sedimentary sequences and granitoids (Engler, 2009).

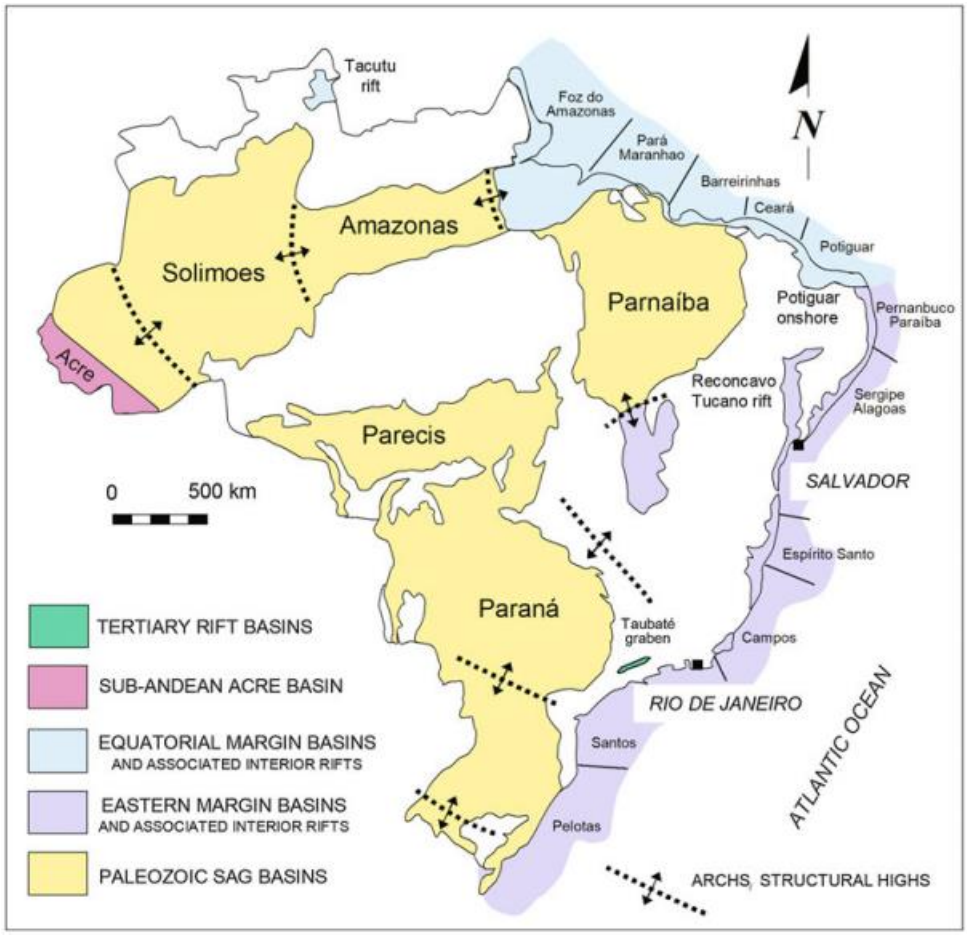

Figure 30: *Sedimentary basins of Brazil (De Alkmim, 2015)*

This wide craton is not exposed in the Amazon River depression which separates the Brazilian Highlands from the Guyana Highlands. This depression includes two sedimentary basins: the Solimoes and the Amazonas Basins (figure 30). These two basins have similar lithological properties. In fact, the topographic high separating the two basins is covered by

Paleozoic sedimentation. Paleozoic sediments are exposed at the rim of the Amazonian Basin, while its central part mainly corresponds to quartzo-kaolinitic Cretaceous sediments (Clapperton, 1993; Roulet et al., 1998; Vital and Stattegger, 2000; Rossetti et al., 2005). Scarce Miocene and Pleistocene-Holocene fluvial deposits are present (Rossetti et al., 2005). In the Salimoes Basin, the Cenozoic sediments cover wider areas, especially in the western part of the basin. They consist of sandstones composed of weathering resistant minerals, sands composed of micas (muscovite, chlorite, biotite) and quartz in variable proportions, and some rare siltstones (Rossetti et al., 2005). In both basins, intrusive Permo-Triassic magmatic rocks are present, although not exposed in the Amazonas Basin (Rossetti et al., 2005).

Southern Brazilian Highlands and Southeast Brazilan Coast

Smaller cratons are surrounded by large orogenic belt areas in the South and southeast of the Amazonian Craton (Cordani and Sato, 1999; Engler, 2009). The Sao Luis Craton (2.2-2.1 Ga) is located south of the Amazon River mouth. This area is also extensively covered by sediments of the Paleozoic Parnaiba Basin and thus the basement is poorly exposed. It is composed of Paleoproterozoic granite-greenstone terrain (tonalites, trondjhemites; Engler, 2009; De Alkmim, 2015).

The Sao Fransisco Craton is separated from the Amazonian Craton by the Brazillia Fold Belt to the west and by the Paranaiba sedimentary basin to the north. This craton contains rocks from 3.4 Ga to 1.2 Ga mainly similar to the Amazonian Craton, including charnockites, tholeiitic volcanic rocks, chemical sediments, gneisses of the amphibolite facies, migmatites, granitoids and associated greenstone belts, flysch deposits, mafic dykes, and Paleo to Mesoproterozoic sediments (pelitic and carbonated sediments; Engler, 2009).

The Borborema Province corresponds to the easternmost part of South America and is located north of the San Francisco Craton (figure 29). This orogenic belt is composed of various basement massifs covered by Proterozoic metasediments largely intruded by Neoproterozoic granites (De Alkmim, 2015). The basement massifs correspond mainly to orthogneisses (from quartz diorite to granite), but meta-ultramafics, metagabbros, amphibolites, and metasediments are locally important (Neves, 2003).

The Parnaiba Basin is located on the northern Brazilian coast (figure 30). It is surrounded by the Amazonian Craton to the West, the Tocantin Province and the San Fransisco Craton to the south, and the Borborema Province to the east. This sedimentary basin is composed of sediments deposited since the Silurian (conglomerates, sandstones). Mesozoic

sediments are fine-grained sandstones and clays. Triassic and Early Jurassic aeolian sandstones are largely intruded by tholeiitic basalts (Paz et al., 2012).

The Tocantin Province is located between the Amazonian and San Fransisco Cratons (figure 29). This orogen is mainly composed of three Neoproterozoic fold belts: the Araguaia, Paraguay, and Brazilia (Fuck et al., 2014). The Brazilia belt is exposed along the western edge of the San Francisco Craton. It is composed of a thick continental margin sequence, ophiolite fragments, and a large juvenile magmatic arc (Fuck et al., 2014). The thick sedimentary sequence has been heterogeneously metamorphosed from granulite facies to unmetamorphosed facies (Pimentel et al., 2011). This sequence includes a high proportion of quartzites (from quartz-rich to micaceous), micaschists (sometimes chlorite-rich), interlayered carbonated rocks, diatomite, phylites, calcschists, and metapelites (Pimentel et al., 2011). The Araguaia belt is located in the Northern part of the Tocantin Province. It corresponds to metamorphosed psamitic and pelitic sequence with minor chemical sediments, mafic and ultramafic rocks (Moura and Gaudette, 1993). The Paraguay belt is located south of the Amazonian Craton, and is exposed west of the Parana Basin (D'el-Rey Silva et al., 2016). It is composed of metamorphosed Neoproterozoic strata (Nogueira et al., 2007) that can be divided into the Cuiaba Group, the Puga formation, the Araras Group, and the upper Paraguay Alto Group (McGee et al., 2015). It includes pelites, diatomite, siliciclastic rocks, and carbonates (Barros et al., 1982; McGee et al., 2015).

The Mantiqueira Province is located along the southeastern coast of South America between the San Fransisco and the Rio de la Plata Craton (figure 29). It is largely covered by Phanerozoic sediments in the southwestern part of the province and it is mostly exposed along the coast and in the northeast (Almeida et al., 1981). In this northeast part, old basement reworked during the upper Precambrian forms most of the outcrop area. This basement can be divided into three massifs: Pelotas, Joinville, Guaxupé Massifs.

The last structure corresponds to the Parana Basin, located south of the South American Shield. It includes sediments from the Late Ordovician to the Late Cretaceous (Horn et al., 2014, Journal of South American Earth Sciences) that can be divided into six depositional sequences (Milani and Ramos, 1998; Milani et al., 2007). These formations are mainly detrital with minor coal and ash deposits (Cagliari et al., 2014; Horn et al., 2014). Interlayered basalts are also present in most of the formations, but a large volcanic pile occurs in the Upper Jurassic to Lower Cretaceous sequence (Milani and Ramos, 1998). It corresponds to voluminous

extrusion of mainly basic tholeiitic basalt with minor acid rhyolites and rhyodacites (Waichel et al., 2012).

2. *Impact of climate on clay mineralogy and isotopic composition*

The geographical distribution of clay mineralogy is strongly linked to past climate and to the composition of the parent-rocks. However, drastic modifications of clay mineral formation driven by climatic condition can be excluded at the studied timescale (<40 ka). Whatever, the important rainfall over the Amazon watershed generates a lot of chemical weathering, and thus, the final product of the chemical weathering (i.e. kaolinite) is clearly dominant in this area (up to 100% at the Amazon River mouth, Guyot et al., 2007; Bayon et al., 2015). South of this Amazon region, the high content in volcanic rocks, and particularly basalts, explain the smectite found over this area (Petschick et al., 1996). Because of the arid conditions over Patagonia and Pampa, it is also possible to find illite and minor amounts of chlorite (Campodonico et al., 2016). However, smectite is dominant in these two regions, as shown by Khondoker et al. (2018).

The isotopic composition of South America can also be regarded as controlled by two regions (see annex 1 for detailed references). The Andes and Patagonia present radiogenic Nd (annexes 1 and 2) and unradiogenic Pb (annexes 1, 4, 5 and 6) and Sr isotopes (annexes 1 and 3). In contrast, the South American Shield is characterized by unradiogenic to strongly unradiogenic Nd isotopes (annexes 1 and 2), and radiogenic to strongly radiogenic Pb (annexes 1, 4, 5, and 6) and Sr isotopes (annexes 1 and 3). In South America, climatic conditions play a key role in the Sr and Pb isotopic composition of weathering products. Indeed, strong rainfalls occurring in equatorial and tropical areas strongly changes isotopic ratios of sediments compared to the source rock (see part I.D of this chapter for details on the impact of chemical weathering on these ratios). Consequently, changes in these isotopes could reflect changes in both chemical weathering and provenance.

C. Africa

The African continent is characterized by rock formations from the first billion years of Earth's history to today, and by tropical to temperate climate with arid and wet conditions.

1. *General geology*

Archean cratons outcrop in Western Africa, Congo and in southern Africa. They are constituted of migmatitic gneiss (tonalities, trondhjemites, granodiorites) separated by greenstone belts and intruded by granitoid plutons. Most of these rocks are metamorphosed

from amphibolite to granulite facies. Later Proterozoic tectonic events (i.e., Panafrican orogenesis) outcrop all along the coastline from the western part of the Gulf of Guinea to Southern Africa. They also comprise a major part of the Western Sahara, and in the Great Lakes region. These rocks are mainly flysch deposits associated with volcanic formation, and intruded by granitic pluton. Magmatism for the last ~40 Myr forms a large igneous province in the Great Lake region.

The Early Paleozoic is marked by the end of the Panafrican orogenesis. Many sedimentary basins are formed in northern Africa and in the Congo depression where sandstones with high content in quartz occurred. Marine deposits are visible in the north of Africa. The Middle Paleozoic is marked by fluvial-glacial deposits. The Paleozoic rocks outcrop in the Sahara, South Africa, and around the Great Lakes.

The Meso-Cenozoic is characterized by sedimentation with fluviatile and lacustrine deposits in the depressions, and by a strong aeolian activity over huge areas. In northern Africa, carbonated deposits are formed during high sea level periods. This period is also marked by a few magmatic phases with the formation of magmatic provinces in the African rift.

2. *Impact of climate on clay mineralogy, and isotopic composition*

Northern Africa is the largest source on Earth of mineral dust (Scheuvens et al., 2013). This area is known for its important input of aeolian dusts to the Equatorial Atlantic (Caquineau et al., 2002). However, the signature of these dusts is likely overprinted by more proximal sources. The most important vectors of sediment to the South Atlantic in Africa are equatorial rivers (including the Condo River) and Namibian loesses (Petschick et al., 1996). The equatorial rivers mostly deliver poorly crystallized smectite, and kaolinite, while Namibian deserts mostly delivers illite (Bremmer and Willis, 1993; Petschick et al., 1996). The isotopic composition of these sources are characterized by unradiogenic Nd, and radiogenic Sr and Pb isotopes (annexes 1 to 6).

D. Circumpolar islands

Along the ACC pathway, a few volcanic islands and plateau are present. Here, we examine the main structures along this pathway.

1. *Kerguelen plateau*

The Kerguelen Plateau is a large (1,250,000 km²) volcanic province induced by the activity of a mantle plume that started at least 120 Myrs ago (Wasilewski et al., 2017) and that is mostly composed of basaltic rocks (Frey et al., 2000). Most of the southern Kerguelen Plateau

formed at ~110 Ma while the northern Kerguelen Plateau formed during the Cenozoic (Frey et al., 2000). |The Kerguelen Plateau can be divided into 4 parts: the South, Central and North Kerguelen Plateau, and the Elan Bank, forming an East-West topographic high on the western flank of the plateau (Frey et al., 2000). Even though these 4 parts present some differences, they are considered as neglictible compared to the difference between the Kerguelen Plateau and Antarctica. Consequently, their geologies and histories is not described in detail in this PhD. The Kerguelen Achipelago that was formed ~30 Myrs ago. It is mostly composed of basalts, but a few trachytic and phonolitic rocks are identified (especially in the south of the archipelago of this plateau; Nougier, 1970; Gautier et al., 1990). In addition, the volcano plutonic complex of Rallier du Baty in the southwest of the island is mostly composed of rhyolitic and trachytic rocks (Nougier, 1970; Gautier et al., 1990). Weathering of the Kerguelen Plateau mostly delivers smectite (up to 90%) associated with minor illite and chlorite (Borchers et al., 2011). The WRAS normalised rare earth element (REE) composition of such volcanic areas is generally enriched in heavy rare earth elements (HREE) compared to light rare earth elements (LREE). The isotopic signature of the Kerguelen Plateau is characterized by radiogenic neodymium ($\varepsilon_{Nd} > -5$; Dossa and Rama Murphy, 1980; Gautier et al., 1990; Weis et al., 1993; Jeandel et al., 2007), and unradiogenic strontium ($^{87}Sr/^{86}Sr < 0.71$; Dossa and Rama Murphy, 1980; Gautier et al., 1990; Weis et al., 1993).

Climate over the Kerguelen Islands is mainly polar to subpolar, and particularly windy. However, most of the plateau being under the sea level, rock alteration is mostly driven by seawater. Under such conditions (i.e., basaltic area), most of the clay minerals formed are smectites. The isotopic composition is radiogenic Nd and unradiongenic Sr.

2. Scotia Sea and South Sandwich Islands

The Scotia Sea is located southwest of the South Atlantic. It is delimited to the west by the Drake Passage. This area corresponds to the narrowest Antarctic Circumpolar Current pathways, being restrained by the southern tip of the South America and the Antarctic Peninsula. To the east, the Scotia Sea is delimited by a subduction zone marked by the South Sandwich Islands and the South Sandwich Trench. These islands correspond to volcanic islands formed of calc-alkaline series rocks. However, due to the Early stage of development of the arc, the poorly evolved rocks from this magmatic series are dominant (i.e. basalts and basaltic andesite). To the orth, the Scotia Sea is delimited by Southern Patagonia, the North Scotia Ridge and South Georgia Island. Southern Patagonia and South Georgia Island are formed of rocks of similar composition (see Andean chain description). To the south, the Scotia Sea is separated

from the Weddell Sea by the Antarctic Peninsula, and the South Scotia Ridge, that are described in the section on Antarctica.

The clay mineral produced in the area are mostly well crystalized smectite (Petschick et al., 1996) and few chlorite. In addition, a lot of chlorite brought from more distal sources by the oceanic currents (mostly ACC) are deposited and transit through the Scotia Sea, as shown by the analyses of bottom sediments from the area (Bout-Roumazeilles, personal communication). The isotopic composition is radiogenic Nd ($\varepsilon_{Nd} > -5$), unradiogenic Sr ($^{87}Sr/^{86}Sr$ ~0.703 for the volcanic islands, $^{87}Sr/^{86}Sr$ ~0.706 and ~0.703 for Patagonia and the Antarctic Peninsula, respectively; and $^{87}Sr/^{86}Sr$ ~ 0.710 for marine sediments in the Scotia Sea due to additional distal sources). The Pb isotopes range from low to moderate isotopic ratios with the Scotia Ridges showing the lowest isotopic ratios, and the Patagonia showing the highest.

Chapter 3. Material and Methods

I. Material

This study is based on sediment samples from three sediment cores: one in the South Atlantic, and two east of the Kerguelen Plateau. The sediment core from the South Atlantic is the MD07-3076Q (44°9.2'S, 14°13.7'W) recovered by the French Vessel *Marion Dufresne* in 2007 on the eastern flank of the Mid-Atlantic Ridge at 3770 m depth. The core chronology is based on planktonic foraminifer radiocarbon dates (37 measurements for the studied interval) and stratigraphic control points (Skinner et al., 2010, 2013, 2014; Gottschalk et al, 2015b). A total of 221 sediment samples were used from this core. Today, LCDW flows over the site. From the seafloor to the surface, the water masses observed in the water column above the study site are the LCDW, NADW, UCDW, and intermediate and surface waters. In nearby deeper oceanic basins, the AABW is also found, and it is thought that particles transported by this bottom water can reach our site by advection and mixing with the LCDW.

The sediment cores located east of the Kerguelen Plateau are the cores MD12-3396Q (latitude: 47° 43.88' S, longitude: 86° 41.71' E, water depth: 3630 m) and MD12-3401Q (latitude: 44° 40.76' S, longitude: 80° 23.62' E, water depth: 3445 m). They were recovered in 2012 during the IndienSud-2 cruise of the French Research Vessel (RV) Marion Dufresne. These sediments core were undated before the PhD. A total of 331 and 409 sediment samples were used from the sediment core MD12-3396Q and MD12-3401Q, respectively. In this thesis, only samples from sediment core MD12-3396Q are presented. Data from core MD12-3401Q and grain-size distribution data from core MD12-3396Q will be presented in a paper in collaboration with Alain Mazaud and Elisabeth Michel. Because these collaborators are the main authors of the paper in prep., and because the paper is still under review, this work is not presented in this manuscript.

II. Methods

A. Preliminary treatment

As explained in chapter 2 part I.D, carbonates may affect the detrital fraction and disrupt clay mineralogy analyses. Consequently, carbonates need to be removed. For that purpose, the sediment is placed in an Erlenmeyer flask with 0.1N HCl solution and is homogenized using a magnetic agitator. After ~2 hours, the acidity of the solution is checked, and HCl (30%) is added until the pH is close to 1 to ensure that all the carbonates are removed. The sediment is then transferred to glass beak and deflocculated by repeated washes using pure water.

B. Grain-size distribution analyses

Grain-size distribution analyses are performed immediately after carbonate removal using an aliquot of the carbonate-free sediment. These analyses were performed using a Malvern Mastersizer 2000 laser (0.02-2000 µm) following standard protocols (Montero-Serrano et al., 2009). The clay-size fraction corresponds to the proportion (in volume) of particles with a diameter smaller than 2 µm, the cohesive silts correspond to the 2 to 10 µm diameter particles, the sortable silts correspond to 10 to 63 µm diameter particles, and the sand fraction to the particles coarser than 63 µm.

C. Clay mineralogy analyses

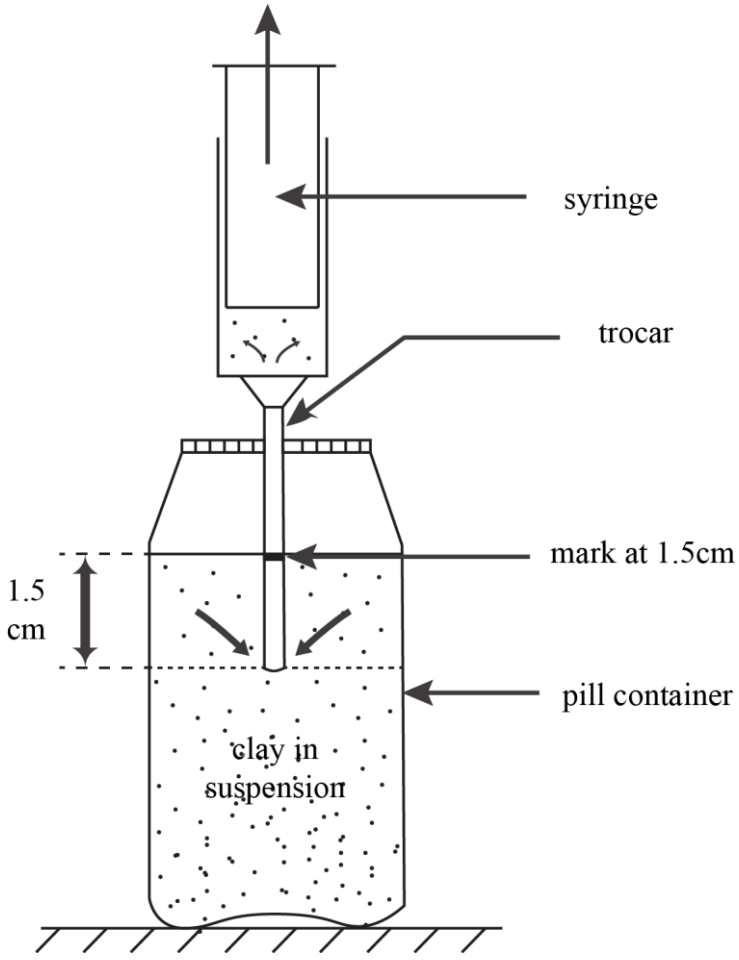

Figure 31: Scheme showing the protocol to extract the size fraction below 2 µm (redrawn from Holtzapfell, 1985).

The clay-size fraction (< 2µm) was isolated by differential settling according to Stoke's Law. Deflocculated sediment is homogenized for 30 seconds using electronic micro homogenizer directly into the beaker. After 1 hour 15 minutes of settling, the upper 1.5 cm is extracted using a trocar (figure 31). This fraction was then concentrated by centrifugation (40

minutes, 3500 rotation per minute) and an aliquot was placed on glass slides. X-ray diagrams were obtained using a Bruker D4Endeavor (standard 30 kV and 30 mA). Each sample is run three times between 2.49 and 32.5°2θ: (1) dried sample, (2) glycolated sample (12 hours in ethylene glycol), and (3) heated sample (490°C for 2 hours).

Each clay mineral is characterized by a diffraction angle obtained in °2θ that is further converted in Angstrom (Å), and appears as peaks on XRD diagrams. This different diffraction angle is caused by the distance between the layers of the clay minerals that is specific to each species of clay. Other peaks can also be observed on XRD diagrams, such as the peaks of quartz, amphiboles, or feldspars. All these peaks are characterized by a first peak, called the main peak, which usually presents the highest intensity, and by harmonics. The proportions of the clay minerals are calculated by determining the area below the first peak according to their crystallographic characteristics (Brown, 1980).

Smectite is characterized by a main peak at 14-15 Å on the air-dried samples that expands at 17 Å after ethylene glycol saturation and collapses at 10 Å after heating. Illite is characterized by basal peak at 10 Å on the 3 runs. Kaolinite and chlorite are measured on their main peak at 7-7.2 Å and further distinguished using pseudo void deconvolution of the kaolinite/chlorite doublet at 3.54/3.58 Å. All measurements and semi quantitative estimations are processed using the McDiff software (Petschick, 2000). The formula used for the calculation of the clay mineral proportion are detailed below:

$$\%smectite = \frac{Area(smectite\ 17Å)}{\sum terrigenous} \times 100$$

$$\%illite = \frac{Area(illite\ 10Å)}{\sum terrigenous} \times 100$$

$$\%kaolinite = Area\ (kaolinite + chlorite) \times \frac{Area(3.58Å)}{Area(3.58Å) + \mathrm{Area}(3.54Å)} \times 100$$

$$\%chlorite = Area\ (kaolinite + chlorite) \times \frac{Area(3.54Å)}{Area(3.58Å) + \mathrm{Area}(3.54Å)} \times 100$$

In addition to the mineral proportions, other parameters can be measured. The index of Esquevin (Esquevin, 1969) is calculated by using the ratio between the intensity of the illite at 10 Å and at 5 Å (illite 5Å/10Å). This index gives information on the composition of the illite that is derived mostly derived from two micas: muscovite and biotite. Ratios below 0.2 indicate that the illite is derived from biotite, whereas ratios above 0.5 indicate an illite derived from

muscovite. The crystallinity of the clay minerals can also be measured by using two methods: the width at half height, and the method of the integral breath (Petschik et al., 1996). In order to allow comparisons with the work of Petschik et al. (1996) in the South Atlantic, the method used in this work is the method of the integral breath. Usually, chlorite and kaolinite are well crystallized, whereas smectite and illite present high range of crystallinities. Consequently, only the crystallinities of smectite and illite are relevant and calculated.

D. Isotopic, trace and rare earth elements

1. *Preliminary procedure*

Isotopic compositions, and trace and rare earth elements have been measured onto 2 sediment cores: the cores MD07-3076Q and MD12-3396Q. These measurements have been determined on isolated grain-size fractions. In both cores, the clay size fraction (0-2 μm) has been measured, whereas additional size fractions have been measured in the South Atlantic core (MD07-3076Q). Indeed, results from grain-size distribution analyses show the occurrence of 2 grain-size modes that vary through time. Consequently, isotopes as well as trace and rare earth elements have also been measured on these grain-size modes in this sediment core.

The clay size fraction (0-2 μm) was isolated by repeated extractions by settling (at least 50 per sample) until no sediment is recovered after concentration by centrifugation. The coarse fraction (20-40 μm in the old section of the core before 11.5 ka cal BP, noted hereafter as ka, and 20-32 μm after 11.5 ka) was isolated by sieving the clay-free residue. The 2-20 μm grain-size fraction is thus the residue of clay separation and coarse fraction sieving. An aliquot of 10 to 150 mg (depending of the sediment quantities available) was then used for chemical procedures.

2. *Trace and rare earth elements*

The HCl solutions are dried at 120°C, and dissolved in 5% HNO_3. An aliquot was taken to obtain a dilution factor close to 5000. For example, to obtain 10 mL of solution (~10 g), 2 mg of original dry sediment are used. Then, the trace element and REE measurements are determined by ICPMS.

3. *Radiogenic isotopes*

Chemical and isotopic measurements were performed at the Faculty of Science of the Vrije Universiteit, Amsterdam. Sediment was digested in closed Savillex^{TM} Teflon beakers using a mixture of concentrated HF and HNO_3 (~2/3 and 1/3, respectively) for a few days at 120°C. After digestion, samples were dried out and re-dissolved in ~6.5N HCl to remove

fluorides. Nd, Sr, and Pb were purified using conventional ion chromatography. Pb isotopes were processed first and purified using AG-X8 200-400 mesh resin. Light rare earth elements (LREE) were isolated using true-spec resin medium (Eichrom^{TM}, 100-150 µm mesh size) and Nd was eluted from the LREE fraction using LN-resin (Eichrom^{TM}, 50-100 µm mesh size). Sr was recovered using a column containing Sr-Spec resin. Nd and Pb measurements were performed by bracketing using respectively CIGO and NBS987 standards on Thermo Scientific Neptune multi-collector inductive coupled plasma-mass spectrometer (MC-ICPMS), whereas Sr measurements were performed on a thermal ionization multi-collector-MS (TIMS). Due to relatively low content of Nd in some of the coarse grain-size fraction (20-32/40µm), Nd measurements of these fractions were also performed by TIMS.

III. Quality control of the data

In this part, few results will be shown and discussed to assess the quality of the data produced. Data considered as contaminated or biased will be excluded and not used for interpretations.

A. Clay mineralogy

The clay mineralogy analysis is based on the visual interpretation of XRD diagrams. To limit any potential bias involved, all the diagrams need to be interpreted by the same person using the same method for all the samples of one study.

In addition, XRD analysis can be disrupted by amorphous minerals that can hardly be removed from the crystalline fraction, such as volcanic glass or diatoms. These minerals, when abundant, can overprint the signal preventing from accurate identification and quantification of the clay association. Sediments from the core MD12-3396Q and MD12-3401Q are located both in the Circum-Antarctic Opal Belt described by Diekmann (2007), and on the Eastern Kerguelen Plateau volcanic province (Dezileau et al., 2000; Borchers et al., 2011). Due to the abudance of opal and of volcanic materials, the rather bad quality of XRD diagrams for these two cores prevents from discriminating accurately chlorite from kaolinite. As a result, the respective proportion of chlorite and kaolinite in this sector is not calculated.

B. Grain-size distribution

The grain-size distribution instrument is calibrated by measuring standards (calibrated spheres). However, such calibration is designed for the study of spherical particles, and some biases may occur when measuring non-spherical particles such as layered clay minerals. In addition, small particles (< 10 µm) are slightly underestimated by the instrument when

measuring small-size standards. As a consequence, when interpreting the data it is necessary to keep in mind that: (1) the flat shape of clay minerals may bias the analysis, (2) <10 µm particles may be slightly underestimated by the instrument.

C. Trace elements

The accuracy of trace element measurements was assessed by measuring blanks, and standards. MAG-1 sediment standards and blanks were processed along with the digestion of sediment in the clean lab as quality controls. Additional geochemical standards DCS and BCR-2 and BHVO2 were also measured.

D. Radiogenic isotopes

The quality of the data produced when measuring isotopes is controlled by measuring standards and blanks. Two types of standards are processed: reference standards designed for the isotopic measurements, and rock/sediment standards treated simultaneously to the samples using the same chemical procedure. Standards used for the isotopic measurements depend on the target element. CIGO (internal standard) and Jndi-1 (Tanaka et al., 2000) standards are used for neodymium isotopes, NBS-987 for strontium isotopes, and NBS-981 for Pb isotopes. The standard processed throughout the PhD is the standard MAG-1. This sample has been chosen because this standard is a deep marine sediment that has similar properties than our samples. Overall the measurements of the standards were consistent with the reference values, as shown in table 1 to 6.

VU code	$^{87}Sr/^{86}Sr$	2σ	$^{143}Nd/^{144}Nd$	2σ
X331	0,722595	0,000012	0,512076	0,000004
X332	0,722724	0,000012	-	-
X557	0,722647	0,00001	-	-
STD	-	-	0,512053	0,000007
Y263	0,72269	0,000009	0,512068	0,00001
Y396	0,722646	0,000014	0,512056	0,000022
Y570	0,722693	0,000008	0,512049	0,000006
Y635	0,722876	0,00001	0,512052	0,000008
REFERENCE VALUE min	0,722638		0,512054	
REFERENCE VALUE mean	0,722806		0,512081	
REFERENCE VALUE max	0,722973		0,512107	
Repeatability				
standard deviation	0,000090		0,000011	
mean	0,722696		0,512059	

Table 1: Sr-Nd isotopic measurements and repeatability calculations of MAG-1 standard. σ corresponds to the internal error.

VU code	$^{206}Pb/^{204}Pb$	2σ	$^{207}Pb/^{204}Pb$	2σ	$^{208}Pb/^{204}Pb$	2σ
X332	18,8593	0,0005	15,6519	0,0007	38,7832	0,0010
X557	18,8774	0,0005	15,6536	0,0008	38,6975	0,0014
REFERENCE VALUE min	18,861		15,6518		38,7968	
REFERENCE VALUE mean	18,8612		15,6539		38,8034	
REFERENCE VALUE max	18,8614		15,656		38,81	
Repeatability						
standard deviation	0,012806		0,001157		0,060607	
mean	18,868312		15,652761		38,740314	

Table 2: *Pb isotopic measurements and repeatability calculations of MAG-1 standard. σ corresponds to the internal error.*

date of measurement	$^{143}Nd/^{144}Nd$	2σ
10/11/2016	0,511334	0,000014
20/03/2017	0,511328	0,000004
20/03/2017	0,511332	0,000005
21/03/2017	0,511321	0,000005
21/03/2017	0,511319	0,000005
06/04/2018	0,511333	0,000004
06/04/2018	0,511326	0,000004
09/04/2018	0,511333	0,000005
14/04/2018	0,511332	0,000003
Repeatability		
standard deviation	0,000006	
mean	0,511329	

Table 3: *Measurements of CIGO Nd standard. σ corresponds to the internal error.*

date of measurement	$^{143}Nd/^{144}Nd$	2σ
06/11/2017	0,512105	0,000012
06/04/2018	0,512099	0,000004
06/04/2018	0,512093	0,000004
09/04/2018	0,512097	0,000004
09/04/2018	0,512091	0,000005
14/04/2018	0,512099	0,000006
REFERENCE VALUE	0,512115	
Repeatability		
standard deviation	0,000005	
mean	0,512097	

Table 4: *Measurements of JNdi-1 Nd standard. σ corresponds to the internal error.*

date of measurement	$^{87}Sr/^{86}Sr$	2σ
XX/05/2016	0,710250	0,000008
XX/05/2016	0,710249	0,000010
XX/05/2016	0,710243	0,000011
XX/05/2016	0,710240	0,000007
17/11/2017	0,710261	0,000008
20/11/2017	0,710237	0,000009
21/11/2017	0,710264	0,000005
26/11/2017	0,710264	0,00001
12/12/2017	0,710254	0,000007
08/04/2018	0,710249	0,000005
10/04/2018	0,710247	0,000007
18/04/2018	0,710239	0,000009
19/04/2018	0,710259	0,000008
Repeatability		
standard deviation	0,000009	
mean	0,710250	

Table 5: *Measurements of NBS987 Sr standard. σ corresponds to the internal error.*

sample	Sr (pg)	Nd (pg)	Pb (pg)
X333	447	burnt	31,4
X334	572	burnt	132
X558	524	burnt	519
blk no name	481	15,2	not measured
Y264	400	250000	486
Y397	49	1000	262
Y571	burnt	Nd-150 not measured	72,5
Y636	160	Nd-150 not measured	Pb not processed

Table 6: *Blank measurements from the PhD.*

In addition to standards, total blank are processed and measured using isotopically enriched spikes (solutions of known concentration and known isotopic composition). All the blank measurements are reported in table 6. The blank procedure for the Sr gave variable and high values (up to 572 pg). However, considering the amount of Sr in our samples (2900 ng on average, and up to 11821 ng), these blanks correspond to less than 1/1000 of the value. As a consequence, the isotopic values obtained do not need blank correction. These relatively high blank values for the Sr can result from a combination of factors: (1) the high quantities of Sr in our samples, (2) the proximity of the beakers (opened) when drying down the samples. This second factor result from technical issue linked to the efficiency of the work in the clean lab that was concentrated over few weeks during the PhD. Indeed, 172 Nd and Sr samples, and 142 Pb samples have been processed in ~25 weeks. Similarly, the Pb blanks are high (up to 519 pg in samples series with high Pb concentrations). However, for the sample series with "normal"

Pb concentrations (~40 ppm, blanks X333, X334, and Y571), the blank values are more typical of those routinely measured in the laboratory and range from 31 to 132 pg. Analysed samples contained at least 121 ng of Pb, and 2800 ng on average. Hence no Pb blank correction was required.

A more detailed discussion of potential contamination is presented below.

1. *Pb contamination*

By looking the ICPMS results, it appeared that some samples had an unexpectedly high concentration in Pb (up to 2250 ppm). These high concentrations are found in the coarse grain-size fractions (2-20 μm and 20-32/40 μm), but not in the <2 μm fraction. In addition, the isotopic composition of Pb is characteristic in these two coarse fractions, and there is a relation between concentration and isotopic composition (see figure 32). Such phenomenon can be explained by the occurrence of coarse particles characterized by high Pb concentration. To identify the nature of these particles, scanning electron microscope (SEM) observations were performed in Lille at the LOG. These studies allow the idenfication of Pb-rich particles that correspond to a Pb, Fe, and Cr alloy, evidencing their anthropogenic nature and thus contamination. This alloy derives from the micro-homogenizer used during Early stages of the chemical procedure. This finding means that the Pb isotope measurements of the two coarse grain-size fractions cannot be used to reconstruct provenances. To avoid such problems in the future, it appears necessary to avoid using a micro-homogenizer during the separation of the grain-size fractions.

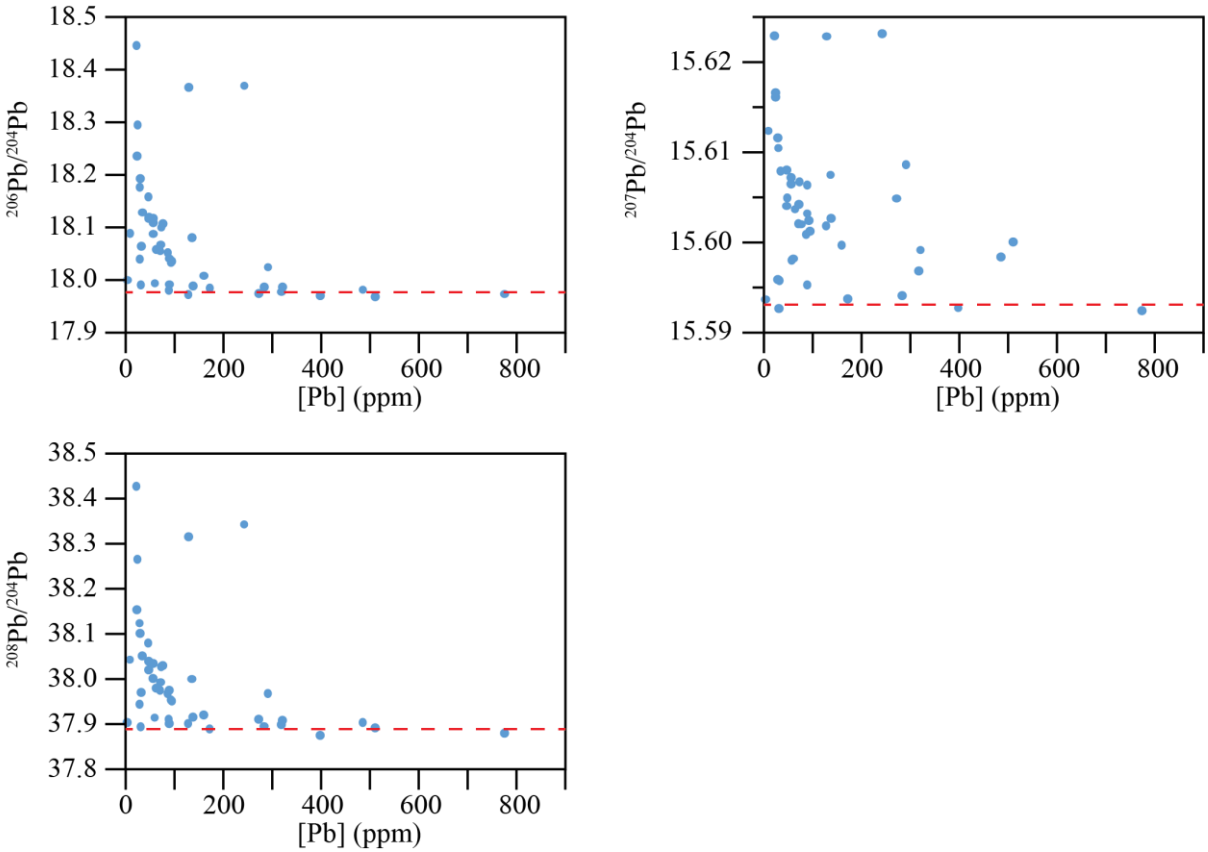

Figure 32: Isotopic composition vs concentration of Pb in the grain-size fractions 2-20 µm and 20-32/40 µm. The red dashed line represent the estimated composition of the micro homogenizer for each isotopic ratio.

To check the validity of the isotopic composition of the clay size fraction, we used the correlation between the concentration and the isotopic composition in the coarse grain-size fraction to calculate the isotopic composition of the micro homogenizer (see figure 32), which gives:

- $^{206}Pb/^{204}Pb \sim 18.0$
- $^{207}Pb/^{204}Pb \sim 15.59$
- $^{208}Pb/^{204}Pb \sim 37.9$

By comparing these values to the isotopic composition of the clay size fraction, we noted that the isotopic composition of our samples varies between two end-members that are not the isotopic composition of the micro homogenizer. In addition, the Pb concentrations of the fine fraction are consistent with what have been observed in marine sediments in the studied area. As a result, we conclude that the clay size fraction is not polluted by the micro homogenizer and can be used for paleoprovenance and paleoclimate reconstructions.

2. *Nd contamination*

When looking at the blank results for Nd isotopes, it appears that the blank procedure was clearly not as good as expected. First, there are no blank results for the series 1 to 3 (X333, X334, and X558, table 6) because the blanks were run as sediment samples instead as blanks. Second, ^{150}Nd spike has been used, but this isotope was not measured in the method used for the analyses due to a misunderstanding. This was caused by the fact that: (1) it was the first blanks the PhD ran on the Neptune, (2) it was the first time that the new operator measured Nd at the VU and communication was not optimum.

The only good blank value measured is the "blk no name" (15 pg, table 6). The highest blank value (250 ng) is an incorrect measurement. This amount of Nd is higher than the average content in classic marine sediments. The small measurement beams indicate that the analysis does not correspond to the actual blank and that most of the ^{150}Nd spike was lost during sample preparation, leading to an incorrect blank determination. Moreover, the isotopic results of the sediment sample processed with this blank are consistent with comparable samples in the same core (see figure 32). In addition, coupled Nd and Sr isotope variations are coherent, as shown on figure 34.

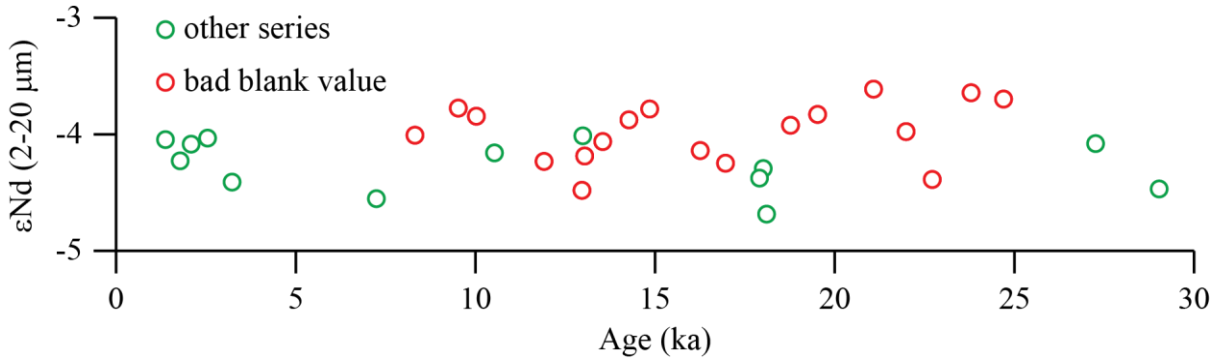

Figure 33: Comparison of Nd isotopic composition of series with bad blank value with others series.

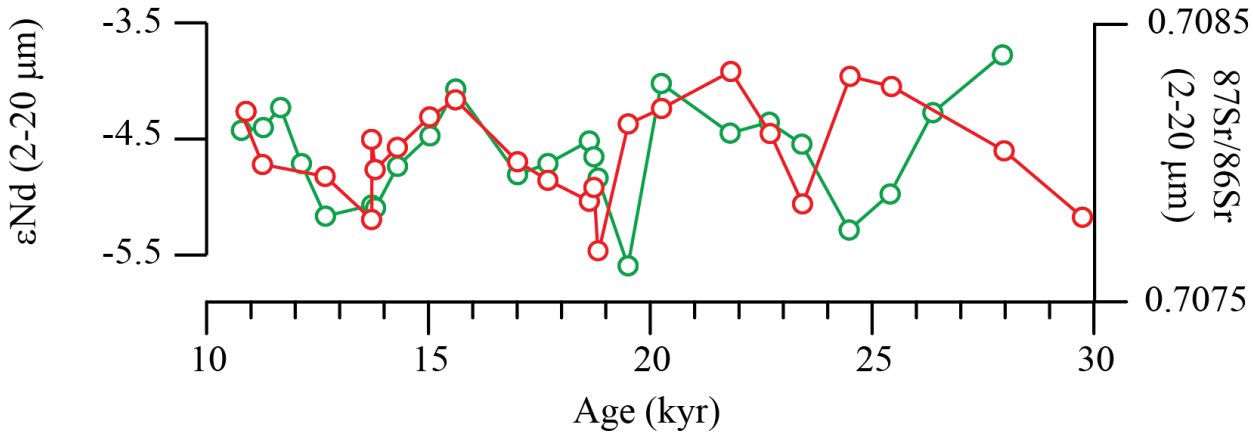

Figure 34: *Comparison of Nd and Sr isotopes results in the 2-20 µm grain-size fraction of core MD07-3076Q.*

Finally, the last high blank (Y397; ~1000 pg, table 6) was due to additional chemical treatment. When loading the Nd samples onto filaments, TaCl was added by mistake. TaCl is usually used to make a ceramic for Sr measurement in order to slow down the evaporation of Sr isotopes during measurements by TIMS. As a result, it was impossible to obtain sufficient Nd evaporation. Consequently, the Nd samples were recovered from the Re filaments. To do so, filaments have been soaked in 10% HNO_3 until the sample is dissolved. Then, the sample was dried down to restart the elution procedure to remove the Re and the Ta from the sample. The Tru-spec columns were used as a clean-up. In order to validate the Nd isotope ratios, 2 duplicates have been made on two samples. These samples were taken from REE pre-fraction collected during the first elution and hence come from the same original sediment sample. The isotopic results are within analytical error (Table 7). Despite the excellent reproducibility, the samples recovered from the filament do not reveal any shift between the LGM and the Holocene, and have a high variability with no apparent link to climatic events. This contrasts with samples from previous measurements that are stable during the Holocene and the LGM, and record a marked shift during the deglaciation (figure 35). Consequently, these values are considered doubtful and are not used in the PhD.

Sample ID	Sample type	$^{143}Nd/^{144}Nd$	SE	Difference
Y387	recovered from the filament	0.512454	0.000005	0.000008
	re-processed duplicate	0.512446	0.000007	
Y393	recovered from the filament	0.512456	0.000005	0.000004
	re-processed duplicate	0.512452	0.000005	

Table 7: *Comparison between samples recovered from the filaments and duplicate from the same original sediment.*

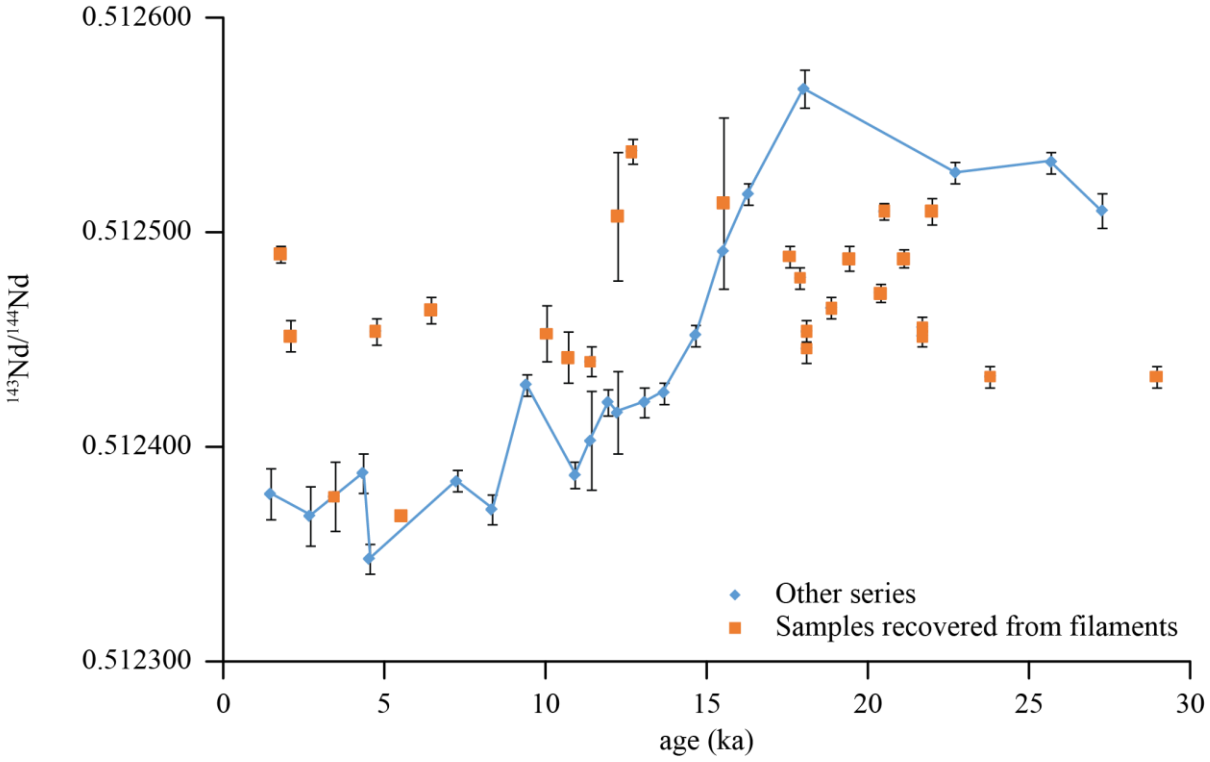

Figure 35: Comparison between isotopic composition of samples recovered from filaments, and isotopic composition of other samples processed normally.

Chapter 4. Radiogenic isotopic and clay mineralogical signatures of terrigenous particles as water-mass tracers: new insights into South Atlantic deep circulation during the Last Termination.

F. Beny[1,2,], V. Bout-Roumazeilles[1], G.R. Davies[2], C. Waelbroeck[3], A. Bory[1], N. Tribovillard[1], M. Delattre[1], R. Abraham[1].*

[1] Laboratoire d'Océanologie et de Géosciences, UMR 8187 CNRS/Univ Lille/ULCO, Cité scientifique, F-59655 Villeneuve d'Ascq, France.

[2] VU University Amsterdam, Department of Earth Sciences, Faculty of Science, De Boelelaan 1085, 1081 HV Amsterdam, The Netherlands.

[3] Laboratoire des Sciences du Climat et de l'Environnement, LSCE/IPSL, UMR 8212 CEA-CNRS-UVSQ, Site de l'Orme des Merisiers, F-91191 Gif sur Yvette Cedex, France

* Corresponding author: beny.francois@gmail.com

Published in Quaternary Science Review. DOI: 10.1016/j.quascirev.2019.106089

Abstract

The past evolution of the Southern Ocean, one of the major components of the climatic system, is still a matter of debate. This study provides new insights into the deep Southern Ocean circulation based on the radiogenic isotopes and clay mineralogical signature of the terrigenous fractions transported by the main deep-water masses to sediments recovered in core MD07-3076Q from the central South Atlantic. This approach successfully permits: (1) provenance identification of the various grain-size fractions (clay, cohesive silt and sortable silt); (2) assignment of each grain-size fraction to a specific water-mass; (3) reconstruction of past changes in the main deep water-mass pathways. These data document the evolution of deep-water masses in the South Atlantic Ocean during the last deglaciation. The Antarctic Bottom Water (AABW) speed and northward extension were maximum at the end of the Last Glacial Maximum (LGM), associated with strong bottom water production in the Weddell Sea, together with a vigorous Lower Circumpolar deep-water (LCDW). In contrast the North Atlantic deep-water (NADW) circulation was weaker than today. The onset of the deglaciation (from 17.5 ka to 15 ka, ~Heinrich Stadial 1, HS 1) was marked by weakening and southerly retreat of the AABW and by an increase of mixing between AABW and LCDW. The speed of the AABW remained at its lowest during the Bølling Allerød (B/A) and the Younger Dryas (YD), and the LCDW slowed and retreated to the south, while the NADW progressively migrated southward, deepened, and strengthened between the beginning of the Bølling Allerød and the Holocene (from ~15 to 10 ka).

Keywords

Last Deglaciation; Paleoceanography; Southern Ocean; South Atlantic; Radiogenic isotopes; Clay mineralogy; Grain-size distribution.

I. Introduction

The Southern Ocean (SO) is a key area for understanding the present and past carbon cycle. Direct observations indicate that the SO is a sink of atmospheric CO_2 today (Le Quéré et al., 2007; Sallée et al., 2012) while it was likely a source of CO_2 to the atmosphere during the deglaciation (Bouttes et al., 2012; Jaccard et al., 2013). Upwelling of CO_2-rich deep-water likely explains most of the CO_2 rise observed during Heinrich Stadials (HS; Ahn and Brook, 2008; Anderson et al., 2009; Fischer et al., 2010; Skinner et al., 2010; Menviel et al., 2014, 2017). Several other processes occurring in the Southern Ocean have also been invoked to explain the deglacial atmospheric CO_2 rise. For example, reduction of biological pump due to reduced iron fertilization (Watson et al., 2000; Wolff et al., 2006; Fischer et al., 2010; Martinez-Garcia et al., 2014); reduced CO_2 solubility due to increased temperature of the ocean (Köhler and Fischer, 2006; Fischer et al., 2010); reduction of sea ice extent (Fischer et al., 2010). As a consequence, the organization and extension of the Southern Ocean deep water-masses (i.e., Atlantic Meridional Overturning Circulation, AMOC; Skinner et al., 2010; Shakun et al., 2012; Toggweiler et al., 2006) were studied, mainly using paleo-hydrological proxies ($\delta^{18}O$, $\delta^{13}C$, ε_{Nd} of sea water, $\Delta^{13}C$; Barker et al., 2009; Vasquez-Riveiros et al., 2010; Skinner et al., 2010, 2013, 2014; Waelbroeck et al., 2011; Gottschalk et al., 2015b). By contrast, the terrigenous particle signal transported by these deep water-masses in the sub-Antarctic Atlantic Ocean remain poorly studied, even though locally it was successfully used to reconstruct the deep ocean circulation dynamical component (Diekmann et al., 2000 – Scotia Sea; Walter et al., 2000 – Scotia Sea and southwest South Atlantic; Kuhn and Diekmann, 2002 – Cape Basin). In this study, we aim to reconstruct the past evolution of deep-water masses (i.e. contribution to sedimentation, vertical and horizontal extensions, and speeds) during the last deglaciation using the signal carried in the terrigenous particles transported by these water masses. Sediment grain-size distribution allows identifying the contribution of distinct oceanic currents (Weltje and Prins, 2007; Weltje, 2012), and reconstructing the speeds of the main deep water-masses (McCave and Hall, 2006; McCave and Andrew, 2019). Grain-size distribution displays distinct modes (Weltje, 2012) that can be attributed to specific physical transport processes (e.g., wind, water currents, ice) and/or transport energy. Because grain-size distribution reflects both carrying vectors (e.g., wind, water currents, ice) and flow speed, several studies focused on the respective isotopic composition of distinct grain-size fractions in order to track distinct provenance patterns (Meyer et al., 2011; Bayon et al., 2015; Beny et al., 2018). Similarly, clay minerals are useful tracers of provenance, erosion balance, weathering, and transportation

pattern of fine-grained sediments (Moriarty et al., 1977; Petschick et al., 1996; Kuhn and Diekmann, 2002; Montero-Serrano et al., 2010). Finally, radiogenic isotope compositions of sediments can be used to decipher the different provenances of terrigenous particles and determine their respective contributions through time (Walter et al., 2000; Bayon et al., 2009).

This study focuses on the South Atlantic Ocean, where northern water-masses (North Atlantic Deep Water, NADW) and southern ones (Lower Circumpolar Deep Water, LCDW and Antarctic Bottom Water, AABW) mix, because this area is key for understanding the atmosphere-ocean exchanges that control CO_2 sequestration/outgassing. The reorganization of these deep water-masses during the deglaciation is still a subject of debate and their impact on deglaciation is not resolved (Barker et al., 2009; Skinner et al., 2010, 2013; Waelbroeck et al., 2011; Adkins, 2013; Menviel et al., 2014, 2015a,b, 2018). Recent studies of the last deglaciation ventilation events in the South Atlantic Ocean demonstrated an apparent synergy between physical and biological processes (Gottschalk et al., 2016), whereas chemical and physical processes appear to be decoupled (Roberts et al., 2016). These contrasting results highlight the lack of constraints on the dynamical aspect of the water-masses mixing. In this paper, we combined grain-size distribution, clay mineralogy, and radiogenic isotope (Sr-Nd-Pb) analyses (on separated grain-size fractions) in order to investigate the evolution (horizontal and vertical extensions, pathways, speed) of deep water-masses in the South Atlantic Ocean during the last termination.

II. General setting

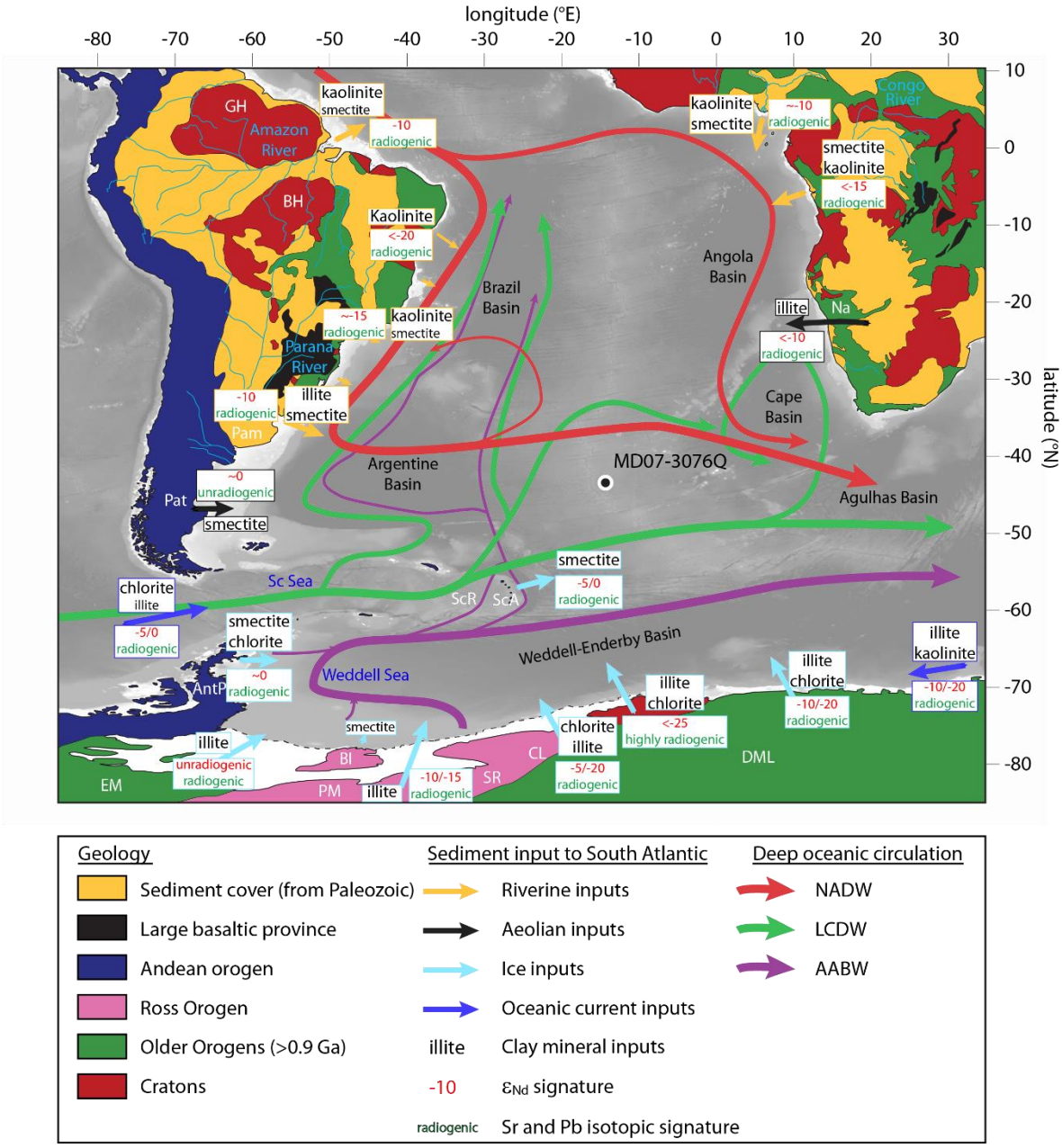

Figure 36: Simplified geological map of the study area. Light blue text names riverine systems, dark blue text names seas, black text names oceanic basins, and white abbreviations names areas. In South America: Guyana Highlands -GH-, Brazilian Highlands -BH-, Argentinian Pampas -Pam-, Patagonia -Pat-; in Africa: Namibian deserts-Na-; in Antarctica: Ellsworth Mountains -EM-, Antarctic Peninsula -AntP-, Pensacola Mountains -PM-, Berkner Islands -BI-, Shackleton Range -SR-, Coats Land -CL-, Dronning Maud Land -DML-. Clay mineral inputs to the South Atlantic Ocean derived from the studies of Petschick et al. (1996);Diekmann et al. (2000); Walter et al. (2000); Guyot et al. (2007); Bayon et al. (2016); and Khondoker et al. (2018).

A. Deep water-masses

Modern South Atlantic deep circulation is characterized by the incursion of the NADW into the Southern Ocean, where it mixes/interacts with both the AABW and the Circumpolar deep-water (CDW; figure 36). The southward NADW mainly flows as Deep Western Boundary Current along the South American Margin before leaving the continental shelf and flowing eastward around 45°S (Reid, 1989; Larqué et al., 1997; Stramma and England, 1999). A branch of the NADW crosses the Atlantic Ocean at the equator before to flow southward along the African margin and to reach the Indian Ocean via the Good Hope Cape (Larqué et al., 1997). In the Southern Ocean, NADW flows between two parts of the CDW: the Upper Circumpolar deep-water (UCDW) flows above, whereas the Lower Circumpolar deep-water flows underneath. The northern extension of the UCDW is very asymmetric with larger extent in the eastern part of the South Atlantic (Larqué et al., 1997). On the west side of the Mid-Atlantic Ridge (MAR), the LCDW penetrates into the Argentine Basin via the Drake Passage and flows northward into the Brazil Basin (Speer and Zend, 1993). On the east of the MAR, the LCDW is a major oceanic feature in the Cape Basin, where it becomes diluted in the Angola Basin (Larqué et al., 1997). The lower part of the LCDW is currently mixed with the upper part of the AABW (Orsi et al., 1999) that is produced heterogeneously along the Antarctic Shelf (Foster and Carmack, 1975; Orsi et al., 1999). Foster and Camarck (1975) demonstrated the formation of a very cold type of bottom water in the vicinity of the shelf break (the Polynyas mode) between 29 and 40°W and along the Antarctic Peninsula's tip, between 35 and 55°W and north of 65°S. Today this production occurs mainly in winter when seawater is close to freezing and becomes saltier due to sea ice formation (Foster and Camarck, 1975; Orsi et al., 1999), which increases its density and promotes convection. This mode is called the Polynyas mode. However, in the Weddell Sea, a second mode of bottom water formation occurs: the Ice Shelf Water mode, which corresponds to bottom water formation under the Antarctic ice shelves due to super-cooling (Krueger et al. and references therein, 2012). The AABW is very thick in the Weddell-Enderby Basin (more than 4000 m; Orsi et al., 1999) and is partially exported to the Argentine Basin via the eastern Scotia Sea (east and west of the South Sandwich Islands) toward the Brazil Basin via the Vema Channel, and to the Agulhas and Crozet basins (Stramma and England, 1999). The AABW is a dominant oceanic feature south of 50°S although its' northern influence extents to around 10°S (Reid et al., 1989).

The characteristics of deep-water masses were not constant through time and the evolution of the AMOC is controversial (Weber and Drijfhout, 2007; Vasquez Riveiros et al.,

2010; Waelbroeck et al., 2011; Howe et al., 2016). Some studies have suggested that during the Last Glacial Maximum (LGM) the NADW was as strong as today but shallower (Curry and Oppo, 2005; Gherardi et al., 2009). Other studies suggest that it was weaker and shallower (Menviel et al., 2012; Howe et al., 2016). The NADW southern extension seems limited during glacial times, whereas southern-born water-masses extended further north (Kuhn and Diekmann, 2002; Skinner et al., 2013). Similarly, modifications of the Antarctic Circumpolar Current (ACC, including the CDW) during the last climatic cycle are still debated. Some studies reported severe modifications of the ACC intensity in the Atlantic (Noble et al., 2012) and Indian (Dezileau et al., 2000; Mazaud et al., 2010) sectors of the Southern Ocean: the activity of the ACC increased during the LGM, probably linked to enhanced westerly winds (Dezileau et al., 2000; Walter et al., 2000; Mazaud et al., 2010). In contrast, other studies support insignificant modification of the ACC in the Atlantic sector of the Southern Ocean (Gersonde et al., 2003) and Drake Passage (McCave et al., 2014). Finally, the evolution of the AABW is also uncertain. Krueger et al. (2012) suggests that the production of AABW was similar during glacial and interglacial, but dropped during terminations (including the last deglaciation). In addition, Menviel et al. (2017) suggest that the "AABW" (corresponding to CDW and AABW in our study) was weaker during the LGM than today. In contrast, other studies suggest enhanced northward flow of AABW via deep western boundary currents in all three major ocean (Pacific: Hall et al., 2001; Govin et al., 2009; Indian: Govin et al., 2009; Atlantic: Govin et al., 2009; Spooner et al., 2018).

Any modifications of the AMOC have a potential effect on carbon storage/outgassing that is tightly controlled by ocean stratification/ventilation, itself resulting from contrasting physical and chemical properties of the water-masses. High ocean stratification – as during the last glacial – inhibits vertical mixing and isolates the deep ocean from the atmosphere. In contrast, ventilation events – breakdown of the stratification that occurred during the last deglaciation – allow CO_2 to upwell from the deep ocean and to be rapidly transferred to the atmosphere (Toggweiler et al., 2006; Barker et al., 2010; Skinner et al., 2010, 2013, 2014; Burke and Robinson, 2012).

B. Geological setting

The Atlantic sector of the Southern Ocean may receive sediments from Antarctica, the Scotia Sea area (i.e., Scotia Arc, southern Patagonia, and northern Antarctic Peninsula) South America, and Africa. Here, we present the general geological structure of these areas, and their respective isotopic signatures (figure 36).

Antarctica corresponds to two distinct geological domains: East and West Antarctica. West Antarctica includes the Ellsworth Mountains (EM), the Antarctic Peninsula (Ant P), the Scotia Arc region (SCA). The geology of the Ellsworth Mountains (figure 36) is poorly known due to the lack of outcrop. These mountains are composed of Precambrian rocks, corresponding mainly to granodiorite orthogneiss intruded by granitic and pegmatitic sheets (Tingey et al., 1991). The isotopic composition of the area is not known, but the age of the rock suggests radiogenic Sr and Pb isotope ratios, and unradiogenic ε_{Nd} (figure 36). This area mostly delivers illite to the sea (Petschick et al., 1996; figure 36). The Antarctic Peninsula, composed of alkaline and calcalkaline magmatic rocks associated with deformed sediments of similar composition (Anderson, 1965; Tingey et al., 1991), is a potential source of terrigenous sediment for CDW and AABW. The Antarctic Peninsula is characterized by radiogenic ε_{Nd}, and low Sr and high Pb isotope ratios (figure 36). Clay minerals from this area mostly correspond to well-crystallized smectite (crystallinity around 1.5, Petschick et al., 1996; figure 36), and chlorite. The Scotia Arc islands rocks are similar to those of the Antarctic Peninsula but with slightly more radiogenic Nd, and slightly less radiogenic Sr and Pb (figure 36). This area exports exclusively well-crystallized smectite to the ocean (crystallinity lower than one; Petschick et al., 1996).

The East Antarctic domain is an old shield with rocks > 0.9 Ga. Rocks from the Pensacola Mountains (PM) to the Shackleton Range (SR) represent the Ross Orogen (i.e., Transantarctic Mountains) and are mainly composed of varied metamorphic rocks aged from the Late Proterozoic to Late Paleozoic (Barrett, 1991; Laird, 1991; Tingey, 1991; Hauptvogel and Passchier and references therein, 2012). The isotopic composition of the area is characterized by unradiogenic Nd, with intermediate to high Sr isotope ratios (figure 36). The Pb isotope composition unknown, as is the case for most of East Antarctica rocks. The few studies reporting Pb isotope ratios have been carried out on feldspars only. The area releases mostly illite and chlorite (Petschick et al., 1996). Smectite is also exported from the Berkner Island, but is found only locally (Petschik et al., 1996). To the east, the Grenville Belts (920 to 1330 Ma) outcrop on the Coats Land (CL) and western Dronning Maud Land (WDML) with a wide range of gneissic and clastic sediments (Capurro, 1955; Anderson, 1965; Tingey et al., 1991) with unradiogenic Nd, and radiogenic Sr isotope ratios (figure 36). Clay minerals produced in this area are mainly chlorite and illite (Petschick et al., 1996). In the northernmost part of the Dronning Maud Land, the old Grunehogna Craton is composed mainly of Archean granitoids (Tingey et al., 1991; Mieth and Jokat, 2014; Pierce et al., 2014) with very

unradiogenic Nd (ε_{Nd}<< -20) and radiogenic Sr ratios (figure 36). The clay minerals generated in that area are mainly chlorite and illite (Petschick et al., 1996).

South America can be divided into two blocks: the recent Andean Orogen, and the old South American Shield. In the Atlantic Sector of the Southern Ocean, the Andean Orogen mostly corresponds to Patagonia (Pat). The geology and the isotopic composition of this region is similar with the Antarctic Peninsula: radiogenic Nd, unradiogenic Sr and Pb isotope ratios, but with higher $^{207}Pb/^{204}Pb$ than the Antarctic Peninsula (figure 36; Olivero and Martinioni, 2001; Sayago et al., 2001 and references therein; Smith et al., 2003; Khondoker et al., 2018). Even if the climate is slightly more humid than in the Antarctic Peninsula, Patagonia also produces mainly well-crystallized smectite (Petschick et al., 1996; Desiage et al., 2018; Khondoker et al., 2018).

The South American Shield is composed of several cratonic areas separated by vast ancient orogenic belts. (Cordani and Sato, 1999; Engler, 2009; Oyhantçabal and Siegesmund, 2011; Siegesmund et al., 2011; de Alkmim, 2015). Cratonic areas are mainly composed of granitoids and a wide range of metamorphic rocks, while orogenic belts are composed of a large variety of metamorphic rocks with high original composition (from the granite to the ophiolite and the juvenile magmatic arc; Almeida et al., 1981; Barros et al., 1982; Moura and Gaudette, 1993; Neves, 2003; de Alkmim, 2015; Nogueira et al., 2007; Pimentel et al., 2011; Fuck et al., 2014; McGee et al., 2015; D'el-Rey Silva et al., 2016). The overall isotopic composition of the South American Shield is radiogenic Sr and Pb, and very unradiogenic Nd isotope ratios (figure 36). South of the South American Shield, a large tholeiitic-basaltic province is known as the Parana basalt (Waichel et al., 2012; Milani and Ramos, 2017). The composition of the Parana basalts differs from the South American Shield with radiogenic Nd, and very low $^{87}Sr/^{86}Sr$ ratio (<0.5; Tapani Ramo et al., 2016).

This South American Shield is drained by important riverine systems such as the Amazon and Parana rivers. The Amazon drains sediments from the Andes, as well as the South American Shield. The South American Shield is characterized by rocks with unradiogenic Nd and radiogenic Sr and Pb (figure 36). The clay mineral exported to the ocean is mainly kaolinite (Petschick et al., 1996; Guyot et al., 2007; Bayon et al., 2015). However, sediments are mainly exported northwards toward the Caribbean Sea. The Parana River drains the southern part of the South American Shield, the Parana basalts, and the north of Patagonia. Its isotopic composition has intermediate Nd, Sr, and Pb isotope ratios (figure 36). Clay minerals transported via this river are illite (~60%; Petschick et al., 1996; Campodonico et al., 2016),

kaolinite, and smectite. Other smaller rivers drain the south of Brazil, and mainly deliver sediments characterized by unradiogenic Nd, and radiogenic Sr and Pb isotope ratios, containing mainly smectite derived from the Parana basalts and kaolinite (figure 36; Petschick et al., 1996). On the other hand, Patagonia and Pampas are dry and windy areas (Clapperton, 1993). Consequently, part of the detrital particles is exported to the ocean via aeolian processes as loess (Mathias et al., 2014). The overall isotopic composition of this smectite-rich loess is radiogenic Nd, unradiogenic Pb and Sr ratios. According to Mathias et al. (2014), the sediment delivery to the southwest Atlantic is currently dominated by loess, and by the Parana River sediments.

A large proportion of the African continent comprises Archean Cratons (western Africa, Congo), and rocks related to the Pan African Orogen. The cratons are composed of gneisses while the Pan African Orogen is mainly composed of flysch deposits associated with volcanic formations, and intruded by granitoids. The overall geochemical composition of Africa is intermediate to very unradiogenic Nd, and intermediate to very radiogenic Sr and Pb isotope ratios (figure 36). Clay minerals formed in the Congo depression are mainly poorly crystallized smectite and kaolinite, whereas the Namibian deserts release illite-rich loess (Bremner and Willis, 1993; Petschick et al., 1996; Bayon et al., 2015; figure 36).

III. Material and methods

A. Material

This study is based on sediment samples from core MD07-3076Q (44°9.2'S, 14°13.7'W) recovered by the French Vessel *Marion Dufresne* in 2007 on the eastern flank of the Mid-Atlantic Ridge at 3770 m depth (figure 36). The core chronology is based on planktonic foraminifer radiocarbon dates (30 measurements for the studied interval) and stratigraphic control points (Skinner et al., 2010, 2013, 2014; Gottschalk et al, 2015b). Today, the site is bathed in the LCDW. From the seafloor to the surface, the water masses observed in the water column above the study site are the LCDW, NADW, UCDW, and intermediate and surface waters. In nearby deeper oceanic basins, the AABW is also found, and it is thought that particles transported by this bottom water can reach our site by advection and mixing with the LCDW.

B. Sample preparation and analytical procedure

All samples were first decarbonated using 0.1N HCl and then deflocculated by repeated washing using pure water.

1. Grain-size distribution

Grain-size distribution was measured on carbonate-free sediment using a Malvern Mastersizer 2000 laser (0.02-2000 µm) following standard protocols (Montero-Serrano et al., 2009). The clay-size fraction corresponds to the proportion (in volume) of particles with a diameter smaller than 2 µm, the cohesive silts correspond to the 2 to 10 µm diameter particles, the sortable silts correspond to the 10 to 63 µm diameter particles, and the sand fraction to the particles coarser than 63 µm.

2. Clay mineralogy

The clay-size fraction (< 2µm) was isolated by differential settling according to Stoke's Law. This fraction was then concentrated by centrifugation (40 minutes, 3500 rotation per minute) and an aliquot was placed on glass slides. X-ray diagrams were obtained using a Bruker D4Endeavor (standard 30 kV and 30 mA). Each sample is run three times between 2.49 and 32.5°2θ: (1) dried sample, (2) glycolated sample (12 hours in ethylene glycol), and (3) heated sample (490°C for 2 hours). The proportion of each clay mineral (smectite, chlorite, illite, and kaolinite) is determined using the main X-ray diffraction peaks (layer and interlayer) on X-ray spectra according to their crystallographic characteristics (Brown, 1980). Smectite is characterized by a main peak at 14-15 Å on the air-dried samples that expands at 17 Å after ethylene glycol saturation and collapses at 10 Å after heating. Illite is characterized by a main peak at 10 Å on the three runs. Kaolinite and chlorite are measured based on their main peak at 7-7.2 Å and further distinguished using pseudo-void deconvolution of the kaolinite/chlorite doublet at 3.54/3.58 Å. All measurements and semi-quantitative estimations are processed using the McDiff software (Petschick, 2000). The index of Esquevin (Esquevin, 1969) corresponds to the ratio between the intensity of the peak of illite at 5 Å and at 10 Å (illite 5Å/10Å). In this study, the crystallinity of illite and smectite has been measured using the method of integral breath to enable comparison with the work of Petschik et al. (1996) in the South Atlantic. High crystallinity (high values of the index) corresponds to badly crystallized mineral.

3. Isotope Analysis

The grain-size distribution recognized three distribution modes. These three grain-size fractions were then isolated in order to examine their provenance. The clay-size fraction (0-2 µm) was isolated by repeated extractions by settling. The coarse fraction (20-40 µm in the old section of the core before 11.5 ka cal BP, noted hereafter as ka, and 20-32 µm after 11.5 ka)

was isolated by sieving the clay-free residue. The 2-20 µm grain-size fraction is thus the residue of clay separation and coarse fraction sieving. An aliquot of 10 to 150 mg (depending of the sediment quantities available) was then used for chemical procedures.

Chemical and isotopic measurements were performed at the Faculty of Science of the Vrije Universiteit, Amsterdam. Sediment was digested in closed Savillex^{TM} Teflon beakers using a mixture of concentrated HF and HNO_3 (~2/3 and 1/3, respectively) for a few days at 120°C. After digestion, samples were dried out and re-dissolved in ~6.5N HCl to remove fluorides. Nd, Sr, and Pb were purified using conventional ion chromatography. Pb isotopes were processed first and purified using AG-X8 200-400 mesh resin. Light rare earth elements (LREE) were isolated using true-spec resin medium (Eichrom^{TM}, 100-150 µm mesh size) and Nd was eluted from the LREE fraction using LN-resin (Eichrom^{TM}, 50-100 µm mesh size). Sr was recovered using Sr resin column. Nd and Pb measurements were performed by bracketing using respectively CIGO and NBS981 standards on Thermo Scientific Neptune multi-collector inductive coupled plasma-mass spectrometer (MC-ICPMS), whereas Sr measurements were performed on a thermal ionization multi-collector-MS (TIMS). Due to relatively low content of Nd in some of the coarse grain-size fraction (20-32/40µm), Nd measurements of these fractions were also performed by TIMS.

IV. Results

A. Grain-size distribution

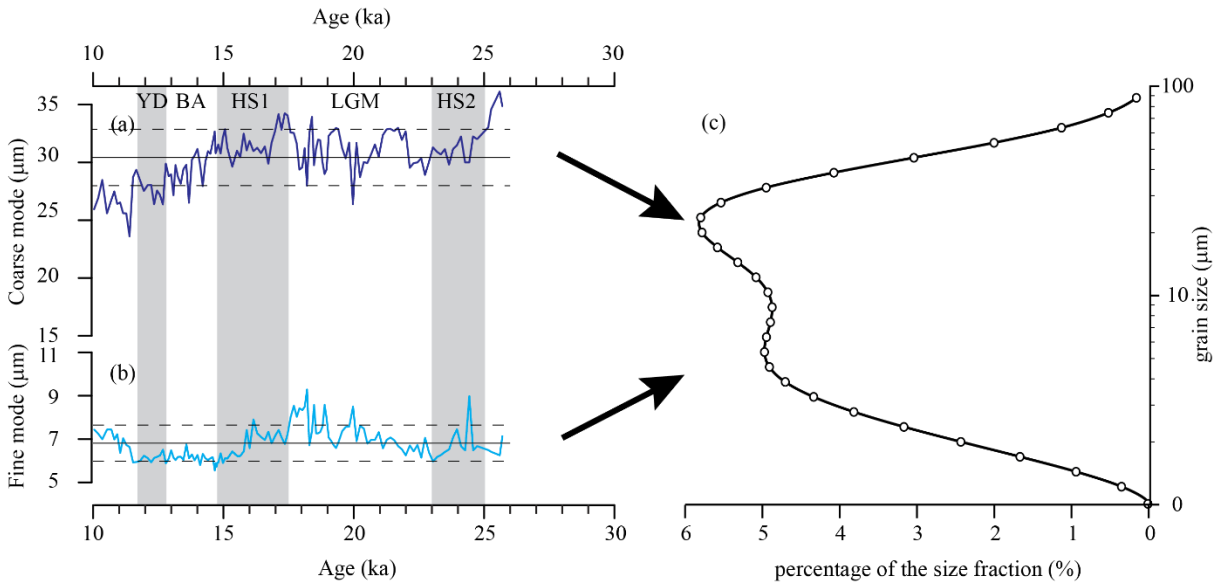

Figure 37: Grain-size results from core MD07-3076Q. (a) and (b) Variation of the coarse and fine grain-size mode values, respectively, through time. Black lines represent the average

value for both grain-size modes while dashed lines represent their standard deviation; (b) typical grain-size distribution curve from the core MD07-3076Q. Two grain-size modes can be identified from the grain-size distribution curve. YD: Younger Dryas, BA: Bølling Allerød, HS: Heinrich Stadial; LGM: Last Glacial Maxima.

The grain-size distribution is bimodal throughout the core (figure 37) with a coarse mode ranging in the sortable silts fraction (from 23.6 and 36.2 μm, average: 30.4, standard deviation: 2.48; annex 7) and a fine mode ranging in the cohesive silts fraction (from 5.6 and 9.3 μm, average: 6.8, standard deviation: 0.8; annex 7). The sortable silt (10-63 μm) fraction is dominant (41 to 52% in volume of the total terrigenous fraction, average: 47%, standard deviation: 2.4; annex 7) and the cohesive silts (2-10 μm) represent 35 to 45% (average: 39%, standard deviation: 2.4; annex 7). The clay (<2 μm) and sand fractions (>63 μm) represent respectively 2 to 5% (average: 3.4%, standard deviation: 0.7; annex 7) and 1 to 6% (average: 3.0, standard deviation: 1.0; annex 7) of the total terrigenous fraction (annex 7).

In details, the mean of the coarse mode (hereafter mentioned as the sortable silt mode) is slightly coarser during the LGM (figure 37.a), and decreases during the deglaciation and reaches its minimum values after the Younger Dryas (YD). The average size of the fine mode (hereafter mentioned as the cohesive silt mode) is maximum at the end of the LGM and displays its lowest values during the deglaciation (figure 37.b).

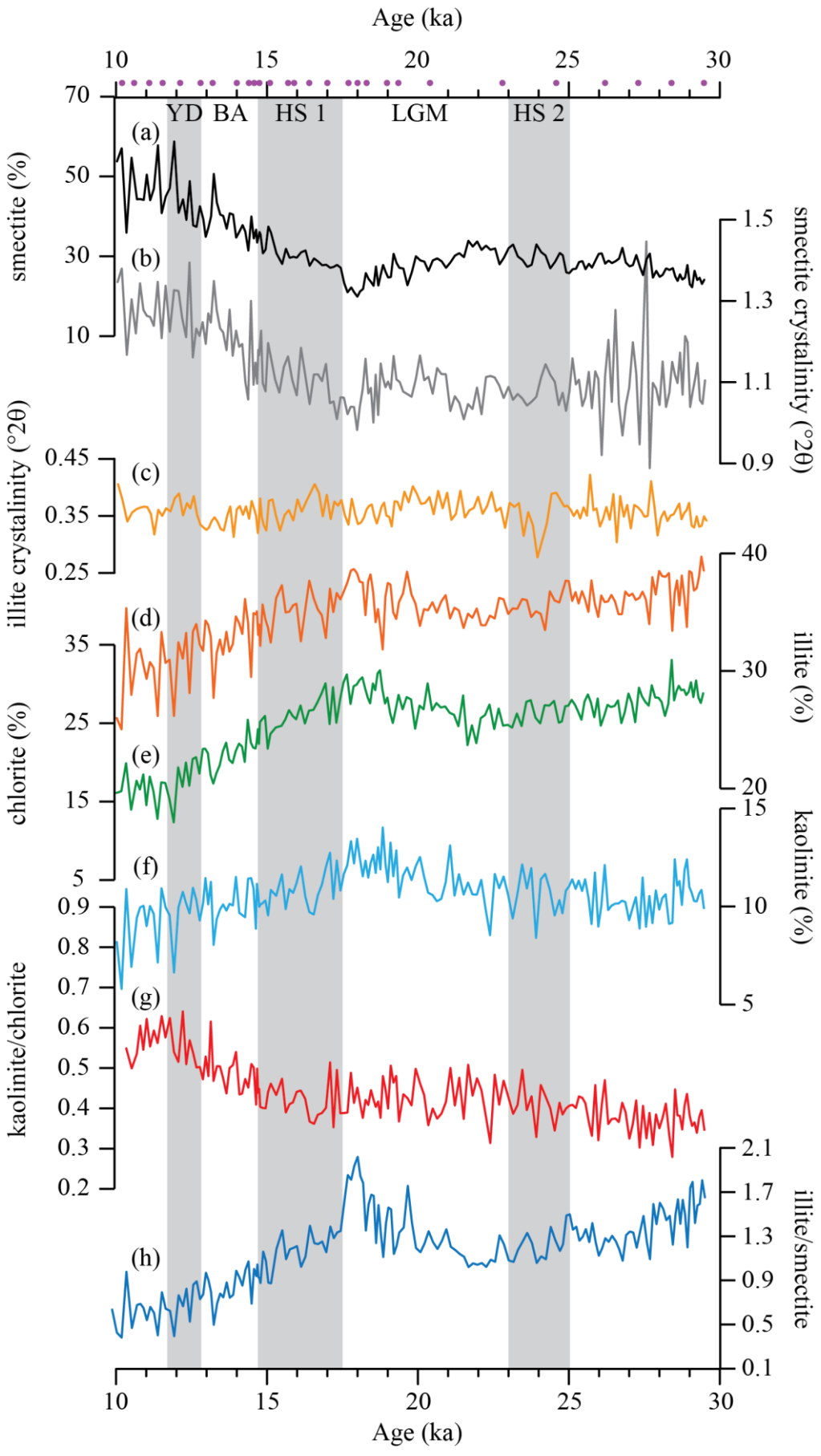

Figure 38: Clay mineral data from core MD07-3076Q. Purple dots represent the radiocarbon dates used for the age model. (a) relative proportion of smectite (%); (b) smectite crystallinity (°2θ); (c) illite crystallinity (°2θ); (b) and (c) note that the lower is the crystallinity index, the better the mineral is crystallized; (d) relative proportion of illite (%); (e) relative proportion of chlorite (%); (f) relative proportion of kaolinite; (g) kaolinite/chlorite ratio (K/C); (h) illite/smectite ratio (I/S).

B. Clay Mineralogy

The clay mineral assemblage is composed of smectite ((S) 18-59%; figure 38.a), illite ((I) 21-40%; figure 38.d), chlorite ((C) 12-33%; figure 38.e), and kaolinite ((K) 5-14%; figure 38.f) with higher smectite content at the end of the deglaciation, and higher illite, chlorite and kaolinite contents during the LGM. The smectite crystallinity ranges from 0.89 and 1.45 (figure 38.b) and varies in phase with the smectite content with slightly higher variability between 25 and 30 ka. The illite crystallinity varies between 0.27 and 0.42 (figure 38.c and 39) without major variation. Clay mineral proportions are relatively stable during the LGM but records a shift during the deglaciation with an increase of smectite compared to the other clay minerals. The smectite crystallinity varies simultaneously with smectite proportion changes. The K/C ratio is stable during the LGM, and increases during the deglaciation. The I/S ratio presents two maxima at the beginning of the record and at the end of the LGM, sharply decreases at the beginning of the HS 1, and steadily decreases during the deglaciation.

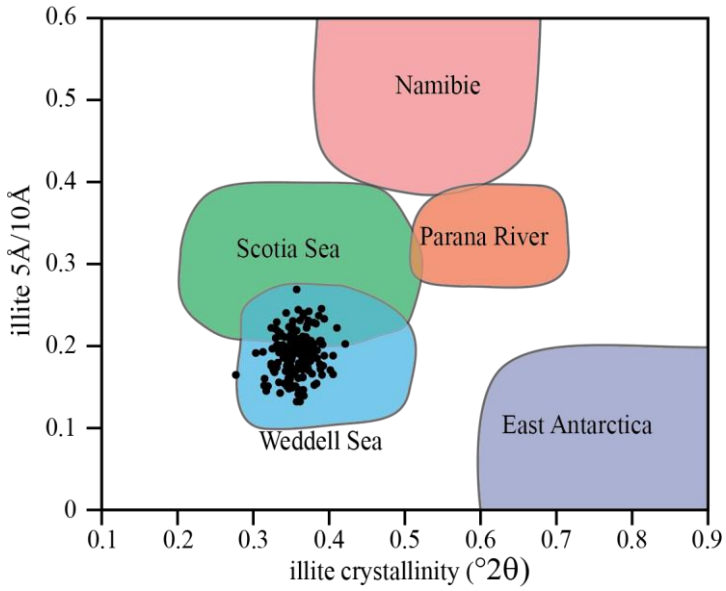

Figure 39: Crystallographic properties of illite from site MD07-3076Q (black dots) and comparison with properties of illite from potential sources to the South Atlantic basin. The data used for comparison are from Petschick et al., (1996). Illite 5Å/10Å ratio gives information on

the chemical properties of illite (Fe-Mg- vs Al-rich illite) while the crystallinity gives clues on the quality of the mineral crystal (high crystallinity: badly crystallized mineral).

C. Radiogenic Isotopes

Isotopic results are presented for the sortable silt mode fraction (20-32/40 μm) and the cohesive silt mode fraction (2–20 μm) and for the clay-size fraction (<2 μm) (annexes 8 to 10). Lead isotope ratios were only been measured on the clay-size fraction (annex 8).

1. Clay-size fraction (<2 μm)

The ε_{Nd} of the clay-size fraction ranges from -7.2 to -4.8. It is relatively stable during the last glacial (<± 0.5 ε_{Nd}), decreases by 2 ε units during the deglaciation and shows minimum values at the end of the deglaciation (figure 40.c). The $^{87}Sr/^{86}Sr$ ratio ranges from 0.711 to 0.712: it is rather high and stable (<± 0.0003), during the last glaciation and displays a rapid decrease at ~15 ka. The ratio records a short rebound at 12.7 ka before reaching its minimum values at the end of the deglaciation (0.7107; figure 40.d). The $^{87}Sr/^{86}Sr$ ratio and the ε_{Nd} show a similar temporal evolution (they both decrease during the deglaciation), which is surprising as in nature they usually record opposite relationship. The three Pb isotope ratios record their lowest values around 25 ka, and increase thereafter. This trend is more pronounced for the $^{207}Pb/^{204}Pb$ ratio during the deglaciation. Some fluctuations of the three ratios are observed during the deglaciation with higher ratios at climatic transitions (LGM/Heinrich Stadial 1 – HS1–, HS1/Bølling-Allerød – B-A – , B-A/Younger Dryas –YD–, Holocene onset), and low values during the middle of the HS1, the middle of the B-A, and the second half of the YD (except for the $^{206}Pb/^{204}Pb$). We note that the Sr isotope rebound observed at 12.7 ka is also associated with variations Pb isotope ratios.

2. Cohesive silt mode fraction (2-20 μm)

The ε_{Nd} of the 2-20 μm grain-size fraction (cohesive silt mode fraction) ranges from -5.5 to -3.9 with the lowest values at 13, 18, 23 and 29 ka (figure 40.b). The $^{87}Sr/^{86}Sr$ ratios are generally constant with higher values around 13, 19, and 24 ka (figure 40.f).

3. Sortable silt mode fraction: (20-32/40 μm)

The ε_{Nd} of the sortable silt mode fraction ranges from -4.9 to -1.4. Values are relatively unchanging during the last glacial period (-2 ± 0.5 ε_{Nd}) but decreases after 18 ka and reaches a minimum (-5) at the end of the deglaciation (figure 40.a). The $^{87}Sr/^{86}Sr$ ratio ranges from 0.708 and 0.710. $^{87}Sr/^{86}Sr$ values are lower during the HS 2, at the beginning of the HS 1, and at the beginning of the YD, while the highest value is recorded at the B-A offset (figure 40.e).

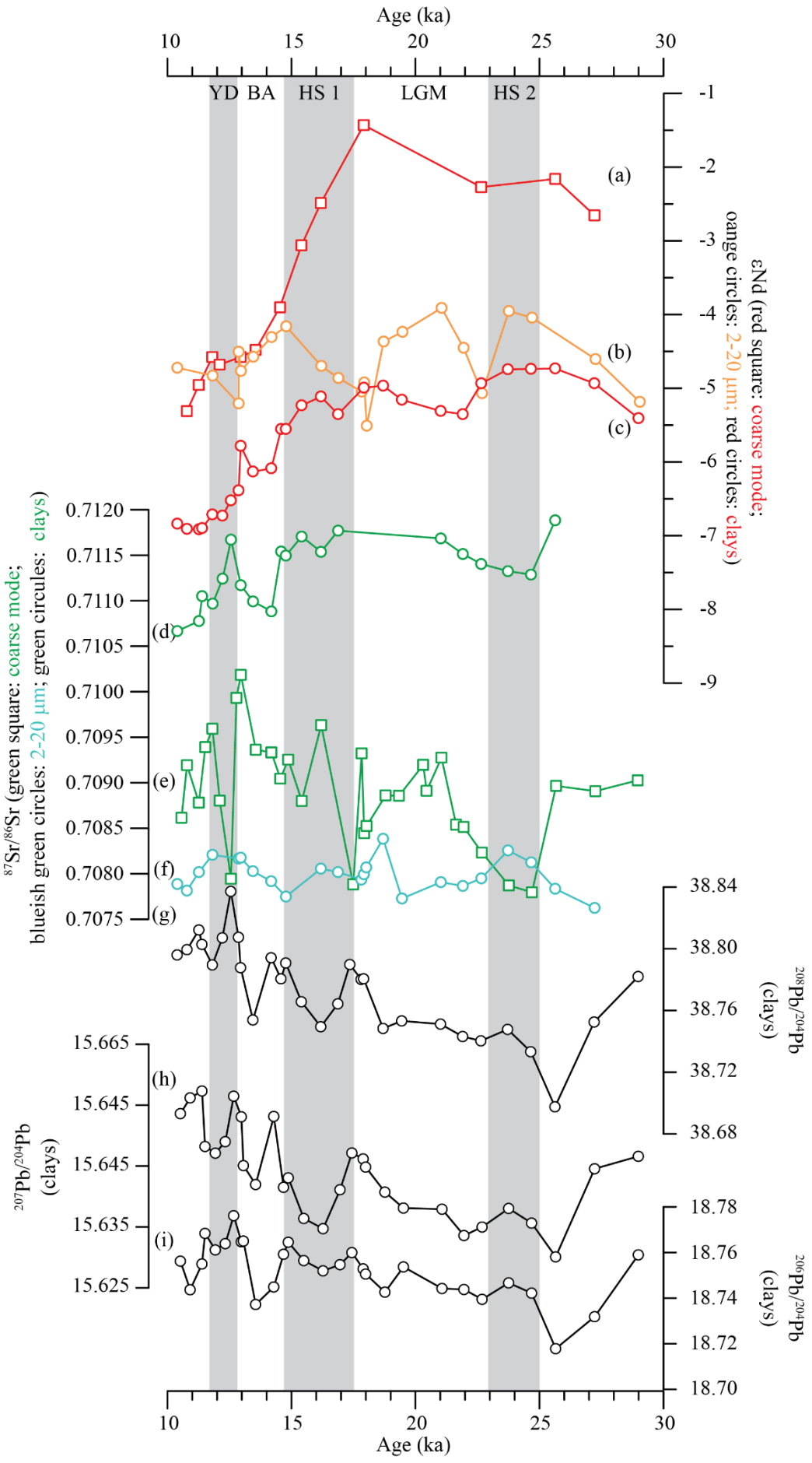

Figure 40: Isotopic results from core MD07-3076Q. (a) ε_{Nd} from the sortable silt mode fraction (20-32/40 μm); (b) ε_{Nd} from the cohesive silt mode fraction (2-20 μm); (c) ε_{Nd} from the clay-size fraction (<2 μm); (d) $^{87}Sr/^{86}Sr$ from the clay-size fraction (<2 μm); (f) $^{87}Sr/^{86}Sr$ from the sortable silt mode fraction (20-32/40 μm); (g) $^{87}Sr/^{86}Sr$ from the cohesive silt mode fraction (2-20 μm); (h) $^{208}Pb/^{204}Pb$, (i) $^{207}Pb/^{204}Pb$, and (j) $^{206}Pb/^{204}Pb$ from the clay-size fraction (<2 μm).

V. Discussion

A. Sediment provenance

1. *Clay size fraction: an overall provenance signal*

To determine the provenance of this grain-size fraction, both clay mineral proportions and radiogenic isotopes have been used. Kaolinite and chlorite have distinct provenances: at present, kaolinite is mainly found at low latitudes where chemical weathering is strong. Brazilian rivers (Amazon and Parana), as well as equatorial and tropical African rivers are characterized by high contents of kaolinite (figure 36). Inherited kaolinite is also found in East Antarctica marine sediments (figure 36), but is transported by the westward Antarctic Coastal Current and remains trapped in the Weddell-Enderby Basin due to the Weddell Gyre circulation (Petschick et al., 1996) and this kaolinite is therefore unlikely to contribute to sedimentation at the studied site. Consequently, kaolinite can be used to trace the low latitude provenance. Conversely, presently, chlorite mainly characterizes high latitude regions, where weak chemical weathering allows its preservation. It is abundant in Antarctica and the Scotia Sea (figure 36). Consequently, chlorite can be considered a tracer of high latitude provenance. Thus, the kaolinite/chlorite ratio (K/C) discriminates southern-born versus northern-born material in the southern Atlantic (Petschick et al., 1996; Kuhn and Diekmann., 2002; Kruger et al., 2008).

Illite provenance is more complex. It is very abundant in the Weddell Sea, Namibian deserts, the Parana River (60% of the delivered sediment), and it is also present, although at lower concentrations (<30%), in the Scotia Sea (figure 36). To decipher the provenance of illite, we used the chemical (5/10Å ratio, i.e., Fe-Mg vs. Al rich illite) and crystallographic properties (crystallinity) of this mineral. Data are compared with the 5/10Å ratio and the crystallinity of illite of potential illite sources from the database of Petschick et al. (1996) (figure 39). This comparison demonstrates that the illite from core MD07-3076Q is similar to illite from the Weddell and Scotia seas while the chemical and crystallographic properties of the illite recovered at site MD07-3076Q is not compatible with a Namibian source. In the Scotia Sea,

illite represents less than 30% of the total clay mineral fraction (from 10-30%; Petschick et al., 1996) and represents a mix of illite coming from the Weddell Sea embayment via the AABW, and illite from the Pacific sector of Antarctica delivered by the CDW (Diekmann et al., 2000; Walter et al., 2000; Petschick et al., 1996). Importantly, in the Weddell Sea, illite represents at least 50% of the total clay mineral fraction (more than 80% in some areas; Petschick et al., 1996). Consequently, the Weddell Sea embayment is considered as the major, source of illite for our studied site.

Smectite has several potential provenances: the Angola Basin, southern South America, Scotia Sea Islands, and Antarctic Peninsula. The crystallinity of this mineral was measured in order to decipher its provenance. The well-crystallized smectite (low crystallinity; figure 38) is compatible with a provenance from southern South America (Pampas and Patagonia), Scotia Arc, or Antarctic Peninsula, which are all characterized by crystallinity lower than 1.5 (Petschick et al., 1996; figure 38). It rules out a contribution of poorly crystallized smectite (crystallinity > 2; Petschick et al., 1996) from Angola. In detail, the crystallinity of the smectite from our studied site likely corresponds to a mix between two types of sources: (1) Patagonia and Antarctic Peninsula with a crystallinity of 1.5; and (2) Scotia Arc with a crystallinity lower than 1.0. Interestingly, the proportion and crystallinity of smectite record very similar variations that suggest a dominant and rather continuous flux of smectite from the Scotia Arc (low crystallinity - ~1.1) during the last glacial period, with a supplementary supply of less well crystallized smectite (slightly higher crystallinity – 1.5; ~20%) from Patagonia or Antarctic Peninsula during the deglaciation (supplementary figures S1 and S2)

In summary, both the proportions of the clay minerals and their crystallographic properties suggest that kaolinite mainly derives from low latitude areas, chlorite originates from Antarctica and the Scotia Sea, while illite mainly derives from the Weddell Sea embayment and smectite is derived from several sources (Scotia Arc, Patagonia, and Antarctic Peninsula). Moreover, mineralogical and crystallographic properties exclude Africa as a source of clay minerals consistent with the dominant westward oceanic circulation in the ACC (figure 36).

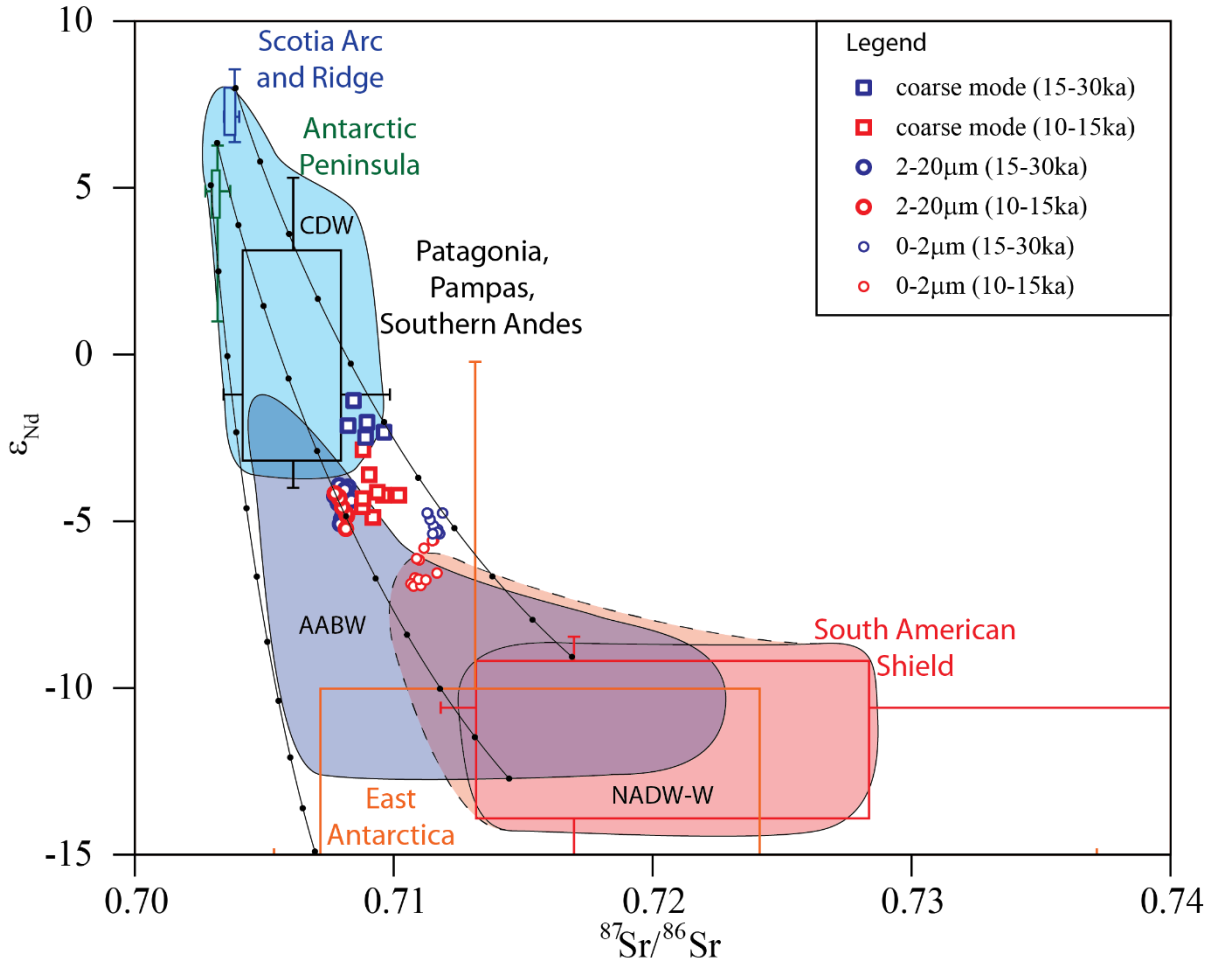

Figure 41: *$^{87}Sr/^{86}Sr$-ε_{Nd} diagram of MD07-3076Q sediments and of potential sources of sediments for the South Atlantic Basin. Boxes representing the reference data delimit the first and the third quartile. The median values are represented by horizontal and vertical lines attached to the boxes for the ε_{Nd} and the $^{87}Sr/^{86}Sr$ ratios, respectively. The short strokes at the end of these lines represent the 10^{th} and 90^{th} percentile values. Accordingly, the box represent 50% of values found for each potential provenance, and 80% is represented with the lines. Data sources: -South American Shield- Allegre et al. (1996); Basile et al. (1997); Walter et al. (2000); de Mahiques (2008); Jeandel et al. (2007), and references therein; Mallmann et al. (2007); Ganade de Araujo et al. (2014); Fuck et al. (2014); -Patagonia, Pampas, Southern Andes- Stern et al. (1990); Grousset et al. (1992); Basile et al. (1997); Walter et al. (2000); Smith et al. (2003); Jeandel et al. (2007), and references therein; Khondoker et al. (2018); -Scotia Arc and Ridge- Jeandel et al. (2007); Harrison et al. (2003);-Antarctic Peninsula- Hole el al. (1993); Kosler et al. (2009); Roy et al. (2007); Lee et al. (2005); -East Antarctica- DePaolo et al. (1982); Luttinen et al. (1998, 2010); Roy et al. (2007); Will et al. (2010).*

The coupled ε_{Nd} - $^{87}Sr/^{86}Sr$ isotope variation of the clay-size fraction (figure 41) reveal a mixed provenance between young sources around the Scotia Sea (Scotia Arc, Antarctic Peninsula, Patagonia) and southern South America (Patagonia and Pampas), and an old source from East Antarctica or the South American Shield (i.e., Brazil and Parana River).

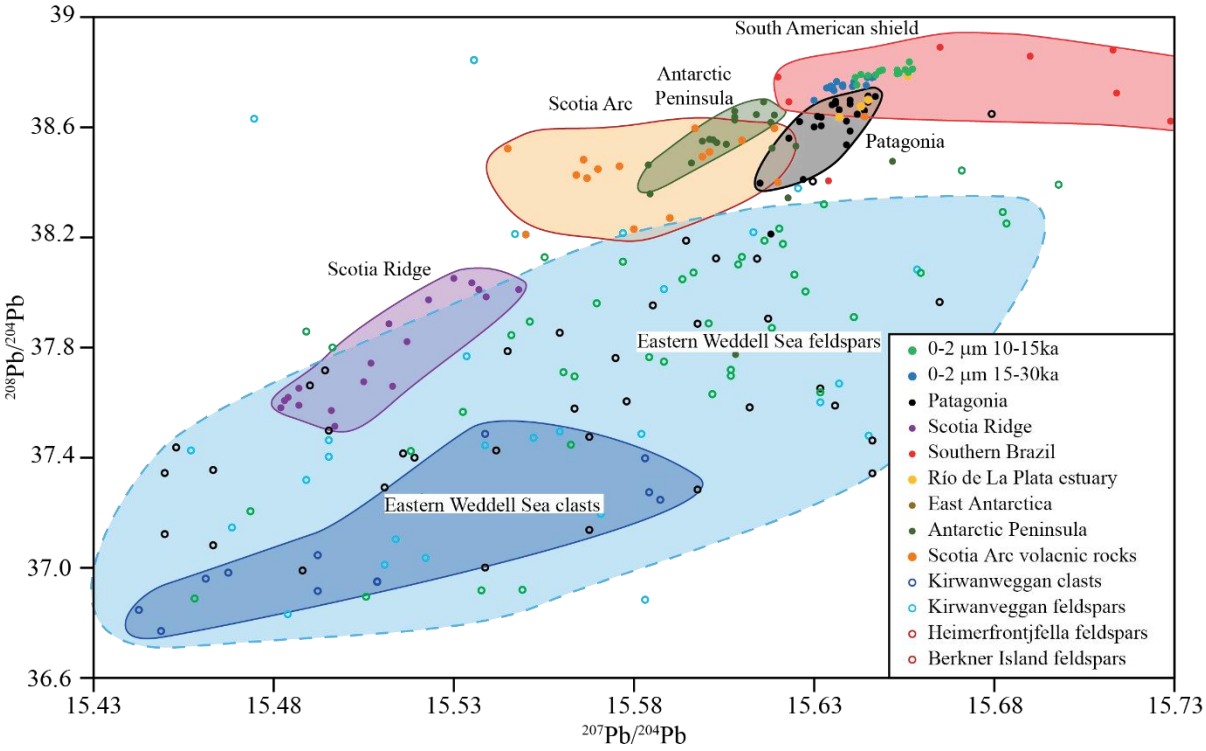

<u>Figure 42:</u> Pb isotope composition of core MD07-3076Q and of potential sources of sediments. The reference data used for comparison are from Fretzdorff et al. (2002), -Scotia Ridge-; Khondoker et al. (2018), -Patagonia-; Cohen and O'Nions (1982); Barreiro (1983), -Scotia Arc-; Lee et al. (2005), Kosler et al. (2009), Flowerdew et al. (2012) -Antarctic Peninsula-, de Mahiques et al. (2007), -South American Shield-; Flowerdew et al., (2012), -Eastern Weddell Sea-.

The coherent Pb isotope variations in figure 42 support this interpretation recording a mix between the Antarctic Peninsula, Scotia Arc, and South American Shield. However, since very few data are available for the Pb isotope compositions of East Antarctica, a contribution from this area cannot be excluded. The three isotopic systems suggest an increased contribution of older material during the deglaciation compared with the LGM. Based solely on Nd and Pb isotope data, it is rather difficult to distinguish South America and East Antarctica as the old end-members during the deglaciation. However, the increase of the K/C ratio during the deglaciation supports the hypothesis of enhanced relative contribution from the South American Shield.

2. *Cohesive silt mode fraction (2-20 μm)*

Both $^{87}Sr/^{86}Sr$ and ε_{Nd} of the cohesive silt mode fraction record limited variation throughout the deglaciation (figure 40). The isotopic results indicate that the provenance is located in Patagonia and in the Antarctic Peninsula, with an additional contribution of old source (South American Shield and/or East Antarctica). These results suggest that no major modification of provenance occurred during the deglaciation. Strontium and Nd isotope ratios do not allow discrimination of the source of old material for the cohesive silt mode fraction. The Nd isotope ratios suggest on average a higher radiogenic contribution for cohesive silts compared with the clay-size fraction (figure 41).

3. *Sortable silt mode fraction (20-32/40 μm)*

Both Sr and Nd isotope ratios of the sortable silt during the LGM record one dominant provenance: the Scotia Sea area (Patagonia, Scotia Arc, Antarctic Peninsula; figure 40). During the deglaciation, an important shift to less radiogenic ε_{Nd} values (4 units) is observed implying an increased contribution of an older end-member such as East Antarctica and/or the South American Shield. However, because East Antarctica and the South American shield have similar Sr and Nd isotope composition, it is not possible to distinguish them with these isotopes (figure 41). Consequently, investigating the main transportation patterns is necessary to identify the source of old material for both the cohesive (2-20 μm) and the sortable silt mode fractions (20-32/40 μm).

In summary, (figure 41) all three grain-size fractions compositions are located between two end-members: the Scotia Sea-southern South America area (Antarctic Peninsula, Scotia Arc and Ridge, Patagonia, Pampas, Southern Andes), and crustal shields (East Antarctica, South American Shield). The clay-size fraction appears the most crustal-like, whereas the sortable silt mode presents the most mantle-like composition. The 2-20 μm grain-size fraction presents the lowest $^{87}Sr/^{86}Sr$, meaning that the difference with the other grain-size fraction is related to distinct provenances rather than grain-size effect. Both the clay size and the sortable silt mode fractions display an increase of the crustal end-member. In the clay size fraction, clay mineralogy enabled the identification of this old crustal source (i.e., the South American Shield).

B. Transportation pattern and palaeoclimatic implications

The provenances of the sediments for the three distinct grain-size fractions have been identified (or partially identified) in the previous section using their mineralogical and

geochemical characteristics. Now, we will focus on identifying their transportation patterns and vectors from the source to the sedimentation site.

Several studies propose that aeolian processes may lead to significant particle transfers from Patagonia into the central Atlantic sector of the Southern Ocean (Hegner et al., 2007; Desiage et al., 2018). The aeolian contribution of loess from Patagonia was enhanced during the LGM as far as Antarctica (Petit et al., 1990; Grousset et al., 1992; Diekmann, 2007; Lambert et al., 2008). Although this hypothesis could be supported by the radiogenic Nd signal observed in both the clay-size and the sortable silt mode fraction during the LGM, the mineralogical of MD07-3076Q sediments is not in agreement with an enhanced contribution from Patagonia. The dominant clay mineral in Patagonia is smectite (up to 95%), and the contribution of Patagonian smectite in our clay-size fraction is lowest during the LGM (figure 38). Consequently, direct aeolian inputs cannot be significant at our site, and oceanic currents appear to be the main contributors to sedimentation (Moriarty, 1977; Petschick et al., 1996; Kuhn and Diekmann, 2002). This means that any aeolian particles from Patagonia delivered to the southwest Atlantic (Mathias et al., 2014) likely reach our site via oceanic transport processes.

The size of particles transported by water flow is directly related to the flow energy, with size increasing with the flow speed. This property was used in previous studies to track the temporal evolution of paleo-current flow (e.g. McCave and Hall, 2006; McCave and Andrews, 2019). Below we show that the different grain-size modes not only correspond to distinct flow speeds, but specific water mass at site MD07-3076Q. Consequently, grain-size modes (2-20 μm and 20-32/40 μm) can be associated to specific deep water-masses.

The clay-size fraction (i.e., the < 2 μm particles) with very high specific surface readily floats and hence can undergo long-range transportation (>500 km). Consequently, particles within this grain-size fraction can be used to record the relative contribution of the main deep-water masses.

1. *Clay-size fraction: the distant terrigenous signal*

The NADW carries fine suspended particles from as far as the Labrador Sea. However, this signal is probably overprinted by the supply of sediments from more proximal sources such as Africa or South America. The western branch of the NADW (NADW-W; i.e., Deep Western Boundary Current) can transport sediments from Brazil, Parana River, Pampas, and Patagonia (figure 36). Both mineralogical and geochemical compositions of the particles transported by the western branch of the NADW are likely controlled by the southern extension of the water-

mass. Currently the western branch drifts away from the South American coast around 45°S. This southern extension likely changed during the last glacial period and deglaciation (Skinner et al., 2010, 2014; Vasquez-Riveiros et al., 2010; Waelbroeck et al., 2011; Gottschalk et al., 2015a,b; Howe et al., 2016). Depending on its southern extent, the NADW is thus able to carry either mostly kaolinite (equatorial Brazil), or kaolinite and smectite (southern Brazil), or illite (Parana River basin), or well-crystallized smectite (crystallinity ~1.5; Patagonia). As shown above, the ε_{Nd} signature of these sediments is more radiogenic when the NADW extends further south (-20 in equatorial Brazil, to ~0 in Patagonia) while the Pb and Sr yield a slightly less radiogenic signature (figures 41 and 42).

The CDW transports sediments from the Scotia Sea area, including Scotia Arc, Patagonia, and the Antarctic Peninsula, as well as from the Weddell Sea when mixing occurs between the lower part of the LCDW and AABW. Then particles transported by the CDW likely record a younger isotopic signature (i.e., more radiogenic ε_{Nd} and unradiogenic Sr and Pb isotopes), and a mineralogical composition dominated by smectite and chlorite, while additional contribution of old material (unradiogenic ε_{Nd} and radiogenic Sr and Pb isotopes) and illite is possible when the LCDW and AABW mix together. In summary, illite is considered as injected into the sedimentary system via the AABW through mixing processes between LCDW and AABW while smectite and chlorite are likely transported by the CDW.

The AABW in the Atlantic sector mainly forms in the Weddell Sea embayment (Orsi et al., 1999), and thus, must carries sediments from its drainage basin (East Antarctica, Antarctic Peninsula), but may also transport sediment winnowed on its pathway such as the Scotia Arc or southern Patagonia in the Argentine Basin. The main clay minerals in the Weddell Sea embayment are illite associated with chlorite. Smectite may be injected in the AABW at the vicinity of the Scotia Arc. Kaolinite is almost absent in both the Weddell Sea embayment and the Scotia Sea area (Patagonia, Antarctic Peninsula and Scotia Arc) and is unlikely to be transported by the AABW. The isotopic composition of fine particles transported by the AABW ranges between two end-members: the very old sediments from East Antarctica ($^{87}Sr/^{86}Sr > 0.72$; $\varepsilon_{Nd} < -20$), and younger material from the Antarctic Peninsula and the Scotia Arc ($^{87}Sr/^{86}Sr \sim 0.70$; $\varepsilon_{Nd} > -5$; intermediate Pb isotope ratios). Consequently, the composition of particles transported by the AABW flowing out of the Weddell Sea is intermediate, with ε_{Nd} around -9 (Walter et al., 2000), and is potentially enriched in young material when entering the Scotia Sea.

The above observations are summarized in annex 5, in which specific isotopic and mineralogical signatures are associated to each deep-water mass. It is clear that the K/C ratio as well as the ε_{Nd} composition reflect northern- versus southern-born water mass contributions (i.e., NADW versus CDW and AABW). Similarly, smectite and illite are transported by distinct water-masses and the illite/smectite ratio (I/S) can efficiently distinguish the AABW from the other water-masses. Thus, this ratio will further be used as a tool for estimating the AABW contribution through time.

The illite/smectite and kaolinite/smectite ratios have been plotted in figure 43. The three end-members for AABW, CDW and NADW are plotted according to the clay composition of their suspended loads. Figure 43 highlights how the relative contribution of the three water masses (i.e., AABW, CDW, and NADW) to clay deposition has changed with time since the LGM. To interpret this figure it is important to keep in mind that changes observed in the contribution one deep-water mass are relative compared to the other water masses. To construct figure 43.b, the proportion of clay particles deposited by each deep-water mass was calculated as described below.

End-member deep-water mass compositions were calculated from the average composition of deep water-masses shown in figure 43.a. Weights are computed as the inverse of the distance between the position of water-mass end-member (x_w;y_w) with x_w=K/C_w and y_w=I/S_w and the position of the data point (x_d;y_d), with x_d=K/C_d and y_d=I/S_d taken from the graph (figure 43.a) for each water-mass: $W_w=1/[\ (x_d-xw)^2+(y_d-y_w)^2]^{1/2}$. The position used for the deep-water masses are: xA_{ABW} = K/C_{AABW} = 0.3 ; y_{AABW} = I/S_{AABW} = 2.5 ; x_{CDW} = K/C_{CDW} = 0.1 ; y_{CDW} = I/S_{CDW} = 1 ; x_{NADW} = K/C_{NADW} = 0.9 ; y_{NADW} = I/S_{NADW} = 1. The values used for the NADW correspond to the mineralogical composition of the NADW during the LGM. As a result, the contribution of NADW to the deposition of clay particles is underestimated (~10%) at the end of the deglaciation while the contribution of the CDW is overestimated (~10%). This choice does not have a strong impact on the contribution of the AABW (less than 4.5%). Second, the percentage of the contribution of each water mass is calculated by bringing the sum of the weights computed to 100: [NADW's contribution] = W_{NADW}/(W_{NADW} + W_{CDW} + W_{AABW}) x 100

To test the validity of this method to reconstruct the evolution of the past deep circulation, we compared our results with those of other water-masses proxies (e.g. seawater ε_{Nd} and $\delta^{13}C$). However, these latter methods proved incapable of distinguishing AABW from CDW. Consequently, we based the comparison on the proportion of the NADW compared to

the southern sourced deep waters. Based on data from the same core, our estimates give comparable results to these two proxies (see annex 6). This suggests that our approach successfully reconstructs the evolution of these three deep-water masses. However, our estimate of the proportion of the NADW is higher than the estimate of Howe et al. (2016) based on ε_{Nd}. This discrepancy can be explained by two factors. First, we were unable to make corrections for concentration differences of particles in the three deep-water masses (i.e., quantity of clay particles per volume of water) due to the large uncertainties involved. In addition, it is very likely that the NADW is more concentrated in clay particles than the AABW and CDW due to sediment source effect (e.g., dry East Antarctica below thick ice sheets vs. humid South America highly drained by equatorial rivers). Consequently, even though our tool successfully reconstruct the variations of the NADW, the contribution of NADW is probably overestimated. In other words, our estimate of NADW contribution to the clay deposition is likely higher than the proportion of NADW (in volume of water). Second, the choice of the end member for the seawater ε_{Nd} of AABW+CDW made by Howe et al. (2016) is debatable (-5.5 during the LGM, -8.5 during the Holocene). Skinner et al. (2013) used a compositional end-member between -5 and -2, which yields a better match with the isotopic composition of seawater Nd at our site (-5.5, Skinner et al., 2013). Therefore, the estimate of Howe et al. (2016) appears to underestimate the contribution of NADW at our site.

From 25 to 20 ka, the CDW is clearly dominant, with a contribution of 50% on average, while the NADW and AABW deliver 35% and 15% of the clay fraction, respectively. The highest contribution of the AABW is observed at the end of the LGM between 20 and 17.5 ka (27% in average, but up to 52% at 18 ka). During this interval, the NADW and CDW deliver respectively 34% and 39% on average. At the end of this period, the mineralogical composition of the fine sediments deposited at site MD07-3076Q suggests that the AABW was dominant. At the beginning of the deglaciation, between 17.5 and 15 ka (i.e., during HS 1), the clay mineral composition of core MD07-3076Q indicates a decreased relative contribution of the AABW end-member (15% on average) associated to an increase of the relative contribution of the CDW (49%) end-member. This observation of an increase of the CDW contribution is supported by the radiogenic ε_{Nd} of the clay-size fraction and a $^{87}Sr/^{86}Sr$ close to the Scotia Arc composition (figures 40 and 41).

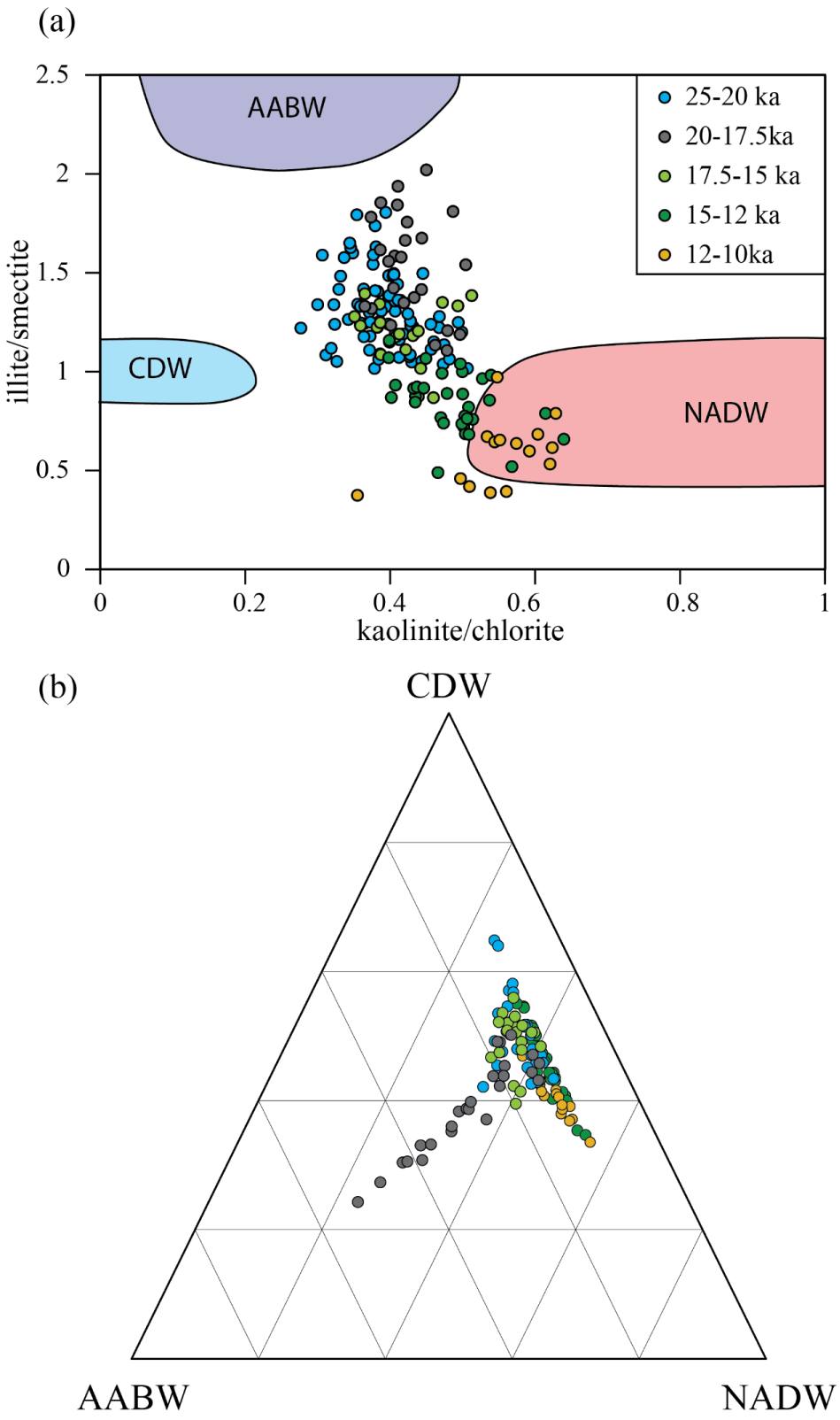

Figure 43: (a) Plot of kaolinite/chlorite vs illite/smectite ratios from core MD07-3076Q from 25 to 10 ka. The composition of deep-water masses has been determined using the data from Petschick et al. (1996). (b) Ternary diagram comparing the contribution of the three deep-water masses to the clay deposition at site MD07-3076Q.

From 15 ka on, the clay mineral composition at the study site records an increasing contribution of the NADW until the end of the deglaciation (at least 47% for the interval 10-12 ka, figure 43). Compared with the LGM this suggests enhanced contribution of the NADW with reduced contributions from the CDW (40% for the interval 10-12 ka) and AABW (13% for the interval 10-12 ka). These results are strongly supported by the sharp decrease in ε_{Nd} and by the concomitant increase of $^{208}Pb/^{204}Pb$ and $^{207}Pb/^{204}Pb$ ratios from the clay size fraction (figures 40 and 42). This corroborates the conclusions based on the *cibicides* $\delta^{13}C$ measured in the same core (figure 44.e, Waelbroeck et al., 2011). In addition, increasing inputs of less crystallized smectite (slightly higher crystallinity: ~1.5, supplementary figure S1) from Patagonia support the southward penetration of the NADW in the southern Atlantic Ocean, consistent with an increasing contribution of the NADW-W to sedimentation at site MD07-3076Q. Interestingly, the transition between B/A (that starts simultaneously with the southern Hemisphere cooling, the Antarctic Cold Reversal) and the YD appears to have no effect on the relative contribution of deep-water masses and shows a continuous increase of the relative contribution of the NADW during these two periods.

Overall, the clay size fraction demonstrates that the contribution of the three deep water-masses changed through time. An increase of contribution of the AABW is recorded at the end of the LGM and is followed by a two-step deglaciation. First, an important reduction of the AABW is observed at the HS 1 onset. Second, an increase in the NADW contribution compared to the CDW is observed during the B/A and YD.

2. *Cohesive silt mode fraction (2-20 μm): an AABW signal*

According to our geochemical data, the provenance of the cohesive silt fraction is dominated by sources from the Scotia Sea area, especially Patagonia and Antarctic Peninsula, and by an old, unidentified, crustal source. According to the modern deep oceanic circulation, only the CDW and AABW are able to transport sediment from the Scotia Sea to the studied site (figure 36). It was also likely the case during the LGM and deglaciation. The AABW and CDW were likely spreading further north while the NADW was likely shallower, and retreated to the north (Kuhn and Diekmann, 2002; Barker et al., 2010; Waelbroeck et al., 2011). These modifications do not affect the continental sources of terrigeneous sediment for the CDW and AABW compared the present day, and the NADW is still unable to transport sediments from the Scotia Sea. Consequently, it excludes the NADW as a transport medium for the cohesive silt mode fraction to site MD07-3076Q. Therefore, because the NADW is also the only water-mass able to transport sediment from the South American Shield to our study site, it excludes

the South American Shield as a source of sediment for the cohesive silt mode fraction, and implies East Antarctica as the source of old material identified in the cohesive silt mode fraction. The terrigenous supplies deriving from East Antarctica/Scotia Sea strongly suggest the AABW has been the dominant carrier of the 2-20 μm grain-size fraction since the LGM. In addition, because the mean isotopic composition of this grain-size fraction transported by the AABW is relatively constant through time (figure 41), the relative contributions of East Antarctica and Scotia Sea area seem to have remained largely unchanged since the LGM.

3. *Sortable silt mode fraction (20-32/40 μm): A LCDW signal*

A part of the particles transported by the AABW and the NADW are derived from old crustal sources (i.e., East Antarctica and South American Shield, respectively). Thence, these two deep-water masses cannot be the source of the sortable silt mode fraction during the LGM. In contrast, the CDW is a good candidate to transport particles solely from the Scotia Sea, as identified for the sortable silt mode fraction during the LGM. Consequently, the only possible source of this grain-size fraction is the CDW. During the deglaciation, the Nd isotope composition of the sortable silt mode fraction became gradually less radiogenic while the $^{87}Sr/^{86}Sr$ ratio fluctuated, suggesting a modification of provenances and/or an additional contribution of less radiogenic Nd source. Such isotopic changes could be explained in two ways; (1) a change in the CDW pathway; (2) the incorporation of terrigenous material by mixing with other water-masses (such as AABW or NADW). The CDW slowed down and migrated southward during the deglaciation in concert with the southward migration of the subpolar and polar fronts (Howard and Prell, 1992; Anderson et al., 2009; Denton et al., 2010). However, such a change in the CDW pathway would have no effect on the terrigenous sources of particles. In contrast, several studies proposed increased ventilation in the Southern Ocean, enabling the degassing of oceanic CO_2 to the atmosphere (Ahn and Brook, 2008; Fischer et al., 2010; Skinner et al., 2010, 2013, 2014; Siani et al., 2013). Currently the base of the LCDW is mixed with the AABW, which was apparently not the case during the LGM (Skinner et al., 2010). The onset of AABW/LCDM mixing could explain the incorporation of unradiogenic terrigenous material from the Weddell Sea embayment (i.e., East Antarctica) into the LCDW. This mechanism likely explains the shift in ε_{Nd} composition during the deglaciation. This hypothesis is supported by the results of Walter et al. (2000) who reported lower ε_{Nd} in terrigenous sediments in the southern Scotia Sea during the interglacial period and interpreted this as higher contribution of sediment from the Weddell Sea embayment due to the mixing of the AABW into the ACC. From 15 ka, the Nd isotope composition of the sortable silt mode

fraction is very close to the one from the cohesive silt mode fraction transported by the AABW. It suggests that the sortable silt mode fraction is specifically transported by the LCDW rather than by the entire CDW. This highlights the fact that the ε_{Nd} variations from the sortable silt mode fraction provide a useful tool to study the mixing between the AABW and LCDW.

4. Paleoceanographic implication

Our results establish that different grain-size modes can be attributed to distinct water-masses and that variation of the particle size of the different grain-size modes (figure 39) can be used to record the variations of flow speed of these water-masses as well as changes in pathways/mixing. This method has the advantage of distinguishing the speed of each water mass instead of giving the average speed of all the water masses, as it is the case for the sortable silt method (McCave and Hall, 2006). During the last glacial period, the large mean particle diameter (>30 μm) of the sortable silt mode fraction reflects strong LCDW activity. At the beginning of the deglaciation, the variation of the mean particle size suggests that the LCDW speed slightly decreased, but remained high. Since ~15 ka, the LCDW speed has been showing a gradual decrease. McCave et al. (2014) observed minor change in the Antarctic Circumpolar Current (which includes the CDW) flow speed at the Drake Passage during the deglaciation. Our observation, however, is consistent with other studies in the south Indian sector of the Southern Ocean indicating that the Antarctic Circumpolar Current (which includes the CDW) flow speed was maximum during the LGM and decreased during the deglaciation (Mazaud et al., 2010), with a notable increase from ~15 ka on (Mazaud et al., in prep.). Altogether, these studies and our results suggest that the weakening of the ACC started at ~15 ka.

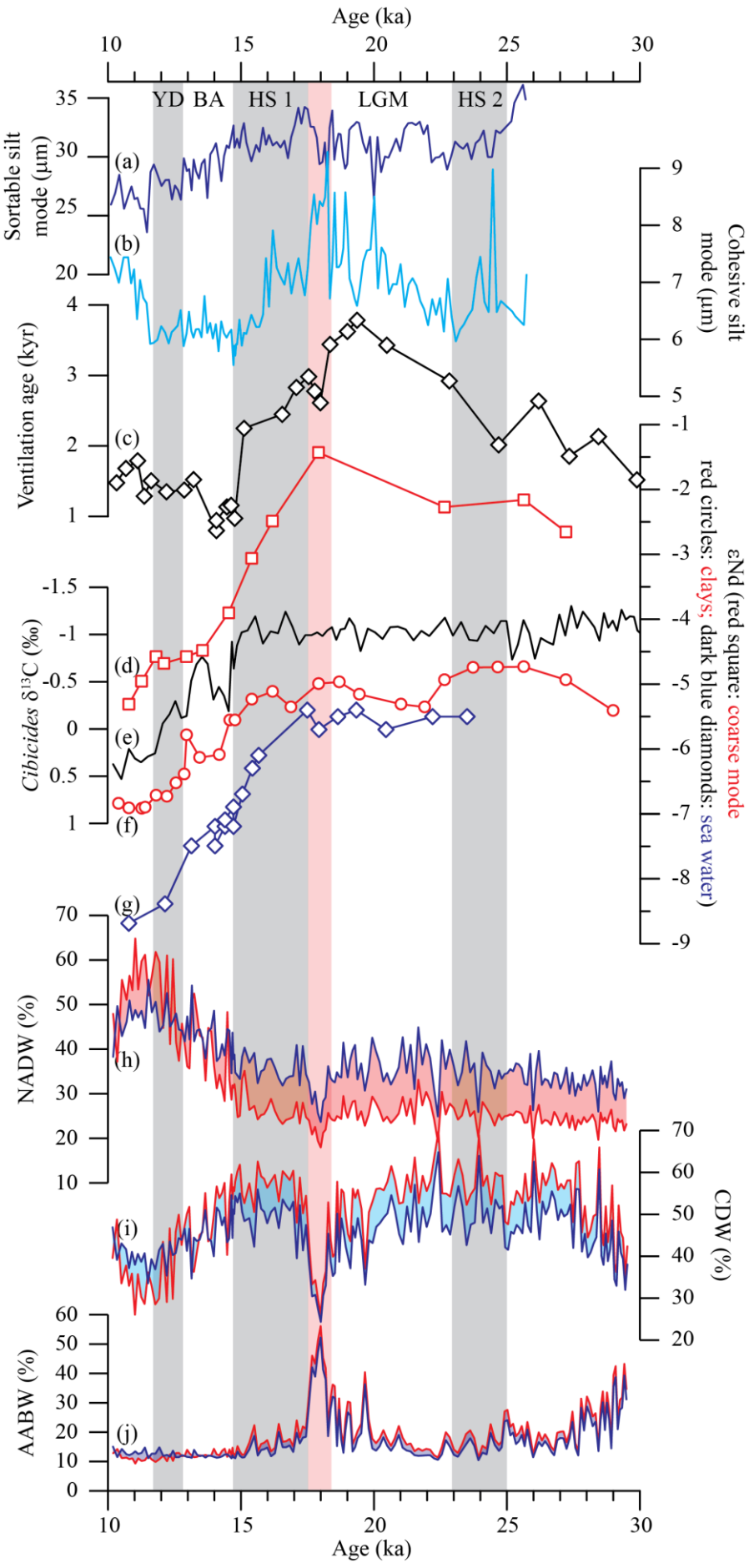

Figure 44: Comparison between paleoceanographic proxies from core MD07-3076Q and data produced in this study. Grey areas delimit the main climatic events and the red band highlights the particularly strong AABW event. (a) size of the sortable silt mode (μm), a proxy of the speed of the LCDW; (b) size of the cohesive silt mode (μm), a proxy of the speed of the AABW; (c) bottom water ventilation age from site MD07-3076Q (data from Skinner et al., 2010); (d) ε_{Nd} from the sortable silt size fraction; (e) Cibicides $\delta^{13}C$ from site MD07-3076Q (Waelbroeck et al., 2011); (f) ε_{Nd} from the cohesive silt size fraction; (g) seawater ε_{Nd} from site MD07-3076Q (Skinner et al., 2013); (h) proportion of clay particles delivered by the NADW (see figure 43.b); (i) proportion of clay particles delivered by the CDW (see figure 43.b); (j) proportion of clay particles delivered by the AABW (see figure 43.b). On curves (h), (i) and (j), the red line represent values calculated using the Holocene end-member of the NADW (I/S = 0.5), while the blue line correspond to the values calculated using the LGM end-member of the NADW (I/S = 1).

From ~26 to 21 ka, the low particle sizes recorded in the cohesive silt mode (figure 37.b, transported by the AABW) indicate slow AABW, which is consistent with the observed moderate relative contribution of AABW in clay particles (figure 43 and 44). In this time interval, one isolated high value is recorded at 24 ka and suggests that, temporarily, AABW activity was stronger. However, no change is registered in the clay minerals (figure 38 and 44). The grain-size data indicate that the AABW became more vigorous from 21 ka to reach its strongest speed at the end of the LGM. This maximum speed is concomitant with the strongest relative contribution of the AABW of the clay record (figures 38.h and 44), as shown by the peak of the illite/smectite ratio (figure 38) illustrated on figure 43. Interestingly, this AABW maximum preceded the HS 1, and both its speed and relative contribution fell at the LGM/HS 1 transition as defined by Missiaen et al. (2019). At the beginning of the deglaciation, the abrupt decrease of the fine grain-size mode indicates a slowdown of the AABW (figure 37). This is supported by a sharp decrease in the illite/smectite ratio in the clay-size fraction (figure 38), which also suggests an abrupt decrease of the relative contribution of the AABW. At ~16 ka, a slowdown of the AABW is indicated by a second sharp decrease of the cohesive silt mode (figure 37), which reaches its lowest values of the entire record, indicating low AABW speed from 16 to 11.5 ka, when the AABW activity increased suddenly and recovered the speed observed before 16 ka.

These variations of the AABW speed could indicate the transition from the Ice Shelf Mode dominated bottom water formation at the end of the LGM to the Polynyas Mode

dominated bottom water formation during interglacial periods. The variations of the cohesive silt mode support a strong AABW during the LGM and the Early Holocene, and a minimum flow during the deglaciation. This minimum flow would result from the reduction of bottom water production via the Ice Shelf Mode and still low production via the Polynyas Mode. Our results confirm the results of Krueger et al. (2012) who demonstrated the relation between the flow speed changes in the Cape Basin and the higher AABW production rates and indicate that the size of the cohesive silt mode is a reliable tracer of the AABW flow speed and hence of AABW production rates in the Weddell Sea.

Overall, the variations of the AABW flow speed and ventilation age are similar, with higher average speeds corresponding to the old ventilation ages. Taken together with the reconstructed vigorous LCDW during the LGM (figure 43.a.), these observations suggest that the deep Southern Ocean was poorly ventilated but with a vigorous circulation. It means that both the AABW and LCDW remained isolated from the surface during the LGM. This conclusion is consistent with our hypothesis that AABW was formed under ice shelves during this period and that the major expansion of sea ice (Bianchi and Gersonde, 2004; Bostock et al., 2012; Adkins 2013) kept the AABW isolated from the atmosphere during the LGM. In addition, poorly ventilated deep Southern Ocean associated with a vigorous deep circulation (i.e., high AABW and LCDW flow) suggests that a barrier existed between the deep ocean and the surface, which is consistent with the study of Howe et al. (2016). In contrast, direct comparison highlights the fact that the peaks of ventilation age and of the AABW flow are not in phase. Indeed, the peaks of the AABW flow (figure 44.b) and of the AABW contribution to clay deposition (figure 44.j) are synchronous with the first decrease in deep-water ventilation ages after the LGM and prior to HS1. Moreover, this well-defined change in the AABW behavior is recorded by two distinct proxies (i.e., clay minerals and grain-size distribution) and in two distinct grain-size fractions (clays and silts). These synchronous changes are associated with a drop in ventilation age prior to the HS 1. The variations in two grain-size fractions that are transported and deposited by distinct dynamic processes indicates a major perturbation in Southern Ocean circulation. Interestingly, the increase in the AABW strength associated to the Early decrease in deep-water ventilation age took place significantly earlier than the changes recorded by the other proxies measured in core MD07-3076Q (i.e., sea water ε_{Nd} between 17.5 and 16 ka, $\delta^{13}C$ at 14.5 ka, $\delta^{18}O$ at 15 ka, LCDW flow speed at 15 ka, NADW proportion at 15 ka) and also precedes the atmospheric CO_2 rise (Bereiter et al., 2015) and the change in the opal flux (Anderson et al., 2009). For the first time, these data indicate a change in the deep

Southern Ocean circulation that is associated with ventilation change that precedes the HS 1. This suggest that the identified large temporary (~1 kyr long) increase in the AABW contribution and flow speed may have had a substantial impact on the deep Southern Ocean ventilation, and by extension, on the deglacial CO_2 rise. Indeed, the magnitude of the change in the AABW behavior has the potential to "break" the hypothetical physical barrier between the deep Southern Ocean and the surface that was responsible of poorly ventilated deep-water during the LGM. This combination of events also explains the unexpected Early fall of the deep-water ventilation age observed at ~18.2 ka.

Conclusion

The mineralogical characteristics of the clay-size fraction provide new insights into the general thermohaline circulation in the southern South Atlantic. The mineralogical signal demonstrates strong influence of both the CDW and AABW during the last glacial period. Clay assemblages reveal a particularly high contribution of the AABW at the end of the LGM, which is interpreted as reflecting strong Ice Shelf Mode bottom water production in the Weddell Sea. The contribution of the CDW and AABW then progressively decreases during the deglaciation together with the growing influence of the NADW (figure 43). Indeed, clay size fraction data monitor the progressive incursion of NADW into the Southern Ocean during the deglaciation from ~15 ka (figure 43), as well as the synchronous southward retreat of the southern-born deep water-masses (i.e., CDW and AABW).

The isotopic compositions of the distinct grain-size modes provides invaluable information. The sortable silt mode fraction helps to trace the LCDW activity whereas the cohesive silt mode fraction is associated with the AABW signal. Consequently, the temporal evolution of flow speeds, pathways and interactions of these deep water-masses can be determined in a very robust way. This study suggests: (1) vigorous LCDW during the LGM and a marked weakening from ~15 ka; (2) strong AABW at the end of the LGM and during the Early Holocene, and weak AABW during the deglaciation between 16 and 11.5 ka. These results suggest a decrease of AABW production rates during the deglaciation that could result from the transition from strong Ice Shelf Mode bottom water production during the LGM to stronger Polynyas Mode bottom water during the Holocene.

The strong LCDW speed observed during the LGM is associated with increased clay deposition by the CDW, and the reduction of LCDW speed since the B/A is accompanied by an increased clay contribution from the NADW. Similarly, the highest AABW speed recorded

at the end of the LGM is concomitant with the highest relative contribution of the AABW to clay mineral deposition. Interestingly, this AABW maximum preceded the HS 1 and both its speed and contribution fell markedly at the LGM/HS 1 transition.

Finally, this study demonstrates that based on (1) the combination of isotopic and mineral investigation of the clay size fraction, (2) the combination of isotopic measurement of isolated grain-size modes and of grain-size distribution results, and (3) a complete synthesis of the potential sources of sediments, it is possible to obtain reliable information on the lithogenic material transported by each deep-water mass. This approach allows efficient tracking of the evolution of distinct water-masses through time, since it helps to isolate the specific signal associated to each water-mass. Based on these observations, we conclude that the increase in the AABW strength at the end of the LGM may have had a substantial impact on the ventilation recovery of the deep Southern Ocean, and by extension, to the deglacial CO_2 rise.

Acknowledgments

We wish to thank Richard Smeets for his invaluable help in the clean lab, Emmeke Bos, Janne Koorneef, and Mathijs van de Ven for the help with TIMS Triton measurements, Bas van der Wagt and Kirsten van Zuilen for Neptune MC-ICPMS measurements. Tristan Lippens is thanked for computer support. We also wish to thank all organizations that provided financial support to the project: the “region Haut de France” and the Vrije Universiteit of Amsterdam. The research was supported by Europlanet 2020 RI, which received funding from the European Union's Horizon 2020 research and innovation programme under grant agreement No 654208. We also want to express our special thanks to the “flotte océanographique française” for retrieving the sediment core used in this study. FB and VBR thanks Monique Gentric for administrative support. CW acknowledges support from the European Research Council ERC grant ACCLIMATE/n° 339108.

Supplementary figures

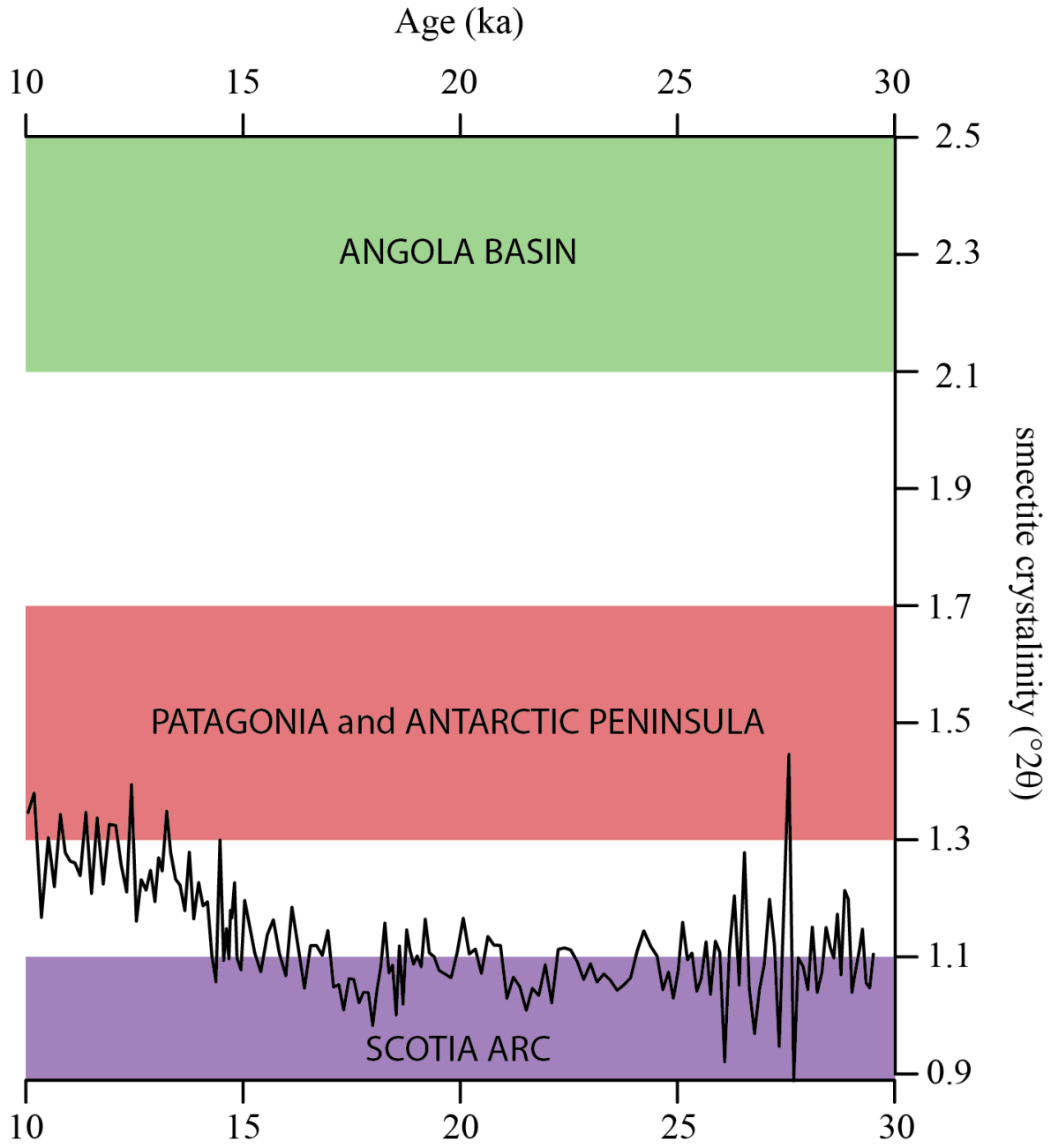

SUPPLEMENTARY FIGURE S1: Crystallinity of smectite from site MD07-3076Q (black curve) and comparison with crystallinity of smectite from potential sources to the South Atlantic basin. The data used for comparison are from Petschick et al., 1996.

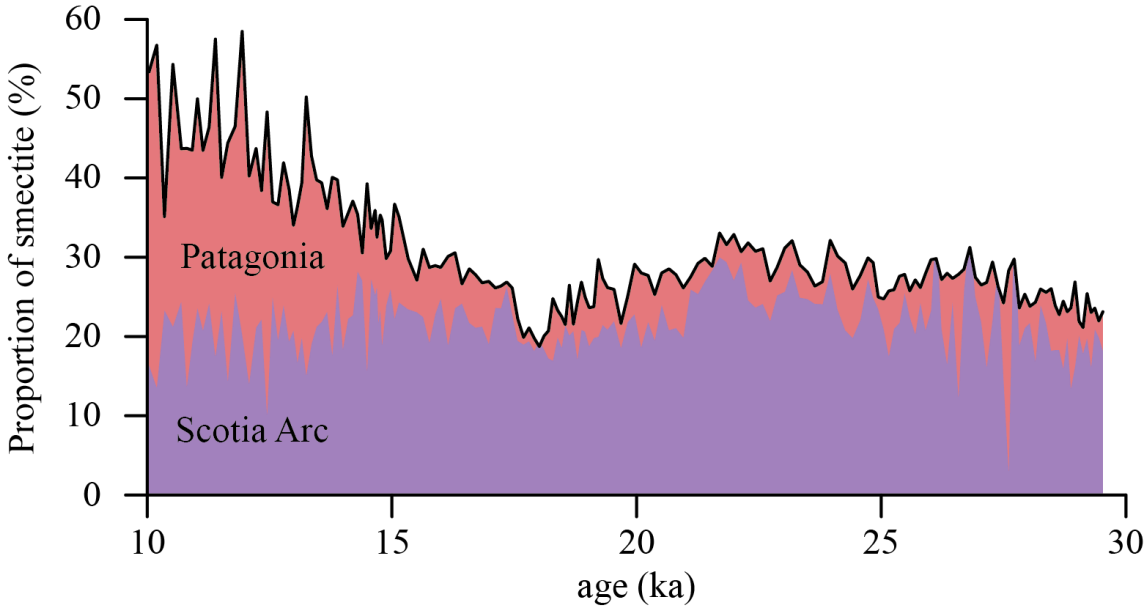

SUPPLEMENTARY FIGURE S2: Contribution of the two types of smectite from site MD07-3076Q. The black line represent the total smectite content, the purple area represent the smectite content from the Scotia Arc, and the red area represent the smectite content from Patagonia. The proportion of the two types of smectite are calculated as followed:

$$[\%\text{Patagonian smectite}] = [\%\text{total smectite}] \times \frac{(\text{sample crystallinity}] - (\text{Scotia Sea crystallinity}]}{(\text{Patagonia crystallinity}] - (\text{Scotia Sea crystallinity}]} \times 100$$

$$[\%\text{Scotia Sea smectite}] = [\%\text{total smectite}] - (\%\text{Patagonian smectite}]$$

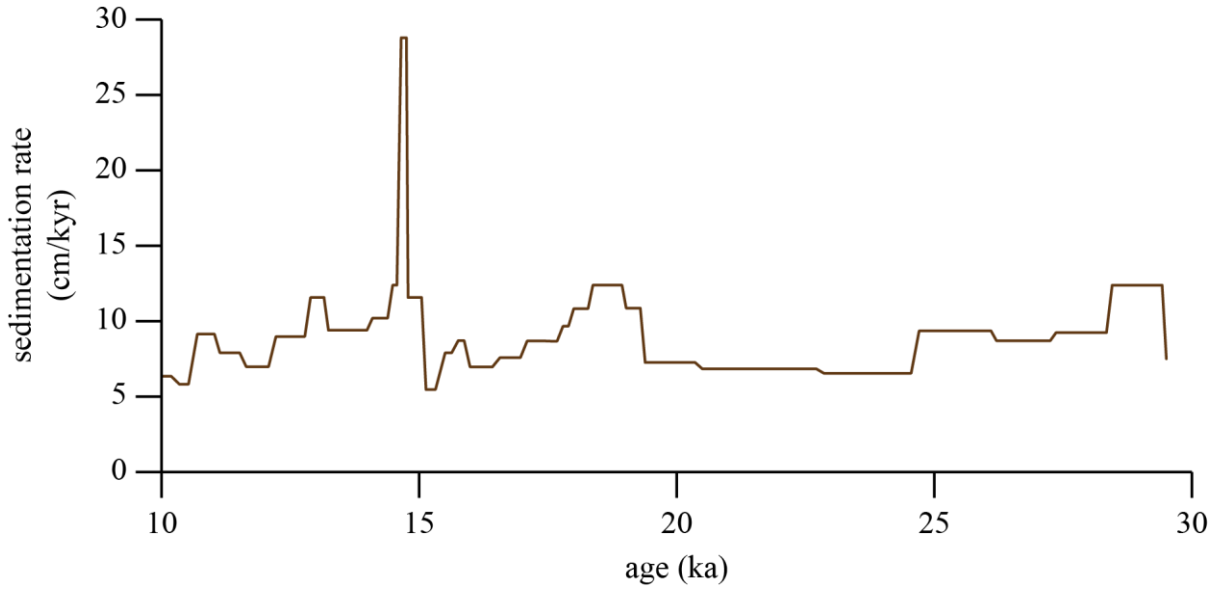

SUPPLEMENTARY FIGURE S3: Sedimentation rate from site MD07-3076Q calculated from the age model published in Skinner et al. (2010, 2013, 2014) and Gottschalk et al. (2015b).

Chapter 5. Holocene climate variability over Patagonia and southern Brazil: insights from geochemical and mineralogical properties of detrital sediments from the deep South Atlantic Ocean.

F. Beny[1,2], V. Bout-Roumazeilles[1], G. Davies[2], L. Skinner[3], C. Waelbroeck[4], J. Gottschalk[5], A. Bory[1], N. Tribovillard[1], R. Abraham[1], M. Delattre[1].

[1] Laboratoire d'Océanologie et de Géosciences, UMR 8187 CNRS/Univ Lille/ULCO, Cité scientifique, F-59655 Villeneuve d'Ascq, France.

[2] VU University Amsterdam, Department of Earth Sciences, Faculty of Science, De Boelelaan 1085, 1081 HV Amsterdam, The Netherlands.

[3] Godwin Laboratory for Palaeoclimate Research, Department of Earth Sciences, University of Cambridge, Downing Street, Cambridge CB2 3EQ, United Kingdom.

[4] Laboratoire des Sciences du Climat et de l'Environnement, LSCE/IPSL, UMR 8212 CEA-CNRS-UVSQ, Site de l'Orme des Merisiers, F-91191 Gif sur Yvette Cedex, France.

[5] Lamont-Doherty Earth Observatory, Colombia University, Palisades NY 10964-8000, United States.

Abstract

Reconstructions of paleoenvironmental conditions over South America are mainly based on continental archives. Here, we provide new insights into past South American climate emphasizing on rainfall distribution and intensity as well as wind strength by studying the nature and provenance of deep sea sediments deposited in the central South Atlantic Ocean (core MD07-3076Q) during the Holocene. By combining clay mineralogy, X-ray fluorescence core scanning data, and Sr-Nd-Pb isotopes of detrital sediments, we show that most of the sedimentary changes in the deep South Atlantic observed during the Holocene can be linked to paleoenvironmental changes over South America (with the exception of the 8.2 ka event). Smectite content and smectite crystallinity are used to estimate the sediment supply from Patagonia while the kaolinite/chlorite ratio (Kaol/Chlo) is considered to represent the contribution of the Parana River, directly recording rainfall distribution over its watershed. The aluminum/potassium (Al/K) ratio was used to reconstruct the degree of chemical weathering over southern South America, and is interpreted as changes in rainfall intensity. These proxies demonstrate that moderately dry conditions associated with weak winds prevailed during early Holocene (11-9 ka), while dryness and wind strength increased thereafter (9-7 ka). The mid-Holocene was the driest and the windiest period of the Holocene, with the strongest winds likely occurring between 6 and 4.5 ka. At the end of the mid-Holocene (~5 ka), environmental conditions became significantly wetter and the wind strength decreased until the beginning of the late-Holocene (~3 ka). The time interval between 3 and 2.2 ka was likely the wettest of the Holocene, before the return to dry conditions at the end of the record.

I. Introduction

Precipitation in South America is primarily controlled by the position (figure 45) of the Intertropical Convergence Zone (ITCZ), the South Atlantic Convergence Zone (SACZ), and the South Westerly Wind Belt (SWWB) at present-day (Cruz et al., 2009; Kylian and Lamy, 2012). The ITCZ causes strong precipitation over equatorial and tropical South America, while the SACZ mostly controls rainfall over the Parana River Basin (i.e. Southern Brazil, Paraguay, Uruguay, South Easternmost Bolivia, and Northern Argentina). The SWWB is linked to strong surface wind stress and rainfall over Southern Patagonia. Reconstructions of past changes in rainfall and wind intensity associated with these atmospheric patterns are mainly based on speleothems (Cruz et al., 2005; 2006; 2009; Novello et al., 2017), lagoons and lakes (Schäbitz, 1994; Barker et al., 2005; Mayr et al., 2007; Sallun et al., 2012; Kaplan et al., 2016; Fontes et al., 2017), terrestrial (Behling et al., 2001; Mansilla et al., 2016), and glacier advance reconstructions (Glasser et al., 2004; Kaplan et al., 2016). Past precipitation patterns on land were also assessed based on marine sediment cores using magnetic properties (Mathias et al., 2014), grain size distribution of detrital sediments (Razik et al., 2013, 2015), and micropaleontological proxies (Razik et al., 2013). However, the sensitivity of rainfall intensity and distribution patterns over South America to changing environmental and climatic conditions, in particular during the Holocene (Kilian and Lamy, 2012), remain insufficiently understood.

The provenance of terrigenous sediments from marine records has proven useful in order to study terrestrial rainfall distribution patterns for instance driven by monsoon systems owing to a direct link to offshore sediment delivery and transport (i.e. Indian monsoon: Clift et al., 2008; Pandarinath, 2009; East Asian Monsoon: Liu et al., 2003; Diekmann et al., 2008; Dou et al., 2012; Li et al., 2015; Zhao et al., 2017, 2018; Beny et al., 2018; African Monsoon: Meyer et al., 2011). The benefits of this approach have so far not been exploited to study South American climate variations. Here, we aim to provide a new record of rainfall distribution patterns and wind strengths over South America by reconstructing the nature and provenance of deep sea sediments from core MD07-3076Q from the central South Atlantic Ocean, including clay mineralogy, elemental sediment composition and radiogenic isotope signatures. This sediment core has previously been used to reconstruct past oceanic circulation changes (Skinner et al., 2010, 2013, 2014; Gottschalk et al., 2015a,b, 2017, 2018; Beny et al., 2020), and may thus allow a distinction between the impact of environmental changes (e.g., precipitation

intensity and distribution, aeolian activity) and oceanic circulation (e.g., sediment transport) on the provenance signal of sediment fractions in the central South Atlantic.

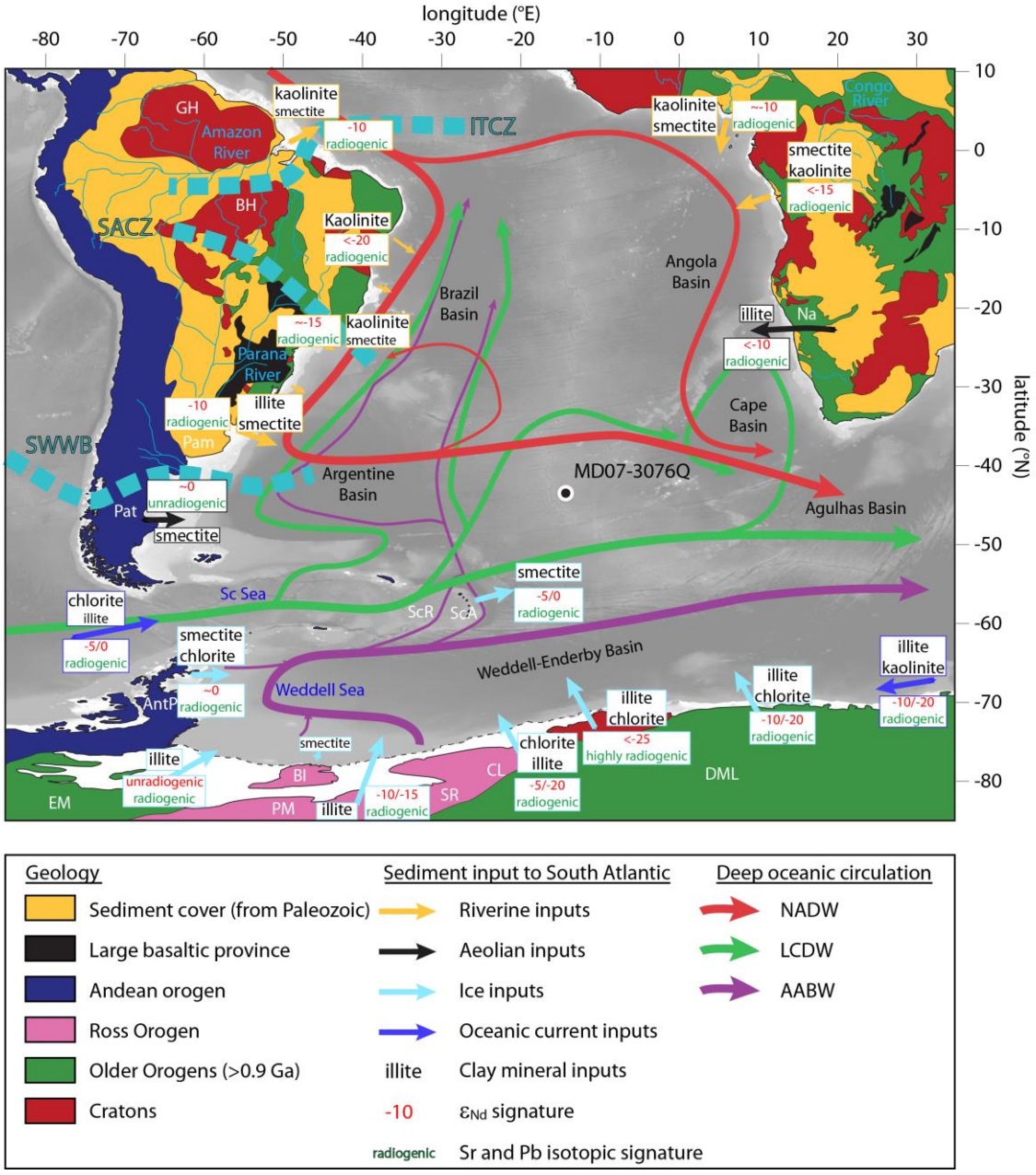

Figure 45: Simplified geological map of the study area showing riverine systems (light blue), seas (dark blue), oceanic basins (black), major geographic areas (white), and main climatic fronts in South America (light blue stippled lines). In South America: Guyana Highlands -GH-, Brazilian Highlands -BH-, Argentinian Pampas -Pam-, Patagonia -Pat-; in Africa: Namibian deserts -Na-; in Antarctica: Ellsworth Mountains -EM-, Antarctic Peninsula -AntP-, Pensacola Mountains -PM-, Berkner Islands -BI-, Shackleton Range -SR-, Coats Land -CL-, Dronning Maud Land -DML-. The northern limit of the modern South Westerly Wind Belt (SWWB) is drawn following the summer mean zonal wind isoline 6 m/s, calculated by Björck

et al. (2012) using the NCEP/NCAR data from Kalnay et al. (1996) for the period 1981-2000; the modern Intertropical Convergence Zone (ITCZ) and South Atlantic Convergence Zone (SACZ) are drawn using the data from Cruz et al. (2009). Clay mineral inputs to the South Atlantic Ocean (boxes) derived from the studies of Petschick et al, (1996), Diekmann et al. (2000), Walter et al. (2000), Guyot et al. (2007), Bayon et al. (2016), and Khondoker et al. (2018).

II. Material and Methods

A. Material

This study is based on sediment samples from marine sediment core MD07-3076Q (44°9.2'S, 14°13.7'W) recovered by the French Research Vessel *Marion Dufresne* during the SOUC cruise in 2007 on the eastern flank of the Mid-Atlantic Ridge at 3770 m water depth (figure 45). The core chronology is based on planktonic foraminifer radiocarbon dates (9 measurements for the studied interval) and additional stratigraphic control points based on planktonic foraminiferal Mg/Ca ratios and assemblage changes (Skinner et al., 2010, 2013, 2014; Gottschalk et al, 2015a).

B. Sample preparation and analytical procedure of the clay fraction

Samples were first decarbonated using 0.1N HCl, and deflocculated by repeated washes using milli-Q water. The clay-size fraction (<2 μm) was isolated by settling according to Stoke's Law, concentrated by centrifugation (40 minutes, 3500 rotation per minute) and then oriented on glass slides. X-ray diffractograms were obtained to determine the clay composition using a Bruker D4Endeavour (standard 30kV and 30mA) coupled with a rapid Lynxeye detector and by running each sample three times between 2.49 and 32.5°2θ in different setups: (1) dried sample, glycolated sample (12 hours in ethylene glycol), and heated sample (490°C for 2 hours). The proportion of each clay mineral (smectite, chlorite, illite, and kaolinite) is determined using the main peak (layer and interlayer) on the X-ray diffraction diagrams according to their crystallographic characteristics (Brown, 1980). Smectite is characterized by a main peak at 14-15 Å on the air-dried samples that expands at 17 Å after ethylene glycol saturation and collapses at 10 Å after heating. Illite is characterized by a basal peak at 10 Å on the 3 runs. Kaolinite and chlorite are measured on their main peak at 7-7.2 Å and further distinguished using pseudo void deconvolution of the kaolinite/chlorite doublet at 3.54/3.58 Å. All measurements and semi-quantitative estimates are processed using the McDiff software (Petschick, 2000). The index of Esquevin (Esquevin, 1969) corresponds to the ratio between the intensity of the peak of illite at

5 Å and at 10 Å (illite 5Å/10Å). The crystallinity of smectite and illite has been measured using the method of integral breath to enable comparison with the work of Petschik et al. (1996) in the South Atlantic. High crystallinity corresponds to low values of the index (Kubler et al., 1969).

An aliquot of ~100 mg from the clay fraction (<2 μm) was separated and used for chemical procedures. Chemical and isotopic measurements were performed at the Faculty of Science of the Vrije Universiteit, Amsterdam. Sediment was digested in closed Savillex™ Teflon beakers using a mixture of concentrated HF and HNO_3 (~2/3 and 1/3, respectively) for a few days at 120°C. After digestion, samples were dried out and re-dissolved in ~6.5N HCl to remove fluorides. Nd, Sr, and Pb were purified using conventional ion chromatography. Pb isotopes were processed first and purified using AG-X8 200-400 mesh resin. Light rare earth elements (LREE) were isolated using true-spec resin medium (Eichrom™, 100-150 μm mesh size) and Nd was eluted from the LREE fraction using LN-resin (Eichrom™, 50-100 μm mesh size). Sr was recovered using Sr resin column. Nd and Pb measurements were performed by bracketing using respectively CIGO and NBS981 standards on Thermo Scientific Neptune multi-collector inductive coupled plasma-mass spectrometer (MC-ICPMS), whereas Sr measurements were performed on a thermal ionization multi-collector-MS (TIMS).

C. X-ray flourescence (XRF) scanning

The XRF core scanner measurement were carried out at the Universtity of Cambridge using an AVAATECH core scanner. *The data is own by Luke Skinner, and detailed method has not been transmitted yet when this PhD manuscript was submitted. Thus, this section will only be completed for publication.*

Because K is easily washed away from rocks by liquid water and Al is one of less mobile element in water, bulk sedimentary XRF Al/K ratio is used as indicator of the degree of chemical weathering, and thus rainfall intensities, over southern South America.

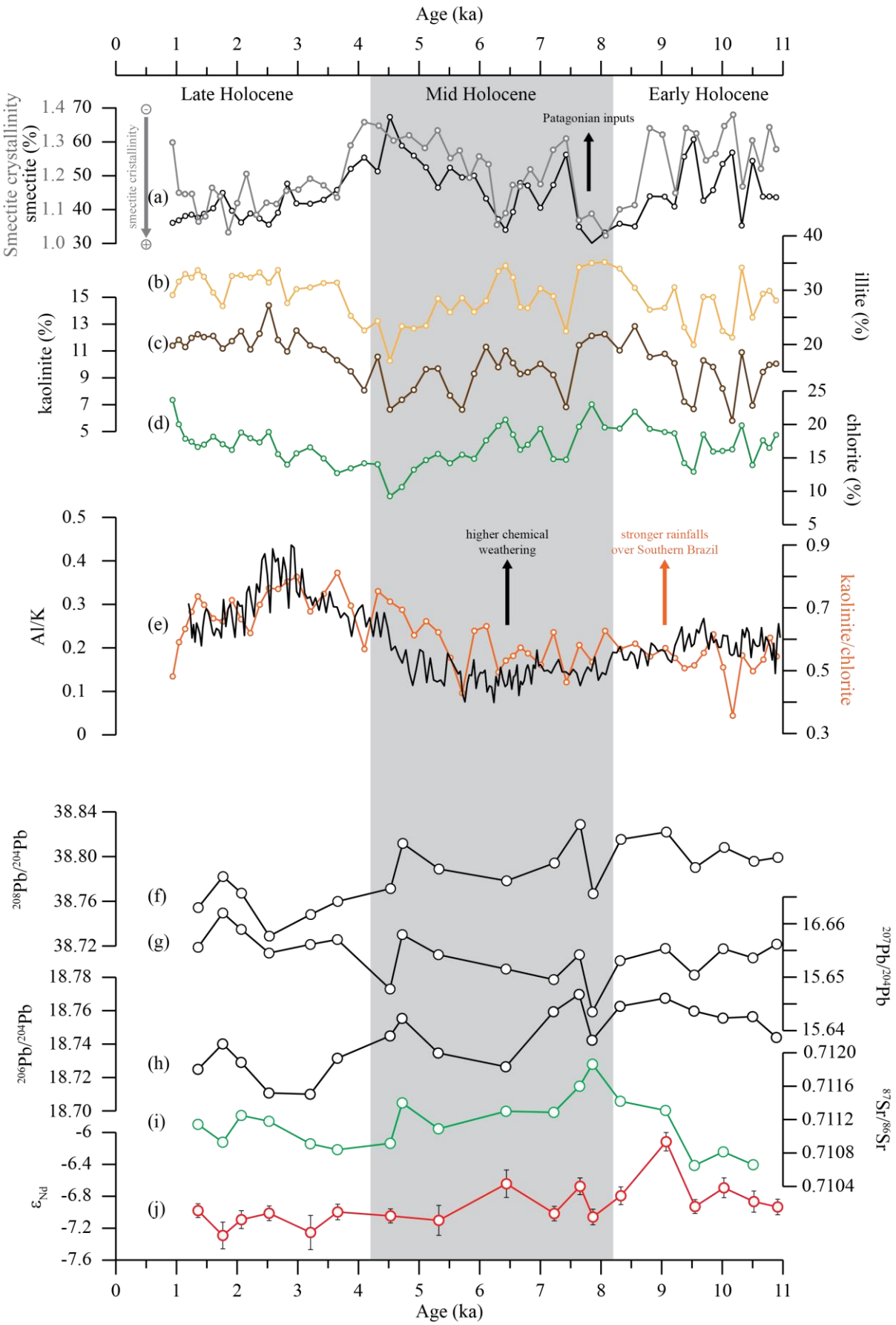

Figure 46: Mineralogical and geochemical composition of Holocene terrigenous sediment of core MD07-3076Q. (a) crystallinity (grey) and proportion of smectite (black); (b) proportion of illite; (c) proportion of kaolinite; (d) proportion of chlorite; (e) bulk sedimentary XRF Al/K ratio (black) and Kaolinite/Chlorite ratio (Kaol/Chlo, orange); (f) $^{208}Pb/^{204}Pb$ of the clay size fraction; (g) $^{207}Pb/^{204}Pb$ of the clay size fraction; (h) $^{206}Pb/^{204}Pb$ of the clay size fraction; (i) $^{87}Sr/^{86}Sr$ of the clay size fraction; (j) ε_{Nd} of the clay size fraction. The error bars on ε_{Nd} corresponds to the 2σ.

III. Results

A. Clay mineralogy

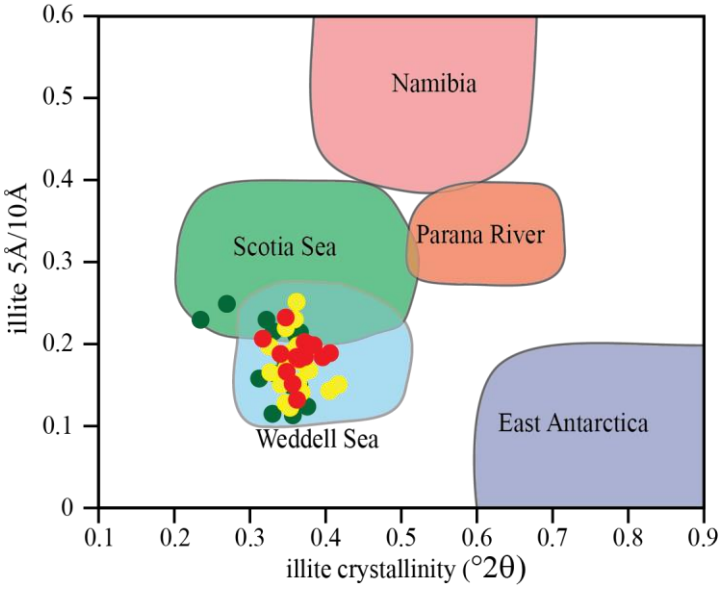

Figure 47: Properties of illite from site MD07-3076Q (Early Holocene: red dots; Mid Holocene: yellow dots; Late Holocene: green dots) and comparison with properties of illite from potential sources to the South Atlantic basin taken from Petschick et al. (1996). The Illite 5Å/10Å ratio gives information on the chemical properties of illite (Fe-Mg- vs Al-rich illite), while the crystallinity largely reflects the quality of the mineral crystal (high crystallinity: badly crystallized mineral).

The clay mineral assemblage is composed of 44% ± 8 of smectite (30-67%) and 29% ± 4 of illite (17-35%) (figure 46, annex 13). Chlorite and kaolinite are less abundant, representing respectively 17% ± 3 (9-24%), and 10 % ± 2 (6-14%) of the clay mineral fraction (figure 46, annex 13). The crystallinity of smectite varies between 1.02°2θ and 1.38°2θ and is closely linked to changes in the proportion of smectite (R^2=0.60) (figure 46), pointing at changes in the provenance of smectite. Both display high values from 11 to 9 ka before present. The

crystallinity of smectite gets reduced between 8.8 and 8.5 ka, then rises from 7.7 to 7.4 ka (figure 46) and is accompanied by similar decrease/increase of the smectite proportion. Both further increase from 7.5 and 4 ka and decrease from 4 to ~3 ka in our study core. Holocene variations of both illite crystallinity and chemistry (Esquevin index, Esquevin, 1969) are not significant when compared with the range of composition of the different sources of illite (figure 47). Properties of illite from site MD07-3076Q are similar to the properties of illite stemming from the Weddell Sea and Scotia Sea (figure 47). However, as demonstrated by Beny et al. (2020), the major source of illite in the central South Atlantic is the Weddell Sea embayment.

The kaolinite/chlorite ratio (Kaol/Chlo) varies between 0.35 and 0.81. It remains fairly invariable until the end of the mid Holocene and increase significantly during the late Holocene (figure 46).

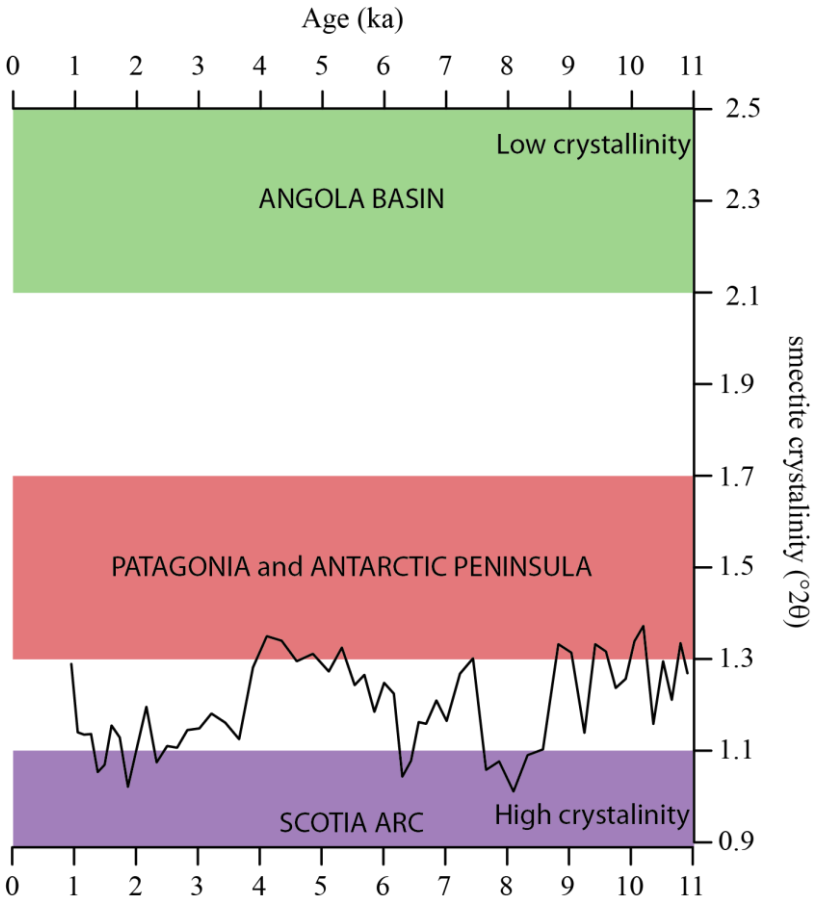

Figure 48: Crystallinity of smectite from site MD07-3076Q (black curve) and comparison with crystallinity of smectite from potential sources to the South Atlantic basin. The data used for comparison are from Petschick et al. (1996).

B. Radiogenic isotopes

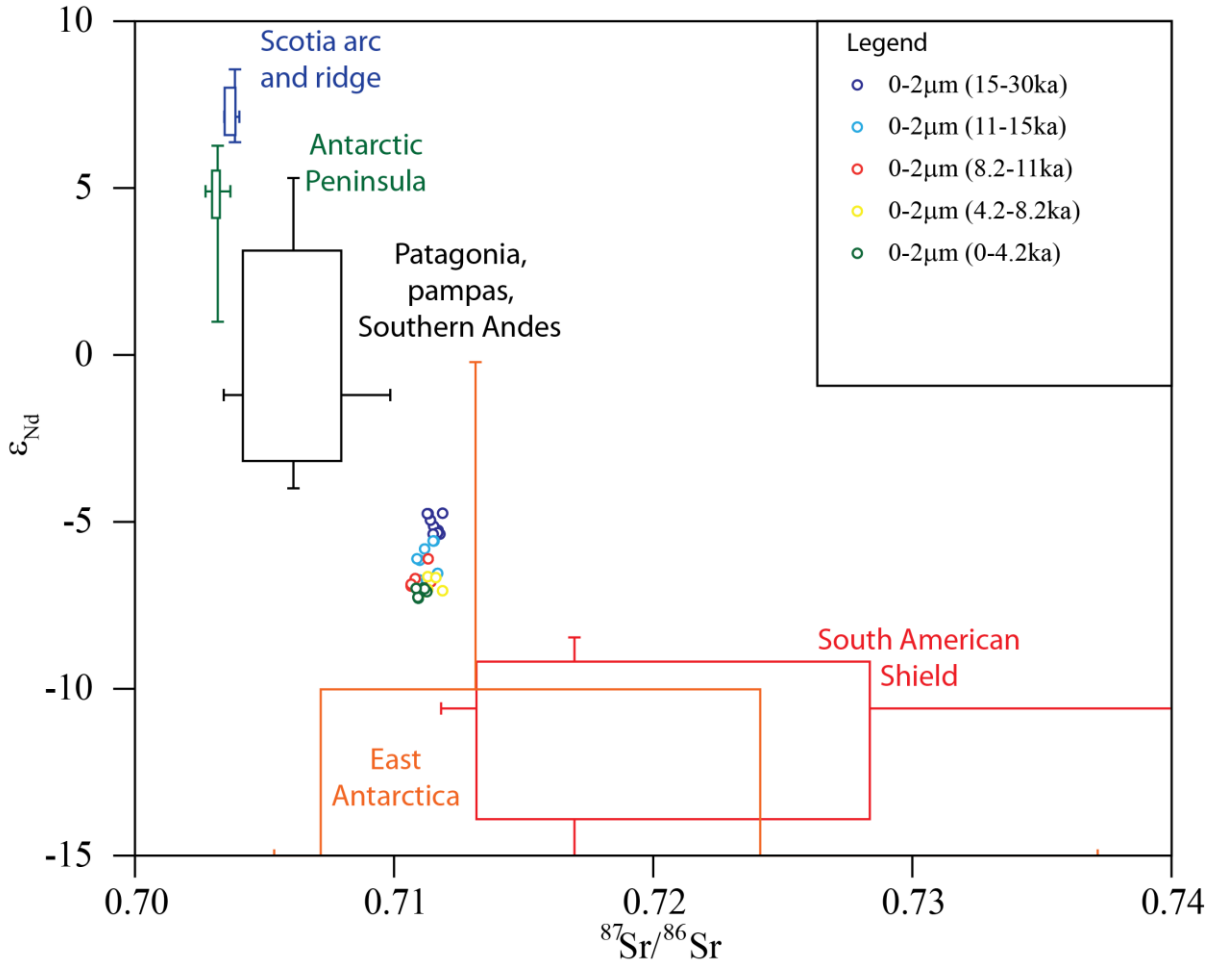

Figure 49: $^{87}Sr/^{86}Sr$-ε_{Nd} *diagram of MD07-3076Q sediments and potential sources of sediments to the South Atlantic Basin. Boxes represent reference data from the South American Shield (Allegre et al., 1996; Basile et al., 1997; Walter et al., 2000; de Mahiques, 2007; Jeandel et al., 2007, and references therein; Mallman et al., 2007; Canade de Aujo et al., 2014; Fuck et al., 2014), Patagonia, Pampas and Southern Andes, (Stern et al., 1990; Grousset et al., 1992; Basile et al., 1997; Walter et al., 2000; Smith et al., 2003; Jeandel et al., 2007, and references therein; Khondoker et al., 2018), Scotia Arc and Ridge (Jeandel et al., 2007; Harrisson et al., 2003), Antarctic Peninsula (Hole el al., 1993; Kosler et al., 2009; Roy et al., 2007; Lee et al., 2005), and East Antarctica (DePaolo et al., 1982; Luttinen et al., 1998, 2010; van de Flierdt, 2007; Roy et al., 2007; Will et al., 2010). Box limits show the 25%- and 75%-quartiles, while whiskers highlight the 10th- and 90th percentiles. The median is represented by horizontal and vertical lines attached to the boxes. Note that the median value for East Antarctica is located exactly at* ε_{Nd}*=-15. The isotopic composition of fine-grained sediment during the last glacial maximum (LGM) and the deglaciation shown for comparison are from Beny et al. (2020).*

The ε_{Nd} signature of the clay fration varies between -7.3 and -6.1 with no significant variations over the Holocene (figures 46 and 49). The $^{87}Sr/^{86}Sr$ ratio changes between 0.7107 and 0.7119 (figures 46 and 49), with a maximum at ~8 ka and a decreasing trend over the rest of the record (figure 46). The $^{206}Pb/^{204}Pb$, $^{207}Pb/^{204}Pb$ and the $^{208}Pb/^{204}Pb$ are between 18.71 and 18.77, 15.64 and 15.66, and between 38.73 and 38.83, respectively (figure 46 and 50). When compared with the Pb signature from potential sources (figure 50), the Pb isotopic composition of the clay size fraction suggests a mix between two end members: a region in the vicinity to the Scotia Sea (that includes Patagonia, Scotia Arc, Antarctic Peninsula, hereafter referred as Scotia Sea area) and the South American shield. All the values to ~5 ka (including glacial and deglacial data from Beny et al., 2020) are located on a mixing line between these two end-members (figure 50). At the end of the Holocene, the isotopic composition of Pb from the clay size fraction deviates from this mixing line by presenting lower $^{208}Pb/^{204}Pb$ compared to $^{207}Pb/^{204}Pb$.

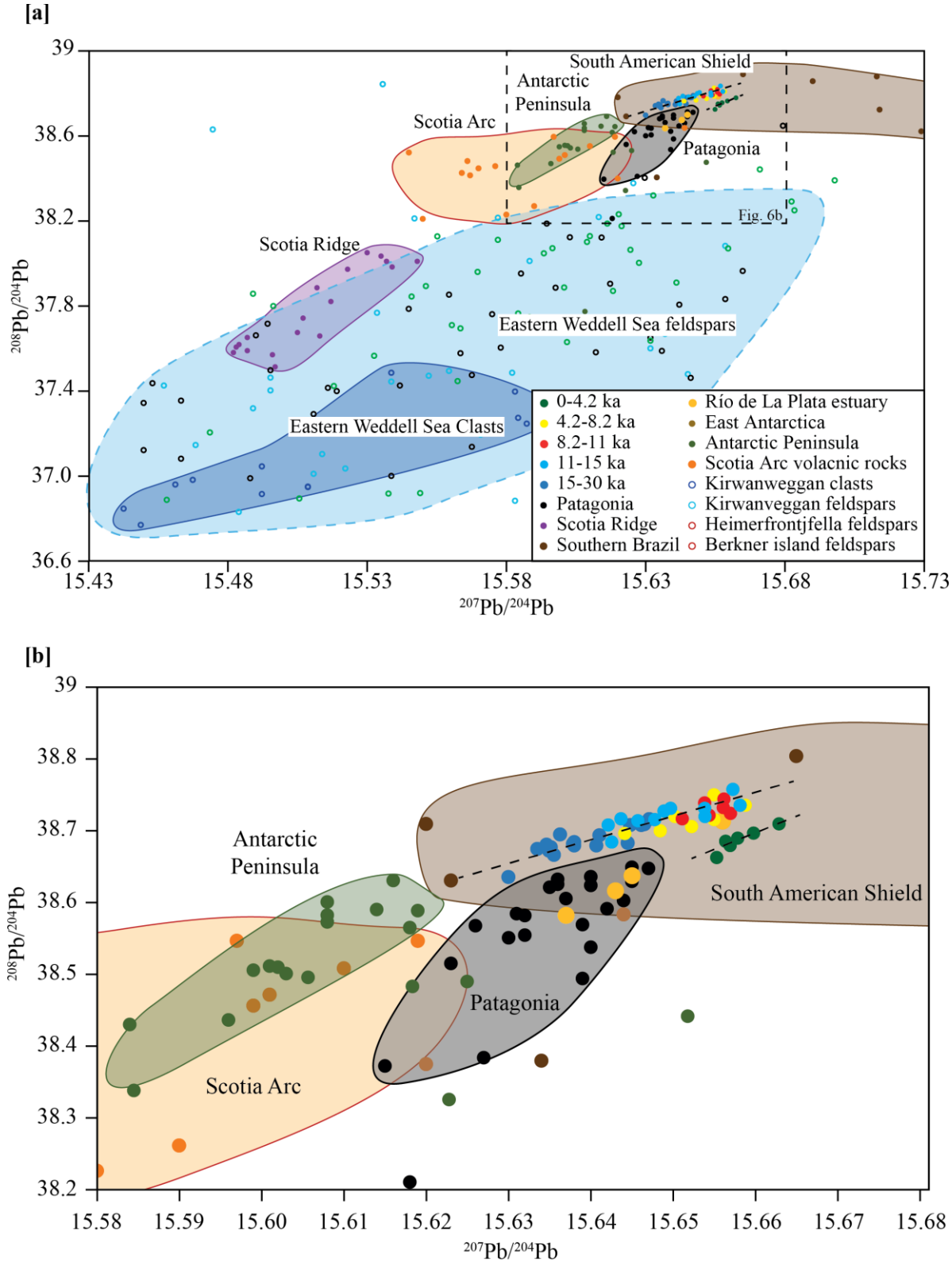

Figure 50: *Lead isotopic composition of the clay fraction from core MD07-3076Q and of potential sources of sediments to the deep South Atlantic. The reference data used for comparison come from Scotia Ridge (Fretzdorff et al.,2002), Patagonia (Khondoker et al., 2018), Scotia Arc(Cohen and O'Nions,, 1982; Barreiro, 1983), Antarctic Peninsula (Lee et al.,*

2005; Kosler et al., 2009; Flowerdew et al., 2012), South American Shield (de Mahiques et al., 2007), and Eastern Weddell Sea (Flowerdew et al., 2012). The data for the studied sediment core for the interval 10-30 ka are taken from Beny et al. (2020). Panel b zooms into the dashed box shown in panel a.

C. XRF scanning

The bulk sedimentary Al/K ratio varies between 0.07 and 0.44, with lowest values during the mid-Holocene, and highest values during the late Holocene (figure 46e). It slightly decreases during the late-mid Holocene transition and increases significantly simultaneously to the Kaol/Chlo ratio during the early Holocene (figure 46e).

IV. Discussion

A. Provenance and transport of fine grained sediments

The provenance of deep central South Atlantic sediments during the deglaciation and the last glacial maximum (LGM) in core MD07-3076Q has been recently investigated (Beny et al., 2020), demonstrating that provenance changes during this period mainly result from modifications by deep ocean circulation. Beny et al. (2020) indicate that at the onset of the Holocene clay-sized sediments were likely advected to our study site by NADW and by southern-sourced deep waters: NADW transporting sediments from South America, Circumpolar Deep Water (CDW) transporting sediments from the Scotia Sea area (Southern Patagonia, Scotia Arc, Antarctic Peninsula), and Antarctic Bottom Water (AABW) carrying particles from the Scotia Arc and the Weddell Sea embayment (figure 45).

Beny et al., (2020) utilize the ε_{Nd} of the clay size fraction to track the relative contribution of NADW compared to AABW and CDW to variable clay composition and -mineralogy during the deglaciation. The relative stability of this tracer during the Holocene (figure 46) suggests that there is no major change in deep water masses configuration during the Holocene. Similarly, the authigenic ε_{Nd} signature of fish debris and mixed benthic foraminifera measured in our study core, considered to reflect the source of deep waters, as well as the *Cibicides* $\delta^{18}O$ and $\delta^{13}C$ are rather constant during the Holocene (Figure 51g and 51j; Waelbroeck et al., 2011; Skinner et al., 2013). This support the notion that the advection of NADW into the South Atlantic was relatively stable, hence having a minor influence on the abundance and geochemistry of the terrigenous clay fraction in the central South Atlantic.

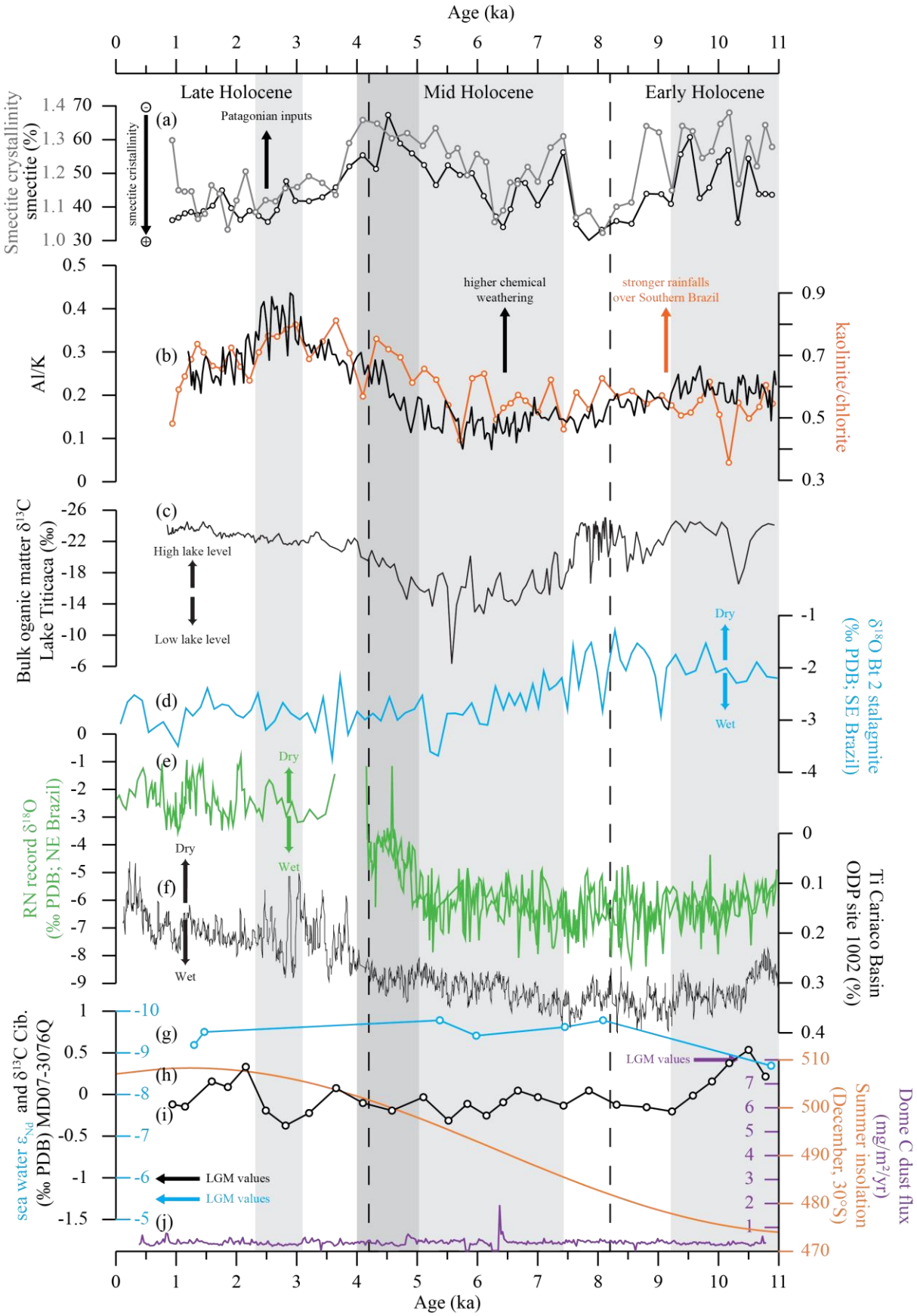

<u>Figure 51:</u> Comparison between proxy data obtained from the terrigenous fraction in core MD07-3076Q and other proxy-records reflecting changes in the South American Monsoon (c-

f), the AMOC (g and i), and of the winds over Antarctica (j). (a) Proportion (black) and crystallinity (grey) of smectite from core MD07-3076Q (South Atlantic; this study); (b) Al/K (black) and Kaol/Chlo ratios (orange) from core MD07-3076Q (South Atlantic; this study); (c) organic matter $\delta^{13}C$ from core NE98-PC2 (Lake Titicaca; Baker et al., 2005); (d) Stalagmite $\delta^{18}O$ from Botuvera Cave (SE Brazil; Cruz et al., 2005); (e) Rio Grande de Norte $\delta^{18}O$ record, obtained from 5 stalagmites recovered in the Rainha, Furna Nova, and Abissal caves (NE Brazil; Cruz et al., 2009), (f) Bulk sedimentary Ti proportion from ODP Site 1002 (Cariaco Basin; Haug et al., 2001), (g) sea water ε_{Nd} (from fish debris and benthic foraminifera; Skinner et al., 2013) from site MD07-3076Q; (h) summer insolation at 30°S (December); (i) Cibicides $\delta^{18}O$ from core MD07-3076Q (Waelbroeck et al., 2011); (j) EPICA Dome C dust flux (Antarctica, Lambert et al., 2012). Y-axes are chosen to encompass the LGM values in order to highlight mismatch in the variability of South American climate proxies (curves (a) to (f)) and the variability of the proxies of Antarctic climate and of the AMOC (curves (g), (i), and (j)). In that purpose, the average value of the LGM is given for curves (g), (i), and (j). Note that EPICA Dome dust flux (j) varied substantially during the LGM, with maximum dust fluxes of 15 mg/m²/yr.

Although short term ~1500 years fluctuations in NADW formation were identified in the northern North Atlantic Ocean (Chapman and Shackleton, 2000; Bond et al., 2001; Oppo et al., 2003), no major change in Atlantic overturning has been reported for the Holocene further to the south (McManus et al., 2004; Vasquez Riveiros et al., 2010; Waelbroeck et al., 2011; Skinner et al., 2013, 2014), except for the 8.2 ka event. This global cooling event of approximately half the magnitude of the Younger Dryas occurred from 8.4 to 8.0 ka (Alley et al., 1997) and was likely caused by catastrophic drainage of Laurentide lakes (Wiersma and Renssen, 2006; Kleiven et al., 2008) delivering freshwater to the North Atlantic and slowing down the Atlantic Meridional Overturning Circulation (AMOC). Significant changes in the clay mineralogy composition of core MD07-3076Q, particularly in the smectite crystallinity and proportions, are observed during this interval (figure 46). These changes suggest a decreased contribution of smectite from Patagonia during the 8.2 ka event, meaning that the ability of NADW to transport smectite to the study site may have been reduced at that time. A slow-down followed by a fast recovery of the AMOC after the 8.2 ka event (LeGrande and Schmidt, 2008; Born and Levermann, 2010) support this notion. For the remainder of the Holocene, the rather constant clay ε_{Nd} signature observed in our study attests to the fact that the AMOC was relatively stable in the South Atlantic Ocean during the Holocene, consistent with previous

findings (McManus et al., 2004; Vasquez Riveiros et al., 2010; Waelbroeck et al., 2011; Skinner et al., 2013, 2014).

The Kaol/Chlo ratio is assumed to reflect northern-sourced versus southern-sourced deep water masses in the South Atlantic during the deglaciation (Kuhn and Diekmann, 2002; Beny et al., 2020). During the mid and the late Holocene, an increase in this ratio suggests an increase of NADW compared to southern-sourced deep water masses (figure 46). The magnitude of this variation in the Kaol/Chlo ratio is similar to the one observed during the deglaciation (Beny et al., 2020), likely suggesting an incursion of NADW into the Southern Ocean at that time. This is inconsistent with other proxies suggesting no major change of the AMOC. Taking advantage of further insights from our new proxy data on chemical weathering intensities we favor a different explanation of the Kaol/Chlo variations during the Holocene, as described below.

Clay-fraction Pb isotopes show important variations after 5 ka in time with the observed Kaol/Chlo increase (figures 46 and 50b). Until ~5 ka, the Pb isotopic signature of the samples suggest a source in the vicinity of the Scotia Sea (Scotia Arc, Antarctic Peninsula, Patagonia) and/or the South American Shield (figure 50). After 5 ka, the values deviate from this mixing line between these two sources and display lower $^{208}Pb/^{204}Pb$ ratios compared to $^{207}Pb/^{204}Pb$ (figure 50).

Pb isotopes are known to be sensitive to chemical weathering due to the higher mobility of the elements from which radiogenic Pb is formed compared to the Pb itself (Shirahata et al., 1980; Silver et al., 1984; Allen and Hajek, 1989As a consequence, chemical weathering can reduce the amount of radiogenic Pb (^{206}Pb, ^{207}Pb, and ^{208}Pb) formed by the radioactive decay of U and Th compared to primordial Pb (^{204}Pb). In our data, the decrease of $^{208}Pb/^{204}Pb$ and of $^{206}Pb/^{204}Pb$ after 5 ka may result from enhanced chemical weathering during the Late Holocene. Similarly to the Pb isotopes, the Kaol/Chlo ratio can be sensitive to chemical weathering because kaolinite is formed by chemical weathering while chlorite is destroyed during these processes.

The co-variation of the XRF Al/K – that can be considered as a chemical weathering proxy – and of the Kaol/Chlo ratios (with constant clay size fraction ε_{Nd}, figure 46) suggests that the Kaol/Chlo ratios reflect changes in chemical weathering. This is consistent with the constant clay ε_{Nd} signature, as it is not sensitive to superficial weathering processes (Faure and Mensing, 2005). We thus argue that the observed change in the Kaol/Chlo ratio and on Pb

isotopes during the Holocene reflect changes in chemical weathering on land instead of provenance and redistribution changes driven by ocean circulation changes, the latter of which remained rather stable/constant in the South Atlantic (Waelbroeck et al., 2011; Skinner et al., 2013, 2014).

B. Chemical weathering variations: insights onto moisture distribution over South America

1. A modification of the signature of the detrital particles from South America

Our dataset implies no major modifications of oceanic configuration throughout the Holocene. We have argued above that the observed changes in Kaol/Chlo, smectite proportion and crystallinity, as well as bulk sedimentary Al/K and clay Pb isotopes reflect changes in chemical weathering on land prior to transport by AABW, CDW and/or NADW to our study site.

Most of the particles transported by AABW hardly interact with liquid water on land: chemical weathering processes are assumed to be negligible in Antarctica and in the Scotia Arc and cannot explain the modulation of Kaol/Chlo, Al/K and of Pb isotopes. Most of the particles transported by CDW come from Southern Patagonia and from the Scotia Arc, with minor contributions from the Antarctic Peninsula (Beny et al., 2020). Even if Patagonia is sensitive to precipitation changes over the Holocene (Glasser et al., 2004; Kilian and Lamy, 2012), which would cause an increase of chemical weathering product, we argue that these modifications are not likely to affect the Kaol/Chlo ratio at our study site as Patagonia delivers mostly smectite to the South Atlantic basin (>90%; Mathias et al., 2014; Khondoker et al., 2018). As a result, we argue that the modulation of Kaol/Chlo and Al/K ratios, as well as of the Pb isotopes of the fine fraction during the Holocene at our study site are not a signal driven by CDW transport.

At the beginning of the Holocene, terrigenous particles from Southern Brazil to Patagonia are delivered to the South Atlantic Ocean by rivers and winds (Petschick et al., 1996; Hegner et al., 2007; Mathias et al., 2014; Desiage et al., 2018) and transported to our site by the NADW (Beny et al., 2020). Vegetation and precipitation changes in South America are closely linked to the migration of the Intertropical Convergence Zone (ITCZ), of the South Atlantic Convergence Zone (SACZ), and of the South Westerly Wind Belt (SWWB). Due to the migrations of these atmospheric systems, South America experienced successive periods of enhanced/reduced rainfalls and wind strength during the Holocene (figure 51; Schäbitz, 1994; Cruz et al., 2009; Kilian and Lamy, 2012; Sallun et al., 2012). Modifications of hydrolysis

conditions (i.e. on the South American continent) are thus likely the main driver of mineralogical and geochemical characteristics of particles formed on land, which are subsequently transported toward the deep South Atlantic basin via NADW during the Holocene.

2. Relation between provenance change, rainfall distribution, and wind strength

Since modifications of the composition of sediment have been identified as the cause of the changes observed in sedimentological and geochemical proxies during the Holocene, we will now focus on characterizing environmental conditions (i.e., rainfall intensity and distribution, wind strength) in South America. According to Mathias et al. (2014), the Parana River and the Patagonian loess are the dominant sources of sediment supplied to the SW Atlantic, with higher contributions of Patagonian loess during dry and windy periods. Parana River sediments contain a large proportion of illite (60%; Mathias et al., 2014) that does not reach our study site (figure 47 and Beny et al., 2020), along with minor contributions from kaolinite, and smectite (Petschick et al., 1996; Campodonico et al., 2016). On the other hand, Patagonian loess are derived from reworked material from the Andes (Sayago et al., 2001). As a result, the clay minerals formed in this region are mostly smectite (~90%, Khondoker et al., 2018). These two areas experienced different moisture conditions throughout the Holocene: Patagonia is a semi-arid desert today, whereas the Parana River basin is located in sub-tropical climate characterized by highly seasonal rainfalls during austral summer (Clapperton, 1993). Consequently, chemical weathering in these two areas is different, with stronger chemical weathering over the Parana River Basin than over Patagonia. Hence, not only rainfall intensities but also rainfall distribution sediment provenance can impact the values of the chemical weathering proxies (e.g., via Al/K and Kaol/Chlo) used in this study. Similarly, wind patterns can also have an important influence on the geochgemical and mineralogical composition of sediments. Indeed, Patagonian loess are mostly transported to the ocean by wind, and stronger winds may increase the relative contribution of Patagonia loess to deep South Atlantic sediments, especially smectite (Mathias et al., 2014; Razik et al., 2013).

To decipher the paleoenvironmental changes in South America recorded with our provenance proxies, it is necessary to identify the main forcing parameters of variations in smectite proportion and crystallinity, the Kaol/Chlo ratio and the Al/K ratio. We argued above that the influence of oceanic circulation on these proxies during the Holocene was negligible, except of the 8.2 kyr event. Our results indicate rather stable conditions in Antarctica, and hence rather constant supply of chlorite to the South Atlantic. As a result, we suggest that the Kaol/Chlo ratio of central South Atlantic marine clays will mainly reflect changes in supply of

kaolinite to the South Atlantic Ocean during the Holocene. This delivery depends on the efficiency of both the production of kaolinite, and the efficiency of river transport. Both processes are controlled by the intensity of rainfall over the river drainage basins. Today, the main sources of kaolinite are the drainage basins of coastal rivers of South Brazil, the Parana River, and the Sao Francisco River. However, the Parana River is the dominant contributor to sediment delivery to the Southwest Atlantic (Razik et al., 2013; Mathias et al., 2014), and thus likely controls the delivery of kaolinite. Consequently, the ratio Kaol/Chlo tracks changes in the intensity of rainfall over the Parana River watershed that is strongly controlled by the position of the SACZ (figure 45).

The XRF Al/K ratio is commonly used as an index for the magnitude of chemical weathering (Bayon et al., 2009), but provenance changes can also have an impact on this ratio (Schneider et al., 1997). Changes of the XRF Al/K ratio can also reflect changes in rainfall distribution (via increased drainage of poorly weathered sediments), as well as changes in aeolian activity (via delivery of mostly physically eroded particles to the ocean that are transported to the central South Atlantic Ocean via oceanic currents). As a result, it is crucial to disentangle the effects of those processes on observed XRF Al/K ratios at our study site.

The driving mechanisms of proportion changes of smectite appear to be complex. At our study site, the proportion and the crystallinity of smectite display a good correlation (R^2 = 0.60), suggesting that the quantity of smectite at the studied site is mainly controlled by supply from Patagonia. We pointed out that AMOC changes associated with the 8.2 kyr event may alter the efficiency of smectite transport by the NADW. However, other phenomena can explain changes in smectite supply throughout the remainder of the Holocene: changes in precipitation and in wind intensity may strongly modify the delivery of Patagonian smectite to the ocean by increasing the drainage of rivers in Patagonia, and/or by increasing the transport of particles to the oceans via aeolian processes. Because provenance proxies are not able to discriminate aeolian versus fluvial processes, the role of stronger winds, stronger rainfalls, or both, in variations of smectite abundance in the South Atlantic remains unconstrained. But as the majority (90%) of clay minerals delivered from Patagonia is smectite, this mineral can still be used as a tracer of the Patagonian provenance, and thus helps to support provenance changes derived from other proxies such as Kaol/Chlo.

3. Paleoenvironmental changes over Southern South America

Paleoenvironmental interpretations require a careful consideration of the advantages and limitations of each proxy applied. In the case of our study, the distance between the

continental source and the studied site (>1000 km) tends to smooth the signal and only large-scale (i.e. regional) processes are likely recorded. Any local effects have thus a negligible impact on our proxy records. As a result, we argue that our work aids to understand large-scale phenomena over the South American continent such as the South American Monsoon System or shifts in the SWWB. In addition, we highlight that our proxies provide qualitative insights into the relative changes in precipitation and wind strength. Secondly, we take advantage of differences between the geochemical and mineralogical signatures of rocks from Patagonia (arid region, with young mantellic rock signatures), and from Brazil (mostly humid, with old crustal signature), allowing to distinguish between source apportionment and processes controlling central South Atlantic sediments.

At the beginning of Holocene (11-9 ka, figure 51), the intermediate XRF Al/K values indicate moderate chemical weathering, and low Kaol/Chlo ratios support a relatively weak sediment delivery by the Parana River, suggesting relatively weak rainfalls over this area. In addition, high content of smectite associated with "high" smectite crystallinity (~1.3°2θ) indicate substantial sediment delivery from Patagonia. At that time, studies suggest that the SWWB was shifted to the south (Razik et al., 2013; Mansilla et al., 2016) and weakened (Moreno et al., 2010; Saunders et al., 2018), which may have also caused a weakening of local winds in Patagonia. This would however contradict our observations of higher sediment (i.e., smectite) supply from Patagonia. However, Mansilla et al. (2016) observed forest expansion in southern Patagonia during the early Holocene and interpreted it as the result of more humid conditions. We hence argue that the contribution of small Patagonian rivers was significantly higher during the early Holocene due to increased rainfalls over southern Patagonia, hence allowing for increased fluvial smectite supply to the South Atlantic.

From ~9 to ~7.4 ka, the Kaol/Chlo ratio remains rather stable, reflecting no significant change in rainfall intensity/distribution over South America, whereas the XRF Al/K ratio suggests a slight decrease in chemical weathering. This suggests that the Parana River Basin suffered from increased dryness during the early to mid-Holocene transition, likely due to a weakening or to a northward migration of the SACZ. Our results also reveal the quasi absence of smectite supply from Patagonia during that time, as the smectite percentage decreases to |35% during this time. As discussed above, this might be related to weak winds and/or weak precipitation over Patagonia, along with changes in the AMOC during the 8.2 ka event.

The period between 7.4 and 5 ka is characterized by the lowest XRF Al/K and Kaol/Chlo ratios of the entire Holocene record suggesting that this period was the driest interval of the

Holocene in southeast South America, indicating relatively weak rainfall caused by the SACZ over the Parana River watershed. This agrees with several studies that assess pollen variations (Behling et al., 2001 – southern Brazilian Highlands; Mansilla et al., 2016 – Southern Patagonia), marine South Atlantic sediments (Razik et al., 2013; Mathias et al., 2014), and palynological record from lake sediments (Schäbitz, 1994 – northern Patagonia). During this interval, the high smectite content suggests enhanced delivery from Patagonia via winds, and moderately low Al/K and low Kaol/Chlo ratios further highlight reduced sediment delivery by Parana River. This is consistent with the occurrence of aeolian deposits from Patagonia on the Southeast Brazilian shelf during the mid-Holocene (Mathias et al., 2014). The high proportion of Patagonian smectite (figure 51) suggest that the SWWB was positioned northward and was promoting strong winds over Patagonia during the mid-Holocene, which is supported by previous studies (Schäbitz, 1994; Razik et al., 2013; Kaplan et al., 2016, Saunders et al., 2018). The period between 6.1 and 4.5 ka corresponds to the highest contribution of Patagonian smectite, suggesting that this interval was the windiest of the entire Holocene. This is supported by similar observations made by Kaplan et al. (2016), supporting our interpretation of strong aeolian sediment supply from Patagonian deserts due to northward intensification of the SWWB between 6.1 and 4.5 ka.

Significant changes occurred during the mid to late Holocene transition (5-3 ka). The increase of both XRF Al/K and Kaol/Chlo ratios suggest enhanced supply from the Parana River, and thus increasing rainfalls over the Parana River watershed. During this period, the observed increase of XRF Al/K ratios suggest increased chemical weathering. This agrees with the variation in the Pb isotopic composition of the clay size fraction, whereby the lowest $^{208}Pb/^{204}Pb$ and $^{206}Pb/^{204}Pb$ ratios during this time interval (figure 50) is interpreted to reflect enhanced chemical weathering (see section III.B.1), as both Sr and Nd isotopic composition of the clay fraction remains unchanged (figure 46). Altogether, these changes indicate enhanced rainfall over the Parana River watershed linked to a shift in the SACZ. At the same time, the contribution of Patagonian smectite falls to almost zero (figures 46 and 48, and supplementary figure S1), which suggests a decrease in aeolian transport during this period likely caused by a migration to the south and/or a weakening of the SWWB. This agrees with continental records (Behling et al., 2001; Glasser et al., 2004; Razik et al., 2013; Kaplan et al., 2016; Mansilla et al., 2016) as well as with marine studies on the SE Brazil Shelf (Mathias et al., 2012) that observe increased precipitation over the Parana River basin and Southern Brazil, while Patagonia became drier and less windy.

The interval between 3-2.2 ka appears to be the most humid of the Holocene in SE South America, as shown by the highest XRF Al/K and Kaol/Chlo ratios of the entire Holocene record. A decreasing trend of the XRF Al/K and Kaol/Chlo ratios, as well as a small increase of the $^{208}Pb/^{204}Pb$ and $^{206}Pb/^{204}Pb$ ratios instead suggest reduced rainfall where after 2.2 ka.

V. Conclusion

In this study, we assessed changes in the provenance of terrigenous sediments in the deep central South Atlantic Ocean to reconstruct the past evolution of rainfall and wind strength over Southern Brazil and Patagonia. Our marine study core provided insights into in the position and intensity of winds and rainfalls at a regional scale, specifically associated with changes of the SWWB and the SACZ, respectively. We were thus able to circumvent complications associated with potential local effects and provide new insights into paleoenvironmental changes over South America during the Holocene.

We show that the AMOC had a negligible impact on provenance variations of sediments in the deep South Atlantic during the Holocene, except for the 8.2 ka event, when a strong perturbation of the AMOC was observed in the North Atlantic. Thus, we argue that most of the mineralogical and geochemical changes observed at our study site reflect changes in the composition of sediments at their source that is strongly determined by rainfall and wind strength changes, and hence riverine and aeolian sediment transport, in southern South America throughout the Holocene.

Variation of smectite content and crystallinity of sediments in the deep South Atlantic mainly result from variations in terrigenous supply from Patagonia because Patagonia is the only source of smectite. We show that changes in terrigenous smectite supply to the central South Atlantic vary during the Holocene and are associated to Patagonian supplies. Because the Kaol/Chlo ratio is controlled by the precipitation intensity over the source area of kaolinite, namely Parana River watershed and Southern Brazil, this ratios was used to identify the contribution of the Parana River as well as changes in precipitation distribution to Holocene kaolinite changes at our study cite. The XRF Al/K ratios serves as measure of the intensity of chemical weathering, and thus rainfall intensities, over southern South America.

Low Kaol/Chlo and intermediate Al/K ratios suggest moderately dry conditions associated with weak winds during Early Holocene (11-9 ka). Decreasing XRF Al/K ratios indicate increased dryness over southern Brazil between the end of the late Holocene to the onset of the mid-Holocene (9-7 ka), with a weak NADW coinciding with the 8.2 ka event

disabling the transport of Patagonian smectite to our marine study site. As shown by the lowest Al/K and Kaol/Chlo ratios, the mid-Holocene was the driest period in South America of the Holocene. This is paralleled by the highest smectite content and crystallinity, indicating that the mid-Holocene was also the windiest period of the Holocene, with a wind intensity maximum probably occurring between 6 and 4.5 ka. At the end of the mid-Holocene (~5 ka), a marked increase of the Kaol/Chlo and AL/K ratios suggest that conditions became significantly wetter while a marked decrease in smectite proportion and crystallinity suggest that the wind strength decreased until the beginning of the late Holocene (~3 ka). As suggested by the highest Al/K and Kaol/Chlo ratios of the Holocene record, we argue that the period between 3 and 2.2 ka was the wettest period in southern South America throughout the Holocene, and was followed by a marked weakening in rainfall to the end of the record indicated by a decrease of the Al/K and Kaol/Chlo ratios.

Finally, our study suggests that the position and strength of the SACZ and of the SWWB were similar to their present-day "average" characteristics during the Early Holocene. Rainfalls associated with the location of SACZ were weak during the mid-Holocene, while the SWWB intensified and shifted further to the north, promoting substantial aeolian activity in Patagonia. The Mid to Late Holocene transition is characterized by a marked strengthening of the SACZ and associated rainfall increase as well as by a marked southward migration and weakening of the SWWB and associated wind systems in Patagonia. The Late Holocene was likely characterized by the stronger SACZ and the weakest SWWB of the Holocene.

VI. Acknowledgment

We wish to thank Richard Smeets for his invaluable help in the clean lab, Emmeke Bos, Janne Koorneef, and Mathijs van de Ven for the help with TIMS Triton measurements, Bas van der Wagt and Kirsten van Zuilen for Neptune MC-ICPMS measurements. Tristan Lippens is thanked for computer support. We also wish to thank all organisations that provided financial support to the project: the "region Haut de France", Europlanet and the Vrije Universiteit of Amsterdam. We also want to express our special thanks to the "flotte océanographique française" for retrieving the sediment core used in this study. FB and VBR thanks Monique Gentric for administrative support. JG acknowledges the German Research Foundation for support through DFG grant GO 2294/2-1. CW acknowledges support from the European Research Council ERC grant ACCLIMATE/n° 339108.

VII. Supplementary figures

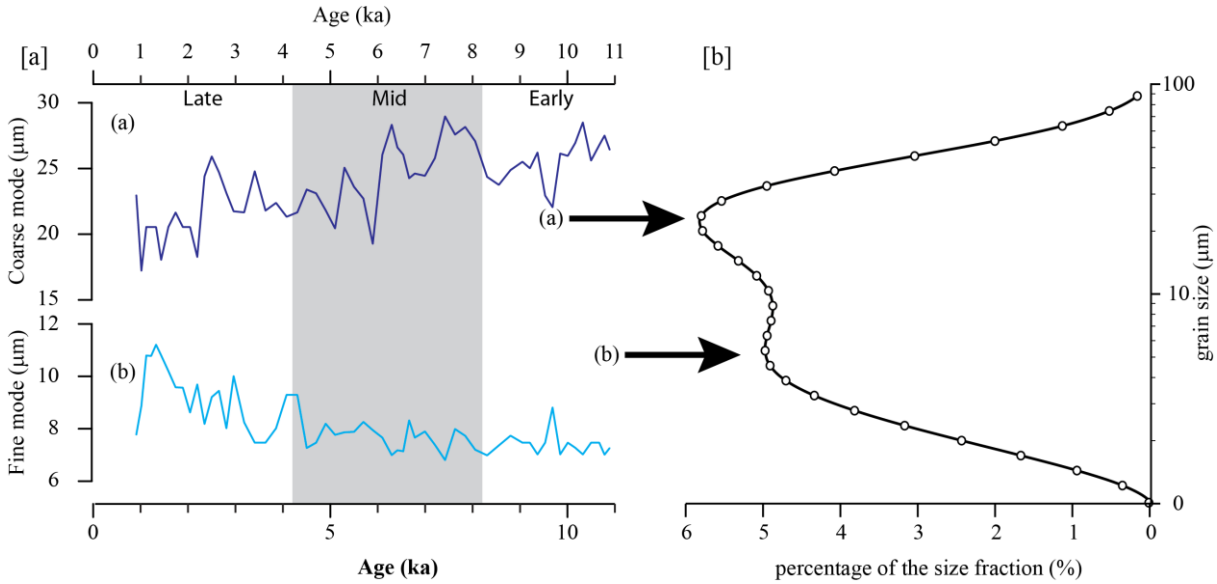

SUPPLEMENTARY FIGURE S1: Grain-size variation during the Holocene observed in sediment core MD07-3076Q (left): (a) coarse grain size mode; (b) fine grain size mode. A typical grain-size distribution curve for core MD07-3076Q obtained in sediment samples from xx-xx cm (right) shows that two grain-size modes can be identified.

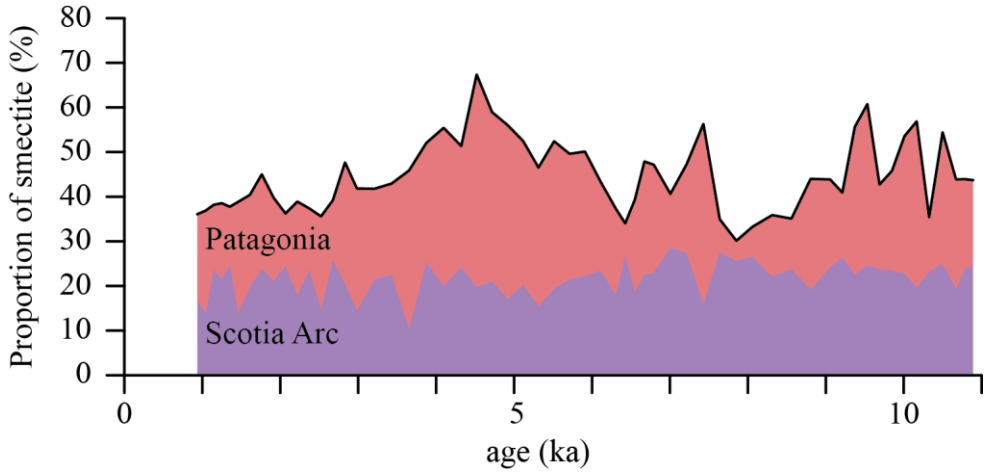

SUPPLEMENTARY FIGURE S2: Abundance variationsof two types of smectite observed at site MD07-3076Q. The black line represents the total smectite content, where the

purple and red area represent the smectite content from the Scotia Arc and from Patagonia, respectively. The proportion of the two types of smectite are calculated as followed:

$$[\%\text{Patagonian smectite}] = [\%\text{total smectite}] \times \frac{[\text{sample crystallinity}] - [\text{Scotia Sea crystallinity}]}{([\text{Patagonia crystallinity}] - [\text{Scotia Sea crystallinity}]} \times 100$$

$$[\%\text{Scotia Sea smectite}] = [\%\text{total smectite}] - [\%\text{Patagonian smectite}]$$

Chapter 6. Geochemical and mineralogical evidence of equatorial export of AABW in the South Indian Sector of the Southern Ocean during Heinrich Stadials.

F. Beny[1,2,], V. Bout-Roumazeilles[1], G.R. Davies[2], A. Mazaud[3], E. Michel[3], J. Gottschalk[4], M. Delattre[1], R. Abraham[1], N. Tribovillard[1], A. Bory[1].*

[1] Laboratoire d'Océanologie et de Géosciences, UMR 8187 CNRS/Univ Lille/ULCO, Cité scientifique, F-59655 Villeneuve d'Ascq, France.

[2] VU University Amsterdam, Department of Earth Sciences, Faculty of Science, De Boelelaan 1085, 1081 HV Amsterdam, The Netherlands.

[3] Laboratoire des Sciences du Climat et de l'Environnement, LSCE/IPSL, UMR 8212 CEA-CNRS-UVSQ, Site de l'Orme des Merisiers, F-91191 Gif sur Yvette Cedex, France

[4] Lamont-Doherty Earth Observatory, Colombia University, Palisades NY 10964-8000, United States.

* Corresponding author

Abstract

The evolution of the Antarctic Circumpolar Current (ACC) and of the Antarctic Bottom Water (AABW) during past major climate changes remains controversial. This study uses coupled trace-element contents and Sr-Nd isotope composition of fine-grain detrital sediments (<2μm) from the sediment core MD12-3396Q recovered east of the Kerguelen Plateau to constrain hydrological changes during the last deglaciation. The sediments studied correspond to a mix between material from the Kerguelen Plateau and Antarctica. Overall, the Kerguelen Plateau is the dominant source of sediment, demonstrating that the ACC is the main sediment conveyor to the site. Provenance proxies, however, show that the contribution from Antarctica reaches 40% during Heinrich Stadials (HS) 1, 2 and 3. We propose that the AABW delivers sediment from Antarctica via the Deep Western Boundary Current (DWBC) flowing northward along the Kerguelen-Crozet Plateau. The AABW delivered 3 times more sediment during HS 1, 2 and 3 than during modern interglacial period, and generated enhanced export of the AABW to the Global Ocean via the DWBC.

I. Introduction

Better knowledge of the past global carbon cycle is crucial to understand how the CO_2 released in the atmosphere by anthropic activity can impact future climate. The oceans acts as a sink for atmospheric CO_2 today (Le Quéré et al., 2007; Sallée et al., 2012), but likely acted as a CO_2 source during specific past climate intervals, called Heinrich Stadials (HS) (Bouttes et al., 2012; Jaccard et al., 2013). Today the Southern Ocean plays a major role in this CO_2 storage and release (Fischer et al., 2010; Adkins et al., 2013). Upwelling of deep CO_2-rich water masses in the Southern Ocean is thought to be responsible for most of the world atmospheric CO_2 rise observed during HS (Ahn and Brook, 2008; Anderson et al., 2009; Fischer et al., 2010; Skinner et al., 2010; Siani et al., 2013; Menviel et al., 2014, 2017). Menviel et al. (2014, 2015, 2017) suggest that the AABW played an important role in CO_2 variations during the HS. Although some studies examined variations of the AABW at glacial/interglacial time scales (Hall et al., 2001; Govin et al., 2009; Krueger et al., 2012; Spooner et al., 2018), little is known about millennial scale variations during HS. Due to a simple oceanographic setting compared to other sectors of the Southern Ocean (Figure 52), the Kerguelen sector is an ideal area to reconstruct past evolution of the AABW. Currently, the Deep Western Boundary Current (DWBC) - flowing below the Antarctic Circumpolar Current (ACC) eastward main core (Figure 52) - promotes the northward export of the AABW along the eastern flank of the Kerguelen Plateau (Aoki et al., 2008; Fukamachi et al, 2010). The variations of the ACC in the vicinity of the Kerguelen Plateau are well constrained for today (Park et al., 2009, 2014), as well as for the last glacial cycle (Bareille et al., 1994; Dezileau et al., 2000; Mazaud et al., in prep.), while the evolution of the AABW since the last glaciation is still poorly studied. In this study, we fill this gap by studying the provenance and transfer of sediments in core MD12-3396Q, located west of the Kerguelen Plateau in the area influenced by the DWBC by examining the coupled variation in clay mineralogy and trace element and Sr-Nd isotope composition.

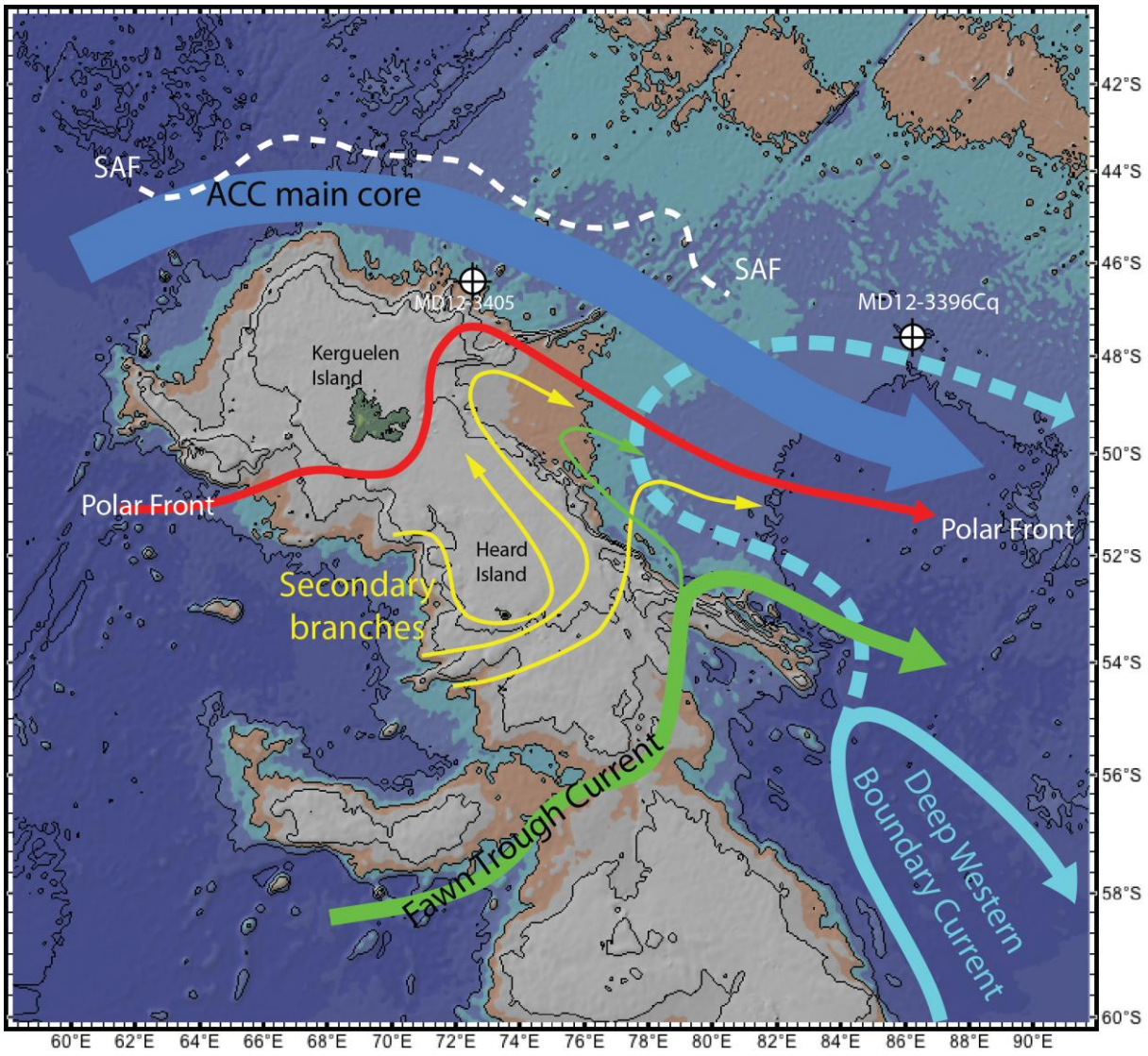

Figure 52: Present-day deep and bottom circulation of the Kerguelen sector of the Southern Ocean. Dark blue, red, yellow and green arrows: present-day organisation of ACC branches according to Park et al. (2009); light blue arrow: present-day DWBC (i.e., AABW) according to Fukamachi et al. (2010); dashed light blue arrow: position of the DWBC during Heinrich Stadial period suggested by geochemical data from this study. SAF: Sub Antarctic Front.

II. Regional settings

A. Oceanography

The Kerguelen-Crozet Plateau is located in the South Indian Sector of the Southern Ocean (figure 52). It constitutes a major obstacle to the eastward flowing ACC that splits into several branches. Currently, two-third of the ACC flow is deflected to the north of the Kerguelen-Crozet Plateau (i.e., ACC-core; 89-94 Sv; Park et al., 2009) and lies south of the Subantarctic Front (SAF). The remaining third of the ACC flows through the Fawn Trough (43

Sv; Park et al., 2009). This southern branch is deflected north along the eastern flank of the Kerguelen-Crozet Plateau and then rejoins the ACC-core (Park et al., 2009). Secondary branches (8 Sv) flow onto the Kerguelen Plateau and associated with the Polar Front (PF; Park et al. 2009; 2014). These branches are very slow when they pass over the Kerguelen Plateau (<5cm/s; Park et al., 2014).

The Kerguelen Plateau also acts as a barrier for the westward flow of the AABW that is deviated northward as the Deep Western Boundary Current (DWBC). The northwestward transport of this current is estimated to be 16 to 22 Sv (Aoki et al., 2008; Fukamachi et al, 2010), of which 8.4 Sv are redirected to the southeast, resulting in a net equatorward export of the AABW of 8 Sv. The AABW forms heterogeneously around Antarctica. According to Aoki et al. (2008), the AABW transported by the DWBC originates from both Adélie Land (between 140 and 150°E, Bindoff et al., 2000) and the Princess Elisabeth Trough (i.e., in the Prydz Bay). Close to the Antarctic continent, the AABW mixes with the westward along slope current from Antarctica (Antarctic Slope Current, ASC, Orsi et al. 1999). This current remains restricted to the Antarctic continental slope while the AABW formed on the continental shelf flows below the ASC and is exported to the deep oceanic basins (figure 53).

The past variations of the ACC and AABW remain controversial. Some previous sedimentological studies indicated stronger ACC during the Last Glacial Maxima (LGM) compared to the Holocene (Bareille et al., 1994; Dezileau et al., 2000; Mazaud et al. 2010, Lynch-Stieglitz et al., 2016, Mazaud et al., in prep.), whereas other detected no major changes since the last glaciation (McCave et al., 2014) or even an increase since the LGM (Lamy et al.,2015) . These studies however were conducted in different area along the ACC path around the globe, so that regional difference in the ACC dynamics may have occurred. The evolution of the DWBC is poorly documented, even though northward expansion of AABW during glacial period has been reported in other areas (Pacific: Hall et al., 2001; Indian: Govin et al., 2009; Atlantic: Govin et al., 2009; Spooner et al., 2018).

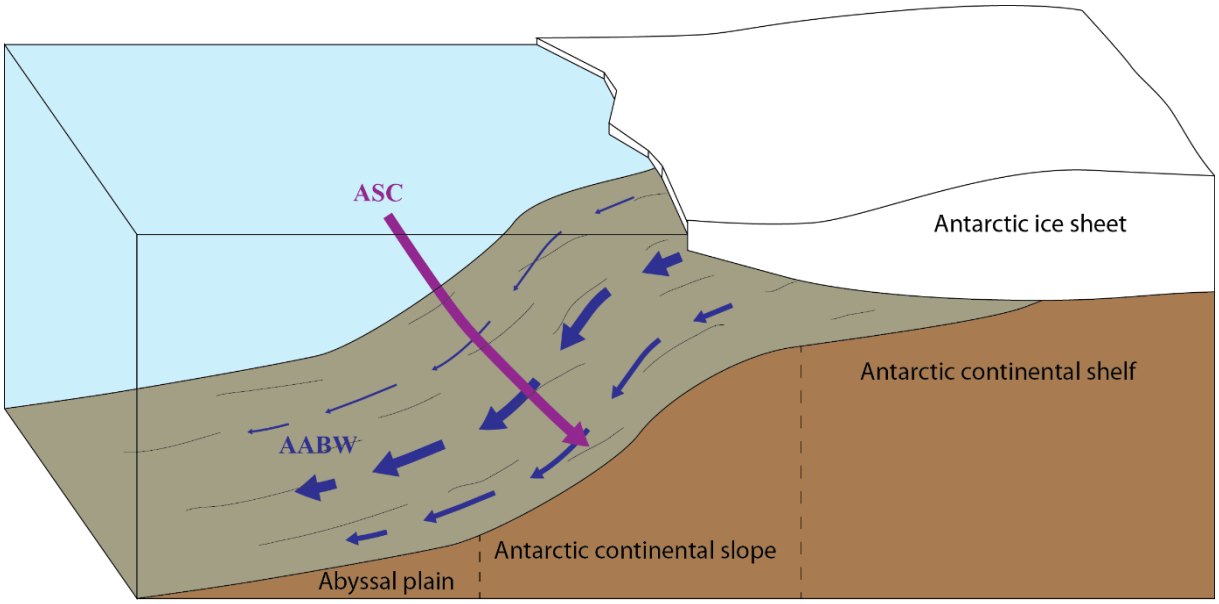

Figure 53: *Organisation of AABW and ASC circulations alongshore Antarctica.*

B. Geological background

The study area receives sediments from two main geographical areas: the Kerguelen Plateau, and East Antarctica. The Kerguelen Plateau is a large (1,250,000 km²) volcanic province induced by the activity of a mantle plume at least 120 Myrs ago (Wasilewski et al., 2017). The Kerguelen Plateau is often divided into 4 geological parts (Frey et al., 2000). However, the difference between these part is assumed to be neglictible for the studied proxies compared to the difference between the plateau and East Antarctica. Consequently, these 4 parts are not distinguished in this study. It is mostly composed of basalts (Gautier et al., 1990; Frey et al., 2000), but a few trachytic and phonolitic rocks are identified (especially in the south of the archipelago of this plateau; Nougier et al., 1970; Gautier et al., 1990; Wasilewski et al., 2017). In addition, the volcano plutonic complex of Rallier du Baty in the southwest of the island is mostly composed of rhyolitic and trachytic rocks. Weathering of the Kerguelen Plateau mostly delivers smectite (up to 90%) associated with minor illite and chlorite (Borchers et al., 2011). The WRAS normalised rare earth element (REE) composition of such volcanic areas is generally enriched in heavy rare earth elements (HREE) compared to light rare earth elements (LREE). The isotopic signature of the Kerguelen Plateau is characterized by radiogenic neodymium ($\varepsilon_{Nd} > -5$; Dossa and Rama Murphy, 1980; Gautier et al., 1990; Weis et al., 1993; Jeandel et al., 2007), and unradiogenic strontium ($^{87}Sr/^{86}Sr < 0.71$; Dossa and Rama Murphy, 1980; Gautier et al., 1990; Weis et al., 1993).

East Antarctica is mostly composed of Archean cratons and Precambrian orogens comprising a variety of granites and granitic gneisses. A Grenville Belt (920-1330 Ma) extends from Enderby Land to Wilkes Land (Tingey, 1981; Tingey, 1982a, b; Tingey, 1991; Pierce et al. and references therein, 2014). Pan-African crustal rocks are locally exposed between these belts in the area of the Denmann Glacier in Queen Mary Land, and on the Eastern flank of the Prydz Bay (Mond, 1972; Barret, 1991). Archean cratons are present on the Enderby coast (Napier Complex), in the southern part of the Prydz Bay (Ruker Terrane), and Adélie Land (Gawler Craton; Tingey et al., 1991). Clay minerals released from these Precambrian areas are mostly chlorite and illite (Moriarty et al., 1977; Petschik et al., 1996). Inherited kaolinite - formed under past wet conditions when Antarctica was close to the equator - is present in the Prydz Bay (Petschik et al., 1996; Whitehead and McKelvey, 2001). The REE composition of East Antarctica is very similar to the upper continental crust. The isotopic compositions of these areas display very unradiogenic neodymium (ε_{Nd} < -20), and radiogenic strontium ($^{87}Sr/^{86}Sr$ > 0.72). Archean cratons such as the Ruker Terrane can reach extreme values with ε_{Nd} close -50 and $^{87}Sr/^{86}Sr$ exceeding 0.8 (see figure 56 for detailed references).

III. Materials and Methods

A. Materials

Core MD12-3396Q (latitude: 47° 43.88’ S, longitude: 86° 41.71’ E, water depth: 3630 m) was taken in 2012 during the IndienSud-2 cruise by the French Research Vessel (RV) *Marion Dufresne*.

The age model of core MD12-3396Q is based on radiocarbon analyses of mono specific planktic foraminifera samples measured at the ARTEMIS facility, Bern (Gottschalk et al., 2018). *Neogloboquadrina pachyderma* was used for datation except for Holocene samples where *G. bulloides* was analysed). 73 samples have been dated yielding ages between 8 and 27.6 ka. The next age measurement is at 34 ka and the age between 27.6 ka and 34 ka was calculated using a linear interpolation, generating a highly uncertain age model for this interval. The sedimentation rate (figure 54) displays many marked variations and a linear interpolation is not representative of the behavior of sedimentation rates in this sediment core.

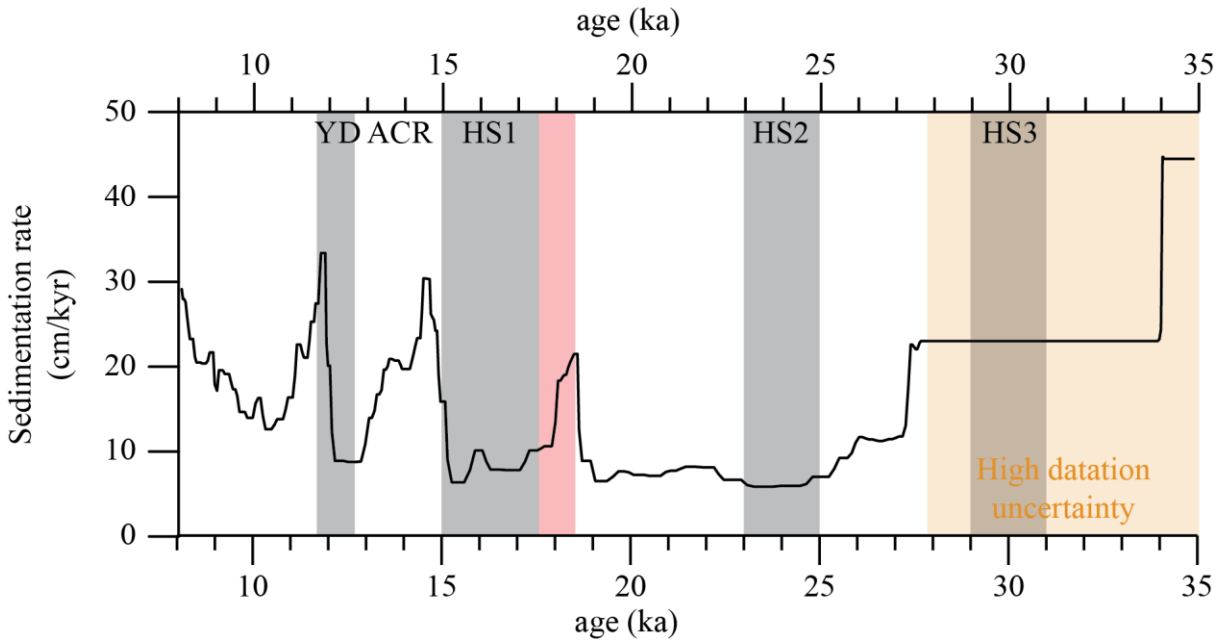

Figure 54: Sedimentation rate of core MD12-3396Q based on the age model described above. Grey areas correspond to Heinrich Stadials; red area indicates substantial northward migration of the AABW in the South Atlantic sector of the Southern Ocean (Beny et al., 2020); orange area indicates the interval of high datation uncertainty (only 2 tie-points over 7 kyr).

B. Sample preparation and analytical procedures

Samples were first decarbonated using 0.1N HCl, and deflocculated by repeated washes using milli-Q water. The clay-size fraction (<2 μm) was isolated by settling according to Stoke's Law. This fraction was then concentrated by centrifugation (40 minutes, 3500 rotation per minute) and an aliquot was oriented on a glass slide. X-ray diffraction patterns were obtained using a Bruker D4Endeavour (standard 30kV and 30mA). Each samples is run three times between 2.49 and 32.5°2θ: (1) dried sample, (2) glycolated sample (12 hours in ethylene glycol), and (3) heated sample (490°C for 2 hours). The proportion of each clay mineral (smectite, illite, and chlorite+kaolinite) is determined using the main X-ray diffraction peaks (layer and interlayer) on X-ray spectra according to their crystallographic characteristics (Brown, 1980). Smectite is characterized by a main peak at 14-15 Å on the air-dried samples that expands at 17 Å after ethylene glycol saturation and collapses at 10 Å after heating. The main peak at 10 Å on the three runs characterizes illite. Kaolinite + chlorite are measured based on their main peak at 7-7.2 Å. The presence of residual opal affect the signal-to-background ratio preventing distinction of kaolinite from chlorite. All measurements and semi-quantitative estimations are processed using the McDiff software (Petschick, 2000).

Trace and rare earth elements and isotopic analyses were carried out on the clay-size fraction (<2 μm). An aliquot of 10 to 150 mg (depending of the sediment quantities available) was then used for chemical analysis at the Faculty of Earth and Life Sciences of the Vrije Universiteit, Amsterdam. Sediment was digested using a mixture of concentrated HF and HNO_3 (~2/3 and 1/3, respectively) for a few days and then dissolved in ~6.5N HCl for a few days. The HCl solutions are dried at 120°C, and redissolved in 5% HNO_3. An aliquot was taken to obtain a dilution factor close to 5000 (e.g., 2 mg of original dry sediment are used to obtain 10mL of solution). Then, the trace element and REE measurements are determined by ICPMS.

Neodymium and strontium isotopes were purified using conventional ion chromatography. Light rare earth elements (LREE) were isolated using true-spec resin medium (Eichrom^{TM}, 100-150 μm mesh size) and Nd was eluted from the LREE fraction using LN-resin (Eichrom^{TM}, 50-100 μm mesh size). Sr was recovered using Sr resin column. Nd measurements were performed by bracketing using CIGO standards on Thermo Scientific Neptune multi-collector inductive coupled plasma-mass spectrometer (MC-ICPMS) when possible, whereas the measurements of low Nd samples (<50 ng) and of Sr isotopes were performed on a thermal ionization multi-collector-MS (TIMS).

IV. Results

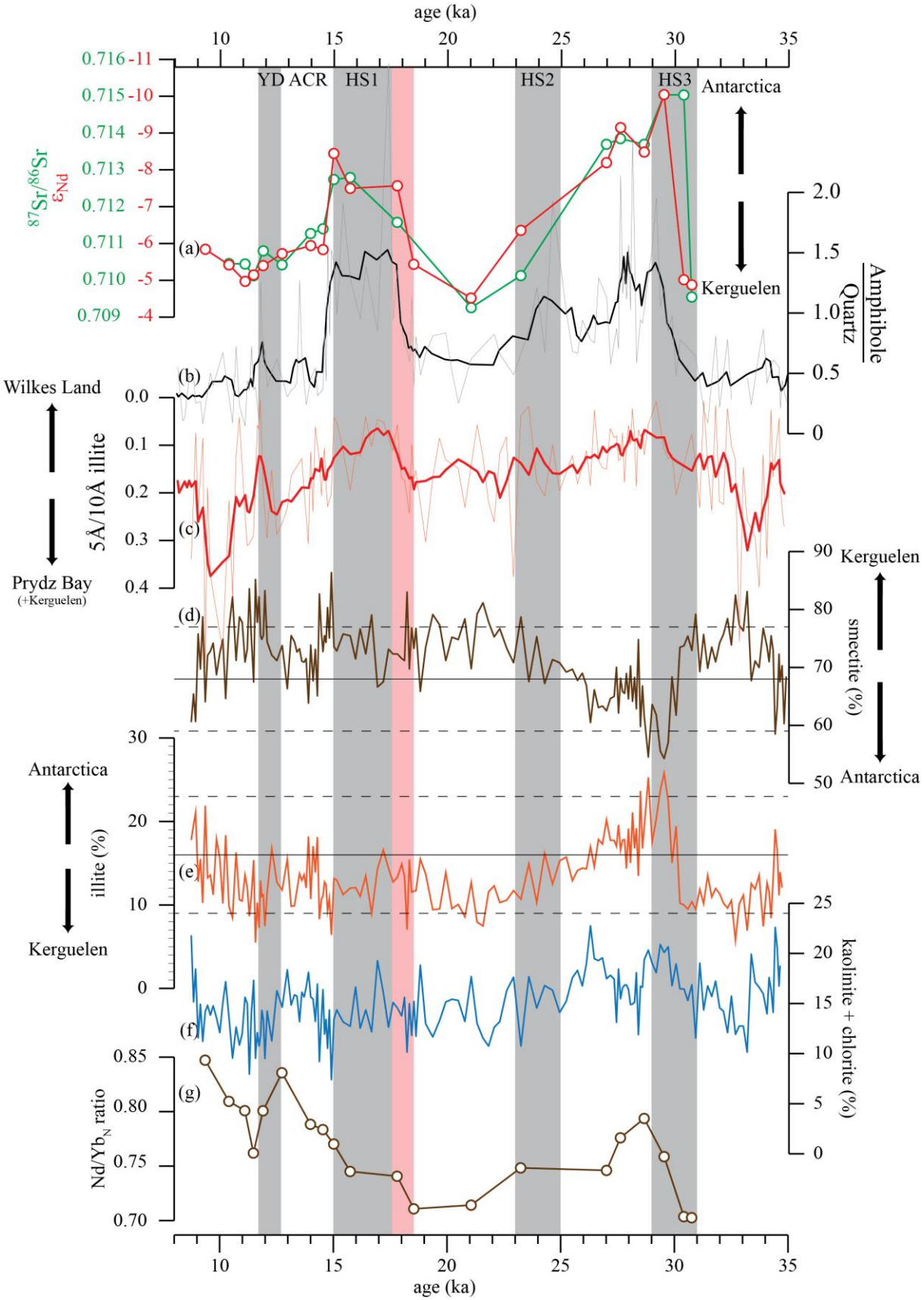

Figure 55: Geochemical and mineralogical proxies from site MD12-3396Q: (a) ε_{Nd} (red) and $^{87}Sr/^{86}Sr$ (green) measured on the clay-size fraction; (b) amphibole/quartz ratio (thin black line, amphibole/quartz ratio, thick black line, 5 points-smoothed signal); (c) chemical properties of the illite (thin red line, illite intensity at 5Å / illite intensity at 10Å ratio, thick red line, 5 points-smoothed signal); (d) smectite proportion (%), black line represent the mean smectite proportion and black dashed lines the standard deviation; (e) illite proportion (%), black line represent the mean smectite proportion and black dashed lines the standard deviation; (f) kaolinite and chlorite proportion (%); (g) Nd/Yb_N ratio (normalized to WRAS).

A. Mineralogy

Clay mineralogy analyses results are detailed in figure 55 and in annex 22. The total clay mineral assemblage is composed of 71±6% of smectite, 15±3% of kaolinite+chlorite and 14±4% of illite (5-26%). Overall, smectite is the dominant clay mineral ranging from 53 to 86%, being less abundant between 30 and 26 ka and between 9 and 8 ka. Relatively higher than average inputs of illite and kaolinite+chlorite correspond to smectite lows. The illite 5Å/10Å ratio ranges from 0.002 to 0.569 (Fe- and Mg-rich illite) with the lowest values (<0.3) corresponding to illite-rich and smectite-depleted intervals. The amphibole/quartz ratio varies between 0.05 and 5.05 with high values associated with low illite 5Å/10Å ratio.

B. Isotopic compositions

The isotopic results are detailed in annex 23 and displayed on figures 55 and 56. The ε_{Nd} varies between -10.1 and -4.5, with lowest values between 30 and 26 ka and between 18 and 15 ka, associated with low illite 5Å/10Å values and high amphibole/quartz ratios (figure 55). The $^{86}Sr/^{87}Sr$ ratios range between 0.70922 and 0.71506 and are correlated to the Nd isotope composition ($R^2 = 0.908$ if an outlier value at 30.433 ka is excluded). This observation, taken together with the fact that Nd isotope composition is relatively insensitive to chemical weathering, suggests that the variations of Sr isotopes track provenance changes rather than chemical weathering variations.

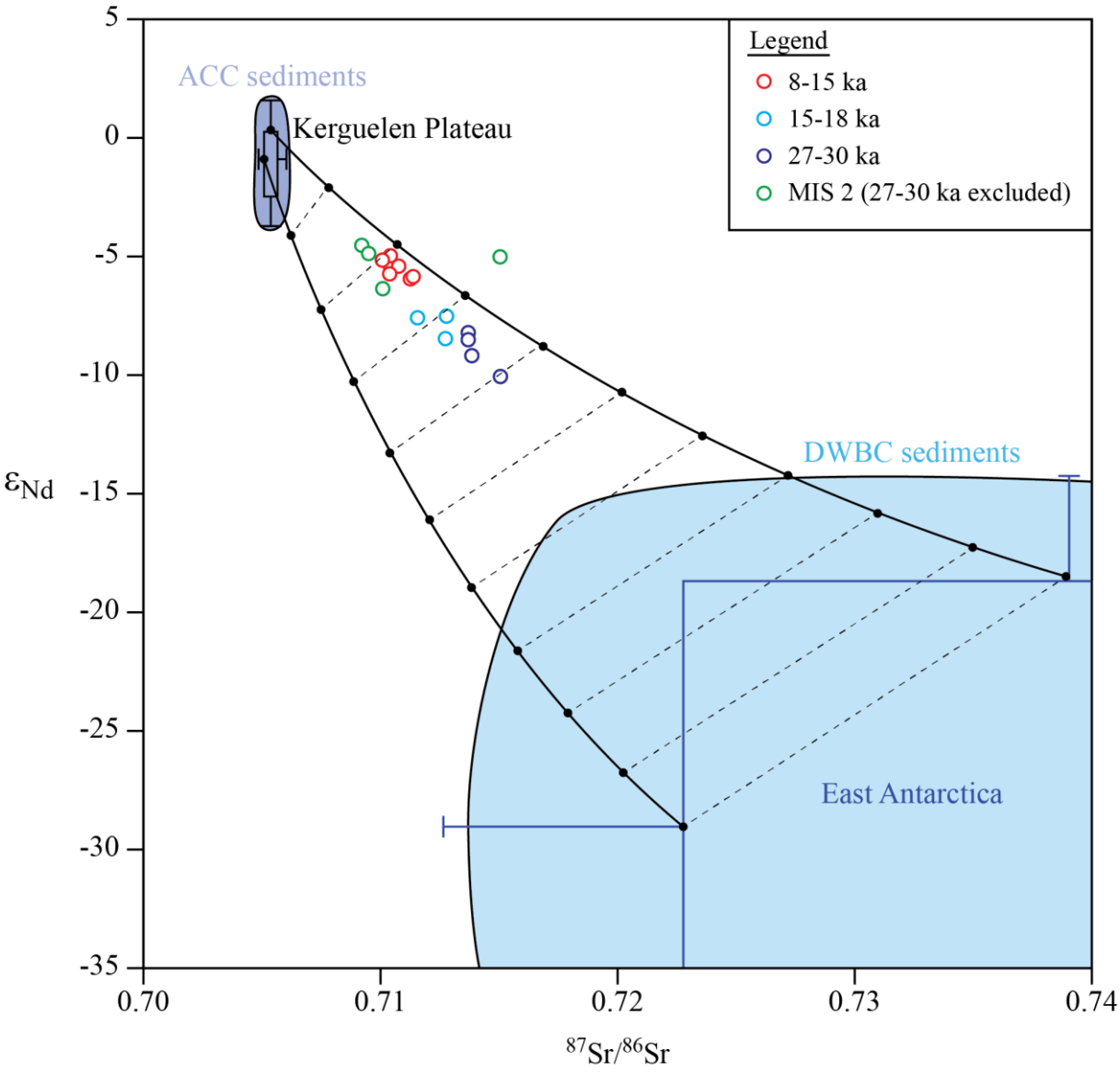

Figure 56: *$^{87}Sr/^{86}Sr$-ε_{Nd} diagram of core MD12-3396Q. Boxes represent the reference data are delimited by the first and the third quartile. The median is represented by horizontal and vertical lines attached to the boxes for the ε_{Nd} and the $^{87}Sr/^{86}Sr$ ratios, respectively. The short strokes at the end of these lines mark the 10th and 90th percentile values. According to this, the box represent 50% of values found for each potential provenance, and 80% is represented with the lines. The black dots on the mixing lines represent 10% intervals by black dots joined by dashed lines. Reference data used to draw the boxes are: -Kerguelen Plateau- Dosso and Rama Murphy, 1980; Gautier et al., 1990; Weis et al., 1993; -East Antarctica- DePaolo et al., 1982; McCulloch and Black, 1984; Black et al., 1987; Grousset et al., 1992; Jeandel et al., 2007; Roy et al., 2007; Van de Flierdt et al., 2007; Boger et al., 2008.*

C. Trace and rare earth elements

Trace element compositions are detailed in annex 24 and representative ratios are presented on figure 57. REE have been normalized to the world river average shale (WRAS; Bayon et al., 2015). In the normalised REE patterns HREE are enriched compared to LREE, expressed by the Nd/Yb_N ratios ranging from 0.70 and 0.85.

Most trace element ratios (Rb/Sr, Rb/Hf, Cs/Hf, Cs/Zr) correlate with isotopic ratios (annex 25), suggesting that provenance changes are the main factor controlling the chemical composition of the sediment at our site. In addition, most of ratios comparing large ion lithophile elements (LILE; Rb, Sr, Cs, Ba) with high field strength elements (HFSE; Zr, Nb, Ti, Hf, Ta) decrease throughout the studied interval (Cs/Zr, Rb/Hf ; figure 57) whereas normalised LREE/ HREE ratios increase through time (La/Nd_N, Nd/Yb_N ; figure 57). Th/Sc ratio behaves similarly to the LILE/HFSE ratio. The apparent enrichment in incompatible trace elements compared to lithophile element across the deglaciation is likely due to an increased contribution of newly exposed minerals that have been previously physically broken up by glacial processes.

Overall, the trace element ratios show a good correlation with radiogenic isotopes. In addition, LILE/HFSE ratios present a decreasing trend through the record, likely due to the progressive retreat of the ice sheets. The low normalised LREE/HREE ratios indicate an important contribution of volcanic material compared to crustal material. In addition, the variations of the Nd/Yb_N display a good correlation with the other geochemical proxies until 15 ka. From this date, the ratio increases and presents a short decrease during the Younger Dryas (YD), suggesting that less volcanic material is delivered compared to crustal material.

Figure 57: Trace and rare earth element ratios from site MD12-3396Q. (a) ε_{Nd} (red) and $^{87}Sr/^{86}Sr$ (green) measured on the clay-size fraction; (b) Rb/Sr ratio; (c) Sm/Nd ratio; (d) Cs/Zr ratio; (e) Rb/Hf ratio; (f) Th/Sc ratio; (g) Nd/Yb_N ratio (normalized to WRAS).

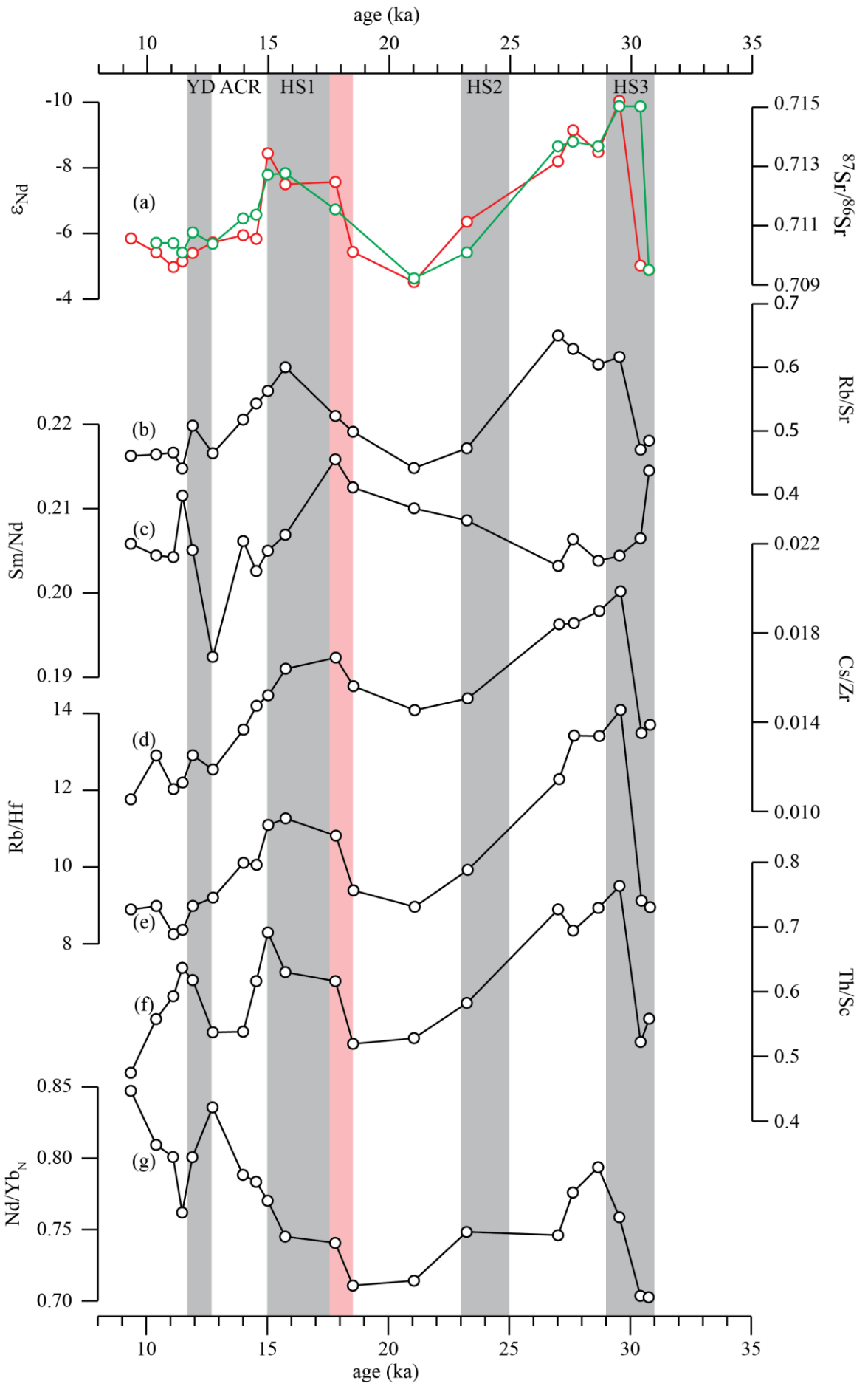

V. Discussion

A. Provenance of marine sediments East of the Kerguelen Plateau

Clay mineral abundance is dominated by smectite, which typically represents more than 70% of the total clay mineral fraction. This indicates a dominant contribution of detrital material derived from the Kerguelen Plateau, which is the nearest and largest productive source of volcanic material. This observation is independently supported by the relative HREE enrichment, as shown by the Nd/Yb_N ratios (figure 55) (Bayon et al., 2015). The second most abundant clay mineral is illite, which constitutes up to 26% of the clay mineral content. In the Indian sector of the Southern Ocean, illite has 2 possible provenances, the Kerguelen Plateau and the Antarctica (Borchers et al., 2001). Illite delivered by the Kerguelen Plateau is clearly muscovitic (5Å/10Å ratio > 0.5), whereas the composition of illite delivered from Antarctica is biotitic (5Å/10Å ratio < 0.2) or a mix biotitic/muscovitic (5Å/10Å ratio from 0.2 to 0.5). This ratio rarely exceeds 0.4 and is generally below 0.25, suggesting that most of the illite comes from Antarctica. Since smectite is mostly delivered by the Kerguelen Plateau, these observations strongly support the idea that illite and smectite have distinct provenances. The chemical composition of illite is controlled by crystallographical properties that can be used to pinpoint the detailed provenance of illite in Antarctica. Borchers et al. (2011) demonstrated that the chemical signature of illite from deep-sea sediment west of the southern Kerguelen Plateau (5Å/10Å ratio = 0.20) is too low to be solely explained by a mix between illite from Prydz Bay (0.15-0.38) and from the Kerguelen Plateau (> 0.6) and suggested that a branch of the Antarctic Slope Current may bring biotitic illite toward the eastern part of the Kerguelen Plateau. In fact, a similar interpretation applies to the illite found at our site located northeast of the Kerguelen Plateau where the contribution of the Kerguelen Plateau compared to Antarctica should be even more significant than the sites studied by Borchers et al. (2011). In particular, between 30 and 26 ka, 24.5 and 23 ka and 17.5 and 15 ka and at 12 ka, the 5Å/10Å ratio drops down to 0.1 and an additional source of illite is necessary to explain these low values. Borchers et al. (2011) pointed out that there was little information about the clay mineral composition west of the study of Moriarty (1977; 100-170°E) to validate this hypothesis. However, very low 5Å/10Å ratio (down to 0.05) occur in Holocene and Quaternary illite-rich sediments off Wilkes Land (Beucherie, unpublished data). The nature of these illite-rich intervals is also highlighted by the geochemical data, with higher LREE/HREE and LILE/HFSE ratios (figure 57), consistent with a higher contribution of terrigenous particles originating from Antarctica. Equally, the isotopic compositions clearly indicate a high contribution of sediments originating from Antarctica.

Indeed, the contribution of East Antarctica varies between 10% and 40% in the total clay-size fraction (figure 56), with higher contribution from Antarctica (characterized by low ε_{Nd} and high $^{87}Sr/^{86}Sr$) associated with higher 5Å/10Å ratio (figure 55). In addition, the amphibole/quartz ratio (figure 55) displays high values during these intervals giving support for an Antarctic provenance as described by Moriarty (1977). These conclusions contrast with a previous study of Dezileau et al. (2000) on ^{230}Th and trace elements, arguing against sources from Antarctica during the LGM compared with the Holocene, and concluding that AABW formation was not significantly different during the LGM. Overall, the provenance of the sediment at our site is dominated by basaltic inputs from the Kerguelen Plateau whereas Antarctica is a minor source of sediments. However, the supply of detrital particles from Antarctica appears higher than expected (up to 40% between 30 and 27 ka), highlighting that equatorial transport of Antarctic deep water masses was previously underestimated.

B. Transport of marine sediments

In the Southern Ocean, several processes may be involved in the transport and deposition of terrigenous sediments. Dezileau et al. (2000) estimated that the contribution of aeolian particles, turbidity current and Ice Rafted Detritus (IRD) on the Southeast Indian Ridge were insignificant. In contrast, many studies in the South Atlantic sector (Petschick et al., 1996; Diekmann et al., 2000; Kuhn and Diekmann, 2002; Krueger et al., 2008; Noble et al., 2012) and in the South Indian sector (Moriarty, 1977; Dezileau et al., 2000; Thamban et al., 2005; Borchers et al., 2011) of the Southern Ocean highlight the importance of oceanic currents in the redistribution of detrital sediments. In the core MD12-3996Q, variations of both clay-size fraction and magnetic susceptibility (Mazaud et al., in prep.) are not synchronous with changes in aeolian dust activities in Antarctica (Petit et al., 1990, Grousset et al., 1992), in sea surface temperature, or in IRD deposits. Consequently, it is concluded that sediments in core MD12-3996Q were mostly transported and deposited by oceanic processes.

In this sector of the Southern Ocean, the ACC is responsible for the transport of material from the Kerguelen Plateau while the AABW - via the DWBC – delivers material from Antarctica (Dezileau et al., 2000; Borchers et al., 2011; Mazaud et al., in prep.). According to the Sr-Nd diagram (figure 56), the contribution of the AABW ranges between 10 and 40%, and does not display significant changes through the deglaciation. In contrast, enhanced contribution of the DWBC occurred during Heinrich Stadials 3 and 1. The increase of the amphibole/quartz ratio during the HS 2 suggests that enhanced contribution of the DWBC also occurred during this interval, but additional isotopic data of well dated samples are required to

confirm this hypothesis. The mineralogical changes are characterized by modifications of illite chemistry (figure 55) indicating changes in sediment provenance. Moreover, these events are also marked by coupled variation in trace elements (figure 57) and Sr and Nd isotope ratios (figures 55 and 56), clearly indicating an increase of the Antarctic contribution. Such changes in provenance imply modification in the mode of AABW formation (which feeds the DWBC) with additional AABW coming from the east Antarctica. This hypothesis is consistent with the work of Borchers et al. (2011) that provided evidence of the existence of an additional branch of the Antarctic Slope Current intermittently feeding the DWBC and delivering biotitic illite. Our data show clear evidences that (1) the delivery of sediment by the AABW coming from the east (especially Wilkes Land illite) is stronger between 30 and 27 ka (figure 56) when illite supply is at a maximum, and (2) that this branch is more vigorous during HS 3, 2, and 1, as the contribution of material from east Antarctica increased (figures 55 and 56).

C. Paleoclimatic implications

The marked increase in sediment delivery by the AABW during HS 3 and 1 in core MD12-3396Q potentially results from several processes including: (1) enhanced sediment production linked to increased ice sheet activity in the Wilkes Land area, (2) stronger Antarctic Slope current, (3) formation of bottom water off Wilkes Land, (4) northward migration of the DWBC, likely related to higher AABW production.

Higher sediment delivery by the unstable ice sheets associated with invigorated DWBC has been previously observed in Miocene sediments at site ODP 375 (Joseph et al., 2002). Unfortunately, this study did not provide any information on the timing of changes and both climate and oceanic configurations in the Miocene were different from today, preventing any direct comparison with our study.

Macintosh et al. (2014) revealed that the retreat of the East Antarctic Ice Sheet since the LGM was not homogenous: some areas such as central Dronning Maud Land or Eastern Wilkes Land were affected by minor changes during the deglaciation, whereas the thickness of the ice sheet was reduced by at least 700 m in the central Wilkes Land (at the Bunger Hills). In addition, the timing of the ice-sheet retreat differs regionally. Precise data about the ice-sheet history in the Wilkes Land are scarce and poorly studied across the LGM. It is thus impossible to build robust conclusions on the role of the Wilkes Land ice sheets on sediment delivery to the ocean. Nevertheless, the ice-sheet retreat began between 30 and 40 kyr while most of the retreat of the East Antarctic Ice Sheet happened progressively between 14 and 6 ka (Macintosh et al., 2014). This progressive ice-sheet recession is consistent with the geochemical data that show a

progressive decrease of the LILE/HFSE ratio values from 30 to 10 ka. Indeed, ice-sheets retreat would expose incompatible elements-bearing minerals broken up through physical erosion during the glaciation. Nevertheless, this progressive ice-sheet retreat is not consistent with the fast and brief detrital inputs from Antarctica observed at our site during HS 1, 2, and 3, ruling out any major sharp terrigenous contribution resulting from ice-sheet destabilization during these climatic events.

No important change of the Antarctic Slope Current during the LGM and the deglaciation has been reported. Moreover, magnetic properties and grain size distribution, interpreted as proxies for current intensity and speed measured on core MD12-3996 (Mazaud et al., in progress) do not display any variations associated with the provenance changes observed between 30 and 26 ka, or during HS3 and HS1. Hence, the observed provenance changes do not appear to result from modification in AABW or ASC speeds.

A northward expansion of the AABW has been recorded in the southern flank of the South Indian Ridge during the MIS 5.5-5.4 transition and interpreted as reflecting higher AABW production due to enhanced sea ice formation (Govin et al., 2009). Other sedimentological evidences of northward expansion of AABW during glacial times in the Atlantic and Pacific sector of the Southern Ocean have also been reported (Hall et al., 2001; Krueger et al., 2012; Spooner et al., 2018). Moreover, rapid perturbations of the Atlantic Meridional Overturning Circulation were revealed by changes in benthic foraminifera preservation during HS 1 to 6, indicating rapid changes in the carbonate compensation depth, interpreted as the result of incursion of southern-sourced bottom water (i.e., AABW from the Weddell Sea; Gottschalk et al., 2015). All these related findings suggest that the AABW reacted rapidly to perturbations induced by the Heinrich Events in the North Atlantic ocean: the AABW expanded northward during HS not only in the Kerguelen Sector but in the entire Southern Ocean. Our results also highlight that the export of the AABW to the global ocean was especially enhanced in the Kerguelen sector during Heinrich Stadials compared to the other areas. In addition, our results pinpoint a specific provenance for some of the bursts of Antarctic detrital material inputs and thus suggest that additional area(s) of production of AABW may have existed at that time. Indeed, specific changes in illite chemistry imply additional inputs of terrigenous material from the Wilkes Land, which is not known for AABW production. These changes are coeval with periods of northward expansion of the AABW and with increases of all materials deriving from Antarctica. Such additional terrigenous inputs from the Wilkes Land thus suggest that AABW production may have occurred off Wilkes Land at that time.

The data indicate the enhanced export of AABW before HS 1 and 2. Due to the high uncertainty in dating of samples older than 27 ka, similar observation cannot be confirmed for HS 3. Nevertheless, the changes observed in the AABW during the HS 1, 2, and possibly 3, cannot result from changes involved by the Heinrich Events (1, 2 and 3, respectively) as these events started after the recorded change in the AABW. In the Atlantic Ocean, Pahnke et al. (2008) and Gutjahr and Lippold (2011) also observed an incursion of southern source deep water (i.e., AABW, CDW, AAIW) ~2 kyr before the Heinrich Event 2. Gutjahr and Lippold (2011) proposed that a change of the Atlantic Meridional Overturning Circulation (AMOC) may have contributed to, or even triggered, the ice sheet instability in the Northern Hemisphere. Here, our data independently support this idea by providing evidences of enhanced production of AABW in the South Indian sector of the Southern Ocean ~2 kyr prior to the Heinrich Event 2.

VI. Conclusions

Based on coupled mineralogical and geochemical variations in sediments deposited at site MD12-3996 record mixing of sediments originating from (1) the Kerguelen Plateau and transported by the ACC, and (2) Antarctica and transported by the AABW via the DWBC. The contribution of the AABW was previously underestimated, especially during Heinrich Stadials. Radiogenic isotopes indicate that the AABW is responsible for up to 40% (at 27 ka) of the terrigenous inputs during these intervals. Moreover, the composition of illite reveals (1) that the provenance of material from Antarctica via the AABW is not constant, and (2) that production of the AABW may have occurred periodically in the Wilkes Land. Data also highlight the rapid and major response of the AABW in response to perturbations of the AMOC during Heinrich Events resulting in northward expansion, and enhanced production with additional formation area (off Wilkes Land) and increased DWBC contribution to thermohaline circulation.

Chapter 7. The role of the Southern Ocean Overturning on Heinrich Event atmospheric CO_2 variations: clues from marine terrigenous sediments.

Abstract

A strong correlation has been observed between Antarctic temperature, Southern Ocean overturning circulation, and atmospheric CO_2, indicating abrupt changes associated with rapid climatic events such as during Heinrich Stadial periods. This work is specifically designed to study the dynamic component of the Southern Ocean deep water masses by using grain size distribution data from well dated sediments (core MD07-3076Q) whose provenance and transportation patterns have been previously determined. This new dataset is compared with (1) previously published data from the same core (2) data from a core located in the Kerguelen sector of the Southern Ocean, and (3) published climatic records. The data establish that Heinrich Events 1 and 2 are preceded by a modification of the Southern Ocean overturning circulation associated with a significant change in the extent of Atlantic Antarctic Bottom Water (AABW) northward. Consequently, this study supports the theory that a change in overturning circulation in the Atlantic and the Southern Ocean played a major role in triggering Heinrich Events. In addition, we demonstrate that the comparison between the two main grain-size modes from core MD07-3076Q is a valuable tool to identify changes in turbulent mixing at the AABW/LCDW (Lower Circumpolar Deep Water) interface. The data indicate enhanced turbulent mixing during rapid climatic events such as Heinrich Events and the Younger Dryas. Turbulent mixing was more intense during HE 2 than during HE 1, even though HE 2 is muted in atmospheric CO_2 records. These results demonstrate that turbulent mixing occurred at the AABW/LCDW interface although water exchange between the deep ocean and the atmosphere were interrupted during the last glacial period. Our results suggest that the apparent disconnection between the deep and surface ocean may be due to a dynamic/physical barrier to turbulent mixing, likely driven by astronomical specific configuration associated with low obliquity that created specific background lockdown surface-to-deep oceanic conditions.

Introduction

In the context of a global warming world due to increased greenhouse gas (including CO_2) release into the atmosphere mainly through anthropic activities, it is crucial to understand the global carbon cycle and how it may impact future climate. In order to estimate these potential impacts, the scientific community concentrates its effort in understanding past reactions of the carbon cycle during rapid climatic perturbations. Most studies focus on the role of the ocean in the cycle since the deep ocean is currently a sink for CO_2, while it appears to have been a source of CO_2 within the past (Anderson et al, 2009; Adkins et al., 2013; Bereiter et al., 2015). In this context, the Southern Ocean plays a key role in modulating atmospheric CO_2 variations during the Quaternary being the most important "window" (or active interface) between the deep ocean and the atmosphere (Anderson et al., 2009; Barker et al., 2009; Skinner et al., 2010, 2013, 2014; Burke and Robinson, 2012; Adkins et al., 2013; Boer and Hogg, 2014; Menviel et al., 2015a,b). Indeed, upwelling of CO_2-rich deep water masses likely explains most of the CO_2 rise observed during Heinrich Stadials (HS; Ahn and Brook, 2008; Anderson et al., 2009; Fischer et al., 2010; Skinner et al., 2010; Menviel et al., 2014, 2017). Other processes occurring in the Southern Ocean can also be invoked to explain deglacial atmospheric CO_2 rise: reduction of the biological pump due to reduced iron fertilization (Watson et al., 2000; Wolff et al., 2006; Fischer et al., 2010; Martinez-Garcia et al., 2014); reduced CO_2 solubility due to increased temperature of the ocean (Köhler and Fischer, 2006; Fischer et al., 2010); and reduction of sea ice extent (Fischer et al., 2010). Despite the crucial role of the Southern Ocean on the CO_2 cycle, no attempt has yet been made to reconstruct past variations of the Southern Ocean overturning during rapid climatic events of the last deglaciation by using detrital sediments, even though they are useful tracers for reconstructing the dynamical component of deep water masses (Hall et al., 2001; McCave and Hall, 2006; McCave and Andrews, 2019; Beny et al., 2020). Here, we explore the evolution of Southern Ocean overturning recorded in the well-dated sediment core MD07-3076Q using a new grain size distribution dataset. Specific attention will be paid to grain size distribution modes in the frame of previously constrained provenance and transportation patterns (Beny et al., 2020). These data will be compared with results from a core located on the Kerguelen sector of the Southern Ocean (Beny et al., in prep. – Chapter 6), and with other previously published paleoceanographic records in order to qualitatively constrain the role of the Southern Ocean on the carbon cycle during rapid climatic changes.

I. Material and Methods

A. Material

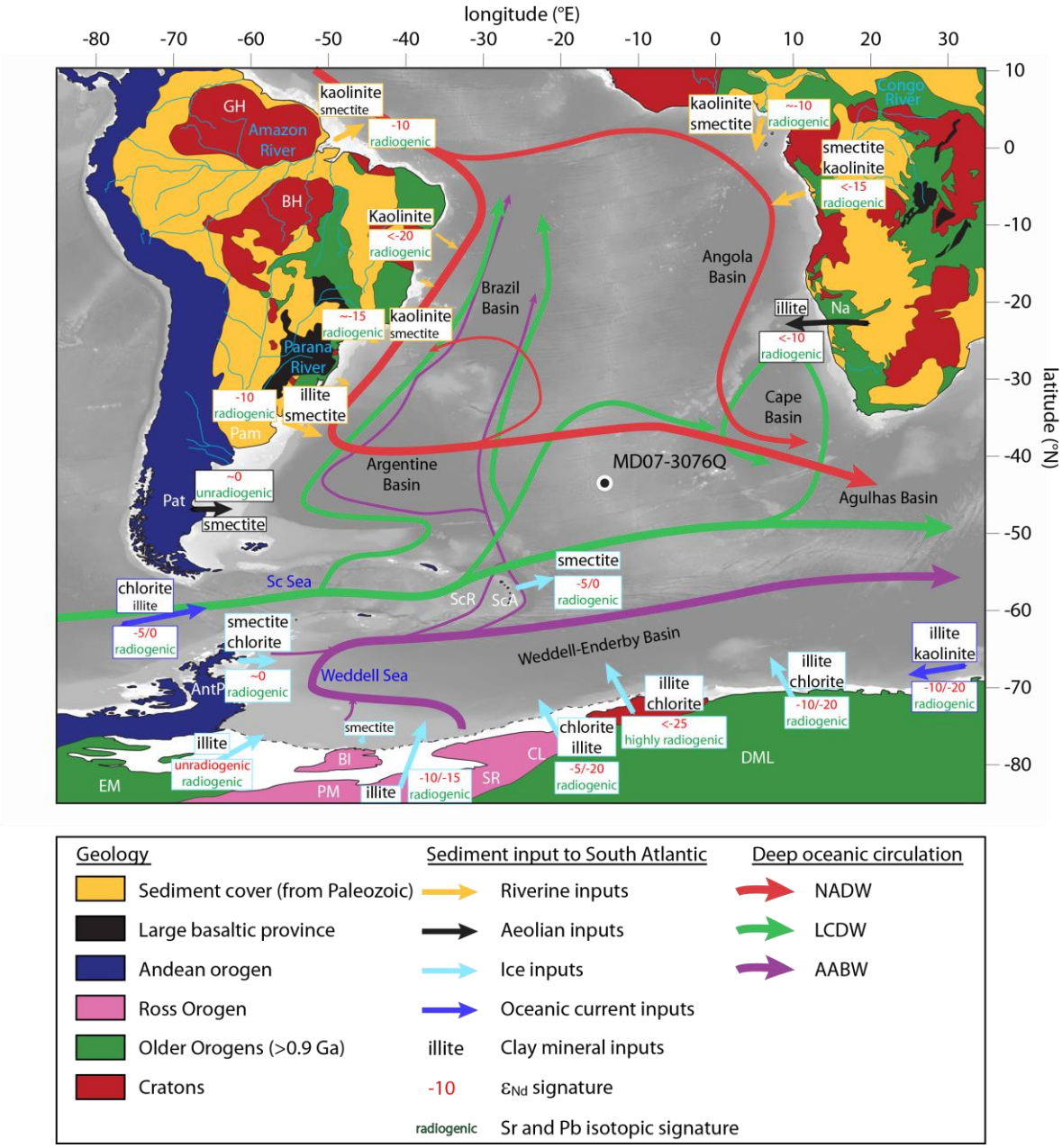

Figure 58: Simplified geological map of the study area. Light blue text riverine systems, dark blue text seas, italic black text oceanic basins, and white abbreviations areas. In South America: Guyana Highlands -GH-, Brazilian Highlands -BH-, Argentinian Pampas -Pam-, Patagonia -Pat-; in Africa: Namibian deserts-Na-; in Antarctica: Ellsworth Mountains -EM-, Antarctic Peninsula -AntP-, Pensacola Mountains –PM–, Berkner Islands -BI-, Shackleton Range -SR-, Coats Land -CL-, Dronning Maud Land -DML-. Clay mineral inputs to the South Atlantic Ocean derived from the studies of Petschick et al.,1996, Guyot et al. 2007, and Bayon et al., 2016, and Khondoker et al.,2018.

This study is based on sediment samples from core MD07-3076Q (44°9.2'S, 14°13.7'W) recovered by the French Vessel *Marion Dufresne* in 2007 on the eastern flank of the Mid-Atlantic Ridge at 3770 m depth (figure 58). The core chronology is based on planktonic foraminifer radiocarbon dates (30 measurements for the studied interval) and stratigraphic control points (Skinner et al., 2010, 2013, 2014; Gottschalk et al, 2015b). Today, the site is bathed in the LCDW (Lower Circumpolar Deep Water). From the seafloor to the surface, the water masses observed in the water column above the study site are the LCDW, North Atlantic Deep Water (NADW), Upper Circumpolar Deep Water (UCDW), and intermediate and surface waters. The Antarctic Bottom Water (AABW) is observed in nearby deep oceanic basins and terrigenous particles transported by this bottom water reach the studied site by advection and mixing with the LCDW.

B. Sample preparation and analytical procedure

The samples were first decarbonated using 0.1N HCl and then deflocculated by repeated washing using milli-Q water. Grain-size distribution was measured on carbonate-free sediment using a Malvern Mastersizer 2000 laser (0.02-2000 μm) following standard protocols (Montero-Serrano et al., 2009). The clay-size fraction corresponds to the proportion of particles with a diameter smaller than 2 μm, the cohesive silts correspond to the 2 to 10 μm diameter particles, the sortable silts correspond to the 10 to 63 μm diameter particles, and the sand fraction to the particles coarser than 63 μm.

II. Results

A. Previous results

The provenance of the sediment from this core during the deglaciation and the LGM were previously discussed (Beny et al., 2020). The clay size fraction (<2 μm) records the relative contribution of past variations of deep water masses relative contributions. Both mineralogy and radiogenic isotopes from the clay size fraction indicate particularly high contribution of AABW during the LGM, followed by an increased contribution of CDW during the early deglaciation. The NADW becomes dominant during the rest the deglaciation associated with its southern incursion into the Southern Ocean (Beny et al., 2020). Beny et al. (2020) demonstrated that the cohesive fraction (2-20 μm grain size fraction) is transported by the AABW, while the sortable fraction (20-32/40 μm grain size fraction) is carried by the LCDW. The isotopic composition of the sediment transported by the AABW is relatively constant ($-5.5<\varepsilon_{Nd}<-3.5$), while the incorporation of AABW component into the LCDW ($-1<\varepsilon_{Nd}$

<-3 during glacial) is suggested by a shift in the ε_{Nd} ($-4.5<\varepsilon_{Nd}<5.5$) during the deglaciation (figures 61c-e). The ε_{Nd} of the clay size fraction reflects the relative contribution of NADW compared with southern sourced deep waters (i.e. AABW and CDW), with enhanced contribution of NADW to clay sedimentation when ε_{Nd} is lower (Beny et al., 2020). Moreover, the ε_{Nd} of the coarse grain size fraction gives insight onto the mixing between LCDW and AABW, with no mixing when ε_{Nd} is close to -2, and active mixing enabling the incorporation of sediment initially transported by the AABW to the LCDW when ε_{Nd} is close to -4 or below (Beny et al., 2020).

B. Results

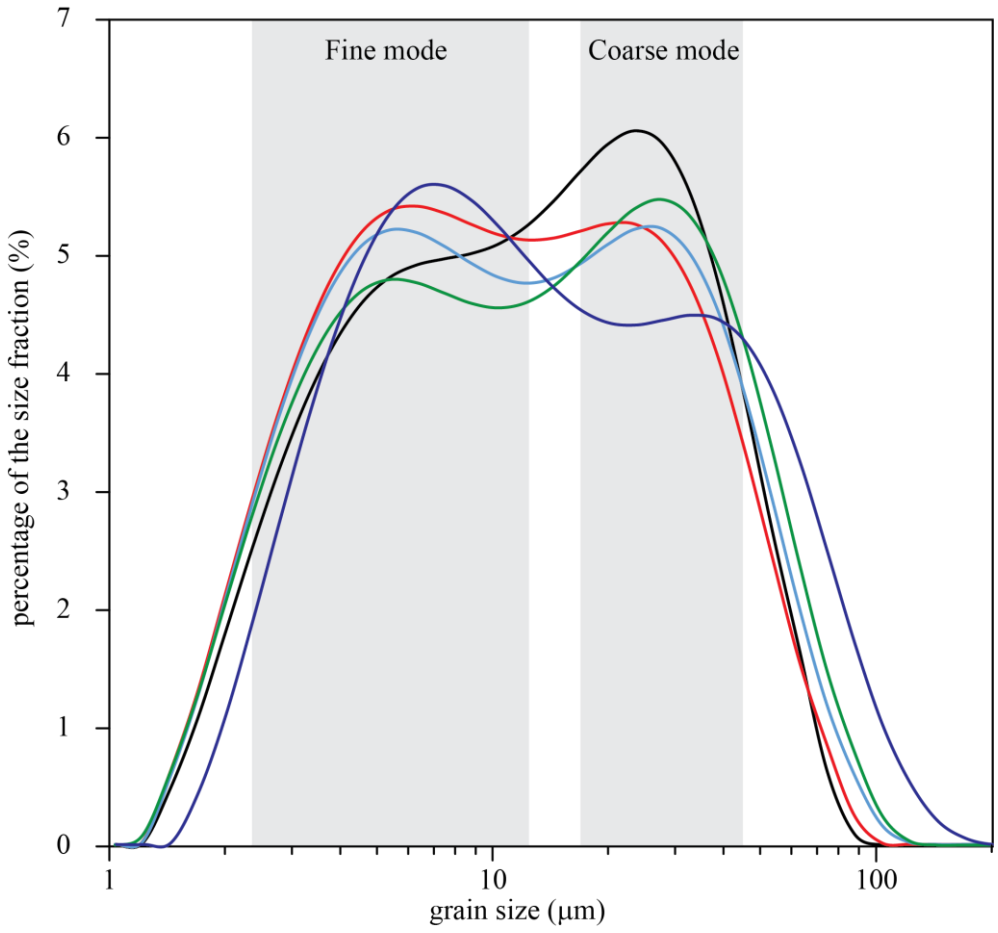

Figure 59: Representative examples of grain size distribution curves from the sediment core MD07-3076Q. These grain size distribution curves indicate a bimodal regime suggesting the presence of 2 main oceanic currents with the dominant mode varying. The fine mode is dominant on the dark blue curve while it is the coarse mode on the black curve. Black curve: 10.03 ka; light blue curve: 15.05 ka; red curve: 18.46 ka; green curve: 21.25 ka; dark blue curve: 24.26 ka.

The grain size curves display a bimodal distribution (figure 59), with a fine mode (2-10µm, transported by the AABW, Beny et al., 2020) and a coarse mode (20-32/40µm, transported by the LCDW, Beny et al., 2020) suggesting the presence of two distinct oceanic regimes. Note that the dominant mode (i.e. the most representative class size) varies throughout the studied interval (figure 60). The dominant mode is generally the coarse grain size mode, except during the Heinrich Events and the Younger Dryas when the fine grain size mode becomes dominant (figure 60). The coarse grain size mode displays the highest abundnce during the LGM, and decrease during the deglaciation. In addition, during Heinrich Stadials and the YD, the size of the coarse grain size mode is slightly smaller, indicating a slight slowdown of the LCDW. The fine grain size mode displays the lowest values between the end of the record and ~22 ka and during the deglaciation. The mode progressively rises from 22 ka to reach its maximum value at 18.3 ka. Then, it decreases rapidly in two periods between 18.3 and 18 ka and 16.2 and 15.8 ka.

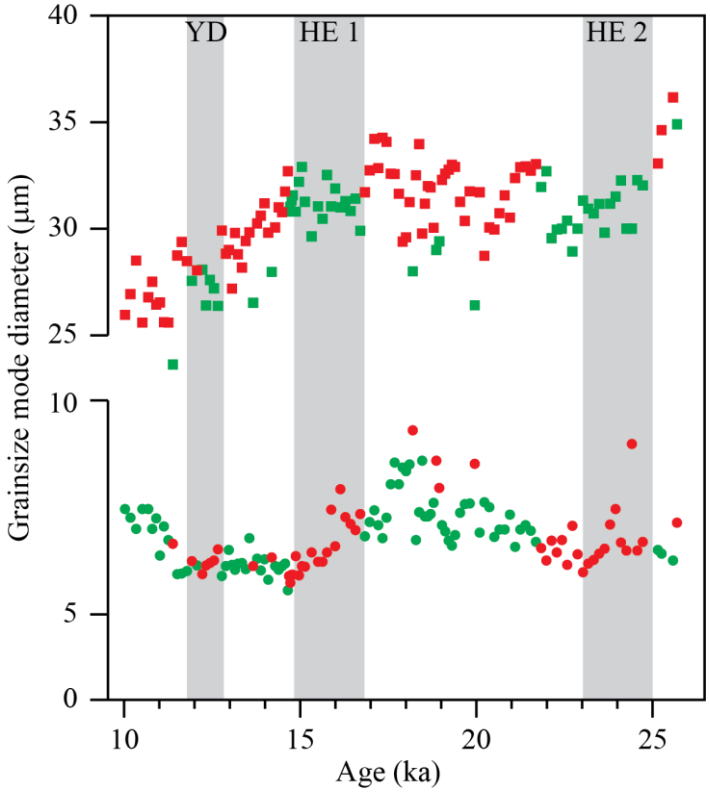

Figure 60: *Main grain size modes shown on figure 57 through time. The coarse grain size mode values are represented by squares while the fine grain size mode values are represented by circles. The dominant mode is represented in red, while the secondary mode is represented in green. This figure shows that the coarse grain size mode is generally dominant. The fine grain size mode becomes dominant during Heinrich Events and the Younger Dryas.*

The ratio of the proportion of particles represented by the fine grain size mode and of the proportion of particles represented by the coarse grain size mode (hereafter referred as Fine/Coarse ratio, figure 61) ranges from 1.20 to 1.88. Values of the Fine/Coarse ratio higher than 1.5 characterize HS 1, HS 2, and the YD, with the highest values during HS 2 (2.14; figure 61). The data also show that the onsets and ends of HS 1 and the YD are marked by sharp rise/drop of the Fine/Coarse ratio, indicating a marked change in the interaction between the LCDW and the AABW. Interestingly, high Fine/Coarse ratios recorded during HS 2 are not restricted to the duration of the stadial: the ratio rises sharply at the HS 2 onset, and remains high until it decreases sharply 0.7-1.2 ka after the end of HS 2.

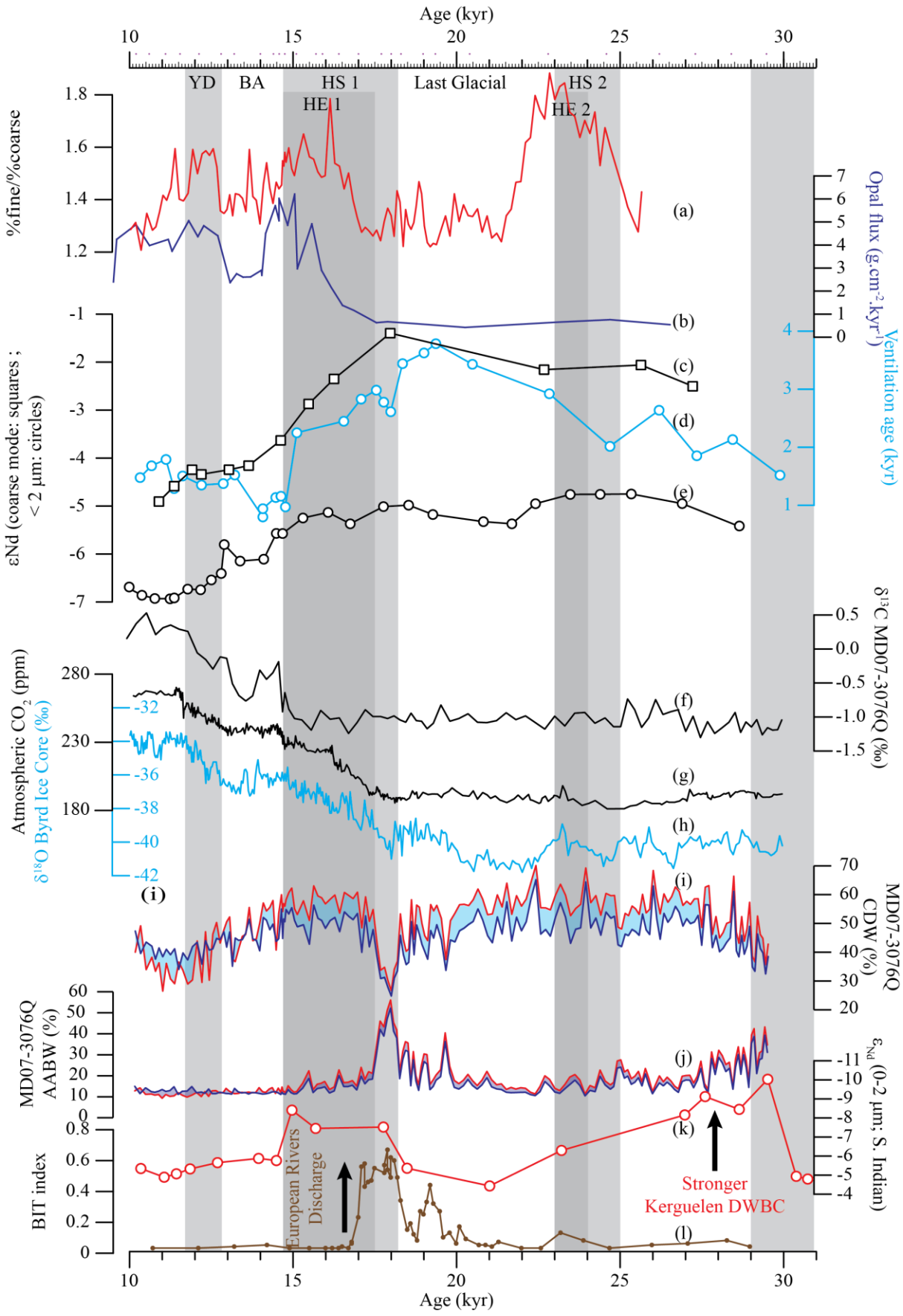

Figure 61: Comparison of data from site MD07-3076Q with the literature. (a) Fine/Coarse ratio from core MD07-3076Q calculated using the ratio of the relative proportion of the fine grain size mode divided by the relative proportion of the coarse grain size mode (this study); (b) opal flux from site TN057-13PC, a proxy of Southern Ocean upwelling (Anderson et al., 2009); (c) Nd isotope composition of the coarse grain size mode from site MD07-3076Q (Beny et al., 2020); (d) Ventilation age from core MD07-3076Q (Skinner et al., 2010); (e) Nd isotope composition of the clay size grain size fraction from site MD07-3076Q (Beny et al., 2020); (f) Cibicides $\delta^{13}C$ from core MD07-3076Q (Waelbroeck et al., 2011); (g) Atmospheric CO_2 concentration calculated from a compilation of Antarctic ice core records. (Bereiter et al., 2015); (h) $\delta^{18}O$ from Byrd ice core (Johnsen et al., 1972); (i) proportion of clay minerals delivered by the CDW from site MD07-3076Q (Beny et al., 2020); (j) proportion of clay minerals delivered by the AABW from site MD07-3076Q (Beny et al., 2020); (k) Nd isotope composition of clay size fraction from site MD12-3396Q in the Kerguelen sector of the Southern Ocean, showing the strength of DWBC (i.e. AABW; Beny et al., in prep. – Chapter 6); (l) BIT (Branched and Isoprenoid Tetraether) index indicating the European rivers discharge of fresh water in the North Atlantic (Ménot et al., 2006).

III. Discussion

A. Grain size mode switches during Heinrich Stadials

A previous study demonstrated that sediment distribution at this site is mainly dominated by two grain size modes that are useful tracers of deep water masses flow speed (i.e. AABW and LCDW, Beny et al., 2020). However, distribution and mean diameter of the dominant mode (see figure 59 representative examples) are varying through time (figure 60). In details, it appears that the coarse grain size mode is generally dominant, except during the YD, and HS 1 and 2 (figure 60).

The Fine/Coarse ratio, reflecting relative contributions of the fine versus coarse grain size mode, is used to summarize the results (figure 61a). This ratio rapidly increases/decreases at the beginning/end of northern hemisphere Heinrich Events (HE 1 and 2 on figure 61), with a slight lead of 1 kyr for the HE 2. Previous studies demonstrated that NADW production is severely reduced or even stopped during Heinrich Events (Hemming, 2004; Robinson and van de Flierdt, 2009). Both fine and coarse grain size modes are transported by southern-born water masses (i.e. AABW and LCDW; Beny et al. 2020), and consequently the Fine/Coarse ratio is unlikely to be directly impacted by the collapse of northern hemisphere ice sheets (Hemming,

2004; Robinson and van de Flierdt, 2009). This new dataset suggests that rapid modifications of both AABW and LCDW, and therefore of the Southern Ocean Overturning, occurred as the NADW production was weakened in the North Atlantic.

Such a stronger export of sediment via the AABW (Fine/Coarse ratio; figure 61a) apparently contrasts with mineralogical results from the same core (illite/smectite ratio; Beny et al., 2020) which support a maximum contribution of AABW during the LGM - due to northward expansion of AABW (from ~20 to ~17.5 ka; figure 61j) – whereas an abrupt reduction of AABW compared to CDW and NADW occurs slightly before the onset of Heinrich Stadial 2 (from 17.7 to 17.5 ka; figure 61j). These observations can be reconciled because clay minerals generally have a non-linear response to dynamic changes of the water masses resulting from their high particle cohesiveness (McCave and Hall and references therein, 2006). In summary, clay mineralogy allows tracing of water mass volume and latitudinal extent, while the Fine/Coarse ratio reflects changes in the dynamic properties of deep water masses.

The speed of AABW or LCDW as recorded by the grain size diameter modes does not display obvious correlation with the Fine/Coarse ratio although this latter parameter is forced by the dynamic characteristics of deep water masses (figure 60 and 61). These data indicate that the speed of the LCDW slightly decreases while the speed of AABW is generally slow during the HE and the YD (figure 60). Consequently, the increased contribution of AABW compared with LCDW to the sedimentation at the studied site does not result from an increase of AABW speed. Moreover, as mineralogical results from the southern South Atlantic suggest that the AABW retreated toward the South slightly before the HS 1 (Beny et al., 2020), a latitudinal shift of the AABW cannot be responsible for the change observed during the HS 1. As a result, it is impossible to explain the enhanced export of AABW compared to LCDW at the studied site during the HS 1 (and during HS 2 and the YD by extrapolation), without involving the advection of particles from the AABW due to enhanced upwelling or turbulence at the AABW/LCDW interface. This interpretation is supported by ε_{Nd} data from the coarse grain size fraction that show incorporation of AABW-derived particles into the LCDW during HS 1 (Beny et al., 2020; figure 61c).

The major slow-down of the AABW indicated by a marked decrease of the size of the fine grain size mode during HS 1 (figure 60) is coeval with an significant increase of opal flux (Anderson et al., 2009), a proxy for the Southern Ocean upwelling (Figure 61b). This suggests a change in the mode of production of AABW. This change is likely due to the retreat of sea

ice (Bianchi and Gersonde, 2004; Menviel et al., 2014) resulting from enhanced poleward export of heat (Barker et al., 2009) that may have promoted changes in AABW speed.

Overall, the Fine/Coarse ratio record changes in the advection of particles transported by the AABW, and by implication, deep ocean mixing. In particular, high values of this ratio (Figure 61a) suggest that deep mixing was stronger during HS 2 than during the HS 1 and the YD. In addition, the synchronicity between the increased Southern Ocean overturning marked by grain size distribution and the onset of Heinrich Events supports the importance of inter-hemispheric seesaw processes (Barker et al., 2009) and questions the role of the southern sourced deep water as a driver of rapid climatic changes.

B. Does a perturbation of the Southern Ocean overturning triggered Heinrich Events?

In the Southern Ocean, the deep western boundary currents (DWBC) are responsible for an important part of the export of AABW toward the Pacific, the Atlantic and the Indian oceans (Hall et al., 2001; Orsi et al., 1999; Aoki et al., 2008; Fukamachi et al, 2010). Beny et al. (in prep. – Chapter 6) demonstrate increased advection of particles transported by the AABW (through the Kerguelen DWBC, a boundary current flowing northward along the eastern flank of the Kerguelen Plateau) during HS2, HS1 and the YD, reflecting enhanced southern overturning. Previous studies also reported an enhanced flow of AABW via DWBC during glacial time compared to interglacial (Pacific: Hall et al., 2001; Govin et al., 2009; Indian: Govin et al., 2009; Atlantic: Govin et al., 2009; Spooner et al., 2018), but the behavior of the Southern Ocean outflow during rapid climate change during the last deglaciation is currently poorly constrained.

Nevertheless, Beny et al., (in prep. – Chapter 6) provide evidence of enhanced DWBC flow during HS 2 and HS 1 in the South Indian sector of the Southern Ocean whereas Gottschalck et al., (2015a, 2018a) showed a major change in AMOC due to rapid southern incursions of NADW into the South Atlantic sector of the Southern Ocean during Dansgaard-Oeschger interstadials. Beny et al. (in prep. – Chapter 6) report that increased AABW outflow toward the South Indian Ocean occurs before Heinrich Events. This observation is similar to findings from Gutjhar and Lippold (2011) and Pahnke et al. (2008) who observed that AAIW incursions into the North Atlantic preceded HE 1 and 2 by ~1-2 kyr. As proposed by Gutjhar and Lippold (2011), these observations suggests that a change in the meridional overturning circulation coming from the Southern Hemisphere may be responsible, or even triggered the

HE 2. They argued that the input of relatively "warm" southern sourced water could favor or even trigger the melting of the Northern Hemisphere ice sheets by transferring heat toward the northern hemisphere. Similarly, Pahnke et al. (2008) proposed that the input of AAIW to the North Atlantic may have stimulated the collapse of North Atlantic convection. In addition, Ahn and Brook (2008) observed a 0-3 kyr lead of atmospheric CO_2 rise over HE, supporting the findings of Pahnke et al. (2008) and Gutjhar and Lippold (2011).

Previous studies also suggest that a perturbation of the meridional overturning circulation happened before the HE 1. Clay minerals (Beny et al. 2020; figure 61j) reveal that the AABW significantly migrates equatorward at around 20 ka. The ε_{Nd} of seawater from Pahnke et al., (2008) reveals an increased contribution of southern-sourced water in the Tobago Basin (i.e. AAIW and "AABW" – corresponding to AABW and CDW undifferentiated in the study) at ~19 ka concomitant with the last deglaciation (He et al., 2013). A second, substantive equatorward migration of AABW is observed in clay minerals from 18.3 to 18.0 ka (Beny et al, 2020) simultaneous with the increase of the ventilation of the Southern Ocean recorded by Skinner et al. (2010) in the same sediment core. Previous studies provided evidence of a slow-down of the AMOC due to reduced fresh water inputs from Northern Hemisphere ice sheets at 18 ka (Hall et al., 2006) while the Southern Ocean deep water circulation was reinvigorated (Bostock et al., 2013). All of these observations suggest that the AMOC, and particularly the Southern Ocean overturning, changed before Heinrich Event 1 (17.5 ka; Missiaen et al., 2019). The perturbation of the AMOC invoked by Guthjar and Lippold (2011) as the trigger of HE 2 may thus also be responsible for the onset of HE 1.

The cause(s) of this early perturbation of the AMOC is not clear, but enhanced northward export of southern-sourced waters appear a key factor. Clay minerals reveal an early migration of AABW in the South Atlantic from 20 ka with a marked peak at 19.7 ka, and a second, more substantive, maximum from 18.3 to 18.0 ka (Beny et al., 2020). Beny et al., (in prep. – Chapter 6; figure 61k) suggest that the enhanced equatorward export of AABW via DWBC east of the Kerguelen Plateau between 18.5 and 14.5 ka may result from increased production of AABW due to the activation of additional areas of bottom water formation off Wilkes Land. Pahnke et al., (2008) showed that AAIW production was reduced in the Pacific Ocean during the northward migration of the AAIW in the Atlantic that occurred before the HE 1 (from ~19 ka). They proposed that AAIW migration into the North Atlantic was probably due to reduced competition with a weakened NADW. Indeed, during the early stage of the deglaciation, this AAIW incursion at ~19 ka (Pahnke et al., 2008) occurs simultaneously with

increased fresh water discharge from European Rivers due to the melting of the European Ice Sheet (Ménot et al., 2006; figure 61l). Together with the meltwater supply from the Laurentide Ice Sheet (MWP1A-0), this freshwater discharge could be responsible for the weakening of the NADW in the North Atlantic at 19 ka (Toucanne et al., 2015). Similarly, the maximum of AABW excursion observed by Beny et al. (2020; figure 61j) at 18ka happened synchronously with the major freshwater discharge from European rivers (Ménot et al., 2006) and with a slowdown of the AMOC (Hall et al., 2006), highlighting the strong interconnection between Southern Ocean overturning and the North Atlantic climate.

In this context, we propose a "southern view" of the scenario initially proposed by Toucanne et al. (2015). The first observed change in ocean circultation happened at ~21 ka with a warming recorded by a drawdown of the quantity of polar foraminiferal species in core TN057-21, interpreted as an early phase of deglacial warming (Barker et al., 2009). Clay minerals reveal an early northward migration of AABW through the South Atlantic, associated to a reduced flow of the LCDW (Beny et al., 2020) at 19.7 ka. Both events indicate that modification of the Southern Ocean overturning precedes any change in the North Atlantic. It supports the proposal of Gutjhar and Lippold (2011) that the Southern Ocean overturning was responsible of the perturbation of the AMOC instead of being a consequence of it. These events are immediately followed by a small retraction of AABW to the south, a small increase of LCDW speed, and by freshwater discharge in the North Atlantic (MWP1A-0) due to the melting of the Northern Hemisphere ice sheet (Clark et al., 2009). This situation promoted slowdown of the AMOC (He et al., 2013; Toucanne et al., 2015) by reducing the production of NADW (Hemming et al., 2004; Robinson and Van de Flierdt, 2009). The reduced competition with the NADW (Pahnke et al., 2008) promoted the incursion of AAIW in the North Atlantic Ocean at 19.3 ka (Pahnke et al., 2008; Gutjahr and Lippold 2011) and a short cooling in the Southern Hemisphere that lasted until the beginning of the HS 1 (Barker et al., 2009). This succession of events supports the idea that heat was likely transported toward the northern hemisphere via the northward migration of southern source water (Panhke et al., 2008), thus exerting a positive feedback on the upcoming collapse of the northern hemisphere ice sheet. Between 18.3 ka and 18.0 ka, a substantive equatorward migration of AABW due to enhanced AABW production (Beny et al., 2020, in prep. – Chapter 6, figure 61j, 61k), is associated with a slowdown of the LCDW (figure 59) and a reduction of the CDW contribution (Beny et al., 2020). These perturbations of the Southern Ocean overturning are coeval to the freshwater supply from European ice sheets that coincides with the beginning of the HS 1 stadial conditions (Ménot et

al., 2006; Toucanne et al., 2015). At 17.5 ka, the southward retreat of the AABW (figure 61j) - due to a reduced production of AABW in the Weddell Sea (Beny et al., 2020) associated with an increased contribution of CDW in the South Atlantic (Beny et al., 2020) – is concomitant with the beginning of the recovery of the Southern Ocean upwelling (Anderson et al., 2009; figure 61b), with the southward migration of the Southern Hemisphere oceanic fronts and subsequent southern hemisphere warming (Barker et al., 2009; Barker and Diz, 2014), and associated atmospheric CO_2 rise (Bereiter et al., 2015; figure 61g). All these events, and in particular the southern sourced waters migration toward the North Atlantic may have exerted a positive feedback on the collapse of Northern Hemisphere ice sheet by transferring heat from below the northern hemisphere ice sheets, as suggested by Gutjahr and Lippold (2011). This collapse released huge amount of freshwater to the North Atlantic, shutting down the AMOC and NADW production (Hemming et al., 2004; Robinson and Van de Flierdt, 2009). These interconnected mechanisms likely amplified the phenomenon initiated by the freshwater discharge from European rivers (e.g. Channel River discharge) or by the southern hemisphere warming. These new findings strongly support the results from the numerical simulation of He et al. (2013), which suggested that the apparent lead of the Southern Hemisphere warming could reflect a bipolar seesaw phenomenon. At the beginning of the HE 1, reduced production of AABW in the Weddell sea associated with an increased contribution of CDW in the South Atlantic (Beny et al., 2020) favored heat transport toward the Southern Hemisphere while the Northern ACC fronts are pushed poleward (Barker et al., 2009). This event likely provoked an increase in wind pressure and wind driven upwelling (Anderson et al., 2009; figure 48b) while the enhanced turbulent mixing between AABW and LCDW recorded by our Fine/Coarse ratio, generated conditions favorable to the release of CO_2 to the atmosphere, with potential positive feedback on the deglaciation (Denton et al., 2010).

To conclude, our data suggest that enhanced Southern Ocean overturning started before and continued during Heinrich Events and could represent the trigger of these events. A small increased seasonality under dry and cold climate in the northern hemisphere (Toucanne et al., 2015) or an early warming in the southern hemisphere (Barker et al., 2009) was likely sufficient to trigger a series of mechanisms amplifying each other through positive feedbacks during the early stages of the deglaciation. An early change in AABW production preceded the northern hemisphere ice sheet melting during MVP1A-0 and HS 2, providing evidence of a seesaw response of the AMOC to southern ocean overturning changes. This new finding gives additional support to the observed rise in CO_2 and Southern Hemisphere temperatures that

preceded the melting of Northern Hemisphere ice sheets during Termination II (Broecker and Henderson, 1998).

C. Implication for atmospheric CO_2 variations

In this study, we give new insights on the major role of the Southern Ocean overturning in setting HS climate and AMOC perturbations. The equatorward transport of AABW due to enhanced mixing or/and production appear especially a major forcing mechanism during rapid climatic events of the last deglaciation (Beny et al., 2020 and in prep. – Chapter 6).

Previous studies proposed that interhemisphic and Pacific/Atlantic seesaw processes lead to enhanced production of AABW (referring in these studies and many others to the combination of AABW and CDW) and of North Pacific Deep Water while both AMOC and NADW experienced weak production, enabling the ventilation of the Southern Ocean and Pacific carbon pool (Menviel et al.,2014, 2015a,b; 2017). Our results clearly support these model outputs for HS 1 by providing evidence of stronger export of AABW in the South Atlantic as well as in the South Indian Ocean (Beny et al., in prep. – Chapter 6). In addition, the observed stronger exports of AABW predate any weakening of the AMOC and NADW production, suggesting that the perturbation caused by the change in AABW production was transferred to the North Atlantic via seesaw processes. Surprisingly, these exports are even stronger during HS 2 depsite HS 2 and HS 3 appearing to be muted in the atmospheric CO_2 signal (Ahn and Brook, 2008; Bereiter et al., 2015). Consequently, our data demonstrates that enhanced Southern Ocean upwelling alone is necessary but not sufficient to drive atmospheric CO_2 rise. Thus, the question arises as to why some HS, such as HS 2, are not associated to atmospheric CO_2 rise, even though enhanced vertical mixing is suggested in the Southern Ocean?

The rather different environmental conditions prevailing during HS2 and HS3 compared with HS1 are likely responsible for the contrasted atmospheric CO_2 response to deep southern ocean ventilation. Orbital forcing, and in particular obliquity may represent the explanation of the contrasting results. Ahn and Brook (2008) observed a poor correlation between ventilation proxies such as $\delta^{13}C$ (Iberian margin) and $\delta^{15}N$ (Chile margin), and the rate of change of atmospheric CO_2 between 19 and 37 ka, a period of low obliquity (Berger and Loutre, 1991). This observation suggest no apparent link between oceanic ventilation and atmospheric CO_2 during this interval of low oblitquity. During this time interval, Barker et al. (2010) also suggested that the amplitude of the oscillation between weak and strong modes of the AMOC was reduced compared to high obliquity intervals. In addition, stratified deep ocean formed

under minimum obliquity periods (at ~27 ka; Zhang et al., 2013; during MIS 4 and the LGM; Barker and Diz, 2014) reducing the strength of the AMOC and thus reduces its capacity to react to perturbation such as Heinrich Events (Zhang et al., 2013).

Obliquity could also have a strong impact on the position of climatic fronts. Fischer et al., (2010) demonstrated that the position of the Polar Front and its role on buoyancy fluxes are both crucial in glacial/deglacial CO_2 variations. Low obliquity is responsible of strong seasonal variations of the latitudinal position of the sub-tropical front during MIS 4 (Barker and Diz, 2014). Similar conditions were likely prevailing during the LGM, and may have had a strong impact on seasonal sea ice extension, and thus, on CO_2 storage/degassing (DeLille et al., 2014). In addition, the reduction of ocean atmosphere exchanges- preventing from CO_2 degassing - may have been stronger during HS 2 than during HS 1 due to extended sea ice cover during the LGM (Bianchi and Gersonde, 2004; Bostock et al., 2012; Adkins 2013).

In addition to orbital forcing, other processes may have contributed to the unexpected muted atmospheric CO_2 signal during HS 2. Increased ocean stratification due to strong salinity gradient between the AABW and NADW (often referred as Glacial North Atlantic Intermediate Water due to their shallow position during glacial time – i.e. above 2000 m; Adkins, 2013) is likely responsible of an important reduction of the exchange between deep ocean and the surface waters during the LGM (Watson and Naveira Garabato, 2006; Wolff et al., 2006; Adkins, 2013). In this context, this salinity gradient could “capped” the deep ocean, preventing exchanges between ventilated deep ocean and surface water during HS 2. This idea is supported by the absence of apparent change in the Southern Ocean opal flux during HS 2 (Anderson et al., 2009; figure 61b) indicating that the vertical mixing observed in our data does not affect the upper part of the ocean. Similarly, Burke and Robinson (2012) argued for ventilation within the deep ocean layers during the HS 2 while the upper ocean remained stratified.

The northward position of the westerly winds (Kohfeld et al., 2013) could alter the efficiency of wind driven Southern Ocean upwelling. Indeed, upwelling generally occurs during strong and poleward retracted westerly winds (Anderson et al., 2009; Denton et al., 2010; Fischer et al., 2010; Menviel et al. 2017). Thus, a more northly position of these winds during low obliquity intervals would prevent them from completing the full ventilation of the ocean. In other words, this driver would not be efficient enough under low obliquity conditions to enable the full ventilation of the Southern Ocean and the degassing of CO_2 to the atmosphere. This conclusion, taken together with the fact deep ventilation is observed when wind is not able to generate upwelling, questions the importance of winds as the driver of the Southern Ocean

upwelling. The active biological pump due to high iron fertilization caused by enhanced dust flux during the LGM (Watson et al., 2000; Wolf et al., 2006; Fischer et al., 2010; Martinez-Garcia et al., 2014) could have counterbalanced the CO_2 release by enhancing the storage of CO_2. Similarly, the tight link between Antarctic temperatures and atmospheric CO_2 (Broecker and Henderson, 1998; Siegenthaler et al., 2005; Ahn and Brook, 2008) suggests that a colder Southern Ocean was probably a better CO_2 trap due to enhanced CO_2 solubility during the LGM (Kohler and Fischer, 2006; Ahn and Brook, 2008; Fischer et al., 2010; Adkins et al., 2013).

To conclude, we suggest that background conditions (i.e. low amplitude between weak and strong AMOC modes, position of the Polar Front, sea ice extent, enhanced stratification due to the formation of saltier AABW, stratified ocean, northward position of the westerly winds, efficient biological pump, colder ocean being a better CO_2 trap) prevailing before HS 2 (and by extension HS 3) possibly driven by low obliquity likely explains the absence of CO_2 rise during this particular HS, even though our data clearly demonstrate deep mixing due to higher AABW production.

IV. Conclusion

Rapid climate variations associated with Heinrich Stadials in the southern south Atlantic (Core MD07-3076Q) as well as in the Kerguelen sector (core MD 12-3396Q) highlight that modifications of Southern Ocean conditions preceded climatic events HS1 and HS 2. Before the HS 1, changes in the Southern Ocean (i.e. warming and AABW equatorward expansion) are immediately followed by the increase of freshwater release from Northern Hemisphere ice sheets. This release would have slowed the production of NADW and enabled the incursion of southern source deep and intermediate waters to the North Atlantic. This incursion would be associated with the transfer of heat toward the northern hemisphere, exerting a positive feedback on the incoming melting of northern hemisphere ice sheets (i.e. HE 1). These changes were associated with a change in AABW production preceding the HE in both the Atlantic and the Kerguelen sector of the Southern Ocean (Beny et al., 2020, in prep. – Chapter 6). Consequently, this work support the model/hypothesis of Pahnke et al. (2008) and of Gutjhar and Lippold (2011) that the Southern Ocean overturning circulation could have triggered the HE.

In this study we demonstrated that: 1) major modifications of the dominant grain size mode are generated by changes in turbulent mixing at the AABW/LCDW interface, and; 2) the sediment fine-to-coarse mode ratio trace the turbulent mixing through time. The coarse grain

size mode is generally dominant, while the fine grain size mode becomes dominant during the YD, HE 1 and HE 2. Surprisingly, mixing in the Southern Atlantic sector appears to be stronger during HE 2 than HE 1, while the HE 2 is muted in the atmospheric CO_2 records. This information is supported by stronger AABW production during the HS 2 compared to HS 1 in the Kerguelen sector of the Southern Ocean. Consequently, we propose that even if deep ocean mixing occurred during the HS 2 as during HS 1, background conditions driven by the low obliquity prevailing during HS 2 (e.g. extended sea ice, ACC fronts located north, strong efficiency of the biological pump, …) likely prevented any large exchanges between the CO_2-rich deep ocean and the atmosphere. This conclusion strongly supports a physical and/or dynamic barrier preventing exchange between the deep ocean and the overlaying water masses during the LGM, and thus favored the storage of CO_2 into the deep ocean although strong AABW production is recorded in the Southern Atlantic and Kerguelen Sector of the Southern Ocean during HS 2.

Chapter 8. General conclusions and perspectives

I. Conclusions

This study allows to draw some major conclusions about sediment provenance, deep water-masses variations, Heinrich Event trigger, and about carbon cycle since the last glacial epoc. These major conclusions are presented below.

Composition of the potential sources of sediments:

In this PhD, the composition of the potential sources of sediment to the South Atlantic sector and of the Kerguelen Sector of the Southern Ocean has been widely investigated. The geology of the potential sources can be simplified according to their geological context: (1) old continental shields (including very old craton and old orogens, generally older than 1 Ga), and (2) modern orogens associated to important volcanic activity. The type (1) is represented by the African continent, East Antarctica, and the South American shield, while the type (2) is represented by the Andean Orogen, the Antarctic Peninsula, and the circumpolar volcanic islands (i.e. Scotia Arc, Kerguelen Plateau). The average composition of these areas and the way it can be impacted by climate conditions is illustrated on figure 62 (already shown in chapter 2)

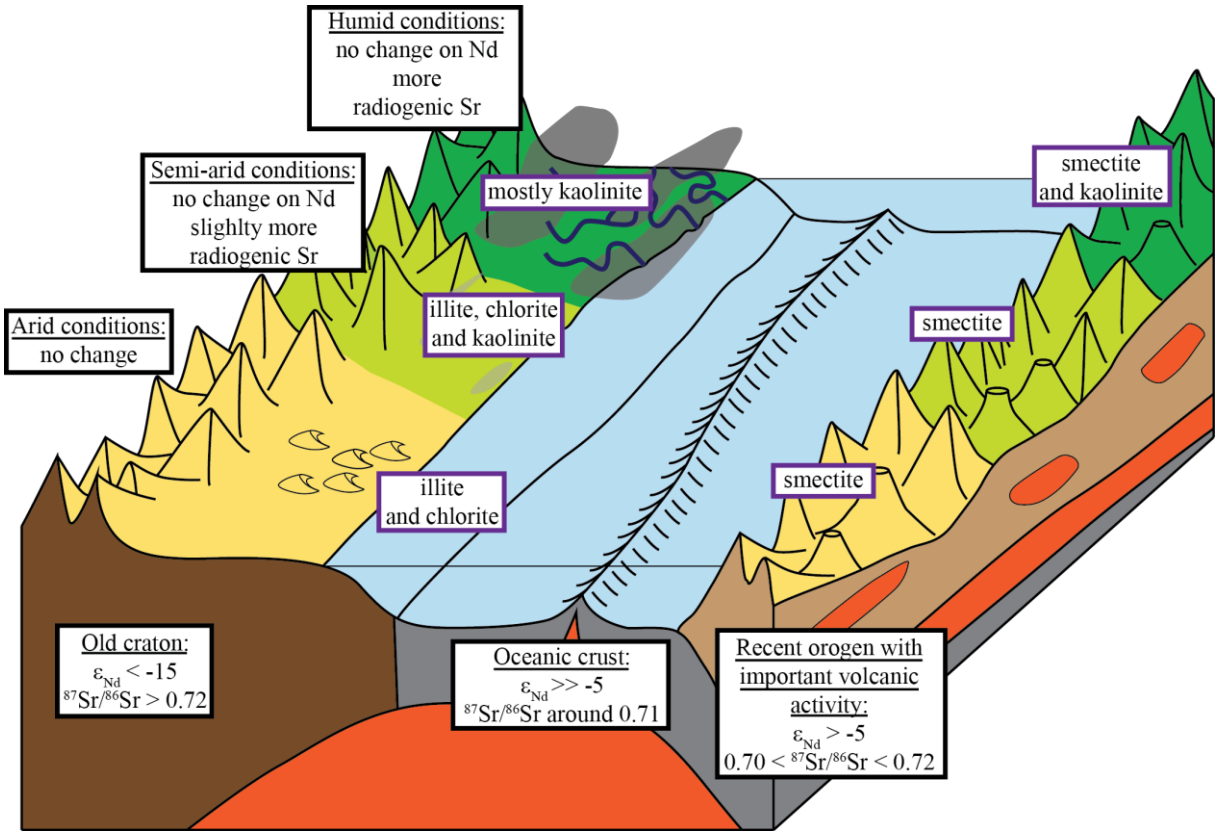

Figure 62: 3D bloc illustrating the isotopic and mineralogical composition of the potential sources of sediments (already shown in Chapter 2)

In this PhD, I also demonstrated that even if climate may affect sediment delivery to the ocean, it does not affect the composition of the sediments located East of the Kerguelen Plateau. By contrast, the composition of South Atlantic sediments is strongly influenced by moisture conditions over South America, especially during the Holocene. I evidenced that the provenance changes observed during the Holocene in the South Atlantic sediment can only result from climatic changes over South America without any significant modifications in the AMOC, except during the 8.2 ka event. I also pinpointed that moderately dry conditions associated to weak winds prevailed during the Late Holocene (11-9 ka). Enhancing dryness and increasing winds occurred thereafter until the Mid-Holocene (9-7 ka), while the NADW was probably weaker in response to the 8.2 ka event. The Mid-Holocene was the driest and the windiest interval, with the strongest winds observed between 6 and 4.5 ka. At the end of the Mid-Holocene (~5 ka), climatic conditions became significantly wetter and the wind strength decreased until the beginning of the Late Holocene (~3 ka). The period between 3 and 2.2 ka was probably the wettest of the Holocene, and was followed by a marked decrease of rainfalls to the end of our record.

Determination of the composition of the specific particles transported by distinct deep-water masses:

An extensive comprehension of continent-ocean transfers associated to a good knowledge of the main water mass pathways enabled to constrain the composition of sediments transported by each deep-water mass. The mineralogical and isotopic composition of these sediments is represented on figure 63 for the South Atlantic sector of the Southern Ocean. In particular, determining the isotopic signatures of different grain-size modes provide clues on understanding the evolution of the main deep-water masses (AABW and LCDW) through time. In the Kerguelen sector, the estimation is easy, as shown on figure 64, since the hydrographical conditions are simple: the ACC transport sediments deriving from the Kerguelen Plateau whereas the AABW transport sediments originating from East Antarctica.

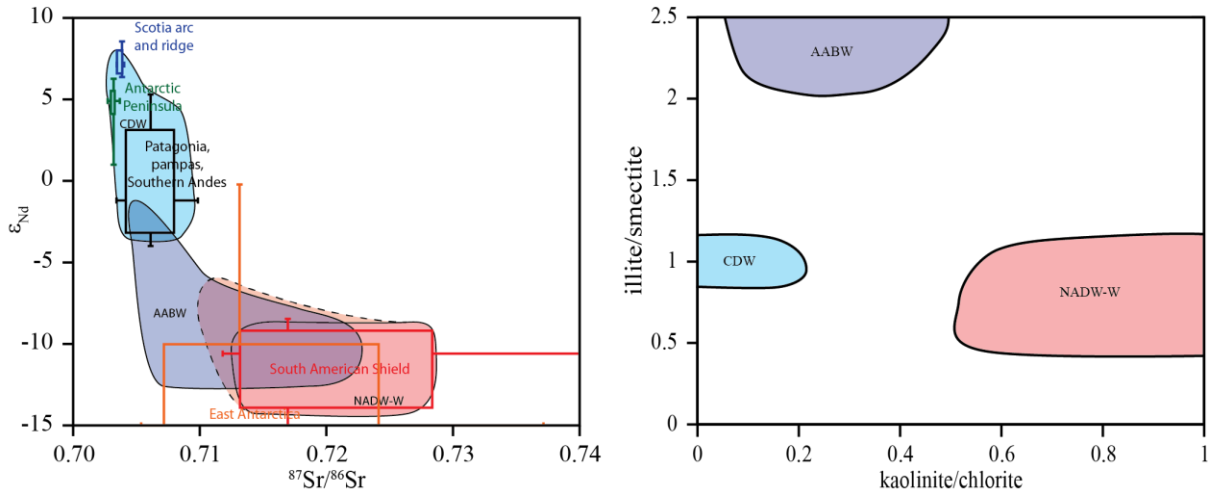

Figure 63: Composition of the sediment transported by deep-water masses in the South Atlantic sector of the Southern Ocean.

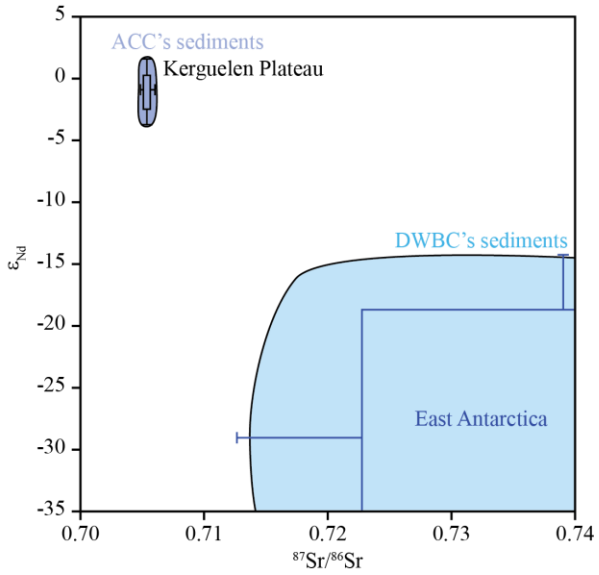

Figure 64: Isotopic composition of the sediment transported by water masses in the Kerguelen sector of the Southern Ocean.

Evolution of the relative contribution of deep-water masses to sedimentation through time:

These estimations allow comparing the relative contribution of each deep-water mass to sedimentation through time. Our method enabled the distinction between the AABW and the CDW, which was not possible using "classical" deep-water mass proxies. Thus, it was possible to estimate the proportion of material delivered by each deep-water mass through time (figure 63), and by extension, the latitudinal modifications of these water masses thoughout the last deglaciation. Overall, our results in the South Atlantic sector support the idea that southern

sourced were stronger during the LGM compared to the Holocene while the NADW was retreated North (see figure 65). In details, our results provide evidence of highly expanded AABW at the end of the LGM (between 20 and 17.5 ka). Then the AABW retreated rapidly due to modifications associated to HS. During the HS 1, the isotopic composition of LCDW sediments suggests that particles transported by the AABW were added to the LCDW suspended load by mixing. During the Bølling-Allerød, the isotopic composition of the clay size fraction as well as the clay mineralogy suggest an increased contribution of the NADW compared to southern born deep-water masse, likely due to the incursion of the NADW into the Southern Ocean and to the deepening of the AMOC at that time.

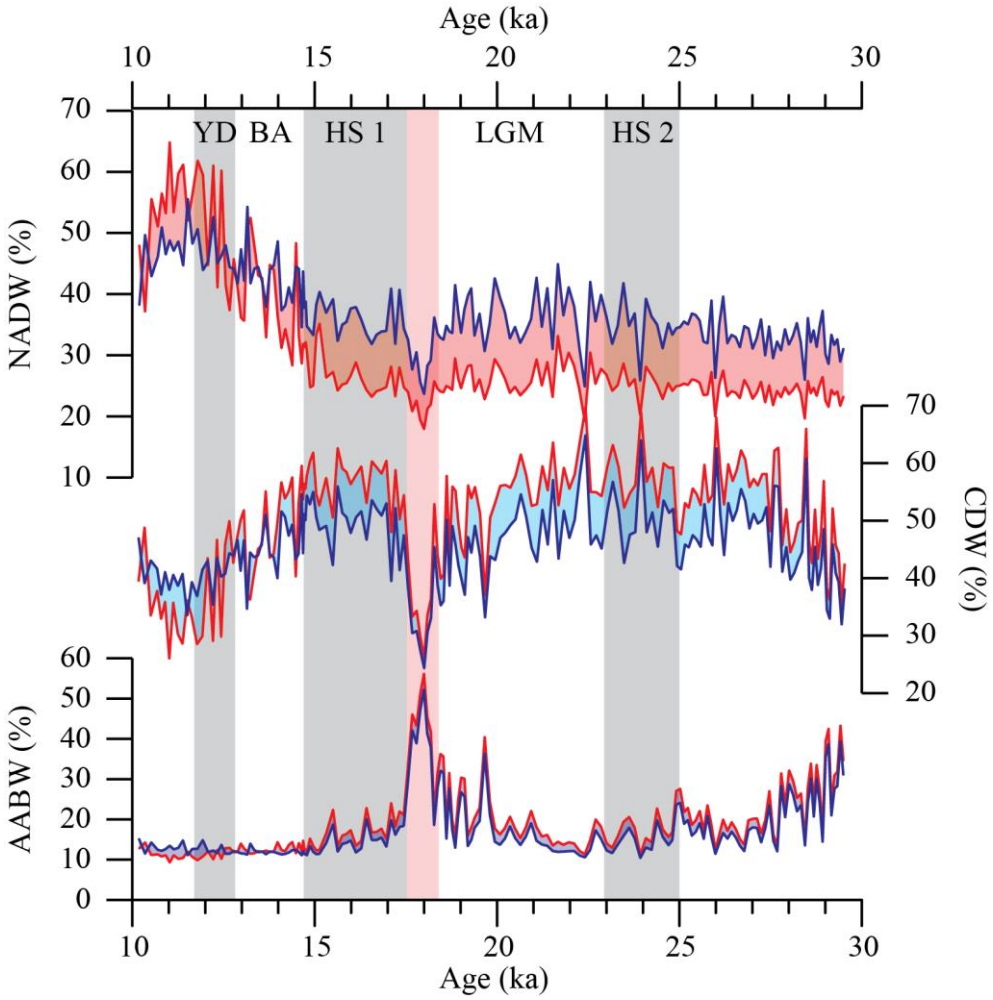

Figure 65: Relative contribution of the deep-water masses at site MD07-3076Q.

In the Kerguelen sector, little provenance changes are associated to the deglaciation. Instead, important provenance changes occurred during and before HS 1, 2, and 3. These provenance changes indicate an increased contribution of the DWBC (a branch of AABW) and suggest that enhanced production of AABW may cause a northward migration of this water

mass during HS 1, HS 2, and HS 3. In addition, mixing calculations show that the contribution of the DWBC to sedimentation is more important than previously thought and that it may have delivered up to 40% of the terrigenous sediment.

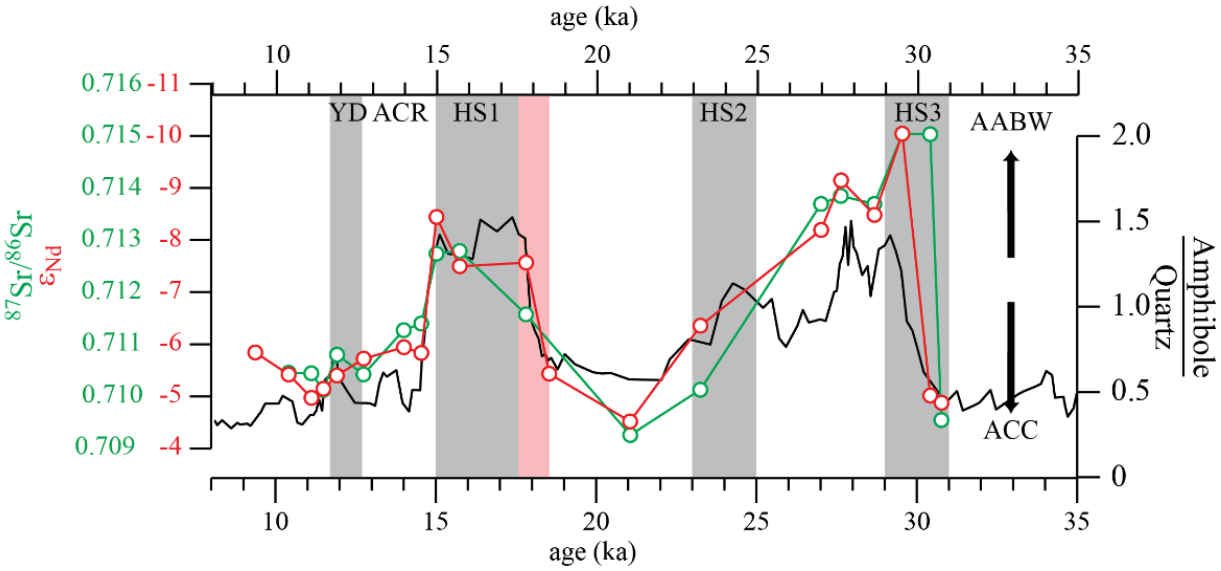

Figure 66: Provenance changes in core MD12-3396Q showing changes of contribution of deep-water masses to sedimentation.

Evolution of deep-water velocity through time:

The use of grain-size distribution, and in particular of grain-size modes enabled the reconstruction of past variations of the oceanic currents flow speed. In the South Atlantic sector, the analysis of the isotopic composition of the two grain-size modes highlighted that these two modes are respectively carried by the AABW (fine grain-size mode) and by the LCDW (coarse grain-size mode). Our results indicate that the AABW speed was: 1) maxima during the end of the LGM (especially between 20 and 17.5 ka, when the AABW extent was important); 2) low during Heinrich Stadials, when the AMOC is shut down, and 3) minimum between the middle of the HS 1 (~16 ka) and the end of the Younger Dryas. The LCDW speed presents a plateau during the LGM until the end of the HS 1. This plateau is punctuated by intervals of higher speed (22-21 ka; 19.5-19 ka; 17.6-17 ka) - the latter being the most significant one - slightly preceding the contraction of the AABW at 17.5 ka. From the onset of the Bølling-Allerød to the end of the record, the LCDW speed is slowly decreasing.

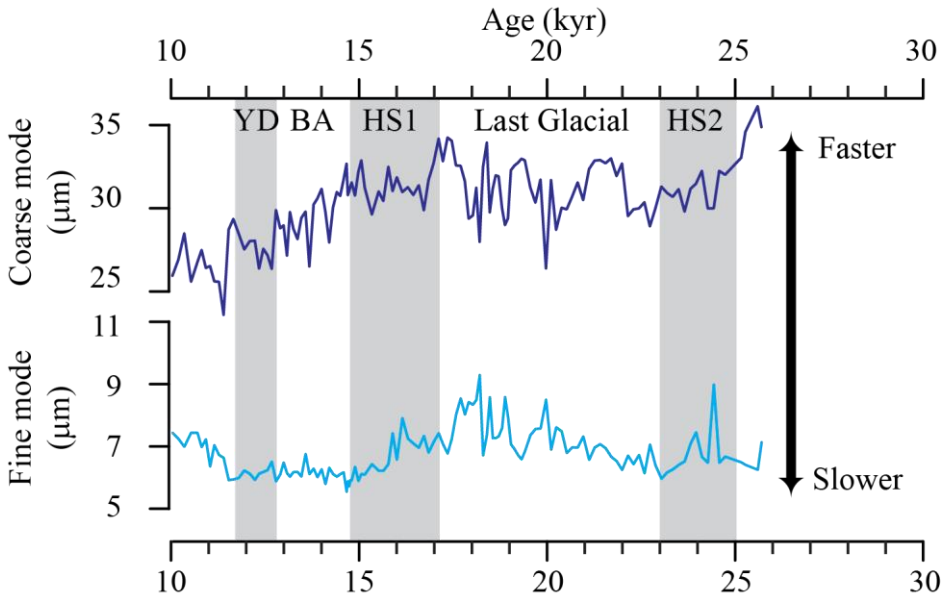

Figure 67: *Size of grain-size modes from site MD07-3076Q indicating speed changes of LCDW (coarse mode) and of AABW (fine mode) in the South Atlantic sector of the Southern Ocean.*

In the Kerguelen Sector, similar observations has been made, but are not presented in this PhD, since these data will appear in a collaborative paper in preparation with Alain Mazaud (first author) and Elisabeth Michel from LSCE (*Laboratoire des Sciences du Climat et de l'Environnement*).

Timing and trigger of the Heinrich Events:

Finally, a careful look at the timing of fast variations associated with Heinrich Stadial (in the Kerguelen sector as well as in the Atlantic sector) shows that modifications of the Southern Ocean preceded the onset of HE 1, 2, and 3 as defined in the northern hemisphere. In addition, our data indicate that Southern Ocean modifications probably favoured the penetration of relatively "warm" southern born water masses into the North Atlantic Ocean, and hence played a major role in the Heinrich Event 1. As a result, I proposed a scenario in which, before the HS 1, an early perturbation in the Southern Ocean (i.e. warming and AABW equatorward expansion) was rapidly transmitted to the North Atlantic and are immediately followed by the increase of fresh water release into the North Atlantic. This early release of fresh water and the associated reduction of NADW production in the North Atlantic would have favoured the penetration of relatively "warm" southern born waters. This incursion would be associated with the transfer of heat toward the northern hemisphere, exerting a positive feedback on the incoming melting of northern hemisphere ice sheets (i.e. HE 1). These changes were associated

with a change in AABW production preceding the HE in both the Atlantic and the Kerguelen sector of the Southern Ocean (Beny et al., 2020, in prep. – Chapter 6). Consequently, this work support the model/hypothesis of Pahnke et al. (2008) and of Gutjhar and Lippold (2011) that the Southern Ocean overturning circulation could have triggered the HE 1, and by extension, HE 2 and 3.

Fast oceanographic changes during the Heinrich Stadials and their implication on carbon cycle:

This study evidenced that the dominant grain-size mode varies through time in the South Atlantic sector. In general, the coarse mode – reflecting the transport by the LCDW – is the "dominant" mode. However, during the YD, and the HE 1 and 2, the fine mode – reflecting transport by the AABW – becomes "dominant". The coarse-to-fine ratio exhibits brutal shifts at both the onset and the offset of Heinrich Events. Such shifts reflect vertical mixing between AABW and LCDW, giving some support to the idea of enhanced upwelling during HE 1 and the YD enabling CO_2 outgassing. However, this ratio displays higher variations during HS 2 than during HE 1 while no atmospheric CO_2 rise occurred during HS 2. Contrasted observations during HS 1, 2, and 3 are also found in the Kerguelen sector where the DWBC displays a higher northward extension during HS 3 than during HS 1. Consequently, deep mixing may have occurred during the HS 2 and 3 whereas ventilation between the deep and surface ocean was inhibited. In order to reconciliate these contrasted obesrvations, I proposed that the low obliquity prevailing at that time was responsible for specific background conditions (e.g. extended sea ice, ACC fronts located north, strong efficiency of the biological pump, etc.) that may have favoured the existence of a physical/dynamical barrier between deep and surface oceanic compartments. Such barrier would have disabled the exchanges between the CO_2-rich deep ocean and the atmosphere during the last glacial period, even though mixing occurred during HS 2 and HS 3 within the deep compartment. Finally, our data suggest the occurrence of a massive AABW northward excursion ~1 kyr before the HS 1. This excursion is associated with a first increase of the ventilation in the South Atlantic Ocean although "classical" deep-water proxies do not evidence any major change in the NADW/southern born water masses ratio. This massive AABW excursion preceeding the HS 1 could be responsible for the breakdown of the physical/dynamical barrier between the deep and surface ocean and thus enabled the interaction of upwelled CO_2-rich water masses with the atmosphere.

II. Perspectives

This PhD work demonstrated the utility of working on distinct grain-size fractions and in particular on grain-size modes when studying oceanic currents. As a result, it would be interesting to test this methods and this set of data (radiogenic isotopes, clay minerals, grain-size distribution) in other areas. The most evident one is the Pacific sector of the Southern Ocean. This sector is less studied, and the composition of the sediment transported by deep-water masses in the area is poorly known. The information coming from the study of terrigenous sediment in the area is then likely to give new insights on the evolution of the Pacific Ocean overturning, and on its role the global carbon cycle and atmospheric CO_2 variations. In addition, data from this area would fill some gaps unravelled during my PhD and will enable robust interpretations applicable to the whole Southern Ocean as well as potential inter-oceanic seesaw processes.

During this PhD work, I had the opportunity to sail on the expedition IODP 374 in the Ross Sea and to recover samples from this area. The ideas behind this project are: 1) to use the method developed during my PhD in new areas where ice plays a major role, and 2) to try distinguishing the terrigenous signal derived from the ice sheets from the signal derived from the oceanic currents during the deglaciation. For the same reason, it could be interesting to test this method in the North Atlantic to check if any link with the South Atlantic can be drawn, and to check if interhemispheric seesaw processes can be observed in the terrigenous sediments.

This method could also be tested for shallower sites where few grain-size modes have been identified in order to catch a grain-size mode transported by UCDW, NADW, or even AAIW. Such a work could be useful to precise the composition of the sediment transported by these water masses. In addition, testing this method at a site close to the boundary between NADW with one other deep-water masse could be useful to track the variation of NADW depth during the Heinrich Stadial and during the Bølling Allerød, when important variations of the NADW depth and strength has been identified.

In this PhD, I highlighted that a lot of changes of AABW punctuated the Heinrich Stadials. Few studies focused on glacial/deglacial changes of AABW by measuring sortable silts within DWBC in several sector of the Southern Ocean, and no grain-size distribution analyses focused on the change of AABW during HS. As a result, it could be interesting to measure the grain-size distributions of core located within DWBC in all sector of the Southern Ocean to estimate the variations of AABW's speed during these short intervals. Similarly, using

a method similar to the study of Spooner et al., (2018; applied at glacial/interglacial resolution only) at high resolution during Heinrich Stadials could also give additional information on the evolution of AABW characteristics through time.

Performing additional analyses on the sites studied during my PhD could also be of interest. First, it could be useful to increase the sampling resolution of some records. In particular, technical issues are responsible for a low resolution in the isotopic composition of neodymium in the coarse grain-size modes in core MD07-3076Q during the LGM. In addition, the onset of the deglaciation shift is poorly constrained, and no sample is recording the HS 2. For similar reasons, there is no Pb isotopic data in the Atlantic sector of the Southern Ocean although these data will help to constrain the provenance change in the sediment core. Due to the lack of time, the Nd and Sr isotopes have only been measured on targeted samples from the core MD12-3396Q in the Kerguelen sector. Consequently, it would be interesting to increase the resolution, and to explore the isotopic composition of the Holocene sediments.

Similarly, due to the lack of time, no isotopic analyses has been performed on site MD12-3401Q. Consequently, it could be interesting to measure a few samples during targeted periods to check the potential arrival of sediment from Antarctica. If these preliminary results are promising, then more samples could be analysed, and it would be interesting to compare these results with core MD12-3396Q.

On the opposite, it is probably useless to carry out isotopic measurement on the grain-size modes from the Kerguelen sector of the Southern Ocean. Indeed, these grain-size modes are both transported by the ACC from the Kerguelen Plateau. Consequently, there is almost no chance to observe any variation of their isotopic composition through time. Similarly, the Pb isotopes in this sector appear unnecessary: the Nd and the Sr isotopes already clearly constrain the provenance changes in the area, and the information that could be added by Pb isotopes will face the lack of data (to not say the absence) on the isotopic composition of Pb of Antarctica.

Finally, this PhD give insights on the specificities of the HS 2 and 3 (i.e. deep mixing without atmospheric CO_2 rise, Southern Ocean overturning reacting before the HE 2). In several aspects, HS 2 is similar to HS 3, as shown in core MD12-3396Q. Consequently, it would give valuable information to deeply explore this period with the same tools to confirm/refute deep mixing during this interval.

Abbreviations

AABW: AntArctic Bottom Water

AAIW: AntArctic Intermediate Water

ACC: Antarctic Circumpolar Current

ACR: Antarctic Cold Reversal

AMOC: Atlantic Merdional Overturning Circulation

ASC: Antarctic Slope Current

B/A and B-A: Bølling Allerød

CDW: Circumpolar Deep Water

CHUR: CHondrite Uniform Reservoir

DWBC: Deep Western Boundary Current

HE: Heinrich Event

HFSE: High Field Strenght Elements

HREE: Heavy Rare Earth Element

HS: Heinrich Stadial

ITCZ: InterTropical Convergence Zone

LCDW: Lower Circumpolar Deep Water

LGM: Last Glacial Maximum

LILE: Large Ion Lithophile Elements

LREE: Light Rare Earth Element

MIS: Marine Isotopic Stage

MRFE: Mantle Rock Forming Elements

MAR: Mid-Atlantic Ridge

NADW: North Atlantic Deep Water

NASC: North American Shale Composite

PAAS: Post Archaean Australian Shales

PF: Polar Front

REE: Rare Earth Element

SACZ: South Atlantic Convergence Zone

SAF: Sub-Antarctic Front

SAMS: South American Monsoon System

SEM: Scanning Electron Microscope

STF: SubTropical Front

SWWB: South Westerly Wind Belt

UCDW: Upper Circumpolar Deep Water

UCC: Upper Continental Crust

WRAS: World River Average Silts

YD: Younger Dryas

References

Adkins, J.F., 2013. The role of deep ocean circulation in setting glacial climates. Paleoceanography 28, 539–561. https://doi.org/10.1002/palo.20046, 2013

Ahn, J., Brook, E.J., 2008. Atmospheric CO2 and Climate on Millennial Time Scales During the Last Glacial Period. Science 322, 83. https://doi.org/10.1126/science.1160832

Allègre, C.J., Dupré, B., Négrel, P., Gaillardet, J., 1996. Sr-Nd-Pb isotope systematics in Amazon and Congo River systems: constraints about erosion processes. Chemical Geology 131, 93–112. https://doi.org/10.1016/0009-2541(96)00028-9

Allen, B.L., Hajek, B.F., 2018. Mineral Occurrence in Soil Environments, in: Minerals in Soil Environments. John Wiley & Sons, Ltd, pp. 199–278. https://doi.org/10.2136/sssabookser1.2ed.c5

Alley, R.B., Mayewski, P.A., Sowers, T., Stuiver, M., Taylor, K.C., Clark, P.U., 1997. Holocene climatic instability: A prominent, widespread event 8200 yr ago. Geology 25, 483–486. https://doi.org/10.1130/0091-7613(1997)025<0483:HCIAPW>2.3.CO;2

An, Z., Porter, S.C., Kutzbach, J.E., Xihao, W., Suming, W., Xiaodong, L., Xiaoqiang, L., Weijian, Z., 2000. Asynchronous Holocene optimum of the East Asian monsoon. Quaternary Science Reviews 19, 743–762. https://doi.org/10.1016/S0277-3791(99)00031-1

Andersen, K.K., Azuma, N., Barnola, J.-M., Bigler, M., Biscaye, P., Caillon, N., Chappellaz, J., Clausen, H.B., Dahl-Jensen, D., Fischer, H., Flückiger, J., Fritzsche, D., Fujii, Y., Goto-Azuma, K., Grønvold, K., Gundestrup, N.S., Hansson, M., Huber, C., Hvidberg, C.S., Johnsen, S.J., Jonsell, U., Jouzel, J., Kipfstuhl, S., Landais, A., Leuenberger, M., Lorrain, R., Masson-Delmotte, V., Miller, H., Motoyama, H., Narita, H., Popp, T., Rasmussen, S.O., Raynaud, D., Rothlisberger, R., Ruth, U., Samyn, D., Schwander, J., Shoji, H., Siggard-Andersen, M.-L., Steffensen, J.P., Stocker, T., Sveinbjörnsdóttir, A.E., Svensson, A., Takata, M., Tison, J.-L., Thorsteinsson, Th., Watanabe, O., Wilhelms, F., White, J.W.C., North Greenland Ice Core Project members, 2004. High-resolution record of Northern Hemisphere climate extending into the last interglacial period. Nature 431, 147–151. https://doi.org/10.1038/nature02805

Anderson, J.J., 1965. Bedrock geology of Antarctica: A summary of exploration, 1831–1962. Geology and Paleontology of the Antarctic 6, 1–70. https://doi.org/10.1029/AR006p0001

Anderson, R.F., Ali, S., Bradtmiller, L.I., Nielsen, S.H.H., Fleisher, M.Q., Anderson, B.E., Burckle, L.H., 2009. Wind-Driven Upwelling in the Southern Ocean and the Deglacial Rise in Atmospheric CO2. Science 323, 1443. https://doi.org/10.1126/science.1167441

Andersson, P.S., Dahlqvist, R., Ingri, J., Gustafsson, Ö., 2001. The isotopic composition of Nd in a boreal river: a reflection of selective weathering and colloidal transport. Geochimica et Cosmochimica Acta 65, 521–527. https://doi.org/10.1016/S0016-7037(00)00535-4

Anhuf, D., Ledru, M.-P., Behling, H., Da Cruz, F.W., Cordeiro, R.C., Van der Hammen, T., Karmann, I., Marengo, J.A., De Oliveira, P.E., Pessenda, L., Siffedine, A., Albuquerque, A.L., Da Silva Dias, P.L., 2006. Paleo-environmental change in Amazonian and African rainforest during the LGM. Palaeogeography, Palaeoclimatology, Palaeoecology 239, 510–527. https://doi.org/10.1016/j.palaeo.2006.01.017

Aoki, S., Fujii, N., Ushio, S., Yoshikawa, Y., Watanabe, S., Mizuta, G., Fukamachi, Y., Wakatsuchi, M., 2008. Deep western boundary current and southern frontal systems of the Antarctic Circumpolar Current southeast of the Kerguelen Plateau. Journal of Geophysical Research: Oceans 113. https://doi.org/10.1029/2007JC004627

Ayliffe, L.K., Marianelli, P.C., Moriarty, K.C., Wells, R.T., McCulloch, M.T., Mortimer, G.E., Hellstrom, J.C., 1998. 500 ka precipitation record from southeastern Australia: Evidence for interglacial relative aridity. Geology 26, 147–150. https://doi.org/10.1130/0091-7613(1998)026<0147:KPRFSA>2.3.CO;2

Baker, P.A., Fritz, S.C., Garland, J., Ekdahl, E., 2005. Holocene hydrologic variation at Lake Titicaca, Bolivia/Peru, and its relationship to North Atlantic climate variation. Journal of Quaternary Science 20, 655–662. https://doi.org/10.1002/jqs.987

Bareille, G., Grousset, F.E., Labracherie, M., Labeyrie, L.D., Petit, J.-R., 1994. Origin of detrital fluxes in the southeast Indian Ocean during the last climatic cycles. Paleoceanography 9, 799–819. https://doi.org/10.1029/94PA01946

Barker, S., Diz, P., 2014. Timing of the descent into the last Ice Age determined by the bipolar seesaw. Paleoceanography 29, 489–507. https://doi.org/10.1002/2014PA002623

Barker, S., Diz, P., Vautravers, M.J., Pike, J., Knorr, G., Hall, I.R., Broecker, W.S., 2009. Interhemispheric Atlantic seesaw response during the last deglaciation. Nature 457, 1097. https://doi.org/10.1038/nature07770

Barker, S., Knorr, G., Edwards, R.L., Parrenin, F., Putnam, A.E., Skinner, L.C., Wolff, E., Ziegler, M., 2011. 800,000 Years of Abrupt Climate Variability. Science 334, 347. https://doi.org/10.1126/science.1203580

Barker, S., Knorr, G., Vautravers, M.J., Diz, P., Skinner, L.C., 2010. Extreme deepening of the Atlantic overturning circulation during deglaciation. Nature Geoscience 3, 567. https://doi.org/10.1038/ngeo921

Barreiro, B., 1983. Lead isotopic compositions of South Sandwich Island volcanic rocks and their bearing on magmagenesis in intra-oceanic island arcs. Geochimica et Cosmochimica Acta 47, 817–822. https://doi.org/10.1016/0016-7037(83)90115-1

Barrett, P.J., 1991. The Devonian to Jurassic Beacon Supergroup of the Transantarctic Mountains and correlatives in other parts of Antarctica, in: The Geology of Antarctica. pp. 120–152.

Barros, A.M., Silva, R.D., Cardoso, O.R.F.A., Freire, F.A., Souza Junior, J.J., Rivetti, M., Luz, D.S., Palmeira, R.C.B., Tassinari, C.C.G., 1982. Geologia, BRASIL. Ministério das Minas e Energia. Projeto RADAMBRASIL Folha SD.

Basile, I., Grousset, F.E., Revel, M., Petit, J.R., Biscaye, P.E., Barkov, N.I., 1997. Patagonian origin of glacial dust deposited in East Antarctica (Vostok and Dome C) during glacial stages 2, 4 and 6. Earth and Planetary Science Letters 146, 573–589. https://doi.org/10.1016/S0012-821X(96)00255-5

Bayon, G., Burton, K.W., Soulet, G., Vigier, N., Dennielou, B., Etoubleau, J., Ponzevera, E., German, C.R., Nesbitt, R.W., 2009. Hf and Nd isotopes in marine sediments: Constraints on global silicate weathering. Earth and Planetary Science Letters 277, 318–326. https://doi.org/10.1016/j.epsl.2008.10.028

Bayon, G., Skonieczny, C., Delvigne, C., Toucanne, S., Bermell, S., Ponzevera, E., André, L., 2016. Environmental Hf–Nd isotopic decoupling in World river clays. Earth and Planetary Science Letters 438, 25–36. https://doi.org/10.1016/j.epsl.2016.01.010

Bayon, G., Toucanne, S., Skonieczny, C., André, L., Bermell, S., Cheron, S., Dennielou, B., Etoubleau, J., Freslon, N., Gauchery, T., Germain, Y., Jorry, S.J., Ménot, G., Monin, L., Ponzevera, E., Rouget, M.-L., Tachikawa, K., Barrat, J.A., 2015. Rare earth elements and neodymium isotopes in world river sediments revisited. Geochimica et Cosmochimica Acta 170, 17–38. https://doi.org/10.1016/j.gca.2015.08.001

Behling, H., Bauermann, S.G., Pereira Neves, P.C., 2001. Holocene environmental changes in the São Francisco de Paula region, southern Brazil. Journal of South American Earth Sciences 14, 631–639. https://doi.org/10.1016/S0895-9811(01)00040-2

Beny, F., Bout-Roumazeilles, V., Davies, G.R., Waelbroeck, C., Bory, A., Tribovillard, N., Delattre, M., Abraham, R., 2020a. Radiogenic isotopic and clay mineralogical signatures of terrigenous particles as water-mass tracers: New insights into South Atlantic deep circulation during the last termination. Quaternary Science Reviews 228, 106089. https://doi.org/10.1016/j.quascirev.2019.106089

Beny, F., Bout-Roumazeilles, V., Davies, G.R., Waelbroeck, C., Bory, A., Tribovillard, N., Delattre, M., Abraham, R., 2020b. Radiogenic isotopic and clay mineralogical signatures of terrigenous particles as water-mass tracers: New insights into South Atlantic deep circulation during the last termination. Quaternary Science Reviews 228, 106089. https://doi.org/10.1016/j.quascirev.2019.106089

Beny, F., Toucanne, S., Skonieczny, C., Bayon, G., Ziegler, M., 2018. Geochemical provenance of sediments from the northern East China Sea document a gradual migration of the Asian Monsoon belt over the past 400,000 years. Quaternary Science Reviews 190, 161–175. https://doi.org/10.1016/j.quascirev.2018.04.032

Bereiter, B., Eggleston, S., Schmitt, J., Nehrbass-Ahles, C., Stocker, T.F., Fischer, H., Kipfstuhl, S., Chappellaz, J., 2015. Revision of the EPICA Dome C CO2 record from 800 to 600 kyr before present. Geophysical Research Letters 42, 542–549. https://doi.org/10.1002/2014GL061957

Berger, A., Loutre, M.F., 1991. Insolation values for the climate of the last 10 million years. Quaternary Science Reviews 10, 297–317. https://doi.org/10.1016/0277-3791(91)90033-Q

Bianchi, C., Gersonde, R., 2004. Climate evolution at the last deglaciation: the role of the Southern Ocean. Earth and Planetary Science Letters 228, 407–424. https://doi.org/10.1016/j.epsl.2004.10.003

Bindoff, N.L., Rosenberg, M.A., Warner, M.J., 2000. On the circulation and water masses over the Antarctic continental slope and rise between 80 and 150°E. Deep Sea Research Part II: Topical Studies in Oceanography 47, 2299–2326. https://doi.org/10.1016/S0967-0645(00)00038-2

Björck, S., Rundgren, M., Ljung, K., Unkel, I., Wallin, Å., 2012. Multi-proxy analyses of a peat bog on Isla de los Estados, easternmost Tierra del Fuego: a unique record of the variable Southern Hemisphere Westerlies since the last deglaciation. Quaternary Science Reviews 42, 1–14. https://doi.org/10.1016/j.quascirev.2012.03.015

Black, L.P., Harley, S.L., Sun, S.S., McCulloch, M.T., 1987. The Rayner Complex of East Antarctica: complex isotopic systematics within a Proterozoic mobile belt. Journal of Metamorphic Geology 5, 1–26. https://doi.org/10.1111/j.1525-1314.1987.tb00366.x

Boger, S.D., Maas, R., Fanning, C.M., 2008. Isotopic and geochemical constraints on the age and origin of granitoids from the central Mawson Escarpment, southern Prince Charles Mountains, East Antarctica. Contrib Mineral Petrol 155, 379–400. https://doi.org/10.1007/s00410-007-0249-x

Bond, G., Kromer, B., Beer, J., Muscheler, R., Evans, M.N., Showers, W., Hoffmann, S., Lotti-Bond, R., Hajdas, I., Bonani, G., 2001. Persistent Solar Influence on North Atlantic Climate During the Holocene. Science 294, 2130. https://doi.org/10.1126/science.1065680

Bond, G.C., Lotti, R., 1995. Iceberg Discharges into the North Atlantic on Millennial Time Scales During the Last Glaciation. Science 267, 1005. https://doi.org/10.1126/science.267.5200.1005

Borchers, A., Voigt, I., Kuhn, G., Diekmann, B., 2011. Mineralogy of glaciomarine sediments from the Prydz Bay–Kerguelen region: relation to modern depositional environments. Antarctic Science 23, 164–179. https://doi.org/10.1017/S0954102010000830

Born, A., Levermann, A., 2010. The 8.2 ka event: Abrupt transition of the subpolar gyre toward a modern North Atlantic circulation. Geochemistry, Geophysics, Geosystems 11. https://doi.org/10.1029/2009GC003024

Bostock, H.C., Barrows, T.T., Carter, L., Chase, Z., Cortese, G., Dunbar, G.B., Ellwood, M., Hayward, B., Howard, W., Neil, H.L., Noble, T.L., Mackintosh, A., Moss, P.T., Moy, A.D., White, D., Williams, M.J.M., Armand, L.K., 2013. A review of the Australian–New Zealand sector of the Southern Ocean over the last 30 ka (Aus-INTIMATE project). Quaternary Science Reviews 74, 35–57. https://doi.org/10.1016/j.quascirev.2012.07.018

Bouttes, N., Paillard, D., Roche, D.M., Waelbroeck, C., Kageyama, M., Lourantou, A., Michel, E., Bopp, L., 2012. Impact of oceanic processes on the carbon cycle during the last termination. Climate of the Past 8, 149–170. https://doi.org/10.5194/CP-8-149-2012

Bremner, J.M., Willis, J.P., 1993. Mineralogy and geochemistry of the clay fraction of sediments from the Namibian continental margin and the adjacent hinterland. Marine Geology 115, 85–116. https://doi.org/10.1016/0025-3227(93)90076-8

Broecker, W.S., Henderson, G.M., 1998. The sequence of events surrounding Termination II and their implications for the cause of glacial-interglacial CO2 changes. Paleoceanography 13, 352–364. https://doi.org/10.1029/98PA00920

Brown, G., 1980. X-ray diffraction procedures for clay mineral identification. Crystal structures of clay minerals and their X-ray identification 305–359.

Burke, A., Robinson, L.F., 2012. The Southern Ocean's Role in Carbon Exchange During the Last Deglaciation. Science 335, 557–561. https://doi.org/10.1126/science.1208163

Cagliari, J., Lavina, E.L.C., Philipp, R.P., Tognoli, F.M.W., Basei, M.A.S., Faccini, U.F., 2014. New Sakmarian ages for the Rio Bonito formation (Paraná Basin, southern Brazil) based on LA-ICP-MS U–Pb radiometric dating of zircons crystals. Journal of South American Earth Sciences 56, 265–277. https://doi.org/10.1016/j.jsames.2014.09.013

Caley, T., Roche, D.M., Renssen, H., 2014. Orbital Asian summer monsoon dynamics revealed using an isotope-enabled global climate model. Nature Communications 5, 5371. https://doi.org/10.1038/ncomms6371

Campodonico, V.A., García, M.G., Pasquini, A.I., 2016. The geochemical signature of suspended sediments in the Parana River basin: Implications for provenance, weathering and sedimentary recycling. CATENA 143, 201–214. https://doi.org/10.1016/j.catena.2016.04.008

Capurro, L.R., 1955. Expedición argentina al Mar de Weddell, diciembre de 1954 a enero de 1955. República Argentina, Ministerio de Marina, Dirección General de Navegación.

Caquineau, S., Gaudichet, A., Gomes, L., Legrand, M., 2002. Mineralogy of Saharan dust transported over northwestern tropical Atlantic Ocean in relation to source regions. Journal of Geophysical Research: Atmospheres 107, AAC 4-1. https://doi.org/10.1029/2000JD000247

Chamley, H., 1989. Clay Minerals, in: Chamley, H. (Ed.), Clay Sedimentology. Springer Berlin Heidelberg, Berlin, Heidelberg, pp. 3–20. https://doi.org/10.1007/978-3-642-85916-8_1

Chapman, M.R., Shackleton, N.J., 2000. Evidence of 550-year and 1000-year cyclicities in North Atlantic circulation patterns during the Holocene. The Holocene 10, 287–291. https://doi.org/10.1191/095968300671253196

Cheng, H., Edwards, R.L., Broecker, W.S., Denton, G.H., Kong, X., Wang, Y., Zhang, R., Wang, X., 2009. Ice Age Terminations. Science 326, 248. https://doi.org/10.1126/science.1177840

Cheng, H., Edwards, R.L., Sinha, A., Spötl, C., Yi, L., Chen, S., Kelly, M., Kathayat, G., Wang, X., Li, X., Kong, X., Wang, Y., Ning, Y., Zhang, H., 2016. The Asian monsoon over the past 640,000 years and ice age terminations. Nature 534, 640.

Cheng, H., Edwards, R.L., Wang, Y., Kong, X., Ming, Y., Kelly, M.J., Wang, X., Gallup, C.D., Liu, W., 2006. A penultimate glacial monsoon record from Hulu Cave and two-phase glacial terminations. Geology 34, 217–220. https://doi.org/10.1130/G22289.1

Cheng, H., Zhang, P.Z., Spötl, C., Edwards, R.L., Cai, Y.J., Zhang, D.Z., Sang, W.C., Tan, M., An, Z.S., 2012. The climatic cyclicity in semiarid-arid central Asia over the past 500,000 years. Geophysical Research Letters 39. https://doi.org/10.1029/2011GL050202

Clapperton, C.M., 1993. Quaternary geology and geomorphology of South America. Elsevier Amsterdam etc.

Clark, P.U., Dyke, A.S., Shakun, J.D., Carlson, A.E., Clark, J., Wohlfarth, B., Mitrovica, J.X., Hostetler, S.W., McCabe, A.M., 2009. The Last Glacial Maximum. Science 325, 710. https://doi.org/10.1126/science.1172873

Clift, P.D., Giosan, L., Blusztajn, J., Campbell, I.H., Allen, C., Pringle, M., Tabrez, A.R., Danish, M., Rabbani, M.M., Alizai, A., Carter, A., Lückge, A., 2008. Holocene erosion of the Lesser Himalaya triggered by intensified summer monsoon. Geology 36, 79–82. https://doi.org/10.1130/G24315A.1

Cohen, R.S., O'Nions, R.K., 1982. Identification of recycled continental material in the mantle from Sr, Nd and Pb isotope investigations. Earth and Planetary Science Letters 61, 73–84. https://doi.org/10.1016/0012-821X(82)90040-1

Cook, C.P., Hemming, S.R., van de Flierdt, T., Pierce Davis, E.L., Williams, T., Galindo, A.L., Jiménez-Espejo, F.J., Escutia, C., 2017. Glacial erosion of East Antarctica in the Pliocene: A comparative study of multiple marine sediment provenance tracers. Chemical Geology 466, 199–218. https://doi.org/10.1016/j.chemgeo.2017.06.011

Cook, K.H., Vizy, E.K., 2006. South American climate during the Last Glacial Maximum: Delayed onset of the South American monsoon. J. Geophys. Res. 111, D02110. https://doi.org/10.1029/2005JD005980

Cordani, U.G., Sato, K., 1999. Crustal evolution of the South American Platform, based on Nd isotopic systematics on granitoid rocks. Episodes-Newsmagazine of the International Union of Geological Sciences 22, 167–173.

Cruz, F.W., Burns, S.J., Karmann, I., Sharp, W.D., Vuille, M., 2006. Reconstruction of regional atmospheric circulation features during the late Pleistocene in subtropical Brazil from oxygen isotope composition of speleothems. Earth and Planetary Science Letters 248, 495–507. https://doi.org/10.1016/j.epsl.2006.06.019

Cruz, F.W., Burns, S.J., Karmann, I., Sharp, W.D., Vuille, M., Cardoso, A.O., Ferrari, J.A., Silva Dias, P.L., Viana, O., 2005. Insolation-driven changes in atmospheric circulation over the past 116,000 years in subtropical Brazil. Nature 434, 63–66. https://doi.org/10.1038/nature03365

Cruz, Francisco W., Burns, S.J., Karmann, I., Sharp, W.D., Vuille, M., Ferrari, J.A., 2006. A stalagmite record of changes in atmospheric circulation and soil processes in the Brazilian subtropics during the Late Pleistocene. Quaternary Science Reviews 25, 2749–2761. https://doi.org/10.1016/j.quascirev.2006.02.019

Cruz, F.W., Vuille, M., Burns, S.J., Wang, X., Cheng, H., Werner, M., Lawrence Edwards, R., Karmann, I., Auler, A.S., Nguyen, H., 2009. Orbitally driven east–west antiphasing of South American precipitation. Nature Geoscience 2, 210.

Cuffey, K.M., Clow, G.D., 1997. Temperature, accumulation, and ice sheet elevation in central Greenland through the last deglacial transition. Journal of Geophysical Research: Oceans 102, 26383–26396. https://doi.org/10.1029/96JC03981

Curry, W.B., Oppo, D.W., 2005. Glacial water mass geometry and the distribution of δ13C of ΣCO2 in the western Atlantic Ocean. Paleoceanography 20. https://doi.org/10.1029/2004PA001021

de Alkmim, F.F., 2015. Geological Background: A Tectonic Panorama of Brazil, in: Vieira, B.C., Salgado, A.A.R., Santos, L.J.C. (Eds.), Landscapes and Landforms of Brazil. Springer Netherlands, Dordrecht, pp. 9–17. https://doi.org/10.1007/978-94-017-8023-0_2

de Almeida, F.F.M., Hasui, Y., de Brito Neves, B.B., Fuck, R.A., 1981. Brazilian structural provinces: An introduction. Earth-Science Reviews 17, 1–29. https://doi.org/10.1016/0012-8252(81)90003-9

De Boer, A.M., Hogg, A.McC., 2014. Control of the glacial carbon budget by topographically induced mixing. Geophysical Research Letters 41, 4277–4284. https://doi.org/10.1002/2014GL059963

de Fátima Rossetti, D., Mann de Toledo, P., Góes, A.M., 2005. New geological framework for Western Amazonia (Brazil) and implications for biogeography and evolution. Quaternary Research 63, 78–89. https://doi.org/10.1016/j.yqres.2004.10.001

de Mahiques, M.M., Tassinari, C.C.G., Marcolini, S., Violante, R.A., Figueira, R.C.L., da Silveira, I.C.A., Burone, L., de Mello e Sousa, S.H., 2008. Nd and Pb isotope signatures on the Southeastern South American upper margin: Implications for sediment transport and source rocks. Marine Geology 250, 51–63. https://doi.org/10.1016/j.margeo.2007.11.007

Deacon, G.E.R., 1937. The hydrology of the Southern Ocean. Discovery Rep. 15, 3–122.

Delille, B., Vancoppenolle, M., Geilfus, N.-X., Tilbrook, B., Lannuzel, D., Schoemann, V., Becquevort, S., Carnat, G., Delille, D., Lancelot, C., Chou, L., Dieckmann, G.S., Tison, J.-L., 2014. Southern Ocean CO2 sink: The contribution of the sea ice. Journal of Geophysical Research: Oceans 119, 6340–6355. https://doi.org/10.1002/2014JC009941

D'el-Rey Silva, L.J.H., Walde, D.H.-G., Saldanha, D.O., 2016. The Neoproterozoic–Cambrian Paraguay Belt, central Brazil: Part I — New structural data and a new approach on the regional implications. Tectonophysics 676, 20–41. https://doi.org/10.1016/j.tecto.2016.03.019

Denton, G.H., Anderson, R.F., Toggweiler, J.R., Edwards, R.L., Schaefer, J.M., Putnam, A.E., 2010. The Last Glacial Termination. Science 328, 1652. https://doi.org/10.1126/science.1184119

DePaolo, D.J., Manton, W.I., Grew, E.S., Halpern, M., 1982. Sm–Nd, Rb–Sr and U–Th–Pb systematics of granulite facies rocks from Fyfe Hills, Enderby Land, Antarctica. Nature 298, 614–618. https://doi.org/10.1038/298614a0

DePaolo, D.J., Wasserburg, G.J., 1976. Nd isotopic variations and petrogenetic models. Geophysical Research Letters 3, 249–252. https://doi.org/10.1029/GL003i005p00249

Desiage, P.-A., Montero-Serrano, J.-C., St-Onge, G., Crespi-Abril, A.C., Giarratano, E., Gil, M.N., Haller, M.J., 2018. Quantifying sources and transport pathways of surface sediments in the Gulf of San Jorge, central Patagonia (Argentina). Oceanography 31, 92–103.

Dezileau, L., Bareille, G., Reyss, J.L., Lemoine, F., 2000. Evidence for strong sediment redistribution by bottom currents along the southeast Indian ridge. Deep Sea Research Part I: Oceanographic Research Papers 47, 1899–1936. https://doi.org/10.1016/S0967-0637(00)00008-X

Diekmann, B., 2007. Sedimentary patterns in the late Quaternary Southern Ocean. Deep Sea Research Part II: Topical Studies in Oceanography 54, 2350–2366. https://doi.org/10.1016/j.dsr2.2007.07.025

Diekmann, B., Hofmann, J., Henrich, R., Fütterer, D.K., Röhl, U., Wei, K.-Y., 2008. Detrital sediment supply in the southern Okinawa Trough and its relation to sea-level and Kuroshio dynamics during the late Quaternary. Marine Geology 255, 83–95. https://doi.org/10.1016/j.margeo.2008.08.001

Diekmann, B., Kuhn, G., Rachold, V., Abelmann, A., Brathauer, U., Fütterer, D.K., Gersonde, R., Grobe, H., 2000. Terrigenous sediment supply in the Scotia Sea (Southern Ocean): response to Late Quaternary ice dynamics in Patagonia and on the Antarctic Peninsula. Palaeogeography, Palaeoclimatology, Palaeoecology 162, 357–387. https://doi.org/10.1016/S0031-0182(00)00138-3

Dosso, L., Murthy, V.R., 1980. A Nd isotopic study of the Kerguelen Islands: Inferences on enriched oceanic mantle sources. Earth and Planetary Science Letters 48, 268–276. https://doi.org/10.1016/0012-821X(80)90190-9

Dou, Y., Yang, S., Liu, Z., Shi, X., Li, J., Yu, H., Berne, S., 2012. Sr–Nd isotopic constraints on terrigenous sediment provenances and Kuroshio Current variability in the Okinawa

Trough during the late Quaternary. Palaeogeography, Palaeoclimatology, Palaeoecology 365–366, 38–47. https://doi.org/10.1016/j.palaeo.2012.09.003

Dunlop, S., 2008. A Dictionary of Weather. OUP Oxford.

Dutt, S., Gupta, A.K., Clemens, S.C., Cheng, H., Singh, R.K., Kathayat, G., Edwards, R.L., 2015. Abrupt changes in Indian summer monsoon strength during 33,800 to 5500 years B.P. Geophysical Research Letters 42, 5526–5532. https://doi.org/10.1002/2015GL064015

Dykoski, C.A., Edwards, R.L., Cheng, H., Yuan, D., Cai, Y., Zhang, M., Lin, Y., Qing, J., An, Z., Revenaugh, J., 2005. A high-resolution, absolute-dated Holocene and deglacial Asian monsoon record from Dongge Cave, China. Earth and Planetary Science Letters 233, 71–86. https://doi.org/10.1016/j.epsl.2005.01.036

Elliot, D.H., 1975. Tectonics of Antarctica: a review. American Journal of Science 275, 45–106.

Engler, A., 2009. The Geology of South America, in: Geology. Encyclopedia of Life Support Systems, p. 11.

Esquevin, J., 1969. Influence de la composition chimique des illites sur leur cristallinité. Bull. Centre Rech. Pau-SNPA 3, 147–153.

Faure, G., Barrett, P.J., 1973. Strontium Isotope Compositions of Non-marine Carbonate Rocks from the Beacon Supergroup of the Transantarctic Mountains. Journal of Sedimentary Research 43.

Faure, G., Mensing, T.M., 2005. Isotopes: principles and applications. Wiley-Blackwell.

Fischer, H., Schmitt, J., Lüthi, D., Stocker, T.F., Tschumi, T., Parekh, P., Joos, F., Köhler, P., Völker, C., Gersonde, R., Barbante, C., Le Floch, M., Raynaud, D., Wolff, E., 2010. The role of Southern Ocean processes in orbital and millennial CO2 variations – A synthesis. Quaternary Science Reviews 29, 193–205. https://doi.org/10.1016/j.quascirev.2009.06.007

Flowerdew, M.J., Tyrrell, S., Riley, T.R., Whitehouse, M.J., Mulvaney, R., Leat, P.T., Marschall, H.R., 2012. Distinguishing East and West Antarctic sediment sources using the Pb isotope composition of detrital K-feldspar. Chemical Geology 292–293, 88–102. https://doi.org/10.1016/j.chemgeo.2011.11.006

Fontes, D., Cordeiro, R.C., Martins, G.S., Behling, H., Turcq, B., Sifeddine, A., Seoane, J.C.S., Moreira, L.S., Rodrigues, R.A., 2017. Paleoenvironmental dynamics in South Amazonia, Brazil, during the last 35,000 years inferred from pollen and geochemical records of Lago do Saci. Quaternary Science Reviews 173, 161–180. https://doi.org/10.1016/j.quascirev.2017.08.021

Ford, A.B., Kistler, R.W., 1980. K—Ar age, composition, and origin of Mesozoic mafic rocks related to Ferrar Group, Pensacola Mountains, Antarctica. New Zealand Journal of Geology and Geophysics 23, 371–390. https://doi.org/10.1080/00288306.1980.10424146

Foster, T.D., Carmack, E.C., 1976. Frontal zone mixing and Antarctic Bottom water formation in the southern Weddell Sea. Deep Sea Research and Oceanographic Abstracts 23, 301–317. https://doi.org/10.1016/0011-7471(76)90872-X

Fraser, K.J., Hawkesworth, C.J., Erlank, A.J., Mitchell, R.H., Scott-Smith, B.H., 1985. Sr, Nd and Pb isotope and minor element geochemistry of lamproites and kimberlites. Earth and Planetary Science Letters 76, 57–70. https://doi.org/10.1016/0012-821X(85)90148-7

Fretzdorff, S., Livermore, R.A., Devey, C.W., Leat, P.T., Stoffers, P., 2002. Petrogenesis of the back-arc east scotia ridge, south Atlantic ocean. Journal of Petrology 43, 1435–1467. https://doi.org/10.1093/petrology/43.8.1435

Frey, F.A., Coffin, M.F., Wallace, P.J., Weis, D., Zhao, X., Wise, S.W., Wähnert, V., Teagle, D.A.H., Saccocia, P.J., Reusch, D.N., Pringle, M.S., Nicolaysen, K.E., Neal, C.R., Müller, R.D., Moore, C.L., Mahoney, J.J., Keszthelyi, L., Inokuchi, H., Duncan, R.A., Delius, H., Damuth, J.E., Damasceno, D., Coxall, H.K., Borre, M.K., Boehm, F., Barling, J., Arndt, N.T., Antretter, M., 2000. Origin and evolution of a submarine large igneous province: the Kerguelen Plateau and Broken Ridge, southern Indian Ocean. Earth and Planetary Science Letters 176, 73–89. https://doi.org/10.1016/S0012-821X(99)00315-5

Fuck, R.A., Dantas, E.L., Pimentel, M.M., Botelho, N.F., Armstrong, R., Laux, J.H., Junges, S.L., Soares, J.E., Praxedes, I.F., 2014. Paleoproterozoic crust-formation and reworking events in the Tocantins Province, central Brazil: A contribution for Atlantica supercontinent reconstruction. Precambrian Research 244, 53–74. https://doi.org/10.1016/j.precamres.2013.12.003

Fukamachi, Y., Rintoul, S.R., Church, J.A., Aoki, S., Sokolov, S., Rosenberg, M.A., Wakatsuchi, M., 2010. Strong export of Antarctic Bottom Water east of the Kerguelen plateau. Nature Geoscience 3, 327.

Ganade de Araujo, C.E., Cordani, U.G., Weinberg, R.F., Basei, M.A.S., Armstrong, R., Sato, K., 2014. Tracing Neoproterozoic subduction in the Borborema Province (NE-Brazil): Clues from U-Pb geochronology and Sr-Nd-Hf-O isotopes on granitoids and migmatites. Lithos 202–203, 167–189. https://doi.org/10.1016/j.lithos.2014.05.015

Gasse, F., 2000. Hydrological changes in the African tropics since the Last Glacial Maximum. Quaternary Science Reviews 19, 189–211. https://doi.org/10.1016/S0277-3791(99)00061-X

Gautier, I., Weis, D., Mennessier, J.-P., Vidal, P., Giret, A., Loubet, M., 1990. Petrology and geochemistry of the Kerguelen Archipelago basalts (South Indian Ocean): evolution of the mantle sources from ridge to intraplate position. Earth and Planetary Science Letters 100, 59–76. https://doi.org/10.1016/0012-821X(90)90176-X

Gersonde, R., Abelmann, A., Brathauer, U., Becquey, S., Bianchi, C., Cortese, G., Grobe, H., Kuhn, G., Niebler, H.-S., Segl, M., Sieger, R., Zielinski, U., Fütterer, D.K., 2003. Last glacial sea surface temperatures and sea-ice extent in the Southern Ocean (Atlantic-Indian sector): A multiproxy approach. Paleoceanography 18. https://doi.org/10.1029/2002PA000809

Gherardi, J.-M., Labeyrie, L., Nave, S., Francois, R., McManus, J.F., Cortijo, E., 2009. Glacial-interglacial circulation changes inferred from 231Pa/230Th sedimentary record in the North Atlantic region. Paleoceanography 24. https://doi.org/10.1029/2008PA001696

Glasser, N.F., Harrison, S., Winchester, V., Aniya, M., 2004. Late Pleistocene and Holocene palaeoclimate and glacier fluctuations in Patagonia. Global and Planetary Change 43, 79–101. https://doi.org/10.1016/j.gloplacha.2004.03.002

Goldstein, S.J., Jacobsen, S.B., 1987. The Nd and Sr isotopic systematics of river-water dissolved material: Implications for the sources of Nd and Sr in seawater. Chemical Geology: Isotope Geoscience section 66, 245–272. https://doi.org/10.1016/0168-9622(87)90045-5

Gottschalk, J., Hodell, D.A., Skinner, L.C., Crowhurst, S.J., Jaccard, S.L., Charles, C., 2018a. Past Carbonate Preservation Events in the Deep Southeast Atlantic Ocean (Cape Basin)

and Their Implications for Atlantic Overturning Dynamics and Marine Carbon Cycling. Paleoceanography and Paleoclimatology 33, 643–663. https://doi.org/10.1029/2018PA003353

Gottschalk, J., Skinner, L.C., Lippold, J., Vogel, H., Frank, N., Jaccard, S.L., Waelbroeck, C., 2016. Biological and physical controls in the Southern Ocean on past millennial-scale atmospheric CO2 changes. Nature Communications 7, 11539. https://doi.org/10.1038/ncomms11539

Gottschalk, J., Skinner, L.C., Misra, S., Waelbroeck, C., Menviel, L., Timmermann, A., 2015a. Abrupt changes in the southern extent of North Atlantic Deep Water during Dansgaard–Oeschger events. Nature Geoscience 8, 950. https://doi.org/10.1038/NGEO2558

Gottschalk, J., Skinner, L.C., Waelbroeck, C., 2015b. Contribution of seasonal sub-Antarctic surface water variability to millennial-scale changes in atmospheric CO2 over the last deglaciation and Marine Isotope Stage 3. Earth and Planetary Science Letters 411, 87–99. https://doi.org/10.1016/j.epsl.2014.11.051

Gottschalk, J., Szidat, S., Michel, E., Mazaud, A., Salazar, G., Battaglia, M., Lippold, J., Jaccard, S.L., 2018b. Radiocarbon Measurements of Small-Size Foraminiferal Samples with the Mini Carbon Dating System (MICADAS) at the University of Bern: Implications for Paleoclimate Reconstructions. Radiocarbon 60, 469–491. https://doi.org/10.1017/RDC.2018.3

Govin, A., Michel, E., Labeyrie, L., Waelbroeck, C., Dewilde, F., Jansen, E., 2009. Evidence for northward expansion of Antarctic Bottom Water mass in the Southern Ocean during the last glacial inception. Paleoceanography 24. https://doi.org/10.1029/2008PA001603

Grant, K.M., Rohling, E.J., Ramsey, C.B., Cheng, H., Edwards, R.L., Florindo, F., Heslop, D., Marra, F., Roberts, A.P., Tamisiea, M.E., Williams, F., 2014. Sea-level variability over five glacial cycles. Nature Communications 5, 5076. https://doi.org/10.1038/ncomms6076

Grousset, F.E., Rognon, P., Coudé-Gaussen, G., Pédemay, P., 1992. Origins of peri-Saharan dust deposits traced by their Nd and Sr isotopic composition. Palaeogeography, Palaeoclimatology, Palaeoecology 93, 203–212. https://doi.org/10.1016/0031-0182(92)90097-O

Gutjahr, M., Lippold, J., 2011. Early arrival of Southern Source Water in the deep North Atlantic prior to Heinrich event 2. Paleoceanography 26. https://doi.org/10.1029/2011PA002114

Guyot, J.L., Jouanneau, J.M., Soares, L., Boaventura, G.R., Maillet, N., Lagane, C., 2007. Clay mineral composition of river sediments in the Amazon Basin. CATENA 71, 340–356. https://doi.org/10.1016/j.catena.2007.02.002

Hall, I.R., McCave, I.N., Shackleton, N.J., Weedon, G.P., Harris, S.E., 2001. Intensified deep Pacific inflow and ventilation in Pleistocene glacial times. Nature 412, 809–812. https://doi.org/10.1038/35090552

Hall, I.R., Moran, S.B., Zahn, R., Knutz, P.C., Shen, C.-C., Edwards, R.L., 2006. Accelerated drawdown of meridional overturning in the late-glacial Atlantic triggered by transient pre-H event freshwater perturbation. Geophysical Research Letters 33. https://doi.org/10.1029/2006GL026239

Harrison, D., Leat, P.T., Burnard, P.G., Turner, G., Fretzdorff, S., Millar, I.L., 2003. Resolving mantle components in oceanic lavas from segment E2 of the East Scotia back-arc ridge, South Sandwich Islands. Geological Society, London, Special Publications 219, 333. https://doi.org/10.1144/GSL.SP.2003.219.01.16

Haug, G.H., Hughen, K.A., Sigman, D.M., Peterson, L.C., Röhl, U., 2001. Southward Migration of the Intertropical Convergence Zone Through the Holocene. Science 293, 1304. https://doi.org/10.1126/science.1059725

Hauptvogel, D.W., Passchier, S., 2012. Early–Middle Miocene (17–14Ma) Antarctic ice dynamics reconstructed from the heavy mineral provenance in the AND-2A drill core, Ross Sea, Antarctica. Global and Planetary Change 82–83, 38–50. https://doi.org/10.1016/j.gloplacha.2011.11.003

He, F., Shakun, J.D., Clark, P.U., Carlson, A.E., Liu, Z., Otto-Bliesner, B.L., Kutzbach, J.E., 2013. Northern Hemisphere forcing of Southern Hemisphere climate during the last deglaciation. Nature 494, 81.

Hegner, E., Dauelsberg, H.J., Rutgers Van Der Loeff, M.M., Jeandel, C., De Baar, H.J.W., 2007. Nd isotopic constraints on the origin of suspended particles in the Atlantic Sector of the Southern Ocean. Geochemistry, Geophysics, Geosystems 8. https://doi.org/10.1029/2007GC001666

Heinonen, J.S., Carlson, R.W., Luttinen, A.V., 2010. Isotopic (Sr, Nd, Pb, and Os) composition of highly magnesian dikes of Vestfjella, western Dronning Maud Land, Antarctica: A key to the origins of the Jurassic Karoo large igneous province? Chemical Geology 277, 227–244. https://doi.org/10.1016/j.chemgeo.2010.08.004

Hemming, S.R., 2004. Heinrich events: Massive late Pleistocene detritus layers of the North Atlantic and their global climate imprint. Reviews of Geophysics 42. https://doi.org/10.1029/2003RG000128

Hemming, S.R., van de Flierdt, T., Goldstein, S.L., Franzese, A.M., Roy, M., Gastineau, G., Landrot, G., 2007. Strontium isotope tracing of terrigenous sediment dispersal in the Antarctic Circumpolar Current: Implications for constraining frontal positions. Geochemistry, Geophysics, Geosystems 8. https://doi.org/10.1029/2006GC001441

Hesse, P.P., McTainsh, G.H., 1999. Last Glacial Maximum to Early Holocene Wind Strength in the Mid-latitudes of the Southern Hemisphere from Aeolian Dust in the Tasman Sea. Quaternary Research 52, 343–349. https://doi.org/10.1006/qres.1999.2084

Hole, M.J., Kempton, P.D., Millar, I.L., 1993. Trace-element and isotopic characteristics of small-degree melts of the asthenosphere: Evidence from the alkalic basalts of the Antarctic Peninsula. Chemical Geology 109, 51–68. https://doi.org/10.1016/0009-2541(93)90061-M

Horn, B.L.D., Melo, T.M., Schultz, C.L., Philipp, R.P., Kloss, H.P., Goldberg, K., 2014. A new third-order sequence stratigraphic framework applied to the Triassic of the Paraná Basin, Rio Grande do Sul, Brazil, based on structural, stratigraphic and paleontological data. Journal of South American Earth Sciences 55, 123–132. https://doi.org/10.1016/j.jsames.2014.07.007

Howard, W.R., Prell, W.L., 1992. Late Quaternary Surface Circulation of the Southern Indian Ocean and its Relationship to Orbital Variations. Paleoceanography 7, 79–117. https://doi.org/10.1029/91PA02994

Howe, J.N.W., Piotrowski, A.M., Noble, T.L., Mulitza, S., Chiessi, C.M., Bayon, G., 2016. North Atlantic Deep Water Production during the Last Glacial Maximum. Nature Communications 7, 11765. https://doi.org/10.1038/ncomms11765

Hu, B., Li, G., Li, J., Bi, J., Zhao, J., Bu, R., 2012. Provenance and climate change inferred from Sr–Nd–Pb isotopes of late Quaternary sediments in the Huanghe (Yellow River)

Delta, China. Quaternary Research 78, 561–571. https://doi.org/10.1016/j.yqres.2012.07.005

Jaccard, S.L., Hayes, C.T., Martínez-García, A., Hodell, D.A., Anderson, R.F., Sigman, D.M., Haug, G.H., 2013. Two Modes of Change in Southern Ocean Productivity Over the Past Million Years. Science 339, 1419. https://doi.org/10.1126/science.1227545

Jeandel, C., Arsouze, T., Lacan, F., Téchiné, P., Dutay, J.-C., 2007. Isotopic Nd compositions and concentrations of the lithogenic inputs into the ocean: A compilation, with an emphasis on the margins. Chemical Geology 239, 156–164. https://doi.org/10.1016/j.chemgeo.2006.11.013

Jo, K., Woo, K.S., Yi, S., Yang, D.Y., Lim, H.S., Wang, Y., Cheng, H., Edwards, R.L., 2014. Mid-latitude interhemispheric hydrologic seesaw over the past 550,000 years. Nature 508, 378.

Johnsen, S.J., Dansgaard, W., Clausen, H.B., Langway, C.C., 1972. Oxygen Isotope Profiles through the Antarctic and Greenland Ice Sheets. Nature 235, 429–434. https://doi.org/10.1038/235429a0

Joseph, L.H., Rea, D.K., van der Pluijm, B.A., Gleason, J.D., 2002. Antarctic environmental variability since the late Miocene: ODP Site 745, the East Kerguelen sediment drift. Earth and Planetary Science Letters 201, 127–142. https://doi.org/10.1016/S0012-821X(02)00661-1

Kalnay, E., Kanamitsu, M., Kistler, R., Collins, W., Deaven, D., Gandin, L., Iredell, M., Saha, S., White, G., Woollen, J., Zhu, Y., Chelliah, M., Ebisuzaki, W., Higgins, W., Janowiak, J., Mo, K.C., Ropelewski, C., Wang, J., Leetmaa, A., Reynolds, R., Jenne, R., Joseph, D., 1996. The NCEP/NCAR 40-Year Reanalysis Project. Bull. Amer. Meteor. Soc. 77, 437–472. https://doi.org/10.1175/1520-0477(1996)077<0437:TNYRP>2.0.CO;2

Kaplan, M.R., Schaefer, J.M., Strelin, J.A., Denton, G.H., Anderson, R.F., Vandergoes, M.J., Finkel, R.C., Schwartz, R., Travis, S.G., Garcia, J.L., Martini, M.A., Nielsen, S.H.H., 2016. Patagonian and southern South Atlantic view of Holocene climate. Quaternary Science Reviews 141, 112–125. https://doi.org/10.1016/j.quascirev.2016.03.014

Khondoker, R., Weiss, D., van de Flierdt, T., Rehkämper, M., Kreissig, K., Coles, B.J., Strekopytov, S., Humphreys-Williams, E., Dong, S., Bory, A., Bout-Roumazeilles, V., Smichowski, P., Cid-Agüero, P., Babinski, M., Losno, R., Monna, F., 2018. New

constraints on elemental and Pb and Nd isotope compositions of South American and Southern African aerosol sources to the South Atlantic Ocean. Geochemistry 78, 372–384. https://doi.org/10.1016/j.chemer.2018.05.001

Kilian, R., Lamy, F., 2012. A review of Glacial and Holocene paleoclimate records from southernmost Patagonia (49–55°S). Quaternary Science Reviews 53, 1–23. https://doi.org/10.1016/j.quascirev.2012.07.017

Kleiven, H. (Kikki) F., Kissel, C., Laj, C., Ninnemann, U.S., Richter, T.O., Cortijo, E., 2008. Reduced North Atlantic Deep Water Coeval with the Glacial Lake Agassiz Freshwater Outburst. Science 319, 60. https://doi.org/10.1126/science.1148924

Kohfeld, K.E., Graham, R.M., de Boer, A.M., Sime, L.C., Wolff, E.W., Le Quéré, C., Bopp, L., 2013. Southern Hemisphere westerly wind changes during the Last Glacial Maximum: paleo-data synthesis. Quaternary Science Reviews 68, 76–95. https://doi.org/10.1016/j.quascirev.2013.01.017

Köhler, P., Fischer, H., 2006. Simulating low frequency changes in atmospheric CO2 during the last 740 000 years. Climate of the Past 2, 57–78.

Košler, J., Magna, T., Mlčoch, B., Mixa, P., Nývlt, D., Holub, F.V., 2009. Combined Sr, Nd, Pb and Li isotope geochemistry of alkaline lavas from northern James Ross Island (Antarctic Peninsula) and implications for back-arc magma formation. Chemical Geology 258, 207–218. https://doi.org/10.1016/j.chemgeo.2008.10.006

Krueger, S., Leuschner, D.C., Ehrmann, W., Schmiedl, G., Mackensen, A., 2012. North Atlantic Deep Water and Antarctic Bottom Water variability during the last 200ka recorded in an abyssal sediment core off South Africa. Global and Planetary Change 80–81, 180–189. https://doi.org/10.1016/j.gloplacha.2011.10.001

Krueger, S., Leuschner, D.C., Ehrmann, W., Schmiedl, G., Mackensen, A., Diekmann, B., 2008. Ocean circulation patterns and dust supply into the South Atlantic during the last glacial cycle revealed by statistical analysis of kaolinite/chlorite ratios. Marine Geology 253, 82–91. https://doi.org/10.1016/j.margeo.2008.04.015

Kübler, B., 1969. Crystallinity of illite. Detection of metamorphism in some frontal parts of the Alpine. Fortschritte der Mineralogie 47, 39–40.

Kuhn, G., Diekmann, B., 2002. Late Quaternary variability of ocean circulation in the southeastern South Atlantic inferred from the terrigenous sediment record of a drift

deposit in the southern Cape Basin (ODP Site 1089). Palaeogeography, Palaeoclimatology, Palaeoecology 182, 287–303. https://doi.org/10.1016/S0031-0182(01)00500-4

Laird, M.G., 1991. The late Proterozoic-middle Palaeozoic rocks of Antarctica, in: The Geology of Antarctica. pp. 74–119.

Lambert, F., Bigler, M., Steffensen, J.P., Hutterli, M., Fischer, H., 2012. Centennial mineral dust variability in high-resolution ice core data from Dome C, Antarctica. Climate of the Past 8, 609–623. https://doi.org/10.5194/cp-8-609-2012

Lambert, F., Delmonte, B., Petit, J.R., Bigler, M., Kaufmann, P.R., Hutterli, M.A., Stocker, T.F., Ruth, U., Steffensen, J.P., Maggi, V., 2008. Dust-climate couplings over the past 800,000 years from the EPICA Dome C ice core. Nature 452, 616. https://doi.org/10.1038/nature06763

Lamy, F., Hebbeln, D., Röhl, U., Wefer, G., 2001. Holocene rainfall variability in southern Chile: a marine record of latitudinal shifts of the Southern Westerlies. Earth and Planetary Science Letters 185, 369–382. https://doi.org/10.1016/S0012-821X(00)00381-2

Larqué, L., Maamaatuaiahutapu, K., Garçon, V., 1997. On the intermediate and deep water flows in the South Atlantic Ocean. Journal of Geophysical Research: Oceans 102, 12425–12440.

Le Quéré, C., Rödenbeck, C., Buitenhuis, E.T., Conway, T.J., Langenfelds, R., Gomez, A., Labuschagne, C., Ramonet, M., Nakazawa, T., Metzl, N., Gillett, N., Heimann, M., 2007. Saturation of the Southern Ocean CO2 Sink Due to Recent Climate Change. Science 316, 1735. https://doi.org/10.1126/science.1136188

Ledbetter, M.T., 1993. Late pleistocene to holocene fluctuations in bottom-current speed in the Argentine Basin mudwave field. Deep Sea Research Part II: Topical Studies in Oceanography 40, 911–920. https://doi.org/10.1016/0967-0645(93)90040-T

Lee, J.I., Park, B.-K., Jwa, Y.-J., Ho Il Yoon, Kyu Chul Yoo, Kim, Y., 2005. Geochemical characteristics and the provenance of sediments in the Bransfield Strait, West Antarctica. Marine Geology 219, 81–98. https://doi.org/10.1016/j.margeo.2005.06.002

Lee, S.R., Cho, M., Hwang, J.H., Lee, B.-J., Kim, Y.-B., Kim, J.C., 2003. Crustal evolution of the Gyeonggi massif, South Korea: Nd isotopic evidence and implications for

continental growths of East Asia. Precambrian Research 121, 25–34. https://doi.org/10.1016/S0301-9268(02)00196-1

LeGrande, A.N., Schmidt, G.A., 2008. Ensemble, water isotope–enabled, coupled general circulation modeling insights into the 8.2 ka event. Paleoceanography 23. https://doi.org/10.1029/2008PA001610

Lévy, M., Bopp, L., Karleskind, P., Resplandy, L., Éthé, C., Pinsard, F., 2013. Physical pathways for carbon transfers between the surface mixed layer and the ocean interior. Global Biogeochemical Cycles 27, 1001–1012. https://doi.org/10.1002/gbc.20092, 2013

Li, T., Xu, Z., Lim, D., Chang, F., Wan, S., Jung, H., Choi, J., 2015. Sr–Nd isotopic constraints on detrital sediment provenance and paleoenvironmental change in the northern Okinawa Trough during the late Quaternary. Palaeogeography, Palaeoclimatology, Palaeoecology 430, 74–84. https://doi.org/10.1016/j.palaeo.2015.04.017

Liebmann, B., Allured, D., 2005. Daily Precipitation Grids for South America. Bull. Amer. Meteor. Soc. 86, 1567–1570. https://doi.org/10.1175/BAMS-86-11-1567

Liu, Z., Trentesaux, A., Clemens, S.C., Colin, C., Wang, P., Huang, B., Boulay, S., 2003. Clay mineral assemblages in the northern South China Sea: implications for East Asian monsoon evolution over the past 2 million years. Marine Geology 201, 133–146. https://doi.org/10.1016/S0025-3227(03)00213-5

Loewy, S.L., Dalziel, I.W.D., Pisarevsky, S., Connelly, J.N., Tait, J., Hanson, R.E., Bullen, D., 2011. Coats Land crustal block, East Antarctica: A tectonic tracer for Laurentia? Geology 39, 859–862. https://doi.org/10.1130/G32029.1

Luttinen, A.V., Leat, P.T., Furnes, H., 2010. Björnnutane and Sembberget basalt lavas and the geochemical provinciality of Karoo magmatism in western Dronning Maud Land, Antarctica. Journal of Volcanology and Geothermal Research 198, 1–18. https://doi.org/10.1016/j.jvolgeores.2010.07.011

Luttinen, A.V., Rämö, O.T., Huhma, H., 1998. Neodymium and strontium isotopic and trace element composition of a Mesozoic CFB suite from Dronning Maud Land, Antarctica: implications for lithosphere and asthenosphere contributions to Karoo magmatism. Geochimica et Cosmochimica Acta 62, 2701–2714. https://doi.org/10.1016/S0016-7037(98)00184-7

Mackintosh, A.N., Verleyen, E., O'Brien, P.E., White, D.A., Jones, R.S., McKay, R., Dunbar, R., Gore, D.B., Fink, D., Post, A.L., Miura, H., Leventer, A., Goodwin, I., Hodgson, D.A., Lilly, K., Crosta, X., Golledge, N.R., Wagner, B., Berg, S., van Ommen, T., Zwartz, D., Roberts, S.J., Vyverman, W., Masse, G., 2014. Retreat history of the East Antarctic Ice Sheet since the Last Glacial Maximum. Quaternary Science Reviews 100, 10–30. https://doi.org/10.1016/j.quascirev.2013.07.024

Mallmann, G., Chemale, F., Ávila, J.N., Kawashita, K., Armstrong, R.A., 2007. Isotope geochemistry and geochronology of the Nico Pérez Terrane, Rio de la Plata Craton, Uruguay. Gondwana Research 12, 489–508. https://doi.org/10.1016/j.gr.2007.01.002

Mansilla, C.A., McCulloch, R.D., Morello, F., 2016. Palaeoenvironmental change in Southern Patagonia during the Lateglacial and Holocene: Implications for forest refugia and climate reconstructions. Palaeogeography, Palaeoclimatology, Palaeoecology 447, 1–11. https://doi.org/10.1016/j.palaeo.2016.01.041

Martínez-García, A., Sigman, D.M., Ren, H., Anderson, R.F., Straub, M., Hodell, D.A., Jaccard, S.L., Eglinton, T.I., Haug, G.H., 2014. Iron Fertilization of the Subantarctic Ocean During the Last Ice Age. Science 343, 1347. https://doi.org/10.1126/science.1246848

Mathias, G.L., Nagai, R.H., Trindade, R.I.F., de Mahiques, M.M., 2014. Magnetic fingerprint of the late Holocene inception of the Río de la Plata plume onto the southeast Brazilian shelf. Palaeogeography, Palaeoclimatology, Palaeoecology 415, 183–196. https://doi.org/10.1016/j.palaeo.2014.03.034

Mawji, E., Schlitzer, R., Dodas, E.M., Abadie, C., Abouchami, W., Anderson, R.F., Baars, O., Bakker, K., Baskaran, M., Bates, N.R., Bluhm, K., Bowie, A., Bown, J., Boye, M., Boyle, E.A., Branellec, P., Bruland, K.W., Brzezinski, M.A., Bucciarelli, E., Buesseler, K., Butler, E., Cai, P., Cardinal, D., Casciotti, K., Chaves, J., Cheng, H., Chever, F., Church, T.M., Colman, A.S., Conway, T.M., Croot, P.L., Cutter, G.A., de Baar, H.J.W., de Souza, G.F., Dehairs, F., Deng, F., Dieu, H.T., Dulaquais, G., Echegoyen-Sanz, Y., Lawrence Edwards, R., Fahrbach, E., Fitzsimmons, J., Fleisher, M., Frank, M., Friedrich, J., Fripiat, F., Galer, S.J.G., Gamo, T., Solsona, E.G., Gerringa, L.J.A., Godoy, J.M., Gonzalez, S., Grossteffan, E., Hatta, M., Hayes, C.T., Heller, M.I., Henderson, G., Huang, K.-F., Jeandel, C., Jenkins, W.J., John, S., Kenna, T.C., Klunder, M., Kretschmer, S., Kumamoto, Y., Laan, P., Labatut, M., Lacan, F., Lam, P.J.,

Lannuzel, D., le Moigne, F., Lechtenfeld, O.J., Lohan, M.C., Lu, Y., Masqué, P., McClain, C.R., Measures, C., Middag, R., Moffett, J., Navidad, A., Nishioka, J., Noble, A., Obata, H., Ohnemus, D.C., Owens, S., Planchon, F., Pradoux, C., Puigcorbé, V., Quay, P., Radic, A., Rehkämper, M., Remenyi, T., Rijkenberg, M.J.A., Rintoul, S., Robinson, L.F., Roeske, T., Rosenberg, M., van der Loeff, M.R., Ryabenko, E., Saito, M.A., Roshan, S., Salt, L., Sarthou, G., Schauer, U., Scott, P., Sedwick, P.N., Sha, L., Shiller, A.M., Sigman, D.M., Smethie, W., Smith, G.J., Sohrin, Y., Speich, S., Stichel, T., Stutsman, J., Swift, J.H., Tagliabue, A., Thomas, A., Tsunogai, U., Twining, B.S., van Aken, H.M., van Heuven, S., van Ooijen, J., van Weerlee, E., Venchiarutti, C., Voelker, A.H.L., Wake, B., Warner, M.J., Woodward, E.M.S., Wu, J., Wyatt, N., Yoshikawa, H., Zheng, X.-Y., Xue, Z., Zieringer, M., Zimmer, L.A., 2015. The GEOTRACES Intermediate Data Product 2014. Marine Chemistry 177, 1–8. https://doi.org/10.1016/j.marchem.2015.04.005

Mayr, C., Wille, M., Haberzettl, T., Fey, M., Janssen, S., Lücke, A., Ohlendorf, C., Oliva, G., Schäbitz, F., Schleser, G.H., Zolitschka, B., 2007. Holocene variability of the Southern Hemisphere westerlies in Argentinean Patagonia (52°S). Quaternary Science Reviews 26, 579–584. https://doi.org/10.1016/j.quascirev.2006.11.013

Mazaud, A., Michel, E., Dewilde, F., Turon, J.L., 2010. Variations of the Antarctic Circumpolar Current intensity during the past 500 ka. Geochemistry, Geophysics, Geosystems 11. https://doi.org/10.1029/2010GC003033

McCave, I.N., Andrews, J.T., 2019. Distinguishing current effects in sediments delivered to the ocean by ice. I. Principles, methods and examples. Quaternary Science Reviews 212, 92–107. https://doi.org/10.1016/j.quascirev.2019.03.031

McCave, I.N., Carter, L., Hall, I.R., 2008. Glacial–interglacial changes in water mass structure and flow in the SW Pacific Ocean. Quaternary Science Reviews 27, 1886–1908. https://doi.org/10.1016/j.quascirev.2008.07.010

McCave, I.N., Crowhurst, S.J., Kuhn, G., Hillenbrand, C.-D., Meredith, M.P., 2014. Minimal change in Antarctic Circumpolar Current flow speed between the last glacial and Holocene. Nature Geoscience 7, 113. https://doi.org/10.1038/ngeo2037

McCave, I.N., Hall, I.R., 2006. Size sorting in marine muds: Processes, pitfalls, and prospects for paleoflow-speed proxies: SIZE SORTING IN MARINE MUDS. Geochem. Geophys. Geosyst. 7, n/a-n/a. https://doi.org/10.1029/2006GC001284

McCulloch, M.T., Black, L.P., 1984. SmNd isotopic systematics of Enderby Land granulites and evidence for the redistribution of Sm and Nd during metamorphism. Earth and Planetary Science Letters 71, 46–58. https://doi.org/10.1016/0012-821X(84)90051-7

McGee, B., Collins, A.S., Trindade, R.I.F., Jourdan, F., 2015. Investigating mid-Ediacaran glaciation and final Gondwana amalgamation using coupled sedimentology and 40Ar/39Ar detrital muscovite provenance from the Paraguay Belt, Brazil. Sedimentology 62, 130–154. https://doi.org/10.1111/sed.12143

McManus, J.F., Francois, R., Gherardi, J.-M., Keigwin, L.D., Brown-Leger, S., 2004. Collapse and rapid resumption of Atlantic meridional circulation linked to deglacial climate changes. Nature 428, 834–837. https://doi.org/10.1038/nature02494

Ménot, G., Bard, E., Rostek, F., Weijers, J.W.H., Hopmans, E.C., Schouten, S., Damsté, J.S.S., 2006. Early Reactivation of European Rivers During the Last Deglaciation. Science 313, 1623. https://doi.org/10.1126/science.1130511

Menviel, L., England, M.H., Meissner, K.J., Mouchet, A., Yu, J., 2014. Atlantic-Pacific seesaw and its role in outgassing CO2 during Heinrich events. Paleoceanography 29, 58–70. https://doi.org/10.1002/2013PA002542

Menviel, L., Joos, F., Ritz, S.P., 2012. Modeling atmospheric CO2, stable carbon isotope and marine carbon cycle changes during the last glacial-interglacial cycle. Quat. Sci. Rev 56, 46–68.

Menviel, L., Spence, P., England, M.H., 2015. Contribution of enhanced Antarctic Bottom Water formation to Antarctic warm events and millennial-scale atmospheric CO2 increase. Earth and Planetary Science Letters 413, 37–50. https://doi.org/10.1016/j.epsl.2014.12.050

Menviel, Laurie, Spence, P., Golledge, N., England, M.H., 2015. Southern Ocean Overturning Role in Modulating High Southern Latitude Climate and Atmospheric CO2 on Millennial Timescales. Nova Acta Leopoldina NF 121, 159–166.

Menviel, L., Spence, P., Yu, J., Chamberlain, M.A., Matear, R.J., Meissner, K.J., England, M.H., 2018. Southern Hemisphere westerlies as a driver of the early deglacial atmospheric CO2 rise. Nature Communications 9, 2503. https://doi.org/10.1038/s41467-018-04876-4

Menviel, L., Yu, J., Joos, F., Mouchet, A., Meissner, K.J., England, M.H., 2017. Poorly ventilated deep ocean at the Last Glacial Maximum inferred from carbon isotopes: A data-model comparison study. Paleoceanography 32, 2–17. https://doi.org/10.1002/2016PA003024

Meyer, I., Davies, G.R., Stuut, J.-B.W., 2011. Grain size control on Sr-Nd isotope provenance studies and impact on paleoclimate reconstructions: An example from deep-sea sediments offshore NW Africa. Geochemistry, Geophysics, Geosystems 12. https://doi.org/10.1029/2010GC003355

Mieth, M., Jokat, W., 2014. Banded iron formation (?) at Grunehogna Craton, East Antarctica – Constraints from aeromagnetic data. Precambrian Research 250, 143–150. https://doi.org/10.1016/j.precamres.2014.06.001

Milani, E.J., Melo, J.H.G., de Souza, P.A., de Gernandes, L.A., França, A.B., 2007. Bacia Do Parana. Boletim de Geoci encias da Petrobras 15, 265–287.

Milani, E.J., Ramos, V.A., 2017. Orogenias paleozóicas no domínio sul-ocidental do Gondwana e os ciclos de subsidência da Bacia do Paraná. Revista Brasileira de Geociências 28, 473–484.

Milankovitch, M.K., 1941. Kanon der Erdbestrahlung und seine Anwendung auf das Eiszeitenproblem. Royal Serbian Academy Special Publication 133, 1–633.

Missiaen, L., Waelbroeck, C., Pichat, S., Jaccard, S.L., Eynaud, F., Greenop, R., Burke, A., 2019. Improving North Atlantic marine core chronologies using 230Th-normalization. Paleoceanography and Paleoclimatology 0. https://doi.org/10.1029/2018PA003444

Mond, A., 1972. Permian sediments of the Beaver Lake area, Prince Charles Mountains. Antarctic Geology and Geophysics 585–589.

Montero-Serrano, J.C., Bout-Roumazeilles, V., Sionneau, T., Tribovillard, N., Bory, A., Flower, B.P., Riboulleau, A., Martinez, P., Billy, I., 2010. Changes in precipitation regimes over North America during the Holocene as recorded by mineralogy and geochemistry of Gulf of Mexico sediments. Global and Planetary Change 74, 132–143. https://doi.org/10.1016/j.gloplacha.2010.09.004

Montero-Serrano, J.C., Bout-Roumazeilles, V., Tribovillard, N., Sionneau, T., Riboulleau, A., Bory, A., Flower, B., 2009. Sedimentary evidence of deglacial megafloods in the

northern Gulf of Mexico (Pigmy Basin). Quaternary Science Reviews 28, 3333–3347. https://doi.org/10.1016/j.quascirev.2009.09.011

Morel, R., 1996. Les sols cultivés. 2e edition Lavoisier. Paris.

Moreno, P.I., Francois, J.P., Moy, C.M., Villa-Martinez, R., 2010. Covariability of the Southern Westerlies and atmospheric CO2 during the Holocene. Geology 38, 727–730. https://doi.org/10.1130/G30962

Moreno, P.I., Lowell, T.V., Jacobson jr, G.L., Denton, G.H., 1999. Abrupt vegetation and climate changes during the last glacial maximumand last termination in the chilean lake district: a case study from canal de la puntilla (41°s). Geografiska Annaler: Series A, Physical Geography 81, 285–311. https://doi.org/10.1111/1468-0459.00059

Moriarty, K.C., 1977. Clay minerals in Southeast Indian Ocean sediments, transport mechanisms and depositional environments. Marine Geology 25, 149–174. https://doi.org/10.1016/0025-3227(77)90051-2

Moura, C.A., Gaudette, H., 1993. Evidence of Brasiliano/Panafrican deformation in the Araguaia belt: implication for Gondwana evolution. Rev. Bras. Geoc 23, 117–123.

Neves, S.P., 2003. Proterozoic history of the Borborema province (NE Brazil): Correlations with neighboring cratons and Pan-African belts and implications for the evolution of western Gondwana. Tectonics 22. https://doi.org/10.1029/2001TC001352

Noble, T.L., Piotrowski, A.M., Robinson, L.F., McManus, J.F., Hillenbrand, C.-D., Bory, A.J.-M., 2012. Greater supply of Patagonian-sourced detritus and transport by the ACC to the Atlantic sector of the Southern Ocean during the last glacial period. Earth and Planetary Science Letters 317–318, 374–385. https://doi.org/10.1016/j.epsl.2011.10.007

Nogueira, A.C.R., Riccomini, C., Sial, A.N., Moura, C.A.V., Trindade, R.I.F., Fairchild, T.R., 2007. Carbon and strontium isotope fluctuations and paleoceanographic changes in the late Neoproterozoic Araras carbonate platform, southern Amazon craton, Brazil. Chemical Geology 237, 168–190. https://doi.org/10.1016/j.chemgeo.2006.06.016

Nougier, J., 1970. Carte géologique de reconnaissance des Iles Kerguelen:(1970). Institut géographique national.

Novello, V.F., Cruz, F.W., Vuille, M., Stríkis, N.M., Edwards, R.L., Cheng, H., Emerick, S., de Paula, M.S., Li, X., Barreto, E. de S., Karmann, I., Santos, R.V., 2017. A high-

resolution history of the South American Monsoon from Last Glacial Maximum to the Holocene. Scientific Reports 7, 44267.

Öhlander, B., Ingri, J., Land, M., Schöberg, H., 2000. Change of Sm-Nd isotope composition during weathering of till. Geochimica et Cosmochimica Acta 64, 813–820. https://doi.org/10.1016/S0016-7037(99)00365-8

Olivero, E.B., Martinioni, D.R., 2001. A review of the geology of the Argentinian Fuegian Andes. Journal of South American Earth Sciences, Mesozoic Palaeontology and Stratigraphy of South America and the South Atlantic 14, 175–188. https://doi.org/10.1016/S0895-9811(01)00016-5

Oppo, D.W., McManus, J.F., Cullen, J.L., 2003. Deepwater variability in the Holocene epoch. Nature 422, 277–277. https://doi.org/10.1038/422277b

Orsi, A.H., Johnson, G.C., Bullister, J.L., 1999. Circulation, mixing, and production of Antarctic Bottom Water. Progress in Oceanography 43, 55–109. https://doi.org/10.1016/S0079-6611(99)00004-X

Orsi, A.H., Whitworth, T., Nowlin, W.D., 1995. On the meridional extent and fronts of the Antarctic Circumpolar Current. Deep Sea Research Part I: Oceanographic Research Papers 42, 641–673. https://doi.org/10.1016/0967-0637(95)00021-W

Oyhantçabal, P., Siegesmund, S., Wemmer, K., 2011. The Río de la Plata Craton: a review of units, boundaries, ages and isotopic signature. International Journal of Earth Sciences 100, 201–220. https://doi.org/10.1007/s00531-010-0580-8

Pahnke, K., Goldstein, S.L., Hemming, S.R., 2008. Abrupt changes in Antarctic Intermediate Water circulation over the past 25,000 years. Nature Geoscience 1, 870.

Palmer, M.R., Edmond, J.M., 1989. The strontium isotope budget of the modern ocean. Earth and Planetary Science Letters 92, 11–26. https://doi.org/10.1016/0012-821X(89)90017-4

Pandarinath, K., 2009. Clay minerals in SW Indian continental shelf sediment cores as indicators of provenance and palaeomonsoonal conditions: a statistical approach. International Geology Review 51, 145–165. https://doi.org/10.1080/00206810802622112

Park, Y.-H., Durand, I., Kestenare, E., Rougier, G., Zhou, M., d'Ovidio, F., Cotté, C., Lee, J.-H., 2014. Polar Front around the Kerguelen Islands: An up-to-date determination and

associated circulation of surface/subsurface waters. Journal of Geophysical Research: Oceans 119, 6575–6592. https://doi.org/10.1002/2014JC010061

Park, Y.-H., Gambéroni, L., 1995. Large-scale circulation and its variability in the south Indian Ocean from TOPEX/POSEIDON altimetry. Journal of Geophysical Research: Oceans 100, 24911–24929. https://doi.org/10.1029/95JC01962

Park, Y.-H., Gambéroni, L., Charriaud, E., 1991. Frontal structure and transport of the Antarctic Circumpolar Current in the south Indian Ocean sector, 40–80°E. Marine Chemistry 35, 45–62. https://doi.org/10.1016/S0304-4203(09)90007-X

Park, Y.-H., Vivier, F., Roquet, F., Kestenare, E., 2009. Direct observations of the ACC transport across the Kerguelen Plateau. Geophysical Research Letters 36. https://doi.org/10.1029/2009GL039617

Paz, S.P.A. da, Angélica, R.S., Neves, R. de F., 2012. Mg-bentonite in the Paranaiba Paleozoic Basin, northern Brazil. Clays and Clay Minerals 60, 265–277. https://doi.org/10.1346/CCMN.2012.0600304

Peterson, R.G., Stramma, L., 1991. Upper-level circulation in the South Atlantic Ocean. Progress in Oceanography 26, 1–73. https://doi.org/10.1016/0079-6611(91)90006-8

Petit, J.R., Mourner, L., Jouzel, J., Korotkevich, Y.S., Kotlyakov, V.I., Lorius, C., 1990. Palaeoclimatological and chronological implications of the Vostok core dust record. Nature 343, 56–58. https://doi.org/10.1038/343056a0

Petschick, R., 2000. MacDiff 4.2. 5.

Petschick, R., Kuhn, G., Gingele, F., 1996. Clay mineral distribution in surface sediments of the South Atlantic: sources, transport, and relation to oceanography. Marine Geology 130, 203–229. https://doi.org/10.1016/0025-3227(95)00148-4

Pierce, E.L., Hemming, S.R., Williams, T., van de Flierdt, T., Thomson, S.N., Reiners, P.W., Gehrels, G.E., Brachfeld, S.A., Goldstein, S.L., 2014. A comparison of detrital U–Pb zircon, 40Ar/39Ar hornblende, 40Ar/39Ar biotite ages in marine sediments off East Antarctica: Implications for the geology of subglacial terrains and provenance studies. Earth-Science Reviews 138, 156–178. https://doi.org/10.1016/j.earscirev.2014.08.010

Pimentel, M.M., Rodrigues, J.B., DellaGiustina, M.E.S., Junges, S., Matteini, M., Armstrong, R., 2011. The tectonic evolution of the Neoproterozoic Brasília Belt, central Brazil, based on SHRIMP and LA-ICPMS U–Pb sedimentary provenance data: A review.

Journal of South American Earth Sciences 31, 345–357. https://doi.org/10.1016/j.jsames.2011.02.011

Piotrowski, A.M., Goldstein, S.L., Hemming, S., R., Fairbanks, R.G., Zylberberg, D.R., 2008. Oscillating glacial northern and southern deep water formation from combined neodymium and carbon isotopes. Earth and Planetary Science Letters 272, 394–405. https://doi.org/10.1016/j.epsl.2008.05.011

Piotrowski, A.M., Goldstein, S.L., Hemming, S.R., Fairbanks, R.G., 2004. Intensification and variability of ocean thermohaline circulation through the last deglaciation. Earth and Planetary Science Letters 225, 205–220. https://doi.org/10.1016/j.epsl.2004.06.002

R. Rintoul, S., W. Hughes, C., Olbers, D., 2001. Chapter 4.6 The antarctic circumpolar current system, in: Siedler, G., Church, J., Gould, J. (Eds.), International Geophysics. Academic Press, pp. 271–XXXVI. https://doi.org/10.1016/S0074-6142(01)80124-8

Rahmstorf, S., England, M.H., 1997. Influence of Southern Hemisphere Winds on North Atlantic Deep Water Flow. J. Phys. Oceanogr. 27, 2040–2054. https://doi.org/10.1175/1520-0485(1997)027<2040:IOSHWO>2.0.CO;2

Raza, W., Ahmad, S.M., Lone, M.A., Shen, C.-C., Sarma, D.S., Kumar, A., 2017. Indian summer monsoon variability in southern India during the last deglaciation: Evidence from a high resolution stalagmite δ18O record. Palaeogeography, Palaeoclimatology, Palaeoecology 485, 476–485. https://doi.org/10.1016/j.palaeo.2017.07.003

Razik, S., Chiessi, C.M., Romero, O.E., von Dobeneck, T., 2013. Interaction of the South American Monsoon System and the Southern Westerly Wind Belt during the last 14kyr. Palaeogeography, Palaeoclimatology, Palaeoecology 374, 28–40. https://doi.org/10.1016/j.palaeo.2012.12.022

Razik, S., Govin, A., Chiessi, C.M., von Dobeneck, T., 2015. Depositional provinces, dispersal, and origin of terrigenous sediments along the SE South American continental margin. Marine Geology 363, 261–272. https://doi.org/10.1016/j.margeo.2015.03.001

Reid, J.L., 2003. On the total geostrophic circulation of the Indian Ocean: flow patterns, tracers, and transports. Progress in Oceanography 56, 137–186. https://doi.org/10.1016/S0079-6611(02)00141-6

Reid, J.L., 1997. On the total geostrophic circulation of the pacific ocean: flow patterns, tracers, and transports. Progress in Oceanography 39, 263–352. https://doi.org/10.1016/S0079-6611(97)00012-8

Reid, J.L., 1994. On the total geostrophic circulation of the North Atlantic Ocean: Flow patterns, tracers, and transports. Progress in Oceanography 33, 1–92. https://doi.org/10.1016/0079-6611(94)90014-0

Reid, J.L., 1989. On the total geostrophic circulation of the South Atlantic Ocean: Flow patterns, tracers, and transports. Progress in Oceanography 23, 149–244. https://doi.org/10.1016/0079-6611(89)90001-3

Rijkenberg, M.J.A., Middag, R., Laan, P., Gerringa, L.J.A., van Aken, H.M., Schoemann, V., de Jong, J.T.M., de Baar, H.J.W., 2014. The distribution of dissolved iron in the west atlantic ocean. PloS one, PloS one 9, e101323. https://doi.org/10.1371/journal.pone.0101323

Rintoul, S.R., 1985. On the Origin and Influence of Adélie Land Bottom Water, in: Ocean, Ice, and Atmosphere: Interactions at the Antarctic Continental Margin. American Geophysical Union (AGU), pp. 151–171. https://doi.org/10.1029/AR075p0151

Roberts, J., Gottschalk, J., Skinner, L.C., Peck, V.L., Kender, S., Elderfield, H., Waelbroeck, C., Vázquez Riveiros, N., Hodell, D.A., 2016. Evolution of South Atlantic density and chemical stratification across the last deglaciation. Proc Natl Acad Sci USA 113, 514. https://doi.org/10.1073/pnas.1511252113

Robinson, L.F., Flierdt, T. van de, 2009. Southern Ocean evidence for reduced export of North Atlantic Deep Water during Heinrich event 1. Geology 37, 195–198. https://doi.org/10.1130/G25363A.1

Roulet, M., Lucotte, M., Saint-Aubin, A., Tran, S., Rhéault, I., Farella, N., De Jesus Da silva, E., Dezencourt, J., Sousa Passos, C.-J., Santos Soares, G., Guimarães, J.-R.D., Mergler, D., Amorim, M., 1998. The geochemistry of mercury in central Amazonian soils developed on the Alter-do-Chão formation of the lower Tapajós River Valley, Pará state, Brazil1The present investigation is part of an ongoing study, the CARUSO project (IDRC-UFPa-UQAM), initiated to determine the sources, fate, and health effects of MeHg in the Lower Tapajós area.1. Science of The Total Environment 223, 1–24. https://doi.org/10.1016/S0048-9697(98)00265-4

Rousseau, D.-D., Wu, N., Pei, Y., Li, F., 2009. Three exceptionally strong East-Asian summer monsoon events during glacial times in the past 470 kyr. Climate of the Past 5, 157–169. https://doi.org/10.5194/cp-5-157-2009

Roy, M., van de Flierdt, T., Hemming, S.R., Goldstein, S.L., 2007. 40Ar/39Ar ages of hornblende grains and bulk Sm/Nd isotopes of circum-Antarctic glacio-marine sediments: Implications for sediment provenance in the southern ocean. Chemical Geology 244, 507–519. https://doi.org/10.1016/j.chemgeo.2007.07.017

Sallée, J.B., Matear, R., Rintoul, S.R., Lenton, A., 2012. Surface to interior pathways of anthropogenic CO2 in the southern hemisphere oceans. Nat. Geosci. 5, 579–584.

Sallun, A.E.M., Sallun Filho, W., Suguio, K., Babinski, M., Gioia, S.M.C.L., Harlow, B.A., Duleba, W., De Oliveira, P.E., Garcia, M.J., Weber, C.Z., Christofoletti, S.R., Santos, C. da S., Medeiros, V.B. de, Silva, J.B., Santiago-Hussein, M.C., Fernandes, R.S., 2012. Geochemical evidence of the 8.2 ka event and other Holocene environmental changes recorded in paleolagoon sediments, southeastern Brazil. Quaternary Research 77, 31–43. https://doi.org/10.1016/j.yqres.2011.09.007

Salt, L.A., van Heuven, S.M.A.C., Claus, M.E., Jones, E.M., de Baar, H.J.W., 2015. Rapid acidification of mode and intermediate waters in the southwestern Atlantic Ocean. Biogeosciences, Biogeosciences 12, 1387?1401. https://doi.org/10.5194/bg-12-1387-2015

Saunders, K.M., Roberts, S.J., Perren, B., Butz, C., Sime, L., Davies, S., Van Nieuwenhuyze, W., Grosjean, M., Hodgson, D.A., 2018. Holocene dynamics of the Southern Hemisphere westerly winds and possible links to CO2 outgassing. Nature Geoscience 11, 650–655. https://doi.org/10.1038/s41561-018-0186-5

Sayago, J.M., Collantes, M.M., Karlson, A., Sanabria, J., 2001. Genesis and distribution of the Late Pleistocene and Holocene loess of Argentina: a regional approximation. Quaternary International 76–77, 247–257. https://doi.org/10.1016/S1040-6182(00)00107-5

Schäbitz, F., 1994. Holocene climatic variations in northern Patagonia, Argentina. Palaeogeography, Palaeoclimatology, Palaeoecology 109, 287–294. https://doi.org/10.1016/0031-0182(94)90180-5

Schellmann, G., Radtke, U., 2010. Timing and magnitude of Holocene sea-level changes along the middle and south Patagonian Atlantic coast derived from beach ridge systems, littoral terraces and valley-mouth terraces. Earth-Science Reviews 103, 1–30. https://doi.org/10.1016/j.earscirev.2010.06.003

Scheuvens, D., Schütz, L., Kandler, K., Ebert, M., Weinbruch, S., 2013. Bulk composition of northern African dust and its source sediments — A compilation. Earth-Science Reviews 116, 170–194. https://doi.org/10.1016/j.earscirev.2012.08.005

Schlitzer, R., Anderson, R.F., Dodas, E.M., Lohan, M., Geibert, W., Tagliabue, A., Bowie, A., Jeandel, C., Maldonado, M.T., Landing, W.M., Cockwell, D., Abadie, C., Abouchami, W., Achterberg, E.P., Agather, A., Aguliar-Islas, A., van Aken, H.M., Andersen, M., Archer, C., Auro, M., de Baar, H.J., Baars, O., Baker, A.R., Bakker, K., Basak, C., Baskaran, M., Bates, N.R., Bauch, D., van Beek, P., Behrens, M.K., Black, E., Bluhm, K., Bopp, L., Bouman, H., Bowman, K., Bown, J., Boyd, P., Boye, M., Boyle, E.A., Branellec, P., Bridgestock, L., Brissebrat, G., Browning, T., Bruland, K.W., Brumsack, H.-J., Brzezinski, M., Buck, C.S., Buck, K.N., Buesseler, K., Bull, A., Butler, E., Cai, P., Mor, P.C., Cardinal, D., Carlson, C., Carrasco, G., Casacuberta, N., Casciotti, K.L., Castrillejo, M., Chamizo, E., Chance, R., Charette, M.A., Chaves, J.E., Cheng, H., Chever, F., Christl, M., Church, T.M., Closset, I., Colman, A., Conway, T.M., Cossa, D., Croot, P., Cullen, J.T., Cutter, G.A., Daniels, C., Dehairs, F., Deng, F., Dieu, H.T., Duggan, B., Dulaquais, G., Dumousseaud, C., Echegoyen-Sanz, Y., Edwards, R.L., Ellwood, M., Fahrbach, E., Fitzsimmons, J.N., Russell Flegal, A., Fleisher, M.Q., van de Flierdt, T., Frank, M., Friedrich, J., Fripiat, F., Fröllje, H., Galer, S.J.G., Gamo, T., Ganeshram, R.S., Garcia-Orellana, J., Garcia-Solsona, E., Gault-Ringold, M., George, E., Gerringa, L.J.A., Gilbert, M., Godoy, J.M., Goldstein, S.L., Gonzalez, S.R., Grissom, K., Hammerschmidt, C., Hartman, A., Hassler, C.S., Hathorne, E.C., Hatta, M., Hawco, N., Hayes, C.T., Heimbürger, L.-E., Helgoe, J., Heller, M., Henderson, G.M., Henderson, P.B., van Heuven, S., Ho, P., Horner, T.J., Hsieh, Y.-T., Huang, K.-F., Humphreys, M.P., Isshiki, K., Jacquot, J.E., Janssen, D.J., Jenkins, W.J., John, S., Jones, E.M., Jones, J.L., Kadko, D.C., Kayser, R., Kenna, T.C., Khondoker, R., Kim, T., Kipp, L., Klar, J.K., Klunder, M., Kretschmer, S., Kumamoto, Y., Laan, P., Labatut, M., Lacan, F., Lam, P.J., Lambelet, M., Lamborg, C.H., Le Moigne, F.A.C., Le Roy, E., Lechtenfeld, O.J., Lee, J.-M., Lherminier, P., Little, S., López-Lora, M., Lu, Y., Masque, P., Mawji, E., Mcclain, C.R., Measures, C., Mehic, S., Barraqueta, J.-L.M.,

van der Merwe, P., Middag, R., Mieruch, S., Milne, A., Minami, T., Moffett, J.W., Moncoiffe, G., Moore, W.S., Morris, P.J., Morton, P.L., Nakaguchi, Y., Nakayama, N., Niedermiller, J., Nishioka, J., Nishiuchi, A., Noble, A., Obata, H., Ober, S., Ohnemus, D.C., van Ooijen, J., O'Sullivan, J., Owens, S., Pahnke, K., Paul, M., Pavia, F., Pena, L.D., Peters, B., Planchon, F., Planquette, H., Pradoux, C., Puigcorbé, V., Quay, P., Queroue, F., Radic, A., Rauschenberg, S., Rehkämper, M., Rember, R., Remenyi, T., Resing, J.A., Rickli, J., Rigaud, S., Rijkenberg, M.J.A., Rintoul, S., Robinson, L.F., Roca-Martí, M., Rodellas, V., Roeske, T., Rolison, J.M., Rosenberg, M., Roshan, S., Rutgers van der Loeff, M.M., Ryabenko, E., Saito, M.A., Salt, L.A., Sanial, V., Sarthou, G., Schallenberg, C., Schauer, U., Scher, H., Schlosser, C., Schnetger, B., Scott, P., Sedwick, P.N., Semiletov, I., Shelley, R., Sherrell, R.M., Shiller, A.M., Sigman, D.M., Singh, S.K., Slagter, H.A., Slater, E., Smethie, W.M., Snaith, H., Sohrin, Y., Sohst, B., Sonke, J.E., Speich, S., Steinfeldt, R., Stewart, G., Stichel, T., Stirling, C.H., Stutsman, J., Swarr, G.J., Swift, J.H., Thomas, A., Thorne, K., Till, C.P., Till, R., Townsend, A.T., Townsend, E., Tuerena, R., Twining, B.S., Vance, D., Velazquez, S., Venchiarutti, C., Villa-Alfageme, M., Vivancos, S.M., Voelker, A.H.L., Wake, B., Warner, M.J., Watson, R., van Weerlee, E., Alexandra Weigand, M., Weinstein, Y., Weiss, D., Wisotzki, A., Woodward, E.M.S., Wu, J., Wu, Y., Wuttig, K., Wyatt, N., Xiang, Y., Xie, R.C., Xue, Z., Yoshikawa, H., Zhang, J., Zhang, P., Zhao, Y., Zheng, L., Zheng, X.-Y., Zieringer, M., Zimmer, L.A., Ziveri, P., Zunino, P., Zurbrick, C., 2018. The GEOTRACES Intermediate Data Product 2017. Chemical Geology 493, 210–223. https://doi.org/10.1016/j.chemgeo.2018.05.040

Schneider, R.R., Price, B., Müller, P.J., Kroon, D., Alexander, I., 1997. Monsoon related variations in Zaire (Congo) sediment load and influence of fluvial silicate supply on marine productivity in the east equatorial Atlantic during the last 200,000 years. Paleoceanography 12, 463–481. https://doi.org/10.1029/96PA03640

Shakun, J.D., Clark, P.U., He, F., Marcott, S.A., Mix, A.C., Liu, Z., Otto-Bliesner, B., Schmittner, A., Bard, E., 2012. Global warming preceded by increasing carbon dioxide concentrations during the last deglaciation. Nature 484, 49. https://doi.org/10.1038/nature10915

Shirahata, H., Elias, R.W., Patterson, C.C., Koide, M., 1980. Chronological variations in concentrations and isotopic compositions of anthropogenic atmospheric lead in

sediments of a remote subalpine pond. Geochimica et Cosmochimica Acta 44, 149–162. https://doi.org/10.1016/0016-7037(80)90127-1

Siani, G., Michel, E., De Pol-Holz, R., DeVries, T., Lamy, F., Carel, M., Isguder, G., Dewilde, F., Lourantou, A., 2013. Carbon isotope records reveal precise timing of enhanced Southern Ocean upwelling during the last deglaciation. Nature Communications 4, 2758.

Siegenthaler, U., Stocker, T.F., Monnin, E., Lüthi, D., Schwander, J., Stauffer, B., Raynaud, D., Barnola, J.-M., Fischer, H., Masson-Delmotte, V., Jouzel, J., 2005. Stable Carbon Cycle–Climate Relationship During the Late Pleistocene. Science 310, 1313. https://doi.org/10.1126/science.1120130

Siegesmund, S., Basei, M., Oyhantçabal, P., 2011. Multi-accretional tectonics at the Rio de la Plata Craton margins: preface. International Journal of Earth Sciences 100, 197–200. https://doi.org/10.1007/s00531-010-0616-0

Sime, L.C., Kohfeld, K.E., Le Quéré, C., Wolff, E.W., de Boer, A.M., Graham, R.M., Bopp, L., 2013. Southern Hemisphere westerly wind changes during the Last Glacial Maximum: model-data comparison. Quaternary Science Reviews 64, 104–120. https://doi.org/10.1016/j.quascirev.2012.12.008

Skinner, L.C., Fallon, S., Waelbroeck, C., Michel, E., Barker, S., 2010. Ventilation of the Deep Southern Ocean and Deglacial CO2 Rise. Science 328, 1147. https://doi.org/10.1126/science.1183627

Skinner, L.C., Scrivner, A.E., Vance, D., Barker, S., Fallon, S., Waelbroeck, C., 2013. North Atlantic versus Southern Ocean contributions to a deglacial surge in deep ocean ventilation. Geology 41, 667–670. https://doi.org/10.1130/G34133.1

Skinner, L.C., Waelbroeck, C., Scrivner, A.E., Fallon, S.J., 2014. Radiocarbon evidence for alternating northern and southern sources of ventilation of the deep Atlantic carbon pool during the last deglaciation. Proc Natl Acad Sci USA 111, 5480. https://doi.org/10.1073/pnas.1400668111

Smith, J., Vance, D., Kemp, R.A., Archer, C., Toms, P., King, M., Zárate, M., 2003. Isotopic constraints on the source of Argentinian loess – with implications for atmospheric circulation and the provenance of Antarctic dust during recent glacial maxima. Earth

and Planetary Science Letters 212, 181–196. https://doi.org/10.1016/S0012-821X(03)00260-7

Speer, K.G., Zenk, W., 1993. The Flow of Antarctic Bottom Water into the Brazil Basin. J. Phys. Oceanogr. 23, 2667–2682. https://doi.org/10.1175/1520-0485(1993)023<2667:TFOABW>2.0.CO;2

Spooner, P.T., Thornalley, D.J.R., Ellis, P., 2018. Grain Size Constraints on Glacial Circulation in the Southwest Atlantic. Paleoceanography and Paleoclimatology 33, 21–30. https://doi.org/10.1002/2017PA003232

Stern, C.R., Frey, F.A., Futa, K., Zartman, R.E., Peng, Z., Kurtis Kyser, T., 1990. Trace-element and Sr, Nd, Pb, and O isotopic composition of Pliocene and Quaternary alkali basalts of the Patagonian Plateau lavas of southernmost South America. Contributions to Mineralogy and Petrology 104, 294–308. https://doi.org/10.1007/BF00321486

Stramma, L., England, M., 1999. On the water masses and mean circulation of the South Atlantic Ocean. Journal of Geophysical Research: Oceans 104, 20863–20883. https://doi.org/10.1029/1999JC900139

Stramma, L., Ikeda, Y., Peterson, R.G., 1990. Geostrophic transport in the Brazil current region north of 20°S. Deep Sea Research Part A. Oceanographic Research Papers 37, 1875–1886. https://doi.org/10.1016/0198-0149(90)90083-8

Tanaka, T., Togashi, S., Kamioka, H., Amakawa, H., Kagami, H., Hamamoto, T., Yuhara, M., Orihashi, Y., Yoneda, S., Shimizu, H., Kunimaru, T., Takahashi, K., Yanagi, T., Nakano, T., Fujimaki, H., Shinjo, R., Asahara, Y., Tanimizu, M., Dragusanu, C., 2000. JNdi-1: a neodymium isotopic reference in consistency with LaJolla neodymium. Chemical Geology 168, 279–281. https://doi.org/10.1016/S0009-2541(00)00198-4

Tapani Rämö, O., Heikkilä, P.A., Pulkkinen, A.H., 2016. Geochemistry of Paraná-Etendeka basalts from Misiones, Argentina: Some new insights into the petrogenesis of high-Ti continental flood basalts. Journal of South American Earth Sciences 67, 25–39. https://doi.org/10.1016/j.jsames.2016.01.008

Thamban, M., Naik, S.S., Mohan, R., Rajakumar, A., Basavaiah, N., D'Souza, W., Kerkar, S., Subramaniam, M.M., Sudhakar, M., Pandey, P.C., 2005. Changes in the source and transport mechanism of terrigenous input to the Indian sector of Southern Ocean during

the late Quaternary and its palaeoceanographic implications. Journal of Earth System Science 114, 443–452. https://doi.org/10.1007/BF02702021

Thornalley, D.J.R., Barker, S., Broecker, W.S., Elderfield, H., McCave, I.N., 2011. The Deglacial Evolution of North Atlantic Deep Convection. Science 331, 202. https://doi.org/10.1126/science.1196812

Thornalley, D.J.R., Elderfield, H., McCave, I.N., 2010. Intermediate and deep water paleoceanography of the northern North Atlantic over the past 21,000 years. Paleoceanography 25. https://doi.org/10.1029/2009PA001833

Tingey, R.J., 1991. The regional geology of Archean and Proterozoic rocks in Antractica., in: The Geology of Antarctica. Oxford University Press, pp. 1–73.

Tingey, R.J., 1982a. Geological map of the southern Prince Charles Mountains, Antarctica.

Tingey, R.J., 1982b. The geologic evolution of the Prince Charles Mountains—an Antarctic Archean cratonic block. Antarctic Geoscience 455–464.

Tingey, R.J., 1981. Geological investigations in Antarctica 1968-1969: The Prydz Bay-Amery ice shelf-prince Charles mountains area. Bureau of Mineral Resources, Geology and Geophysics.

Tingey, R.J., Laird, M.J., Barret, P.J., Ford, A.B., Himmelberg, P.F., Barker, P.F., Dalziel, I.W., Storey, B.C., LeMasurier, W.E., Rex, D.C., Anderson, J.B., Bentley, C.R., Denton, G.H., Prentice, M.L., Burckle, L.H., McKelvey, B.C., Cooper, R.A., Shergold, J.H., Thomson, M.R.A., Truswell, E.M., Young, G.C., Colbert, E.H., Behrent, J.C., Rowler, P.D., Williams, P.L., Pride, D.E., Cassidy, W.A., 1991. The geology of Antarctica. Oxford University Press.

Toggweiler, J.R., Russell, J.L., Carson, S.R., 2006. Midlatitude westerlies, atmospheric CO2, and climate change during the ice ages. Paleoceanography 21. https://doi.org/10.1029/2005PA001154

Toucanne, S., Soulet, G., Freslon, N., Silva Jacinto, R., Dennielou, B., Zaragosi, S., Eynaud, F., Bourillet, J.-F., Bayon, G., 2015. Millennial-scale fluctuations of the European Ice Sheet at the end of the last glacial, and their potential impact on global climate. Quaternary Science Reviews 123, 113–133. https://doi.org/10.1016/j.quascirev.2015.06.010

Tsuchiya, M., Talley, L.D., McCartney, M.S., 1994. Water-mass distributions in the western South Atlantic; A section from South Georgia Island (54S) northward across the equator. Journal of Marine Research 52, 55–81. https://doi.org/10.1357/0022240943076759

Urbano, L., 2011. Global Atmospheric Circulation and Biomes.

van de Flierdt, T., Goldstein, S.L., Hemming, S.R., Roy, M., Frank, M., Halliday, A.N., 2007. Global neodymium–hafnium isotope systematics — revisited. Earth and Planetary Science Letters 259, 432–441. https://doi.org/10.1016/j.epsl.2007.05.003

Vázquez Riveiros, N., Waelbroeck, C., Skinner, L., Roche, D.M., Duplessy, J.-C., Michel, E., 2010. Response of South Atlantic deep waters to deglacial warming during Terminations V and I. Earth and Planetary Science Letters 298, 323–333. https://doi.org/10.1016/j.epsl.2010.08.003

Vera, C., Higgins, W., Amador, J., Ambrizzi, T., Garreaud, R., Gochis, D., Gutzler, D., Lettenmaier, D., Marengo, J., Mechoso, C.R., Nogues-Paegle, J., Dias, P.L.S., Zhang, C., 2006. Toward a Unified View of the American Monsoon Systems. J. Climate 19, 4977–5000. https://doi.org/10.1175/JCLI3896.1

Vidal, L., Schneider, R.R., Marchal, O., Bickert, T., Stocker, T.F., Wefer, G., 1999. Link between the North and South Atlantic during the Heinrich events of the last glacial period. Climate Dynamics 15, 909–919. https://doi.org/10.1007/s003820050321

Vital, H., Stattegger, K., 2000. Major and trace elements of stream sediments from the lowermost Amazon River. Chemical Geology 168, 151–168. https://doi.org/10.1016/S0009-2541(00)00191-1

Waelbroeck, C., Skinner, L.C., Labeyrie, L., Duplessy, J.-C., Michel, E., Vazquez Riveiros, N., Gherardi, J.-M., Dewilde, F., 2011. The timing of deglacial circulation changes in the Atlantic. Paleoceanography 26. https://doi.org/10.1029/2010PA002007

Waichel, B.L., de Lima, E.F., Viana, A.R., Scherer, C.M., Bueno, G.V., Dutra, G., 2012. Stratigraphy and volcanic facies architecture of the Torres Syncline, Southern Brazil, and its role in understanding the Paraná–Etendeka Continental Flood Basalt Province. Journal of Volcanology and Geothermal Research 215–216, 74–82. https://doi.org/10.1016/j.jvolgeores.2011.12.004

Walter, H.J., Hegner, E., Diekmann, B., Kuhn, G., Rutgers van der loeff, M.M., 2000. Provenance and transport of terrigenous sediment in the south Atlantic Ocean and their relations to glacial and interglacial cycles: Nd and Sr isotopic evidence. Geochimica et Cosmochimica Acta 64, 3813–3827. https://doi.org/10.1016/S0016-7037(00)00476-2

Wang, Y., Cheng, H., Edwards, R.L., Kong, X., Shao, X., Chen, S., Wu, J., Jiang, X., Wang, X., An, Z., 2008. Millennial- and orbital-scale changes in the East Asian monsoon over the past 224,000 years. Nature 451, 1090. https://doi.org/10.1038/nature06692

Wang, Y.J., Cheng, H., Edwards, R.L., An, Z.S., Wu, J.Y., Shen, C.-C., Dorale, J.A., 2001. A High-Resolution Absolute-Dated Late Pleistocene Monsoon Record from Hulu Cave, China. Science 294, 2345. https://doi.org/10.1126/science.1064618

Wasilewski, B., Doucet, L.S., Moine, B., Beunon, H., Delpech, G., Mattielli, N., Debaille, V., Delacour, A., Grégoire, M., Guillaume, D., Cottin, J.-Y., 2017. Ultra-refractory mantle within oceanic plateau: Petrology of the spinel harzburgites from Lac Michèle, Kerguelen Archipelago. Lithos 272–273, 336–349. https://doi.org/10.1016/j.lithos.2016.12.010

Watson, A.J., Bakker, D.C.E., Ridgwell, A.J., Boyd, P.W., Law, C.S., 2000. Effect of iron supply on Southern Ocean CO2 uptake and implications for glacial atmospheric CO2. Nature 407, 730–733. https://doi.org/10.1038/35037561

Watson, A.J., Naveira Garabato, A.C., 2006. The role of Southern Ocean mixing and upwelling in glacial-interglacial atmospheric CO2 change. Tellus B: Chemical and Physical Meteorology 58, 73–87. https://doi.org/10.1111/j.1600-0889.2005.00167.x

Wayne Nesbitt, H., Markovics, G., 1997. Weathering of granodioritic crust, long-term storage of elements in weathering profiles, and petrogenesis of siliciclastic sediments. Geochimica et Cosmochimica Acta 61, 1653–1670. https://doi.org/10.1016/S0016-7037(97)00031-8

Weber, S.L., Drijfhout, S.S., 2007. Stability of the Atlantic Meridional Overturning Circulation in the Last Glacial Maximum climate. Geophysical Research Letters 34. https://doi.org/10.1029/2007GL031437

Weis, D., Frey, F.A., Leyrit, H., Gautier, I., 1993. Kerguelen Archipelago revisited: geochemical and isotopic study of the Southeast Province lavas. Earth and Planetary Science Letters 118, 101–119. https://doi.org/10.1016/0012-821X(93)90162-3

Weltje, G.J., 2012. Quantitative models of sediment generation and provenance: State of the art and future developments. Sedimentary Geology 280, 4–20. https://doi.org/10.1016/j.sedgeo.2012.03.010

Weltje, G.J., Prins, M.A., 2007. Genetically meaningful decomposition of grain-size distributions. Sedimentary Geology 202, 409–424. https://doi.org/10.1016/j.sedgeo.2007.03.007

White, W.M., 2007. Trace Elements, in: Geochemistry. pp. 258–312.

Whitehead, J.M., McKelvey, B.C., 2001. The stratigraphy of the Pliocene—lower Pleistocene Bardin Bluffs Formation, Amery Oasis, northern Prince Charles Mountains, Antarctica. Antarctic Science 13, 79–86. https://doi.org/10.1017/S0954102001000128

Wiersma, A.P., Renssen, H., 2006. Model–data comparison for the 8.2kaBP event: confirmation of a forcing mechanism by catastrophic drainage of Laurentide Lakes. Quaternary Science Reviews 25, 63–88. https://doi.org/10.1016/j.quascirev.2005.07.009

Will, T.M., Frimmel, H.E., Zeh, A., Le Roux, P., Schmädicke, E., 2010. Geochemical and isotopic constraints on the tectonic and crustal evolution of the Shackleton Range, East Antarctica, and correlation with other Gondwana crustal segments. Precambrian Research 180, 85–112. https://doi.org/10.1016/j.precamres.2010.03.005

Wilson, A.H., Carlson, R.W., 1989. A SmNd and Pb isotope study of Archaean greenstone belts in the southern Kaapvaal Craton, South Africa. Earth and Planetary Science Letters 96, 89–105. https://doi.org/10.1016/0012-821X(89)90125-8

Wolff, E.W., Fischer, H., Fundel, F., Ruth, U., Twarloh, B., Littot, G.C., Mulvaney, R., Röthlisberger, R., de Angelis, M., Boutron, C.F., Hansson, M., Jonsell, U., Hutterli, M.A., Lambert, F., Kaufmann, P., Stauffer, B., Stocker, T.F., Steffensen, J.P., Bigler, M., Siggaard-Andersen, M.L., Udisti, R., Becagli, S., Castellano, E., Severi, M., Wagenbach, D., Barbante, C., Gabrielli, P., Gaspari, V., 2006. Southern Ocean sea-ice extent, productivity and iron flux over the past eight glacial cycles. Nature 440, 491–496. https://doi.org/10.1038/nature04614

Yu, J., Anderson, R.F., Rohling, E.J., 2014. Deep Ocean Carbonate Chemistry and Glacial-Interglacial Atmospheric CO_2 Changes. Oceanography 27, 16–25.

Yuan, D., Cheng, H., Edwards, R.L., Dykoski, C.A., Kelly, M.J., Zhang, M., Qing, J., Lin, Y., Wang, Y., Wu, J., Dorale, J.A., An, Z., Cai, Y., 2004. Timing, Duration, and Transitions of the Last Interglacial Asian Monsoon. Science 304, 575. https://doi.org/10.1126/science.1091220

Zhang, R., Delworth, T.L., 2007. Impact of the Atlantic Multidecadal Oscillation on North Pacific climate variability. Geophysical Research Letters 34. https://doi.org/10.1029/2007GL031601

Zhang, X., Lohmann, G., Knorr, G., Xu, X., 2013. Different ocean states and transient characteristics in Last Glacial Maximum simulations and implications for deglaciation. Clim. Past 9, 2319–2333. https://doi.org/10.5194/cp-9-2319-2013

Zhao, D., Wan, S., Clift, P.D., Tada, R., Huang, J., Yin, X., Liao, R., Shen, X., Shi, X., Li, A., 2018. Provenance, sea-level and monsoon climate controls on silicate weathering of Yellow River sediment in the northern Okinawa Trough during late last glaciation. Palaeogeography, Palaeoclimatology, Palaeoecology 490, 227–239. https://doi.org/10.1016/j.palaeo.2017.11.002

Zhao, D., Wan, S., Toucanne, S., Clift, P.D., Tada, R., Révillon, S., Kubota, Y., Zheng, X., Yu, Z., Huang, J., Jiang, H., Xu, Z., Shi, X., Li, A., 2017. Distinct control mechanism of fine-grained sediments from Yellow River and Kyushu supply in the northern Okinawa Trough since the last glacial. Geochemistry, Geophysics, Geosystems 18, 2949–2969. https://doi.org/10.1002/2016GC006764

Ziegler, M., Diz, P., Hall, I.R., Zahn, R., 2013. Millennial-scale changes in atmospheric CO2 levels linked to the Southern Ocean carbon isotope gradient and dust flux. Nature Geoscience 6, 457. https://doi.org/10.1038/ngeo1782

Annexes

Annex 1: isotopic data from the litterature

la tude (°N)	longitude (E°)	region (when given)	locality (when given)	grain size frac on (when given)	$^{143}Nd/^{144}Nd$	ε_{Nd}	[Nd] (ppm)	$^{87}Sr/^{86}Sr$	[Sr] (ppm)	$^{206}Pb/^{204}Pb$	$^{207}Pb/^{204}Pb$	$^{208}Pb/^{204}Pb$	[Pb] (ppm)	number of sample	type of sample (when given)	reference
-12,12	12,36	Africa	Angola Basin			-24,9	9							1	core n− TE7-S (1760m)	Jeandel et al., 2007 and references therein
-14,53	10,23	Africa	Angola basin			-18,8	22							1	core n− MD96-2091 (3569m)	Jeandel et al., 2007 and references therein
-25,36	13,23	Africa	Cape basin			-12,2	10							1	core n− MD96-2087 (1028m)	Jeandel et al., 2007 and references therein
-30,58	13,28	Africa	Cape Basin			-11,6	22							1	core n− VM19-240 (3103m)	Jeandel et al., 2007 and references therein
-25,5	11,3	Africa	Cape Basin			-11,6	16							1	core n− RC13-229 (4191m)	Jeandel et al., 2007 and references therein
-29,42	12,56	Africa	Cape basin			-11,0	8							1	core n− MD96-2085 (3001m)	Jeandel et al., 2007 and references therein
-6	12	Africa	Congo			-16,1	35							1	river sediment & n− KZAI-01	Jeandel et al., 2007 and references therein
-19	49	Africa	E Madagascar			-22,1	24							7	rocks	Jeandel et al., 2007 and references therein
-27	33	Africa	Kaapvaal Craton			-30,0	29							41	rocks	Jeandel et al., 2007 and references therein
-33	23	Africa	South Africa			-9,5	37							9	rocks	Jeandel et al., 2007 and references therein
-32	28	Africa	South Africa			-9,2	30							3	rocks	Jeandel et al., 2007 and references therein
-20	34,5	Africa	Zimbabwe			-14,5	15							12	rocks	Jeandel et al., 2007 and references therein
		Africa	Congo	bulk	0,511958	-13,3		0,72257		18,47	15,703	38,75		1	suspended par cles (5m below river's surface)	Allegre et al, 1996
		Africa	Congo	bulk	0,511873	-14,9		0,72333		18,121	15,638	38,44		1	suspended par cles (5m below river's surface)	Allegre et al, 1996
		Africa	Congo	bulk	0,511865	-15,1		0,72583		18,731	15,732	39,23		1	suspended par cles (5m below river's surface)	Allegre et al, 1996
		Africa	Congo	bulk	0,511686	-18,6		0,72839						1	suspended par cles (5m below river's surface)	Allegre et al, 1996
		Africa	Congo	bulk	0,511795	-16,4		0,7316		19,1	15,784	39,35		1	suspended par cles (5m below river's surface)	Allegre et al, 1996
		Africa	Congo	bulk	0,511804	-16,3		0,73398		18,536	15,722	39,06		1	suspended par cles (5m below river's surface)	Allegre et al, 1996
		Africa	Congo	bulk	0,511833	-15,7		0,73639		18,919	15,767	39,08		1	suspended par cles (5m below river's surface)	Allegre et al, 1996
		Africa	Congo	bulk	0,511739	-17,5		0,74668		19,78	15,872	39,5		1	suspended par cles (5m below river's surface)	Allegre et al, 1996
		Africa	Congo	bulk	0,511712	-18,1				19,07	15,853	39,78		1	suspended par cles (5m below river's surface)	Allegre et al, 1996
		Africa	Congo	bulk	0,511765	-17,0								1	suspended par cles (5m below river's surface)	Allegre et al, 1996
-23	15	Africa	Gobabeb	bulk	0,512285	-6,9		0,721688						1	loess	Grousset et al, 1992
-23	15	Africa	Gobabeb	bulk	0,512219	-8,2		0,7232						1	loess	Grousset et al, 1992
-23	15	Africa	Gobabeb	bulk	0,512234	-7,9		0,724816						1	loess	Grousset et al, 1992
-23	15	Africa	Gobabeb	bulk	0,512243	-7,7		0,725423						1	loess	Grousset et al, 1992
3	-6	Africa	Ivory Coast			-9,1	46							1	dust n− JL-42	Jeandel et al., 2007 and references therein
-27,5	20	Africa	Kalahari	bulk	0,512444	-3,8		0,746431						1	loess	Grousset et al, 1992
-27,5	20	Africa	Kalahari	0-5 m	0,512382	-5,0		0,747157						1	loess	Grousset et al, 1992
-27	16	Africa	Luderitz	bulk	0,511534	-21,5		0,723115						1	loess	Grousset et al, 1992
-29	17	Africa	Orangemund	bulk	0,512478	-3,1		0,716897						1	loess	Grousset et al, 1992
-29	17	Africa	Orangemund	bulk	0,511997	-12,5		0,721911						1	loess	Grousset et al, 1992
		Africa	South Africa	whole rock	0,51224	-7,8		0,70949		17,796	15,524	37,796		1	micas brearing kimberlite	Fraser et al, 1985
		Africa	South Africa	whole rock	0,51217	-9,1		0,70956		17,869	15,545	37,9		1	micas brearing kimberlite	Fraser et al, 1985
		Africa	South Africa	whole rock				0,70957		17,909	15,518	37,94		1	micas brearing kimberlite	Fraser et al, 1985
		Africa	South Africa	whole rock	0,51219	-8,7		0,70959		17,889	15,57	37,95		1	micas brearing kimberlite	Fraser et al, 1985
		Africa	South Africa	whole rock	0,51217	-9,1		0,70968		17,994	15,534	37,978		1	micas brearing kimberlite	Fraser et al, 1985
		Africa	South Africa	whole rock	0,51217	-9,1		0,71064		17,739	15,482	37,701		1	micas brearing kimberlite	Fraser et al, 1985
		Africa	South Africa	whole rock	0,51217	-9,1		0,71188		18,245	15,574	38,23		1	micas brearing kimberlite	Fraser et al, 1985
27,5	31	Africa	South Africa	whole rock	0,51081	-35,7	18							1	dacite	Wilson and Carlson, 1989
27,5	31	Africa	South Africa	whole rock	0,510863	-34,6	19							1	dacite	Wilson and Carlson, 1989
27,5	31	Africa	South Africa	whole rock	0,511081	-30,4	70							1	rhyolite	Wilson and Carlson, 1989
27,5	31	Africa	South Africa	whole rock	0,511175	-28,5	80							1	rhyolite	Wilson and Carlson, 1989
27,5	31	Africa	South Africa	whole rock	0,511844	-15,5	11			14,813	14,751	34,8		1	basalt	Wilson and Carlson, 1989
27,5	31	Africa	South Africa	whole rock	0,511934	-13,7	17							1	basalt	Wilson and Carlson, 1989
27,5	31	Africa	South Africa	whole rock	0,511959	-13,2	16							1	basalt	Wilson and Carlson, 1989
27,5	31	Africa	South Africa	whole rock	0,511978	-12,9	10			19,729	16,036	40,52		1	basal c koma i te	Wilson and Carlson, 1989
27,5	31	Africa	South Africa	whole rock	0,511979	-12,9	15			16,753	15,569	37,13		1	basalt	Wilson and Carlson, 1989
27,5	31	Africa	South Africa	whole rock	0,51198	-12,8	11			27,486	17,813	48,28		1	basal c koma i te	Wilson and Carlson, 1989
27,5	31	Africa	South Africa	whole rock	0,511988	-12,7	10			15,826	14,954	36,17		1	basal c koma i te	Wilson and Carlson, 1989
27,5	31	Africa	South Africa	whole rock	0,512	-12,4	1							1	basal c koma i te	Wilson and Carlson, 1989
27,5	31	Africa	South Africa	whole rock	0,512019	-12,1	11			13,411	14,281	33,39		1	basal c koma i te	Wilson and Carlson, 1989
27,5	31	Africa	South Africa	whole rock	0,512047	-11,5	16							1	basalt	Wilson and Carlson, 1989
27,5	31	Africa	South Africa	whole rock	0,512049	-11,5	17			19,35	16,016	40,3		1	basalt	Wilson and Carlson, 1989
27,5	31	Africa	South Africa	whole rock	0,512069	-11,1	11							1	basal c koma i te	Wilson and Carlson, 1989
27,5	31	Africa	South Africa	whole rock	0,512094	-10,6	16							1	basalt	Wilson and Carlson, 1989
27,5	31	Africa	South Africa	whole rock	0,512145	-9,6	6							1	basalt	Wilson and Carlson, 1989
27,5	31	Africa	South Africa	whole rock	0,512156	-9,4	9			26,628	17,993	49,35		1	basalt	Wilson and Carlson, 1989
27,5	31	Africa	South Africa	whole rock	0,512186	-8,8	2			29,196	17,921	48,84		1	basal c koma i te	Wilson and Carlson, 1989
27,5	31	Africa	South Africa	whole rock	0,512195	-8,6	5							1	basalt	Wilson and Carlson, 1989
27,5	31	Africa	South Africa	whole rock	0,512266	-7,3	3			16,826	15,927	36,63		1	basal c koma i te	Wilson and Carlson, 1989
27,5	31	Africa	South Africa	whole rock	0,512268	-7,2	7							1	basal c koma i te	Wilson and Carlson, 1989
27,5	31	Africa	South Africa	whole rock	0,512321	-6,2	8			40,176	20,658	62,01		1	basal c koma i te	Wilson and Carlson, 1989
27,5	31	Africa	South Africa	whole rock	0,512352	-5,6	8			30,337	18,235	48,69		1	basal c koma i te	Wilson and Carlson, 1989
27,5	31	Africa	South Africa	whole rock	0,51237	-5,2	6			14,98	14,762	35,41		1	koma i te	Wilson and Carlson, 1989
27,5	31	Africa	South Africa	whole rock	0,512374	-5,1	13							1	basal c koma i te	Wilson and Carlson, 1989
27,5	31	Africa	South Africa	whole rock	0,512401	-4,6	6							1	koma i te	Wilson and Carlson, 1989
27,5	31	Africa	South Africa	whole rock	0,512477	-3,1	6							1	koma i te	Wilson and Carlson, 1989
27,5	31	Africa	South Africa	whole rock	0,512514	-2,4	6							1	koma i te	Wilson and Carlson, 1989
27,5	31	Africa	South Africa	whole rock	0,512519	-2,3	6							1	koma i te	Wilson and Carlson, 1989
27,5	31	Africa	South Africa	whole rock	0,512523	-2,2	6							1	koma i te	Wilson and Carlson, 1989
27,5	31	Africa	South Africa	whole rock	0,512524	-2,2	6			16,871	15,201	37,2		1	koma i te	Wilson and Carlson, 1989
27,5	31	Africa	South Africa	whole rock	0,512547	-1,8	6			16,144	15,035	36,65		1	koma i te	Wilson and Carlson, 1989
27,5	31	Africa	South Africa	whole rock	0,512547	-1,8	6			20,321	16,169	40,94		1	koma i te	Wilson and Carlson, 1989
27,5	31	Africa	South Africa	whole rock	0,512548	-1,8	7							1	basal c koma i te	Wilson and Carlson, 1989
27,5	31	Africa	South Africa	whole rock	0,512595	-0,8	6							1	koma i te	Wilson and Carlson, 1989
27,5	31	Africa	South Africa	whole rock	0,512617	-0,4	6			16,434	15,192	36,95		1	koma i te	Wilson and Carlson, 1989
27,5	31	Africa	South Africa	whole rock	0,512683	0,9	5			18,653	15,762	39,48		1	koma i te	Wilson and Carlson, 1989
27,5	31	Africa	South Africa	whole rock	0,512694	1,1	7			24,491	17,074	44,13		1	koma i te	Wilson and Carlson, 1989
27,5	31	Africa	South Africa	whole rock	0,512747	2,1	5			22,432	16,674	41,58		1	basal c koma i te	Wilson and Carlson, 1989
27,5	31	Africa	South Africa	whole rock	0,512764	2,5	4							1	basal c koma i te	Wilson and Carlson, 1989

latitude (°N)	longitude (E°)	region (when given)	locality (when given)	grain size fraction (when given)	$^{143}Nd/^{144}Nd$	ε_{Nd}	[Nd] (ppm)	$^{87}Sr/^{86}Sr$	[Sr] (ppm)	$^{206}Pb/^{204}Pb$	$^{207}Pb/^{204}Pb$	$^{208}Pb/^{204}Pb$	[Pb] (ppm)	number of sample	type of sample (when given)	reference
27,5	31	Africa	South Africa	whole rock	0,512941	5,9	6			16,121	15,347	35,65		1	basalt	Wilson and Carlson, 1989
27,5	31	Africa	South Africa	whole rock	0,513	7,1	9			17,758	15,713	37,83		1	basaltic komatiite	Wilson and Carlson, 1989
27,5	31	Africa	South Africa	whole rock	0,513038	7,8	3			17,553	15,621	37,48		1	basaltic komatiite	Wilson and Carlson, 1989
27,5	31	Africa	South Africa	whole rock	0,516143	68,4	0							1	peridotite	Wilson and Carlson, 1989
27,5	31	Africa	South Africa	whole rock	0,516436	74,1	0							1	peridotite	Wilson and Carlson, 1989
27,5	31	Africa	South Africa	whole rock	0,516776	80,7	0							1	peridotite	Wilson and Carlson, 1989
27,5	31	Africa	South Africa	whole rock	0,518892	122,0	0							1	peridotite	Wilson and Carlson, 1989
27,5	31	Africa	South Africa	whole rock	0,519612	136,0	0							1	peridotite	Wilson and Carlson, 1989
27,5	31	Africa	South Africa	whole rock	0,519638	136,5	0							1	peridotite	Wilson and Carlson, 1989
27,5	31	Africa	South Africa	whole rock	0,522474	191,9	0							1	peridotite	Wilson and Carlson, 1989
27,5	31	Africa	South Africa	whole rock	0,522702	196,3	0							1	peridotite	Wilson and Carlson, 1989
27,5	31	Africa	South Africa	whole rock						15,567	14,907	35,85		1	komatiite	Wilson and Carlson, 1989
27,5	31	Africa	South Africa	whole rock			31							1	dacite	Wilson and Carlson, 1989
27,5	31	Africa	South Africa	whole rock						19,118	15,84	39,97		1	komatiite	Wilson and Carlson, 1989
27,5	31	Africa	South Africa	whole rock						21,909	16,493	42,16		1	komatiite	Wilson and Carlson, 1989
27,5	31	Africa	South Africa	whole rock						24,778	17,018	42,73		1	basaltic komatiite	Wilson and Carlson, 1989
27,5	31	Africa	South Africa	whole rock						31,961	18,588	45,8		1	basaltic komatiite	Wilson and Carlson, 1989
27,5	31	Africa	South Africa	whole rock						30,337	18,236	48,69		1	basaltic komatiite	Wilson and Carlson, 1989
27,5	31	Africa	South Africa	whole rock						31,213	18,637	52,39		1	basaltic komatiite	Wilson and Carlson, 1989
27,5	31	Africa	South Africa	whole rock						41,86	20,802	67,33		1	basalt	Wilson and Carlson, 1989
-23	15	Africa	Walvis Bay	bulk	0,512404	-4,6		0,722826						1	loess	Grousset et al, 1992
-6	6	Africa		bulk	0,511775	-16,8								1	marine sediment	Bayon et al, 2009
-5	8	Africa		bulk	0,511807	-16,2								1	marine sediment	Bayon et al, 2009
-5	7	Africa		bulk	0,511815	-16,1								1	marine sediment	Bayon et al, 2009
-25,6	13,3861	Africa		bulk	0,512009	-12,3								1	marine sediment	Bayon et al, 2009
-25,6	13,3861	Africa		bulk	0,512062	-11,2								1	marine sediment	Bayon et al, 2009
-25,6	13,3861	Africa		bulk	0,512087	-10,7								1	marine sediment	Bayon et al, 2009
-25,6	13,3861	Africa		bulk	0,512089	-10,7								1	marine sediment	Bayon et al, 2009
-25,6	13,3861	Africa		bulk	0,512108	-10,3								1	marine sediment	Bayon et al, 2009
-63,5	-59	Antarctica	Scotia arc	whole rock		5,7	21							4	rocks	Jeandel et al., 2007 and references therein
-66	141	Antarctica	Adelie Land	bulk		-24,9		0,736836						1	plateforme	Grousset et al, 1992
-67	140	Antarctica	Adelie Land	bulk	0,512198	-8,6		0,760816						1	moraine	Grousset et al, 1992
-67	140	Antarctica	Adelie Land	0-5 µm	0,512117	-10,2		0,774102						1	moraine	Grousset et al, 1992
-74,65	124,167	Antarctica	Adelie Land	bulk	0,512894	5,0		0,708707						1	dust	Grousset et al, 1992
-72,6043	-6,2072	Antarctica	Annandagstoppane	feldspar						26,6584	17,7865	35,0361		1	granite	Flowerdew et al., 2012
-72,6035	-6,213	Antarctica	Annandagstoppane	feldspar						18,8218	15,8725	34,5087		1	granite	Flowerdew et al., 2012
-72,6035	-6,213	Antarctica	Annandagstoppane	feldspar						20,2765	16,1987	36,8552		1	granite	Flowerdew et al., 2012
-70	-70	Antarctica	Antarctic Peninsula	whole rock	0,512952	6,1		0,70269						1	-	Hole et al, 1993
-70	-70	Antarctica	Antarctic Peninsula	whole rock	0,51292	5,5		0,7027						1	tephrite	Hole et al, 1993
-70	-70	Antarctica	Antarctic Peninsula	whole rock	0,51296	6,3		0,7027						1	tephrite	Hole et al, 1993
-70	-70	Antarctica	Antarctic Peninsula	whole rock	0,512878	4,7		0,70272						1	-	Hole et al, 1993
-70	-70	Antarctica	Antarctic Peninsula	whole rock	0,512883	4,8		0,70276						1	-	Hole et al, 1993
-70	-70	Antarctica	Antarctic Peninsula	whole rock	0,51288	4,7		0,7028						1	tephrite	Hole et al, 1993
-66	-61	Antarctica	Antarctic Peninsula	whole rock	0,51299	6,9		0,7028						1	alkaline basalt	Hole et al, 1993
-66	-61	Antarctica	Antarctic Peninsula	whole rock	0,512994	6,9		0,7028						1	-	Hole et al, 1993
-66	-61	Antarctica	Antarctic Peninsula	whole rock	0,512924	5,6		0,703						1	-	Hole et al, 1993
-70	-70	Antarctica	Antarctic Peninsula	whole rock	0,51294	5,9		0,703						1	basanite	Hole et al, 1993
-66	-61	Antarctica	Antarctic Peninsula	whole rock	0,51294	5,9		0,703						1	tholeite	Hole et al, 1993
-70	-70	Antarctica	Antarctic Peninsula	whole rock	0,51296	6,3		0,703						1	alkaline basalt	Hole et al, 1993
-70	-70	Antarctica	Antarctic Peninsula	whole rock	0,512923	5,6		0,70305						1	-	Hole et al, 1993
-66	-61	Antarctica	Antarctic Peninsula	whole rock	0,51291	5,3		0,70306						1	-	Hole et al, 1993
-66	-61	Antarctica	Antarctic Peninsula	whole rock	0,512957	6,2		0,70308						1	-	Hole et al, 1993
-66	-61	Antarctica	Antarctic Peninsula	whole rock	0,512904	5,2		0,70309						1	-	Hole et al, 1993
-66	-61	Antarctica	Antarctic Peninsula	whole rock	0,51296	6,3		0,7031						1	alkaline basalt	Hole et al, 1993
-66	-61	Antarctica	Antarctic Peninsula	whole rock				0,70313						1	-	Hole et al, 1993
-66	-61	Antarctica	Antarctic Peninsula	whole rock	0,51283	3,7		0,70325						1	-	Hole et al, 1993
-66	-61	Antarctica	Antarctic Peninsula	whole rock	0,5128036	3,2		0,70326						1	-	Hole et al, 1993
-66	-61	Antarctica	Antarctic Peninsula	whole rock	0,51284	3,9		0,7033						1	tholeite	Hole et al, 1993
-70	-70	Antarctica	Antarctic Peninsula	whole rock	0,51286	4,3		0,7033						1	olivine bearing basalt	Hole et al, 1993
-70	-70	Antarctica	Antarctic Peninsula	whole rock	0,512863	4,4		0,70331						1	-	Hole et al, 1993
-66	-61	Antarctica	Antarctic Peninsula	whole rock	0,512852	4,2		0,70336						1	-	Hole et al, 1993
-70	-80	Antarctica	Antarctic Peninsula			-4,1	55							1	core n− ELT42-09	Jeandel et al., 2007 and references therein
-66	-72	Antarctica	Antarctic Peninsula			-3,2	0							1	core n−2	Jeandel et al., 2007 and references therein
-65	-70	Antarctica	Antarctic Peninsula			1,1	0							1	core n−1	Jeandel et al., 2007 and references therein
-69,5	-70,9	Antarctica	Antarctic Peninsula			5,5	38							6	rocks	Jeandel et al., 2007 and references therein
-63,81233333	-57,83166667	Antarctica	Antarctic Peninsula	whole rock	0,51289	4,9		0,703175		18,953	15,608	38,637		1	basalt lava flow	Kosler et al., 2009
-63,869	-58,108	Antarctica	Antarctic Peninsula	whole rock	0,512888	4,9		0,703188		18,932	15,614	38,646		1	basalt lava flo	Kosler et al., 2009
-63,852	-58,059	Antarctica	Antarctic Peninsula	whole rock	0,512903	5,2		0,703211		18,829	15,584	38,463		1	dolerite volcanic plug	Kosler et al., 2009
-63,80883333	-57,8245	Antarctica	Antarctic Peninsula	whole rock	0,512891	4,9		0,703216		18,916	15,608	38,626		1	basalt lava flow	Kosler et al., 2009
-63,81766667	-57,94166667	Antarctica	Antarctic Peninsula	whole rock	0,512899	5,1		0,703216		18,745	15,596	38,47		1	dolerite lava flow	Kosler et al., 2009
-63,88616667	-57,903	Antarctica	Antarctic Peninsula	whole rock	0,512905	5,2		0,703222		18,849	15,599	38,549		1	dolerite dyke	Kosler et al., 2009
-63,8745	-58,079	Antarctica	Antarctic Peninsula	whole rock	0,512866	4,4		0,703256		18,974	15,616	38,692		1	dolerite lava flow	Kosler et al., 2009
-63,82716667	-57,9365	Antarctica	Antarctic Peninsula	whole rock	0,512895	5,0		0,703256		18,894	15,602	38,554		1	dolerite lava flow	Kosler et al., 2009
-63,81233333	-57,83166667	Antarctica	Antarctic Peninsula	whole rock	0,512889	4,9		0,703281		18,972	15,608	38,658		1	basalt lava flow	Kosler et al., 2009
-63,811	-57,88916667	Antarctica	Antarctic Peninsula	whole rock	0,512903	5,2		0,703281		18,859	15,618	38,617		1	basalt pillow breccia	Kosler et al., 2009
-63,809	-57,91666667	Antarctica	Antarctic Peninsula	whole rock	0,512866	4,4		0,703369		18,775	15,625	38,531		1	dolerite volcanic plug	Kosler et al., 2009
-63,79216667	-57,81	Antarctica	Antarctic Peninsula	whole rock	0,512884	4,8		0,703387		18,855	15,601	38,556		1	basalt pillow lava	Kosler et al., 2009
-63,797	-57,80083333	Antarctica	Antarctic Peninsula	whole rock	0,512896	5,0		0,703737		18,841	15,603	38,544		1	basalt pillow lava	Kosler et al., 2009
-63,80316667	-57,95166667	Antarctica	Antarctic Peninsula	whole rock	0,512818	3,5		0,703948		18,857	15,619	38,644		1	basalt dyke	Kosler et al., 2009
62,95983333	60,66066667	Antarctica	Antarctic Peninsula	whole rock	0,513004	7,1	24	0,703714		18,629	15,585	38,358		1	marine sediment	Lee et al., 2005
62,23366667	58,32883333	Antarctica	Antarctic Peninsula	whole rock	0,512846	4,1	25	0,705187		18,680	15,618	38,523		1	marine sediment	Lee et al., 2005

latitude (°N)	longitude (E°)	region (when given)	locality (when given)	grain size fraction (when given)	$^{143}Nd/^{144}Nd$	ε_{Nd}	[Nd] (ppm)	$^{87}Sr/^{86}Sr$	[Sr] (ppm)	$^{206}Pb/^{204}Pb$	$^{207}Pb/^{204}Pb$	$^{208}Pb/^{204}Pb$	[Pb] (ppm)	number of sample	type of sample (when given)	reference
63,151	61,07416667	Antarctica	Antarctic Peninsula	whole rock	0,512747	2,1	20	0,705618		18,721	15,606	38,538		1	marine sediment	Lee et al., 2005
-69,99	-80,4	Antarctica	Antarctic Peninsula	0-63 µm	0,51242	-4,3	55							1	marine sediment	Roy et al, 2007
-67,18	-74,78	Antarctica	Antarctic Peninsula	0-63 µm	0,512469	-3,3	38							1	marine sediment	Roy et al, 2007
-65,95	-70,25	Antarctica	Antarctic Peninsula	0-63 µm	0,512685	0,9	41							1	marine sediment	Roy et al, 2007
-67,37	49,2	Antarctica	Antarctica	whole rock		-38,2	37							7	rocks	Jeandel et al., 2007 and references therein
-75,9424	-70,3359	Antarctica	Bean Peaks	feldspar						19,3417	15,7815	39,0881		1	granite	Flowerdew et al., 2012
		Antarctica	Berkner	feldspar						14,717	14,687	35,674		1	basal ice core sand	Flowerdew et al., 2012
		Antarctica	Berkner	feldspar						15,706	14,825	33,961		1	basal ice core sand	Flowerdew et al., 2012
		Antarctica	Berkner	feldspar						15,714	14,969	35,745		1	basal ice core sand	Flowerdew et al., 2012
		Antarctica	Berkner	feldspar						15,819	14,821	38,423		1	basal ice core sand	Flowerdew et al., 2012
		Antarctica	Berkner	feldspar						16,444	15,155	36,924		1	basal ice core sand	Flowerdew et al., 2012
		Antarctica	Berkner	feldspar						16,465	15,199	37,864		1	basal ice core sand	Flowerdew et al., 2012
		Antarctica	Berkner	feldspar						16,776	15,2	36,915		1	basal ice core sand	Flowerdew et al., 2012
		Antarctica	Berkner	feldspar						16,94	15,422	37,082		1	basal ice core sand	Flowerdew et al., 2012
		Antarctica	Berkner	feldspar						17,038	15,472	37,998		1	basal ice core sand	Flowerdew et al., 2012
		Antarctica	Berkner	feldspar						17,435	15,28	36,371		1	basal ice core sand	Flowerdew et al., 2012
		Antarctica	Berkner	feldspar						17,474	15,511	37,416		1	basal ice core sand	Flowerdew et al., 2012
		Antarctica	Berkner	feldspar						17,595	15,523	37,438		1	basal ice core sand	Flowerdew et al., 2012
		Antarctica	Berkner	feldspar						17,597	15,462	37,345		1	basal ice core sand	Flowerdew et al., 2012
		Antarctica	Berkner	feldspar						17,626	15,459	37,123		1	basal ice core sand	Flowerdew et al., 2012
		Antarctica	Berkner	feldspar						17,696	15,459	36,991		1	basal ice core sand	Flowerdew et al., 2012
		Antarctica	Berkner	feldspar						17,701	15,496	37,4		1	basal ice core sand	Flowerdew et al., 2012
		Antarctica	Berkner	feldspar						17,708	15,526	37,499		1	basal ice core sand	Flowerdew et al., 2012
		Antarctica	Berkner	feldspar						17,714	15,503	37,356		1	basal ice core sand	Flowerdew et al., 2012
		Antarctica	Berkner	feldspar						17,741	15,472	37,292		1	basal ice core sand	Flowerdew et al., 2012
		Antarctica	Berkner	feldspar						17,764	15,518	37,525		1	basal ice core sand	Flowerdew et al., 2012
		Antarctica	Berkner	feldspar						17,774	15,428	37,001		1	basal ice core sand	Flowerdew et al., 2012
		Antarctica	Berkner	feldspar						17,78	15,545	37,344		1	basal ice core sand	Flowerdew et al., 2012
		Antarctica	Berkner	feldspar						17,83	15,649	37,965		1	basal ice core sand	Flowerdew et al., 2012
		Antarctica	Berkner	feldspar						17,857	15,667	37,717		1	basal ice core sand	Flowerdew et al., 2012
		Antarctica	Berkner	feldspar						17,867	15,502	37,138		1	basal ice core sand	Flowerdew et al., 2012
		Antarctica	Berkner	feldspar						17,876	15,573	37,605		1	basal ice core sand	Flowerdew et al., 2012
		Antarctica	Berkner	feldspar						17,91	15,583	37,579		1	basal ice core sand	Flowerdew et al., 2012
		Antarctica	Berkner	feldspar						17,922	15,569	37,476		1	basal ice core sand	Flowerdew et al., 2012
		Antarctica	Berkner	feldspar						17,966	15,573	37,427		1	basal ice core sand	Flowerdew et al., 2012
		Antarctica	Berkner	feldspar						17,984	15,548	37,463		1	basal ice core sand	Flowerdew et al., 2012
		Antarctica	Berkner	feldspar						17,998	15,649	37,663		1	basal ice core sand	Flowerdew et al., 2012
		Antarctica	Berkner	feldspar						18,072	15,498	37,285		1	basal ice core sand	Flowerdew et al., 2012
		Antarctica	Berkner	feldspar						18,154	15,602	37,787		1	basal ice core sand	Flowerdew et al., 2012
		Antarctica	Berkner	feldspar						18,217	15,551	37,589		1	basal ice core sand	Flowerdew et al., 2012
		Antarctica	Berkner	feldspar						18,227	15,639	37,807		1	basal ice core sand	Flowerdew et al., 2012
		Antarctica	Berkner	feldspar						18,239	15,645	37,833		1	basal ice core sand	Flowerdew et al., 2012
		Antarctica	Berkner	feldspar						18,248	15,661	37,762		1	basal ice core sand	Flowerdew et al., 2012
		Antarctica	Berkner	feldspar						18,25	15,58	37,854		1	basal ice core sand	Flowerdew et al., 2012
		Antarctica	Berkner	feldspar						18,282	15,565	37,583		1	basal ice core sand	Flowerdew et al., 2012
		Antarctica	Berkner	feldspar						18,308	15,616	37,652		1	basal ice core sand	Flowerdew et al., 2012
		Antarctica	Berkner	feldspar						18,344	15,635	37,905		1	basal ice core sand	Flowerdew et al., 2012
		Antarctica	Berkner	lithic						18,385	15,621	38,123		1	basal ice core sand	Flowerdew et al., 2012
		Antarctica	Berkner	feldspar						18,429	15,618	38,124		1	basal ice core sand	Flowerdew et al., 2012
		Antarctica	Berkner	lithic						18,453	15,607	38,039		1	basal ice core sand	Flowerdew et al., 2012
		Antarctica	Berkner	feldspar						18,473	15,752	37,953		1	basal ice core sand	Flowerdew et al., 2012
		Antarctica	Berkner	lithic						18,562	15,59	37,887		1	basal ice core sand	Flowerdew et al., 2012
		Antarctica	Berkner	feldspar						18,567	15,602	38,188		1	basal ice core sand	Flowerdew et al., 2012
		Antarctica	Berkner	lithic						18,655	15,599	38,404		1	basal ice core sand	Flowerdew et al., 2012
		Antarctica	Berkner	lithic						18,825	15,633	38,649		1	basal ice core sand	Flowerdew et al., 2012
		Antarctica	Berkner	feldspar						19,008	15,681	38,582		1	basal ice core sand	Flowerdew et al., 2012
		Antarctica	Berkner	feldspar						19,494	15,784	36,186		1	basal ice core sand	Flowerdew et al., 2012
-67	102	Antarctica	Bunger Hills	bulk				0,72512						1	moraine	Basile et al, 1997
-66,7833	-64,0042	Antarctica	Cole Peninsula	feldspar						18,7858	15,6515	38,4703		1	granite	Flowerdew et al., 2012
		Antarctica	Dronning Maud Land	feldspar						17,589	15,555	37,234		1	granite gneiss	Flowerdew et al., 2012
		Antarctica	Dronning Maud Land	feldspar						17,571	15,511	37,074		1	granite gneiss	Flowerdew et al., 2012
		Antarctica	Dronning Maud Land	feldspar						17,491	15,529	36,829		1	granite gneiss	Flowerdew et al., 2012
		Antarctica	Dronning Maud Land	feldspar						19,739	16,101	33,206		1	Annadagstoppane granite	Flowerdew et al., 2012
		Antarctica	Dronning Maud Land	feldspar						21,729	16,532	33,248		1	Annadagstoppane granite	Flowerdew et al., 2012
		Antarctica	Dronning Maud Land	feldspar						16,546	15,159	32,746		1	Annadagstoppane granite	Flowerdew et al., 2012
		Antarctica	Dronning Maud Land	feldspar						17,312	15,58	36,84		1	granite gneiss	Flowerdew et al., 2012
		Antarctica	Dronning Maud Land	feldspar						17,119	15,444	36,498		1	granite gneiss	Flowerdew et al., 2012
		Antarctica	Dronning Maud Land	feldspar						17,317	15,588	36,885		1	granite gneiss	Flowerdew et al., 2012
-70	20	Antarctica	Dronning Maud Land			-14,0	60							3	core	Jeandel et al., 2007 and references therein
-74,62333333	-9,983333333	Antarctica	Dronning Maud Land	whole rock	0,51284	3,9	16	0,70386	337					1	Björnnutane mountains	Luttinen et al., 2010
-74,63	-10	Antarctica	Dronning Maud Land	whole rock	0,512861	4,4	10	0,70386	298,4					1	Björnnutane mountains	Luttinen et al., 2010
-74,62333333	-9,983333333	Antarctica	Dronning Maud Land	whole rock	0,512713	1,5	19	0,70394	378					1	Björnnutane mountains	Luttinen et al., 2010
-74,62333333	-9,983333333	Antarctica	Dronning Maud Land	whole rock	0,51268	0,8	14	0,70409	302,7					1	Björnnutane mountains	Luttinen et al., 2010
-74,61833333	-10,025	Antarctica	Dronning Maud Land	whole rock	0,512785	2,9	12	0,70426	218,6					1	Björnnutane mountains	Luttinen et al., 2010
-74,47666667	-8,138333333	Antarctica	Dronning Maud Land	whole rock	0,51269	1,0	11	0,70475	146,6					1	Sembberget mountains	Luttinen et al., 2010
-74,47666667	-8,138333333	Antarctica	Dronning Maud Land	whole rock	0,512689	1,0	14	0,70531	154,6					1	Sembberget mountains	Luttinen et al., 2010
-74,47666667	-8,138333333	Antarctica	Dronning Maud Land	whole rock	0,512673	0,7	15	0,70561	165,1					1	Sembberget mountains	Luttinen et al., 2010
-74,47666667	-8,138333333	Antarctica	Dronning Maud Land	whole rock	0,51251	-2,5	14	0,70568	172,6					1	Sembberget mountains	Luttinen et al., 2010
-74,62333333	-9,983333333	Antarctica	Dronning Maud Land	whole rock	0,512511	-2,5	21	0,70577	188					1	Sembberget mountains	Luttinen et al., 2010
-74,47666667	-8,138333333	Antarctica	Dronning Maud Land	whole rock	0,512537	-2,0	18	0,70616	162,7					1	Sembberget mountains	Luttinen et al., 2010
-74,62333333	-9,983333333	Antarctica	Dronning Maud Land	whole rock	0,512316	-6,3	15	0,7062	296,4					1	Björnnutane mountains	Luttinen et al., 2010

latitude (°N)	longitude (E°)	region (when given)	locality (when given)	grain size fraction (when given)	$^{143}Nd/^{144}Nd$	ε_{Nd}	[Nd] (ppm)	$^{87}Sr/^{86}Sr$	[Sr] (ppm)	$^{206}Pb/^{204}Pb$	$^{207}Pb/^{204}Pb$	$^{208}Pb/^{204}Pb$	[Pb] (ppm)	number of sample	type of sample (when given)	reference
-74,61833333	-10,06	Antarctica	Dronning Maud Land	whole rock	0,51234	-5,8	14	0,70663	289,5					1	Björnnutane mountains	Luttinen et al., 2010
-74,62333333	-9,983333333	Antarctica	Dronning Maud Land	whole rock	0,512304	-6,5	22	0,7069	310					1	Björnnutane mountains	Luttinen et al., 2010
-74,61833333	-10,025	Antarctica	Dronning Maud Land	whole rock	0,512474	-3,2	13	0,70815	122,7					1	Sembberget mountains	Luttinen et al., 2010
-74,62333333	-9,983333333	Antarctica	Dronning Maud Land	whole rock	0,512394	-4,8	23	0,70926	145					1	Sembberget mountains	Luttinen et al., 2010
-74,47666667	-8,138333333	Antarctica	Dronning Maud Land	whole rock	0,512373	-5,2	17	0,70937	147,5					1	Sembberget mountains	Luttinen et al., 2010
-65,4	36,72	Antarctica	Dronning Maud Land	0-63 µm	0,511749	-17,3	20							1	marine sediment	Roy et al, 2007
-68,61	10,97	Antarctica	Dronning Maud Land	0-63 µm	0,512074	-11,0	65							1	marine sediment	Roy et al, 2007
-70	-5,08	Antarctica	Dronning Maud Land	0-63 µm	0,511867	-15,0	95							1	marine sediment	van de Flierdt, 2007
-80,34166667	-24,03583333	Antarctica	Dronning Maud Land	whole rock	0,51262	-0,4	14	0,7035	187	21,0113	15,7579	40,9695		1	felsic amphibolite	Will et al., 2010
-80,39166667	-29,52166667	Antarctica	Dronning Maud Land	whole rock	0,51205	-11,5	60	0,70632	1127	17,4717	15,5074	37,9251		1	amphibolite	Will et al., 2010
-80,63666667	-20,6375	Antarctica	Dronning Maud Land	whole rock	0,512311	-6,4	65	0,70666	576	18,7319	15,6587	38,661		1	felsic amphibolite	Will et al., 2010
-80,60133333	-19,09166667	Antarctica	Dronning Maud Land	whole rock	0,512311	-6,4	65	0,70666	576	18,7319	15,6587	38,661		1	metagranite	Will et al., 2010
-80,38466667	-29,651	Antarctica	Dronning Maud Land	whole rock				0,70666	576	18,7319	15,6587	38,661		1	metasyenodiorite	Will et al., 2010
-80,53916667	-19,60166667	Antarctica	Dronning Maud Land	whole rock	0,51266	0,4	21	0,7071	258	21,2545	15,7692	40,4688		1	amphibolite	Will et al., 2010
-80,34166667	-24,03583333	Antarctica	Dronning Maud Land	whole rock	0,51266	0,4	21	0,7071	258	21,2545	15,7692	40,4688		1	garnet bearing amphibolite	Will et al., 2010
-80,65666667	-25,05166667	Antarctica	Dronning Maud Land	whole rock	0,51102	-31,6	130	0,71028	1939	17,1038	15,5286	39,2776		1	metadiorite	Will et al., 2010
-80,37583333	-29,7075	Antarctica	Dronning Maud Land	whole rock	0,51224	-7,8	90	0,71228	378	19,3482	15,631	40,6719		1	amphibolite	Will et al., 2010
-80,39166667	-29,52166667	Antarctica	Dronning Maud Land	whole rock				0,72028	320	18,3403	15,6198	38,4063		1	garnet bearing metagranite	Will et al., 2010
-80,40466667	-29,65833333	Antarctica	Dronning Maud Land	whole rock	0,5122	-8,5	12	0,72219	305	19,9927	15,9193	38,1389		1	metadiorite	Will et al., 2010
-80,72433333	-25,76816667	Antarctica	Dronning Maud Land	whole rock				0,72219	305	19,9927	15,9193	38,1389		1	amphibolite	Will et al., 2010
-80,40466667	-29,65833333	Antarctica	Dronning Maud Land	whole rock				0,72478	267	18,7179	15,6563	38,4092		1	garnet bearing metagranite	Will et al., 2010
-80,40466667	-29,65833333	Antarctica	Dronning Maud Land	whole rock				0,72604	281	18,7008	15,6561	38,4485		1	metadiorite	Will et al., 2010
-80,37583333	-29,7075	Antarctica	Dronning Maud Land	whole rock	0,512065	-11,2	75							1	amphibolite	Will et al., 2010
-80,72433333	-25,76816667	Antarctica	Dronning Maud Land	whole rock	0,5122	-8,5	12							1	amphibolite	Will et al., 2010
-80,38466667	-29,651	Antarctica	Dronning Maud Land	whole rock	0,512264	-7,3	76							1	orthogneiss	Will et al., 2010
-80,4025	-29,54033333	Antarctica	Dronning Maud Land	whole rock	0,512311	-6,4	65							1	felsic amphibolite	Will et al., 2010
-80,40266667	-29,6705	Antarctica	Dronning Maud Land	whole rock	0,512687	1,0	32							1	metadioritic orthogneiss	Will et al., 2010
-78	165	Antarctica	Dry Valley	0-30 µm	0,512175	-9,0		0,7128678						1	sand	Basile et al, 1997
-72,1667	-62,3333	Antarctica	E Palmer Land	feldspar						18,7348	15,6459	38,5795		1	granitoid	Flowerdew et al., 2012
		Antarctica	Enderby Land	whole rock	0,511175	-28,5		0,73003						1	rayner complex paragneiss	Black et al., 1987
		Antarctica	Enderby Land	whole rock				0,73233						1	rayner complex paragneiss	Black et al., 1987
		Antarctica	Enderby Land	whole rock				0,7347						1	rayner complex paragneiss	Black et al., 1987
		Antarctica	Enderby Land	whole rock				0,73353						1	rayner complex paragneiss	Black et al., 1987
		Antarctica	Enderby Land	whole rock				0,73701						1	rayner complex paragneiss	Black et al., 1987
		Antarctica	Enderby Land	whole rock				0,7275						1	rayner complex paragneiss	Black et al., 1987
		Antarctica	Enderby Land	whole rock				0,7296						1	rayner complex paragneiss	Black et al., 1987
		Antarctica	Enderby Land	whole rock				0,74127						1	rayner complex paragneiss	Black et al., 1987
		Antarctica	Enderby Land	whole rock				0,79608						1	rayner complex paragneiss	Black et al., 1987
		Antarctica	Enderby Land	whole rock	0,510791	-36,0		0,83148						1	rayner complex pegmatite	Black et al., 1987
		Antarctica	Enderby Land	whole rock	0,510682	-38,2		0,82156						1	rayner complex orthogneiss	Black et al., 1987
		Antarctica	Enderby Land	whole rock	0,510462	-42,4		0,82562						1	rayner complex granite	Black et al., 1987
		Antarctica	Enderby Land	whole rock				0,82618						1	rayner complex granite	Black et al., 1987
		Antarctica	Enderby Land	whole rock				0,8313						1	rayner complex granite	Black et al., 1987
		Antarctica	Enderby Land	whole rock				0,82969						1	rayner complex granite	Black et al., 1987
		Antarctica	Enderby Land	whole rock	0,51071	-37,6		0,80019						1	rayner complex orthogneiss	Black et al., 1987
		Antarctica	Enderby Land	whole rock	0,510692	-38,0		0,7165						1	rayner complex anothosic gneiis	Black et al., 1987
		Antarctica	Enderby Land	whole rock				0,73512						1	rayner complex anothosic gneiis	Black et al., 1987
		Antarctica	Enderby Land	whole rock				0,72133						1	rayner complex anothosic gneiis	Black et al., 1987
		Antarctica	Enderby Land	whole rock				0,72252						1	rayner complex anothosic gneiis	Black et al., 1987
		Antarctica	Enderby Land	whole rock				0,7567						1	rayner complex anothosic gneiis	Black et al., 1987
		Antarctica	Enderby Land	whole rock				0,72942						1	rayner complex anothosic gneiis	Black et al., 1987
		Antarctica	Enderby Land	whole rock				0,71978						1	rayner complex anothosic gneiis	Black et al., 1987
		Antarctica	Enderby Land	whole rock				0,72231						1	rayner complex anothosic gneiis	Black et al., 1987
		Antarctica	Enderby Land	whole rock				0,72301						1	rayner complex anothosic gneiis	Black et al., 1987
		Antarctica	Enderby Land	whole rock	0,510573	-40,3		0,73795						1	rayner complex anothosic gneiis	Black et al., 1987
		Antarctica	Enderby Land	whole rock				0,74604						1	charnockite	Black et al., 1987
		Antarctica	Enderby Land	whole rock				0,74651						1	charnockite	Black et al., 1987
		Antarctica	Enderby Land	whole rock				0,74852						1	charnockite	Black et al., 1987
		Antarctica	Enderby Land	whole rock				0,75045						1	charnockite	Black et al., 1987
		Antarctica	Enderby Land	whole rock				0,74509						1	charnockite	Black et al., 1987
		Antarctica	Enderby Land	whole rock				0,74855						1	charnockite	Black et al., 1987
-65	50	Antarctica	Enderby Land	whole rock	0,51085	-34,9		0,7078						1	2 pyroxenes garnet bearing granulite	DePaolo et al, 1982
-65	50	Antarctica	Enderby Land	whole rock	0,51019	-47,8		0,7134						1	quartzofeldspathic granulite	DePaolo et al, 1982
-65	50	Antarctica	Enderby Land	whole rock	0,50944	-62,4		0,7157						1	quartzofeldspathic granulite	DePaolo et al, 1982
-65	50	Antarctica	Enderby Land	whole rock	0,50961	-59,1		0,7164						1	magnesian pyroxene bearing granulite	DePaolo et al, 1982
-65	50	Antarctica	Enderby Land	whole rock	0,50969	-57,5		0,7189						1	bounded iron formation	DePaolo et al, 1982
-65	50	Antarctica	Enderby Land	whole rock	0,50996	-52,2		0,7372						1	magnesian pyroxene bearing granulite	DePaolo et al, 1982
-65	50	Antarctica	Enderby Land	whole rock	0,50943	-62,6		0,816						1	quartzofeldspathic granulite	DePaolo et al, 1982
		Antarctica	Enderby Land	whole rock	0,50913	-68,4	16	0,79991	129,2					1	charnockite	McCulloch, 1984
		Antarctica	Enderby Land	whole rock	0,50936	-63,9	6	0,83517	99,8					1	charnockite	McCulloch, 1984
		Antarctica	Enderby Land	whole rock	0,50979	-55,6	10	0,74362	93,6					1	charnockite	McCulloch, 1984
		Antarctica	Enderby Land	whole rock	0,50917	-67,7	5	0,83196	133,1					1	charnockite	McCulloch, 1984
		Antarctica	Enderby Land	whole rock	0,50939	-63,4	13	0,77116	176,2					1	leuconorite	McCulloch, 1984
		Antarctica	Enderby Land	whole rock	0,50997	-52,0	7	0,73648	72					1	leuconorite	McCulloch, 1984
		Antarctica	Enderby Land	whole rock	0,51032	-45,2	6	0,76422	54,6					1	leuconorite	McCulloch, 1984
		Antarctica	Enderby Land	whole rock	0,51034	-44,8	47	0,70884	185,5					1	gabbro	McCulloch, 1984
		Antarctica	Enderby Land	whole rock	0,51067	-38,4	21	0,70565	131					1	gabbro	McCulloch, 1984
		Antarctica	Enderby Land	whole rock	0,51007	-50,1	30	0,70654	249,7					1	gabbro	McCulloch, 1984
-74,014	-77,4799	Antarctica	FitzGerald Bluffs	feldspar						18,7541	15,617	38,33		1	granite	Flowerdew et al., 2012
-75,1	-12,7833	Antarctica	Heimefrontfjella	feldspar						17,732	15,5942	37,5521		1	granite gneiss	Flowerdew et al., 2012
-74,2833	-9,6333	Antarctica	Heimefrontfjella	feldspar						17,6307	15,5435	36,9856		1	granite gneiss	Flowerdew et al., 2012

latitude (°N)	longitude (E°)	region (when given)	locality (when given)	grain size fraction (when given)	$^{143}Nd/^{144}Nd$	ε_{Nd}	[Nd] (ppm)	$^{87}Sr/^{86}Sr$	[Sr] (ppm)	$^{206}Pb/^{204}Pb$	$^{207}Pb/^{204}Pb$	$^{208}Pb/^{204}Pb$	[Pb] (ppm)	number of sample	type of sample (when given)	reference
		Antarctica	Heimefrontfjella	feldspar						17,115	15,518	37,011		1	Permian sandstone	Flowerdew et al., 2012
		Antarctica	Heimefrontfjella	feldspar						17,124	15,529	37,037		1	Permian sandstone	Flowerdew et al., 2012
		Antarctica	Heimefrontfjella	feldspar						17,382	15,492	36,832		1	Permian sandstone	Flowerdew et al., 2012
		Antarctica	Heimefrontfjella	feldspar						17,529	15,521	37,104		1	Permian sandstone	Flowerdew et al., 2012
		Antarctica	Heimefrontfjella	feldspar						17,695	15,576	37,196		1	Permian sandstone	Flowerdew et al., 2012
		Antarctica	Heimefrontfjella	feldspar						17,797	15,477	37,147		1	Permian sandstone	Flowerdew et al., 2012
		Antarctica	Heimefrontfjella	feldspar						17,814	15,587	37,487		1	Permian sandstone	Flowerdew et al., 2012
		Antarctica	Heimefrontfjella	feldspar						17,817	15,503	37,464		1	Permian sandstone	Flowerdew et al., 2012
		Antarctica	Heimefrontfjella	feldspar						17,864	15,466	37,427		1	Permian sandstone	Flowerdew et al., 2012
		Antarctica	Heimefrontfjella	feldspar						17,909	15,231	36,48		1	Permian sandstone	Flowerdew et al., 2012
		Antarctica	Heimefrontfjella	feldspar						17,935	15,373	36,87		1	Permian sandstone	Flowerdew et al., 2012
		Antarctica	Heimefrontfjella	feldspar						17,972	15,497	37,32		1	Permian sandstone	Flowerdew et al., 2012
		Antarctica	Heimefrontfjella	feldspar						18,003	15,545	37,445		1	Permian sandstone	Flowerdew et al., 2012
		Antarctica	Heimefrontfjella	feldspar						18,016	15,558	37,473		1	Permian sandstone	Flowerdew et al., 2012
		Antarctica	Heimefrontfjella	feldspar						18,162	15,648	37,48		1	Permian sandstone	Flowerdew et al., 2012
		Antarctica	Heimefrontfjella	feldspar						18,188	15,553	38,213		1	Permian sandstone	Flowerdew et al., 2012
		Antarctica	Heimefrontfjella	feldspar						18,288	15,404	36,934		1	Permian sandstone	Flowerdew et al., 2012
		Antarctica	Heimefrontfjella	feldspar						18,348	15,542	38,844		1	Permian sandstone	Flowerdew et al., 2012
		Antarctica	Heimefrontfjella	feldspar						18,348	15,542	38,844		1	Permian sandstone	Flowerdew et al., 2012
		Antarctica	Heimefrontfjella	feldspar						18,378	15,503	37,404		1	Permian sandstone	Flowerdew et al., 2012
		Antarctica	Heimefrontfjella	feldspar						18,501	15,582	38,216		1	Permian sandstone	Flowerdew et al., 2012
		Antarctica	Heimefrontfjella	feldspar						18,501	15,593	38,012		1	Permian sandstone	Flowerdew et al., 2012
		Antarctica	Heimefrontfjella	feldspar						18,52	15,661	38,084		1	Permian sandstone	Flowerdew et al., 2012
		Antarctica	Heimefrontfjella	feldspar						18,608	15,617	38,219		1	Permian sandstone	Flowerdew et al., 2012
		Antarctica	Heimefrontfjella	feldspar						18,671	15,629	38,379		1	Permian sandstone	Flowerdew et al., 2012
		Antarctica	Heimefrontfjella	feldspar						18,689	15,64	37,669		1	Permian sandstone	Flowerdew et al., 2012
		Antarctica	Heimefrontfjella	feldspar						18,705	15,54	37,769		1	Permian sandstone	Flowerdew et al., 2012
		Antarctica	Heimefrontfjella	feldspar						18,723	15,414	37,477		1	Permian sandstone	Flowerdew et al., 2012
		Antarctica	Heimefrontfjella	feldspar						18,908	15,565	37,496		1	Permian sandstone	Flowerdew et al., 2012
		Antarctica	Heimefrontfjella	feldspar						19,038	15,483	38,631		1	Permian sandstone	Flowerdew et al., 2012
		Antarctica	Heimefrontfjella	feldspar						19,047	15,635	37,602		1	Permian sandstone	Flowerdew et al., 2012
		Antarctica	Heimefrontfjella	feldspar						19,096	16,013	39,28		1	Permian sandstone	Flowerdew et al., 2012
		Antarctica	Heimefrontfjella	feldspar						19,256	15,734	39,101		1	Permian sandstone	Flowerdew et al., 2012
		Antarctica	Heimefrontfjella	feldspar						19,528	15,738	39,586		1	Permian sandstone	Flowerdew et al., 2012
-68,1717	-65,2312	Antarctica	Joerg Peninsula	feldspar						18,75	15,6518	38,4762		1	granodiorite	Flowerdew et al., 2012
-72,17	-0,0586	Antarctica	Kirwanveggan	feldspar						17,4099	15,4498	37,9708		1	syenite	Flowerdew et al., 2012
		Antarctica	Kiwanveggan	clast						17,226	15,393	36,608		1	Permian gritstone	Flowerdew et al., 2012
		Antarctica	Kiwanveggan	clast						17,572	15,311	36,513		1	Permian gritstone	Flowerdew et al., 2012
		Antarctica	Kiwanveggan	clast						17,628	15,423	36,725		1	Permian gritstone	Flowerdew et al., 2012
		Antarctica	Kiwanveggan	clast						17,702	15,47	36,961		1	Permian gritstone	Flowerdew et al., 2012
		Antarctica	Kiwanveggan	clast						17,748	15,452	36,847		1	Permian gritstone	Flowerdew et al., 2012
		Antarctica	Kiwanveggan	feldspar						17,752	15,5	36,916		1	Permian gritstone	Flowerdew et al., 2012
		Antarctica	Kiwanveggan	clast						17,806	15,476	36,983		1	Permian gritstone	Flowerdew et al., 2012
		Antarctica	Kiwanveggan	feldspar						17,897	15,5	37,046		1	Permian gritstone	Flowerdew et al., 2012
		Antarctica	Kiwanveggan	clast						17,931	15,516	36,949		1	Permian gritstone	Flowerdew et al., 2012
		Antarctica	Kiwanveggan	clast						18	15,592	37,247		1	Permian gritstone	Flowerdew et al., 2012
		Antarctica	Kiwanveggan	clast						18,05	15,458	36,771		1	Permian gritstone	Flowerdew et al., 2012
		Antarctica	Kiwanveggan	clast						18,174	15,516	36,951		1	Permian gritstone	Flowerdew et al., 2012
		Antarctica	Kiwanveggan	feldspar						18,275	15,588	37,398		1	Permian gritstone	Flowerdew et al., 2012
		Antarctica	Kiwanveggan	clast						18,311	15,545	37,487		1	Permian gritstone	Flowerdew et al., 2012
		Antarctica	Kiwanveggan	clast						18,325	15,589	37,275		1	Permian gritstone	Flowerdew et al., 2012
		Antarctica	Kiwanveggan	feldspar						18,339	15,41	36,959		1	Permian gritstone	Flowerdew et al., 2012
		Antarctica	Kiwanveggan	feldspar						18,341	15,482	37,206		1	Permian gritstone	Flowerdew et al., 2012
		Antarctica	Kiwanveggan	feldspar						18,595	15,611	37,72		1	Permian gritstone	Flowerdew et al., 2012
		Antarctica	Kiwanveggan	feldspar						18,839	15,614	38,13		1	Permian gritstone	Flowerdew et al., 2012
		Antarctica	Kiwanveggan	feldspar						16,55	15,514	36,234		1	Jurassic sandstone	Flowerdew et al., 2012
		Antarctica	Kiwanveggan	feldspar						16,971	15,555	36,921		1	Jurassic sandstone	Flowerdew et al., 2012
		Antarctica	Kiwanveggan	feldspar						17,054	15,467	36,889		1	Jurassic sandstone	Flowerdew et al., 2012
		Antarctica	Kiwanveggan	feldspar						17,399	15,513	36,896		1	Jurassic sandstone	Flowerdew et al., 2012
		Antarctica	Kiwanveggan	feldspar						17,479	15,528	37,256		1	Jurassic sandstone	Flowerdew et al., 2012
		Antarctica	Kiwanveggan	feldspar						17,551	15,568	37,448		1	Jurassic sandstone	Flowerdew et al., 2012
		Antarctica	Kiwanveggan	feldspar						17,581	15,544	36,918		1	Jurassic sandstone	Flowerdew et al., 2012
		Antarctica	Kiwanveggan	feldspar						17,663	15,635	37,638		1	Jurassic sandstone	Flowerdew et al., 2012
		Antarctica	Kiwanveggan	feldspar						17,698	15,429	37,254		1	Jurassic sandstone	Flowerdew et al., 2012
		Antarctica	Kiwanveggan	feldspar						17,747	15,631	38,004		1	Jurassic sandstone	Flowerdew et al., 2012
		Antarctica	Kiwanveggan	feldspar						17,75	15,628	38,065		1	Jurassic sandstone	Flowerdew et al., 2012
		Antarctica	Kiwanveggan	feldspar						17,772	15,539	37,567		1	Jurassic sandstone	Flowerdew et al., 2012
		Antarctica	Kiwanveggan	feldspar						17,827	15,611	37,698		1	Jurassic sandstone	Flowerdew et al., 2012
		Antarctica	Kiwanveggan	feldspar						17,861	15,606	37,631		1	Jurassic sandstone	Flowerdew et al., 2012
		Antarctica	Kiwanveggan	feldspar						17,892	15,589	37,765		1	Jurassic sandstone	Flowerdew et al., 2012
		Antarctica	Kiwanveggan	feldspar						17,931	15,575	37,961		1	Jurassic sandstone	Flowerdew et al., 2012
		Antarctica	Kiwanveggan	feldspar						17,96	15,525	37,425		1	Jurassic sandstone	Flowerdew et al., 2012
		Antarctica	Kiwanveggan	feldspar						18,018	15,497	37,858		1	Jurassic sandstone	Flowerdew et al., 2012
		Antarctica	Kiwanveggan	feldspar						18,02	15,593	37,749		1	Jurassic sandstone	Flowerdew et al., 2012
		Antarctica	Kiwanveggan	feldspar						18,054	15,569	37,696		1	Jurassic sandstone	Flowerdew et al., 2012
		Antarctica	Kiwanveggan	feldspar						18,059	15,504	37,801		1	Jurassic sandstone	Flowerdew et al., 2012
		Antarctica	Kiwanveggan	feldspar						18,089	15,685	38,251		1	Jurassic sandstone	Flowerdew et al., 2012
		Antarctica	Kiwanveggan	feldspar						18,104	15,622	37,872		1	Jurassic sandstone	Flowerdew et al., 2012
		Antarctica	Kiwanveggan	feldspar						18,106	15,566	37,711		1	Jurassic sandstone	Flowerdew et al., 2012
		Antarctica	Kiwanveggan	feldspar						18,115	15,557	37,895		1	Jurassic sandstone	Flowerdew et al., 2012
		Antarctica	Kiwanveggan	feldspar						18,142	15,598	38,049		1	Jurassic sandstone	Flowerdew et al., 2012

latitude (°N)	longitude (E°)	region (when given)	locality (when given)	grain size fraction (when given)	$^{143}Nd/^{144}Nd$	ε_{Nd}	[Nd] (ppm)	$^{87}Sr/^{86}Sr$	[Sr] (ppm)	$^{206}Pb/^{204}Pb$	$^{207}Pb/^{204}Pb$	$^{208}Pb/^{204}Pb$	[Pb] (ppm)	number of sample	type of sample (when given)	reference
		Antarctica	Kiwanveggan	feldspar						18,156	15,62	38,189		1	Jurassic sandstone	Flowerdew et al., 2012
		Antarctica	Kiwanveggan	feldspar						18,178	15,662	38,071		1	Jurassic sandstone	Flowerdew et al., 2012
		Antarctica	Kiwanveggan	feldspar						18,198	15,605	37,888		1	Jurassic sandstone	Flowerdew et al., 2012
		Antarctica	Kiwanveggan	feldspar						18,213	15,613	38,102		1	Jurassic sandstone	Flowerdew et al., 2012
		Antarctica	Kiwanveggan	feldspar						18,246	15,601	38,073		1	Jurassic sandstone	Flowerdew et al., 2012
		Antarctica	Kiwanveggan	feldspar						18,247	15,699	38,392		1	Jurassic sandstone	Flowerdew et al., 2012
		Antarctica	Kiwanveggan	feldspar						18,273	15,552	37,845		1	Jurassic sandstone	Flowerdew et al., 2012
		Antarctica	Kiwanveggan	feldspar						18,3	15,582	38,112		1	Jurassic sandstone	Flowerdew et al., 2012
		Antarctica	Kiwanveggan	feldspar						18,3	15,644	37,911		1	Jurassic sandstone	Flowerdew et al., 2012
		Antarctica	Kiwanveggan	feldspar						18,311	15,636	38,321		1	Jurassic sandstone	Flowerdew et al., 2012
		Antarctica	Kiwanveggan	feldspar						18,315	15,625	38,176		1	Jurassic sandstone	Flowerdew et al., 2012
		Antarctica	Kiwanveggan	feldspar						18,327	15,684	38,292		1	Jurassic sandstone	Flowerdew et al., 2012
		Antarctica	Kiwanveggan	feldspar						18,334	15,624	38,232		1	Jurassic sandstone	Flowerdew et al., 2012
		Antarctica	Kiwanveggan	feldspar						18,384	15,561	38,128		1	Jurassic sandstone	Flowerdew et al., 2012
		Antarctica	Kiwanveggan	feldspar						18,418	15,673	38,443		1	Jurassic sandstone	Flowerdew et al., 2012
		Antarctica	Kiwanveggan	feldspar						18,418	15,796	38,627		1	Jurassic sandstone	Flowerdew et al., 2012
-77,8	-34,9	Antarctica	Littlewood Nunataks	feldspar						17,937	15,5103	37,1149		1	granite	Flowerdew et al., 2012
-69,9417	-64,4217	Antarctica	Mount Charity	feldspar						18,5771	15,6228	38,3436		1	granite	Flowerdew et al., 2012
-80,55	-96,7167	Antarctica	Mount Woolard	feldspar						18,6853	15,6605	38,5244		1	granite	Flowerdew et al., 2012
-80,4178	-29,3722	Antarctica	North Shackletons	feldspar						18,208	15,608	37,9545		1	granite	Flowerdew et al., 2012
-80,3886	-29,64	Antarctica	North Shakletons	feldspar						17,5421	15,4943	37,8259		1	granite	Flowerdew et al., 2012
		Antarctica	Pensacola Mountains	whole rock				0,716						12	Permian rocks (Beacon supergroup)	Faure and Barret, 1973
		Antarctica	Pensacola Mountains	whole rock				0,7252						3	Devonianc rocks (Beaacon supergroup)	Faure and Barret, 1973
		Antarctica	Pensacola province	feldspar						18,323	15,631	38,76		1	Thiel Mountain granite	Flowerdew et al., 2012
		Antarctica	Pensacola province	feldspar						18,194	15,594	37,672		1	Thiel Mountain granite	Flowerdew et al., 2012
		Antarctica	Pensacola province	feldspar						18,213	15,605	37,698		1	Thiel Mountain granite	Flowerdew et al., 2012
-83,9125	-56,5081	Antarctica	Pensacolas	feldspar						18,3898	15,6154	37,9841		1	granite	Flowerdew et al., 2012
-83,5681	-54,8108	Antarctica	Pensacolas	feldspar						18,4131	15,6076	38,0524		1	granite gneiss	Flowerdew et al., 2012
		Antarctica	Prince Charles Mountains	whole rock	0,51117	-28,6	40	0,7757	194,5					1	-	Boger et al., 2008
		Antarctica	Prince Charles Mountains	whole rock	0,51149	-22,4	106	0,70968	1636					1	-	Boger et al., 2008
		Antarctica	Prince Charles Mountains	whole rock	0,51033	-45,0	23	0,70751	892,5					1	-	Boger et al., 2008
		Antarctica	Prince Charles Mountains	whole rock	0,5112	-28,1	33	0,75639	167,5					1	-	Boger et al., 2008
		Antarctica	Prince Charles Mountains	whole rock	0,51128	-26,5	12	0,74271	251,1					1	-	Boger et al., 2008
		Antarctica	Prince Charles Mountains	whole rock	0,51115	-29,0	71	0,74596	260,7					1	-	Boger et al., 2008
		Antarctica	Prince Charles Mountains	whole rock	0,51129	-26,3	3	0,73904	228,7					1	-	Boger et al., 2008
-65	60	Antarctica	Prydz Bay			-18,8	39							3	core	Jeandel et al., 2007 and references therein
-65,65	60,68	Antarctica	Prydz Bay	0-63 µm	0,511655	-19,2	31							1	marine sediment	Roy et al, 2007
-66,66	77,9	Antarctica	Prydz Bay	0-63 µm	0,511544	-21,3	47							1	marine sediment	van de Flierdt, 2007
-61,12	71,27	Antarctica	Prydz Bay	0-63 µm	0,511681	-18,7	40							1	marine sediment	van de Flierdt, 2007
-67,41	74,47	Antarctica	Prydz Bay	0-63 µm	0,51173	-17,7								1	marine sediment	van de Flierdt, 2007
-80,7617	-25,6083	Antarctica	Read Mountains	feldspar						15,9469	15,3406	35,2839		1	granite gneiss	Flowerdew et al., 2012
-80,5111	-29,3667	Antarctica	Read Mountains	feldspar						19,9269	16,1329	40,1852		1	granite gneiss	Flowerdew et al., 2012
-80	0	Antarctica	Ross Sea			-20,8	12							1		Jeandel et al., 2007 and references therein
-70	170	Antarctica	Ross Sea			-6,8	46							3	core	Jeandel et al., 2007 and references therein
-73,54	176,96	Antarctica	Ross Sea	0-63 µm	0,512262	-7,3								1	marine sediment	Roy et al, 2007
-64,2	170,08	Antarctica	Ross Sea	0-63 µm	0,512498	-2,7								1	marine sediment	Roy et al, 2007
-71,96	178,6	Antarctica	Ross Sea	0-63 µm	0,512283	-6,9	46							1	marine sediment	van de Flierdt, 2007
-56,5	-30,75	Antarctica	Scotia Sea	bulk	0,512969	6,5		0,70344		19,3462	15,6422	39,1027		1	Scotia Sea Ridge	Harrison et al., 2003
-56,5	-30,75	Antarctica	Scotia Sea	bulk	0,512975	6,6		0,703444		19,3156	15,5868	38,9295		1	Scotia Sea Ridge	Harrison et al., 2003
-56,5	-30,75	Antarctica	Scotia Sea	bulk	0,512977	6,6		0,703453		19,1941	15,5833	38,8289		1	Scotia Sea Ridge	Harrison et al., 2003
-56,5	-30,75	Antarctica	Scotia Sea	bulk	0,512999	7,0		0,703454		19,3208	16,6212	39,0284		1	Scotia Sea Ridge	Harrison et al., 2003
		Antarctica	Shackleton range	feldspar						20,33	16,228	40,512		1	Read Mountains granite	Flowerdew et al., 2012
		Antarctica	Shackleton range	feldspar						19,899	16,135	40,348		1	Read Mountains granite	Flowerdew et al., 2012
		Antarctica	Shackleton range	feldspar						19,733	16,071	39,984		1	Read Mountains granite	Flowerdew et al., 2012
80,34166667	24,03583333	Antarctica	Shackleton Range	whole rock	0,51262	-0,4	14	0,7035	187	40,9695	15,7579	21,0113		1	felsic amphibolite	Will et al., 2010b
80,39166667	29,52166667	Antarctica	Shackleton Range	whole rock	0,51205	-11,5	60	0,70632	1127	37,9251	15,5074	17,4717		1	amphibolite	Will et al., 2010b
80,38466667	29,651	Antarctica	Shackleton Range	whole rock	0,51209	-10,7	65	0,70666	576	38,661	15,6587	18,7319		1	metasyenodiorite	Will et al., 2010b
80,60133333	19,09166667	Antarctica	Shackleton Range	whole rock	0,51266	0,4	21	0,7071	258	40,4688	15,7692	21,2545		1	garnet bearing amphibolite	Will et al., 2010b
80,65666667	25,05166667	Antarctica	Shackleton Range	whole rock	0,51102	-31,6	130	0,71028	1939	39,2776	15,5286	17,1038		1	metadiorite	Will et al., 2010b
80,37583333	29,7075	Antarctica	Shackleton Range	whole rock	0,51224	-7,8	90	0,71228	378	40,6719	15,631	19,3482		1	amphibolite	Will et al., 2010b
80,50633333	19,20466667	Antarctica	Shackleton Range	whole rock	0,51193	-13,8	11	0,71556	134	39,8358	16,1052	19,9802		1	amphibolite	Will et al., 2010b
80,39166667	29,52166667	Antarctica	Shackleton Range	whole rock	0,51204	-11,7	26	0,72028	320	38,4063	15,6198	18,3403		1	garnet bearing metagranite	Will et al., 2010b
80,72433333	25,76816667	Antarctica	Shackleton Range	whole rock	0,51199	-12,6	18	0,72219	305	38,1389	15,9193	19,9927		1	amphibolite	Will et al., 2010b
80,40466667	29,65833333	Antarctica	Shackleton Range	whole rock	0,512	-12,4	50	0,72478	267	38,4092	15,6563	18,7179		1	garnet bearing metagranite	Will et al., 2010b
80,40466667	29,65833333	Antarctica	Shackleton Range	whole rock	0,51199	-12,6	41	0,72604	281	38,4485	15,6561	18,7008		1	metadiorite	Will et al., 2010b
80,50633333	19,20466667	Antarctica	Shackleton Range	whole rock	0,51182	-16,0	14	0,73186	233	39,3181	15,856	18,4557		1	amphibolite	Will et al., 2010b
80,50633333	19,20466667	Antarctica	Shackleton Range	whole rock	0,51185	-15,4	17	0,73776	138	39,2159	15,8373	18,3276		1	amphibolite	Will et al., 2010b
80,38466667	29,651	Antarctica	Shackleton Range	whole rock	0,51149	-22,4	72							1	metasyenodiorite	Will et al., 2010b
80,4025	29,54033333	Antarctica	Shackleton Range	whole rock	0,51152	-21,8	44							1	felsic amphibolite	Will et al., 2010b
80,50633333	19,20466667	Antarctica	Shackleton Range	whole rock	0,511678	-18,7	27							1	hb-bi gneiss	Will et al., 2010b
80,72333333	25,93833333	Antarctica	Shackleton Range	whole rock	0,511804	-16,3	27							1	amphibolite	Will et al., 2010b
80,37583333	29,7075	Antarctica	Shackleton Range	whole rock	0,512065	-11,2	75							1	amphibolite	Will et al., 2010b
80,39166667	29,52166667	Antarctica	Shackleton Range	whole rock	0,512081	-10,9	37							1	metagranodiorite	Will et al., 2010b
80,71833333	25,925	Antarctica	Shackleton Range	whole rock	0,512082	-10,8	13							1	amphibolite	Will et al., 2010b
80,4025	29,54033333	Antarctica	Shackleton Range	whole rock	0,51215	-9,5	33							1	metadiorite	Will et al., 2010b
80,4025	29,54033333	Antarctica	Shackleton Range	whole rock	0,512183	-8,9	31							1	garnet bearing amphibolite	Will et al., 2010b
80,72433333	25,76816667	Antarctica	Shackleton Range	whole rock	0,5122	-8,5	12							1	amphibolite	Will et al., 2010b
80,38466667	29,651	Antarctica	Shackleton Range	whole rock	0,512264	-7,3	76							1	orthogneiss	Will et al., 2010b
80,4025	29,54033333	Antarctica	Shackleton Range	whole rock	0,512296	-6,7	39							1	garnet bearing amphibolite	Will et al., 2010b
80,4025	29,54033333	Antarctica	Shackleton Range	whole rock	0,512311	-6,4	65							1	felsic amphibolite	Will et al., 2010b
		Antarctica	South Sandwich Islands	whole rock						18,587	15,545	38,522	0,53	1	volcanic rock	Barreiro et al., 1983

latitude (°N)	longitude (E°)	region (when given)	locality (when given)	grain size fraction (when given)	$^{143}Nd/^{144}Nd$	ε_{Nd}	[Nd] (ppm)	$^{87}Sr/^{86}Sr$	[Sr] (ppm)	$^{206}Pb/^{204}Pb$	$^{207}Pb/^{204}Pb$	$^{208}Pb/^{204}Pb$	[Pb] (ppm)	number of sample	type of sample (when given)	reference
		Antarctica	South Sandwich Islands	whole rock						18,56	15,564	38,426	1,89	1	volcanic rock	Barreiro et al., 1983
		Antarctica	South Sandwich Islands	whole rock						18,6	15,566	38,482	0,79	1	volcanic rock	Barreiro et al., 1983
		Antarctica	South Sandwich Islands	whole rock						18,513	15,567	38,415	2,02	1	volcanic rock	Barreiro et al., 1983
		Antarctica	South Sandwich Islands	whole rock						18,578	15,57	38,448	2,14	1	volcanic rock	Barreiro et al., 1983
		Antarctica	South Sandwich Islands	whole rock						18,583	15,576	38,458	1,7	1	volcanic rock	Barreiro et al., 1983
		Antarctica	South Sandwich Islands	whole rock						18,603	15,597	38,596	4,72	1	volcanic rock	Barreiro et al., 1983
		Antarctica	South Sandwich Islands	whole rock						18,575	15,599	38,493	3,7	1	volcanic rock	Barreiro et al., 1983
		Antarctica	South Sandwich Islands	whole rock						18,567	15,601	38,51		1	volcanic rock	Barreiro et al., 1983
		Antarctica	South Sandwich Islands	bulk						18,622	15,61	38,398	14,1	1	pelagic sediment	Barreiro et al., 1983
		Antarctica	South Sandwich Islands	bulk						18,608	15,61	38,447		1	pelagic sediment	Barreiro et al., 1983
		Antarctica	South Sandwich Islands	whole rock						18,626	15,61	38,552	1,93	1	volcanic rock	Barreiro et al., 1983
		Antarctica	South Sandwich Islands	bulk						18,716	15,61	38,618		1	pelagic sediment	Barreiro et al., 1983
		Antarctica	South Sandwich Islands	bulk						18,484	15,613	38,453	11,6	1	pelagic sediment	Barreiro et al., 1983
		Antarctica	South Sandwich Islands	bulk						18,614	15,616	38,446	7,4	1	pelagic sediment	Barreiro et al., 1983
		Antarctica	South Sandwich Islands	bulk						18,694	15,617	38,587	9,33	1	pelagic sediment	Barreiro et al., 1983
		Antarctica	South Sandwich Islands	whole rock						18,637	15,619	38,596	1,8	1	volcanic rock	Barreiro et al., 1983
		Antarctica	South Sandwich Islands	bulk						18,641	15,62	38,519	15,5	1	pelagic sediment	Barreiro et al., 1983
		Antarctica	South Sandwich Islands	bulk						18,74	15,638	38,679	14,8	1	pelagic sediment	Barreiro et al., 1983
		Antarctica	South Sandwich Islands	whole rock						18,658	15,644	38,638	0,61	1	volcanic rock	Barreiro et al., 1983
		Antarctica	South Sandwich Islands	bulk						18,793	15,655	38,777		1	pelagic sediment	Barreiro et al., 1983
		Antarctica	South Sandwich Islands	bulk						18,677	15,656	38,603		1	pelagic sediment	Barreiro et al., 1983
		Antarctica	South Sandwich Islands	bulk						18,604	15,663	38,497	11,6	1	pelagic sediment	Barreiro et al., 1983
		Antarctica	South Sandwich Islands	bulk						18,71	15,681	38,662		1	pelagic sediment	Barreiro et al., 1983
		Antarctica	South Sandwich Islands	bulk						18,802	15,693	38,804	3,96	1	pelagic sediment	Barreiro et al., 1983
		Antarctica	South Sandwich Islands	whole rock	0,51305	8,0		0,70384		18,44	15,57	36,28		1	volcanic rock	Cohen and O'Nions, 1982
		Antarctica	South Sandwich Islands	whole rock	0,51307	8,4		0,70386		18,41	15,58	38,23		1	volcanic rock	Cohen and O'Nions, 1982
		Antarctica	South Sandwich Islands	whole rock	0,51314	9,8		0,70386		18,42	15,55	38,21		1	volcanic rock	Cohen and O'Nions, 1982
		Antarctica	South Sandwich Islands	whole rock	0,51304	7,8		0,70399		18,45	15,62	38,4		1	volcanic rock	Cohen and O'Nions, 1982
		Antarctica	South Sandwich Islands	whole rock	0,51301	7,3		0,70414		18,41	15,59	38,27		1	volcanic rock	Cohen and O'Nions, 1982
-72,2608	1,2847	Antarctica	Sverdrupfjella	feldspar						17,3385	15,5539	37,6427		1	granite gneiss	Flowerdew et al., 2012
-72,1053	1,4797	Antarctica	Sverdrupfjella	feldspar						16,4526	15,6337	37,6068		1	granite	Flowerdew et al., 2012
-72,1032	1,4792	Antarctica	Sverdrupfjella	feldspar						16,5396	15,6448	37,6607		1	syenite	Flowerdew et al., 2012
-72,095	1,2171	Antarctica	Sverdrupfjella	feldspar						16,972	15,473	37,3318		1	granite gneiss	Flowerdew et al., 2012
		Antarctica	Theron Mountains	zircon						18,358	15,494	37,888		1	Permian sandstone	Flowerdew et al., 2012
		Antarctica	Theron Mountains	zircon						18,479	15,539	38,086		1	Permian sandstone	Flowerdew et al., 2012
		Antarctica	Theron Mountains	zircon						18,507	15,59	38,241		1	Permian sandstone	Flowerdew et al., 2012
		Antarctica	Theron Mountains	zircon						18,538	15,597	38,232		1	Permian sandstone	Flowerdew et al., 2012
		Antarctica	Theron Mountains	zircon						18,552	15,644	38,358		1	Permian sandstone	Flowerdew et al., 2012
		Antarctica	Theron Mountains	zircon						18,556	15,614	38,25		1	Permian sandstone	Flowerdew et al., 2012
		Antarctica	Theron Mountains	zircon						18,557	15,607	38,269		1	Permian sandstone	Flowerdew et al., 2012
		Antarctica	Theron Mountains	zircon						18,581	15,627	38,316		1	Permian sandstone	Flowerdew et al., 2012
		Antarctica	Theron Mountains	zircon						18,582	15,607	38,27		1	Permian sandstone	Flowerdew et al., 2012
		Antarctica	Theron Mountains	zircon						18,611	15,612	38,251		1	Permian sandstone	Flowerdew et al., 2012
		Antarctica	Theron Mountains	zircon						18,617	15,628	38,256		1	Permian sandstone	Flowerdew et al., 2012
		Antarctica	Theron Mountains	zircon						18,651	15,695	38,56		1	Permian sandstone	Flowerdew et al., 2012
		Antarctica	Theron Mountains	zircon						18,655	15,638	38,306		1	Permian sandstone	Flowerdew et al., 2012
		Antarctica	Theron Mountains	zircon						18,657	15,712	38,536		1	Permian sandstone	Flowerdew et al., 2012
		Antarctica	Theron Mountains	zircon						18,657	15,679	38,427		1	Permian sandstone	Flowerdew et al., 2012
		Antarctica	Theron Mountains	zircon						18,661	15,683	38,46		1	Permian sandstone	Flowerdew et al., 2012
		Antarctica	Theron Mountains	zircon						18,664	15,646	38,35		1	Permian sandstone	Flowerdew et al., 2012
		Antarctica	Theron Mountains	zircon						18,671	15,654	38,405		1	Permian sandstone	Flowerdew et al., 2012
		Antarctica	Theron Mountains	zircon						18,671	15,729	38,555		1	Permian sandstone	Flowerdew et al., 2012
		Antarctica	Theron Mountains	zircon						18,681	15,641	38,417		1	Permian sandstone	Flowerdew et al., 2012
		Antarctica	Theron Mountains	zircon						18,698	15,665	38,408		1	Permian sandstone	Flowerdew et al., 2012
		Antarctica	Theron Mountains	zircon						18,699	15,698	38,548		1	Permian sandstone	Flowerdew et al., 2012
		Antarctica	Theron Mountains	zircon						18,713	15,728	38,558		1	Permian sandstone	Flowerdew et al., 2012
		Antarctica	Theron Mountains	zircon						18,73	15,655	38,415		1	Permian sandstone	Flowerdew et al., 2012
		Antarctica	Theron Mountains	zircon						18,733	15,642	38,387		1	Permian sandstone	Flowerdew et al., 2012
		Antarctica	Theron Mountains	zircon						18,747	15,76	38,549		1	Permian sandstone	Flowerdew et al., 2012
		Antarctica	Theron Mountains	zircon						18,847	15,698	38,556		1	Permian sandstone	Flowerdew et al., 2012
		Antarctica	Theron Mountains	zircon						19,044	15,621	38,559		1	Permian sandstone	Flowerdew et al., 2012
		Antarctica	Theron Mountains	lithic						19,051	15,499	38,683		1	Permian sandstone	Flowerdew et al., 2012
		Antarctica	Theron Mountains	lithic						19,26	15,738	39,115		1	Permian sandstone	Flowerdew et al., 2012
		Antarctica	Theron Mountains	lithic						19,541	15,754	39,64		1	Permian sandstone	Flowerdew et al., 2012
-85,0133	-91,7667	Antarctica	Thiel Mountains	feldspar						18,2525	15,6247	37,7714		1	porphiry	Flowerdew et al., 2012
-85,0133	-90,2833	Antarctica	Thiel Mountains	feldspar						18,3018	15,6082	37,7745		1	granite	Flowerdew et al., 2012
		Antarctica	Vestfjella	whole rock	0,512985	6,8	13	0,703112	220	18,111	15,491	37,69	0,93	1	highly magnesian dykes	Heinonen, 2010
		Antarctica	Vestfjella	whole rock	0,512958	6,2	24	0,703118	321	18,122	15,504	37,78	1,79	1	highly magnesian dykes	Heinonen, 2010
		Antarctica	Vestfjella	whole rock	0,513008	7,2	19	0,7032	303	17,961	15,473	37,52	1,27	1	highly magnesian dykes	Heinonen, 2010
		Antarctica	Vestfjella	whole rock	0,513004	7,1	15	0,703302	263	18,103	15,489	37,73	1,03	1	highly magnesian dykes	Heinonen, 2010
		Antarctica	Vestfjella	whole rock	0,513	7,1	9	0,703348	234	17,825	15,492	37,57	0,65	1	highly magnesian dykes	Heinonen, 2010
		Antarctica	Vestfjella	whole rock	0,513014	7,3	9	0,703692	161	17,701	15,437	38,31	1,07	1	highly magnesian dykes	Heinonen, 2010
		Antarctica	Vestfjella	whole rock	0,513006	7,2	13	0,703833	240	18,256	15,543	37,74	0,84	1	highly magnesian dykes	Heinonen, 2010
		Antarctica	Vestfjella	whole rock	0,512829	3,7	32	0,703844	455	18,26	15,598	37,79	2,34	1	highly magnesian dykes	Heinonen, 2010
		Antarctica	Vestfjella	whole rock	0,512757	2,3	27	0,704572	516	18,351	15,597	38,26	2,27	1	highly magnesian dykes	Heinonen, 2010
		Antarctica	Vestfjella	whole rock	0,512589	-1,0	6	0,70481	151	17,809	15,523	37,17	0,91	1	highly magnesian dykes	Heinonen, 2010
		Antarctica	Vestfjella	whole rock	0,512523	-2,2	7	0,705088	119	17,203	15,44	37,16	1,24	1	highly magnesian dykes	Heinonen, 2010
		Antarctica	Vestfjella	whole rock	0,512688	1,0	27	0,70518	415	17,38	15,535	38,28	2,08	1	highly magnesian dykes	Heinonen, 2010
		Antarctica	Vestfjella	whole rock	0,512055	-11,4	5	0,708039	66	17,374	15,541	37,93	0,72	1	highly magnesian dykes	Heinonen, 2010
		Antarctica	Vestjella	whole rock	0,512730	1,8	32	0,704468	287,5					1	lava	Luttinen et al., 1998
		Antarctica	Vestjella	whole rock	0,512768	2,5	28	0,704563	374,9					1	dolerite dyke	Luttinen et al., 1998

latitude (°N)	longitude (E°)	region (when given)	locality (when given)	grain size fraction (when given)	$^{143}Nd/^{144}Nd$	ε_{Nd}	[Nd] (ppm)	$^{87}Sr/^{86}Sr$	[Sr] (ppm)	$^{206}Pb/^{204}Pb$	$^{207}Pb/^{204}Pb$	$^{208}Pb/^{204}Pb$	[Pb] (ppm)	number of sample	type of sample (when given)	reference
		Antarctica	Vestjella	whole rock	0,512732	1,8	14	0,704926	291,7					1	lava	Luttinen et al., 1998
		Antarctica	Vestjella	whole rock	0,512706	1,3	9	0,705001	427					1	lava	Luttinen et al., 1998
		Antarctica	Vestjella	whole rock	0,512720	1,6	12	0,705279	532,2					1	lava	Luttinen et al., 1998
		Antarctica	Vestjella	whole rock	0,512631	-0,1	11	0,706343	239,9					1	lava	Luttinen et al., 1998
		Antarctica	Vestjella	whole rock	0,512533	-2,0	24	0,7066	411,1					1	lava	Luttinen et al., 1998
		Antarctica	Vestjella	whole rock	0,512007	-12,3	22	0,707139	499,7					1	lava	Luttinen et al., 1998
		Antarctica	Vestjella	whole rock	0,512277	-7,0	16	0,707265	271,7					1	lava	Luttinen et al., 1998
		Antarctica	Vestjella	whole rock	0,511859	-15,2	19	0,70735	430,4					1	lava	Luttinen et al., 1998
		Antarctica	Vestjella	whole rock	0,511746	-17,4	27	0,708245	629					1	lava	Luttinen et al., 1998
		Antarctica	Vestjella	whole rock	0,511804	-16,3	13	0,708289	464,5					1	lava	Luttinen et al., 1998
		Antarctica	Vestjella	whole rock	0,511814	-16,1	13	0,70832	466					1	lava	Luttinen et al., 1998
-77,15	-40,5	Antarctica	Weddell Sea			-10,4	19							1	core n− PS1016-1 (702m)	Jeandel et al., 2007 and references therein
-75	-40	Antarctica	Weddell Sea			-8,0	70							2	core	Jeandel et al., 2007 and references therein
-74,4	-35,05	Antarctica	Weddell Sea			-7,7	11							1	core n− PS1490-2 (497m)	Jeandel et al., 2007 and references therein
-60,95	-45,42	Antarctica	Weddell Sea			-6,2	24							1	core n− D-ORC-15 (290m)	Jeandel et al., 2007 and references therein
-66,05	-55,32	Antarctica	Weddell Sea			-5,7	21							1	core n− PS2805-1 (466m)	Jeandel et al., 2007 and references therein
-66,5	-45,62	Antarctica	Weddell Sea	0-63 μm	0,512147	-9,6	75							1	marine sediment	van de Flierdt, 2007
-62	-20,01	Antarctica	Weddell Sea	0-63 μm	0,512201	-8,5	65							1	marine sediment	van de Flierdt, 2007
		Antarctica	West Antarctic Province	feldspar						18,679	15,657	38,469		1	Graham Land granite	Flowerdew et al., 2012
		Antarctica	West Antarctic Province	feldspar						18,576	15,642	38,381		1	Graham Land granite	Flowerdew et al., 2012
		Antarctica	West Antarctic Province	feldspar						18,751	15,55	38,297		1	Graham Land granite	Flowerdew et al., 2012
-70	-120	Antarctica	West Antarctica	bulk		-3,7	53							5	core	Jeandel et al., 2007 and references therein
-70	-120,17	Antarctica	West Antarctica	0-63 μm	0,512358	-5,5	66							1	marine sediment	Roy et al, 2007
-70,17	-106,64	Antarctica	West Antarctica	0-63 μm	0,5124	-4,6	38							1	marine sediment	Roy et al, 2007
-70,42	-99,25	Antarctica	West Antarctica	0-63 μm	0,51247	-3,3	55							1	marine sediment	Roy et al, 2007
-70,1	-122,26	Antarctica	West Antarctica	0-63 μm	0,512502	-2,7	58							1	marine sediment	Roy et al, 2007
-70,14	-102,82	Antarctica	West Antarctica	0-63 μm	0,512399	-4,7	47							1	marine sediment	van de Flierdt, 2007
-82,6833	-104,2	Antarctica	Whitmore Mountains	feldspar						18,68	15,6356	38,3162		1	granite	Flowerdew et al., 2012
-65	120	Antarctica	Wilkes Land			-14,3	47							7	core	Jeandel et al., 2007 and references therein
-66,08	145,02	Antarctica	Wilkes Land	0-63 μm	0,511765	-17,0	34							1	marine sediment	Roy et al, 2007
-65,22	138,88	Antarctica	Wilkes Land	0-63 μm	0,511815	-16,1	43							1	marine sediment	Roy et al, 2007
-65,55	141,1	Antarctica	Wilkes Land	0-63 μm	0,511817	-16,0	38							1	marine sediment	Roy et al, 2007
-64,67	132,98	Antarctica	Wilkes Land	0-63 μm	0,511876	-14,9	75							1	marine sediment	Roy et al, 2007
-61,04	114,81	Antarctica	Wilkes Land	0-63 μm	0,511927	-13,9	48							1	marine sediment	Roy et al, 2007
-64,43	119,98	Antarctica	Wilkes Land	0-63 μm	0,512006	-12,3	48							1	marine sediment	Roy et al, 2007
-60	105	Antarctica	Wilkes Land	0-63 μm	0,511881	-14,8								1	marine sediment	van de Flierdt, 2007
-64,83	150,49	Antarctica	Wilkes Land	0-63 μm	0,512003	-12,4	47							1	marine sediment	van de Flierdt, 2007
67	93	Antarctica		bulk	0,511538	-21,5		0,7249						1	marine sediment	Basile et al, 1997
-50,58	2,9	Atlantic	Antarctic Circum, Current			-4,8	18							1	core n− RC13-255 (3332m)	Jeandel et al., 2007 and references therein
45,04	-7,59	Atlantic	Biscay abyssal plain			-9,9	36							1	core n− TE1-M (4526m)	Jeandel et al., 2007 and references therein
13	-80	Atlantic	Carribean_Plateau			4,1	10							1	rocks (average)	Jeandel et al., 2007 and references therein
14	-18	Atlantic	Continental Shelf (Senegal)			-14,5	42							1	loess n−Ro	Jeandel et al., 2007 and references therein
14,38	-17,27	Atlantic	Dakar (Senegal)			-16,2	3							1	loess n−Est	Jeandel et al., 2007 and references therein
64	-57	Atlantic	Davis Strait			-27,5	27							1	core n− HU87-033-007 (823m)	Jeandel et al., 2007 and references therein
62	-53	Atlantic	Davis Strait			-24,1	31							1	core n− HU87-033-008 (2424m)	Jeandel et al., 2007 and references therein
68	8	Atlantic	East Greenland			-15,1	40							1	core n− JM 98 624	Jeandel et al., 2007 and references therein
31,58	-4,25	Atlantic	Er Rachidia (Morocco)			-13,6	33							1	loess n−Elra	Jeandel et al., 2007 and references therein
62	-7	Atlantic	Faeroe Island			-6,5	7							1	core n− Rom1	Jeandel et al., 2007 and references therein
28,59	-8,55	Atlantic	Foum el Hassan (Morocco)			-17,1	39							1	loess n−Foum	Jeandel et al., 2007 and references therein
14,08	-16,3	Atlantic	Foundiougne (Senegal)			-14,3	28							1	loess n−Foun	Jeandel et al., 2007 and references therein
36	-10	Atlantic	Gibraltar			-8,5	21							1	dust n− JL-50	Jeandel et al., 2007 and references therein
65,1	-50,07	Atlantic	Greenland			-34,3	83							1	stream sediment n− 105862	Jeandel et al., 2007 and references therein
65,07	-49,56	Atlantic	Greenland			-33,0	54							1	stream sediment n− 110528	Jeandel et al., 2007 and references therein
65,08	-49,53	Atlantic	Greenland			-26,1	40							1	stream sediment n− 105894	Jeandel et al., 2007 and references therein
65,1	-49,48	Atlantic	Greenland			-24,2	46							1	stream sediment n− 110326	Jeandel et al., 2007 and references therein
40,3	-76	Atlantic	Hudson (U,S,A)			-11,3	46							1	river sediment	Jeandel et al., 2007 and references therein
60,57	-22,08	Atlantic	Iceland basin			3,4	21							1	core n− SU-9033 (2400m)	Jeandel et al., 2007 and references therein
60	-38	Atlantic	Irminger Basin			-7,9	30							1	core n− HU91-045-051 (2949m)	Jeandel et al., 2007 and references therein
11,43	-12,35	Atlantic	Labe (Guinea)			-12,1	22							1	loess n−Lab	Jeandel et al., 2007 and references therein
55	-55	Atlantic	Labrador Sea			-27,7	30							1	core n− HU91-045-005 (530m)	Jeandel et al., 2007 and references therein
59	-59	Atlantic	Labrador Sea			-17,0	22							1	core n− HU90-013-020 (2865m)	Jeandel et al., 2007 and references therein
60	-46	Atlantic	Labrador Sea			-16,5	32							1	core n− HU90-013-006 (1105m)	Jeandel et al., 2007 and references therein
59,5	-48	Atlantic	Labrador Sea			-8,8	36							1	core n− HU90-013-011 (2805m)	Jeandel et al., 2007 and references therein
11,2	-75	Atlantic	Magdalena (Colombia)			-8,3	27							1	river sediment	Jeandel et al., 2007 and references therein
30	-89	Atlantic	Mississippi (U,S,A)			-10,9	33							1	river sediment	Jeandel et al., 2007 and references therein
58	-2	Atlantic	N British Isles			-10,6	40							18	rocks & river sediments	Jeandel et al., 2007 and references therein
72,9	-13,99	Atlantic	N-E Greenland			-13,7	27							1	core n−MD99-2308Hy (2520m)	Jeandel et al., 2007 and references therein
43,29	-45,15	Atlantic	Newfoundland Basin			-24,5	22							1	core n− TE2-S (4415m)	Jeandel et al., 2007 and references therein
56,5	-13,75	Atlantic	North West Ireland			-11,1	26							1	core n− KS 73134 (2300m)	Jeandel et al., 2007 and references therein
45,4	-10,5	Atlantic	North West Spain			-11,6	26							1	core n− Inter-B1 (2588m)	Jeandel et al., 2007 and references therein
65	6,8	Atlantic	Norway			-14,0	10							1	sandstones	Jeandel et al., 2007 and references therein
18,09	-15,58	Atlantic	Nouakchott (Mauritania)			-17,1	56							1	loess n−Nou	Jeandel et al., 2007 and references therein
17	-18,3	Atlantic	off St Louis (Senegal)			-14,6	14							1	aerosols n− SL	Jeandel et al., 2007 and references therein
34,41	-1,45	Atlantic	Oujda (Morocco)			-11,8	30							1	loess n−Ouj	Jeandel et al., 2007 and references therein
53	-1	Atlantic	S British Isles			-13,5	37							14	rocks & river sediments	Jeandel et al., 2007 and references therein
63,4	-18,5	Atlantic	S Iceland			7,6	54							1	stream sed,	Jeandel et al., 2007 and references therein
8	-17,5	Atlantic	Sierra Leone Basin			-14,4	38							1	aerosols n− A18	Jeandel et al., 2007 and references therein
49	-68	Atlantic	St Lawrence (Canada)			-5,3	52							1	river sediment	Jeandel et al., 2007 and references therein
47,5	-8,5	Atlantic	West Britain			-11,6	26							1	core n− Flux-8 (2120m)	Jeandel et al., 2007 and references therein
22,44	-12,21	Atlantic	Zouerate (Mauritania)			-17,8	39							1	loess	Jeandel et al., 2007 and references therein
66,5	-60	Atlantic	Baffin Bay			-25,8	11							1	core n− HU74026-557PC	Jeandel et al., 2007 and references therein

latitude (°N)	longitude (E°)	region (when given)	locality (when given)	grain size fraction (when given)	$^{143}Nd/^{144}Nd$	ε_{Nd}	[Nd] (ppm)	$^{87}Sr/^{86}Sr$	[Sr] (ppm)	$^{206}Pb/^{204}Pb$	$^{207}Pb/^{204}Pb$	$^{208}Pb/^{204}Pb$	[Pb] (ppm)	number of sample	type of sample (when given)	reference
69	-72,12	Atlantic	Baffin Bay			-23,1	11							1	core n− HU77027-002TWC	Jeandel et al., 2007 and references therein
67	25	Atlantic	Baltic Sea			-19,4	13							1	sediments	Jeandel et al., 2007 and references therein
14	-18	Atlantic	Gambie			-13,6	31							1	dust n− JL-46	Jeandel et al., 2007 and references therein
20,32	-13,08	Atlantic	Mauritania			-17,9	4							1	loess n−Atar	Jeandel et al., 2007 and references therein
4,55	-21,07	Atlantic	W Guinea			-18,6	40							1	core n− VM22-189 (2525m)	Jeandel et al., 2007 and references therein
21,2	-18,15	Atlantic	W Mauritania			-14,8	25							1	core n− K09 (2002m)	Jeandel et al., 2007 and references therein
19,29	-17,17	Atlantic	W Mauritania			-14,3	22							1	core n− K02 (1407m)	Jeandel et al., 2007 and references therein
25,02	-16,39	Atlantic	W Morocco			-15,3	32							1	core n− K20b (1445m)	Jeandel et al., 2007 and references therein
23,44	-17,16	Atlantic	W Morocco			-14,4	27							1	core n− K15 (1000m)	Jeandel et al., 2007 and references therein
32,24	-10,25	Atlantic	W Morocco			-13,0	33							1	core n− K25 (3165m)	Jeandel et al., 2007 and references therein
34,2	-7,01	Atlantic	W Morocco			-11,7	35							1	core n− K23 (730m)	Jeandel et al., 2007 and references therein
13,5	-18,57	Atlantic	W Senegal			-15,7	32							1	core n− VM22-196 (3728m)	Jeandel et al., 2007 and references therein
11,03	-59,58	Atlantic	West Indies			-13,3	29							1	core n− RC16-44 (1639m)	Jeandel et al., 2007 and references therein
12,55	-59,37	Atlantic	West Indies			-11,6	28							1	core n− GS7605-53 (1685m)	Jeandel et al., 2007 and references therein
3,4	-48,4	Atlantic	West Indies			-10,7	23							1	core n− RC16-168 (836m)	Jeandel et al., 2007 and references therein
13,03	-60,35	Atlantic	West Indies			-9,6	27							1	core n− GS7605-48 (2430m)	Jeandel et al., 2007 and references therein
14,72	-59,64	Atlantic	West Indies			-9,1	21							1	core n− GS7605-11 (2625m)	Jeandel et al., 2007 and references therein
-36	136	Australia	South australia			-21,1	22							7	rocks	Jeandel et al., 2007 and references therein
-33,32	115,63	Australia	SW Australia			1,7	14							3	rocks	Jeandel et al., 2007 and references therein
-34,42	115,4	Australia	SW Australia (id)			-4,6	11							2	rocks	Jeandel et al., 2007 and references therein
-43	147	Australia	tasmania			-5,2	13							12	dolerites	Jeandel et al., 2007 and references therein
-20	119	Australia	W Australia			-15,1	20							6	river sediment	Jeandel et al., 2007 and references therein
-18,5	124	Australia	great sandy desert NW	bulk	0,512447	-3,7		0,732307						1	loess	Grousset et al, 1992
-18,5	124	Australia	great sandy desert NW	bulk				0,76336						1	loess	Grousset et al, 1992
-31	142	Australia	SE desert	bulk	0,512037	-11,7		0,721822						1	loess	Grousset et al, 1992
-31	142	Australia	SE desert	bulk	0,512446	-3,7		0,723238						1	loess	Grousset et al, 1992
-31	142	Australia	SE desert	0-5 µm	0,512128	-9,9		0,740074						1	loess	Grousset et al, 1992
		Australia	West Australia	bulk	0,51198	-12,8		0,71134		17,573	15,753	38,425		1	lamproite	Fraser et al, 1985
		Australia	West Australia	bulk	0,51211	-10,3		0,71251						1	lamproite	Fraser et al, 1985
		Australia	West Australia	bulk	0,51209	-10,7		0,71258						1	lamproite	Fraser et al, 1985
		Australia	West Australia	bulk	0,51197	-13,0		0,71471		17,384	15,714	38,314		1	lamproite	Fraser et al, 1985
		Australia	West Australia	bulk	0,51204	-11,7		0,715		17,575	15,737	38,185		1	lamproite	Fraser et al, 1985
		Australia	West Australia	bulk	0,51194	-13,6		0,71745		17,274	15,728	37,94		1	lamproite	Fraser et al, 1985
		Australia	West Australia	bulk	0,51184	-15,6		0,71753						1	lamproite	Fraser et al, 1985
		Australia	West Australia	bulk	0,51187	-15,0		0,71807						1	lamproite	Fraser et al, 1985
		Australia	West Australia	bulk	0,51167	-18,9		0,71811						1	lamproite	Fraser et al, 1985
		Australia	West Australia	bulk	0,51167	-18,9		0,71878						1	lamproite	Fraser et al, 1985
		Australia	West Australia	bulk	0,51183	-15,8		0,71916						1	lamproite	Fraser et al, 1985
		Australia	West Australia	bulk	0,51181	-16,2		0,71958		17,293	15,736	37,887		1	lamproite	Fraser et al, 1985
		Australia	West Australia	bulk	0,51181	-16,2		0,72039						1	lamproite	Fraser et al, 1985
		Australia	West Australia	bulk	0,51189	-14,6		0,72089						1	lamproite	Fraser et al, 1985
		Australia	West Australia	bulk	0,51182	-16,0		0,72093		17,228	15,76	37,87		1	lamproite	Fraser et al, 1985
-60	-45	Drake Passage	South Orkney Island	whole rock	0,512369	-5,2	13	0,71166						1	gneiss	Walter et al, 2000
-60	-45	Drake Passage	South Orkney Island	whole rock	0,512365	-5,3	94	0,71753						1	pelite	Walter et al, 2000
-23,37	38,85	Indian	Agulhas current			-15,5	33							1	core n− VM19-214 (3092m)	Jeandel et al., 2007 and references therein
-29,63	32,87	Indian	Agulhas current			-15,3	22							1	core n− VM14-77 (1818m)	Jeandel et al., 2007 and references therein
-31,5	32,6	Indian	Agulhas current			-13,4	24							1	core n− RC17-69 (3380m)	Jeandel et al., 2007 and references therein
-35,78	18,45	Indian	Agulhas current			-11,2	22							1	core n− RC11-86 (2829m)	Jeandel et al., 2007 and references therein
12,46	96,04	Indian	Andaman Sea			-11,3	29							1	core n− RC12-344 (2140m)	Jeandel et al., 2007 and references therein
10,12	95,03	Indian	Andaman Sea			-10,0	24							1	core n− MD77-169 (2360m)	Jeandel et al., 2007 and references therein
14,3	93,07	Indian	Andaman Sea			-9,3	24							1	core n− MD77-176 (1375m)	Jeandel et al., 2007 and references therein
11,45	94,09	Indian	Andaman Sea			-9,2	22							1	core n− MD77-171 (1760m)	Jeandel et al., 2007 and references therein
17,11	93,05	Indian	Andaman Sea (Northern)			-8,6	17							1	core n− MD77-178 (2459m)	Jeandel et al., 2007 and references therein
-8	127	Indian	banda sea shelf			-12,4	20							1	sediments	Jeandel et al., 2007 and references therein
18,21	91,01	Indian	Bay of Bengal (Northern)			-12,8	24							1	core n− MD77-179 (1986m)	Jeandel et al., 2007 and references therein
18,28	89,51	Indian	Bay of Bengal (Northern)			-12,6	30							1	core n− MD77-180 (1986m)	Jeandel et al., 2007 and references therein
9,39	81,45	Indian	Bay of Bengal (Western)			-16,2	25							1	core n− VM29-21 (3724m)	Jeandel et al., 2007 and references therein
11,32	81,42	Indian	Bay of Bengal (Western)			-16,1	26							1	core n− VM29-20 (3557m)	Jeandel et al., 2007 and references therein
16,38	85,24	Indian	Bay of Bengal (Western)			-15,1	28							1	core n− VM29-18 (2816m)	Jeandel et al., 2007 and references therein
14,42	83,35	Indian	Bay of Bengal (Western)			-13,9	21							1	core n− VM29-19 (3182m)	Jeandel et al., 2007 and references therein
21	90	Indian	Ganges (India)			-15,7	36							1	river sediment	Jeandel et al., 2007 and references therein
11,6	43,15	Indian	Gulf of Aden			6,3	30							1	core n− V-55 (900m)	Jeandel et al., 2007 and references therein
24	67	Indian	Indus (Pakistan)			-12,2	34							1	river sediment	Jeandel et al., 2007 and references therein
-7,21	103,07	Indian	Java trench			-13,8	35							1	core n− CA30-M (6454m)	Jeandel et al., 2007 and references therein
0,4	73,3	Indian	Maldives			6,4	8							1	core n− 115-713A-19R-2 (2266m)	Jeandel et al., 2007 and references therein
-4,08	145,05	Indian	Manam volcano			7,1	18							1	rocks basalt	Jeandel et al., 2007 and references therein
-10	60	Indian	Mascarene ridge			7,3	4							1	core n− 115-707C-27R-6 (1552m)	Jeandel et al., 2007 and references therein
9	107	Indian	Mekong (Cambodgia)			-9,5	41							1	river sediment	Jeandel et al., 2007 and references therein
26	35	Indian	Red Sea			-9,1	31							1	aerosols n− MR83	Jeandel et al., 2007 and references therein
-6,02	88,57	Indian	Sunda			-7,7	8							1	core n− V34-55 (2996m)	Jeandel et al., 2007 and references therein
-8,25	107,11	Indian	Sunda			-3,1	17							1	core n− V33-75 (3396m)	Jeandel et al., 2007 and references therein
-8,7	106,43	Indian	Sunda			-2,8	14							1	core n− V33-77 (3014m)	Jeandel et al., 2007 and references therein
-7,9	106,4	Indian	Sunda			-2,6	13							1	core n−V33-79 (3000m)	Jeandel et al., 2007 and references therein
-9,06	130,13	Indian	Timor			-9,3	17							1	core n− V28-341 (750m)	Jeandel et al., 2007 and references therein
5	92	Indian	W Indian			-13,8	12							1	dust n− JL-13	Jeandel et al., 2007 and references therein
-59	85	Kerguelen Plateau	Southern_Kerguelen			-0,5	10							1	rocks (average)	Jeandel et al., 2007 and references therein
-65	83	Kerguelen Plateau	kerguelen			-8,0	21							6	sediments	Jeandel et al., 2007 and references therein
-49	69	Kerguelen Plateau	kerguelen			0,0	25							25	basalts	Jeandel et al., 2007 and references therein
-49,25	69,7	Kerguelen Plateau	Ballons Mounts	whole rock	0,51272	1,6		0,70464						1	metabasalt	Gautier et al, 1990
-49,25	69,7	Kerguelen Plateau	Ballons Mounts	whole rock	0,51259	-0,9		0,70521						1	trachybasanite	Gautier et al, 1990
-49,3	69,3	Kerguelen Plateau	Central plateau	whole rock	0,51275	2,2		0,70483		18,467	15,528	38,817	1,98	1	basalt	Gautier et al, 1990

latitude (°N)	longitude (E°)	region (when given)	locality (when given)	grain size fraction (when given)	$^{143}Nd/^{144}Nd$	ε_{Nd}	[Nd] (ppm)	$^{87}Sr/^{86}Sr$	[Sr] (ppm)	$^{206}Pb/^{204}Pb$	$^{207}Pb/^{204}Pb$	$^{208}Pb/^{204}Pb$	[Pb] (ppm)	number of sample	type of sample (when given)	reference
-49,3	69,3	Kerguelen Plateau	Central plateau	whole rock	0,51273	1,8		0,70488		18,377	15,539	38,813	1,64	1	basalt	Gautier et al, 1990
-49,3	69,3	Kerguelen Plateau	Central plateau	whole rock				0,70488						1	basalt	Gautier et al, 1990
-49,3	69,3	Kerguelen Plateau	Central plateau	whole rock				0,70494						1	basalt	Gautier et al, 1990
-49,233	70,153	Kerguelen Plateau	Château Mounts	whole rock	0,51262	-0,4		0,70508		18,444	15,565	39,007	1,85	1	picritic basalt	Gautier et al, 1990
-49,233	70,153	Kerguelen Plateau	Château Mounts	whole rock	0,51262	-0,4		0,70509						1	basalt	Gautier et al, 1990
-49,233	70,153	Kerguelen Plateau	Château Mounts	whole rock	0,51262	-0,4		0,70513						1	mugearite	Gautier et al, 1990
-49,3139	69,0414	Kerguelen Plateau	Cook Glacier	whole rock	0,512447	-3,7	10	0,70548	369					1	alkaline basalt	Dosso et Rama Murphy, 1980
-49,2	70,1	Kerguelen Plateau	Courbet peninsula	whole rock	0,512543	-1,9	8	0,70522	824					1	nepheline bearing basalt	Dosso et Rama Murphy, 1980
-49,2	70,1	Kerguelen Plateau	Courbet peninsula	whole rock	0,512462	-3,4		0,7055	666					1	nepheline bearing basalt	Dosso et Rama Murphy, 1980
-49,2	70,1	Kerguelen Plateau	Courbet peninsula	whole rock	0,512412	-4,4	14	0,70553	662					1	trachyte	Dosso et Rama Murphy, 1980
-49,2943	69,9837	Kerguelen Plateau	Crozier Mount	whole rock	0,51261	-0,5		0,70506						1	hawaiite	Gautier et al, 1990
-49,65	68,77	Kerguelen Plateau	Gaby Island	whole rock	0,51275	2,2		0,70497	304	18,607	15,579	39,212	2,3	1	basalt	Weis et al, 1993
-49,65	68,77	Kerguelen Plateau	Gaby Island	whole rock	0,51265	0,2		0,70532	364	18,435	15,556	39,065	8,1	1	trachyte	Weis et al, 1993
-49,66	70	Kerguelen Plateau	Jeanne d'arc peninsula	whole rock	0,512346	-5,7	8	0,70572	474					1	alkaline basalt	Dosso et Rama Murphy, 1980
-49,66	70	Kerguelen Plateau	Jeanne d'arc peninsula	whole rock	0,512444	-3,8		0,70588	1535					1	trachyte	Dosso et Rama Murphy, 1980
-49,66	70	Kerguelen Plateau	Jeanne d'arc peninsula	whole rock				0,70511	599	18,562	15,566	39,166	4,2	1	basalt	Weis et al, 1993
-49,66	70	Kerguelen Plateau	Jeanne d'arc peninsula	whole rock	0,5127	1,2		0,70518	419	18,543	15,566	39,116	2,7	1	basalt	Weis et al, 1993
-49,66	70	Kerguelen Plateau	Jeanne d'arc peninsula	whole rock	0,51261	-0,5		0,70526	407	18,379	15,559	39,03	2,4	1	basalt	Weis et al, 1993
-49,66	70	Kerguelen Plateau	Jeanne d'arc peninsula	whole rock	0,51254	-1,9		0,70562	1097	18,263	15,569	38,923	8,5	1	basanite	Weis et al, 1993
-49,66	70	Kerguelen Plateau	Jeanne d'arc peninsula	whole rock	0,51256	-1,5		0,70599	203	18,15	15,562	38,909	20	1	phonolite	Weis et al, 1993
-49,66	70	Kerguelen Plateau	Jeanne d'arc peninsula	whole rock	0,51251	-2,5		0,70612	98	18,064	15,538	38,684	33	1	phonolite	Weis et al, 1993
-49,66	70	Kerguelen Plateau	Jeanne d'arc peninsula	whole rock	0,51265	0,2		0,70678	82	18,273	15,582	39,041	36	1	phonolite	Weis et al, 1993
-49,66	70	Kerguelen Plateau	Jeanne d'arc peninsula	whole rock	0,51265	0,2		0,7092	26	18,137	15,568	39,163	7,1	1	trachite	Weis et al, 1993
-49,66	70	Kerguelen Plateau	Jeanne d'arc peninsula	whole rock	0,51261	-0,5		0,7095	29	18,427	15,556	39,094	8,4	1	trachite	Weis et al, 1993
-49,66	70	Kerguelen Plateau	Jeanne d'arc peninsula	whole rock	0,51261	-0,5			10	18,147	15,556	38,717	54	1	phonolite	Weis et al, 1993
-48,8	69	Kerguelen Plateau	Loranchet peninsula	whole rock	0,512711	1,4	6	0,70463	646					1	basanite	Dosso et Rama Murphy, 1980
-48,8	69	Kerguelen Plateau	Loranchet peninsula	whole rock	0,51274	2,0		0,7043		18,302	15,558	38,391	4,7	1	basalt	Gautier et al, 1990
-48,8	69	Kerguelen Plateau	Loranchet peninsula	whole rock	0,51266	0,4		0,70471		18,504	15,55	38,957	1,6	1	basalt	Gautier et al, 1990
-49,4558	69,4747	Kerguelen Plateau	Mont Blanc	whole rock	0,512551	-1,7		0,70512	540					1	basalt	Dosso et Rama Murphy, 1980
-49,6	68,93	Kerguelen Plateau	Rallier du Baty	whole rock	0,512549	-1,7		0,70553	783					1	gabbro	Dosso et Rama Murphy, 1980
-49,6	68,93	Kerguelen Plateau	Rallier du Baty	whole rock	0,512535	-2,0	16	0,7056	393					1	granite	Dosso et Rama Murphy, 1980
-49,6	68,93	Kerguelen Plateau	Rallier du Baty	whole rock	0,512546	-1,8		0,7056	1,92					1	syenite	Dosso et Rama Murphy, 1980
-49,6	68,93	Kerguelen Plateau	Rallier du Baty	whole rock	0,512499	-2,7		0,70767	728					1	gabbro	Dosso et Rama Murphy, 1980
-49,6	68,93	Kerguelen Plateau	Rallier du Baty	whole rock	0,512535	-2,0	11							1	granite	Dosso et Rama Murphy, 1980
-49,6	70,15	Kerguelen Plateau	Ronarc'h peninsula	whole rock	0,51265	0,2		0,70519	471	18,44	15,553	39,012	2,5	1	basalte	Weis et al, 1993
-49,6	70,15	Kerguelen Plateau	Ronarc'h peninsula	whole rock	0,51266	0,4		0,7052	380	18,526	15,591	39,165	2,2	1	basalte	Weis et al, 1993
-49,6	70,15	Kerguelen Plateau	Ronarc'h peninsula	whole rock	0,51272	1,6		0,70527	406	18,539	15,591	39,193	2,3	1	basalte	Weis et al, 1993
-49,6	70,15	Kerguelen Plateau	Ronarc'h peninsula	whole rock	0,51262	-0,4		0,7055	1494	18,427	15,556	39,094	14	1	tephrite	Weis et al, 1993
-49,6	70,15	Kerguelen Plateau	Ronarc'h peninsula	whole rock	0,51254	-1,9		0,70562	1153	18,487	15,568	39,163	14	1	tephrite	Weis et al, 1993
-49,6	70,15	Kerguelen Plateau	Ronarc'h peninsula	whole rock	0,51256	-1,5		0,70569	235	18,084	15,548	38,718	34	1	phonolite	Weis et al, 1993
-49,6	70,15	Kerguelen Plateau	Ronarc'h peninsula	whole rock	0,51249	-2,9		0,70576	1274	18,071	15,56	38,879	8,1	1	basanite	Weis et al, 1993
-49,6	70,15	Kerguelen Plateau	Ronarc'h peninsula	whole rock	0,51251	-2,5			1125	18,05	15,556	38,63	5,9	1	basanite	Weis et al, 1993
-49,63	70	Kerguelen Plateau	SE Province	whole rock	0,51259	-0,9		0,70503						1	basalt	Gautier et al, 1990
-49,35	69,72	Kerguelen Plateau	West Island	whole rock	0,512448	-3,7		0,70562	1090					1	gabbro	Dosso et Rama Murphy, 1980
-49,35	69,72	Kerguelen Plateau	West Island	whole rock	0,512479	-3,1	28	0,70576	1187					1	gabbro	Dosso et Rama Murphy, 1980
-49,35	69,72	Kerguelen Plateau	West Island	whole rock	0,512461	-3,5		0,70583	820					1	gabbro	Dosso et Rama Murphy, 1980
-49,35	69,72	Kerguelen Plateau	West Island	whole rock	0,51254	-1,9		0,70538		18,334	15,552	38,807	3,6	1	basalt	Gautier et al, 1990
-49,35	69,72	Kerguelen Plateau	West Island	whole rock	0,5125	-2,7		0,70564		18,234	15,545	38,978	8,1	1	basalt	Gautier et al, 1990
-41	172,4	New Zealand	New Zealand			1,2	5							8	rocks	Jeandel et al., 2007 and references therein
54,37	-145,59	Pacific	Alaska Basin			1,6	17							1	core n− SS13-S (4111m)	Jeandel et al., 2007 and references therein
47	152	Pacific	C, Kurile (Simushir)			10,1	11							1	basalt andesite n− 135-81	Jeandel et al., 2007 and references therein
2,42	121,32	Pacific	Celebes Basin			4,2	19							1	core n− BA16-M (5336m)	Jeandel et al., 2007 and references therein
46,3	-124	Pacific	Colombia (U,S,A)			-6,6	30							1	river sediment	Jeandel et al., 2007 and references therein
3	-83	Pacific	Costa Rica rift			9,8	5							1	core n− 143R-1 (3640m)	Jeandel et al., 2007 and references therein
4,1	-95,6	Pacific	E Pacific			-3,4	13							1	core n− DSDP 503B	Jeandel et al., 2007 and references therein
13	-91	Pacific	Guatemala			2,0	19							1	core n− 495	Jeandel et al., 2007 and references therein
37	126	Pacific	Hangang (South-Korea)			-16,9	39							1	river sediment	Jeandel et al., 2007 and references therein
36,39	130,58	Pacific	Japan Basin			-9,3	33							1	core n− BA23-M (2111m)	Jeandel et al., 2007 and references therein
53	177	Pacific	Kiska Island			8,5	12							1	basalt rock n −54-452	Jeandel et al., 2007 and references therein
-20,13	-176,82	Pacific	Lau basin			7,5	5							1	core n− 135-836A-3HCC (2466m)	Jeandel et al., 2007 and references therein
-18,5	-177,3	Pacific	Lau basin			8,8	5							1	core n− 135-835B-3R2 (2905m)	Jeandel et al., 2007 and references therein
-18,57	-177,87	Pacific	Lau basin			9,2	10							1	core n− 135-834B-33R-1 (2690m)	Jeandel et al., 2007 and references therein
19,06	-105,3	Pacific	Middle America trench			1,3	26							1	core n− CA25-M (4912m)	Jeandel et al., 2007 and references therein
47,09	-119,18	Pacific	Moses lake (E,U)			-6,0	24							1	core n− Moses Lake	Jeandel et al., 2007 and references therein
-35,1	139,17	Pacific	Murray Bridge (Australia)			-6,0	15							1	diss load river n− Murray	Jeandel et al., 2007 and references therein
46,3	161,4	Pacific	N Pacific			-0,5	12							1	core n− V20-122	Jeandel et al., 2007 and references therein
50,51	155,39	Pacific	N, Kurile (Alaid volcano)			7,6	18							1	basalt rock n− B-11-575	Jeandel et al., 2007 and references therein
49,56	154,08	Pacific	N, Kurile (Beliankin)			7,7	17							1	basalt rock n− B-11-72/5	Jeandel et al., 2007 and references therein
48,59	153,29	Pacific	N, Kurile (Chirinkotan)			7,3	20							1	andesite rock n− B-11-527	Jeandel et al., 2007 and references therein
48,23	153,45	Pacific	N, Kurile (Lovushki)			9,6	5							1	basalt andesite n− B-11-113/2	Jeandel et al., 2007 and references therein
35	129	Pacific	Nakdongang (South-Korea)			-13,4	31							1	river sediment	Jeandel et al., 2007 and references therein
25	115	Pacific	Nanking			-10,2	35							1	loess n− Nanking	Jeandel et al., 2007 and references therein
46,3	-131,7	Pacific	NE Pacific			-6,1	19							1	core n− TT175-83P	Jeandel et al., 2007 and references therein
-45	171	Pacific	New Zealand			-5,3	32							1	loess n− BP2 & BP4	Jeandel et al., 2007 and references therein
-10	160	Pacific	Ontong_Java_Plateau			1,8	10							1	rocks (average)	Jeandel et al., 2007 and references therein
-16,92	-73,73	Pacific	Peru Chile slope			-3,2	20							1	core n− CA27-S (3603m)	Jeandel et al., 2007 and references therein
-7,35	-81,24	Pacific	Peru Chile trench			-5,0	24							1	core n− CA29-M (5856m)	Jeandel et al., 2007 and references therein
-17,3	146,15	Pacific	Queensland			-6,3	32							1	core n− BB 9979 W	Jeandel et al., 2007 and references therein
37,5	-123	Pacific	San Francisco Bay (U,S,A)			-3,6	21							1	river sediment	Jeandel et al., 2007 and references therein
-3,6	-83,9	Pacific	SE Pacific			-4,3	9							1	core n− V19-29	Jeandel et al., 2007 and references therein
34,5	127,5	Pacific	Sumjingang (South-Korea)			-18,4	38							1	river sediment	Jeandel et al., 2007 and references therein

latitude (°N)	longitude (E°)	region (when given)	locality (when given)	grain size fraction (when given)	$^{143}Nd/^{144}Nd$	ε_{Nd}	[Nd] (ppm)	$^{87}Sr/^{86}Sr$	[Sr] (ppm)	$^{206}Pb/^{204}Pb$	$^{207}Pb/^{204}Pb$	$^{208}Pb/^{204}Pb$	[Pb] (ppm)	number of sample	type of sample (when given)	reference
7	110	Pacific	W Pacific			-10,6	16							1	dust n− JL-25	Jeandel et al., 2007 and references therein
23	119	Pacific	W Pacific			-9,6	42							1	dust n− JL-17	Jeandel et al., 2007 and references therein
18,13	-104,36	Pacific	West Mexico Basin			4,2	15							1	core n− CA24-S (680m)	Jeandel et al., 2007 and references therein
-31,5	152,2	Pacific	Wingham (Australia)			-1,3	16							1	diss load river n− Manning	Jeandel et al., 2007 and references therein
31	123	Pacific	Yangtze (China)			-10,7	32							1	river sediment	Jeandel et al., 2007 and references therein
35	126	Pacific	Youngsangang (South-Korea)			-13,2	36							1	river sediment	Jeandel et al., 2007 and references therein
-65,95	-70,25	Pacific		0-63 µm				0,705281						1	marine sediment	Hemming et al., 2007
-61,18	-75,93	Pacific		0-63 µm				0,706946						1	marine sediment	Hemming et al., 2007
-70,42	-99,26	Pacific		0-63 µm				0,707928						1	marine sediment	Hemming et al., 2007
-67,18	-74,78	Pacific		0-63 µm				0,708198						1	marine sediment	Hemming et al., 2007
-70,1	-122,26	Pacific		0-63 µm				0,709086						1	marine sediment	Hemming et al., 2007
-70,14	-102,82	Pacific		0-63 µm				0,70979						1	marine sediment	Hemming et al., 2007
-70	-120,17	Pacific		0-63 µm				0,712846						1	marine sediment	Hemming et al., 2007
-71,96	178,6	Pacific		0-63 µm				0,714642						1	marine sediment	Hemming et al., 2007
-64,83	150,49	Pacific		0-63 µm				0,725643						1	marine sediment	Hemming et al., 2007
-70,17	-106,64	Pacific		0-63 µm				0,73182						1	marine sediment	Hemming et al., 2007
0	-50	South America	Amazon			-9,2	35							1	river sediment	Jeandel et al., 2007 and references therein
7,5	-48	South America	Amazon			-10,2	42							6	river sediment	Jeandel et al., 2007 and references therein
-42	-72	South America	Chile			2,1	19							26	rocks	Jeandel et al., 2007 and references therein
-11	-36	South America	Sao Francisco (Brazil)			-12,9	31							1	river sediment	Jeandel et al., 2007 and references therein
-52,55	-60,28	South America	South Falkland Basin			-4,4	14							1	core n− TE6-S (472m)	Jeandel et al., 2007 and references therein
		South America	Amazon	bulk	0,512185	-8,8		0,71319		18,93	15,675	38,85		1	suspended particles (5m below river's surface)	Allegre et al, 1996
		South America	Amazon	bulk	0,512235	-7,9		0,71327		18,9	15,669	38,84		1	suspended particles (5m below river's surface)	Allegre et al, 1996
		South America	Amazon	bulk	0,511925	-13,9		0,71698		18,95	15,675	38,82		1	suspended particles (5m below river's surface)	Allegre et al, 1996
		South America	Amazon	bulk	0,512094	-10,6		0,72146		18,94	15,707	39,03		1	suspended particles (5m below river's surface)	Allegre et al, 1996
		South America	Amazon	bulk	0,511732	-17,7		0,72835		19,17	15,803	39,16		1	suspended particles (5m below river's surface)	Allegre et al, 1996
		South America	Amazon	bulk	0,512027	-11,9		0,73352		18,67	15,659	38,84		1	suspended particles (5m below river's surface)	Allegre et al, 1996
		South America	Amazon	bulk	0,5115	-22,2		0,74683		19,95	15,924	39,93		1	suspended particles (5m below river's surface)	Allegre et al, 1996
		South America	Amazon	bulk	0,511606	-20,1		0,7564		18,96	15,678	38,92		1	suspended particles (5m below river's surface)	Allegre et al, 1996
		South America	Amazon	bulk						18,95	15,675	38,92		1	suspended particles (5m below river's surface)	Allegre et al, 1996
		South America	Amazon					0,7109						1	river sediment	Palmer et al., 1989
-49,75	-73,55	South America	Andes			-1,4	18							2	adakites	Jeandel et al., 2007 and references therein
-52,33	-73,4	South America	Andes			1,1	16							4	adakites	Jeandel et al., 2007 and references therein
-38	-72	South America	Andes			2,5	19							26	rocks	Jeandel et al., 2007 and references therein
-23,85	-70,3	South America	Andes			5,5	9							8	rocks	Jeandel et al., 2007 and references therein
-46,2	-76	South America	Andes			5,6	21							10	basalts	Jeandel et al., 2007 and references therein
-54,95	-70,24	South America	Andes			9,8	28							1	adakites n−Ck-3-198	Jeandel et al., 2007 and references therein
-36	-70	South America	Andes	whole rock				0,70385						1	basalt	Stern et al, 1990
-41	-67	South America	Andes	whole rock	0,51274	2,0		0,704		18,56	15,62	38,57		1	basalt	Stern et al, 1990
-35	-69	South America	Andes	whole rock	0,51279	3,0		0,70404		18,62	15,61	38,53		1	basalt	Stern et al, 1990
-36	-70	South America	Andes	whole rock				0,70412						1	basalt	Stern et al, 1990
-39	-70	South America	Andes	whole rock				0,70422						1	basalt	Stern et al, 1990
-41	-70	South America	Andes	whole rock	0,51287	4,5		0,70423						1	basalt	Stern et al, 1990
-35	-68	South America	Andes	whole rock	0,51278	2,8		0,70431		8,52	15,59	38,36		1	basalt	Stern et al, 1990
-35	-69	South America	Andes	whole rock				0,70436						1	basalt	Stern et al, 1990
-45	-69	South America	Andes	whole rock	0,51264	0,0		0,70489		18,26	15,53	38,3		1	basalt	Stern et al, 1990
-44	-68	South America	Andes	whole rock	0,51265	0,2		0,70512		18,45	15,59	38,51		1	basalt	Stern et al, 1990
-72,17	-50,31	South America	Argentino Lake, El Calafate, Southern Patagonia	bulk	0,512544	-1,8				18,714	15,638	38,698		1	rural top soil, bed sediment	Khondoker ???
-69,51	-51,16	South America	Bahia Grande, Southern Patagonia	bulk	0,512575	-1,2				18,701	15,632	38,636		1	rural top soil, bed sediment	Khondoker ???
-69,53	-51,09	South America	Bahia Grande, Southern Patagonia	bulk	0,512511	-2,5				18,748	15,64	38,698		1	rural top soil, bed sediment	Khondoker ???
-68,39	-52,99	South America	Bahia San Sebastian, Southern Patagonia	bulk	0,512669	0,6				18,696	15,623	38,56		1	rural top soil, bed sediment	Khondoker ???
-68,39	-53,04	South America	Bahia San Sebastian, Southern Patagonia	bulk	0,512477	-3,1				18,781	15,645	38,713		1	rural top soil, bed sediment	Khondoker ???
-68,5	-53,14	South America	Bahia San Sebastian, Southern Patagonia	bulk	0,512463	-3,4				18,614	15,639	38,536		1	rural top soil, bed sediment	Khondoker ???
-68,57	-53,17	South America	Bahia San Sebastian, Southern Patagonia	bulk	0,512486	-3,0				18,668	15,64	38,586		1	rural top soil, bed sediment	Khondoker ???
-68,57	-53,2	South America	Bahia San Sebastian, Southern Patagonia	bulk	0,512505	-2,6				18,755	15,64	38,684		1	rural top soil, bed sediment	Khondoker ???
-68,57	-53,23	South America	Bahia San Sebastian, Southern Patagonia	bulk	0,512488	-2,9				18,771	15,645	38,691		1	rural top soil, bed sediment	Khondoker ???
-68,52	-53,32	South America	Bahia San Sebastian, Southern Patagonia	bulk	0,512477	-3,1				18,776	15,647	38,711		1	rural top soil, bed sediment	Khondoker ???
-33,47	59,3	South America	Baradero	bulk	0,512459	-3,5		0,70895	203					1	loess	Smith et al., 2003
-33,47	59,3	South America	Baradero	bulk	0,51243	-4,1		0,708987	216					1	loess	Smith et al., 2003
-33,47	59,3	South America	Baradero	bulk	0,512432	-4,0		0,709387	191					1	loess	Smith et al., 2003
-33,47	59,3	South America	Baradero	bulk	0,512361	-5,4		0,709612	209					1	loess	Smith et al., 2003
-33,47	59,3	South America	Baradero	bulk	0,512339	-5,8		0,709927						1	loess	Smith et al., 2003
-7	-37	South America	Borborema Province	whole rock	0,5121	-11,1	47	0,7185	510,8					9	Borborema Province	Canade de Aujo et al., 2014
-71,03	-43,02	South America	Chaiten Volcano, Southern Volcanic Zone	bulk	0,512586	-1,0				18,812	15,643	38,763		1	volcanic clasts and tephras	Khondoker ???
-71,03	-43,02	South America	Cotopaxi Volcano, Northern Volcanic Zone	bulk	0,512816	3,5				18,765	15,635	38,623		1	volcanic clasts and tephras	Khondoker ???
-28,7	66,06	South America	El Lambedero	bulk	0,512405	-4,5		0,711274	227					1	loess	Smith et al., 2003
-28,7	66,06	South America	El Lambedero	bulk	0,512308	-6,4		0,711894						1	loess	Smith et al., 2003
-28,7	66,06	South America	El Lambedero	bulk	0,51232	-6,2		0,712134	264					1	loess	Smith et al., 2003
-28,7	66,06	South America	El Lambedero	bulk	0,512316	-6,3		0,712331	289					1	loess	Smith et al., 2003
-34,54	58,01	South America	Gorina	bulk	0,51246	-3,5		0,707557						1	loess	Smith et al., 2003
-34,54	58,01	South America	Gorina	bulk	0,512552	-1,7		0,707592	232					1	loess	Smith et al., 2003
-34,54	58,01	South America	Gorina	bulk	0,512554	-1,6		0,707617	521					1	loess	Smith et al., 2003
-34,54	58,01	South America	Gorina	bulk	0,512478	-3,1		0,707624						1	loess	Smith et al., 2003
-34,54	58,01	South America	Gorina	bulk	0,512482	-3,0		0,707701	222					1	loess	Smith et al., 2003
-34,54	58,01	South America	Gorina	bulk	0,5125	-2,7		0,708551						1	loess	Smith et al., 2003
-37,57	57,38	South America	Hipódromo	bulk	0,512583	-1,1		0,705914	371					1	loess	Smith et al., 2003
-37,57	57,38	South America	Hipódromo	bulk	0,512581	-1,1		0,705964						1	loess	Smith et al., 2003
-37,57	57,38	South America	Hipódromo	bulk	0,512594	-0,9		0,705986	310					1	loess	Smith et al., 2003
-37,57	57,38	South America	Hipódromo	bulk	0,512577	-1,2		0,706207	347					1	loess	Smith et al., 2003
-31,39	64,64	South America	Lozada	bulk	0,512468	-3,3		0,707904	522					1	loess	Smith et al., 2003
-31,39	64,64	South America	Lozada	bulk	0,512458	-3,5		0,708089						1	loess	Smith et al., 2003

latitude (°N)	longitude (E°)	region (when given)	locality (when given)	grain size fraction (when given)	$^{143}Nd/^{144}Nd$	ε_{Nd}	[Nd] (ppm)	$^{87}Sr/^{86}Sr$	[Sr] (ppm)	$^{206}Pb/^{204}Pb$	$^{207}Pb/^{204}Pb$	$^{208}Pb/^{204}Pb$	[Pb] (ppm)	number of sample	type of sample (when given)	reference
-31,39	64,64	South America	Lozada	bulk	0,512469	-3,3		0,708135	315					1	loess	Smith et al., 2003
-31,39	64,64	South America	Lozada	bulk	0,512452	-3,6		0,70827	320					1	loess	Smith et al., 2003
-37,5	-57	South America	Mar Del Plata	bulk	0,512928	5,7		0,706297						1	dust	Grousset et al, 1992
-38	-59	South America	Pampa	bulk	0,512939	5,9		0,70604						1	dust	Grousset et al, 1992
-38	-59	South America	Pampa	bulk	0,512611	-0,5		0,706072						1	dust	Grousset et al, 1992
-38	-59	South America	Pampa	bulk	0,513064	8,3		0,708049						1	dust	Grousset et al, 1992
-27,2585	-51,2192	South America	Parana	whole rock	0,512375	-5,1	24	0,1617	336,8					1	parana basalt	Tapami Ramo et al., 2016
-27,3043	-54,2001	South America	Parana	whole rock	0,512377	-5,1	23	0,2085	327,4					1	parana basalt	Tapami Ramo et al., 2016
-27,2416	-54,3532	South America	Parana	whole rock	0,512371	-5,2	24	0,2211	329,8					1	parana basalt	Tapami Ramo et al., 2016
-25,6845	-54,4396	South America	Parana	whole rock	0,512349	-5,6	51	0,2383	462,2					1	parana basalt	Tapami Ramo et al., 2016
-27,2348	-54,0391	South America	Parana	whole rock	0,512355	-5,5	23	0,2412	337,2					1	parana basalt	Tapami Ramo et al., 2016
-27,2514	-54,1863	South America	Parana	whole rock	0,512405	-4,5	27	0,248	289,8					1	parana basalt	Tapami Ramo et al., 2016
-27,1551	-53,9564	South America	Parana	whole rock	0,512363	-5,4	30	0,3312	350,7					1	parana basalt	Tapami Ramo et al., 2016
-27,0554	-54,8235	South America	Parana	whole rock	0,512397	-4,7	23	0,3797	328,9					1	parana basalt	Tapami Ramo et al., 2016
-27,0389	-54,1335	South America	Parana	whole rock	0,512354	-5,5	27	0,3826	270,5					1	parana basalt	Tapami Ramo et al., 2016
-26,7554	-54,921	South America	Parana	whole rock	0,512383	-5,0	46							1	parana basalt	Tapami Ramo et al., 2016
-34,5	-59	South America	Parana River			-10,3	37							1	river sediment	Jeandel et al., 2007 and references therein
		South America	Parana river					0,7139						1	river sediment	Palmer et al., 1989
-35	-58	South America	Parana River			-9,0	40							1	river sed,	Jeandel et al., 2007 and references therein
-52	-69	South America	Patagonia	whole rock	0,51292	5,5		0,70316		19,14	15,62	38,8		1	basalt	Stern et al, 1990
-52	-69	South America	Patagonia	whole rock	0,51291	5,3		0,70317		18,96	15,61	38,63		1	basalt	Stern et al, 1990
-47	-70	South America	Patagonia	whole rock	0,5129	5,1		0,70321		19,37	15,6	38,84		1	basalt	Stern et al, 1990
-47	-70	South America	Patagonia	whole rock	0,51291	5,3		0,70322		19,38	15,64	39,23		1	basalt	Stern et al, 1990
-52	-69	South America	Patagonia	whole rock	0,51292	5,5		0,70324		19,01	15,62	38,77		1	basalt	Stern et al, 1990
-52	-69	South America	Patagonia	whole rock	0,51291	5,3		0,70328		18,95	15,68	38,75		1	basalt	Stern et al, 1990
-52	-69	South America	Patagonia	whole rock				0,70333						1	basalt	Stern et al, 1990
-50	-70	South America	Patagonia	whole rock	0,5129	5,1		0,7035		18,67	15,6	38,45		1	basalt	Stern et al, 1990
-50	-70	South America	Patagonia	whole rock				0,70354						1	basalt	Stern et al, 1990
-50	-70	South America	Patagonia	whole rock	0,51287	4,5		0,70356		18,65	15,58	38,6		1	basalt	Stern et al, 1990
-42	-70	South America	Patagonia	whole rock				0,7037						1	basalt	Stern et al, 1990
-48	-70	South America	Patagonia	whole rock	0,51276	2,4		0,70387		18,55	15,58	38,46		1	basalt	Stern et al, 1990
-47	-68	South America	Patagonia	whole rock				0,70405						1	basalt	Stern et al, 1990
-47	-70	South America	Patagonia	whole rock				0,70406						1	basalt	Stern et al, 1990
-43	-67	South America	Patagonia Plateau	bulk	0,512825	3,6		0,706599						1	dust	Grousset et al, 1992
-41	-73	South America	Puerto Mont	-	0,512805	3,3	19	0,704478						1	loess	Walter et al, 2000
-54	-69	South America	Punta Arenas	bulk	0,512625	-0,3		0,706642						1	dust	Basile et al, 1997
-53	-71	South America	Punta Arenas	silt	0,512472	-3,2	23	0,70631						1	moraine	Walter et al, 2000
-53	-71	South America	Punta Arenas	clay	0,512468	-3,3	26	0,710397						1	moraine	Walter et al, 2000
-71,11	-53,29	South America	Punta Arenas, Southern Patagonia	bulk	0,512814	3,4				18,534	15,615	38,397		1	rural top soil, bed sediment	Khondoker ???
-71,11	-53,29	South America	Punta Arenas, Southern Patagonia	bulk	0,512561	-1,5				18,697	15,632	38,605		1	rural top soil, bed sediment	Khondoker ???
-71,64	-40,76	South America	Puyehue Volcano, lakeside near La Angostura	bulk	0,512831	3,8				18,57	15,617	38,506		1	volcanic clasts and tephras	Khondoker ???
-71,16	-40,62	South America	Puyehue Volcano, Southern Volcanic Zone	bulk	0,512829	3,7				18,601	15,621	38,538		1	volcanic clasts and tephras	Khondoker ???
-71,16	-41,06	South America	Puyehue Volcano, Southern Volcanic Zone	bulk	0,512841	4,0				18,59	15,612	38,505		1	volcanic clasts and tephras	Khondoker ???
0	-78	South America	Quito	-	0,512863	4,4	13	0,704164						1	loess	Walter et al, 2000
-34	-55	South America	Rio de la Plata	bulk	0,511735	-17,6	43	0,7106625						22	Nico Perez terrane	Mallman et al., 2007
-51,5	-69	South America	Rio Gallegos	bulk	0,512733	1,9								1	dust	Basile et al, 1997
-69,53	-51,81	South America	Rio Gallegos, Southern Patagonia	bulk	0,512599	-0,8				18,725	15,626	38,62		1	rural top soil, bed sediment	Khondoker ???
-69,6	-51,71	South America	Rio Gallegos, Southern Patagonia	bulk	0,512623	-0,3				18,722	15,631	38,639		1	rural top soil, bed sediment	Khondoker ???
-68,07	-53,59	South America	Rio Grande, Southern Patagonia	bulk	0,512461	-3,5				18,707	15,639	38,622		1	rural top soil, bed sediment	Khondoker ???
-68,07	-53,59	South America	Rio Grande, Southern Patagonia	bulk	0,512448	-3,7				18,737	15,644	38,66		1	rural top soil, bed sediment	Khondoker ???
-67,8	-53,83	South America	Rio Grande, Southern Patagonia	bulk	0,512463	-3,4				18,772	15,636	38,686		1	rural top soil, bed sediment	Khondoker ???
-69,28	-51,73	South America	Rio Grande, Southern Patagonia	bulk	0,51254	-1,9				18,707	15,63	38,601		1	rural top soil, bed sediment	Khondoker ???
-69,28	-51,73	South America	Rio Grande, Southern Patagonia	bulk	0,512582	-1,1				18,327	15,618	38,212		1	rural top soil, bed sediment	Khondoker ???
-69,64	-51,63	South America	Rio Grande, Southern Patagonia	bulk	0,512559	-1,5				18,719	15,642	38,647		1	rural top soil, bed sediment	Khondoker ???
-68,9	-49,97	South America	Rio Santa Cruz, El Calafate, Southern Patagonia	bulk	0,512576	-1,2				18,711	15,635	38,681		1	rural top soil, bed sediment	Khondoker ???
-68,9	-49,97	South America	Rio Santa Cruz, El Calafate, Southern Patagonia	bulk	0,512573	-1,3				18,461	15,627	38,41		1	rural top soil, bed sediment	Khondoker ???
-68,56	-49,83	South America	Rio Santa Cruz, El Calafate, Southern Patagonia	bulk	0,51257	-1,3				18,715	15,636	38,694		1	rural top soil, bed sediment	Khondoker ???
-68,94	-50,24	South America	Rio Santa Cruz, Southern Patagonia	bulk	0,512598	-0,8				18,757	15,637	38,663		1	rural top soil, bed sediment	Khondoker ???
-33	-70	South America	Santiago	-	0,512872	4,6	12	0,704155						1	loess	Walter et al, 2000
-12,5	-47,5	South America	Tocantin Province	whole rock	0,511571	-20,8	39							131	Tocantin Province	Fuck et al., 2014
-58,51	-34,6	South America	Urban Area, Buenos Aires	50-100µm	0,511957	-13,3				18,158	15,619	38,094		1	road dusts	Khondoker ???
-68,57	-53,17	South America	Urban Area, Buenos Aires	50-100µm	0,51184	-15,6				18,141	15,631	38,104		1	road dusts	Khondoker ???
-58,49	-34,65	South America	Urban Area, Buenos Aires	50-100µm	0,511946	-13,5				18,154	15,629	38,126		1	road dusts	Khondoker ???
-58,49	-34,65	South America	Urban Area, Buenos Aires	50-100µm	0,511633	-19,6				18,187	15,639	38,233		1	road dusts	Khondoker ???
-58,51	-34,6	South America	Urban Area, Buenos Aires	50-100µm	0,511704	-18,2				18,165	15,618	38,128		1	road dusts	Khondoker ???
-68,57	-53,17	South America	Urban Area, Buenos Aires	50-100µm	0,51166	-19,1				18,084	15,633	38,1		1	road dusts	Khondoker ???
-58,49	-34,65	South America	Urban Area, Buenos Aires	<10µm	0,511785	-16,6				18,19	15,64	38,2		1	urban aerosols	Khondoker ???
-58,49	-34,65	South America	Urban Area, Buenos Aires	<10µm	0,51194	-13,6				18,186	15,629	38,182		1	urban aerosols	Khondoker ???
-58,49	-34,65	South America	Urban Area, Sao Paulo	<10µm	0,511852	-15,3				18,634	15,676	38,364		1	urban aerosols	Khondoker ???
-46,72	-23,56	South America	Urban Area, Sao Paulo	<10µm						18,192	15,621	37,959		1	urban aerosols	Khondoker ???
-46,72	-23,56	South America	Urban Area, Sao Paulo	<10µm						18,096	15,615	37,879		1	urban aerosols	Khondoker ???
-46,72	-23,56	South America	Urban Area, Sao Paulo	<10µm						18,189	15,618	38,036		1	urban aerosols	Khondoker ???
-46,72	-23,56	South America	Urban Area, Sao Paulo	<10µm	0,511915	-14,1				18,518	15,655	38,092		1	urban aerosols	Khondoker ???
-52	-73	South America	Ushuaia	bulk	0,51263	-0,2		0,7077						1	dust	Basile et al, 1997
-38,43	-56,7	South America		bulk	0,512555	-1,6		0,7053						1	marine sediment	Basile et al, 1997
-44,1	-33,92	South America		bulk	0,512466	-3,4		0,7063						1	marine sediment	Basile et al, 1997
-48,15	-64,38	South America		bulk	0,512434	-4,0		0,7069						1	marine sediment	Basile et al, 1997
-40,43	-61,23	South America		bulk	0,512542	-1,9		0,7073						1	marine sediment	Basile et al, 1997
-54,17	-64,97	South America		bulk	0,512506	-2,6		0,7077						1	marine sediment	Basile et al, 1997
-52,68	-59,15	South America		bulk	0,512255	-7,5		0,7116						1	marine sediment	Basile et al, 1997
-35,67	-56,57	South America		bulk	0,512153	-9,5		0,7128						1	marine sediment	Basile et al, 1997

latitude (°N)	longitude (E°)	region (when given)	locality (when given)	grain size fraction (when given)	$^{143}Nd/^{144}Nd$	ε_{Nd}	[Nd] (ppm)	$^{87}Sr/^{86}Sr$	[Sr] (ppm)	$^{206}Pb/^{204}Pb$	$^{207}Pb/^{204}Pb$	$^{208}Pb/^{204}Pb$	[Pb] (ppm)	number of sample	type of sample (when given)	reference
-50,58	2,9	South Atlantic	-	0-63 µm				0,708034						1	marine sediment (LGM)	Hemming et al., 2007
-53,18	-0,35	South Atlantic	-	0-63 µm				0,70899						1	marine sediment (LGM)	Hemming et al., 2007
-53,05	-16,45	South Atlantic	-	0-63 µm				0,709372						1	marine sediment (LGM)	Hemming et al., 2007
-50,87	-9,87	South Atlantic	-	0-63 µm				0,709935						1	marine sediment	Hemming et al., 2007
-53,05	-16,45	South Atlantic	-	0-63 µm				0,710432						1	marine sediment	Hemming et al., 2007
-48,57	5,13	South Atlantic	-	0-63 µm				0,711339						1	marine sediment	Hemming et al., 2007
-48,57	5,13	South Atlantic	-	0-63 µm				0,712455						1	marine sediment (LGM)	Hemming et al., 2007
-50,58	2,9	South Atlantic	-	0-63 µm				0,712999						1	marine sediment	Hemming et al., 2007
-64,7817	-68,455	South Atlantic	Antarctic Peninsula	bulk	0,51278	2,8	14	0,706829						1	marine sediment	Walter et al, 2000
-43,85	27,6	South Atlantic	Cape basin	0-63 µm				0,709249						1	marine sediment	Hemming et al., 2007
-46,75	-0,05	South Atlantic	Cape basin	0-63 µm				0,710119						1	marine sediment (LGM)	Hemming et al., 2007
-46,75	-0,05	South Atlantic	Cape basin	0-63 µm				0,710681						1	marine sediment	Hemming et al., 2007
-46,75	-0,05	South Atlantic	Cape basin	0-63 µm				0,710703						1	marine sediment	Hemming et al., 2007
-42,52	11,67	South Atlantic	Cape basin	0-63 µm				0,710954						1	marine sediment (LGM)	Hemming et al., 2007
-43,85	27,6	South Atlantic	Cape basin	0-63 µm				0,712521						1	marine sediment (LGM)	Hemming et al., 2007
-42,52	11,67	South Atlantic	Cape basin	0-63 µm				0,714206						1	marine sediment	Hemming et al., 2007
-68,61	10,97	South Atlantic	Dronning Maud Land	0-63 µm				0,715989						1	marine sediment	Hemming et al., 2007
-70	-5,08	South Atlantic	Dronning Maud Land	0-63 µm				0,721725						1	marine sediment	Hemming et al., 2007
-43,37	-36,1	South Atlantic	Fakland Basin	0-63 µm				0,709081						1	marine sediment (LGM)	Hemming et al., 2007
-47,95	-23,7	South Atlantic	Fakland Basin	0-63 µm				0,709265						1	marine sediment (LGM)	Hemming et al., 2007
-43,37	-36,1	South Atlantic	Fakland Basin	0-63 µm				0,709916						1	marine sediment	Hemming et al., 2007
-54,38	-22,13	South Atlantic	Fakland Basin	0-63 µm				0,710805						1	marine sediment (LGM)	Hemming et al., 2007
-54,38	-22,13	South Atlantic	Fakland Basin	0-63 µm				0,713399						1	marine sediment	Hemming et al., 2007
-53,545	-45,2917	South Atlantic	Scotia Sea	silt	0,51249	-2,9	19	0,706465						1	marine sediment	Walter et al, 2000
-53,545	-45,2917	South Atlantic	Scotia Sea	silt	0,512483	-3,0	18	0,706974						1	marine sediment	Walter et al, 2000
-53,545	-45,2917	South Atlantic	Scotia Sea	silt	0,512429	-4,1	20	0,707068						1	marine sediment	Walter et al, 2000
-53,545	-45,2917	South Atlantic	Scotia Sea	silt	0,512456	-3,6	18	0,707231						1	marine sediment	Walter et al, 2000
-53,545	-45,2917	South Atlantic	Scotia Sea	bulk	0,512462	-3,4	20	0,707249						1	marine sediment	Walter et al, 2000
-53,545	-45,2917	South Atlantic	Scotia Sea	bulk	0,512496	-2,8	19	0,70733						1	marine sediment	Walter et al, 2000
-53,545	-45,2917	South Atlantic	Scotia Sea	bulk	0,512468	-3,3	21	0,70745						1	marine sediment	Walter et al, 2000
-53,545	-45,2917	South Atlantic	Scotia Sea	silt	0,512426	-4,1	17	0,707577						1	marine sediment	Walter et al, 2000
-53,545	-45,2917	South Atlantic	Scotia Sea	silt	0,51245	-3,7	20	0,707989						1	marine sediment	Walter et al, 2000
-53,545	-45,2917	South Atlantic	Scotia Sea	silt	0,512465	-3,4	21	0,708441						1	marine sediment	Walter et al, 2000
-53,545	-45,2917	South Atlantic	Scotia Sea	bulk	0,51242	-4,3	22	0,70852						1	marine sediment	Walter et al, 2000
-53,545	-45,2917	South Atlantic	Scotia Sea	bulk	0,512407	-4,5	19	0,708793						1	marine sediment	Walter et al, 2000
-59,7883	-42,683	South Atlantic	Scotia Sea	bulk	0,512427	-4,1	22	0,708975						1	marine sediment	Walter et al, 2000
-53,545	-45,2917	South Atlantic	Scotia Sea	bulk	0,512413	-4,4	16	0,70903						1	marine sediment	Walter et al, 2000
-53,545	-45,2917	South Atlantic	Scotia Sea	bulk	0,512416	-4,3	20	0,70907						1	marine sediment	Walter et al, 2000
-53,545	-45,2917	South Atlantic	Scotia Sea	bulk	0,512416	-4,3	17	0,709404						1	marine sediment	Walter et al, 2000
-59,7883	-42,683	South Atlantic	Scotia Sea	bulk	0,512405	-4,5	22	0,709633						1	marine sediment	Walter et al, 2000
-53,545	-45,2917	South Atlantic	Scotia Sea	clay	0,512459	-3,5	19	0,709756						1	marine sediment	Walter et al, 2000
-59,7883	-42,683	South Atlantic	Scotia Sea	bulk	0,512389	-4,9	23	0,709814						1	marine sediment	Walter et al, 2000
-53,545	-45,2917	South Atlantic	Scotia Sea	bulk	0,512362	-5,4	18	0,710037						1	marine sediment	Walter et al, 2000
-59,7883	-42,683	South Atlantic	Scotia Sea	bulk	0,512387	-4,9	22	0,710123						1	marine sediment	Walter et al, 2000
-59,7883	-42,683	South Atlantic	Scotia Sea	bulk	0,512374	-5,1	23	0,710232						1	marine sediment	Walter et al, 2000
-59,7883	-42,683	South Atlantic	Scotia Sea	bulk	0,512398	-4,7	24	0,710451						1	marine sediment	Walter et al, 2000
-53,545	-45,2917	South Atlantic	Scotia Sea	clay	0,512427	-4,1	20	0,710533						1	marine sediment	Walter et al, 2000
-59,7883	-42,683	South Atlantic	Scotia Sea	bulk	0,51235	-5,6	22	0,710907						1	marine sediment	Walter et al, 2000
-53,545	-45,2917	South Atlantic	Scotia Sea	clay	0,512342	-5,8	21	0,711433						1	marine sediment	Walter et al, 2000
-53,545	-45,2917	South Atlantic	Scotia Sea	clay	0,512303	-6,5	22	0,711895						1	marine sediment	Walter et al, 2000
-59,7883	-42,683	South Atlantic	Scotia Sea	bulk	0,512343	-5,8	18	0,712344						1	marine sediment	Walter et al, 2000
-59,7883	-42,683	South Atlantic	Scotia Sea	bulk	0,512313	-6,3	23	0,713268						1	marine sediment	Walter et al, 2000
-59,7883	-42,683	South Atlantic	Scotia Sea	bulk	0,512299	-6,6	24	0,713808						1	marine sediment	Walter et al, 2000
-53,545	-45,2917	South Atlantic	Scotia Sea	clay	0,512354	-5,5	23	0,713959						1	marine sediment	Walter et al, 2000
-53,545	-45,2917	South Atlantic	Scotia Sea	clay	0,512349	-5,6	25	0,714296						1	marine sediment	Walter et al, 2000
-59,7883	-42,683	South Atlantic	Scotia Sea	bulk	0,512251	-7,5	16	0,714346						1	marine sediment	Walter et al, 2000
-59,7883	-42,683	South Atlantic	Scotia Sea	bulk	0,512211	-8,3	24	0,71732						1	marine sediment	Walter et al, 2000
-53,545	-45,2917	South Atlantic	Scotia Sea	clay	0,512411	-4,4	15	0,719958						1	marine sediment	Walter et al, 2000
-53,545	-45,2917	South Atlantic	Scotia Sea	bulk	0,512436	-3,9	20							1	marine sediment	Walter et al, 2000
-69,4167	-95,023	South Atlantic	Scotia Sea	silt	0,512613	-0,5	27	0,706137						1	marine sediment	Walter et al, 2000
-62,9967	-89,493	South Atlantic	Scotia Sea	silt	0,51253	-2,1	22	0,707731						1	marine sediment	Walter et al, 2000
-69,4167	-95,023	South Atlantic	Scotia Sea	bulk	0,512503	-2,6	24	0,707765						1	marine sediment	Walter et al, 2000
-50,7483	-85,6883	South Atlantic	Scotia Sea	silt	0,51243	-4,1	22	0,708647						1	marine sediment	Walter et al, 2000
-56,02	-84,905	South Atlantic	Scotia Sea	silt	0,512427	-4,1	22	0,708705						1	marine sediment	Walter et al, 2000
-62,9967	-89,493	South Atlantic	Scotia Sea	bulk	0,512483	-3,0	18	0,708749						1	marine sediment	Walter et al, 2000
-50,7483	-85,6883	South Atlantic	Scotia Sea	bulk	0,512436	-3,9	21	0,708823						1	marine sediment	Walter et al, 2000
-50,7483	-85,6883	South Atlantic	Scotia Sea	clay	0,512396	-4,7	28	0,709051						1	marine sediment	Walter et al, 2000
-41,2867	-14,5	South Atlantic	Scotia Sea	silt	0,512401	-4,6	15	0,709077						1	marine sediment	Walter et al, 2000
-41,287	-14,5	South Atlantic	Scotia Sea	bulk	0,512367	-5,3	15	0,709171						1	marine sediment	Walter et al, 2000
-41,2867	-14,5	South Atlantic	Scotia Sea	silt	0,512237	-7,8	7	0,709183						1	marine sediment	Walter et al, 2000
-56,02	84,905	South Atlantic	Scotia Sea	bulk	0,512404	-4,6	19	0,709203						1	marine sediment	Walter et al, 2000
-56,02	-84,905	South Atlantic	Scotia Sea	clay	0,512341	-5,8	24	0,710092						1	marine sediment	Walter et al, 2000
-62,9967	-89,493	South Atlantic	Scotia Sea	clay	0,512449	-3,7	22	0,710197						1	marine sediment	Walter et al, 2000
-69,4167	-95,023	South Atlantic	Scotia Sea	clay	0,512459	-3,5	23	0,710242						1	marine sediment	Walter et al, 2000
-41,287	-14,5	South Atlantic	Scotia Sea	bulk	0,512211	-8,3	6	0,710439						1	marine sediment	Walter et al, 2000
-41,2867	-14,5	South Atlantic	Scotia Sea	clay	0,512405	-4,5	20	0,710439						1	marine sediment	Walter et al, 2000
-61,583	-45,7068	South Atlantic	Scotia Sea	bulk	0,512322	-6,2	24	0,711861						1	marine sediment	Walter et al, 2000
-41,2867	-14,5	South Atlantic	Scotia Sea	clay	0,512257	-7,4	29	0,712918						1	marine sediment	Walter et al, 2000
-74,6783	-35,083	South Atlantic	Scotia Sea	bulk	0,512244	-7,7	11							1	marine sediment	Walter et al, 2000
-66,0867	-56,5317	South Atlantic	Scotia Sea	bulk	0,512346	-5,7	21							1	marine sediment	Walter et al, 2000
-61,983	-61,983	South Atlantic	Scotia Sea	bulk	0,512717	1,5	11							1	marine sediment	Walter et al, 2000

latitude (°N)	longitude (E°)	region (when given)	locality (when given)	grain size fraction (when given)	$^{143}Nd/^{144}Nd$	ε_{Nd}	[Nd] (ppm)	$^{87}Sr/^{86}Sr$	[Sr] (ppm)	$^{206}Pb/^{204}Pb$	$^{207}Pb/^{204}Pb$	$^{208}Pb/^{204}Pb$	[Pb] (ppm)	number of sample	type of sample (when given)	reference
-77,255	-40,833	South Atlantic	Weddell Sea	bulk	0,512105	-10,4	19	0,723735						1	marine sediment	Walter et al, 2000
-62	-20,01	South Atlantic	Weddell-Enderby basin	0-63 µm				0,729523						1	marine sediment	Hemming et al., 2007
-45,65	48,28	South Indian		0-63 µm				0,703868						1	marine sediment	Hemming et al., 2007
-36,98	59,98	South Indian		0-63 µm				0,705947						1	marine sediment	Hemming et al., 2007
-36,98	59,98	South Indian		0-63 µm				0,706217						1	marine sediment (LGM)	Hemming et al., 2007
-57,48	36,17	South Indian		0-63 µm				0,707678						1	marine sediment	Hemming et al., 2007
-52,2	54,47	South Indian		0-63 µm				0,708249						1	marine sediment	Hemming et al., 2007
-49,57	30,02	South Indian		0-63 µm				0,708507						1	marine sediment (LGM)	Hemming et al., 2007
-50,47	59,58	South Indian		0-63 µm				0,709322						1	marine sediment	Hemming et al., 2007
-50,47	59,58	South Indian		0-63 µm				0,709582						1	marine sediment (LGM)	Hemming et al., 2007
-44,5	31,18	South Indian		0-63 µm				0,709874						1	marine sediment	Hemming et al., 2007
-52,8	54,08	South Indian		0-63 µm				0,709885						1	marine sediment (LGM)	Hemming et al., 2007
-38	51,18	South Indian		0-63 µm				0,710242						1	marine sediment (LGM)	Hemming et al., 2007
-54,48	53,05	South Indian		0-63 µm				0,710579						1	marine sediment (LGM)	Hemming et al., 2007
-53,52	36,63	South Indian		0-63 µm				0,710589						1	marine sediment	Hemming et al., 2007
-61,04	114,81	South Indian		0-63 µm				0,710616						1	marine sediment	Hemming et al., 2007
-40,3	74,57	South Indian		0-63 µm				0,710725						1	marine sediment	Hemming et al., 2007
-52,2	54,47	South Indian		0-63 µm				0,710931						1	marine sediment (LGM)	Hemming et al., 2007
-57,48	36,17	South Indian		0-63 µm				0,711768						1	marine sediment (LGM)	Hemming et al., 2007
-40,3	74,57	South Indian		0-63 µm				0,713113						1	marine sediment (LGM)	Hemming et al., 2007
-49,57	30,02	South Indian		0-63 µm				0,713882						1	marine sediment	Hemming et al., 2007
-38	51,18	South Indian		0-63 µm				0,714613						1	marine sediment	Hemming et al., 2007
-66,08	145,02	South Indian		0-63 µm				0,7249						1	marine sediment	Hemming et al., 2007
-64,67	132,98	South Indian		0-63 µm				0,727889						1	marine sediment	Hemming et al., 2007
-61,12	71,27	South Indian		0-63 µm				0,728087						1	marine sediment	Hemming et al., 2007
-65,4	36,72	South Indian		0-63 µm				0,730219						1	marine sediment	Hemming et al., 2007
-60	105	South Indian		0-63 µm				0,730345						1	marine sediment	Hemming et al., 2007
-64,43	119,98	South Indian		0-63 µm				0,734381						1	marine sediment	Hemming et al., 2007
-65,55	141,1	South Indian		0-63 µm				0,737042						1	marine sediment	Hemming et al., 2007
-66,66	77,9	South Indian		0-63 µm				0,737219						1	marine sediment	Hemming et al., 2007
-65,22	137,88	South Indian		0-63 µm				0,738862						1	marine sediment	Hemming et al., 2007
-65,65	60,68	South Indian		0-63 µm				0,741609						1	marine sediment	Hemming et al., 2007
54	-166		Akutan Island			7,4	20							3	basalt rock	Jeandel et al., 2007 and references therein
36,1	-3,2		Alboran Sea			-10,1	30							1	core n− KS 8231 (855m)	Jeandel et al., 2007 and references therein
54	170		aleutians			7,4	12							3	basalts	Jeandel et al., 2007 and references therein
-10	122		banda			-3,3	12							2	basalts	Jeandel et al., 2007 and references therein
13,25	-50,5		Barbados			-12,0	43							4	aerosols	Jeandel et al., 2007 and references therein
20,25	121,9		Batan			-2,8	6							13	rocks	Jeandel et al., 2007 and references therein
46,3	-15,06		Bay of Biscay			-11,6	25							3	core	Jeandel et al., 2007 and references therein
-5	150		Bismarck New Britain			8,3	4							20	rocks	Jeandel et al., 2007 and references therein
54	-169		Bogoslov Island			7,2	26							2	rocks	Jeandel et al., 2007 and references therein
27	140		Bonin islands			2,3	2							4	rocks	Jeandel et al., 2007 and references therein
19,83	-97,34		C American arc			1,5	21							18	rocks	Jeandel et al., 2007 and references therein
13	-95		C American arc			5,9	13							29	rocks	Jeandel et al., 2007 and references therein
28	-14		Canaries Island			-12,8	35							2	aerosols	Jeandel et al., 2007 and references therein
12,5	-24,5		Cap Verde Basin			-12,0	37							2	aerosols	Jeandel et al., 2007 and references therein
35	110		China (Lanzhou)			-9,7	26							2	loess	Jeandel et al., 2007 and references therein
-12	44		Comoros			3,4	42							19	rocks	Jeandel et al., 2007 and references therein
42	9		Corsica			-13,0	28							5	aerosols	Jeandel et al., 2007 and references therein
10	-85		costa rica coast			7,3	9							46	rocks	Jeandel et al., 2007 and references therein
12	43		djibouti			5,0	30							72	basalts	Jeandel et al., 2007 and references therein
69	-28		E Greenland			4,0	8							41	rocks	Jeandel et al., 2007 and references therein
70,5	-28		E_Greenland			4,0	8							41	rocks	Jeandel et al., 2007 and references therein
-4	132		East Seram			-8,7	24							11	core	Jeandel et al., 2007 and references therein
-7	132		East Serua			-8,1	22							12	core	Jeandel et al., 2007 and references therein
37	129		East South-Korea			-23,9	39							3	rocks	Jeandel et al., 2007 and references therein
-9	128		East Timor			-9,5	20							12	core	Jeandel et al., 2007 and references therein
17,5	41		Eastern Ertrea			-4,2	22							7	rocks	Jeandel et al., 2007 and references therein
35,8	-8,7		Gibraltar			-11,8	22							1	core n− KS 8228 (2798m)	Jeandel et al., 2007 and references therein
66	-37		Greenland SE			-26,0	45							18	rocks	Jeandel et al., 2007 and references therein
11,6	42,5		Gulf of Aden			6,2	25							3	rocks	Jeandel et al., 2007 and references therein
12	48		Gulf of Aden			10,0	10							20	rocks	Jeandel et al., 2007 and references therein
65	-22		Iceland			8,0	17							55	rocks	Jeandel et al., 2007 and references therein
62	-7		Iles Faroes			7,0	34							43	rocks	Jeandel et al., 2007 and references therein
-8,3	124,2		Indonesia			-1,9	31							12	rocks	Jeandel et al., 2007 and references therein
25	37		Indus shelf			-11,2	0							1	core n− ID-18	Jeandel et al., 2007 and references therein
35	140		izu chain (japon)			7,7	12							3	basalts	Jeandel et al., 2007 and references therein
71	-8		Jan-Mayen			5,0	41							8	basalts	Jeandel et al., 2007 and references therein
-21	55,5		La Reunion			4,0	24							16	volcanic	Jeandel et al., 2007 and references therein
70	-135		Mackenzie (Canada)			-14,3	16							1	river sediment	Jeandel et al., 2007 and references therein
15	145		Mariana			6,7	2							3	rocks	Jeandel et al., 2007 and references therein
72,3	-27		N-E Greenland			-29,8	32							5	rocks	Jeandel et al., 2007 and references therein
53	-134		NE Pacific Ocean			9,6	13							6	rocks	Jeandel et al., 2007 and references therein
71	-27		N-E_Greenland			-29,8	32							5	rocks	Jeandel et al., 2007 and references therein
10	150		new britain			7,4	18							4	basalts	Jeandel et al., 2007 and references therein
-15	168		New Hebrides Arc			7,4	14							28	rocks	Jeandel et al., 2007 and references therein
32	31		Nile (Egypt)			-3,3	34							1	river sediment	Jeandel et al., 2007 and references therein
37,62	-119		NW USA			-0,5	22							4	rocks	Jeandel et al., 2007 and references therein
-1,2	132,65		Papua New Guinea			4,1	4							4	rocks	Jeandel et al., 2007 and references therein
45	12		Po			-10,8	27							1	river part	Jeandel et al., 2007 and references therein
43	5		Rhone			-9,7	26							1	river part	Jeandel et al., 2007 and references therein

latitude (°N)	longitude (E°)	region (when given)	locality (when given)	grain size fraction (when given)	$^{143}Nd/^{144}Nd$	ε_{Nd}	[Nd] (ppm)	$^{87}Sr/^{86}Sr$	[Sr] (ppm)	$^{206}Pb/^{204}Pb$	$^{207}Pb/^{204}Pb$	$^{208}Pb/^{204}Pb$	[Pb] (ppm)	number of sample	type of sample (when given)	reference
65	-34		S-E_Greenland			-38,0	15							11	rocks	Jeandel et al., 2007 and references therein
37	36		Seyhan			-6,2	10							1	river part	Jeandel et al., 2007 and references therein
36,8	-7,8		South Andalousia			-8,4	30							1	core n− KC 8221 (580m)	Jeandel et al., 2007 and references therein
-6	106		sunda			0,0	21							4	basalts	Jeandel et al., 2007 and references therein
37	36,2		Tarsus			-6,3	11							1	river part	Jeandel et al., 2007 and references therein
54	-168		Unalaska Island (Al Is)			7,6	13							2	basalt rock	Jeandel et al., 2007 and references therein
27	-113,6		Vizcaino peninsula, mex			7,6	15							5	adakite	Jeandel et al., 2007 and references therein
60,5	5,25		W Norway			-14,0	17							2	rocks	Jeandel et al., 2007 and references therein
15	43		W Yemen			4,1	37							52	rocks	Jeandel et al., 2007 and references therein
-5	149,3		Witu Islands			8,3	16							8	rocks	Jeandel et al., 2007 and references therein
20	40		Saudi Arabia			5,0	30							28	basalts	Jeandel et al., 2007 and references therein
16	-62		West Indies			5,5	10							10	basalts	Jeandel et al., 2007 and references therein

Annex 2: map of Nd isotopic data from the litterature

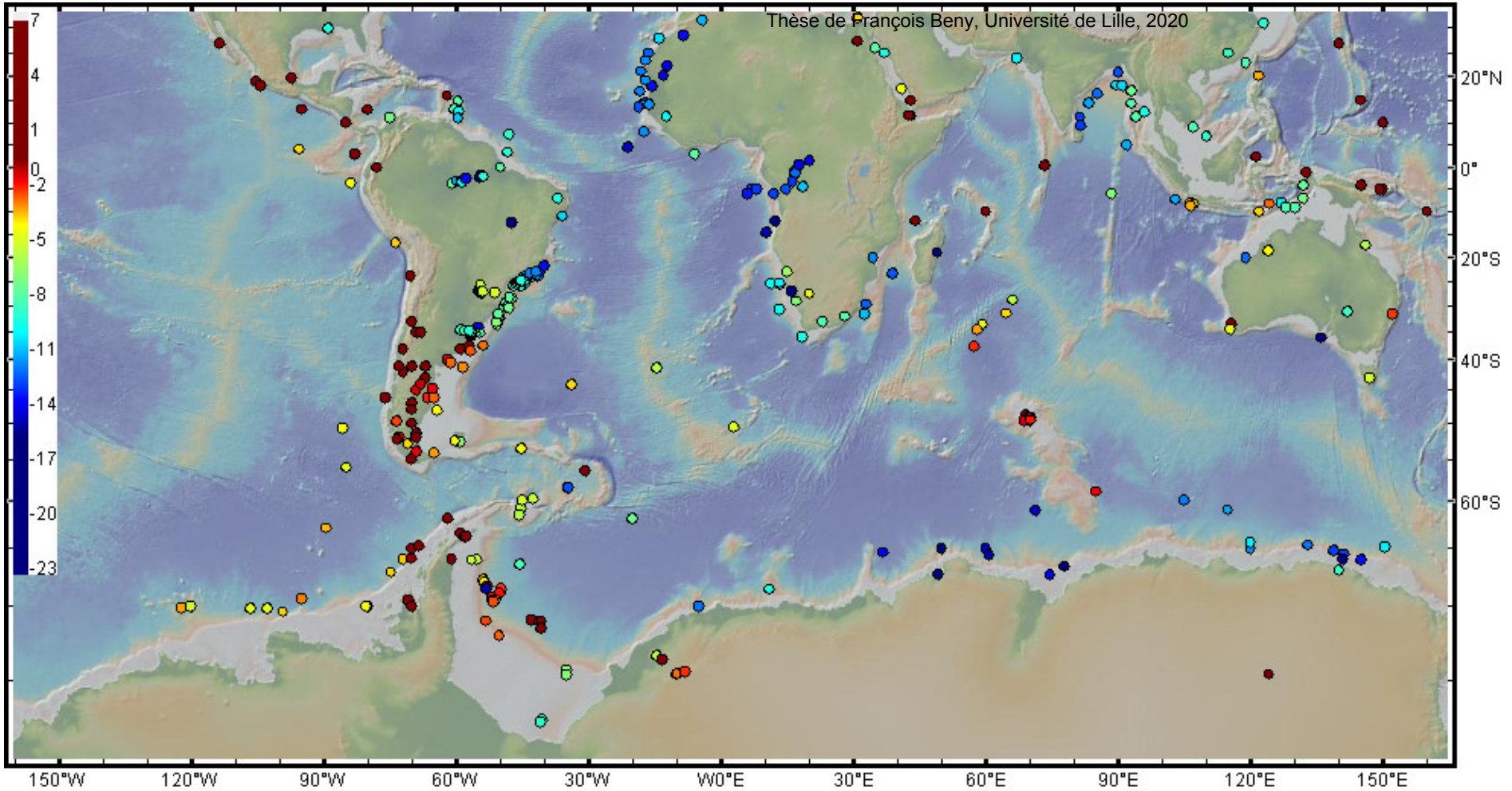

Annex 3: map of Sr isotopic data from the litterature

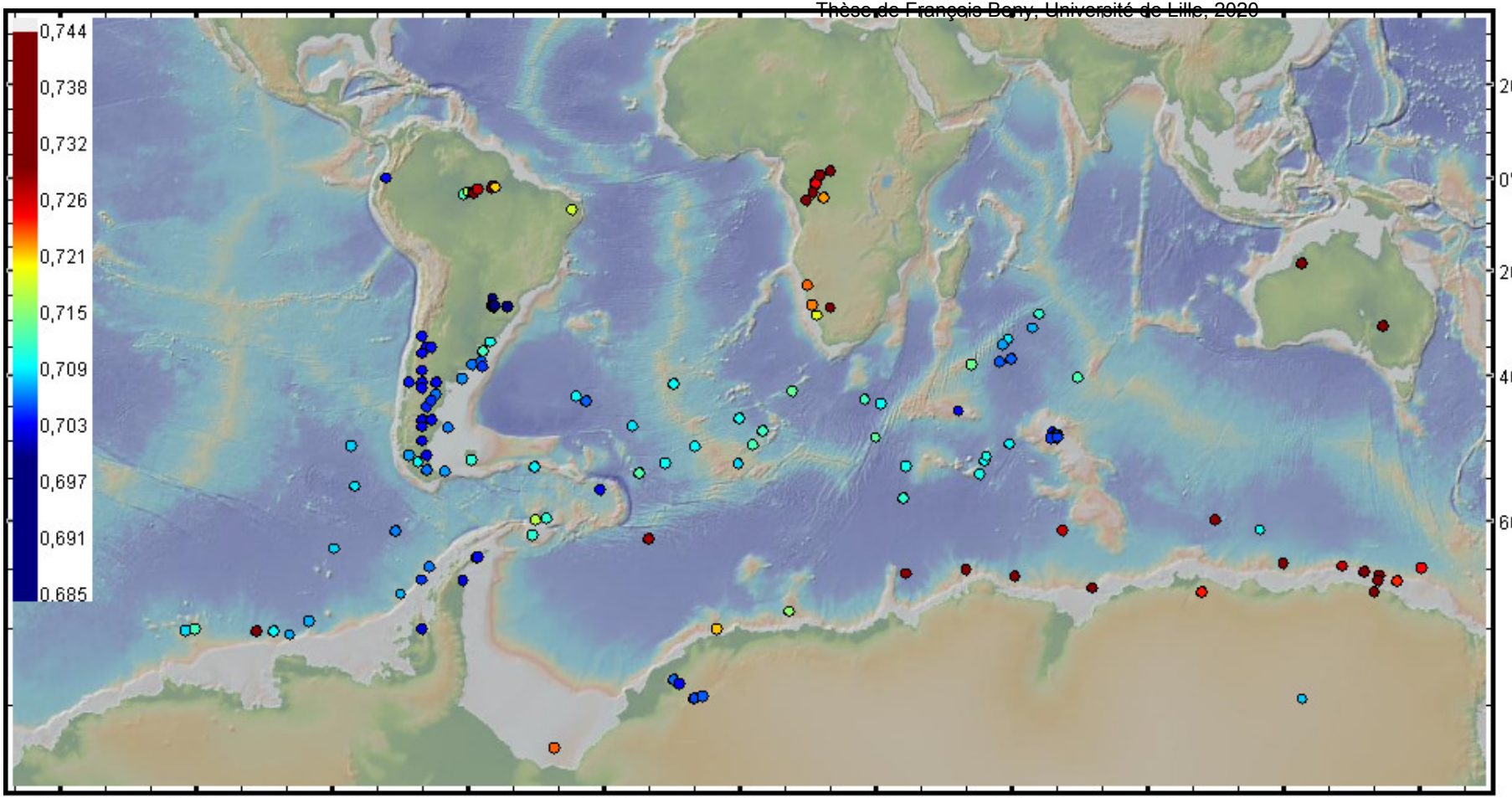

Annex 4: map of ^{206}Pb isotopic data from the litterature

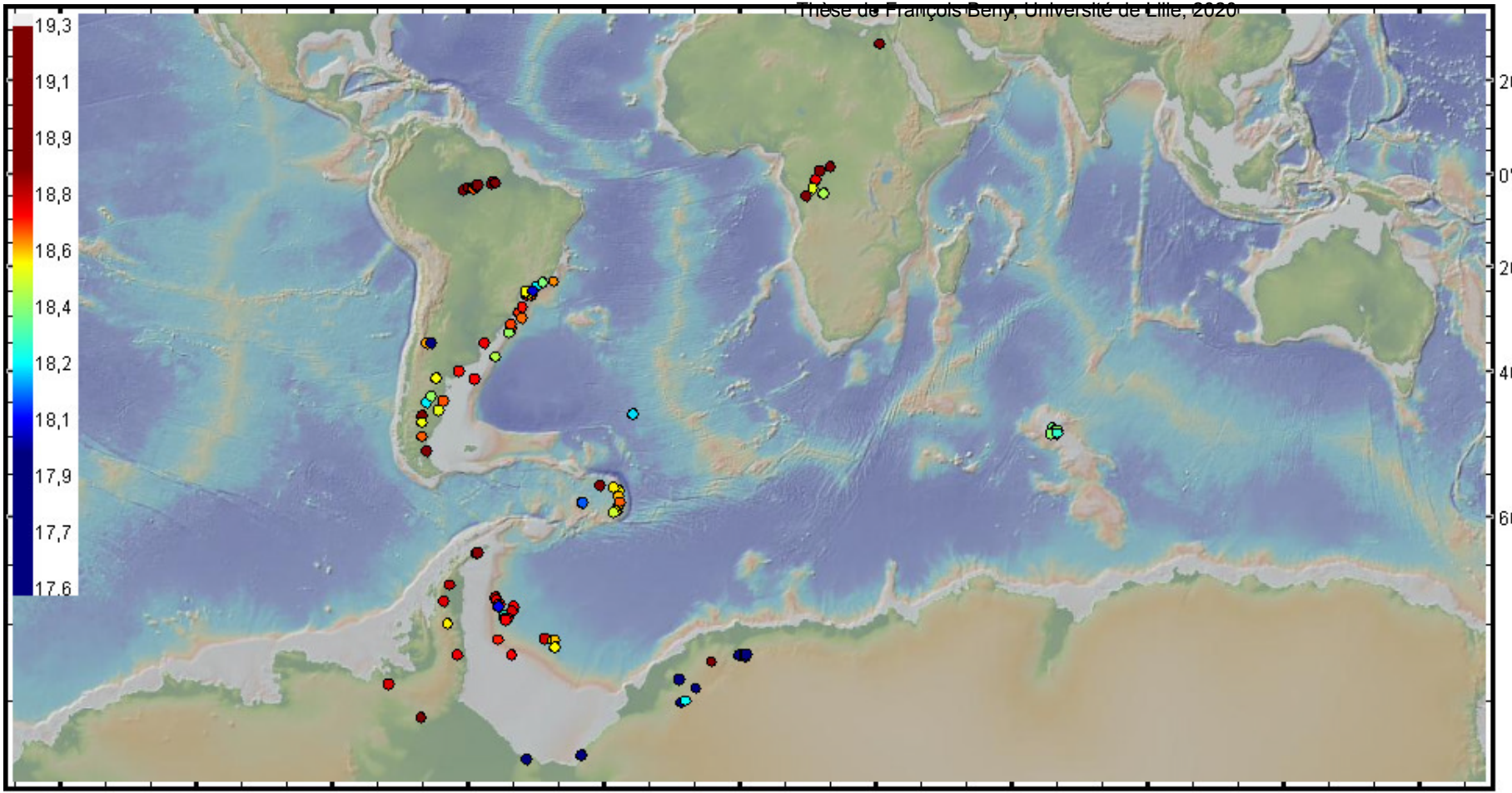

Annex 5: map of ^{207}Pb isotopic data from the litterature

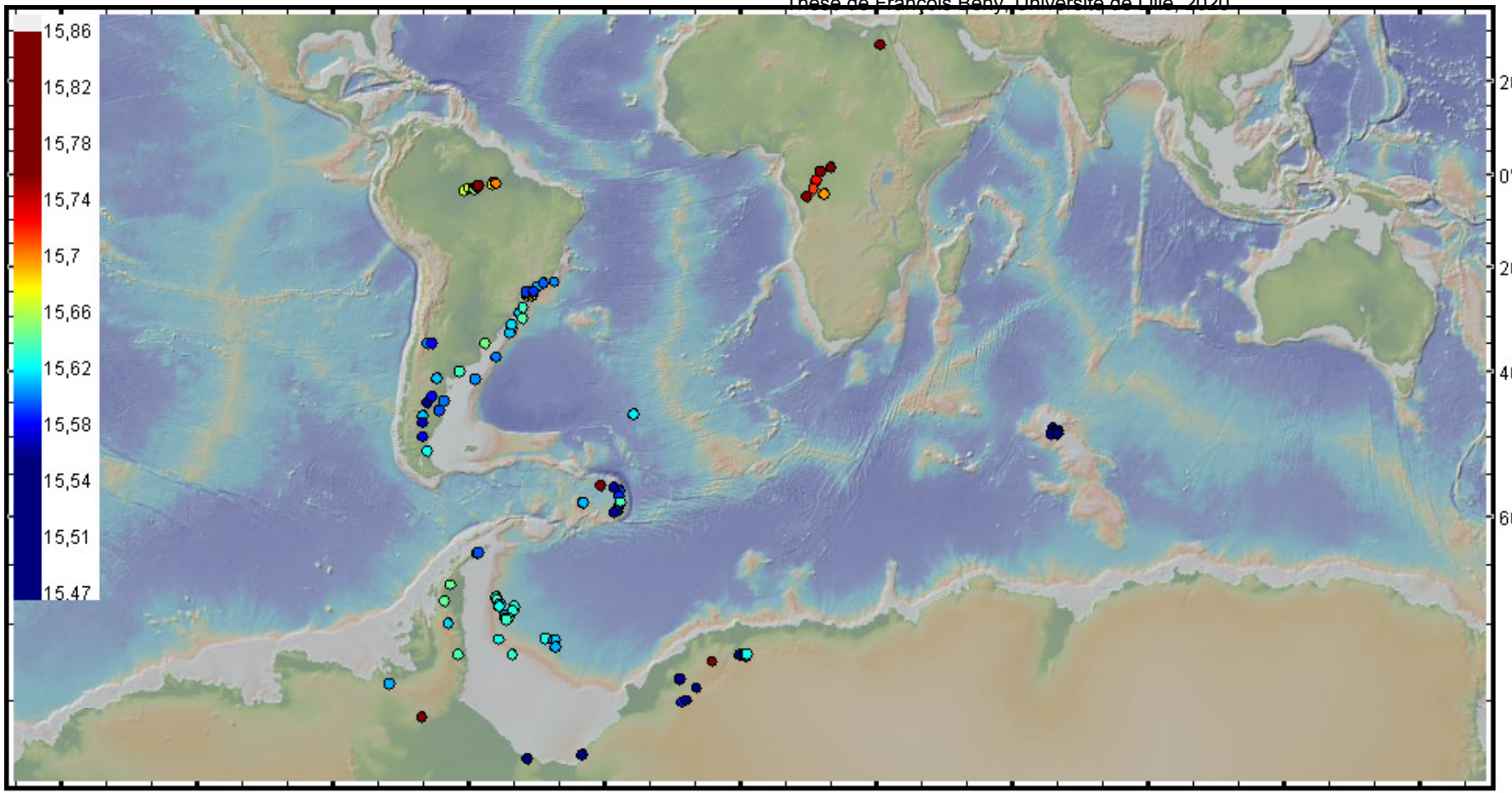

Annex 6: map of ^{208}Pb isotopic data from the litterature

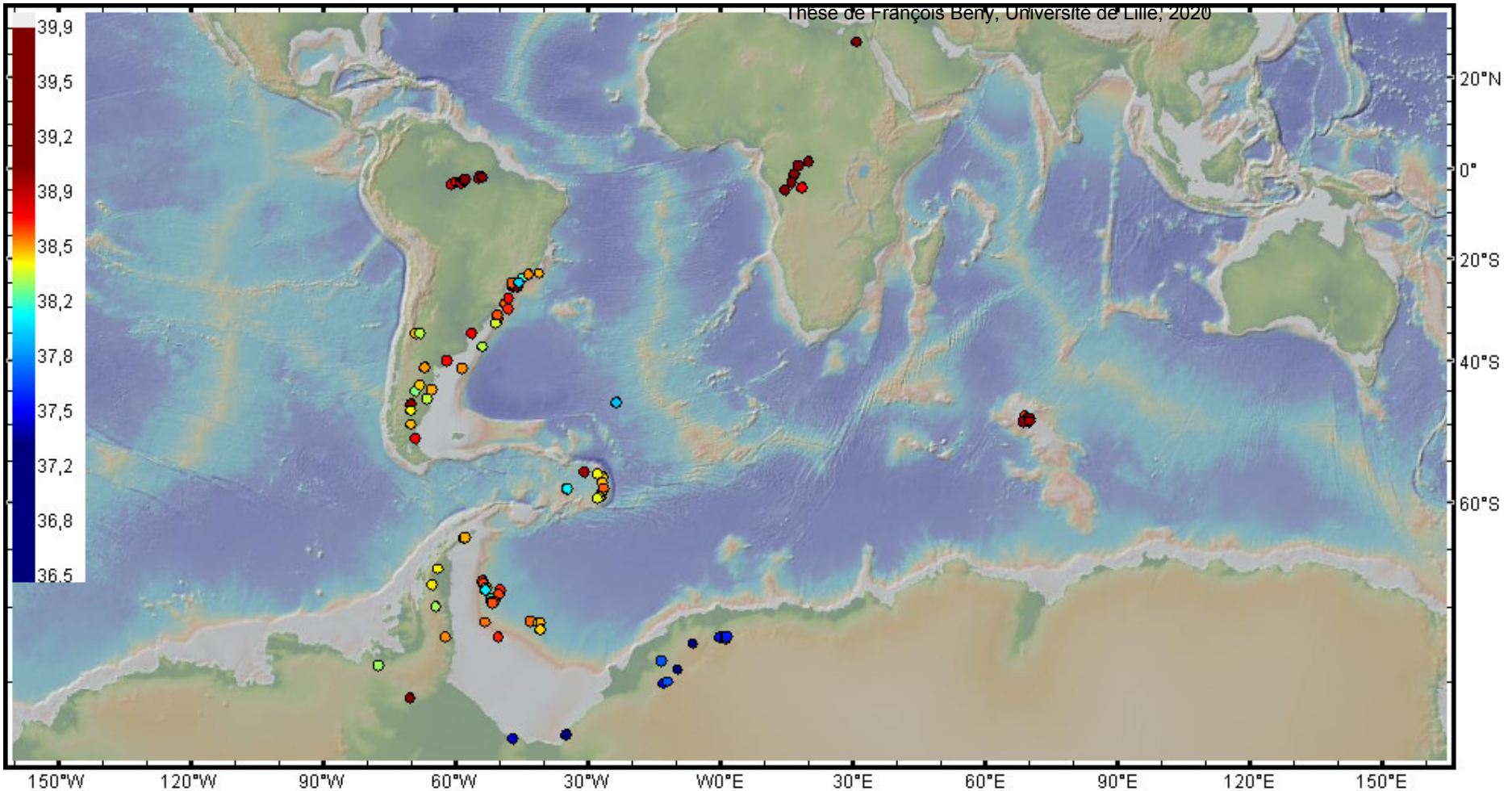

Annex 7: Average values of the different proxies for the entire record, the LGM, and the deglaciation.

	average (10-30 ka)	LGM (25-17 ka)	Deglaciation (17-11.7 ka)	standard deviation (10-30 ka)
fine mode (μm)	6.8	7.2	6.3	0.8
coarse mode (μm)	30.4	31.3	30.4	2.5
clay fraction (%)	3.4	3.0	3.8	0.7
sortable silts (10-63 μm; %)	47.0	47.2	46.2	2.4
cohesive silts (2-10 μm; %)	39.4	38.8	40.2	2.4
sand (%)	3.0	3.5	2.6	1.0
smectite (%)	30.7	26.7	35.7	7.9
illite (%)	33.5	34.7	31.7	3.3
chlorite (%)	25.1	27.2	22.3	4.2
kaolinite (%)	10.6	11.4	10.3	1.3
I/S	1.2	1.3	0.9	0.3
K/C	0.4	0.4	0.5	0.1
ε_{Nd} (<2 μm)	-5.8	-5.0	-6.0	0.8
ε_{Nd} (fine mode)	-4.6	-4.6	-4.7	0.4
ε_{Nd} (coase mode)	-3.3	-1.8	-3.7	1.2
$^{87}Sr/^{86}Sr$ (<2 μm)	0.71130	0.71144	0.71136	0.00036
$^{87}Sr/^{86}Sr$ (fine mode)	0.70795	0.70800	0.70798	0.00019
$^{87}Sr/^{86}Sr$ (coase mode)	0.70889	0.70859	0.70926	0.00058
$^{208}Pb/^{204}Pb$ (<2 μm)	38.774	38.775	38.785	0.012
$^{207}Pb/^{204}Pb$ (<2 μm)	15.644	15.639	15.645	0.008
$^{206}Pb/^{204}Pb$ (<2 μm)	18.752	18.749	18.758	0.030

Annex 8: Isotopic composition from the clay size fraction (<2 μm) from sediment core MD07-3076Q. σ corresponds to the internal error.

depth (cm)	age (ka)	$^{143}Nd/^{144}Nd$	2σ	ε_{Nd}	$^{87}Sr/^{86}Sr$	2σ	$^{206}Pb/^{204}Pb$	2σ	$^{207}Pb/^{204}Pb$	2σ	$^{208}Pb/^{204}Pb$	2σ
51	10.03	0.512295	0.000006	-6.7	0.710814	0.000015	18.7555	0.0003	15.6553	0.0006	38.8083	0.0008
54	10.52	0.512286	0.000007	-6.9	0.710660	0.000010	18.7563	0.0003	15.6536	0.0006	38.7958	0.0008
57	10.91	0.512282	0.000005	-6.9			18.7438	0.0008	15.6562	0.0010	38.7993	0.0017
61	11.39	0.512282	0.000006	-6.9	0.710770	0.000011	18.7551	0.0003	15.6573	0.0006	38.8121	0.0007
62	11.52	0.512283	0.000005	-6.9	0.711048	0.000010	18.7685	0.0003	15.6482	0.0005	38.8027	0.0007
65	11.93	0.512293	0.000004	-6.7	0.710966	0.000007	18.7613	0.0003	15.6471	0.0005	38.7894	0.0006
68	12.33	0.512292	0.000006	-6.8	0.711240	0.000009	18.7640	0.0004	15.6490	0.0007	38.8070	0.0008
71	12.67	0.512302	0.000007	-6.5	0.711670	0.000012	18.7762	0.0003	15.6564	0.0006	38.8372	0.0008
74	12.98	0.512309	0.000005	-6.4			18.7648	0.0008	15.6530	0.0009	38.8073	0.0017
75	13.07	0.512340	0.000004	-5.8	0.711167	0.000011	18.7651	0.0003	15.6450	0.0005	38.7875	0.0008
80	13.56	0.512322	0.000004	-6.2	0.710987	0.000010	18.7374	0.0003	15.6419	0.0005	38.7535	0.0007
87	14.29	0.512325	0.000006	-6.1	0.710880	0.000010	18.7451	0.0005	15.6531	0.0007	38.7940	0.0013
92	14.69	0.512352	0.000006	-5.6	0.711540	0.000011	18.7593	0.0003	15.6414	0.0005	38.7803	0.0006
96	14.88	0.512352	0.000005	-5.6	0.711493	0.000010	18.7646	0.0003	15.6430	0.0005	38.7906	0.0007
101	15.51	0.512369	0.000006	-5.3	0.711706	0.000010	18.7565	0.0003	15.6363	0.0008	38.7654	0.0007
107	16.28	0.512375	0.000005	-5.1	0.711535	0.000009	18.7521	0.0003	15.6346	0.0007	38.7491	0.0007
112	16.97	0.512363	0.000005	-5.4	0.711769	0.000010	18.7548	0.0003	15.6410	0.0007	38.7640	0.0007
116	17.45						18.7601	0.0005	15.6471	0.0008	38.7896	0.0015
120	17.91						18.7530	0.0003	15.6461	0.0006	38.7800	0.0007
121	18.01	0.512381	0.000005	-5,0			18.7507	0.0003	15.6351	0.0007	38.7448	0.0006
130	18.79	0.512382	0.000005	-5,0			18.7428	0.0003	15.6406	0.0007	38.7479	0.0006
138	19.54	0.512373	0.000005	-5.2			18.7538	0.0003	15.6380	0.0007	38.7528	0.0007
149	21.10	0.512365	0.000004	-5.3	0.711683	0.000011	18.7444	0.0004	15.6378	0.0007	38.7508	0.0008
155	21.98	0.512362	0.000006	-5.4	0.711510	0.000010	18.7440	0.0006	15.6335	0.0010	38.7428	0.0021
160	22.72	0.512384	0.000005	-5,0	0.711400	0.000011	18.7397	0.0003	15.6349	0.0007	38.7399	0.0007
167	23.80	0.512394	0.000005	-4.8	0.711323	0.000012	18.7468	0.0004	15.6379	0.0008	38.7474	0.0007
173	24.72	0.512394	0.000004	-4.8	0.711286	0.000011	18.7424	0.0003	15.6355	0.0008	38.7328	0.0006
182	25.69	0.512394	0.000005	-4.8	0.711883	0.000010	18.7182	0.0003	15.6299	0.0007	38.6969	0.0006
196	27.27	0.512384	0.000004	-5,0			18.7321	0.0009	15.6445	0.0010	38.7522	0.0019

214	29.04	0.512360	0.000004	-5.4		18.7591	0.0009	15.6465	0.0011	38.7818	0.0019

Annex 9: Isotopic composition from the sortable silt mode fraction (20-32/40 μm) from sediment core MD07-3076Q. σ corresponds to the internal standard error of the measurement.

depth (cm)	age (ka)	$^{143}Nd/^{144}Nd$	2σ	ε_{Nd}	$^{87}Sr/^{86}Sr$	2σ
51	10.03				0.708365	0.000009
55	10.69				0.708616	0.000008
57	10.91	0.512387	0.000006	-4.9	0.709192	0.000005
61	11.39	0.512403	0.000023	-4.6	0.708783	0.000013
63	11.64				0.709392	0.000005
65	11.93	0.512421	0.000006	-4.2	0.709592	0.000004
67	12.22	0.512416	0.000019	-4.3	0.708802	0.000010
71	12.67				0.707945	0.000005
73	12.89				0.709932	0.000006
75	13.07	0.512421	0.000007	-4.2	0.710185	0.000005
81	13.67	0.512425	0.000005	-4.1	0.709362	0.000005
87	14.29				0.709334	0.000009
91	14.65	0.512452	0.000005	-3.6	0.709046	0.000005
97	14.97				0.709254	0.000005
101	15.51	0.512491	0.000013	-2.9	0.708801	0.000007
107	16.28	0.512518	0.000005	-2.3	0.709632	0.000005
117	17.57				0.707884	0.000007
120	17.91				0.709324	0.000006
121	18.01	0.512567	0.000009	-1.4	0.708447	0.000005
122	18.10				0.708526	0.000006
131	18.87				0.708860	0.000008
137	19.40				0.708856	0.000009
144	20.37				0.709198	0.000006
145	20.51				0.708912	0.000009
149	21.10				0.709277	0.000007
153	21.69				0.708541	0.000008
155	21.98				0.708515	0.000010
160	22.72	0.512528	0.000005	-2.1	0.708235	0.000005
167	23.80				0.707873	0.000006
173	24.72				0.707796	0.000005
182	25.69	0.512533	0.000005	-2,0	0.708965	0.000005
196	27.27	0.512510	0.000008	-2.5	0.708907	0.000005
213	28.96				0.709026	0.000008

Annex 10: Isotopic composition from the cohesive silt mode fraction (2-20 μm) from sediment core MD07-3076Q. σ corresponds to the internal standard error of the measurement.

depth (cm)	age (ka)	$^{143}Nd/^{144}Nd$	2σ	ε_{Nd}	$^{87}Sr/^{86}Sr$	2σ
51	10.03	0.512419	0.000006	-4.3	0.707880	0.000009
54	10.52	0.512395	0.000006	-4.7	0.707870	0.000012
57	10.91				0.707797	0.000005
61	11.39				0.708000	0.000009
65	11.93	0.512390	0.000007	-4.8	0.708190	0.000009
74	12.98	0.512370	0.000006	-5.2	0.708150	0.000009
74	12.98	0.512407	0.000008	-4.5	0.707662	0.000030
75	13.07	0.512393	0.000005	-4.8	0.708160	0.000009
80	13.56	0.512403	0.000006	-4.6	0.708010	0.000010
87	14.29	0.512417	0.000007	-4.3	0.707900	0.000010
96	14.88	0.512424	0.000007	-4.2	0.707730	0.000010
107	16.28	0.512396	0.000006	-4.7	0.708040	0.000009
112	16.97	0.512388	0.000006	-4.9	0.708000	0.000008
120	17.91	0.512379	0.000006	-5.1	0.707918	0.000008
121	18.01	0.512385	0.000005	-4.9	0.707975	0.000005
122	18.10	0.512355	0.000006	-5.5	0.708052	0.000011
130	18.79	0.512413	0.000006	-4.4	0.708370	0.000010
138	19.54	0.512420	0.000005	-4.2	0.707710	0.000010
149	21.1	0.512437	0.000005	-3.9	0.707890	0.000008
155	21.98	0.512409	0.000006	-4.5	0.707850	0.000009
160	22.72	0.512377	0.000006	-5.1	0.707930	0.000011
167	23.80	0.512435	0.000005	-4,0	0.708240	0.000013
173	24.72	0.512430	0.000006	-4.1	0.708110	0.000009
182	25.69				0.707816	0.000005
196	27.27	0.512401	0.000006	-4.6	0.707607	0.000008
214	29.04	0.512371	0.000005	-5.2		

Annex 11: Synthesis of the mineralogical signature of the sediment transported by the three main deep water-masses. Crosses are given when increased delivery from a specific deep water mass increase the relative proportion of the clay mineral. As an example, it can be read as followed: "an enhanced delivery of terrigenous sediment from CDW increases the proportion of smectite and chlorite at site MD07-3076Q"

	smectite	illite	kaolinite	chlorite
NADW-W	X		X	
CDW	X			X
AABW		X		X

Annex 12: Correlation factors (R^2) between deep water mass proxies and the contribution of NADW to clay mineral deposition. All the data comes from the same sediment core (MD07-3076Q) and only samples from the same intervals (i.e. same depth) have been used to calculate the correlation factors. The correlation factor between the ε_{Nd} from clay particles and the ε_{Nd} from sea water is also high (higher than 0.8), but we chose not to report it in the table because of the low number of samples measured on the same interval (n = 6 instead of at least 14).

	NADW contribution to clay deposition (calculated using Holocene end member)	NADW contribution to clay deposition (calculated using LGM end member)	ε_{Nd} (clay)
cibicides $\delta^{13}C$	0,74	0,64	0,8
ε_{Nd} (seawater)	0,81	0,64	-

Annex 13: proportion of clay minerals in core MD07-3076Q

depth (cm)	age (ka)	total terrigenous	smectite (%)	illite (%)	chlorite (%)	kaolinite (%)	I/S	K/C
0	0,9	140,2	35,9	29,1	23,7	11,4	0,8	0,5
1	1,0	83,8	36,7	31,5	20,0	11,8	0,9	0,6
2	1,1	62,6	37,9	33,0	17,8	11,3	0,9	0,6
3	1,3	64,3	38,4	32,3	17,4	11,9	0,8	0,7
4	1,4	62,1	37,5	33,7	16,6	12,2	0,9	0,7
5	1,5	70,7	38,6	32,4	16,9	12,0	0,8	0,7
6	1,6	72,7	40,2	29,5	18,2	12,1	0,7	0,7
7	1,8	74,0	44,8	27,0	17,0	11,2	0,6	0,7
8	1,9	61,7	39,5	32,6	16,2	11,7	0,8	0,7
9	2,1	64,0	36,1	32,7	18,8	12,4	0,9	0,7
10	2,2	72,1	38,7	32,3	17,9	11,1	0,8	0,6
11	2,4	66,2	37,2	33,2	17,3	12,3	0,9	0,7
12	2,5	70,6	35,4	31,4	18,9	14,4	0,9	0,8
13	2,7	58,9	39,0	33,7	15,5	11,8	0,9	0,8
14	2,8	84,5	47,5	27,6	13,9	10,9	0,6	0,8
15	3,0	75,0	41,7	30,2	15,6	12,5	0,7	0,8
16	3,2	81,9	41,6	30,5	16,5	11,4	0,7	0,7
17	3,4	80,0	42,8	31,3	14,9	11,1	0,7	0,7
18	3,7	68,1	45,7	31,4	12,7	10,3	0,7	0,8
19	3,9	108,8	51,9	25,2	13,4	9,5	0,5	0,7
20	4,1	103,3	55,3	22,5	14,2	8,0	0,4	0,6
21	4,3	97,6	51,2	24,3	14,0	10,5	0,5	0,8
22	4,5	124,9	67,3	16,9	9,2	6,6	0,3	0,7
23	4,7	112,2	58,8	23,3	10,6	7,3	0,4	0,7
24	4,9	113,0	55,9	22,9	13,2	8,1	0,4	0,6
25	5,1	102,5	52,4	23,4	14,6	9,6	0,4	0,7
26	5,3	90,9	46,4	28,4	15,5	9,7	0,6	0,6
27	5,5	101,2	52,3	25,9	14,2	7,6	0,5	0,5
28	5,7	87,2	49,4	28,5	15,4	6,6	0,6	0,4
29	5,9	107,3	50,0	25,9	14,8	9,3	0,5	0,6
30	6,1	93,7	43,2	28,0	17,6	11,3	0,6	0,6
31	6,3	54,3	37,0	33,5	19,8	9,8	0,9	0,5
32	6,4	68,5	33,8	34,5	20,7	11,0	1,0	0,5
33	6,6	87,4	39,2	32,3	18,5	10,1	0,8	0,5
34	6,7	76,7	47,8	26,8	16,2	9,3	0,6	0,6
35	6,8	100,4	47,0	26,7	16,9	9,4	0,6	0,6
36	7,0	87,2	40,4	30,2	19,3	10,0	0,7	0,5
37	7,2	105,9	47,2	28,8	14,8	9,2	0,6	0,6
38	7,4	113,5	56,2	22,4	14,7	6,8	0,4	0,5
39	7,7	78,0	34,7	34,2	19,7	11,4	1,0	0,6
40	7,9	80,4	29,9	35,0	23,0	12,1	1,2	0,5
41	8,1	82,2	33,1	35,2	19,5	12,2	1,1	0,6
42	8,3	83,0	35,7	33,9	19,4	11,0	1,0	0,6
43	8,6	86,3	34,9	30,4	21,9	12,8	0,9	0,6
44	8,8	121,5	43,8	26,3	19,3	10,5	0,6	0,5
45	9,1	113,3	43,7	26,7	18,9	10,8	0,6	0,6
46	9,2	100,8	40,8	30,5	18,7	10,1	0,7	0,5
47	9,4	123,9	55,6	23,1	14,2	7,2	0,4	0,5
48	9,6	143,8	60,7	19,8	12,9	6,6	0,3	0,5

depth (cm)	age (ka)	total terrigenous	smectite (%)	illite (%)	chlorite (%)	kaolinite (%)	I/S	K/C
49	9,7	114,2	42,5	28,7	18,5	10,3	0,7	0,6
50	9,9	111,8	45,6	28,7	15,9	9,8	0,6	0,6
51	10,0	136,4	53,4	22,4	16,0	8,2	0,4	0,5
52	10,2	136,1	56,8	21,2	16,2	5,8	0,4	0,4
53	10,3	103,8	35,1	34,1	19,8	10,9	1,0	0,5
54	10,5	116,7	54,3	24,9	13,9	6,9	0,5	0,5
55	10,7	102,8	43,7	29,3	17,6	9,4	0,7	0,5
56	10,8	125,4	43,8	29,8	16,5	9,9	0,7	0,6
57	10,9	123,6	43,5	28,1	18,4	10,0	0,6	0,5
58	11,0	116,4	50,0	26,6	14,5	9,0	0,5	0,6
59	11,1	126,2	43,5	28,4	18,1	10,0	0,7	0,6
60	11,3	128,2	46,4	27,8	16,2	9,6	0,6	0,6
61	11,4	147,2	57,5	22,7	12,7	7,1	0,4	0,6
62	11,5	135,0	40,1	31,6	17,4	10,9	0,8	0,6
63	11,6	155,6	44,5	28,3	17,3	9,9	0,6	0,6
64	11,8	116,6	46,5	28,7	15,3	9,5	0,6	0,6
65	11,9	143,8	58,5	22,6	12,3	6,6	0,4	0,5
66	12,1	144,2	40,2	30,5	19,3	9,9	0,8	0,5
67	12,2	128,8	43,7	28,8	16,8	10,7	0,7	0,6
68	12,3	132,3	38,4	31,5	19,9	10,1	0,8	0,5
69	12,4	144,0	48,3	25,1	16,9	9,6	0,5	0,6
70	12,6	138,2	37,0	31,7	20,4	10,9	0,9	0,5
71	12,7	124,0	36,6	32,5	20,6	10,3	0,9	0,5
72	12,8	139,7	42,0	30,3	18,5	9,3	0,7	0,5
73	12,9	143,1	38,6	29,6	21,7	10,2	0,8	0,5
74	13,0	126,3	34,0	32,8	21,7	11,4	1,0	0,5
75	13,1	130,5	36,4	32,4	21,1	10,1	0,9	0,5
76	13,2	134,4	39,4	31,1	18,3	11,2	0,8	0,6
77	13,2	145,9	50,2	24,6	17,2	8,0	0,5	0,5
78	13,3	123,1	42,8	29,3	18,5	9,3	0,7	0,5
79	13,5	129,2	39,8	30,8	19,6	9,8	0,8	0,5
80	13,6	125,4	39,4	29,2	21,3	10,1	0,7	0,5
81	13,7	122,1	36,1	31,6	22,5	9,8	0,9	0,4
82	13,8	134,8	40,1	29,5	20,3	10,1	0,7	0,5
83	13,9	113,7	39,8	30,3	19,8	10,0	0,8	0,5
84	14,0	126,5	33,9	33,3	21,3	11,5	1,0	0,5
85	14,1	124,3	35,5	32,5	22,3	9,7	0,9	0,4
86	14,2	114,3	37,1	31,4	22,0	9,5	0,8	0,4
87	14,3	105,4	35,4	35,1	20,0	9,4	1,0	0,5
88	14,4	96,4	30,6	32,6	25,4	11,4	1,1	0,4
89	14,5	131,3	39,3	26,8	22,5	11,4	0,7	0,5
90	14,6	111,2	33,6	33,6	21,8	10,9	1,0	0,5
91	14,7	109,3	35,9	33,5	21,7	8,8	0,9	0,4
92	14,7	106,2	32,6	33,9	22,4	11,1	1,0	0,5
93	14,7	128,6	34,0	31,3	24,2	10,6	0,9	0,4
94	14,8	121,8	35,3	32,4	22,3	10,0	0,9	0,4
95	14,8	131,9	34,7	30,1	25,1	10,1	0,9	0,4
96	14,9	117,5	29,8	34,5	25,5	10,2	1,2	0,4
97	15,0	118,5	30,8	33,0	25,9	10,3	1,1	0,4

depth (cm)	age (ka)	total terrigenous	smectite (%)	illite (%)	chlorite (%)	kaolinite (%)	I/S	K/C
98	15,1	136,6	36,7	32,1	21,7	9,5	0,9	0,4
99	15,1	135,0	35,1	30,5	23,6	10,8	0,9	0,5
100	15,3	124,6	29,8	35,2	24,4	10,5	1,2	0,4
101	15,5	110,9	27,1	36,6	24,6	11,6	1,4	0,5
102	15,6	117,4	31,0	33,7	25,4	9,8	1,1	0,4
103	15,8	117,1	28,7	33,8	26,6	10,9	1,2	0,4
104	15,9	119,9	29,0	34,5	25,9	10,7	1,2	0,4
105	16,0	126,4	28,7	34,6	25,5	11,2	1,2	0,4
106	16,1	126,8	30,1	30,6	27,2	12,0	1,0	0,4
107	16,3	109,0	30,6	34,0	24,9	10,5	1,1	0,4
108	16,4	106,3	26,6	37,1	26,6	9,7	1,4	0,4
109	16,6	115,6	28,5	35,2	26,7	9,6	1,2	0,4
110	16,7	115,6	27,8	34,0	27,6	10,6	1,2	0,4
111	16,8	114,5	26,8	33,4	28,7	11,1	1,2	0,4
112	17,0	119,9	26,9	31,0	30,1	12,0	1,1	0,4
113	17,1	107,2	26,2	36,2	24,9	12,7	1,4	0,5
114	17,2	108,3	26,3	33,7	29,6	10,4	1,3	0,4
115	17,3	103,8	26,9	35,8	25,0	12,3	1,3	0,5
116	17,5	109,5	26,1	35,1	28,0	10,8	1,3	0,4
117	17,6	103,0	22,3	36,0	30,1	11,6	1,6	0,4
118	17,7	102,2	19,9	36,8	31,2	12,1	1,9	0,4
119	17,8	92,2	21,1	38,2	27,4	13,3	1,8	0,5
120	17,9	95,9	19,8	38,3	29,7	12,2	1,9	0,4
121	18,0	86,3	18,8	37,9	29,9	13,5	2,0	0,4
122	18,1	95,5	20,1	37,0	30,5	12,5	1,8	0,4
123	18,2	104,9	20,7	36,9	30,8	11,5	1,8	0,4
124	18,3	115,2	24,8	33,4	29,4	12,3	1,3	0,4
125	18,4	105,4	23,3	37,0	28,2	11,5	1,6	0,4
126	18,5	106,8	22,5	37,8	27,5	12,2	1,7	0,4
127	18,5	108,3	21,5	35,8	30,1	12,6	1,7	0,4
128	18,6	111,2	26,5	32,7	29,2	11,7	1,2	0,4
129	18,7	100,8	21,6	34,1	31,3	13,0	1,6	0,4
130	18,8	106,8	24,3	32,1	31,7	11,9	1,3	0,4
131	18,9	110,5	26,9	29,8	29,3	14,0	1,1	0,5
132	18,9	116,8	25,0	35,4	27,5	12,2	1,4	0,4
133	19,0	95,2	23,6	36,9	28,3	11,2	1,6	0,4
134	19,1	104,3	23,8	36,7	26,3	13,3	1,5	0,5
135	19,2	111,5	29,8	33,7	25,0	11,5	1,1	0,5
136	19,3	102,9	27,3	33,0	26,8	12,9	1,2	0,5
137	19,4	99,7	26,2	34,8	28,6	10,4	1,3	0,4
138	19,5	98,0	26,0	35,7	26,7	11,6	1,4	0,4
139	19,7	101,0	21,7	38,1	28,3	12,0	1,8	0,4
140	19,8	104,2	25,0	35,6	28,0	11,3	1,4	0,4
141	20,0	111,6	29,1	34,6	24,2	12,0	1,2	0,5
142	20,1	118,1	28,0	32,2	27,2	12,5	1,2	0,5
143	20,2	101,4	27,7	34,1	26,7	11,5	1,2	0,4
144	20,4	115,9	25,3	33,9	30,1	10,7	1,3	0,4
145	20,5	109,4	28,0	34,8	26,6	10,6	1,2	0,4
146	20,7	113,3	28,5	33,7	27,6	10,2	1,2	0,4

depth (cm)	age (ka)	total terrigenous	smectite (%)	illite (%)	chlorite (%)	kaolinite (%)	I/S	K/C
148	21,0	109,6	26,1	35,6	27,1	11,2	1,4	0,4
149	21,1	110,2	27,5	33,1	26,3	13,1	1,2	0,5
150	21,2	102,8	29,2	34,2	26,0	10,5	1,2	0,4
151	21,4	93,6	29,9	33,9	24,5	11,6	1,1	0,5
152	21,5	90,2	28,9	32,0	28,5	10,6	1,1	0,4
153	21,7	92,8	33,1	33,6	22,1	11,2	1,0	0,5
154	21,8	107,2	31,6	33,1	24,7	10,6	1,0	0,4
155	22,0	92,6	32,9	34,1	22,4	10,6	1,0	0,5
156	22,1	101,7	30,7	32,3	25,6	11,4	1,1	0,4
157	22,3	106,4	31,8	32,3	26,0	9,8	1,0	0,4
158	22,4	107,0	30,8	33,4	27,4	8,5	1,1	0,3
159	22,6	106,7	31,1	33,1	24,2	11,7	1,1	0,5
160	22,7	111,0	27,0	35,3	26,8	10,9	1,3	0,4
161	22,9	115,0	28,7	35,1	24,7	11,5	1,2	0,5
162	23,0	119,0	31,2	33,5	24,7	10,5	1,1	0,4
163	23,2	107,3	32,1	34,1	24,4	9,4	1,1	0,4
164	23,3	114,8	29,1	34,1	26,2	10,6	1,2	0,4
165	23,5	94,9	28,1	35,1	24,6	12,1	1,2	0,5
166	23,6	97,0	26,4	35,0	27,7	10,9	1,3	0,4
167	23,8	103,5	26,9	33,2	27,9	12,0	1,2	0,4
168	24,0	94,9	32,1	33,8	25,7	8,4	1,1	0,3
169	24,1	114,7	30,1	33,6	24,9	11,4	1,1	0,5
170	24,3	109,7	29,3	31,8	27,3	11,7	1,1	0,4
171	24,4	112,7	26,0	36,0	27,2	10,8	1,4	0,4
172	24,6	110,4	27,7	35,0	27,8	9,5	1,3	0,3
173	24,7	114,6	29,9	34,8	25,0	10,3	1,2	0,4
174	24,8	103,7	29,3	35,9	25,2	9,6	1,2	0,4
175	24,9	101,3	25,0	37,1	27,1	10,8	1,5	0,4
176	25,0	95,0	24,8	37,0	27,2	11,0	1,5	0,4
177	25,2	117,6	25,7	34,9	28,0	11,4	1,4	0,4
178	25,3	115,9	25,9	35,9	27,3	10,9	1,4	0,4
179	25,4	112,9	27,6	34,7	26,4	11,3	1,3	0,4
180	25,5	102,4	27,8	36,0	25,4	10,8	1,3	0,4
181	25,6	107,6	25,8	35,1	27,7	11,4	1,4	0,4
182	25,7	116,3	27,2	33,7	28,7	10,4	1,2	0,4
183	25,8	102,5	26,2	37,1	27,6	9,1	1,4	0,3
184	25,9	115,0	27,9	34,6	25,7	11,7	1,2	0,5
185	26,0	106,5	29,7	33,2	28,1	9,0	1,1	0,3
186	26,1	104,3	29,8	35,5	24,6	10,0	1,2	0,4
187	26,2	103,1	27,2	34,8	25,9	12,1	1,3	0,5
188	26,3	102,9	28,0	34,9	27,3	9,8	1,2	0,4
189	26,5	106,9	27,4	35,6	27,0	10,0	1,3	0,4
190	26,6	103,0	27,9	34,8	27,2	10,1	1,3	0,4
191	26,7	110,2	28,5	33,5	27,9	10,1	1,2	0,4
192	26,8	101,5	31,2	33,5	25,0	10,3	1,1	0,4
193	26,9	99,6	27,5	35,9	26,4	10,2	1,3	0,4
194	27,0	100,1	26,5	35,5	28,8	9,3	1,3	0,3
195	27,2	96,4	26,8	35,7	27,6	9,9	1,3	0,4
196	27,3	99,4	29,4	35,0	25,1	10,5	1,2	0,4

depth (cm)	age (ka)	total terrigenous	smectite (%)	illite (%)	chlorite (%)	kaolinite (%)	I/S	K/C
197	27,4	105,1	26,3	35,3	29,5	8,9	1,3	0,3
198	27,5	103,6	24,2	35,9	28,4	11,5	1,5	0,4
199	27,6	103,6	28,3	35,1	27,7	8,9	1,2	0,3
200	27,7	109,5	29,8	32,5	27,2	10,5	1,1	0,4
201	27,8	102,0	23,6	37,5	29,8	9,1	1,6	0,3
202	27,9	98,7	25,3	35,6	28,3	10,8	1,4	0,4
203	28,0	102,4	23,8	38,1	28,2	9,8	1,6	0,3
204	28,1	107,9	24,3	37,6	27,7	10,4	1,5	0,4
205	28,3	97,8	26,0	37,5	25,9	10,6	1,4	0,4
206	28,4	110,6	25,6	37,9	27,4	9,1	1,5	0,3
207	28,5	115,8	26,0	31,8	33,1	9,1	1,2	0,3
208	28,6	104,5	23,9	35,8	27,9	12,4	1,5	0,4
209	28,6	112,9	22,8	37,1	29,0	11,0	1,6	0,4
210	28,7	127,8	24,5	34,5	29,8	11,3	1,4	0,4
211	28,8	117,6	23,1	37,6	29,2	10,1	1,6	0,3
212	28,9	134,2	23,6	35,2	29,3	11,9	1,5	0,4
213	29,0	113,0	26,9	32,1	28,6	12,4	1,2	0,4
214	29,0	105,4	21,9	38,1	29,0	11,0	1,7	0,4
215	29,1	108,5	21,2	37,9	30,2	10,7	1,8	0,4
216	29,2	100,4	25,4	36,0	28,3	10,3	1,4	0,4
217	29,3	112,6	23,0	36,3	30,4	10,2	1,6	0,3
218	29,4	107,7	23,6	37,5	28,3	10,6	1,6	0,4
219	29,4	100,2	22,0	39,7	27,5	10,8	1,8	0,4
220	29,5	119,8	23,1	38,2	28,8	9,9	1,7	0,3

Annex 14: Crystalinity and chemistry of illite and smectite from core MD07-3076Q

depth (cm)	age (ka)	smectite crystallinity	illite crystallinity	illite 5Å/10Å
0	0,9	1,298	0,269	0,249
1	1,0	1,149	0,365	0,146
2	1,1	1,145	0,376	0,124
3	1,3	1,145	0,361	0,211
4	1,4	1,063	0,330	0,115
5	1,5	1,079	0,336	0,163
6	1,6	1,164	0,366	0,214
7	1,7	1,138	0,331	0,215
8	1,9	1,031	0,333	0,164
9	2,0	1,118	0,235	0,229
10	2,2	1,205	0,354	0,149
11	2,3	1,084	0,312	0,158
12	2,5	1,119	0,322	0,229
13	2,7	1,115	0,344	0,163
14	2,8	1,155	0,365	0,149
15	3,0	1,158	0,344	0,187
16	3,2	1,191	0,361	0,185
17	3,4	1,171	0,347	0,159
18	3,7	1,135	0,357	0,113
19	3,9	1,289	0,342	0,154
20	4,1	1,358	0,347	0,178
21	4,3	1,348	0,361	0,251
22	4,6	1,304	0,327	0,165
23	4,8	1,319	0,343	0,152
24	5,1	1,281	0,350	0,154
25	5,3	1,334	0,378	0,168
26	5,5	1,251	0,347	0,219
27	5,7	1,274	0,368	0,141
28	5,8	1,193	0,347	0,128
29	6,0	1,257	0,364	0,194
30	6,2	1,233	0,352	0,177
31	6,3	1,054	0,341	0,150
32	6,4	1,088	0,359	0,230
33	6,6	1,172	0,326	0,197
34	6,7	1,168	0,363	0,198
35	6,9	1,218	0,348	0,170
36	7,0	1,174	0,369	0,177
37	7,2	1,276	0,405	0,143
38	7,4	1,310	0,364	0,154
39	7,7	1,067	0,353	0,122
40	7,9	1,087	0,417	0,150
41	8,1	1,021	0,350	0,188
42	8,3	1,099	0,396	0,183
43	8,6	1,112	0,384	0,199
44	8,8	1,340	0,347	0,232
45	9,0	1,321	0,372	0,202
46	9,2	1,148	0,317	0,206
47	9,4	1,341	0,348	0,166

depth (cm)	age (ka)	smectite crystallinity	illite crystallinity	illite 5Å/10Å
48	9,6	1,325		0,210
49	9,8	1,245	0,361	0,184
50	9,9	1,265	0,373	0,184
51	10,1	1,347	0,406	0,189
52	10,2	1,380	0,378	0,199
53	10,4	1,167	0,340	0,188
54	10,5	1,304	0,356	0,151
55	10,7	1,220	0,362	0,132
56	10,8	1,343	0,365	0,181
57	10,9	1,278	0,366	0,184
58	11,0	1,264	0,366	0,162
59	11,1	1,260	0,353	0,217
60	11,3	1,238	0,317	0,146
61	11,4	1,347	0,361	0,146
62	11,5	1,209	0,350	0,206
63	11,7	1,337	0,364	0,174
64	11,8	1,225	0,358	0,133
65	11,9	1,326	0,381	0,153
66	12,1	1,325	0,390	0,207
67	12,2	1,258	0,351	0,170
68	12,3	1,211	0,373	0,203
69	12,4	1,394	0,363	0,201
70	12,6	1,161	0,385	0,195
71	12,7	1,232	0,352	0,172
72	12,8	1,214	0,335	0,156
73	12,9	1,248		0,192
74	13,0	1,194	0,326	0,197
75	13,1	1,270	0,330	0,210
76	13,2	1,247	0,341	0,211
77	13,3	1,349	0,348	0,173
78	13,3	1,277	0,341	0,186
79	13,5	1,233	0,327	0,171
80	13,6	1,223	0,325	0,223
81	13,7	1,179	0,351	0,215
82	13,8	1,279	0,367	0,240
83	13,9	1,165	0,313	0,193
84	14,0	1,227	0,362	0,202
85	14,1	1,187	0,368	0,187
86	14,2	1,194	0,352	0,195
87	14,3	1,101	0,367	0,140
88	14,4	1,057	0,345	0,151
89	14,5	1,300	0,377	0,207
90	14,6	1,094	0,361	0,191
91	14,6	1,148	0,350	0,170
92	14,7	1,096	0,320	0,151
93	14,7	1,179	0,340	0,202
94	14,8	1,167	0,381	0,229
95	14,8	1,227	0,348	0,224

depth (cm)	age (ka)	smectite crystallinity	illite crystallinity	illite 5Å/10Å
96	14,9	1,098	0,334	0,192
97	15,0	1,078	0,324	0,179
98	15,1	1,196	0,377	0,185
99	15,2	1,153	0,379	0,191
100	15,3	1,106	0,351	0,185
101	15,4	1,074	0,324	0,176
102	15,6	1,137	0,352	0,149
103	15,7	1,164	0,360	0,178
104	15,9	1,106	0,342	0,187
105	16,0	1,068	0,379	0,189
106	16,1	1,185	0,358	0,270
107	16,3	1,114	0,375	0,197
108	16,4	1,046		0,186
109	16,6	1,119	0,406	0,166
110	16,7	1,119	0,391	0,203
111	16,8	1,102	0,349	0,201
112	17,0	1,145	0,387	0,238
113	17,1	1,048	0,344	0,176
114	17,2	1,053	0,375	0,207
115	17,3	1,009	0,368	0,174
116	17,5	1,063	0,378	0,166
117	17,6	1,062	0,352	0,225
118	17,7	1,021	0,335	0,193
119	17,8	1,040	0,380	0,203
120	17,9	1,039	0,353	0,196
121	18,0	0,983	0,336	0,143
122	18,1	1,042	0,339	0,196
123	18,2	1,083	0,347	0,195
124	18,3	1,158	0,362	0,231
125	18,4	1,072	0,368	0,177
126	18,5	1,086	0,370	0,211
127	18,5	1,001	0,350	0,176
128	18,6	1,118	0,337	0,216
129	18,7	1,019	0,350	0,182
130	18,8	1,146	0,367	0,237
131	18,9	1,112	0,374	0,243
132	18,9	1,087	0,351	0,221
133	19,0	1,102	0,349	0,173
134	19,1	1,083	0,331	0,201
135	19,2	1,164	0,376	0,182
136	19,3	1,107	0,375	0,188
137	19,4	1,100	0,360	0,172
138	19,5	1,077	0,393	0,176
139	19,7	1,070	0,374	0,170
140	19,8	1,064	0,402	0,171
141	20,0	1,107	0,389	0,172
142	20,1	1,166	0,371	0,222
143	20,2	1,105	0,373	0,175

depth (cm)	age (ka)	smectite crystallinity	illite crystallinity	illite 5Å/10Å
144	20,4	1,113	0,383	0,228
145	20,5	1,071	0,353	0,189
146	20,7	1,135	0,394	0,233
147	20,8	1,120	0,363	0,204
148	21,0	1,119	0,391	0,165
149	21,1	1,029	0,343	0,195
150	21,2	1,065	0,353	0,167
151	21,4	1,049	0,394	0,189
152	21,5	1,008	0,347	0,148
153	21,7	1,046	0,360	0,161
154	21,8	1,034	0,364	0,188
155	22,0	1,087	0,384	0,155
156	22,1	1,021	0,354	0,166
157	22,3	1,113	0,368	0,177
158	22,4	1,115	0,392	0,202
159	22,6	1,112	0,358	0,219
160	22,7	1,092	0,365	0,190
161	22,9	1,061	0,329	0,173
162	23,0	1,088	0,373	0,231
163	23,2	1,057	0,366	0,174
164	23,3	1,071	0,373	0,188
165	23,5	1,060	0,315	0,152
166	23,6	1,043	0,357	0,170
167	23,8	1,052	0,333	0,218
168	24,0	1,064	0,277	0,165
169	24,1	1,111		0,203
170	24,3	1,144	0,336	0,213
171	24,4	1,118	0,389	0,207
172	24,6	1,101	0,391	0,246
173	24,7	1,043		0,193
174	24,8	1,074	0,367	0,146
175	24,9	1,029	0,368	0,207
176	25,0	1,077	0,361	0,179
177	25,2	1,159	0,350	0,208
178	25,3	1,095	0,360	0,195
179	25,4	1,106	0,346	0,183
180	25,5	1,041	0,365	0,144
181	25,6	1,063	0,350	0,190
182	25,7	1,125	0,422	0,203
183	25,8	1,036	0,360	0,141
184	25,9	1,127	0,363	0,174
185	26,0	1,108	0,332	0,174
186	26,1	0,921	0,345	0,194
187	26,2	1,114	0,366	0,172
188	26,3	1,204	0,343	0,169
189	26,5	1,052	0,388	0,178
190	26,6	1,278	0,304	0,192
191	26,7	1,046	0,385	0,185

depth (cm)	age (ka)	smectite crystallinity	illite crystallinity	illite 5Å/10Å
192	26,8	0,969	0,349	0,191
193	26,9	1,044	0,370	0,208
194	27,0	1,087	0,328	0,168
195	27,2	1,198	0,369	0,197
196	27,3	1,122	0,366	0,162
197	27,4	0,947	0,359	0,192
198	27,5	1,197	0,349	0,159
199	27,6	1,446	0,350	0,152
200	27,7	0,888	0,411	0,222
201	27,8	1,098	0,366	0,212
202	27,9	1,084	0,316	0,160
203	28,0	1,043	0,347	0,161
204	28,1	1,151	0,358	0,209
205	28,3	1,039	0,341	0,154
206	28,4	1,075	0,351	0,197
207	28,5	1,150	0,353	0,231
208	28,6	1,117		0,212
209	28,6	1,098	0,372	0,226
210	28,7	1,173	0,344	0,240
211	28,8	1,069	0,355	0,203
212	28,9	1,214	0,360	0,245
213	29,0	1,198	0,373	0,194
214	29,1	1,039	0,333	0,202
215	29,1	1,076	0,330	0,221
216	29,2	1,110	0,350	0,203
217	29,3	1,147	0,331	0,230
218	29,4	1,056	0,333	0,180
219	29,5	1,047	0,350	0,175
220	29,5	1,105	0,342	0,194

Annex 15: grain size distribution data from core MD07-3076Q

depth (cm)	age (ka)	clays (%)	cohesive silts (%)	non cohesive silts (%)	sand (%)	coarse mode (μm)	fine mode (μm)	coarse mode (%)	fine mode (%)	coarse/fine	fine/coarse
0	0,9	3,23	40,87	46,40	2,14	22,92	7,76	29,43	51,37	0,57	1,75
1	1,0	2,45	43,76	45,56	0,80	17,17	8,87	28,84	55,99	0,52	1,94
2	1,1	1,85	40,94	48,64	0,84	20,50	10,79	30,96	53,77	0,58	1,74
3	1,3	1,86	39,09	49,07	2,25	20,50	10,77	31,25	51,12	0,61	1,64
4	1,4	1,82	39,37	49,54	1,55	20,50	11,20	31,65	51,68	0,61	1,63
5	1,5	2,08	40,44	49,36	0,73	18,00	10,79	31,91	52,46	0,61	1,64
6	1,6	2,01	40,38	49,22	0,94	20,50	10,20	31,70	52,39	0,61	1,65
7	1,8	1,94	39,35	49,54	1,69	21,61	9,57	31,93	50,84	0,63	1,59
8	1,9	2,23	40,93	48,99	0,55	20,50	9,56	31,74	52,68	0,60	1,66
9	2,1	2,21	41,42	48,06	1,01	20,50	8,60	30,99	52,96	0,59	1,71
10	2,2	2,27	41,02	48,55	0,89	18,22	9,68	31,40	52,80	0,59	1,68
11	2,4	2,42	40,67	48,86	1,00	24,39	8,16	31,89	51,68	0,62	1,62
12	2,5	2,35	38,70	50,44	1,37	25,90	9,19	32,99	49,51	0,67	1,50
13	2,7	2,68	39,47	49,56	1,25	24,69	9,44	32,42	50,36	0,64	1,55
14	2,8	2,69	39,39	50,17	0,82	23,10	8,00	33,03	50,57	0,65	1,53
15	3,0	2,71	40,42	49,02	0,86	21,70	10,00	32,08	51,69	0,62	1,61
16	3,2	2,78	41,44	47,71	1,07	21,63	8,23	31,04	52,54	0,59	1,69
17	3,4	2,80	39,12	49,97	1,17	24,77	7,45	32,86	49,83	0,66	1,52
18	3,7	3,22	41,05	48,53	0,42	21,76	7,45	31,95	52,22	0,61	1,63
19	3,9	2,70	40,05	49,57	0,72	22,36	8,00	32,56	51,24	0,64	1,57
20	4,1	2,56	40,86	48,59	0,90	21,29	9,29	31,63	52,22	0,61	1,65
21	4,3	2,84	40,90	48,28	0,98	21,63	9,28	31,48	52,08	0,60	1,65
22	4,5	3,53	41,00	47,44	1,27	23,37	7,24	31,04	51,50	0,60	1,66
23	4,7	3,24	39,88	49,58	0,51	23,08	7,45	32,73	50,77	0,64	1,55
24	4,9	3,78	41,68	47,34	0,50	21,78	8,17	31,05	52,51	0,59	1,69
25	5,1	3,54	42,62	46,65	0,47	20,40	7,75	30,51	53,65	0,57	1,76
26	5,3	3,21	39,65	48,92	1,36	25,05	7,85	32,09	50,06	0,64	1,56
27	5,5	3,66	40,56	48,14	0,89	23,58	7,87	31,60	51,09	0,62	1,62
28	5,7	3,47	40,41	47,56	1,69	22,68	8,25	31,01	51,01	0,61	1,64
29	5,9	3,56	42,82	46,43	0,42	19,22	7,93	30,27	53,94	0,56	1,78
30	6,1	3,06	38,94	49,74	1,43	26,04	7,64	32,79	49,21	0,67	1,50

depth (cm)	age (ka)	clays (%)	cohesive silts (%)	non cohesive silts (%)	sand (%)	coarse mode (μm)	fine mode (μm)	coarse mode (%)	fine mode (%)	coarse/fine	fine/coarse
31	6,3	2,97	38,20	50,11	1,84	28,33	6,97	32,98	48,00	0,69	1,46
32	6,4	2,96	39,46	49,13	1,56	26,60	7,16	32,23	49,63	0,65	1,54
33	6,6	3,20	39,97	48,83	1,21	26,04	7,12	32,08	50,22	0,64	1,57
34	6,7	3,53	39,89	48,61	1,21	24,24	8,30	31,94	50,36	0,63	1,58
35	6,8	3,29	40,20	47,80	1,76	24,60	7,64	31,10	50,63	0,61	1,63
36	7,0	3,32	40,82	47,93	1,04	24,43	7,88	31,25	51,47	0,61	1,65
37	7,2	3,30	39,88	48,92	1,11	25,78	7,37	32,14	50,21	0,64	1,56
38	7,4	3,41	37,76	50,55	1,57	28,97	6,78	33,49	47,37	0,71	1,41
39	7,7	3,09	38,14	50,65	1,28	27,58	7,97	33,41	48,23	0,69	1,44
40	7,9	2,92	38,13	50,37	1,63	28,15	7,71	33,07	48,19	0,69	1,46
41	8,1	3,14	39,14	49,45	1,37	27,07	7,18	32,44	49,22	0,66	1,52
42	8,3	3,47	41,64	46,88	1,19	24,34	6,96	30,53	52,06	0,59	1,71
43	8,6	3,24	40,94	46,80	2,10	23,74	7,34	30,35	51,42	0,59	1,69
44	8,8	3,62	39,88	48,97	0,85	24,87	7,72	32,34	50,28	0,64	1,55
45	9,1	3,36	39,08	49,50	1,20	25,50	7,45	32,54	49,41	0,66	1,52
46	9,2	3,53	39,14	49,77	0,84	25,01	7,45	32,89	49,59	0,66	1,51
47	9,4	3,54	37,34	50,47	1,87	26,20	7,00	33,36	47,41	0,70	1,42
48	9,6	3,12	39,60	49,73	0,70	22,90	7,45	32,73	50,59	0,65	1,55
49	9,7	2,51	38,96	50,09	1,22	22,02	8,80	32,60	50,24	0,65	1,54
50	9,9	3,78	38,13	50,26	1,07	26,12	7,00	33,24	48,19	0,69	1,45
51	10,0	3,34	38,06	51,13	0,72	25,95	7,45	33,98	48,40	0,70	1,42
52	10,2	3,36	38,60	50,24	1,11	26,93	7,26	33,28	48,64	0,68	1,46
53	10,3	3,14	36,52	51,69	1,80	28,51	7,00	34,24	46,27	0,74	1,35
54	10,5	3,18	38,78	49,95	1,20	25,59	7,45	32,84	49,21	0,67	1,50
55	10,7	3,49	37,59	50,40	1,68	26,78	7,45	33,21	47,58	0,70	1,43
56	10,8	3,84	37,98	49,92	1,50	27,50	6,99	32,89	47,72	0,69	1,45
57	10,9	3,67	38,97	49,34	1,27	26,43	7,24	32,48	49,01	0,66	1,51
58	11,0	4,21	39,89	47,88	1,33	26,54	6,36	31,37	49,67	0,63	1,58
59	11,1	4,07	39,63	48,59	1,03	25,61	7,05	32,00	49,71	0,64	1,55
60	11,3	3,89	40,34	47,80	1,26	25,59	6,74	31,32	50,40	0,62	1,61
61	11,4	4,02	42,38	45,78	1,11	23,62	6,64	29,73	52,67	0,56	1,77

depth (cm)	age (ka)	clays (%)	cohesive silts (%)	non cohesive silts (%)	sand (%)	coarse mode (μm)	fine mode (μm)	coarse mode (%)	fine mode (%)	coarse/fine	fine/coarse
62	11,5	5,21	38,42	46,33	3,15	28,74	5,93	29,88	47,44	0,63	1,59
63	11,6	5,17	38,37	46,45	3,07	29,38	5,95	29,89	47,34	0,63	1,58
64	11,8	4,24	39,93	47,14	1,97	28,47	6,00	30,74	49,30	0,62	1,60
65	11,9	3,75	42,03	44,98	2,27	27,55	6,24	28,80	51,73	0,56	1,80
66	12,1	3,89	41,04	46,30	1,96	28,04	6,14	30,00	50,61	0,59	1,69
67	12,2	4,09	41,99	44,98	2,14	28,07	5,94	28,96	51,44	0,56	1,78
68	12,3	4,05	42,17	45,22	1,76	26,39	6,14	29,15	51,93	0,56	1,78
69	12,4	3,92	41,66	45,22	2,25	27,59	6,19	28,98	51,30	0,56	1,77
70	12,6	3,83	42,17	45,09	1,98	27,21	6,25	28,91	51,94	0,56	1,80
71	12,7	3,77	41,23	46,38	1,67	26,37	6,52	29,88	51,17	0,58	1,71
72	12,8	5,14	37,48	46,71	3,64	29,92	5,89	29,97	46,32	0,65	1,55
73	12,9	4,20	38,62	48,44	1,90	28,82	6,12	31,56	47,97	0,66	1,52
74	13,0	3,82	38,42	48,05	2,70	29,00	6,50	31,06	47,87	0,65	1,54
75	13,1	4,47	39,71	47,54	1,49	27,18	6,15	30,92	49,30	0,63	1,59
76	13,2	3,98	38,29	48,21	2,57	29,79	6,04	31,28	47,44	0,66	1,52
77	13,2	3,91	39,63	47,26	2,25	28,80	6,19	30,53	49,09	0,62	1,61
78	13,3	4,05	39,71	47,49	1,86	28,17	6,19	30,79	49,24	0,63	1,60
79	13,5	4,08	39,45	47,36	2,22	29,43	6,05	30,65	48,74	0,63	1,59
80	13,6	3,44	38,19	48,24	2,96	29,82	6,77	31,05	47,68	0,65	1,54
81	13,7	4,48	42,26	45,21	1,28	26,51	6,12	29,09	52,04	0,56	1,79
82	13,8	3,65	39,16	47,10	2,98	30,25	6,30	30,21	48,48	0,62	1,60
83	13,9	3,85	39,35	47,33	2,49	30,61	6,03	30,54	48,50	0,63	1,59
84	14,0	3,78	37,34	48,33	3,43	31,19	6,28	31,14	46,39	0,67	1,49
85	14,1	4,29	40,19	46,24	2,43	29,81	5,81	29,82	49,31	0,60	1,65
86	14,2	3,83	41,29	45,79	2,05	27,96	6,33	29,31	51,00	0,57	1,74
87	14,3	3,95	39,80	46,65	2,56	30,06	6,12	29,95	49,08	0,61	1,64
88	14,4	3,86	39,07	47,43	2,59	31,00	6,04	30,55	48,17	0,63	1,58
89	14,5	3,73	40,36	46,41	2,46	30,77	6,12	29,75	49,64	0,60	1,67
90	14,6	3,69	39,49	46,40	3,21	31,74	6,18	29,54	48,65	0,61	1,65
91	14,7	4,37	40,07	45,60	3,05	32,70	5,56	29,22	48,71	0,60	1,67
92	14,7	4,20	41,37	44,92	2,53	30,79	5,90	28,65	50,53	0,57	1,76

depth (cm)	age (ka)	clays (%)	cohesive silts (%)	non cohesive silts (%)	sand (%)	coarse mode (μm)	fine mode (μm)	coarse mode (%)	fine mode (%)	coarse/fine	fine/coarse
93	14,7	4,46	41,02	44,97	2,62	31,03	5,73	28,72	50,01	0,57	1,74
94	14,8	4,23	41,58	44,37	2,77	31,33	5,93	28,11	50,72	0,55	1,80
95	14,8	4,24	41,00	44,79	2,91	31,56	5,92	28,42	50,08	0,57	1,76
96	14,9	3,60	41,41	44,42	3,26	30,79	6,35	27,90	50,91	0,55	1,82
97	15,0	4,25	40,64	45,03	3,00	32,21	5,90	28,58	49,64	0,58	1,74
98	15,1	3,87	39,85	45,25	3,79	32,89	6,13	28,57	48,89	0,58	1,71
99	15,1	4,05	41,14	44,96	2,69	31,26	6,11	28,45	50,42	0,56	1,77
100	15,3	3,68	42,45	44,25	2,34	29,64	6,44	27,79	52,21	0,53	1,88
101	15,5	3,72	41,19	44,86	3,03	31,04	6,23	28,35	50,58	0,56	1,78
102	15,6	3,86	41,43	45,31	2,28	30,46	6,23	28,78	50,92	0,57	1,77
103	15,8	3,46	40,43	45,83	2,93	32,52	6,45	28,91	49,85	0,58	1,72
104	15,9	2,83	39,63	46,73	3,13	31,04	7,44	29,29	49,66	0,59	1,70
105	16,0	3,44	40,34	46,23	2,68	31,88	6,59	29,28	49,87	0,59	1,70
106	16,1	2,41	43,43	44,22	2,12	31,00	7,92	27,21	54,77	0,50	2,01
107	16,3	2,80	40,49	46,05	2,99	31,28	7,27	28,76	50,56	0,57	1,76
108	16,4	3,01	40,43	46,07	2,93	30,82	7,11	28,89	50,36	0,57	1,74
109	16,6	3,19	39,41	47,17	2,75	31,40	6,97	29,84	49,08	0,61	1,64
110	16,7	2,98	39,91	46,49	3,03	29,90	7,35	29,20	49,94	0,58	1,71
111	16,8	3,16	38,79	47,54	3,11	31,71	6,81	30,23	48,28	0,63	1,60
112	17,0	3,04	37,24	48,16	4,00	32,73	7,15	30,52	46,61	0,65	1,53
113	17,1	2,76	35,63	48,41	5,41	34,22	7,43	30,49	44,80	0,68	1,47
114	17,2	3,04	36,89	48,92	3,64	32,83	7,09	31,15	46,19	0,67	1,48
115	17,3	2,97	36,61	48,72	4,17	34,27	6,78	30,97	45,63	0,68	1,47
116	17,5	2,79	35,86	48,94	4,76	34,07	7,26	31,04	45,01	0,69	1,45
117	17,6	2,65	36,03	48,94	4,66	32,58	8,03	30,96	45,55	0,68	1,47
118	17,7	2,60	35,54	49,97	4,11	32,57	8,55	31,70	45,13	0,70	1,42
119	17,8	2,54	36,91	49,04	3,78	31,64	8,03	31,04	46,70	0,66	1,50
120	17,9	2,64	37,79	48,73	3,16	29,40	8,43	30,86	47,95	0,64	1,55
121	18,0	2,84	37,60	49,19	2,76	29,59	8,35	31,28	47,62	0,66	1,52
122	18,1	2,71	35,94	49,80	3,85	31,24	8,50	31,67	45,58	0,69	1,44
123	18,2	2,73	38,95	48,48	2,20	28,00	9,29	30,75	49,69	0,62	1,62

depth (cm)	age (ka)	clays (%)	cohesive silts (%)	non cohesive silts (%)	sand (%)	coarse mode (μm)	fine mode (μm)	coarse mode (%)	fine mode (%)	coarse/fine	fine/coarse
124	18,3	3,06	38,60	47,51	3,39	32,50	6,73	30,13	47,98	0,63	1,59
125	18,4	2,94	35,44	49,90	4,09	33,97	7,38	31,75	44,58	0,71	1,40
126	18,5	2,60	37,51	48,74	3,38	29,77	8,58	30,73	47,66	0,64	1,55
127	18,5	3,15	37,33	49,22	2,87	31,18	7,28	31,47	46,87	0,67	1,49
128	18,6	3,02	36,85	49,30	3,35	31,99	7,28	31,48	46,28	0,68	1,47
129	18,7	2,92	37,03	48,79	3,72	31,94	7,34	31,01	46,52	0,67	1,50
130	18,8	2,84	38,09	48,29	3,17	30,04	7,60	30,59	47,96	0,64	1,57
131	18,9	2,43	39,26	47,87	2,65	29,00	8,59	30,09	49,98	0,60	1,66
132	18,9	2,56	38,58	47,87	3,25	29,41	7,95	30,12	48,74	0,62	1,62
133	19,0	2,87	37,12	49,11	3,36	32,29	7,08	31,28	46,52	0,67	1,49
134	19,1	3,18	36,20	50,00	3,18	32,58	6,93	32,05	45,36	0,71	1,42
135	19,2	3,27	35,94	50,08	3,32	32,76	6,72	32,19	44,98	0,72	1,40
136	19,3	3,17	36,09	49,71	3,64	33,00	6,60	31,90	45,07	0,71	1,41
137	19,4	3,13	35,90	49,86	3,67	32,89	6,85	31,96	44,96	0,71	1,41
138	19,5	2,91	36,72	49,44	3,45	31,27	7,37	31,59	46,21	0,68	1,46
139	19,7	2,92	37,30	48,49	3,73	30,36	7,57	30,79	46,96	0,66	1,53
140	19,8	2,85	35,91	49,34	4,27	31,75	7,58	31,38	45,27	0,69	1,44
141	20,0	2,57	38,39	48,02	3,26	26,41	8,51	30,23	48,77	0,62	1,61
142	20,1	3,09	37,07	48,36	4,03	31,71	6,90	30,81	46,36	0,66	1,50
143	20,2	2,98	38,13	48,20	3,16	28,72	7,62	30,62	48,00	0,64	1,57
144	20,4	2,99	37,41	48,54	3,50	30,05	7,50	30,86	47,08	0,66	1,53
145	20,5	3,39	37,66	48,37	3,28	29,96	6,80	30,99	47,07	0,66	1,52
146	20,7	3,15	37,64	47,58	4,17	30,73	6,98	30,21	47,07	0,64	1,56
147	20,8	3,14	36,35	48,89	4,20	31,56	6,98	31,25	45,56	0,69	1,46
148	21,0	2,89	37,21	48,24	4,14	30,52	7,33	30,64	46,76	0,66	1,53
149	21,1	3,21	36,44	49,44	3,55	32,37	6,58	31,73	45,50	0,70	1,43
150	21,2	2,94	36,39	49,03	4,15	32,88	6,97	31,27	45,57	0,69	1,46
151	21,4	2,85	36,06	49,88	3,68	32,92	7,08	31,88	45,27	0,70	1,42
152	21,5	2,75	37,92	48,60	3,22	32,73	6,96	30,92	47,38	0,65	1,53
153	21,7	2,96	38,20	47,87	3,51	33,02	6,68	30,39	47,50	0,64	1,56
154	21,8	3,08	39,56	46,19	3,78	31,96	6,54	29,19	48,96	0,60	1,68

depth (cm)	age (ka)	clays (%)	cohesive silts (%)	non cohesive silts (%)	sand (%)	coarse mode (μm)	fine mode (μm)	coarse mode (%)	fine mode (%)	coarse/fine	fine/coarse
155	22,0	3,37	39,58	45,80	3,95	32,70	6,26	28,97	48,74	0,59	1,68
156	22,1	3,24	41,80	44,80	2,74	29,55	6,71	28,08	51,71	0,54	1,84
157	22,3	3,44	42,08	44,27	2,89	29,95	6,44	27,78	51,80	0,54	1,86
158	22,4	3,26	43,75	42,68	2,86	30,00	6,74	26,42	53,94	0,49	2,04
159	22,6	3,77	43,21	42,58	3,21	30,37	6,15	26,55	52,73	0,50	1,99
160	22,7	2,93	41,97	43,43	3,99	28,92	7,07	26,72	52,11	0,51	1,95
161	22,9	3,70	44,83	41,45	2,72	30,00	6,40	25,60	54,83	0,47	2,14
162	23,0	4,04	43,69	41,82	3,28	31,32	5,97	26,01	53,02	0,49	2,04
163	23,2	3,67	43,99	41,42	3,59	30,94	6,18	25,55	53,55	0,48	2,10
164	23,3	3,65	44,42	41,60	2,99	30,71	6,27	25,66	54,14	0,47	2,11
165	23,5	3,45	42,84	42,79	3,48	31,16	6,42	26,47	52,53	0,50	1,98
166	23,6	3,48	42,85	43,28	2,99	29,82	6,53	26,89	52,70	0,51	1,96
167	23,8	2,86	41,08	44,16	4,20	31,18	7,10	27,24	51,07	0,53	1,87
168	24,0	2,62	42,14	44,21	3,23	31,50	7,46	27,20	52,71	0,52	1,94
169	24,1	3,15	42,05	44,10	3,20	32,26	6,68	27,39	51,84	0,53	1,89
170	24,3	3,28	43,60	43,42	2,37	30,00	6,49	27,10	53,54	0,51	1,98
171	24,4	1,97	39,12	47,02	3,69	30,00	8,98	28,92	50,28	0,58	1,74
172	24,6	3,25	42,67	43,87	2,82	32,27	6,49	27,34	52,39	0,52	1,92
173	24,7	3,11	41,58	44,85	2,98	32,02	6,68	28,02	51,35	0,55	1,83
177	25,2	3,43	39,33	47,08	2,82	33,05	6,50	29,87	48,67	0,61	1,63
178	25,3	3,43	38,53	47,59	3,03	34,62	6,42	30,12	47,62	0,63	1,58
181	25,6	3,51	36,68	48,38	3,95	36,15	6,26	30,64	45,31	0,68	1,48
182	25,7	2,82	38,37	46,59	4,48	34,89	7,14	29,05	47,86	0,61	1,65

Annex 16: Sr and Nd isotopic data from the clay size fraction from core MD07-3076Q. 2σ correspond to the internal error.

depth (cm)	age (ka)	$^{143}Nd/^{144}Nd$	$2\sigma (x10^{-6})$	ε_{Nd}	$^{87}Sr/^{86}Sr$	$2\sigma (x10^{-6})$
4	1,4	0,512280	4	-7,0	0,711143	10
7	1,8	0,512264	9	-7,3	0,710930	8
9	2,1	0,512274	6	-7,1	0,711250	10
12	2,5	0,512278	5	-7,0	0,711180	10
16	3,2	0,512266	11	-7,3	0,710910	9
18	3,7	0,512279	5	-7,0	0,710840	9
20	4,1	0,512266	6	-7,3		
22	4,5	0,512277	5	-7,0	0,710916	11
23	4,7				0,711400	11
26	5,3	0,512274	10	-7,1	0,711090	8
32	6,4	0,512297	9	-6,6	0,711300	9
37	7,2	0,512278	5	-7,0	0,711287	10
39	7,7	0,512296	5	-6,7	0,711600	10
40	7,9	0,512276	5	-7,1	0,711863	10
42	8,3	0,512290	6	-6,8	0,711420	9
45	9,1	0,512324	6	-6,1	0,711310	9
48	9,6	0,512283	4	-6,9	0,710651	10
51	10,0	0,512295	6	-6,7	0,710814	15
54	10,5	0,512286	7	-6,9	0,710660	10
57	10,9	0,512282	5	-6,9		
61	11,4	0,512282	6	-6,9	0,710770	11
62	11,5	0,512283	5	-6,9	0,711048	10
65	11,9	0,512293	4	-6,7	0,710966	7
68	12,3	0,512292	6	-6,8	0,711240	9
71	12,7	0,512302	7	-6,5	0,711670	12
74	13,0	0,512309	5	-6,4		
75	13,1	0,512340	4	-5,8	0,711167	11
80	13,6	0,512322	4	-6,2	0,710987	10
87	14,3	0,512325	6	-6,1	0,710880	10
92	14,7	0,512352	6	-5,6	0,711540	11
96	14,9	0,512352	5	-5,6	0,711493	10
101	15,5	0,512369	6	-5,3	0,711706	10
107	16,3	0,512375	5	-5,1	0,711535	9
112	17,0	0,512363	5	-5,4	0,711769	10
121	18,0	0,512381	5	-5,0		
130	18,8	0,512382	5	-5,0		
138	19,5	0,512373	5	-5,2		
149	21,1	0,512365	4	-5,3	0,711683	11
155	22,0	0,512362	6	-5,4	0,711510	10
160	22,7	0,512384	5	-5,0	0,711400	11
167	23,8	0,512394	5	-4,8	0,711323	12
173	24,7	0,512394	4	-4,8	0,711286	11
182	25,7	0,512394	5	-4,8	0,711883	10
196	27,3	0,512384	4	-5,0		
214	29,0	0,512360	4	-5,4		

Annex 17: Sr and Nd isotopic data from the 2-20μm grain size fraction from core MD07-3076Q. 2σ correspond to the internal error.

depth	age	$^{143}Nd/^{144}Nd$	$2\sigma(x10^{-6})$	ε_{Nd}	$^{87}Sr/^{86}Sr$	$2\sigma(x10^{-6})$
4	1,4	0,512404	7	-4,6	0,707996	9
7	1,8	0,512390	9	-4,8	0,708023	11
9	2,1	0,512401	7	-4,6	0,708027	8
12	2,5	0,512405	4	-4,5	0,708174	8
16	3,2	0,512376	13	-5,1	0,708174	9
37	7,2	0,512365	4	-5,3	0,708431	5
42	8,3	0,512407	9	-4,5	0,708430	11
48	9,6	0,512424	5	-4,2	0,707920	9
51	10,0	0,512419	6	-4,3	0,707880	9
54	10,5	0,512395	6	-4,7	0,707870	12
57	10,9		0		0,707797	5
61	11,4		0		0,708000	9
65	11,9	0,512390	7	-4,8	0,708190	9
74	13,0	0,512370	6	-5,2	0,708150	9
74	13,0	0,512407	8	-4,5	0,707662	30
75	13,1	0,512393	5	-4,8	0,708160	9
80	13,6	0,512403	6	-4,6	0,708010	10
87	14,3	0,512417	7	-4,3	0,707900	10
96	14,9	0,512424	7	-4,2	0,707730	10
107	16,3	0,512396	6	-4,7	0,708040	9
112	17,0	0,512388	6	-4,9	0,708000	8
120	17,9	0,512379	6	-5,1	0,707918	8
121	18,0	0,512385	5	-4,9	0,707975	5
122	18,1	0,512355	6	-5,5	0,708052	11
130	18,8	0,512413	6	-4,4	0,708370	10
138	19,5	0,512420	5	-4,2	0,707710	10
149	21,1	0,512437	5	-3,9	0,707890	8
155	22,0	0,512409	6	-4,5	0,707850	9
160	22,7	0,512377	6	-5,1	0,707930	11
167	23,8	0,512435	5	-4,0	0,708240	13
173	24,7	0,512430	6	-4,1	0,708110	9
182	25,7		0		0,707816	5
196	27,3	0,512401	6	-4,6	0,707607	8

Annex 18: Sr and Nd isotopic data from the 20-32/40μm grain size fraction from core MD07-3076Q. 2σ correspond to the internal error.

depth (cm)	age (ka)	$^{143}Nd/^{144}Nd$	$2\sigma(x10^{-6})$	ε_{Nd}	$^{87}Sr/^{86}Sr$	$2\sigma(x10^{-6})$
1	1,0				0,707928	8
5	1,5	0,512378	12	-5,07	0,709799	5
7	1,8	0,512490	4	-2,89		
9	2,1	0,512452	7	-3,63	0,709409	10
13	2,7	0,512368	14	-5,27	0,709893	4
15	3,0				0,709394	14
17	3,4	0,512377	16	-5,09		
21	4,3	0,512388	9	-4,88	0,709838	5
22	4,5	0,512348	7	-5,66	0,710234	5
23	4,7	0,512454	6	-3,59	0,708831	12
27	5,5	0,512368	6	-5,27		
32	6,4	0,512464	6	-3,39	0,708972	14
37	7,2	0,512384	5	-4,95	0,709614	5
39	7,7				0,708981	15
42	8,3	0,512371	7	-5,21	0,710158	4
45	9,1				0,708257	9
47	9,4	0,512429	5	-4,07	0,70892	5
51	10,0	0,512453	13	-3,61	0,708365	9
55	10,7	0,512442	12	-3,82	0,708616	8
57	10,9	0,512387	6	-4,90	0,709192	5
61	11,4	0,512403	23	-4,58	0,708783	13
61	11,4	0,512440	7	-3,86		
63	11,6				0,709392	5
65	11,9	0,512421	6	-4,23	0,709592	4
67	12,2	0,512416	19	-4,33	0,708802	10
67	12,2	0,512508	30	-2,54		
71	12,7	0,512538	6	-1,95	0,707945	5
73	12,9				0,709932	6
75	13,1	0,512421	7	-4,23	0,710185	5
81	13,7	0,512425	5	-4,15	0,709362	5
87	14,3				0,709334	9
91	14,7	0,512452	5	-3,62	0,709046	5
97	15,0				0,709254	5
101	15,5	0,512491	13	-2,86	0,708801	7
101	15,5	0,512514	40	-2,42		
107	16,3	0,512518	5	-2,34	0,709632	5
117	17,6	0,512489	5	-2,91	0,707884	7
120	17,9	0,512479	5	-3,10	0,709324	6
121	18,0	0,512567	9	-1,38	0,708447	5
122	18,1	0,512454	5	-3,59	0,708526	6
122	18,1	0,512446	7	-3,75		
131	18,9	0,512465	5	-3,37	0,70886	8
137	19,4	0,512488	6	-2,93	0,708856	9
144	20,4	0,512472	4	-3,24	0,709198	6
145	20,5	0,512510	4	-2,50	0,708912	9
149	21,1	0,512488	4	-2,93	0,709277	7
153	21,7	0,512456	5	-3,55	0,708541	8
153	21,7	0,512452	5	-3,63		0

depth (cm)	age (ka)	$^{143}Nd/^{144}Nd$	2σ ($x10^{-6}$)	ε_{Nd}	$^{87}Sr/^{86}Sr$	2σ ($x10^{-6}$)
155	22,0	0,512510	6	-2,50	0,708515	10
160	22,7	0,512528	5	-2,15	0,708235	5
167	23,8	0,512433	5	-4,00	0,707873	6
173	24,7				0,707796	5
182	25,7	0,512533	5	-2,05	0,708965	5
196	27,3	0,512510	8	-2,49	0,708907	5
213	29,0	0,512433	5	-4,00	0,709026	8

Annex 19: Pb isotopic data from the clay size fraction from core MD07-3076Q. 2σ correspond to the internal error.

depth	age	$^{206}Pb/^{204}Pb$	2σ (x10^{-4})	$^{207}Pb/^{204}Pb$	2σ (x10^{-4})	$^{208}Pb/^{204}Pb$	2σ (x10^{-4})	$^{207}Pb/^{206}Pb$	2σ (x10^{-5})	$^{208}Pb/^{206}Pb$	2σ (x10^{-6})
4	1,4	18,725	3	15,656	5	38,754	6	0,836	2	2,070	9
7	1,8	18,740	3	15,662	7	38,782	8	0,836	3	2,069	9
9	2,1	18,729	3	15,659	6	38,767	7	0,836	3	2,070	9
12	2,5	18,710	3	15,654	5	38,729	6	0,837	2	2,070	9
16	3,2	18,710	3	15,656	6	38,748	8	0,837	2	2,071	9
18	3,7	18,731	4	15,657	7	38,760	10	0,836	3	2,069	9
22	4,5	18,745	3	15,648	5	38,771	6	0,835	2	2,068	13
23	4,7	18,755	3	15,658	5	38,812	6	0,835	2	2,069	13
26	5,3	18,734	3	15,654	8	38,789	7	0,836	4	2,070	14
32	6,4	18,726	4	15,651	8	38,778	8	0,836	4	2,071	15
37	7,2	18,759	3	15,649	5	38,794	6	0,834	3	2,068	12
39	7,7	18,770	3	15,654	6	38,829	8	0,834	2	2,069	17
40	7,9	18,742	3	15,643	5	38,767	7	0,835	2	2,068	12
42	8,3	18,763	4	15,653	6	38,815	8	0,834	3	2,069	16
45	9,1	18,767	3	15,655	7	38,822	9	0,834	3	2,069	19
48	9,6	18,760	3	15,650	5	38,790	6	0,834	2	2,068	11
51	10,0	18,756	3	15,655	6	38,808	8	0,835	3	2,069	17
54	10,5	18,756	3	15,654	6	38,796	8	0,835	2	2,068	15
57	10,9	18,744	8	15,656	10	38,799	17	0,835	3	2,070	18
61	11,4	18,755	3	15,657	6	38,812	7	0,835	2	2,069	15
62	11,5	18,768	3	15,648	5	38,803	7	0,834	2	2,067	13
65	11,9	18,761	3	15,647	5	38,789	6	0,834	2	2,067	13
68	12,3	18,764	4	15,649	7	38,807	8	0,834	3	2,068	18
71	12,7	18,776	3	15,656	6	38,837	8	0,834	3	2,068	18
74	13,0	18,765	8	15,653	9	38,807	17	0,834	3	2,068	24
75	13,1	18,765	3	15,645	5	38,788	8	0,834	2	2,067	19
80	13,6	18,737	3	15,642	5	38,753	7	0,835	2	2,068	12
87	14,3	18,745	5	15,653	7	38,794	13	0,835	3	2,070	28
92	14,7	18,759	3	15,641	5	38,780	6	0,834	2	2,067	11
96	14,9	18,765	3	15,643	5	38,791	7	0,834	2	2,067	12
101	15,5	18,757	3	15,636	8	38,765	7	0,834	4	2,067	10
107	16,3	18,752	3	15,635	7	38,749	7	0,834	3	2,066	12

depth	age	$^{206}Pb/^{204}Pb$	2σ ($x10^{-4}$)	$^{207}Pb/^{204}Pb$	2σ ($x10^{-4}$)	$^{208}Pb/^{204}Pb$	2σ ($x10^{-4}$)	$^{207}Pb/^{206}Pb$	2σ ($x10^{-5}$)	$^{208}Pb/^{206}Pb$	2σ ($x10^{-6}$)
112	17,0	18,755	3	15,641	7	38,764	7	0,834	4	2,067	11
116	17,5	18,760	5	15,647	8	38,790	15	0,834	3	2,068	37
120	17,9	18,753	3	15,646	6	38,780	7	0,834	3	2,068	14
121	18,0	18,751	3	15,635	7	38,745	6	0,834	4	2,066	13
130	18,8	18,743	3	15,641	7	38,748	6	0,834	3	2,067	11
138	19,5	18,754	3	15,638	7	38,753	7	0,834	3	2,066	14
149	21,1	18,744	4	15,638	7	38,751	8	0,834	3	2,067	11
155	22,0	18,744	6	15,633	10	38,743	21	0,834	4	2,067	54
160	22,7	18,740	3	15,635	7	38,740	7	0,834	3	2,067	11
167	23,8	18,747	4	15,638	8	38,747	7	0,834	4	2,067	13
173	24,7	18,742	3	15,636	8	38,733	6	0,834	4	2,067	13
182	25,7	18,718	3	15,630	7	38,697	6	0,835	3	2,067	12
196	27,3	18,732	9	15,644	10	38,752	19	0,835	3	2,069	25
214	29,0	18,759	9	15,647	11	38,782	19	0,834	4	2,067	24

Annex 20: Pb isotopic data of the cohesive silt mode fraction from core MD07-3076Q. 2σ correspond to the internal error.

depth	age	$^{206}Pb/^{204}Pb$	$2\sigma(x10^{-4})$	$^{207}Pb/^{204}Pb$	$2\sigma(x10^{-4})$	$^{208}Pb/^{204}Pb$	$2\sigma(x10^{-4})$	$^{207}Pb/^{206}Pb$	$2\sigma(x10^{-5})$	$^{208}Pb/^{206}Pb$	$2\sigma(x10^{-6})$
4	1,4	17,978	4	15,602	7	37,907	10	0,868	3	2,108	16
7	1,8	17,992	4	15,599	6	37,913	9	0,867	2	2,107	17
9	2,1	18,294	5	15,619	7	38,249	12	0,854	3	2,091	18
12	2,5	18,275	5	15,622	8	38,235	12	0,855	3	2,092	20
16	3,2	18,293	9	15,619	10	38,253	19	0,854	3	2,091	20
37	7,2	18,164	7	15,608	9	38,100	18	0,859	4	2,098	37
40	7,9	17,977	5	15,597	7	37,895	12	0,868	3	2,108	20
42	8,3	18,193	4	15,612	7	38,138	9	0,858	3	2,096	18
48	9,6	18,011	3	15,600	5	37,935	7	0,866	2	2,106	14
51	10,0	17,970	3	15,596	6	37,883	8	0,868	3	2,108	19
54	10,5	18,248	7	15,609	8	38,194	15	0,855	3	2,093	24
57	10,9	17,982	6	15,597	9	37,898	16	0,867	3	2,108	33
65	11,9	18,111	5	15,605	8	38,043	15	0,862	3	2,100	39
74	13,0	18,127	3	15,609	5	38,065	7	0,861	2	2,100	15
74	13,0	18,231	5	15,607	9	38,162	13	0,856	4	2,093	24
75	13,1	18,374	3	15,620	7	38,330	8	0,850	3	2,086	15
80	13,6	18,322	3	15,619	6	38,278	8	0,852	3	2,089	15
87	14,3	17,994	3	15,598	6	37,913	7	0,867	3	2,107	14
96	14,9	18,387	3	15,621	7	38,346	7	0,850	3	2,085	14
107	16,3	18,053	3	15,605	6	37,986	8	0,864	3	2,104	18
112	17,0	18,195	3	15,601	7	38,111	8	0,857	3	2,095	18
120	17,9	18,483	10	15,618	12	38,432	21	0,845	4	2,079	20
121	18,0	18,462	6	15,627	8	38,428	12	0,846	3	2,081	17
122	18,1	18,412	5	15,621	8	38,369	12	0,848	3	2,084	20
130	18,8	18,367	3	15,618	6	38,310	8	0,850	3	2,086	18
138	19,5	18,346	3	15,619	6	38,305	7	0,851	3	2,088	14
149	21,1	18,424	4	15,620	6	38,382	9	0,848	3	2,083	18
155	22,0	18,438	3	15,622	6	38,401	7	0,847	3	2,083	15
160	22,7	18,135	3	15,607	5	38,071	7	0,861	3	2,099	17
167	23,8	18,301	3	15,618	5	38,258	7	0,853	3	2,090	15
173	24,7	18,400	3	15,619	6	38,351	8	0,849	3	2,084	20
182	25,7	18,368	5	15,621	8	38,319	11	0,850	3	2,086	18
196	27,3	18,103	6	15,603	10	38,029	13	0,862	4	2,101	22
214	29,0	18,434	6	15,619	10	38,385	15	0,847	4	2,082	26

Annex 21: Pbisotopic data of the sortable silt mode fraction from core MD07-3076Q. 2σ correspond to the internal error.

depth	age	$^{206}Pb/^{204}Pb$	$2\sigma(x10^{-4})$	$^{207}Pb/^{204}Pb$	$2\sigma(x10^{-4})$	$^{208}Pb/^{204}Pb$	$2\sigma(x10^{-4})$	$^{207}Pb/^{206}Pb$	$2\sigma(x10^{-5})$	$^{208}Pb/^{206}Pb$	$2\sigma(x10^{-6})$
1	1,0	18,082	4	15,608	6	38,002	8	0,863	3	2,102	15
5	1,5	17,971	5	15,593	8	37,876	12	0,868	3	2,108	26
7	1,8	18,026	5	15,609	9	37,970	12	0,866	4	2,106	25
9	2,1	18,108	7	15,602	9	38,031	14	0,862	4	2,100	22
13	2,7	18,042	3	15,606	6	37,976	7	0,865	4	2,105	29
15	3,0	18,371	7	15,623	10	38,345	15	0,850	4	2,087	24
17	3,4	18,367	6	15,623	8	38,318	14	0,851	3	2,086	26
21	4,3	17,993	5	15,595	8	37,903	13	0,867	3	2,107	27
22	4,5	17,970	3	15,600	5	37,893	6	0,868	2	2,109	11
23	4,7	17,989	5	15,599	9	37,911	13	0,867	4	2,107	26
27	5,5	17,979	5	15,597	8	37,901	12	0,867	4	2,108	25
32	6,4	17,983	5	15,598	8	37,906	12	0,867	3	2,108	26
37	7,2	18,001	5	15,594	9	37,905	17	0,866	3	2,106	39
39	7,7	18,119	14	15,598	13	38,035	31	0,861	3	2,099	47
42	8,3	17,992	3	15,593	6	37,895	9	0,867	2	2,106	23
45	9,1	18,101	3	15,607	7	38,029	8	0,862	3	2,101	16
47	9,4	17,996	4	15,598	8	37,916	11	0,867	3	2,107	24
51	10,0	17,975	4	15,592	7	37,881	8	0,867	4	2,107	19
55	10,7	18,056	3	15,602	6	37,977	7	0,864	3	2,103	16
57	10,9	17,976	5	15,605	8	37,913	14	0,868	3	2,109	30
61	11,4	18,054	3	15,601	6	37,970	8	0,864	3	2,103	18
63	11,6	17,975	3	15,602	7	37,903	7	0,868	3	2,109	20
65	11,9	17,983	4	15,603	7	37,913	12	0,868	3	2,108	23
67	12,2	18,238	3	15,616	6	38,156	8	0,856	3	2,092	16
71	12,7	18,121	3	15,604	6	38,021	8	0,861	3	2,098	17
73	12,9	17,986	4	15,594	8	37,890	12	0,867	3	2,107	23
75	13,1	18,091	5	15,612	8	38,045	13	0,863	3	2,103	29
81	13,7	17,990	5	15,603	8	37,917	12	0,867	3	2,108	26
87	14,3	18,010	3	15,600	6	37,923	8	0,866	2	2,106	15
91	14,7	18,065	6	15,596	8	37,972	14	0,863	3	2,102	27
97	15,0	17,988	4	15,594	7	37,897	12	0,867	3	2,107	27
101	15,5	18,110	3	15,607	5	38,038	7	0,862	2	2,100	13

depth	age	$^{206}Pb/^{204}Pb$	2σ ($x10^{-4}$)	$^{207}Pb/^{204}Pb$	2σ ($x10^{-4}$)	$^{208}Pb/^{204}Pb$	2σ ($x10^{-4}$)	$^{207}Pb/^{206}Pb$	2σ ($x10^{-5}$)	$^{208}Pb/^{206}Pb$	2σ ($x10^{-6}$)
107	16,3	18,090	3	15,607	7	38,002	8	0,863	3	2,101	18
117	17,6	18,194	4	15,611	7	38,103	9	0,858	3	2,094	20
120	17,9	18,178	4	15,612	7	38,126	9	0,859	3	2,097	20
121	18,0	18,042	3	15,596	6	37,945	9	0,864	3	2,103	15
122	18,1	18,160	4	15,608	6	38,081	8	0,859	2	2,097	13
131	18,9	18,060	3	15,604	8	37,981	7	0,864	4	2,103	13
137	19,4	18,034	3	15,602	7	37,956	7	0,865	3	2,105	14
144	20,4	18,118	3	15,605	6	38,042	9	0,861	3	2,100	25
145	20,5	18,130	3	15,608	7	38,054	8	0,861	3	2,099	17
149	21,1	18,037	3	15,601	7	37,952	7	0,865	4	2,104	16
153	21,7	18,296	3	15,617	6	38,268	7	0,854	3	2,092	15
155	22,0	18,069	4	15,604	7	37,995	10	0,864	3	2,103	21
160	22,7	18,050	3	15,603	5	37,968	6	0,864	3	2,104	10
167	23,8	18,126	3	15,604	5	38,040	6	0,861	2	2,099	9
173	24,7	18,138	3	15,602	5	38,037	7	0,860	2	2,097	16
182	25,7	18,007	3	15,601	6	37,928	7	0,866	2	2,106	12
196	27,3	17,980	3	15,599	6	37,898	8	0,868	4	2,108	27
213	29,0	18,447	4	15,623	6	38,430	10	0,847	3	2,083	22

Annex 22: Clay mineralogical composition of detrital sediment from site MD12-3396Q.

depth (cm)	smectite (%)	illite (%)	chlorite and kaolinite (%)	5Å/10Å illite	amphibole/quartz
200	53	25	22	0,141	0,47
202	61	18	22	0,337	-
204	65	20	15	-	0,47
206	61	21	18	0,073	0,25
208	76	13	12	0,240	-
210	70	15	15	-	0,26
212	79	10	11	0,083	0,07
214	64	22	14	0,569	-
216	72	13	15	0,187	-
218	73	14	14	0,371	0,50
220	74	11	15	-	0,39
222	69	18	14	-	0,00
224	72	16	12	-	0,00
226	75	10	15	0,531	0,67
228	65	18	17	-	0,49
230	77	10	14	0,214	-
232	82	8	9	0,422	0,08
234	71	16	13	0,123	0,72
236	79	11	11	0,039	0,22
238	78	10	12	-	-
240	71	14	16	0,242	0,05
242	73	12	15	0,310	0,43
244	84	9	8	0,306	0,35
246	75	11	14	-	0,72
248	67	15	17	0,289	0,36
250	85	5	9	-	0,38
252	78	10	12	0,056	-
254	82	7	11	0,064	0,10
256	75	13	12	0,002	1,25
258	75	11	14	-	0,87
260	76	11	13	0,196	0,59
262	83	7	9	-	0,69
264	74	11	14	0,293	0,38
266	72	17	11	0,150	0,50
268	71	13	16	0,286	0,61
270	74	12	15	0,263	-
272	66	15	18	0,231	0,30
274	75	10	15	0,162	0,36
276	74	10	16	-	0,37
278	73	12	16	-	0,42
280	73	14	13	-	1,27
282	71	13	16	0,126	0,62
284	71	14	16	-	-
286	71	12	17	-	0,23
288	64	18	18	0,306	-
290	74	11	16	0,112	0,45
292	68	17	15	0,238	-
294	73	14	13	0,059	0,54
296	65	18	17	-	0,31

298	83	8	9	0,129	-
300	76	11	14	0,205	-
302	73	11	16	0,138	0,36
304	75	13	12	0,104	0,87
306	74	12	13	0,183	0,43
308	80	9	10	0,227	1,56
310	75	11	14	-	0,81
312	86	6	7	0,201	1,52
314	74	13	13	0,040	1,40
316	73	13	14	0,050	0,98
318	76	11	13	0,108	1,91
320	75	12	13	0,193	1,28
322	71	12	17	0,116	-
324	77	11	12	0,121	0,95
326	72	13	14	0,038	1,39
328	79	9	12	0,100	-
330	66	14	19	0,044	0,84
332	67	17	16	0,049	-
334	73	14	13	0,084	3,08
336	72	13	15	0,109	0,94
338	72	13	15	0,054	1,36
340	71	15	14	0,168	0,89
342	71	13	16	0,172	0,73
344	83	7	10	-	0,68
346	70	15	15	0,242	0,59
348	77	11	12	0,096	1,14
350	73	12	15	0,168	0,39
352	77	12	12	0,151	0,80
354	66	15	19	0,151	0,48
356	73	14	13	0,302	0,66
358	79	9	12	0,166	0,81
360	77	9	13	0,083	-
362	71	14	15	0,129	0,83
364	75	9	15	0,129	0,51
366	75	10	15	0,146	0,25
368	78	9	13	0,229	-
370	70	13	18	-	0,62
372	79	8	13	0,055	-
374	81	7	11	0,121	-
376	78	12	11	0,217	-
378	75	12	13	0,260	0,82
380	77	10	13	0,115	0,65
382	73	10	16	0,080	-
384	71	12	18	0,376	0,48
386	79	11	11	0,036	-
388	67	15	18	0,016	0,85
390	75	10	15	0,174	1,21
392	67	16	17	0,204	0,67
394	71	12	16	0,097	1,93
396	71	15	14	0,195	-

398	69	16	15	-	1,01
400	70	13	18	0,119	0,68
402	68	14	18	0,179	0,66
404	69	14	17	-	0,94
406	67	14	19	0,109	-
408	60	17	23	0,184	0,77
410	66	15	19	0,023	0,75
412	63	18	19	0,129	1,29
414	63	17	20	0,146	-
416	62	20	17	0,148	1,13
418	65	18	18	0,063	0,57
420	65	18	17	0,082	-
422	70	17	13	0,078	0,87
424	62	20	18	0,131	0,70
426	68	17	15	0,126	2,14
428	66	18	17	0,072	1,16
430	65	18	17	0,177	1,35
432	69	14	17	0,096	1,11
434	64	19	16	0,056	1,56
436	70	15	15	0,096	1,03
438	64	21	15	0,021	2,45
440	68	17	15	0,076	-
442	63	19	18	0,185	0,58
444	75	13	12	0,066	-
446	60	24	17	0,080	0,94
448	67	17	17	0,073	0,91
450	61	19	19	0,119	-
454	54	25	20	0,054	1,30
458	64	17	19	-	1,56
462	62	20	18	0,006	1,96
466	55	24	21	-	1,05
470	54	26	20	0,106	1,21
474	57	22	21	0,127	0,85
478	68	15	17	0,117	0,98
482	62	19	19	0,203	0,47
486	73	10	16	-	0,78
490	74	10	16	-	-
494	75	9	15	-	-
498	73	10	17	0,074	-
502	79	9	11	0,139	0,63
506	69	12	19	0,230	-
510	76	10	14	0,005	0,20
514	70	14	17	0,137	0,08
518	73	11	16	0,236	-
522	71	12	17	0,014	0,81
526	74	11	15	0,217	0,21
530	76	10	14	0,222	-
534	78	10	12	0,020	0,78
538	74	10	16	0,100	0,28
542	82	6	12	0,128	-

546	77	10	13	0,512	5,05
550	76	11	13	0,145	-

Annex 23: Isotopic composition of detrital sediment from site MD12-3396Q.

depth (cm)	143Nd/144Nd	2σ	ε_{Nd}	87Sr/86Sr	2σ
214	0,512338	0,000007	-5,85	-	-
230	0,512360	0,000005	-5,42	0,710425	0,000013
240	0,512383	0,000005	-4,97	0,710416	0,000014
248	0,512374	0,000005	-5,15	0,710089	0,000009
260	0,512361	0,000005	-5,40	0,710775	0,000006
270	0,512344	0,000011	-5,73	0,710392	0,000010
290	0,512333	0,000006	-5,95	0,711252	0,000009
302	0,512339	0,000008	-5,84	0,711383	0,000009
314	0,512204	0,000008	-8,46	0,712735	0,000011
320	0,512253	0,000006	-7,51	0,712787	0,000009
338	0,512249	0,000008	-7,58	0,711559	0,000009
350	0,512359	0,000006	-5,44	-	-
370	0,512406	0,000009	-4,52	0,709215	0,000008
386	0,512312	0,000012	-6,37	0,710098	0,000010
416	0,512217	0,000007	-8,21	0,713699	0,000010
426	0,512168	0,000009	-9,17	0,713855	0,000009
450	0,512202	0,000008	-8,50	0,713698	0,000009
470	0,512122	0,000013	-10,07	0,715062	0,000009
490	0,512381	0,000008	-5,02	0,715052	0,000009
498	0,512388	0,000008	-4,88	0,709510	0,000009

Annex 24: Trace and rare earth elements of detrital sediment from site MD12-3396Q.

depth (cm)	214	230	240	248	260	270	290	302	314	320	338
Li	16,7	15,6	17,2	19,5	19,8	18,4	18,7	22,9	24,4	23,1	23,6
Be	1,1	1,0	1,0	1,1	1,4	1,2	1,1	1,2	1,3	1,3	1,4
Sc	18,2	14,3	15,9	17,9	17,6	16,4	16,4	19,1	19,3	19,6	19,9
Ti	5357,6	4514,7	5851,8	7207,0	6865,7	6051,4	3959,0	7282,6	8314,5	7831,4	8880,5
V	73,2	62,3	77,6	102,8	95,3	87,4	82,1	106,9	126,5	122,2	132,3
Cr	76,3	51,6	65,1	78,6	71,7	75,1	64,6	70,9	80,3	76,5	86,9
Co	10,0	10,2	9,9	12,0	13,0	12,6	12,7	13,9	14,9	15,1	15,2
Ni	44,7	29,2	31,6	36,0	36,7	46,2	40,6	43,0	47,8	41,1	49,1
Cu	24,5	24,1	25,1	31,8	28,8	27,1	21,6	24,7	41,7	40,6	40,4
Zn	108,5	74,5	81,7	96,7	93,2	93,1	76,4	90,8	100,4	91,0	99,0
Ga	12,6	10,6	12,5	14,0	14,0	12,6	12,3	14,8	15,5	15,3	15,8
Sr	83,0	72,1	87,4	110,9	95,6	92,5	84,2	104,2	119,3	107,4	125,9
Rb	38,1	33,3	40,6	48,7	48,5	42,9	43,5	56,6	67,1	64,4	65,8
Y	6,6	5,6	7,0	8,3	8,1	7,2	6,9	8,7	9,7	9,0	9,5
Zr	195,2	152,5	203,7	238,2	220,3	193,2	174,5	226,1	258,9	233,5	243,8
Nb	22,7	19,1	26,2	31,0	28,7	24,8	15,0	28,6	31,6	29,3	30,1
Mo	4,6	0,9	3,4	4,8	2,7	4,2	2,5	3,5	4,4	2,6	5,8
In	0,3	0,3	0,3	0,4	0,4	0,3	0,3	0,5	0,5	0,5	0,4
Sn	1,7	1,5	2,0	2,7	2,5	2,1	1,3	2,8	3,0	2,6	2,9
Sb	0,9	0,8	1,0	1,1	0,8	0,7	0,5	1,0	1,6	0,8	1,2
Cs	2,1	1,9	2,2	2,7	2,8	2,3	2,4	3,3	3,9	3,8	4,1
Ba	278,5	265,7	265,4	346,9	317,4	289,5	263,7	458,5	407,7	350,8	342,7
La	8,3	7,1	8,7	10,0	9,8	9,1	8,6	10,5	11,4	10,5	10,7
Ce	15,4	13,6	16,4	19,1	18,8	17,3	16,2	20,2	21,7	20,0	20,4
Pr	1,8	1,6	1,9	2,2	2,1	2,0	1,9	2,3	2,5	2,3	2,3
Nd	6,4	5,6	6,9	8,0	7,9	7,3	6,8	8,5	9,1	8,4	8,5
Sm	1,3	1,1	1,4	1,7	1,6	1,4	1,4	1,7	1,9	1,7	1,8
Eu	0,4	0,3	0,4	0,5	0,5	0,5	0,4	0,6	0,6	0,6	0,7
Tb	0,2	0,2	0,2	0,3	0,3	0,2	0,2	0,3	0,3	0,3	0,3
Gd	1,2	1,1	1,3	1,6	1,5	1,4	1,2	1,6	1,8	1,7	1,7
Dy	1,2	1,1	1,3	1,6	1,5	1,4	1,3	1,7	1,8	1,7	1,8
Ho	0,2	0,2	0,3	0,3	0,3	0,3	0,3	0,3	0,4	0,3	0,4
Er	0,7	0,6	0,8	0,9	0,9	0,8	0,8	1,0	1,1	1,0	1,0
Tm	0,1	0,1	0,1	0,1	0,1	0,1	0,1	0,2	0,2	0,2	0,2
Yb	0,7	0,6	0,8	1,0	0,9	0,8	0,8	1,0	1,1	1,0	1,1
Lu	0,1	0,1	0,1	0,1	0,1	0,1	0,1	0,1	0,2	0,1	0,2
Hf	4,3	3,7	4,9	5,8	5,4	4,7	4,3	5,6	6,0	5,7	6,1
Ta	1,5	1,3	1,8	2,1	1,9	1,6	0,3	1,9	2,1	2,0	2,0
W	2,3	1,8	2,0	2,1	2,5	1,5	0,2	2,0	1,6	2,2	1,5
Re	0,0	0,0	0,0	0,0	0,0	0,0	0,0	0,0	0,0	0,0	0,0
Pb	3,8	3,6	4,4	5,0	4,9	4,1	3,7	5,3	5,9	5,6	5,8
Tl	0,2	0,2	0,2	0,3	0,3	0,3	0,3	0,3	0,4	0,3	0,4
Bi	0,1	0,3	0,1	0,2	0,1	0,1	0,1	0,1	0,1	0,1	0,1
Th	8,6	7,9	9,4	11,4	10,9	8,8	8,8	11,7	13,3	12,3	12,2
U	0,8	0,6	0,8	0,9	0,9	0,8	0,8	1,0	1,2	1,1	1,3

depth (cm)	350	370	386	416	426	450	470	490	498
Li	15,7	22,0	24,1	24,6	24,2	25,3	23,7	17,4	18,9
Be	0,9	1,5	1,5	1,6	1,4	1,6	1,4	1,2	1,4
Sc	14,5	19,6	20,0	18,4	18,4	18,2	17,2	15,4	15,4
Ti	6255,5	9303,4	9677,2	7879,9	7710,7	7735,2	6911,7	6448,1	6801,6
V	90,7	135,5	136,6	120,9	122,0	121,9	105,7	92,4	98,0
Cr	70,5	80,7	87,4	82,0	86,9	87,4	85,4	75,3	86,5
Co	10,6	16,0	16,6	14,3	14,7	14,8	14,0	11,6	12,3
Ni	44,1	48,4	50,0	40,4	46,6	47,6	46,2	38,1	45,1
Cu	30,1	42,4	42,4	44,2	38,4	40,3	33,6	31,2	32,6
Zn	69,4	98,6	107,8	97,5	98,1	96,2	94,9	84,5	85,3
Ga	10,9	15,9	16,8	16,5	16,1	16,9	15,6	13,2	13,9
Sr	83,2	132,4	141,5	114,3	117,8	128,5	119,2	100,6	102,1
Rb	41,4	58,3	66,7	74,3	74,1	77,6	73,4	47,2	49,4
Y	6,4	9,8	10,5	10,2	10,2	10,7	9,7	8,0	8,4
Zr	178,2	262,6	273,1	241,0	228,6	232,5	208,6	212,7	222,2
Nb	21,1	31,4	33,9	28,7	30,0	30,1	27,4	25,8	27,1
Mo	5,4	4,4	4,5	3,0	4,9	4,8	6,4	5,1	6,0
In	0,3	0,4	0,5	0,5	0,5	0,5	0,4	0,3	0,4
Sn	0,9	1,8	3,3	3,1	3,1	3,0	2,8	2,2	2,4
Sb	0,3	0,4	1,1	0,8	0,9	1,1	1,3	0,9	0,8
Cs	2,8	3,8	4,1	4,4	4,2	4,4	4,1	2,9	3,1
Ba	255,7	394,0	424,7	339,4	389,3	363,6	320,7	211,5	234,2
La	6,8	10,3	11,4	11,6	11,7	12,8	11,5	8,5	9,0
Ce	13,1	19,9	22,5	22,4	22,7	24,6	22,0	16,4	17,4
Pr	1,5	2,3	2,6	2,6	2,6	2,8	2,6	1,9	2,0
Nd	5,5	8,5	9,6	9,5	9,4	10,3	9,2	6,9	7,3
Sm	1,2	1,8	2,0	1,9	1,9	2,1	1,9	1,4	1,6
Eu	0,4	0,7	0,7	0,7	0,6	0,7	0,6	0,5	0,6
Tb	0,2	0,3	0,3	0,3	0,3	0,3	0,3	0,2	0,3
Gd	1,2	1,8	1,9	1,9	1,9	2,0	1,8	1,4	1,5
Dy	1,2	1,8	2,0	1,9	1,8	2,0	1,8	1,5	1,6
Ho	0,2	0,4	0,4	0,4	0,4	0,4	0,4	0,3	0,3
Er	0,7	1,1	1,1	1,1	1,1	1,2	1,0	0,9	0,9
Tm	0,1	0,2	0,2	0,2	0,2	0,2	0,2	0,1	0,1
Yb	0,7	1,1	1,2	1,2	1,1	1,2	1,1	0,9	1,0
Lu	0,1	0,2	0,2	0,2	0,2	0,2	0,2	0,1	0,1
Hf	4,4	6,5	6,7	6,0	5,5	5,8	5,2	5,2	5,5
Ta	1,3	2,1	2,2	1,9	2,0	2,0	1,8	1,7	1,8
W	0,9	1,4	1,4	1,4	1,3	1,2	1,2	1,2	1,4
Re	0,0	0,0	0,0	0,0	0,0	0,0	0,0	0,0	0,0
Pb	3,4	5,1	6,0	5,9	5,8	6,3	5,9	4,0	3,9
Tl	0,2	0,3	0,3	0,4	0,4	0,4	0,4	0,3	0,3
Bi	0,1	0,1	0,1	0,1	0,1	0,1	0,1	0,1	0,1
Th	7,5	10,3	11,7	13,4	12,7	13,3	13,2	8,0	8,6
U	0,9	1,3	1,4	1,4	1,3	1,3	1,3	1,2	1,3

	143Nd/144Nd	87Sr/86Sr
143Nd/144Nd	-	0,9076
87Sr/86Sr	0,9076	-
Rb/Sr	0,7758	0,8901
Sm/Nd	0,0224	0,0523
Ti/V	0,5952	0,5419
La/Nb	0,6397	0,7398
La/Hf	0,5268	0,6589
Th/Sc	0,6914	0,8008
Nb/Yb	0,5043	0,5475
Rb/Y	0,8804	0,8842
Rb/Nb	0,8163	0,8131
Rb/Ta	0,8019	0,7902
Rb/Zr	0,8444	0,868
Rb/Hf	0,9084	0,8948
Ba/Nb	0,0223	0,0137
Ba/Ta	0,0827	0,0614
Ba/Zr	0,0932	0,0641
Ba/Hf	0,0826	0,0576
Cs/Nb	0,5861	0,6019
Cs/Ta	0,5784	0,5956
Cs/Zr	0,6863	0,7047
Cs/Hf	0,7581	0,7365
Nd (ppm)	0,4688	0,3644
Sr (ppm)	0,2186	0,0641
∑REE (WRAS)	0,4079	0,2784
La/Yb (WRAS)	0,0011	0,0049
La/Nd (WRAS)	0,0008	0,0047
Dy/Yb (WRAS)	0,1697	0,3027
Nd/Yb (WRAS)	0,0036	0,0048

Annex 25: Correlation factor R2 between the isotopic composition and element ratios of sediment from site MD12-3396Q. The correlation is good to excellent between trace element ratios shown and the isotopic composition, while there is no correlation between rare earth element ratios and the isotopes. Interestingly, the sum of normalized rare earth elements present a relatively good correlation with the isotopes

Résumé

Cette thèse apporte de nouvelles perspectives sur la circulation profonde de l'Océan Austral et sur le cycle du CO2. Elle se base sur la signature géochimique et minéralogique de la fraction terrigène des sédiments récupérés dans le secteur Atlantique Sud (carotte MD07-3076Q) et Indien Sud (MD12-3396Q) de l'Océan Austral.

Grâce à une étude préliminaire rigoureuse des processus de transfert Continent-Océan permettant l'étude de la provenance des sédiments dans l'Océan Autral, il a été possible de démontrer la nécessité de travailler sur plusieurs fractions granulométriques dans l'Atlantique Sud pour pouvoir retracer efficacement les différentes masses d'eau. Une telle approche a permis : (1) l'identification de la provenance de différentes fractions granulométriques ; (2) l'assignation de chaque fraction granulométrique à une masse d'eau spécifique ; (3) la reconstruction de l'évolution passée des principales masses d'eau profondes ; (4) de reconstruire les changements paléoenvironnementaux en Amérique du Sud pendant l'Holocène.

Cette thèse a permis de faire la distinction entre les AABW et l'ACC (Courant Circumpolaire Antarctique, qui comprend la CDW) dans les deux secteurs étudiés de l'Océan Austral. Cela a rendu possible la quantification de la contribution relative à la sédimentation des principales masses d'eau dans chaque secteur (i.e. AABW, CDW, et NADW dans le secteur Atlantique Sud ; ACC et AABW dans le secteur Indien Sud). Grâce à cette distinction, il a été possible de fournir des évidences d'activités encore inconnues de l'AABW au court du temps, et d'étudier les interactions dynamiques entre les AABW et la CDW dans le secteur Atlantique Sud de l'Océan Austral. De plus, cette thèse démontre que les évènements d'Heinrich (HE) 1, 2, et 3 sont précédés par une modification de la circulation profonde de l'Océan Austral. Les données indiquent également que, même si aucun changement dans le CO_2 atmosphérique n'est observé pendant l'HE 2, la turbulence était plus forte pendant l'HE 2 que pendant l'HE 1. Cela suggère que les échanges entre l'océan profond et l'atmosphère pourraient avoir été coupés en raison de la présence d'une barrière dynamique/physique pendant la dernière période glaciaire. A la toute fin de cette dernière période glaciaire, nos données indiquent un « pulse » de la vitesse et de l'extension vers le Nord de la AABW dans le secteur Atlantique de l'Océan Austral. Ce « pulse » est concomitant de la première augmentation de la ventilation enregistrée dans la même carotte de sédiment et se termine avec le début du stadial d'Heinrich (HS) 1, une période d'augmentation du CO_2 atmosphérique. Ces observations suggèrent que cette rapide incursion de la AABW dans l'Océan Atlantique Sud serait responsable de la rupture de la barrière physique/dynamique séparant l'océan profond, riche en CO_2, et la surface, permettant ainsi l'échange entre ces eaux riches en CO_2 et l'atmosphère pendant l'HS 1, et donc l'augmentation du CO_2 atmosphérique pendant la dernière déglaciation.

Abstract

This PhD thesis provides new insights into both the deep Southern Ocean circulation and CO_2 cycle based on geochemical, radiogenic isotopes and clay mineralogical signatures of the terrigenous fractions transported by the main deep-water masses using sediment cores recovered in the South Atlantic sector (core MD07-3076Q, central South Atlantic) and in the South Indian sector (core MD12-3396Q) of the Southern Ocean. Thanks to a careful study of continent-ocean transfer processes enabling the study of the provenance of particles in the Southern Ocean, it was possible to demonstrate that working on distinct grain-size fractions in the South Atlantic Ocean is necessary to efficiently track different water masses. Such an approach successfully permits: (1) provenance identification of the various grain-size fractions (clay, cohesive silt and sortable silt); (2) an assignment of each grain-size fraction to a specific water-mass; (3) the reconstruction of the main deep water-mass pathways past changes, (4) to reconstruct paleoenvironmental changes over South America during the Holocene. In addition, this study successfully permits the distinction between the AABW and the ACC (that includes CDW) in both sectors of the Southern Ocean. This enabled the quantification of the relative contribution to sedimentation of all the main deep-water masses in each sector (i.e. AABW, CDW and NADW in the South Atlantic sector; ACC and AABW in the South Indian sector). Thanks to this distinction, it was possible to provide evidences of previously unknown AABW activities through time, and to study the dynamical interactions between the AABW and the LCDW in the South Atlantic sector of the Southern Ocean. Moreover, we show that Heinrich Events (HE) 1, 2 and 3 are preceded by a modification of the Southern Ocean overturning circulation. Our data also indicate that the turbulent mixing was stronger during HE 2 than during HE 1, even though HE 2 is muted in atmospheric CO_2 records. This suggests that the exchanges between the deep ocean and the atmosphere might have been disabled due to dynamical/physical barrier resulting from background conditions involved by low obliquity during the last glacial period. At the very end of this glacial period, our data indicate a substantial "pulse" of AABW speed and northern extent in the South Atlantic sector of the Southern Ocean. This "pulse" is concomitant with the first increase of the ventilation recorded in the same sediment core and ends with the beginning of the HS 1, a period of rising atmospheric CO_2. These observations suggest that this rapid incursion of AABW into the South Atlantic Ocean may be responsible of the breakdown of the physical/dynamical barrier between the deep CO_2-rich ocean and the surface, enabling the exchange between these CO_2-rich waters and the atmosphere during the HS 1, and thus, the rise of atmospheric CO_2 during the last deglaciation.